THE YOUNG LOCAL UNIVERSE

Sponsored by

- EUROPEAN RESEARCH
- TRAINING NETWORK

XXXIXth Rencontres de Moriond
XXIVth Moriond Astrophysics Meetings
La Thuile, Aosta Valley, March 21 – 28, 2004

The Young Local Universe
Series: Moriond Astrophysics Meetings

Thế Giới Publishers
Printed in Vietnam
GPXB: 3-1111/XB-QLXB (13-7-2005)
VN-TG-31111-1

ISBN

Proceedings of the XXXIXth RENCONTRES DE MORIOND

XXIVth Moriond Astrophysics Meetings

La Thuile, Aosta Valley, Italy March 21 - 28, 2004

THE YOUNG LOCAL UNIVERSE

edited by

Almas Chalabaev

Thierry Montmerle

Jean Trân Thanh Vân

THẾ GIỚI

PUBLISHERS

The Astrophysics Session of the XXXIXth Rencontres de Moriond

Was organized by

J. Trân Thanh Vân (Orsay)

Scientific Advisory Committee:

J. Alves (Garching)
D. Breitschwerdt (Vienna)
C. Cesarsky (Garching)
F. Combes (Paris)
Y. Fukui (Nagoya)
T. Heckman (Baltimore)
T. Henning (Heidelberg)
V. Icke (Leiden)
J. Knödlseder (Toulouse)
D. Kunth (Paris)
A. Maeder (Geneva)
F. Palla (Florence)
M. Tagger (Saclay)
H. Zinnecker (Potsdam)

Program Committee:

P. André (Saclay)
J. Bouvier (Grenoble)
A. Chalabaev (Grenoble)
D. Elbaz (Saclay)
D. Galli (Firenze)
B. Lefloch (Grenoble)
M. McMaughrean (Potsdam)
R. Neri
M. Sauvage (Saclay)
J. Tran Thanh Van (Orsay)

2004 RENCONTRES DE MORIOND

The XXXIXth Rencontres de Moriond were held in La Thuile, Vallée d'Aoste, Italie.

The first meeting took place at Moriond in the French Alps in 1966. There, experimental as well as theoretical physicists not only shared their scientific preoccupations, but also the household chores. The participants in the first meeting were mainly French physicists interested in electromagnetic interactions. In subsequent years, a session on high energy strong interactions was also added.

The main purpose of these meetings is to discuss recent developments in contemporary physics and also to promote effective collaboration between experimentalists and theorists in the field of elementary particle physics. By bringing together a relatively small number of participants, the meeting helps to develop better human relations as well as a more thorough and detailed discussion of the contributions.

This concern of research and experimentation of new channels of communication and dialogue which from the start animated the Moriond meetings, inspired us to organize a simultaneous meeting of biologists on Cell Differenciation (1980) and to create the Moriond Astrophysics Meeting (1981). In the same spirit, we have started a new series on Condensed Matter Physics in January 1994. Common meetings between biologists, astrophysicists, condensed matter physicists and high energy physicists are organized to study the implications of the advances of one field into the others. I hope that these conferences and lively discussions may give birth to new analytical methods or new mathematical languages.

At the XXXIXth Rencontres de Moriond in 2004, four Physics sessions, and one Astrophysics session were held :

* January 25 - February 1	"Quantum Information and Decoherence in Nanosystems"
* March 21-28	"Electroweak Interactions and Unified Theories"
	"The Young Local Universe"
* March 28 -April 4	"QCD and High Energy Hadronic Interactions"
	"Exploring the Universe "

I thank the organizers of the XXXIXth Rencontres de Moriond:

. C. Glattli, T. Martin, B. Pannetier and M. Sanquer, for the "Quantum Information and Decoherence in Nanosystems" session.

. A. Abada, A. Blondel, S. Davidson, P. Fayet, J.-M. Frère, H. Frisch, P. Hernandez, M. Knecht, L. Krauss, J. P. Lees, S. Loucatos, F. Montanet, L. Okun, A. Pich, L.Randall, G. Unal, D. Wood, and F. Zwirner for the "Electroweak Interactions and Unified Theories" session,

. T. Montmerle, J. Bouvier, A. Chalabaev, B. Lefloch, M. Guélin, D. Elbaz, M. Sauvage, for the "The Young Local Universe" session.

. E. Augé, E. Berger, S. Bethke, A. Capella, D. Denegri, Y. Dokshitzer, N. Glover, B. Klima, L. Kluberg, G. Korchemsky, L. McLerran, L. Montanet, B. Pietrzyk, Chung-I Tan and U. Wiedemann for the "QCD and High Energy Hadronic Interactions" session,

. R. Ansari, J. G. Bartlett, S. Caroll, J. Dumarchez, Y. Giraud-Héraud, D. Langlois, C. Magneville, Y. Mellier, P. Rosati and M. Treyer for the "Exploring the Universe" sesssion, and the conference secretariat : C. Barthélemy, I. Cossin, E. Hautefeuille, G. Hérent, M. Y. Joguet, Pham Duy Tu, F. Warin and V. Zorica.

I am also grateful to Enrico Belli, Fillippo Lucchini, Gian Luca Mazzeo, and Gian Franco Raino who contributed through their hospitality and cooperation to the well-being of the participants, enabling them to work in a relaxed atmosphere.

These Rencontres were sponsored by the European Union "Improving Human Research Potential" Program, the Centre National de la Recherche Scientifique (INSU, SPM and FP), the Centre National d'Études Spatiales, the Institut National de Physique Nucléaire et de Physique des Particules (IN2P3-CNRS), the Commissariat à l'Energie Atomique (DAPNIA) and the National Science Foundation. I would like to express my thanks for their encouraging support.

I sincerely wish that a fruitful exchange and an efficient collaboration between the physicists and the astrophysicists will arise from these Rencontres as from the previous ones.

J. Trân Thanh Vân

Preface

The "Young Local Universe" conference was held in the week of March 21-28, 2004 in the beautiful setting of La Thuile, Val d'Aosta, Italy. The conference was the XXIVth Astrophysics Meeting of the well-established "Rencontres de Moriond" series. Its goal was to bring together researchers and students working on the ISM and star formation, from our Galaxy to nearby galaxies, as far away as molecular clouds and star-forming regions can be resolved by modern ground-based and space observatories. The corresponding distances span a range of roughly six orders of magnitude, from 50 pc to 10-20 Mpc.

The main effort was devoted to bring together in an "integrated" fashion participants from galactic and extragalactic backgrounds. As a result, the meeting was attended by nearly 70 participants, who had the opportunity to exchange points of view and confront their visions of galactic and extragalactic star formation at different scales and in different environments.

The conference program included galactic topics such as the Gould Belt, the so-called Local Bubble, giant HII regions, galactic starburst-like regions of massive star formation, and extragalactic topics such as the Local Group (LMC, SMC, etc.), extragalactic bubbles, colliding galaxies and mergers (Antennae, etc.). The first results from the ultra-violet observatory GALEX were presented. Many theoretical issues were also discussed: cloud core collapse, the role of metallicity and nucleosynthetic evolution, feedback effects from massive stars (winds, supernovae), interstellar turbulence and magnetic fields, irradiation effects by high-energy particles, triggered star formation, etc.

The "Young Local Universe" conference was supported by the European Research and Training Network "Formation and Evolution of Young Stellar Clusters" (coordinator: M. McCaughrean, Potsdam).

The Program Committee consisted of Thierry Montmerle (Chair), Jerôme Bouvier, Almas Chalabaev, Bertrand Lefloch (LAOG,Grenoble); Roberto Neri (IRAM); Philippe André, David Elbaz, Marc Sauvage (CEA/DAPNIA/SAp, Saclay); Mark McCaughrean (Potsdam); Daniele Galli (Firenze), and Jean Tran Thanh Van (LPT, Orsay).

The program was elaborated with useful inputs from the Scientific Advisory Committee: João Alves (ESO), Dieter Breitschwerdt (Vienna), Catherine Cesarsky (ESO), Françoise Combes (Paris), Yasuo Fukui (Nagoya), Tim Heckman (Baltimore), Thomas Henning (Heidelberg), Vincent Icke (Leiden), Jörgen Knödlseder (Toulouse), Daniel Kunth (Paris), André Maeder (Geneva), Francesco Palla (Florence), Michel Tagger (Saclay), and Hans Zinnecker (Potsdam).

We are gratefull to all of them for their active participation and their help in putting up what we believe was an original approach towards a global, multiwavelength and multiscale view of star formation in the local universe. We also thank the staff of the "Rencontres de Moriond" for their logistical help.

Last but not least, our special thanks to Hans Zinnecker whose photos illustrate this book.

A. Chalabaev, T. Montmerle, J. Tran Than Van

Contents

Introductory lecture

Part 1. The origin of the stellar mass function

Part 2. Initial conditions of star formation and environmental effects

Part 3. Feedback effects from massive stars

Part 4. Galactic and extragalctic modes of star formation

Part 5. Extreme conditions for star formation

Introductory Lecture

GLOBAL STAR FORMATION FROM $z = 5 \times 10^{-8}$ to $z = 20$

LEO BLITZ

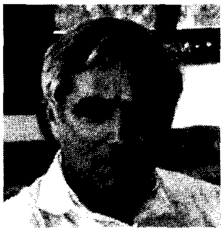

Astronomy Department, University of California
Berkeley, California 94720, USA

Starting with the assertion that the problem of isolated, single star formation is essentially solved, this paper examines some of the missing steps needed to go from there to understanding the star formation history of the Universe. Along the way, some results on the formation of star clusters in the Milky Way and the properties of GMCs in nearby galaxies are briefly examined,

Keywords: Stars: formation; ISM: general; Galaxies: evolution

1 Introduction

The field of star formation exploded with the advent of millimeter-wave and infrared detectors in the 1970s. Prior to that it was a field with a few lonely but brilliant workers such as George Herbig and Adriaan Blaauw who managed to identify young stars and regions of star formation from their optically determined properties alone. Both realized that the regions of most recent star formation were always associated with dark dust clouds, and understood that the earliest stages of star formation would only be probed by penetrating the veil of dust obscuration. Since that time, the field of star formation has expanded to include not just the nearest accessible regions, but the farthest reaches of the Universe as well. Using what we've learned about local star formation, reasonable speculations and simulations have now been attempted to guess at what the first stars in the Universe might have been like (Abel, Bryan & Norman 2002) [1].

The field of star formation remains a rich area of research with many unsolved problems and thus continues to attract a coterie of young inventive scientists. In this article I give a personal view of where some parts of the field are headed, especially those areas that touch on star formation in galaxies. Clearly, in such a short space, I can cover only a few topics, and even those, rather cursorily.

2 What Do We Really Want to Know?

I begin by making the outrageous claim that the problem of low-mass, single star formation is essentially solved, due in large part to the work of Frank Shu, Richard Larson and a number of others. This is not to say that there aren't still questions that are worth asking, but that the most interesting questions are more in the realm of planet formation than star formation. The remaining star formation issues are questions more of detail, rather than questions of a fundamental nature about how stars form. I illustrate this point with reference to what I believe is the most well known image in the scientific literature on the subject of star formation, which is shown here as Figure 1 (Shu, Adams & Lizano 1987) [16]. (Jeff Hester's beautiful image of the elephant trunk structures in the Eagle Nebula is more well known, but is reproduced primarily in the popular press).

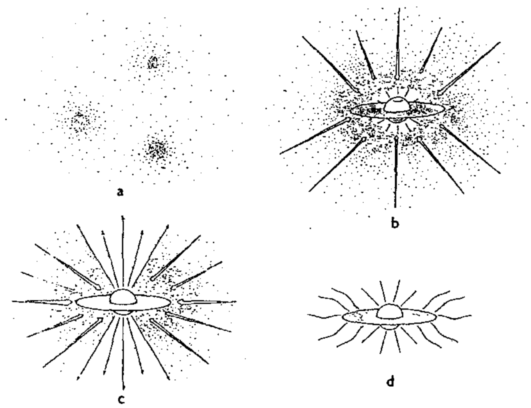

Figure 1: Figure taken from the 1987 review of low-mass star formation by Shu, Adams, and Lizano, giving the four principle stages of star formation. Although there has been some refinement of these stages, there is general agreement among astronomers that star and solar system formation occur according to this picture, which allows detailed quantitative estimates to be made to compare with observations.

This sketch represents the four stages of star formation which are now generally accepted as how low-mass, single stars form. Stars begin as gravitationally unstable condensations in cold, dense molecular clouds, forming a prestellar core observable in the near infrared as material continues to rain in on it. The higher angular momentum material forms a disk, and the system develops a bipolar outflow and jet which removes the angular momentum from the system, while initially disrupting and clearing out the infalling material. The star becomes visible as a T-Tauri star, and the disk ultimately becomes the raw material from which planets form. Magnetic fields play a central role in the dynamics, and add computational complexity, but almost surely determine the onset of collapse and the bipolar outflows. Diverse observations have a good theoretical underpinning, and little work is now done without either explicitly or implicitly invoking this picture.

On the other end of the distance scale, deep observations with the HST, Keck and SCUBA, have made it possible to determine the star formation history of the Universe, which is shown in Figure 2 (Steidel et al. 1999) [20]. This plot, widely known as the Madau plot (Madau et al. 1996) [8], has been modified by others (e.g. Rowan-Robinson 2002 [14]), but its main features are well established: at early times there is a constant, or nearly constant star formation rate per comoving Mpc until about $z = 2$, at which time the star formation rate steadily falls by about an order of magnitude until the present epoch. One of the great challenges is to apply what we know about the details of star formation in the nearest regions to fill in the missing pieces needed to obtain Figure 2. The goal is to obtain not only the correct shape, but the correct amplitude of the Madau function.

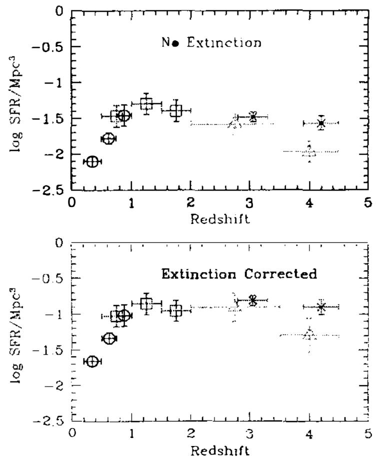

Figure 2: The star formation rate in the universe as a function of redshift. The units on the ordinate are $M_{\odot}$ Mpc^{-3} yr^{-1} based on the work of (Steidel et al. 1999).

2.1 Some of the Missing Pieces

High Mass Star Formation

The first problem is that the star formation rate in the Universe is determined from the light of the most massive stars, but most of what we know about star formation applies only to low mass stars. Getting an evolutionary picture of high mass star formation remains difficult observationally because of the rapid destruction of their surroundings by high mass protostars. Without a good set of observations it is difficult to make progress in the theory. For example, only a small number of candidate high mass prestellar cores have been identified, and little has been written about the relationship of these cores to their surrounding molecular clouds. Nevertheless, considerable progress should be possible in the near term from observations with a new generation of millimeter-wave interferometers: CARMA and ALMA, the Spitzer Space Telescope, and SOFIA.

The Formation of Stars in Clusters

If the problem of how individual low-mass stars form is essentially solved, and if high-mass star formation is next, we only get to the first rung of the ladder that ends at the Madau plot. Stars do not typically form as isolated objects, but rather in clusters, and little is known about clustered star formation. For example, do massive clumps form massive star clusters? What determines the star formation efficiency of a particular cluster forming clump? Are the stars that form in a cluster different from those that form in looser aggregates? Are the prestellar cores that form star clusters in the gas clumps the same as those identified with single star formation?

The study of clustered star formation is in such a primitive state that even some of the most basic questions have not yet been addressed. For example, it would seem that high mass stars are the last to form in clusters (lest they dissociate the gas from which the accompanying low mass stars form), and they appear to form in the cluster centers. But how can this be the case since high mass protostars should have the shortest dynamical times, and if formed in the centers of the clumps, should form first since the density of the gas is highest there. Although there have been several guesses at a solution (e.g. Stahler, Palla & Ho 2000 [19]; Bonnell, Bate & Zinnecker 1998 [4]), no explanation seems compelling yet.

Universality of the IMF

The calibration of the vertical scale in Figure 2 assumes that the IMF is invariant at all epochs and in all galaxies. But how universal is the IMF? To predict how it might or might not vary in other galaxies, and at other epochs, we need to know what physical or stochastic processes determine it. Very little is known about how the initial mass function is produced, though new work by Shu, Li, & Allen (2004) [17] promises some progress on that subject.

The Formation of Stars in Galaxies

It may be a long time before it is possible to understand enough about the details of star formation to predict how star formation proceeds on galactic scales in GMCs. Nevertheless, it may be possible to circumvent this issue by learning how GMCs form and then determining how star formation proceeds *on average* in these GMCs. With this approach one would need to know how the physical conditions in GMCs differ in various galaxy types, in different locations within a galaxy, and with changes in metallicity. While this may seem like a daunting task, improvements in instrumentation now make it possible to survey entire galaxies at high enough resolution to make significant progress. Some early results are discussed below.

The last step in getting to the Madau plot is then extrapolating what we know about global star formation in normal galaxies to the star formation in starbursts and AGN. In other words, why do particular galaxies become starbursts, and how much star formation comes from particular galaxy or merger? This step is important because a significant fraction of the light of galaxies comes from starbursts, and the fraction of starbursts seems to change with z.

Initial conditions, Initial Conditions, Initial conditions

What ties all of these points together is that to make the step from single star formation to the Madau plot, it is necessary not only to learn about the physical processes involved, which requires a combination of theory and observation, but to understand what the initial conditions are that give rise to variations in each step. For example, even if the process of isolated single star formation is essentially solved, we really have no idea how the intial conditions, the star forming cores, are produced. Furthermore, we don't know whether the IMF reflects the mass spectrum of prestellar cores as suggested by Motte, Andre & Neri (1998) [9] and Testi & Sargent(1998) [21], or the process of star formation itself (Shu, Li, & Allen 2004 [17]). The beautiful work by Alves, Lada & Lada (2001) [2] suggests that the initial configuration for star formation may be better represented by a Bonner-Ebert sphere rather than a singular isothermal sphere (Shu 1977) [15]. Does this make a significant difference in the star that is produced? What are the initial conditions in a GMC that produce the difference between relatively isolated star formation (as in Taurus) and clustered star formation (as in Orion)? What are the initial conditions that give rise to the number and distribution of GMCs in a galaxy?

My own view is that we cannot know too much about typical initial conditions and how they vary. Therefore, there cannot be too much emphasis on trying to determine what the intial conditions are for forming individual low mass and high mass stars, for forming stars in clusters (why, for example, do some become globular clusters?), and for forming GMCs in the disks and centers of normal and starburst galaxies.

3 A Few Relevant Results

3.1 Beyond Single Star Formation

One of the first attemps to study to study the formation of star clusters observationally was done by Elizabeth Lada (Lada 1992) [7], who made the first survey of dense gas in an entire GMC (Orion B) using the molecular tracer CS. She found that the embedded stars are found primarily in clusters, and that the clusters form only in the densest condensations: those identified by their CS emission. Subsequently, Phelps & Lada (1997) [11] made another advance with their near IR imaging of some of the ^{13}CO clumps in the Rosette Molecular Cloud. They were able to identify 7 embedded clusters associated with the centers of 7 massive clumps of molecular gas identified previously by Williams, Blitz & Stark (1995) [22]. These 7 clusters were all associated with far IR IRAS sources, and 5 were previously unknown. Thus what appeared to be single point sources in the IRAS data turned out to be embedded star clusters. Figure 3 shows a plot of the clumps in the Rosette vs. the gravitational boundedness of the clumps, plotted as M_{grav}/M_{lum} where $M_{grav} = RV^2/G$, $M_{lum} = X \int \int \int T_A dv dx dy$ and X is the usual CO-to-H_2 conversion factor.

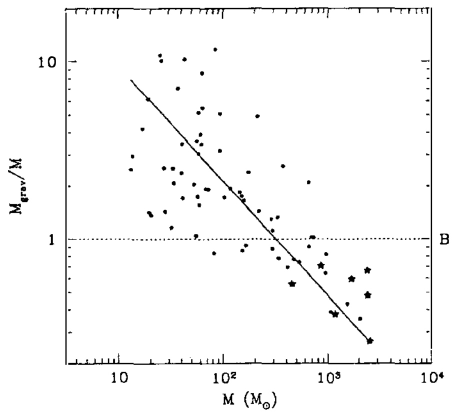

Figure 3: Plot of the ratio of gravitational binding energy to kinetic energy of the clumps in the Rosette Molecular Cloud from Williams, et al.(1995). The horizontal line represents a clump that is marginally self gravitating; clumps that are not self-gravitating are presumably pressure bound. The clumps containing IRAS sources are shown with stars. These are largely coincident with the embedded dlusters found in the infrared by Phelps & Lada (1997).

The clusters identified by Phelps & Lada [11] are identified with the most massive, gravitationally bound clumps (Williams et al., 1995) [22]. But what is it about the star-forming clumps that produces a great many star-forming cores simultaneously? In other words, what is it that is communicated through a clump in a crossing time to let all parts know that they must produce stars simultaneously? What determines how many stars form within a given clump? Do the clumps even have embedded cores that are distinct, recognizable entities? The Phelps & Lada work also provides an efficient way to find embedded clusters, and, *en passant*, demonstrates that the clumps are real, long-lived entities, rather than ephemeral turbulent structures, as some authors have suggested (otherwise the star clusters would not have had enough time to form in them).

3.2 Star Formation on Galactic Scales

Understanding clustered star formation will likely solve the problem of how star formation takes place within an individual molecular cloud. How then do we extrapolate to larger scales, to the scale of an entire galaxy? A reasonable question to ask is whether we need to know all of the details of the star formation process to address star formation on galactic scales. That is, since we know that star formation takes place only in molecular clouds, and that the star formation efficiency in molecular clouds tends to be small ($\sim 5\%$), with relatively little variation in normal galaxies, perhaps the question of how stars form in galaxies reduces to a question of how the molecular clouds themselves form? That is, if we can understand how the ISM turns molecular gas into GMCs, and we can understand how the different conditions within GMCs translate into different star formation efficiencies and perhaps even IMFs, then it should be possible to determine the global star formation rate from just the gas content and other physical conditions within the galaxies.

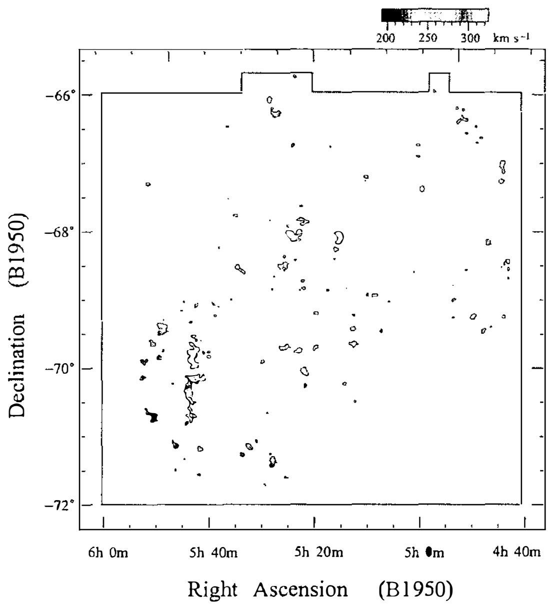

Figure 4: Map of the GMCs found in the LMC by Mizuno et al. (2001). These cover essentially the entire face of the galaxy, but cover only a small fraction of the surface, necessitating a large effort to obtain the map.

To this end, it is useful to have complete surveys of individual GMCs in entire galaxies not just unresolved images of the molecular gas, This has become possible only in the last few years, but for only a few galaxies; only two such maps have been published. The first was the LMC which has been nearly completely mapped by Mizuno et al. (2001) [10] using the 4m Nanten telescope (see Figure 4). More recently, Engargiola et al. (2003) [6] have used the BIMA array to make a 759 field mosaic of M33 at 15$''$ resolution ($\sim$ 50 pc – see Figure 5). Both of these images indicate the difficulty in surveying galaxies for individual GMCs: the surface filling fraction of GMCs in galactic disks is small (see Figure 4), and the resolution needed to determine the cloud properties is high, requiring either large amounts of telescope time for Local Group objects, or high sensitivity interferometric mosaics for galaxies farther away. For both the LMC and M33, followup observations at high resolution were needed to resolve the molecular clouds in each case.

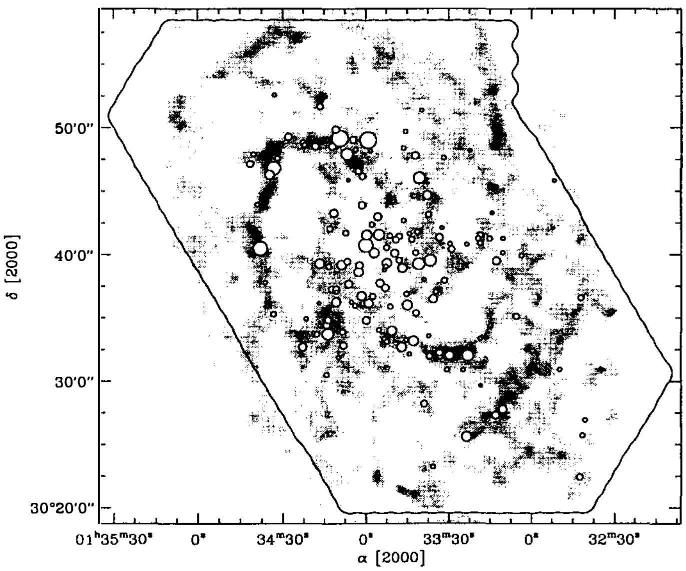

Figure 5: The molecular clouds catalogued by Engargiola et al. (2003), shown as white dots enclosed by black circles, superimposed on an HI map from the data of Deul and van der Hulst (1987). The diameter of each dot is proportional to the H_2 mass of each GMC. Notice both the filamentary structure of the HI and the good correspondence between the filaments and the location of the GMCs.

Other galaxies that have been fully mapped to date but not yet published include the SMC (Mizuno et al.), IC10 (Leroy et al.), and M31 (Muller and Guelin); these maps were all presented at this YLU conference. Although there has been a herculean effort to map the molecular gas in M31, the resolution (90 pc) appears to be too low to resolve clouds blended in the beam in many directions (Muller, this conference). Followup interferometric observations will be needed to obtain the properties of the GMCs. The central region of M64 has also been mapped at high enough resolution to measure the molecular cloud properties in the nuclear region where the surface filling fraction of molecular gas approaches unity (Rosolowsky & Blitz 2005) [13]. The disk has not been observed at comparably high resolution.

The image of M33 seen in Figure 5 shows something quite striking and new: essentially all of the individual GMCs lie on filaments of HI. Note, though, that the filaments show little variation in surface density with radius, but that the GMCs become very sparse at radii more than about 12′ from the center. Averaged over annuli, the atomic gas surface density is nearly constant with radius, falling by only a factor of two over 7 kpc, but the molecular gas surface density is exponential with a scale length of 1.4 kpc. Because there is a great deal of HI where there is no CO, the H_2 must have formed from the HI, rather than the converse. But why do the GMCs become so sparse beyond about 3 kpc?

The close association of the molecular clouds with the filaments implies a maximum lifetime for the GMCs of ~ 20 Myr, based on the mean velocity difference between the CO and HI along the same line of sight. A significantly longer lifetime would cause a spatial separation between the atomic and molecular gas. It thus appears that the filaments are a necessary, but not sufficient condition for the formation of molecular clouds. What, produces the radial abundance gradient of molecular gas, and thus the radial variation of the star formation rate?

One possibility is that the filaments are really the boundaries of 'holes', large regions relatively devoid of HI, caused by supernova explosions in a previous generation of OB associations. However, the large holes in Figure 5 are not associated with catalogued OB associations (Deul & van der Hulst 1987) [5]. In any event, energies of $\sim 10^{53}$ ergs are needed to evacuate the large holes, implying that 100 or more O stars would have been formed in each, leaving bright stellar clusters and diffuse x-ray emission at the centers of the emply regions, which are not observed.

Could it be that the radial variation is due to a change in the ratio of CO/H_2, the so-called "X" factor produced by the known abundance gradient in M33? This possibility was investigated by Rosolowsky et al. (2003) [12] who showed that if X is determined by equating the luminous CO mass with the virial mass of resolved clouds in M33, X shows no variation with metallicity or radius. This can be seen from Figure 6.

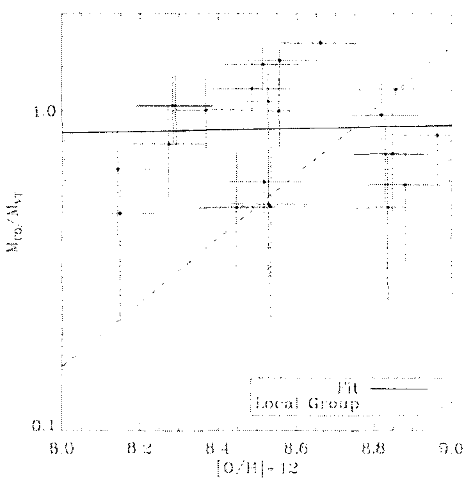

Figure 6: A plot of the X-factor as a function of metallicity in M33. The X-factor is given as a ratio of the value in M33 vs. the locally determined value of 2 $\times 10^{20}$ cm^{-2} (K kms^{-1})$^{-1}$. The dashed line plots the trend from Arimoto et al. (1996) summarizing similar measurements throughout the Local Group.

Wong & Blitz (2002) [23] have proposed that the fraction of molecular gas at a particular radius in a galaxy is the result of interstellar pressure, based on interferometric observations of six nearby spiral galaxies. Blitz & Rosolowsky (2004) [3] showed that pressure modulated molecular cloud formation implies that the radius in a galaxy where the atomic/molecular surface density is unity should occur at a constant *stellar* surface density. An investigation of 30 galaxies showed this constancy to be good to within 50%. Thus it seems reasonable to conclude that hydrostatic pressure plays a significant role in the formation of molecular clouds.

But if hydrostatic pressure is the main culprit in forming GMCs, how do the GMCs vary from galaxy to galaxy where interstellar pressure might be quite varied? With current telescopes, we have data only for GMCs in the Local Group galaxies, and the published data are only available for the Milky Way, the LMC and M33. If we examine the cumulative mass distribution of GMCs for each galaxy (but separating the inner Milky Way from the outer Milky Way), we see that there are significant differences from one galaxy to another (Figure 7). In this figure, the mass distribution is normalized to the most massive cloud observed, and the distribution for M33 is significantly steeper than that of the other galaxies. The mass function is independent of resolution, and the differences in slope are significant.

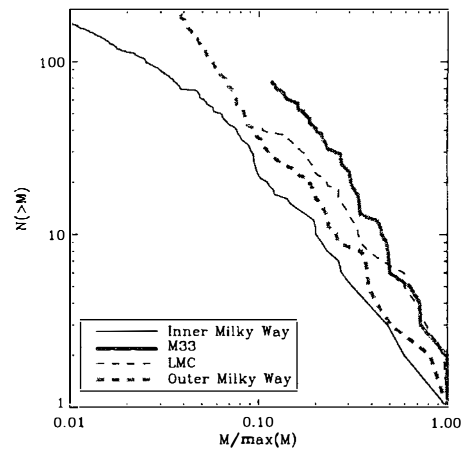

Figure 7: The cumulative mass distribution in three Local Group galaxies, with the inner and outer Milky Way plotted separately. This plot shows that there are significant differences in the mass spectrum from galaxy to galaxy, with the inner Milky Way giving a power law in dN/dM of -1.6, and M33 giving a power law index of -2.3.

We may also ask whether the clouds show differences, for example, in the size-linewidth relation observed for clouds in the Milky Way. Figure 8 shows a plot of hundreds of clouds in the Milky Way, M33, and the LMC, with a line of slope 1/2 superimposed on the data. Evidently, the clouds in these galaxies obey the same size-linewidth relation with no zero-point offset: $\Delta V \propto R^{1/2}$.

This plot suggests that if all of the clouds in these galaxies are self-gravitating, the surface density of the clouds is constant with a relative scatter given by the scatter in Figure 8. That is, since $\Delta V \propto R^{1/2}$, and $M \propto R(\Delta V)^2/\mathrm{G}$, then $M/R^2 = const.$ But the mean internal pressure of GMCs can be written: $P_{int} = \alpha(\pi/2)G\Sigma_g{}^2$, where Σ_g is the gas surface density of the clouds and α is a constant near unity that depends on the cloud geometry. Thus, the GMCs that compose Figure 8 have the same mean internal pressure, regardless of size, regardless of the galaxy they

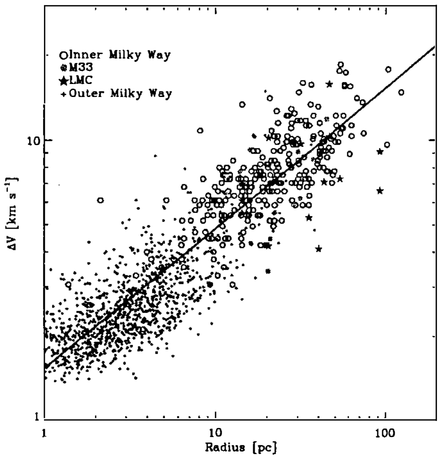

r

Figure 8: Size-linewidth relation for resolved GMCs in the same galaxies plotted in Figure 7. The clouds in all three galaxies appear to follow the same relation with $\Delta V \propto R^{1/2}$. Corrections have been applied to the published data to treat all of the data identically, and to correct for beam effects.

are in and regarless of the external pressure.

This gives us a way of understanding how the IMF might indeed be constant from galaxy to galaxy, at least for galaxies similar to those in Figure 8. That is, if the mean internal pressure of all GMCs in the disk of a galaxy is the same, then the range of pressures within a GMC might also be the same, and the star-forming cores might therefore also be quite similar. It is important to keep in mind, however, that even if true it might apply only in the disks of galaxies. In the bulge regions, the hydrostatic pressure of the gas is likely to be two to three orders of magnitude higher than that in the disk (e.g. Spergel & Blitz (1992) [18]. In these regions, the external pressure can significantly exceed the mean internal pressure of a few $\times 10^5$ cm^{-3} K of the clouds in the disk. In the bulge regions, the GMCs must be different from those in the disk, and may well give rise to stars with a different IMF.

Studying global star formation is only in its infancy and new instruments coming on line and being developed should provide the sensitive high resolution data needed to get from single star formation to the Madau plot. Equally important is to have those who work on local star formation interact closely with those working on global star formation on a regular basis as has happened in this conference.

Acknowledgments

I'd like to thank Charlie Lada who commented on an early version of this manuscript and Steve Stahler for a useful discussion. Erik Rosolowsky prepared a number of the figures in this paper.

References

1. Abel, T., Bryan, G. L., & Norman, M. L. 2002, Science, 295, 93
2. Alves, J. F., Lada, C. J., & Lada, E. A. 2001, Nature, 409, 159

3. Blitz, L., & Rosolowsky, E. 2004, ApJL, 612, L29
4. Bonnell, I. A., Bate, M. R., & Zinnecker, H. 1998, MNRAS, 298, 93
5. Dcul, E. R., & van der Hulst, J. M. 1987, A&AS, 67, 509
6. Engargiola, G., Plambeck, R. L., Rosolowsky, E., & Blitz, L. 2003, ApJS, 149, 343
7. Lada, E. A. 1992, ApJL, 393, L25
8. Madau, P., Ferguson, H. C., Dickinson, M. E., Giavalisco, M., Steidel, C. C., & Fruchter, A. 1996, MNRAS, 283, 1388
9. Motte, F., Andre, P., & Neri, R. 1998, A&AS, 336, 150
10. Mizuno, N., et al. 2001, PASJ, 53, 971
11. Phelps, R. L., & Lada, E. A. 1997, ApJ, 477, 176
12. Rosolowsky, E., Engargiola, G., Plambeck, R., & Blitz, L. 2003, ApJ, 599, 258
13. Rosolowsky, E., & Blitz, L. 2005, ApJ, in press
14. Rowan-Robinson, M. 2001, ApJ, 549, 745
15. Shu, F. H. 1977, ApJ, 214, 488
16. Shu, F. H., Adams, F. C., & Lizano, S. 1987, ARA&A, 25, 23
17. Shu, F. H., Li, Z., & Allen, A. 2004, ApJ, 601, 930
18. Spergel, D. N., & Blitz, L. 1992, Nature, 357, 665
19. Stahler, S. W., Palla, F., & Ho, P. T. P. 2000, Protostars and Planets IV, 327
20. Steidel, C. C., Adelberger, K. L., Giavalisco, M., Dickinson, M., & Pettini, M. 1999, ApJ, 519, 1
21. Testi, L., & Sargent, A. I. 1998, ApJL, 508, L91
22. Williams, J. P., Blitz, L., & Stark, A. A. 1995, ApJ, 451, 252
23. Wong, T., & Blitz, L. 2002, ApJ, 569, 157

Part 1

The origin of the stellar mass function

Star Formation and the IMF

H. Zinnecker

Astrophysikalisches Institut Potsdam, An der Sternwarte 16, D-14482 Potsdam, Germany

The stellar Initial Mass Function or IMF is fundamentally related to the origin of stellar masses. Star formation processes like hierarchical fragmentation or competitive accretion are likely to determine the IMF (log-normal or power-law prediction), but also hybrid models can be considered. Alternatively one can also ask what we can infer from the observed IMF in various star forming regions about the physical processes at work, in particular the observation of a universal IMF (currently under debate). This is a short summary of what I discussed as a key note address at the beginning of the EC-RTN workshop on the young local universe (YLU) at La Thuile.

Keywords: Stars: formation, Stars: luminosity function, mass function, ISM: clouds, HII regions

1 Preview

In this key note address, I will discuss the origin of stellar masses and stellar mass distribution (IMF). The IMF, as defined by Salpeter (1955), is the "relative probability for the creation of stars of mass near M_* at a particular time", assuming that this probability is time-independent. First I give some historical background, by listing a number of relevant IMF papers, then I discuss the physical principles behind log-normal and power-law IMFs. I end by wondering why the IMF should or should not be universal.

2 Historical background:

To be brief, I will just list some useful IMF papers that everyone in the field should have read. Here we go (in a temporal order):

Salpeter (1955), Miller and Scalo (1979), Lequeux (1979), Cohen and Kuhi (1979), Zinnecker (1982), Zinnecker (1984, 1985), Larson (1982, 1985), Elmegreen (1985), Scalo (1986, the big review), Kroupa, Tout, and Gilmore (1993), Zinnecker, McCaughrean, and Wilking (1993), Silk

(1995), Adams and Fatuzzo (1996), Bonnell et al. (1997), Elmegreen (1997, 2002), Scalo (1998), Meyer et al. (2000), Klessen (2001), Kroupa (2002), Pudritz (2002), Chabrier (2003), Bate, Bonnell, and Bromm (2003), Lada and Lada (2003), Elmegreen and Shadmehri (2003), Shu, Li, and Allen (2004), Basu and Jones (2004). Apologies to anyone whose paper I may have missed.

3 The shape of the IMF: log-normal vs. power-law

3.1 Log-Normal IMF

Log-normal IMFs can result from random hierarchical fragmentation, as described in the thesis of Zinnecker (1981, 1984), based on the Larson-Bodenheimer collapse-and-fragmentation cascade (Larson 1972, Bodenheimer 1978), where the spin angular momentum of a cloud is converted into orbital angular momentum of the central fragments, until the angular momentum problem of star formation is solved after several steps (typically about 5, just enough to apply the central limit theorem of statistics). Such a cascade process can roughly explain the mass dispersion of of the "observed" log-normal part of the IMF (Zinnecker 1984). An earlier, but extremely simplified version of this model is due to Larson (1973); later, a much more sophisticated version was published by Adams and Fatuzzo (1996), who did not bother to quote the earlier work.

A random hierarchical process (sequential in time) is a special case of a random multiplicative process which itself is more general. Star formation as a random multiplicative process, discussed at the famous Les Houches Summer School 1983, would not only include a temporal sequence of fragmentation steps but would also incorporate simultaneous influences which represent the initial conditions for the onset of the fragmentation process. The set of random variables in the multiplicative process which may affect a particular stellar mass is the mixture of initial conditions, such as density, temperature, specific angular momentum, strength of turbulence, mass-to-magnetic flux ratio, and the geometry of the initial condensation (Zinnecker 1985). Although these initial conditions may not all be statistically independent, we may assume approximate factorization. In the simplest case, the stellar mass would be given by the Jeans mass ($M_J \sim n^{-1/2} T^{3/2}$) which factorizes exactly into functions of cloud density n and cloud temperature T. For the observed range in gas density and temperature ($n = 10^3 - 10^6\, cm^{-3}$, $T = 10 - 50\, K$), the Jeans masses obtained are in the range of observed stellar masses ($M_J = 0.1 - 100\, M_\odot$). Most likely, however, things are not so simple, and many more than two random factors enter the game, as described above. If so, the central limit theorem will apply and the resulting stellar mass spectrum will be Gaussian in log-mass (i.e. the logarithm of a product will the sum of the logarithms of random variables, and for independent measurements or variables the sum will be a Gaussian distribution). I believe, this was first hinted upon by Miller and Scalo (1979).

3.2 Power-Law IMF

Here, we basically repeat the arguments that led to the first model of competitive accretion in a proto-cluster cloud (Zinnecker 1982). Competitive accretion in protostellar clusters occurs as individual protostars compete gravitationally for the reservoir of gas. As fragmentation is highly inefficient, there remains a large mass of gas that can dominate the gravitational potential. Accretion of this gas onto the protostars can then determine the final stellar masses.

The evolution of a protocluster cloud consists of a global collapse or contraction, while locally the denser fragments quickly collapse and condense on their own. Under the assumption that collisions and coalescence of protostellar fragments will not (or only rarely) occur, the number of protostellar fragments is (approximately) conserved. It is this assumption that keeps the model simple, i.e. amenable to a linear kinetic approach:

$$\frac{\partial N}{\partial t} + \frac{\partial}{\partial M}\left(\dot{M} N\right) = 0 \quad (1)$$

Here is $N = N(M,t)$ is the number of fragments with instantaneous mass between M and $M + dM$ at time t, and $\dot{M}$ is the accretion rate of each fragment which depends only on the instantaneous mass of the fragments. Equation (1) can be solved, once the accretion rate is given. What is the correct accretion rate? In the limit of the gravitational potential being dominated by the stars (and not by the gas, whose self-gravity can thus be largely ignored), the accretion rate to be adopted is the Bondi-Hoyle accretion rate, i.e.

$$\dot{M} \sim M^2 \quad (2)$$

For a recent review on Bondi-Hoyle accretion, see Edgar (2004).

Another implicit assumption to be able to solve equation (1) is a constant uniform gas density in the protocluster (despite exhausting the gas reservoir during Bondi-Hoyle accretion). This means that the proportionality constant in equation (2) is constant and time-independent. With all these assumptions the asymptotic solution for equation (1) is

$$N\left(M,t\right) \sim M^{-2} \quad (3)$$

(asymptotic means for large masses and long times). The result compares favourably with the well-known Salpeter power-law IMF with a slope of -2.35. The asymptotic shape of N(M,t) will be frozen in after the most massive stars start ionizing the remaining gas and drive it out of the cluster on a short timescale. The mass distribution given in equation (3) can be intuitively understood from equation (2) which implies that stars with initially small differences in mass will aquire large differences in the end, due to the non-linear nature of the accretion rate (according to the principle: the rich get richer, the richer get richest). [a]

Substantial refinements of the above model were made by Bonnell et al. (1997, 2001) and, lately, by Bonnell, Bate, and Vine (2003). Their numerical studies have shown that competitive accretion results in a large range of masses, with stars in the center of the cluster accreting more gas due to their location in the deepest part of the potential. Indeed, competitive accretion predicts a two power-law IMF, reminiscent of a log-normal turnover (as observed). Low-mass stars accrete the majority of their mass in a gas dominated regime where tidal forces limit their eventual mass, resulting in a shallow IMF. Higher mass stars accrete their mass in the stellar dominated cores of the cluster with accretion rates dominated by the Bondi-Hoyle accretion process, resulting in a steeper IMF.

3.3 Hybrid IMF: log-normal peak and power-law tail

Just days before this workshop a new theoretical paper on the origin of the IMF appeared, which took me by surprise. It describes a hydrid model of the IMF with a simple explanation of how to turn an originally log-normal mass distribution into one with a power- law tail (Basu and Jones 2004). The basic idea to achieve this miracle is to couple a mass-dependent accretion rate with an exponential distribution of accretion times (the probability of stopping accretion is constant in time). Clearly, protostars will not all accrete for the same time, and a distribution of accretion times will skew the final distribution away from a log-normal. I am happy to popularize this model, as I like it very much (too bad I did not have the idea myself)!

The authors note that, different from Zinnecker's (1982) non-linear accretion model, their model yields a power-law upper mass distribution even if the initial masses were all the same.

[a] In the more modern picture of gravo-turbulent star formation, the protocluster cloud would be supported against collapse by turbulent motions, while supersonic collisions of the turbulent streams of gas would provide the dense gravitationally unstable fragments (see Padoan and Nordlund 2002, MacLow and Klessen 2004).

They also note that the distribution of accretion timescales may play a role to "understand" the outcome of a realistic IMF in detailled global simulations of star formation, such as those of Bate, Bonnell, and Bromm (2003). The accretion timescales may be controlled by the local dynamical time which can differ from place to place in a proto-cluster. Although the spatial structure of turbulence may contribute to power-law fragment masses (e.g. thresholded regions in density fields with log-normal probability density functions; cf. Elmegreen 2002, Pudritz 2002) as seen in the clump mass observations summarized by André et al. (2000), Basu and Jones (2004) may be on the right track in claiming that the temporal effect that they have studied goes a long way to explain a power-law tail of the IMF, while keeping a log-normal peak near and around the Jeans-mass.

I also appreciate Basu and Jones' (2004) reminder of Zipf's law, which states that city sizes (number of inhabitants) are distributed as a power-law. I went to great length to check this for myself for Germany, and indeed obtained a result which is very close to a logarithmic slope of -1. I encourage the EC participants of this meeting to test the Zipf-Zinnecker conjecture for their own native country.

4 Universality of the IMF

What does it mean for star formation processes if the (upper) IMF turns out to be universal? How can it possibly be that the IMF is universal? It means that the physical processes must be rather robust, which could be the case if the spatial structure of the proto-cluster clouds is always self-similar, and if gravity plays the dominant role in protostellar accretion. Interestingly, Scalo (2005) has collected observational evidence for a non-universal (intermediate-mass) IMF in young open clusters. On the other hand, Chabrier (2005) noted that the difference in the low-mass IMF between Pop II globular clusters and Pop I open clusters (and field stars) is rather small, despite a huge difference in metallicity and hence in the cooling efficiency of the corresponding proto-cluster gas. It is unclear which conclusions one should draw from all this data. Are there compensating density-temperature effects (Zinnecker 1995) or is there a global self-regulation of the IMF, perhaps due to radiative or mechanical feedback (Whitworth and Zinnecker 2004; J. Melnick, private communication)?

From a theoretical point of view, we saw that the model of Basu & Jones can generate a universal slope x of the upper IMF, provided that the ratio of the death rate to the growth rate (=x) is constant (the death rate is related to the e-folding time in the exponential distribution of accretion times, while the growth rate is the logarithmic protostellar accretion rate). On the other hand, it is expected that the low-mass end and the peak (i.e. the log-normal part) of the IMF are not universal and depend on the Jeans mass which itself depends on the heating and cooling of the dense gas and hence on the star formation environment and atomic/molecular/dust physics (cf. Larson 2005).

Finally we have to remind ourselves that the IMF is just a first order quantity describing the outcome of star formation; there are second order "details" like the binary frequency as well as the binary separation and mass ratio distribution that relate to the finer fragmentation of star forming molecular clouds; additional clues about a universal fragmentation pattern (mass partitioning) may be gleaned from the changes of binary properties of stars in different environments.

5 Epilogue

Major "puzzles" that have come up during THIS conference included the following:

a) the role of supersonic turbulence in star formation (J. Silk): is turbulence in giant molecular clouds primarily due to internal or external energy sources? What is the role of protostellar winds?

b) dynamical versus quasi-static protostellar evolution (J. Tan): what is the age and age spread of the Orion Trapezium Cluster?

c) the low-mass IMF in different star forming regions (J. Bouvier): is the low-mass IMF in the Taurus association different from that in the Trapezium Cluster?

d) the origin of massive stars (R. Chini): always disk accretion (like in M17) or sometimes collisions of intermediate-mass protostars (like in W3-IR5 UCHII region)?

e) the origin of free floating substellar objects (E. Martin): what is the IMF of free-floating planetary-mass objects (like S Ori 70 in the sigma Ori cluster)?

f) the nature of Cygnus OB2 (F. Palla): why does the Cyg OB2 super star cluster (some 100 massive stars) not affect its cloud environment?

g) the mass spectrum of giant molecular clouds (H. Zinnecker): Why is the GMC mass spectrum different between LMC (Fukui), M33 (Blitz), and M31 (Mueller)?

h) Is the IMF different in regions of triggered star formation? (one of the 25 IMF questions raised on H. Zinnecker's poster, published elsewhere (in IMF@50 Proc.)).

Acknowledgments

This is the time to thank Mark McCaughrean for running our young stellar clusters EC Research Training Network (the sponsor of our workshop). This network is now expiring, but we hope it will not be the end of the collaboration. I particularly benefitted from extensive discussions with my theory friends Ian Bonnell, Francesco Palla, and Ant Whitworth. Thank you! I acknowledge help from Ulf Hanschur at AIP to finish this article. I also thank Almas Chalabaev for his patience with the manuscript and Thierry Montmerle for the invitation to speak.

References

1. Adams, F.C. & Fatuzzo, M. 1996, ApJ, 464, 256
2. André, P., Ward-Thompson, D., & Barsony, M. 2000, *Protostars and Planets IV*, ed. V. Mannings, A.P. Boss, & S.S. Russell (Tucson: University of Arizona Press), p. 59
3. Basu, Sh. & Jones, C.E. 2004, MNRAS, 347, L47
4. Bate, M.R., Bonnell, I.A., & Bromm, V. 2003, MNRAS, 339, 577
5. Bodenheimer, P. 1978, ApJ, 224, 488
6. Bonnell, I.A., *et al.* 1997, MNRAS, 285, 201
7. Bonnell, I.A., *et al.* 2001, MNRAS, 324, 573
8. Bonnell, I.A., Bate, M.R., & Vine, St.G. 2003, MNRAS, 343, 413
9. Chabrier, G. 2003, PASP, 115, 763
10. Chabrier, G. 2005, IMF@50 conference (in press)
11. Cohen, M. & Kuhi, L.V. 1979, ApJS, 41, 743
12. Edgar, R. 2004, NewAR, 48, 843

13. Elmegreen, B.G. 1985, in *Birth and Infancy of Stars*, (NATO: Les Houches 61), p. 257
14. Elmegreen, B.G. 1997, ApJ, 486, 944
15. Elmegreen, B.G. 2002, ApJ, 577, 206
16. Elmegreen, B.G. & Shadmehri, M. 2003, MNRAS, 338, 817
17. Klessen, R.S. 2001, ApJ, 556, 837
18. Kroupa, P., Tout, Ch.A., & Gilmore, G. 1993, MNRAS, 262, 545
19. Kroupa, P. 2002, Science, 295, 82
20. Lada, Ch.J. & Lada, E.A. 2003, ARAA, 41, 57
21. Larson, R.B. 1972, MNRAS, 157, 121
22. Larson, R.B. 1973, MNRAS, 161, 133
23. Larson, R.B. 1982, MNRAS, 200, 159
24. Larson, R.B. 1985, MNRAS, 214, 379
25. Larson, R.B. 2005, IMF@50 conference (in press) and astro-ph 04123357
26. Lequeux, J. 1979, A&A, 71, 1
27. MacLow, M.-M. & Klessen, R. 2004, RvMP, 76, 125
28. Meyer, M.R., *et al.* 2000, in *Protostars and Planets IV*, ed. V. Mannings, A.P. Boss, & S.S. Russell (Tucson: University of Arizona Press), p. 121
29. Miller, G.E. & Scalo, J.M. 1979, ApJS, 41, 513
30. Padoan, P. & Nordlund, Å. 2002, ApJ, 576, 870
31. Pudritz, R.E. 2002, Science, 295, 68
32. Salpeter, E.E. 1955, ApJ, 121, 161
33. Scalo, J.M. 1986, in*Fundamentals of Cosmic Physics*, vol. 11, P. 1
34. Scalo, J.M. 1998, in *The Stellar Initial Mass Function*, ed. G. Gilmore & Debbie H. (ASP Conference Series, Vol. 142), p. 201
35. Scalo, J.M. 2005, IMF@50 conference (in press)
36. Shu, F.H., Li, Z.-Y., & Allen, A. 2004, ApJ, 601, 930
37. Silk, J. 1995, ApJ, 438, L41
38. Whitworth, A.P. & Zinnecker, H., 2004, A&A, 427, 299
39. Zinnecker, H. 1981, PhD Thesis Techn. Univ. Munich, MPI-PAE report (Garching: Max-Planck Institut für Physik und Astrophysik, Institut für Extraterrestrische Physik)
40. Zinnecker, H. 1982, in *Symposium on the Orion Nebula To Honor Henry Draper*, ed. A.E. Glassgold, P.J. Huggins, & E.L. Schucking, Ann. New York Acad. Science, 395, 226
41. Zinnecker, H. 1984, MNRAS, 210, 43
42. Zinnecker, H. 1985, in *Birth and Infancy of Stars*, (NATO: Les Houches 61), p. 473
43. Zinnecker, H., McCaughrean, M.J., & Wilking, B.A. 1993, in *Protostars and Planets III*, ed. E.H. Levy & J.I. Lunine (Tucson: University of Arizona Press), p. 429
44. Zinnecker 1995, in *The bottom of the Main Sequence and Beyond*, ed. C.G. Tinney (ESO Astrophysics Symposia), p. 257

Evolution from dense cores to protostars in low-mass star forming regions

T. Onishi (1), A. Mizuno (2), A. Kawamura (1), K. Tachihara (3), Y. Fukui (1)

(1) Department of Astrophysics, Nagoya University, Chikusa-ku, Nagoya, 464-8602, Japan
(2) Solar-Terrestrial Environment Laboratory, Nagoya University, 3-13 Honohara, Toyokawa, Aichi, 442-8507, Japan
(3) Astrophysikalisches Institut der Universität von Jena, Schillergässchen 2-3, D-07745 Jena, Germany

We present the results of a survey for dense molecular cores toward nearby low-mass star forming regions. We identified 179 $C^{18}O$ cores in total, and found that the intensity of $C^{18}O$ emission is a good tracer of the star formation activity. In particular, the column density of the $C^{18}O$ has a good positive correlation with the probability of star formation and has a threshold value for star formation. We also found that turbulent decay is indicated by diminishing dV from the starless to the star-forming cores. The mass spectrum of the $C^{18}O$ cores can not be fitted by a single power-law function, and the index of the high-mass end resembles the stellar IMF. Based on the $C^{18}O$ data above, we have carried out $H^{13}CO^+(J=1-0)$ observations. The observed regions include Taurus, Ophiuchus, Chamaeleon, Pipe Nebula, Lupus, and so on. These starless condensations are compact (R$\lesssim$0.1 pc) and of high density ($\gtrsim 10^5$ cm^{-3}) and thus are highly probable candidates for protostellar condensations just before star formation. The time scale of the starless condensations is estimated to be $\sim 4 \times 10^5$ yr from the statistical analysis, and is several times larger than the free-fall time scale of gas with 10^5 cm^{-3}, $\sim 10^5$ yr. A comparison of masses between starless condensations and those with stars indicates that most of the starless condensations will not experience fragmentation except for binary formation, i.e, these condensations are a fundamental unit of star formation. The mass spectrum of the condensations is very steep and similar to that of the stellar IMF. Subsequent higher transition-line studies found the densest starless condensation, which is only less than 10^4 years away from the moment of protostar formation

Keywords: Stars: formation – ISM: clouds – ISM: molecules – ISM: kinematics and dynamics

1 Introduction

Stars are formed in molecular cloud cores. It is of crucial importance to understand the mechanism of star formation to study the evolution of galaxies and the universe. The study of star

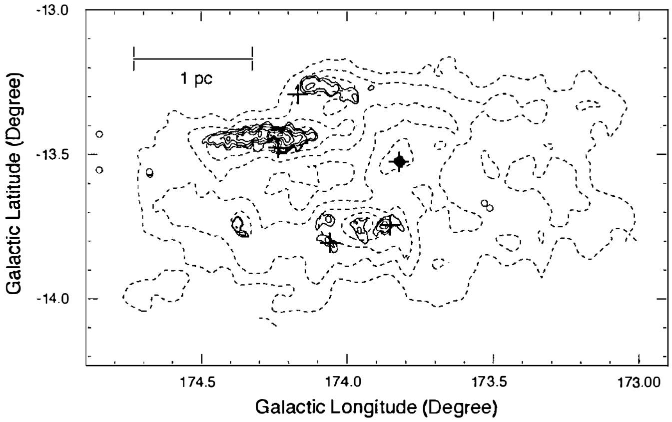

Figure 1: Contour maps of $C^{18}O$ (dashed lines) and $H^{13}CO^+$ ($J = 1-0$) toward HCL2 region (Onishi et al. 2002). A cross indicates an IRAS source that has cold infrared spectra. Open circles indicate T Tauri Stars (Herbig & Bell 1988).

formation has been largely advanced by detections of protostars accompanying outflow phenomenon. However, there still remain a number of unresolved problems in the study of dense molecular cores prior to protostar formation. This is mainly because surveys of dense cores have been biased toward known optical and/or infrared features.

We thus have carried out a molecular-line survey for dense cores in an unbiased way toward $\sim$10 low-mass star forming regions in the lines mainly of $C^{18}O$ and $H^{13}CO^+$($J = 1 - 0$). The observed regions include Taurus, Ophiuchus, Chamaeleon, Lupus, and so on. All the data were taken purely based on molecular data; all the observations have been made based on ^{13}CO observations that reveal entire distribution of gas of an intermediate density of $n(H_2) \sim 10^3 cm^{-3}$. With these observations, we have obtained a uniform and almost complete sample of dense cores with a density $n(H_2)$ from 10^4 to $10^6 cm^{-3}$ in the observed star forming regions. This enables us to study the evolution of dense cores to protostars statistically for the first time. It is to be noted that a big advantage of molecular line observations over continuum observations is that the velocity dispersion of a core can be measured in order to determine the dynamical status. This information is crucial to find gravitationally bound structures that directly lead to a star formation.

More recently, astronomers' efforts toward the understanding of star formation have been sharply focused on detecting an extremely early stage of protostar formation in a dense molecular condensation. Outstanding issues in this regard include the origin of the initial mass function, IMF, the detailed elucidation of each stage of star formation from protostellar condensations to very young protostars, and to understand them based on a reasonable theoretical framework. Fairly young protostars formed in them have been observed as molecular outflows and are sometimes designated as Class I or Class 0 objects whose evolutionary time scale is in the order of 10^5 yr (e.g., Lada 1987; Fukui et al. 1989; André et al. 1993). However, a study of the moment of protostar formation whose time scale is $\lesssim 10^4$ yr has not yet been done because of the difficulty of detecting such a rare event. In order to look into the evolution of starless condensations, it is essential to estimate their density as accurately as possible. The most reliable and straightforward probe of the evolution is the density. We carried out multitransition-line observations in order to do so, and this led us to a detection of a protostellar condensation that is very close to the moment of the formation of a protostellar core.

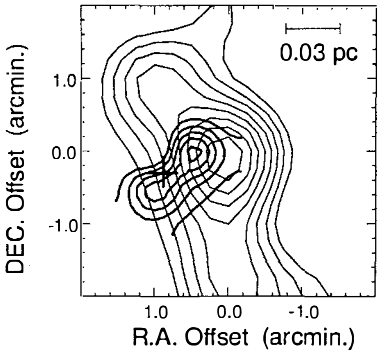

Figure 2: A map of integrated intensity of MC35 in Taurus in $H^{13}CO^{+}(J = 1-0)$ (thin) and in $H^{13}CO^{+}(J = 3-2)$ (thick). This is the second densest starless condensation. The center is $\alpha(1950) = 4^h32^m34^s8$, $\delta(1950) = 24°2'57''$.

2 Observations

2.1 Dense Core Survey in the Line of $C^{18}O(J = 1-0)$

We have carried out dense core surveys in $C^{18}O(J = 1-0)$ with NANTEN and the 4m radio telescopes at Nagoya University. The telescopes provide the same angular resolution of 2.7 arcmin(HPBW) at 109GHz. The nearby star forming regions we have observed include Taurus (Onishi et al. 1996, 1998), L1333 (Obayashi et al. 1998), Ophiuchus (Tachihara et al. 2000), Lupus (Hara et al. 1999), Corona Australis (Yonekura et al. 1999), Camaeleon (Mizuno et al. 1999), Southern Coalsack (Kato et al. 1999) and Pipe nebula (Onishi et al. 1999a). All these molecular clouds are located at a distance of 130-180pc and sufficient spatial resolution of ~0.1 pc is archived. These $C^{18}O$ observations were carried out based on the ^{13}CO surveys as mentioned in the introduction, and therefore, we now have a uniform sample of dense cores in almost all nearby low-mass star forming regions.

2.2 Compact Condensation Survey in the Line of $H^{13}CO^{+}(J = 1-0)$

We carried out a survey for high-density molecular cloud condensations in the line of $H^{13}CO^{+}$ $(J = 1-0)$ with the 45-m telescope at Nobeyama Radio Observatory (NRO) and SEST 15-m telescope toward Taurus, Ophiuchus, Chamaeleon, Lupus, and Pipe nebula. In the present paper, we will focus on the result toward Taurus star-forming region with the 45-m telescope. The 45-m telescope has a full beam width at a half-maximum of 20", which corresponds to 0.01 pc at a distance of 140 pc at 86.75433 GHz, the frequency of the $H^{13}CO^{+}(J = 1-0)$ line. This molecule traces the gas with $n(H_2) \gtrsim 10^5$ cm^{-3}. The observations were started from January 1992, and the first result was published elsewhere (Mizuno et al. 1994). Mizuno et al. (1994) observed targets toward all the protostar-like IRAS sources and several starless condensations. They reported a detection of 15 $H^{13}CO^{+}(J = 1-0)$ compact cores. The present survey was carried out on the basis of an extensive $C^{18}O$ survey made with the 4-m telescope at Nagoya University (Onishi et al. 1996). This $C^{18}O$ survey revealed the entire distribution of the molecular gas of density $n(H_2) \sim 10^4$ cm^{-3} at a scale of 0.1 pc in Taurus. The $H^{13}CO^{+}$ survey covered all the area whose H_2 column density derived from $C^{18}O$ observations is $> 1\times10^{22}$ cm^{-2}, and thus, high density gas of $n(H_2) > 10^5$ cm^{-3} is considered to be fully detected (Figure 1).

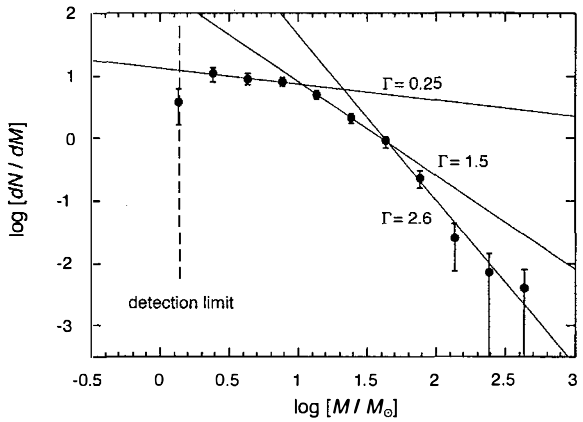

Figure 3: Mass spectrum of the $C^{18}O$ cores. Three solid lines show the best-fit functions of different mass ranges.

2.3 Density Measurements by High-Transition Line Observations of the Protostellar Condensations

In order to further study the evolution of the condensations, we need to obtain their densities more accurately. The best method to determine the density is to observe them with different transitions of the same molecule. In particular, we found that the $H^{13}CO^+(J = 3-2)$ is one of the best probes for the density because the intensity is much more sensitive to density than that in the $1-0$ line by LVG analysis. Twenty of the starless compact condensations were observed in the lines of $HCO^+(J = 3-2, 4-3)$ and $H^{13}CO^+(J = 3-2, 4-3)$ at CSO in August, 1997 and January, 2000. The beam sizes of the $J = 4-3$ and $J = 3-2$ lines were ~24" and 32", respectively. The observation indicates that most of the starless condensations have a density of $n(H_2) \sim 10^5$ cm^{-3}, whereas only a few have a density of $\sim 10^6$ cm^{-3} (e.g., Figure 2). One of the condensations, MC 27, the 27-th condensation in our catalog, is found to have the highest density of $\sim (8 \pm 1) \times 10^5$ cm^{-3}, significantly larger than those of the other starless condensations of $\lesssim 1-2 \times 10^5$cm^{-3}. This result strongly suggests that MC 27 is the most evolved starless condensation in Taurus. In order to pursue the evolutional status of MC 27, we describe the detailed characteristics and discuss the implications on the process of star formation in section 3.

3 Results and Discussion

3.1 $C^{18}O$ Dense Cores

Our observations in the $C^{18}O$ line revealed 179 dense cores in the observed regions. The cores are classified into 3 categories in terms of their star-formation activities as starless, star-forming, and cluster-forming, and their numbers are 136, 36, and 7, respectively. Cores with active star formation tend to have larger M, $N(H_2)$, and $n(H_2)$, and there seems to be a threshold value for star formation of $N(H_2)$ at $\sim 9 \times 10^{21}$cm^{-2}, which was originally suggested for the Taurus region by Onishi et al.(1998). Virial analysis of the cores shows that most are gravitationally bound and that the virial ratios are close to unity. The star formation efficiency derived from the total mass of the $C^{18}O$ cores is nearly constant at ~10%, nearly independent of the total core mass. We found that star-forming cores, not cluster forming cores, have a smaller linewidth than the starless cores of the same mass range. This indicates that turbulent decay leads to star

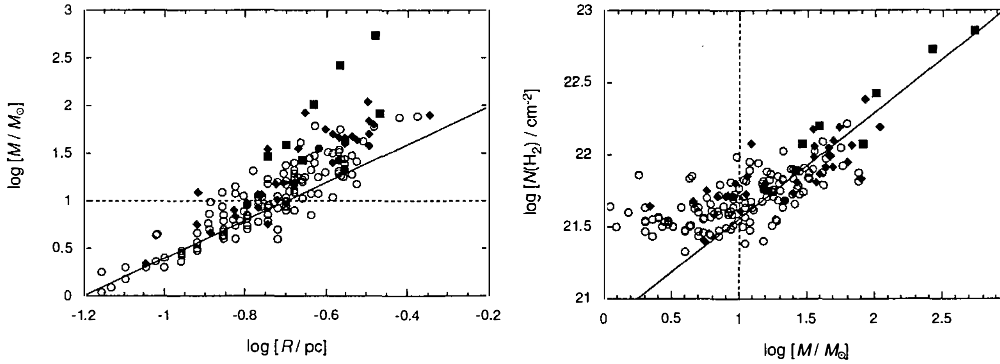

Figure 4: Left: Log-log plot of M versus R. Open circles, diamonds, and squares denote the starless, star-forming, and cluster-forming cores, respectively. The dotted line shows $M = 10M_{\odot}$. The solid line denotes the relation of $M \propto R^2$. Right: Log-log plot of N versus M. The solid line denotes the best-fit function of $N(H_2) \propto M^{-0.74}$ for the cores of $M > 10M_{\odot}$.

formation in the cores.

The mass spectrum of the cores is poorly fitted by a single power-low function. The power-law index in dN/dM is subject to change from 0.25 in the low-mass range to 2.6 in the high-mass range (Figure 3). The correlations among the M, R, and N shown in Figure 4 indicate how the cores evolve to form stars. For low-mass cores with $M < 10M_{\odot}$, the mass is almost proportional to the radius. On the other hand, the mass depends on the column density with constant radius for the higer-mass cores, i.e., the volume density increases with constant radius to increase the mass. There also seems to be a maximum radius of 0.3 pc, possibly related to the Jeans mass including the turbulent motion or magnetic field. It is to be noted here that there is no linewidth-size relation in the present sample. These results are summarized in Tachihara et al. (2002).

3.2 Mass Spectrum of Molecular Condensations

The mass spectrum of the cloud cores reflects the mechanism of their formation and disruption, and should be related to the stellar Initial Mass Function (IMF). It has been a long-standing question how the mass spectrum of the cloud cores is related to the local stellar IMF. The mass spectrum of molecular clouds or cores is surprisingly universal, not depending on the region studied and is found to be $dN/dM \sim M^{-(1.5-1.7)}$ (Dobashi et al. 1996; Yonekura et al. 1997; Kawamura et al. 1998, and see Table 4 of Yonekura et al. 1997), whereas the stellar IMF is $dN/dM \sim M^{-2.35}$ (Salpeter 1955). Our results, however, indicate the mass spectrum of the present condensations as $dN/dM \sim M^{-2.5}$ for $M > 3.5M_{\odot}$ (Figure 5). The slope is much steeper than that for lower-density molecular clouds. A similar result was found for dust condensations in cluster-forming cloud cores in ρ Ophiuchi cloud by Motte, André & Neri (1998). They detected 58 starless clumps and found that the mass spectrum is in the form of $dN/dM \sim M^{-2.5}$ above 0.5 $M_{\odot}$. However, the error in the slope is larger because there are only 9 clumps with a mass of > 0.5 $M_{\odot}$ in their sample. Testi & Sargent (1998) also found a similar result for dust condensations in cluster-forming cloud cores in the Serpens core in the form of $dN/dM \sim M^{-2.1}$, somewhat smaller slope index. Our result shows that the mass spectrum of gas condensations of $n(H_2) \sim 10^5$ cm^{-3} in one of the famous isolated and spontaneous star forming regions is much steeper than that of molecular clouds.

Next, we shall compare the mass spectrum with the IMF in further detail. Scalo (1998) and

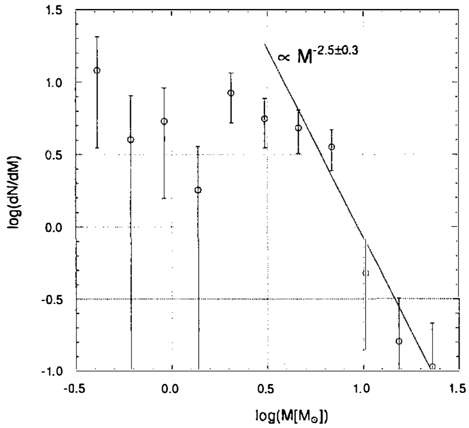

Figure 5: Mass spectrum of the 45 starless $H^{13}CO^+$ condensations. The straight line represents the best fit for $M > 3.5M_\odot$. The mass is derived by assuming that actual mass is propotional to the total $H^{13}CO^+$ luminosity, which is found to be propotional to the virial mass. When we adopt virial masses, the result is also the same.

Kroupa (2001) discussed the averaged stellar IMF and summarized that the slope of the IMF is different according to the mass range. For the stars with a mass larger than $\sim 0.5\ M_\odot$, the IMF has a slope index, α, of ~ 2.3, which is similar to that of the present condensations for $> 3.5\ M_\odot$. The slope of the stellar IMF gets shallower as the mass decreases. The turn over is also seen in the mass spectrum of the present condensations. $H^{13}CO^+$ condensations with a mass $\gtrsim 1M_\odot$ were considered to be almost fully detected in the present survey. Therefore, although the error is large because of the small number of the condensations with a small mass, the turnover is seen actually in Figure 5 for lower mass even if we consider the error and is not an effect of the incompleteness of the survey.

Here, we assume a star formation efficiency, mass of stars divided by mass of the gas plus stars, to be uniform. The average mass of the condensations are $\sim 3\ M_\odot$. The average stellar mass of YSOs with the similar luminosity is assumed to be $\sim 0.5\ M_\odot$ from the results of Hogerheijde et al.(1997) with an error of a factor of ~ 2 or more. Then, the star formation efficiency in the present sample is calculated to be $\sim 17\%$. A condensation mass of 1 $M_\odot$, where the turn over is actually seen, corresponds a stellar mass of 0.17 $M_\odot$, where the turn over is also seen in the averaged stellar IMF. This result shows that the shape of the mass spectrum of $H^{13}CO^+$ condensations is roughly similar to that of the IMF under the assumption. This implies that the mass of a young star is determined by the mass of the condensation if the assumption is correct. Namely, this suggests that the stellar IMF may be the result of the fragmentation process from less-dense cores (e.g., $C^{18}O$ cores) to the condensations, not the result of a way of accretion onto the star or the difference when the accretion stops. The assumption we adopted here, however, must be carefully checked, and further theoretical studies on fragmentation of dense gas are undoubtedly needed to better understand the origin of IMF.

3.3 Time Scale of the Molecular Condensations

It has been widely assumed that low-mass stars are formed in highly magnetically subcritical cloud cores, leading to quasi-static contraction of the cloud core via ambipolar diffusion (see, e.g., Shu, Adams, & Lizano 1987). However, a recent theoretical work brought up an important question on the physical state of cloud cores. Nakano (1998) claimed that cloud cores which will form low-mass stars should be magnetically supercritical. If a star is formed in a highly magnetically subcritical condensation via ambipolar diffusion, the time scale of the condensation process must be nearly equal to the magnetic flux loss time, which is more than 10 times longer than the free-fall time, whereas the time scale of the dissipation of turbulence is several times the free-fall time. Ciolek & Basu (2001) also suggested that the time scale of less subcritical condensations by ambipolar diffusion can be a few times the free-fall time.

Here, we estimate the time scale of the condensations in each evolutionary stage. Because the time scale of the condensations cannot be derived directly, a statistical method is used in order to derive it. If we assume steady star formation rate, the ratio of the number of objects at each stage is proportional to that of the time scale of each stage. This assumption seems plausible in Taurus because the amount of gas is sufficiently large compared to the total mass of the pre-main sequence stars (e.g., Ungerecht & Thaddeus 1987; Mizuno et al. 1995) and because stars have been formed at a roughly constant rate for the past 1– 2×10^6 yr in Taurus (Kenyon & Hartmann 1995). The measure of time is estimated from the number and age of T Tauri stars because the age can be estimated on the H-R diagram. There are $\sim$ 100 pre-main-sequence stars with ages of $\lesssim 10^6$ yr in Taurus (Kenyon et al. 1990). Thus, if we find N condensations of a given kind, the associated timescale is $\sim (10^6/100) \times N$ yr. We use this method in order to estimate the time scale of each stage in the following.

The condensations are expected to evolve in turn as follows; starless condensations, MC 27, condensations with a young protostar, and the remnant condensations. The numbers of condensations in each stage are 44, 1, 4, and 3, respectively (Onishi et al. 2002). This indicates that the time scales of condensations of each stage are estimated to be $\sim 4 \times 10^5$ yr, $\sim 1 \times 10^4$ yr, 3×10^4 yr, and 3×10^4 yr. It is to be noted that we consider here that the evolutionary stage of MC 27 is different from those of starless condensations, because MC 27 has unique properties among starless condensations as described in section 2.2. The detailed discussion on the evolutionary stage of MC 27 is described in section 3.4.

The time scale of the starless condensations, $\sim 4 \times 10^5$ yr, is several times larger than free-fall time scale of gas with 10^5 cm^{-3}, $\sim 10^5$ yr. This means that some other mechanisms are needed to support for self-gravitating condensations, and magnetic force is considered to be the crucial ingredient (see, Shu et al. 1993). If a condensation is a highly subcritical one that are supported against its self-gravity by magnetic force, the condensation is expected to contract as the magnetic field is lost by ambipolar diffusion (Lizano & Shu 1989). However, the magnetic flux loss time is more than 10 times larger than the free-fall time, which is larger than that of the present starless condensations. Turbulence decay of super-critical condensations (Nakano 1998) or ambipolar difussion of less subcritical condensations (e.g., Ciolek & Basu 2001) has a shorter time scale down to a few-several times the free-fall time, which is consistent with the present value.

On the other hand, the time scale of MC 27 is much shorter than that of the starless condensations. The central density is as much as $\sim 10^6$cm^{-3}. The free-fall time of gas with $n(\mathrm{H_2}) \sim 10^6$ cm^{-3} is $\sim 3 \times 10^4$ yr, which is similar to the time scale of MC27, $\sim 1 \times 10^4$ yr, as estimated above. This means that MC27 is dynamically contracting. These facts strongly suggest that MC 27 is dynamically collapsing and is very close to the moment of the formation of a protostellar core within a time scale of $\sim 10^4$ yr.

The short time scale for condensations with young protostars indicates that the main accretion from the surrounding gas of $n(\mathrm{H_2}) \sim 10^{5-6}$cm^{-3} continues only for $\sim 3 \times 10^4$ yr. This time scale is also consistent with the free-fall time of gas with $n(\mathrm{H_2}) \sim 10^6$ cm^{-3}. The density of $n(\mathrm{H_2}) \sim 10^6$ cm^{-3} corresponds to the radius of $\sim$0.005 pc (1000 AU), and the mass within the radius is $\sim 0.5\ M_\odot$ if we assume a density distribution of $n \sim \mathrm{r}^{-2}$. These facts suggest that once a dynamical accretion occurs, the mass of a star accrete onto the circumstellar disk and/or directly onto the star in the dynamical time scale of $\sim 3 \times 10^4$ yr.

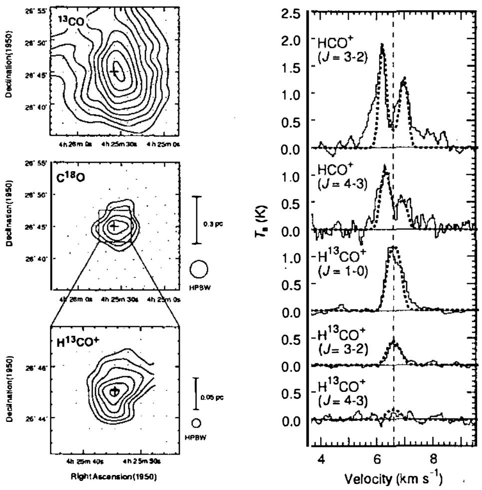

Figure 6: Left:Contour maps of ^{13}CO J = 1–0, C^{18}O J = 1–0, and H^{13}CO$^+$ J = 1–0 total intensity of MC 27. The first two were obtained with the Nagoya 4-m telescope and the last was obtained with the Nobeyama 45-m telescope. The position of the center of the H^{13}CO$^+$ map is indicated by crosses. The position is $\alpha(1950) = 4^h25^m34^s5$, $\delta(1950) = 26°45'4''$. Right:Spectra of the center of MC 27 taken with the 10.4-m telescope at the Caltech Submillimeter Observatory (CSO), except for H^{13}CO$^+$ J = 1–0 with the 45-m telescope. The names of the lines are indicated in the figure. The dashed lines are model-fitted spectra by a Monte-Carlo simulation. The fitted model has a constant infall velocity of 0.2 km s^{-1} only within 3000 AU from the center.

3.4 MC 27: the Moment of the Formation of a Protostellar Core

One of the condensations, named MC 27 in our surveyed molecular condensations, exhibits fairly strong and narrow H^{13}CO$^+$ emission of the J =3–2, and 1–0 transitions, as well as self-reversed profiles of HCO$^+$ J =4–3 and 3–2 (Figure 6). The LVG analysis shows that MC 27 has a density of $\sim 10^6$cm^{-3} within ~1000 AU at the center, while the other starless condensations have a density of $\sim 10^5$cm^{-3} toward the observed position. MC 27 shows a sharply peaked density distribution; the molecular intensity is well fitted by a power-law density distribution of r^{-2} over 0.02 pc $< r <$ 0.2 pc. A statistical analysis indicates a very short time scale of $\sim 10^4$ yr, which is consistent with a free-fall time scale for a density of $\sim 10^6$ cm^{-3}. These properties strongly suggest that MC 27 is in a very early stage of star formation. We will show the details in the following.

Figure 6 shows the ^{13}CO, C^{18}O, and H^{13}CO$^+$ $J = 1 - 0$ integrated intensity maps of MC 27 (Mizuno et al. 1994; Mizuno et al. 1995; Onishi et al. 1996, 1998). These maps indicate that MC 27 has a nearly circularly symmetric shape from the low-density region of 10^3cm^{-3} up to the high-density region of 10^5cm^{-3}. The integrated intensity distribution of C^{18}O and H^{13}CO$^+$ $J = 1 - 0$ can be fitted by a single power-law ranging in the form of $N \sim r^{-0.9\pm0.2}$ and $N \sim r^{-0.8\pm0.1}$, respectively, for $0.02 \lesssim$ r $\lesssim 0.2$ pc after correcting for beam dilution. If we take into account its symmetric shape, it is likely that the density distribution follows a power law of $\sim r^{-(1.8-1.9)}$, whereas the index values of a typical starless condensation are $-1 - -1.5$ (Ward-Thompson et al. 1994). MC 27 therefore shows one of the steepest density distribution among starless condensations.

Figure 6 also shows the spectra of HCO$^+$ $J = 3-2, 4-3$ and H^{13}CO$^+$ $J = 1-0, 3-2, 4-3$ obtained toward the center of MC 27. The broad and asymmetric profiles of the HCO$^+$ $J = 3-2$ and $4-3$ lines indicate a large optical depth and self-absorption due to the foreground gas. This self-absorption is likely to be caused by dense gas of $n(\mathrm{H_2}) \sim 10^5$ cm^{-3}, physically associated

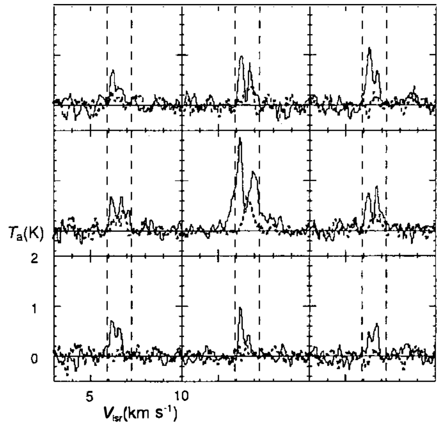

Figure 7: Profile maps of HCO^+ J = 3–2(solid) and $H^{13}CO^+$ J = 3–2 (dashed) of MC 27. The observed grid spacing is 30$''$, corresponding to 4000 AU. The $H^{13}CO^+$ J = 3–2 profiles are scaled by 1.67. The broken lines drawn vertically indicate V_{lsr} = 5.9 and 7.2 km s^{-1}.

with MC 27. The HCO^+ $J = 3 - 2$ line has apparent wing-like velocity components at $V_{lsr} \lesssim$ 5.8 and $V_{lsr} \gtrsim$ 7.4 km s^{-1}. The profile maps of HCO^+ $J = 3 - 2$ in figure 7 show that the wing-velocity components are seen only toward the center. On the other hand, the $J = 1 - 0$ and $3 - 2$ spectra of less-abundant $H^{13}CO^+$ have single and narrow profiles of line-width $\Delta v \sim$ 0.6 km s^{-1}, comparable to those of the others without stars, while the $J = 4 - 3$ emission is not detected with the present sensitivity. The profile maps of $H^{13}CO^+$ $J = 3 - 2$ in figure 7 show that the high-density region is very compact within $\lesssim$ 15" of the $H^{13}CO^+$ $J = 1 - 0$ peak, i.e., $\lesssim$ 2000 AU.

The HCO^+ asymmetric profile with a brighter blue peak of the HCO^+ profiles is qualitatively explicable by an infall motion in a collapsing spherical cloud (e.g., Zhou et al. 1993). In order to test quantitatively how the infall model is applicable to MC 27, we carried out a model fitting using Monte-Carlo simulations (Bernes 1979). The simulation indicates that the infall velocity at 2000–3000 AU should be 0.2–0.3 km s^{-1} while it is less than 0.3 km s^{-1} at ~1000 AU. This derived infall velocity profile can be explained by a dynamical-collapse model of supercritical condensation $\sim 10^{3-4}$ yr prior to formation of the first protostellar core (See Onishi et al. 1999b).

As discussed above, MC 27 is unique among the starless condensations in Taurus. In particular, it has the largest density of ~10^6 cm^{-3}. This is significantly higher than that of the other present starless condensations, $\sim 10^5$ cm^{-3}, typical of low-mass star-forming regions. This suggests that MC 27 is the most evolved starless condensation in terms of gravitational collapse. The time scale of MC 27 is very short, $\sim 10^4$ yr, as mentioned in section 3.3. The upper limit for the luminosity, $\sim 0.1\ L_\odot$ (Kenyon & Hartmann 1995), can be used to further constrain the evolutionary stage. We shall assume a steady mass-accretion rate given by $\dot{M} = 0.975 c_s^3/G$ (Shu 1977) , where c_s is the effective sound speed, $2 \times 10^{-6}\ M_\odot$ yr^{-1} for 10 K molecular gas. The accretion luminosity is calculated as $L_{acc} = GM_*\dot{M}/R_*$, where M_* is the stellar mass and R_* is the stellar radius. The luminosity being $\lesssim 0.1\ L_\odot$ implies a stellar mass of $\lesssim 0.01\ M_\odot$ if we adopt a stellar radius of 1.5 $R_\odot$ for stellar mass of $\lesssim 0.3\ M_\odot$ from the numerical simulation by Stahler (1988). The age of a 0.01 $M_\odot$ protostar under a constant mass-accretion rate is then calculated to be $\sim 10^4$ yr, consistent with that of MC 27 derived above. Therefore, even if MC 27 has already formed a star, the age of the star must be $\lesssim 10^4$ yr. Such a low-luminosity protostellar object in the early stage of star formation has been studied in previous theoretical work (e.g., Boss & Yorke 1995). According to Boss and Yorke (1995), a luminosity $\lesssim 0.1\ L_\odot$ corresponds to a stage younger than $\sim 2 - 10^4$ yr, which they call Class –I. At this stage, the first protostellar core consisting of molecular hydrogen may have been formed or, alternatively, the second (final) protostellar core may have been just formed.

Infall motion has been claimed for another starless condensation in L1544 based on asymmetric self-absorbed profiles (Tafalla et al. 1998). Although L1544 was not part of our original survey, we recently mapped it in $H^{13}CO^+(J = 1-0)$(Onishi et al. 2004, in preparation). The molecular gas of L1544 is spatially more extended than that of MC27 in the line of $H^{13}CO^+(J = 1-0)$. The index of the density profile of L1544 has been derived to be ~ -1.5 and the spatial distribution of the L1544 molecular cloud is not circularly symmetric, especially in the $J = 1-0$ line of $C^{18}O$ (Tafalla et al. 1998, see also Tafalla, this volume). The spherically asymmetric distribution of the molecular gas in L1544 makes any discussion of infall inconclusive, since the self-absorption feature is easily affected by the distribution of the surrounding low-density gas. Molecular line observations with higher-J transitions are necessary to estimate a density higher than $\sim 10^5$ cm^{-3}, as discussed above. We observed the core center of L1544 ($\alpha(1950) = 5^h 1^m 12\overset{s}{.}5$, $\delta(1950) = 25°6'40''$) in $H^{13}CO^+(J = 3-2)$ by using the CSO telescope. The peak antenna temperature is observed to be $\sim$ 0.1K, while that of MC27 is $\sim$ 0.4K. This suggests that the density of L1544 toward the position is lower than that of MC27 and is estimated to be a few $\times 10^5$ cm^{-3}, which is a typical value for the other starless $H^{13}CO^+(J = 1-0)$ condensations (Onishi et al. 2002). Additional mapping observations should reveal the evolutionary status of L1544 more precisely.

We next discuss the wing feature of the HCO^+ $J = 3-2$ line. These wings are localized toward the center of MC 27, at $\lesssim$ 1500 AU. The model fitting discussed above indicates that the origin is probably due to outflow. The estimated dynamical time scale for the wings is $\sim 10^4$ yr or smaller, which is consistent with that of MC 27. If the wing feature is really due to outflow, this result indicates that the outflow phenomenon occurs at a very early stage of protostellar collapse. Recent theoretical calculations (e.g. Kudoh & Shibata 1997) indeed show that outflow can begin at a very early stage of dynamical collapse after a rotating disk is formed, and that the velocity of the protostellar jet is estimated to be around the Keplerian velocity. If a protostellar core of 0.01 $M_\odot$ has already formed in MC 27, the inner gas can have a Keplerian velocity of $\gtrsim$ 10 km s^{-1} at the inner edge of the disk, which can be a cause of the outflow. High-resolution interferometric observations in higher-J transitions could be used to probe the inner structure of MC 27, thus allowing us to study the origin and onset of the outflow.

Submillimeter molecular observations of starless condensations revealed a starless condensation, MC 27, that is only less than $\sim 10^4$ yr away from the moment of protostar formation. The present study suggests the importance of the molecular observations in higher transition lines to measure the density accurately and then to investigate the evolutionary stage. Moreover, the detection of condensations like MC 27 is important to study the process of dynamical collapse. Further studies of dense molecular condensations are needed for other star-forming regions, such as Ophiuchus, Chamaeleon and Lupus, since the number of condensations like MC 27 is only $\sim$ 1/100 of the young stars of age $\sim 10^6$ yr because of its very short time scale of $\sim 10^4$ yr. With these further studies, we can obtain a better comprehensive understanding of the most basic problem, how a protostar is formed via the contraction of molecular gas.

References

1. André P., Ward-Thompson D., & Barsony M. 1993, ApJ 406, 122
2. Bernes, C. 1979, A&A, 73, 67
3. Boss A.P.,& Yorke H.W. 1995, ApJ 439, L55
4. Ciolek, G.E., & Basu, S. 2001, ApJ, 547, 272

5. Dobashi, K., Bernard, J.P.,& Fukui, Y. 1996, ApJ, 466, 282
6. Fukui Y., Iwata T., Takaba H., Mizuno A., Ogawa H., Kawabata K.,& Sugitani K. 1989, Nature 342, 161
7. Hogerheijde, M. R., Dishoeck, E. F., Blake, G. A., & van Langevelde, H. J., 1997, ApJ, 489, 293
8. Kato, S., Mizuno, N., Asayama, S., *et al.* 1999, PASJ, 51,883
9. Kawamura, A., Onishi, T., Yonekura, Y., Dobashi, K., Mizuno, A., Ogawa, H.,& Fukui, Y. 1998, ApJS, 117, 387
10. Kenyon S.J., Hartmann L.W., Strom K.M.,& Strom S.E. 1990, AJ 99, 869
11. Kenyon S.J.,& Hartmann L. 1995, ApJS 101, 117
12. Kroupa, P. 2001, MNRAS, 322, 231
13. Kudoh T.,& Shibata K. 1997, ApJ 476, 632
14. Lada C.J. 1987, in IAU Symp. 115, Star forming regions , ed. M. Peimbert, J. Jugaku (D. Reidel:Dordrecht) p1
15. Lizano S.,& Shu F.H. 1989, ApJ 342, 834
16. Hara, A., Tachihara, K., Mizuno, A., *et al.* 1999, PASJ, 51, 895
17. Herbig G.H.,& Bell K.R 1988 Lick Obs. Bull. Ser., No. 1111
18. Mizuno, A., Onishi, T., Hayashi, M., Ohashi, N., Sunada, K., Hasegawa, T.,& Fukui, Y. 1994, Nature, 368, 719
19. Mizuno A., Onishi T., Yonekura Y., Nagahama T., Ogawa H., & Fukui Y. 1995, ApJ 445, L161
20. Mizuno, A., Hayakawa, T., Tachihara, K., *et al.* 1999, PASJ, 51, 859
21. Motte F., André P.,& Neri R. 1998, A&A 336, 150
22. Nakano T. 1998, ApJ 494, 587
23. Obayashi, A., Kun, M., Sato, F., Yonekura, Y., & Fukui, Y. 1998, AJ, 115, 274
24. Onishi, T., Mizuno, A., Kawamura, A., Ogawa, H., & Fukui, Y. 1996, ApJ, 465, 815
25. Onishi, T., Mizuno, A., Kawamura, A., Ogawa, H., & Fukui, Y. 1998, ApJ, 502, 296
26. Onishi, T., Kawamura, A., Abe, R., Yamaguchi, N., Saito, H., Moriguchi, Y., Mizuno, A., Ogawa, H., & Fukui, Y. 1999a, PASJ, 51, 871
27. Onishi, T., Mizuno, A.,& Fukui, Y. 1999b, PASJ, 51, 257
28. Onishi, T., Mizuno, A., Kawamura, A., Tachihara, K., & Fukui, Y. 2002, ApJ, 575, 815
29. Salpeter, E.E. 1955, ApJ, 121, 161
30. Scalo, J. M. 1998, in The Stellar Initial Mass Function, eds. G. Gilmore & D. Howell (San Francisco; ASP), 201
31. Shu F.H. 1977, ApJ 214, 488
32. Shu F.H., Adams F.C.,& Lizano S. 1987, ARA&A 25, 23
33. Shu F., Najita J., Galli D., Ostriker E.,& Lizano S. 1993, in Protostars and Planets III, ed. Levy, E.H., & Lunine, J.I.(Tucson & London: The University of Arizona Press), p.3
34. Stahler S.W. 1988, ApJ 332, 804
35. Tachihara, K., Mizuno, A., & Fukui, Y. 2000, ApJ, 528, 817
36. Tachihara, K., Onishi, T., Mizuno, A., & Fukui, Y. 2002, A&A, 385, 909
37. Tafalla M., Mardones D., Myers P.C., Caselly P., Bachiller R.,& Benson P.J. 1998, ApJ, 504, 900
38. Testi L.,& Sargent A.I. 1998, ApJ 508, L91
39. Ungerechts H.,& Thaddeus P. 1987, ApJS 63, 645
40. Yonekura, Y., Dobashi, K., Mizuno, A., Ogawa, H.,& Fukui, Y. 1997, ApJS, 110, 21
41. Yonekura, Y., Mizuno, N., Saito, H., *et al.* 1999, PASJ, 51, 911
42. Ward-Thompson D., Scott P.F., Hills R.E.,& André P. 1994, MNRAS 268, 276
43. Zhou, S., Evans, N.J.II, Köpe, C.,& Walmsley, C.M. 1993, ApJ, 404, 232

Santé !

The Origin of the IMF from Core Mass Functions

S.P. Goodwin, A.P. Whitworth & D. Ward-Thompson

Department of Physics & Astronomy, Cardiff University
5 The Parade, Cardiff, CF24 3YB, UK

We examine the initial mass functions (IMFs) of stars produced by different molecular core mass functions. Simulations suggest that more massive cores produce more stars, so we propose a model in which the average number of stars formed in a core is equal to the initial number of Jeans masses in that core. Small-N systems decay through dynamical interactions, ejecting low-mass stars and brown dwarfs which populate the low-mass tail of the IMF. Stars which remain in cores are able to competitively accrete more gas and become more massive. We deduce the forms of the core mass functions required to explain the IMFs of Taurus, Orion, IC 348 and NGC 2547. These core mass functions fall into two categories - one which peaks at a few $M_\odot$ to explain Taurus and NGC 2547, and one that peaks at around $0.2M_\odot$ to explain Orion and IC 348.

Keywords: Stars - formation, Stars - mass function

1 Introduction

All stars form in dense molecular cores (eg. André et al. 2000). Observations of the densest cores, known as prestellar cores (Ward-Thompson et al. 1994), show that their mass functions are remarkably similar to the IMF of field stars (Motte et al. 1998; Testi & Sargent 1998; Motte et al. 2001). This suggests that the form of the IMF may be directly related to the form of the core mass function (CMF).

Most stars $> 1M_\odot$ exist in binary or multiple systems (eg. Duquennoy & Mayor 1991). Most of these multiple systems *must* form as such, since it has been shown that dynamical evolution is unable to significantly alter the initial binary properties or population (Kroupa 1995). Therefore many cores must produce multiple objects and so the IMF cannot be a simple mapping of the CMF.

In a previous paper (Goodwin et al. 2004c) we showed that the IMF of Taurus could be explained if all of the stars in Taurus formed from cores of a few solar masses, a CMF similar to

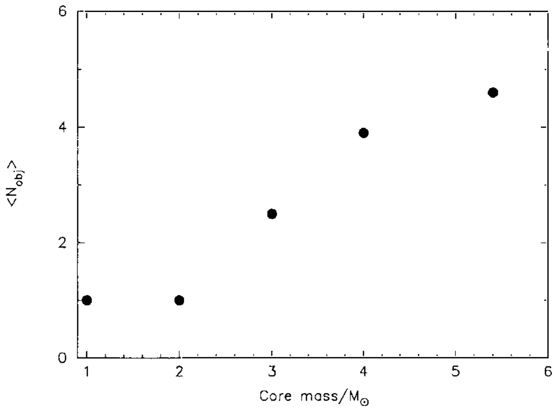

Figure 1: The average number of objects $< N_{\rm obj} >$ formed in cores of different masses, each with the same initial turbulent virial ratio $\alpha_{\rm turb} = E_{\rm turb}/|\Omega| = 0.1$. The average number of objects scales roughly linearly with the initial number of Jeans masses in the core.

that observed by Onishi et al. (2002). In this contribution we investigate the effect of changing the CMF on the IMF and multiplicity of star forming regions.

2 Multiple star formation in cores

Recent studies have shown that within massive ($> 5M_\odot$) turbulent cores, multiple star formation is the norm (Bate et al. 2002, 2003; Delgado Donate et al. 2004; Goodwin et al. 2004a,b). A significant population of low-mass stars and brown dwarfs is formed by ejections from unstable multiple systems in these cores.

Delgado Donate et al. (2003) modelled the origin of the IMF by assuming that fragmentation in cores is scale-free: ie. that all cores produce the same number of objects (stars and brown dwarfs) and that the masses of these objects scale with the mass of the core. By convolving the outcome of star formation in a $1M_\odot$ core with a core mass function (CMF) they obtained an IMF. However, Goodwin et al. (in preparation) find that the number of objects that form depends strongly upon the mass of a core, with low-mass cores being far less able to form multiple objects than more massive cores. Fig. 1 shows the average number of objects that form in cores of different masses but with the same initial thermal and turbulent virial ratios (the ratio of the initial thermal or turbulent energy to the initial potential energy). The average number of objects that form is approximately one per initial Jeans mass ($\sim 1M_\odot$).

Given that most stars form in multiple systems and the number of stars forming in a core might be expected to increase with the mass of the core, we propose a simple model for the formation of stars within cores and the relationship of stellar masses and multiplicities to the core mass (the core-to-star relationship):

- Cores form an average number of objects (stars and/or brown dwarfs) approximately equal to the initial number of Jeans masses in the core (eg. Goodwin et al. in prep).
- Multiple systems with ≥ 3 members are initial unstable and will decay to a stable system within a few $\times 10^4$ yrs through the ejection of low-mass stars and brown dwarfs (cf. Reipurth & Clarke 2001; Bate et al. 2002; Sterzik & Durisen 2003; Goodwin et al. 2004a).

The initial mass function (IMF) is then due to the convolution of the core mass function (CMF) *and* the core-to-star relationships in these different cores.

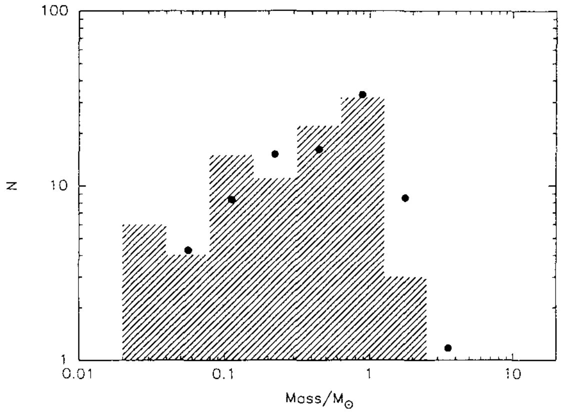

Figure 2: The IMFs of Taurus (histogram, from Luhman et al. 2003a) and NGC 2547 (points, from Jeffries et al. 2004). NGC 2547 has been normalised to contain the same total number of stars as Taurus for ease of comparison.

We assume a form for the CMF - in this case a log-normal which may have different variances above and below the mean - and randomly sample cores from that CMF. A core then produces N_* objects where N_* is drawn from a gaussian of mean $M_{\rm core}$ (where $M_{\rm core}$ is the core mass in solar masses) with $\sigma = 2$. N_* is then rounded to the nearest integer ≥ 1.

If $N_* \leq 3$ then N_* stars are formed of mean mass $\epsilon M_{\rm core}/N_*$ (we assume that the core-to-star efficiency $\epsilon = 0.75$ in all cases).

If $N_* > 3$ then $N_* - 3$ stars are ejected with masses drawn uniformly from a logarithmic distribution between $0.02 M_\odot$ and $0.1 \epsilon M_{\rm core}$. The remaining three stars then distribute the rest of the mass in the core between themselves such that their individual masses are $\epsilon(M_{\rm core} - M_{\rm ej})/3$ (where $M_{\rm ej}$ is the mass of ejected stars).

3 Results

3.1 The IMFs of Taurus and NGC 2547

Both Taurus (Luhman et al. 2003a) and NGC 2547 (Jeffries et al. 2004) have similar MFs. Both of these MFs show a significant peak at $\sim 1 M_\odot$, with a rapid drop above this peak, and a rather flatter decline into the brown dwarf regime, as illustrated in Fig. 2 (where the MF of NGC 2547 has been normalised to have the same total number of stars as Taurus for ease of comparison). The similarity between the two MFs is clear.

Fig 3 shows the results of applying our model to a log-normal CMF of mean $\log \bar{M}_{\rm core} = 0.5$ and $\sigma_{\log M_{\rm core}} = 0.1$ (illustrated by the dashed-line in Fig 3) which is a reasonable approximation to the CMF of Taurus as observed by Onishi et al. (2001). The hashed histogram is the observed IMF of Taurus (Luhman et al. 2003a) and it compares well to the open histogram given by our model. The open circles show the contribution to the IMF from ejected stars and brown dwarfs. The binary fraction is very high in our model as the vast majority of stars have formed in multiple systems, only the ejected component has a low multiplicity. This again compares well with the high observed multiplicity in Taurus (Duchêne 1999).

This agrees well with the results of Goodwin et al. (2004c), the IMF is a combination of a peak of bound systems with average stellar mass $\approx 1 M_\odot$ which remain bound in the cores, and a flat low-mass tail of ejected brown dwarfs and low-mass stars.

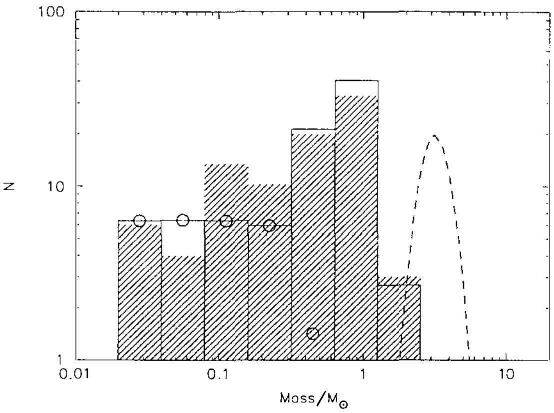

Figure 3: The open histogram shows the IMF resulting from the CMF shown by the dashed line. Open circles show the contribution to each bin of ejected stars and brown dwarfs. The hashed histogram shows the Luhman et al. (2003a) Taurus IMF. Both histograms are normalised to contain the same number of stars.

3.2 The IMFs of Orion and IC 348

Orion has an IMF that is very similar to the field (Muench et al. 2002). Fig. 4 shows the fit to the Orion IMF given by a CMF of mean $\log\bar{M}_{\rm core} = -0.8$ and $\sigma_{\log M_{\rm core}} = 0.3$ (lower) and $= 0.7$ (upper).

Figure 4 reproduces the IMF of Orion well with a wide, flat peak between 0.1 and $0.6 M_\odot$, falling at both ends, with an approximately Salpeter slope at high-masses. Fig. 5 shows the binary fraction as a function of primary mass. This model fits the observed field binary fractions quite well, except at lower masses where it is assumed that all ejected stars and brown dwarfs are single (which is not always the case, a low fraction of ejected stars are multiples, see Goodwin et al. 2004b).

IC 348 has an IMF that is very similar to Orion except that it is relatively deficient in brown dwarfs (Luhman et al. 2003b). Fig. 6 shows the fit to the IMF of IC 348 using a CMF of mean $\log\bar{M}_{\rm core} = -0.8$ and $\sigma_{\log M_{\rm core}} = 0.1$ (lower) and $= 0.7$ (upper). This is almost identical to the CMF used to model Orion, but the lower extent of the CMF is far smaller (0.1 compared to 0.3 in the Orion CMF). Almost no brown dwarfs are formed in cores in IC 348, they are all the result of ejections from higher-mass cores.

4 Conclusions

Using a simple model of fragmentation in cores we are able to match the IMFs of Taurus, NGC 2547, Orion and IC 348 with different core mass functions.

The IMFs of Taurus and NGC 2547 are well-fitted with a CMF that peaks at a few solar masses, which matches the observed CMF of Taurus (Onishi et al. 2002). This CMF reproduces the peaks in these IMFs at $\sim 1 M_\odot$. Most solar-type stars are formed in multiple systems, explaining the very high observed binary fraction in Taurus (Duchêne 1999).

To fit the IMFs of Orion and IC 348 requires CMFs that peak at only a few tenths of a solar mass. The lack of brown dwarfs in IC 348 as compared to Orion can be explained by a CMF that does not extend as far into the brown dwarf regime in IC 348. The binary fractions in Orion and IC 348 are close to those observed in the field.

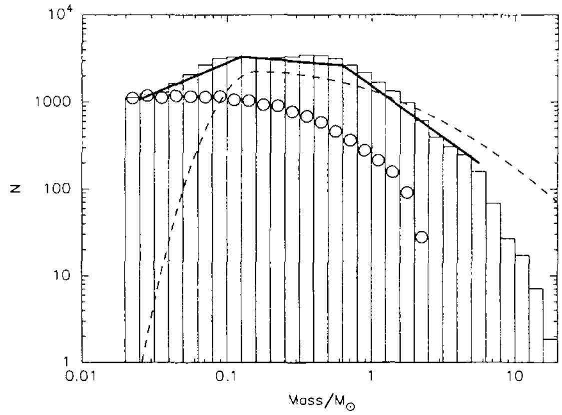

Figure 4: The IMF of Orion (solid line, from Muench et al. 2002) is well-fitted by the open histogram produced by the CMF shown by the dashed-line. As in fig. 3, the circles show the contribution to the IMF from ejected stars.

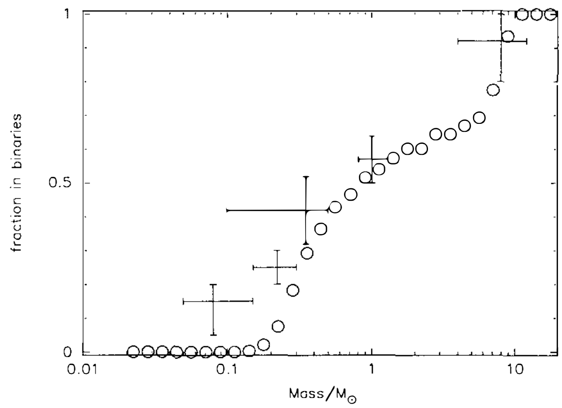

Figure 5: The binary fraction of stars in the model of Orion as a function of primary mass (Open circles). The error bars show the observations of the field binary fraction adapted from Sterzik & Durisen (2003).

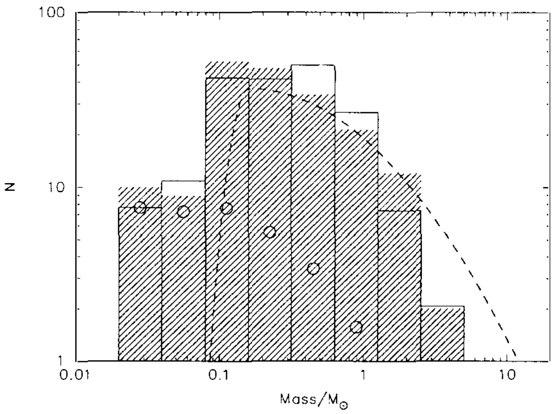

Figure 6: The IMF of IC 348 (hashed histogram, from Luhman et al. 2003b) is well-fitted by the open histogram produced by the CMF shown by the dashed-line. As in fig. 3, the circles show the contribution to the IMF from ejected stars.

Acknowledgements

SPG is a UK Astrophysical Fluids Facility (UKAFF) Fellow.

References

1. André, P., Ward-Thompson, D. & Barsony, M. 2000, *Protostars and Planets IV* (University of Arizona Press, Tucson; Eds. V. Mannings, A. P. Boss & S. S. Russell), p.59
2. Bate, M. R., Bonnell, I. A. & Bromm, V. 2002, MNRAS, 332, L65
3. Bate, M. R., Bonnell, I. A. & Bromm, V. 2003, MNRAS, 339, 577
4. Delgardo Donate, E., Clarke, C. J. & Bate, M. R. 2003, MNRAS, 342, 926
5. Delgardo Donate, E., Clarke, C. J. & Bate, M. R. 2004, MNRAS, 347, 759
6. Duchêne, G. 1999, A&A, 341, 547
7. Duquennoy, A & Mayor, M. 1991, A&A, 248, 485
8. Goodwin, S. P., Whitworth, A. P. & Ward-Thompson, D. 2004a, A&A,
9. Goodwin, S. P., Whitworth, A. P. & Ward-Thompson, D. 2004b, A&A,
10. Goodwin, S. P., Whitworth, A. P. & Ward-Thompson, D. 2004c, A&A,
11. Jeffries, R. D., Naylor, T., Devey, C. R. & Totten, E. J. 2004, astro-ph/0404028
12. Kroupa, P. 1995, MNRAS, 277, 1522
13. Luhman, K. L., Briceño, C., Stauffer, J. R., Hartmann, L., Barrado y Navascués, D. & Nelson, C. 2003a, ApJ, 590, 348
14. Luhman, K. L., Stauffer, J. R., Muench, A. A., Rieke, G. H., Lada, E. A., Bouvier, J. & Lada, C. J. 2003b, ApJ, 594, 758
15. Motte, F., André, P. & Neri, R. 1998, A&A, 336, 150
16. Motte, F., André, P., Ward-Thompson, D. & Bontemps, S. 2001, A&A, 372, L41
17. Muench, A. A., Lada, E. A., Lada, C. J. & Alves, J. 2002, ApJ, 573, 366
18. Onishi, T., Mizuno, A., Kawamura, A., Tachihara, K & Fukui, Y. 2002, ApJ, 575, 950
19. Reipurth, B. & Clarke, C. J. 2001, AJ, 122, 432
20. Sterzik, M. F. & Durisen, R. H. 2003, A&A, 400, 1031
21. Testi, L. & Sargent, A. 1998, ApJ, 508, L91
22. Ward-Thompson, D., Scott, P. F., Hills, R. E. & André, P. 1994, MNRAS, 268, 276

LOW-MASS SUBSTELLAR CANDIDATES IN NGC 2264

TIM KENDALL[1], JEROME BOUVIER[1], ESTELLE MORAUX[2] and DAVID JAMES[3]

1. Laboratoire d'Astrophysique de Grenoble, BP 53X, 38041 Grenoble Cedex, France
2. Institute of Astronomy, University of Cambridge, Madingley Road, Cambridge, CB3 0HA, UK
3. Physics & Astronomy Dept., Vanderbilt University, 1807 Station B, Nashville, TN 37235 USA

NGC 2264 is a young (3 Myr), populous star forming region for which our optical studies have revealed a very high density of potential brown dwarf (BD) candidates - 236 in $< 1\,\mathrm{deg}^2$ - from the substellar limit down to $\sim 20\,\mathrm{M_{Jup}}$. Candidate BD were first selected using wide field (I, z) band imaging with CFHT/12K, by reference to current theoretical isochrones. Subsequently, around 50% of the I, z sample were found to have near-infrared (2MASS) photometry, allowing further selection by comparison with the location of DUSTY isochrones in colour-colour diagrams involving combinations of I,J,H and K colours. After rejection of objects with only upper limits to J, six candidates were selected from the $I-K, J-H$ diagram which afforded the best separation of candidate and field objects; of these, 2 also lie close to the model predictions in the $I-J, I-K$ and $I-J, H-K$ plots. After dereddening, all six remain probable very low-mass NGC2264 members, in spite of their low A_V, while a different group of objects are shown to be highly reddened background giants. A further three brighter (at I) objects selected by their $I-J, I-K$ colours, lie at the substellar limit and are likely cluster objects, as are 2 intermediate mass objects selected by their $I-K$ and $H-K$ colours. These objects potentially constitute a hitherto unknown population of young, low-mass BD in this region; only slighty deeper observations could reveal a new laboratory for the study of near-planetary-mass objects.

Keywords: stars: low mass, brown dwarfs – infrared: stars – surveys – Galaxy: open clusters and associations

1 Introduction

Within the last few years the observational study of substellar objects ($M < 0.072\,M_\odot$) has undergone spectacular and rapid development, opening up new perspectives on the formation of such objects within molecular clouds. Large numbers of BD have now been found in star-forming regions, young clusters and the field[1,2,3,4] and physical models of the atmospheres of BD constructed[5,6], opening up the possibility of confrontation between observations and theoretical predictions of the physical properties of BD. However, the core issues of the form of the substellar initial mass function (IMF) and its dependence on environment remain to be addressed. The discovery of BD in widely differing environments does suggest their formation is directly linked to the star formation process, and early estimates of the substellar IMF in the solar neighbourhood have indicated that BD are nearly as numerous as stars. Within this broad framework, two competing scenarios have been put forward for BD formation; the first simply that they form as stars do, i.e. by the gravitational collapse of low mass molecular cloud cores[7]; the second postulates the dynamical ejection of the lowest mass protostars, leading to BD formation since the ejected fragments are unable to futher accrete[8]. To distinguish between these possibilities and to obtain unbiased estimates of the substellar IMF, observations of statistically complete, homogeneous populations of BD are needed in a wide variety of environments with different ages. Such a deep, wide-field imaging survey has been performed in the I, z bands with CFHT/12K/MegaCam: "Brown dwarfs and the substellar mass function: Clues to the star formation process", initiated by J. Bouvier and collaborators.

The study of NGC 2264 introduced here is only a small part (0.6 deg^2) of the whole survey, which, for the first time, has covered significant areas (70 deg^2) of star-forming environments, pre-main sequence clusters and older open clusters (ages 1–600Myr) with the aim of reaching $I \sim 24$ which corresponds to 25 M_{Jup} at the distance of Taurus (140 pc) for age 10 Myr and extinction $A_v = 10$ mag; in all of the targeted regions, the limiting mass is in the range 10–40 M_{Jup} and NGC 2264, because of its youth and relative proximity (3 Myr, 770 pc [9, 10]), is probed to the lower end of this mass range with the current observations.

2 Young brown dwarfs in star-forming regions (SFRs)

Young BD (with ages 1–3 Myr) are now being uncovered (for a recent compilation see [11]) but the census remains very incomplete to date. The CFHT project as a whole has now discovered a substantial sample of candidate young substellar objects - several hundred to date - which can be studied statistically with confidence and which can provide targets for observations in other wavelength regimes (eg. with the Spitzer Telescope). The youth of such objects ensures that their population has not yet suffered from important dynamical (and stellar) evolution, other than dynamical effects potentially associated with their formation. This is a point worth underlining, since observations of young SFRs have the potential to distinguish the two BD formation mechanisms outlined in Sect. 1 by their resultant spatial distributions. If BD always form exactly as stars do, one would expect them to trace the regions of the highest density of low-mass stars. However, in any dynamical ejection scenario, a deficit of BD may be expected in the central regions of young star-forming clusters; their initial velocities (~ 1 km s^{-1}) [12] moving them away from their birth sites at $\sim 0.3°$/Myr (at 140 pc). Such a deficit would therefore be observable in all nearby young SFRs.

Comparison with young SFRs with a range of environmental conditions (from the low density regions such as Taurus to regions where stars are forming in very massive clusters, such as Upper Scorpius) also permits investigation of the sensitivity of the low-mass end of the IMF to local conditions. Sufficiently large coeval populations are not yet available to perform such studies with confidence, but recent studies are beginning to address such questions. As an example, 30 substellar candidates have been identified in Taurus in a 3.6 deg^2 region using CFHT/12K data which reached to $I = 23.5$. Spectroscopic follow-up led to the identification of four BD in Taurus[13] with spectral types later than M7. In Taurus, $\sim$10 BD are now known [14], and appear to be spatially correlated with regions of highest stellar density. In Upper Scorpius, initial studies [15] have found 18 candidate BD of which 5 show signs of ongoing accretion. We will compare our initial findings on NGC 2264 in Sect. 4; here we will note that the much larger BD populations being uncovered by CFHT/12K, when fully analysed, promise a more robust statistical treatment of these issues.

3 Candidate NGC 2264 brown dwarfs: Optical and near-infrared colour selection

The pre-reduction and analysis of these date have been performed using CFHT Elixir pipelines[a] and innovative point-spread function fitting techniques developed by E. Bertin at the Institut d'Astrophysique de Paris[b]. Full details of these methods will be published in a later paper. A first selection of candidates was made by choosing those redder than the long dashed line in Fig. 1., which shows optically selected candidates in NGC 2264 between the substellar limit and $\sim 10 M_{Jup}$, by comparison with the state-of-the-art DUSTY models, specially created by Baraffe et al. to take account of the CFHT I, z filter responses (see[5] and references therein for full details of these models). All 236 such I, z candidates (squares in Fig. 1) have been visually inspected on both I and z frames and all found to be stellar in nature, i.e. there are no artifacts due to nebulosity, field edges, bad columns, bright stars etc. As can be seen in Fig. 1, we estimate our data are complete to $I \sim 22$, or 12 M_{Jup} for age 2 Myr. Cross-correlation with the 2MASS all sky release data has yielded 101 counterparts to the I, z candidates with JHK magnitudes accurate to $\pm$ 0.3 magnitudes or better (a further 29 have only upper limits to J (and for 5, K). These counterparts are plotted in Fig. 2(a) as large squares, together with the complete set of 2MASS data within the optically surveyed area (crosses), in the $I - K$, $J - H$ colour-colour diagram. It is clear that this diagram provides an excellent separation between candidates and field objects. A number of candidates are extremely red, with $I - K \sim 6$ and $I - J \sim 3$–4; the latter colour being typical of field objects with late M or L spectral types, e.g.[16].

[a] www.cfht.hawaii.edu

[b] www.terapix.iap.fr

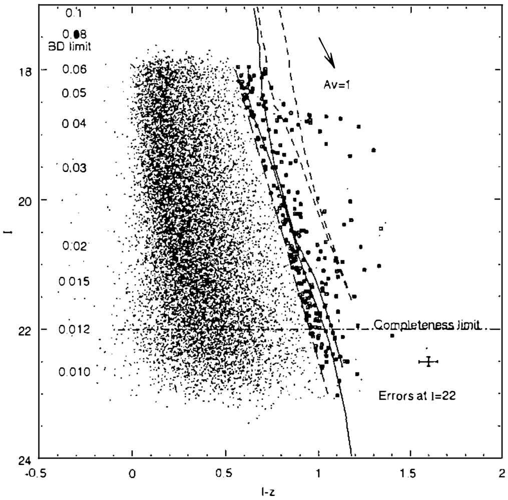

Figure 1: (I,$I - z$) colour-magnitude diagram built using long (360 sec) exposures of NGC 2264. The solid isochrones are DUSTY models for an ages 2 and 5 Myr; the dashed isochrones are the NextGen models at the same ages. All isochrones are for a distance of 770 pc. 236 BD candidates (squares) were selected to be redward of the sloping straight line (long dash). Small dots redward of this line were rejected from the candidacy on visual inspection. The mass scale (in $M_\odot$) is for the 2 Myr models; it and the estimated completeness limit are indicated.

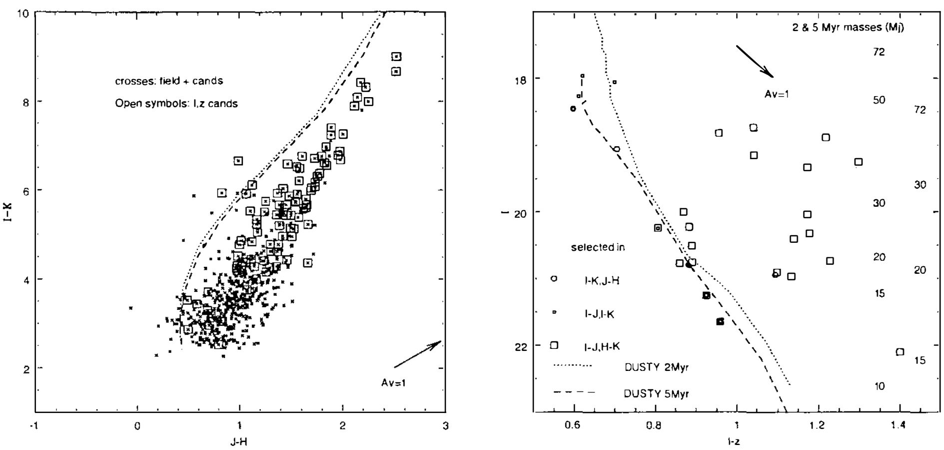

Figure 2: (a, Left): All I, z candidates with 2MASS (squares) and all 2MASS points (field and candidates, crosses) in the $I - K, J - H$ colour-colour diagram. Note the separation of the two populations and the reddening vector. The dashed curve is the 5 Myr DUSTY isochrone; the dotted, 1 Myr. Figure 2: (b, Right): Final selection of candidates from colour indices in I, J, H, K, plotted in the ($I, I - z$) diagram, and excluding objects with only JK upper limits. It is clear that the the $H - K$ colour is least efficient at selecting objects near the model loci. DUSTY isochrones only are plotted as in Fig. 1. Candidates were selected from their locations in the $I - K, J - H$ diagram *and* two other colour combinations (see key). Typical errors in I and $I - z$ are small, $\sim$0.1 mag. (see Fig. 1).

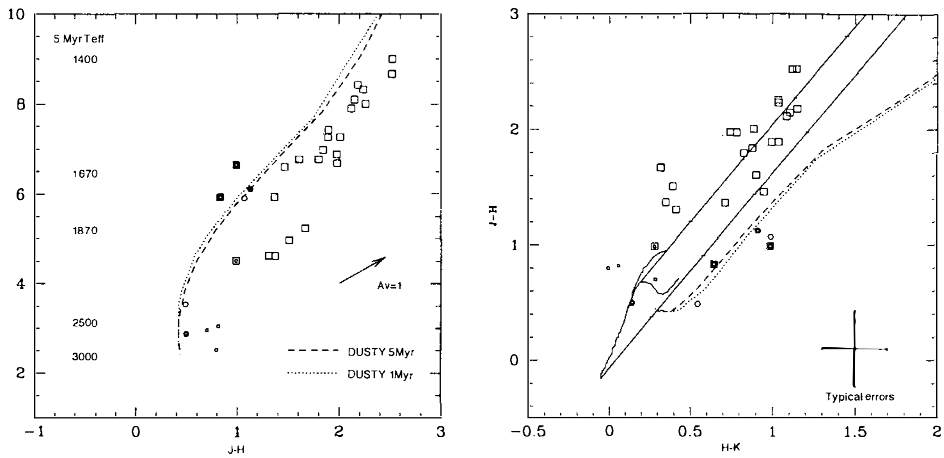

Figure 3: (a, Left): Final census of near-infrared selected objects plotted in the $I - K$, $J - H$ diagram, as an aid to visualizing the selection space. Note the T_{eff} scale based on $I - K$ colour. Figure 3: (b, Right): Location in the JHK diagram. The reddening band (RB) is shown (each horizontal tickmark represents $A_V = 5$), together with loci for dwarfs and giants. Objects selected only in $I - J, H - K$ are clearly more likely to be reddened contaminants; the most promising candidates lie away from the RB and close to the DUSTY isochrones in this plot. Some may have small K-band excesses. 1 and 5 Myr DUSTY isochrones are plotted as for Fig. 3(a). Typical 2MASS errors are given; the error in $I - K$ is somewhat smaller than in $J - H$ or $H - K$, as it is dominated by that in K and the error in I from our 12K data is comparatively small.

To further refine our sample, we have followed similar methods to those of[14, 17] in Taurus, using combinations of I, J, H, K colour-colour diagrams to select those optical candidates which lie on or close to the model isochrones in these diagrams. For the similarly young and extinction affected NGC 2264 region, our finding that the $I - K, J - H$ diagram yields the best separation between field 2MASS objects and candidate BD is in agreement with these authors. In practice, we have chosen candidates lying close to the isochrone in Fig. 2(a), after discarding I, z candidates with only upper limits to J or K. Fig. 2(b) shows objects selected in various colour combinations (see key) re-plotted in the $I, I - z$ diagram, and, in Fig. 3(a), the $I - K, J - H$ diagram. It can be clearly seen that objects selected by $I - J, H - K$ colours *only* (open squares in Figs. 2(b) and 3(a)) do not as a group fall close to the cluster isochrones in $I, I - z$ and these objects are almost certainly reddened background giants. Indeed, in a conventional JHK colour-colour diagram (Fig. 3(b)) many objects *only* selected by their $I - J, H - K$ colours lie within the reddening band However, candidates selected in the $I - J, I - K$ and, especially, $I - K, J - H$ diagrams. tend to lie away from the reddening band, and closer to the cluster isochrone. They can therefore can be considered much more likely to be substellar NGC 2264 members. Such candidates are plotted by small open squares and open hexagons in Figs. 2(b) and 3.

These arguments are backed up by simple dereddening in $J - H$ where all objects have been taken to the low-mass tip of the dwarf sequence in Fig. 3(b), and subsequently replotted in the $I, I - z$ diagram (Fig. 4(a)). To deredden z, we interpolate the interstellar reddening laws of[18] to find A_z/A_V=0.406, taking the optimum sensitivity of the z filter at 9800Å, as given by the CFHT website. As a group, the $I - J, H - K$ selected objects are proven to be highly reddened with A_V ranging up to ~ 17. Only one such object might be considered a member by reference to its position near the tip of the 2 Myr isochrone in $I, I - z$; one further candidate is simultaneously selected in $I - J, I - K$ and has a predicted mass near 40 M_{Jup}. Six objects, all part of the $I - K, J - H$ selection, lie close to the isochrones with masses ranging down to 20 M_{Jup}, and three more chosen by their $I - J, I - K$ colours only are clustered near the model predictions very close to the BD limit. Therefore, the total number of probable substellar members found in NGC 2264 and reported here is eleven.

4 Discussion and concluding remarks

The first and most important point concerns the masses of our candidates, derived from their I magnitudes after dereddening, by comparison with theoretical models for 2 and 5 Myr plotted for a distance modulus 9.4. For the

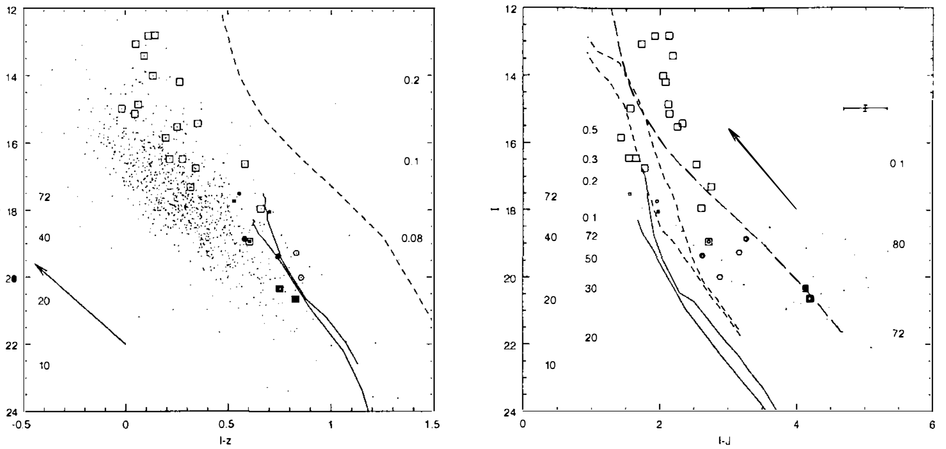

Figure 4: (a, Left): Locations of objects in $I, I - z$ after simple dereddening described in the text. Most $H - K$ selected objects (open squares) are clearly in the background. The dots are a locus of *all* 2MASS points in the region, similarly dereddened; the locus of all field points. The best cluster candidates selected by the methods described here lie noticeably away from this locus. The arrow represents the dereddening vector for $A_V = 5$. 2 and 5 Myr DUSTY isochrones are plotted as solid curves for which the mass scale at left is for 2 Myr; the dash is the location of a 5 Gyr isochrone, representing the field, at 60pc. (b, Right): As Fig. 4(a) but for $I, I - J$. DUSTY isochrones are solid curves, short dashes NextGen, for 1 and 5 Myr ages. The long dash is the field isochrone for 60 pc. Dots are locations before dereddening. Mass scales are for the 5 Myr DUSTY (extreme left), 2 Myr NextGen (left) and the field model (right). The possibility that the two points lying on it at ~ 75 M_{Jup} are *foreground field objects* is discussed in the text. A typical errorbar is shown.

11 most probable cluster members shown in Fig. 4(a) and discussed above, predicted masses range between the substellar limit and close to 20 M_{Jup}.

However we caution that the photometric methods used in this work do not rule out that some of the candidate BD may be background giant or faint foreground contaminants. This is an important point, in the light of the obvious existence of strong and variable extinction intrinsic to the NGC 2264 region itself as discussed at length by [10] (and references therein), and in the foreground, since the region lies close to the galactic plane. Clearly, our methods can distinguish background giants. However, [10] draw attention to the surprising fact that a number of *known* NGC 2264 members exhibit only the reddening expected in this line of sight at $b = 2°$, $E_{B-V} \sim 0.5$. Presumably, these members must lie on the near edge of the cloud and be unaffected by reddening intrinsic to the cluster nebulosity itself. The eleven objects suggested here as substellar members have A_v typically in the range 0–3 and *not more than 4*, as apart from the objects we have clearly identified as background giants suffering $\sim$ 15 magnitudes of extinction. Their A_v are therefore perfectly consistent with cluster membership, although they may be preferentially located on the near edge of the cloud.

This discussion brings to the point the question of contamination by *foreground* objects. It is seen from inspection of the $I, I - J$ diagram in Fig. 4(b) that the candidates are spread in colour between the cluster models and an isochrone plotted for age 5 Gyr (i.e. representing the *field* population) at a distance chosen to be 60 pc to bisect the two candidates selected in all colours and shown as triply overplotted points. For reasons which we defer to a future paper, the question of foreground contamination is not raised by the location of the same isochrone in $I, I - z$ (Fig. 4(a)). However, the status of these 2 objects in particular, as questioned by their dereddened $I - J$ colour, can be further investigated. These objects have A_v of 1.25 and 2.7, as determined by our method. At first sight, it would appear that it is very unlikely that a foreground object at 60 pc would suffer such extinction, supporting the claim that they are true NGC 2264 members with masses not near the BD limit but instead much lower. Indeed, for one of these objects the 2MASS J-magnitude is flagged "D" and its $I - J$ colour might be bluer (nearer the cluster isochrone) than plotted; the other is flagged "C" and may also be bluer by at least the typical error shown in Fig. 4(b).

Further general arguments favourable to the identification of these eleven candidates as NGC 2264 members are provided by the observation of clear separation of I, z selected objects from the field in the $I - K$, $J - H$ diagram and by the classical $J - H, H - K$ diagram (Fig. 3(b)), in which the location of DUSTY isochrones has *not* been employed for candidate selection. It can be readily seen that, even before any dereddening, the best candidates as a group here lie away from the reddening band, while other initially plausible candidates, selected using their $I - J$ and $H - K$ colours only, are more scattered over the diagram, often lying within the reddening band. A similar separation identifies background giants in the dereddened $I, I - z$ plot. Such observations further strengthen the effectiveness of our photometric selection methods, with $I - K, J - H$ selected candidates preferentially located closest to the DUSTY isochrones in all colour-colour and colour-magnitude diagrams. The location of a few candidates in JHK also raises the possibility that they have K-band excesses, which might indicate ongoing accretion, and can be tested first by photometric observations in the thermal infrared with Spitzer. Current studies do not easily show whether the presence of disks might be still expected around young BD at the age of NGC 2264, and our candidates provide a good opportunity to constrain disk ages in this way.

It is clear however that near-infrared spectroscopy is also required to confirm candidates on the basis of their T_{eff} and surface gravities, which will be significantly less than foreground, evolved field objects owing to the young age of the region.

In conclusion, there is a strong likelihood that our preliminary work has indeed uncovered a small initial sample of low mass brown dwarfs, some of which may have masses only twice the deuterium burning limit. Deeper near-infrared photometry than given by 2MASS is likely to identify more of our I, z candidates as near-planetary mass BD. If so, then NGC 2264 will prove to be a new astrophysical laboratory, intermediate in stellar density between Orion and Taurus, where the formation mechanisms of such objects in star-forming environments can be investigated.

Acknowledgments

TRK and DJJ acknowledge support from the 5th Framework European Union Research Training Network "The Formation and Evolution of Young Stellar Clusters" (RTN1-1999-00436) and TRK from the French *Ministère du Recherche*. EM acknowledges support from PPARC.

References

1. Bejar, V.J.S., Martín, E.L., Zapatero-Osorio, M.R., et al. 2001, ApJ, 556, 830
2. Moraux, E., Bouvier, J., Stauffer, J.R., & Cuillandre, J.-C. 2003, A&A, 400, 891
3. Chabrier, G. 2002, ApJ, 567, 404
4. Chabrier, G. 2003, PASP, 115, 763
5. Baraffe, I., Chabrier, G., Barman, T.S., et al. 2003, A&A, 402, 701
6. Chabrier, G., et al., 2000, ApJ, 542, 464
7. Padoan, P., & Nordlund, A. 2002, ApJ, 576, 870
8. Reipurth, B., & Clarke, C. 2001, AJ, 122, 432
9. Lamm, M.H., Bailer-Jones, C.A.L., Mundt, R., et al. 2004, A&A, 417, 557
10. Rebull, L.M., Makidon, R.B., Strom, S.E., et al. 2002, AJ, 123, 1528
11. Basri, G. 2000, ARA&A, 38, 485
12. Sterzik, M.F., & Durisen, R,H. 2003, A&A, 400, 1031
13. Martín, E.L., Dougados, C., Magnier, E., et al. 2001, ApJ, 561, L195
14. Briceno, C., Luhman, K.L., Hartmann, L., et al. 2002, ApJ, 580, 317
15. Martín, E.L., Delfosse, X., & Guieu, S. 2004, AJ, 127, 449
16. Kendall, T.R., Delfosse, X., Martín, E.L., & Forveille, T. 2004, A&A, 416, L17
17. Luhman, K.L., Briceno, C., Stauffer, J.R., et al. 2003, ApJ, 590, 348
18. Rieke, G.H., & Lebovsky, M.J., 1985, ApJ., 288, 618

Competitive accretion and the initial mass function

Ian A. Bonnell

School of Physics and Astronmy, University of St Andrews,
North Haugh, St Andrews, KY16 9SS, UK.

Competitive accretion in stellar clusters is a simple physical mechanism to explain the observed initial mass function of stars. In this model, stars attain their final masses by accreting gas within a clustered environment, with a few centrally located stars accreting significantly more than the rest to become high-mass stars. The IMF arises due to the detailed physics of the accretion process. In young, gas-dominated clusters, accretion is controlled by the tidal radius of individual stars. In contrast, where stars dominate the potential, as first occurs in the core of a cluster, the accretion is controlled by the Bondi-Hoyle radius. The combination of these two accretion processes results in a two power-law IMF with a shallow power-law, $\gamma \approx -1.5$, for low-mass stars which accrue their mass in the gas dominated regime whereas higher mass stars have a steeper, $\gamma \approx -2.5$, IMF as their mass is predominantly due to accretion in the core of a cluster. Numerical simulations of the fragmentation and formation of a stellar cluster show that the final stellar masses are due to competitive accretion and that this results in a realistic IMF. Competitive accretion also naturally results in a mass segregated cluster and in a direct correlation between the richness of a cluster and the mass of the most massive star therein.

1 Introduction

There have been many models advanced to explain the origin of the initial mass function (IMF) of stars (eg., Meyer et al.2000). These models are based either on the physics of fragmentation (Larson 1985; Elmegreen 1997; Padoan & Nordlund 2002) on accretion (Zinnecker 1982, Larson 1992, Bonnell et al.2001b) or on feedback from young stars (Silk 1995, Adams & Fatuzzo 1996). Although how exactly feedback can produce the IMF is at best complicated, both fragmentation and accretion rely on simple physics. For fragmentation to produce the IMF requires that the distribution of fragment masses map directly onto that of stars. This mechanism is particularly attractive as observations of star-less cores in Ophiuchus appears to follow a stellar-like IMF (Motte et al.1998) although this does not appear to be true in some regions of Orion

(Coppin et al. 2000). In order for fragmentation to occur, individual cores must contain a Jeans mass, the minimum mass to be gravitationally bound.

The Jeans mass of a core of density ρ and temperature T is given by

$$M_J = \left(\frac{5R_gT}{2G\mu}\right)^{3/2}\left(\frac{4}{3}\pi\rho\right)^{-1/2}, \tag{1}$$

where R_g is the gas constant, G is the gravitational constant, and μ is the mean molecular weight. Thus, even if the gas is isothermal as is generally the case in molecular clouds, a distribution of densities results in a distribution of Jeans masses and thus can yield a mass function. The required structure can either be thought of as fractal (Elmegreen 1997) or as due to the observed supersonic 'turbulence' observed in molecular clouds (Padoan & Nordlund 2002).

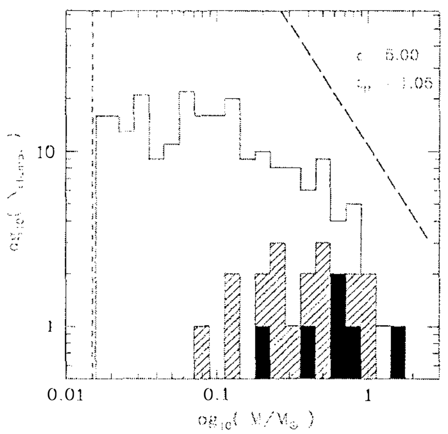

Figure 1: The mass distribution of pre-stellar cores is plotted from a simulation of a turbulent molecular cloud The histogram plots all cores while the hashed are denotes those that are thermally bound while the black areas denote those that are totally bound. The small subset of cores which are actually bound does not resemble the stellar IMF (Clark & Bonnell 2004)..

One problem with a fragmentation model for the IMF is that the more massive cores must be less dense if they contain just one Jeans mass, and are thus not going to fragment into several smaller pieces. This implies that more massive stars should be well separated at distances greater than the Jeans radius, the minimum radius for an object to be gravitationally bound:

$$R_J = \left(\frac{5R_gT}{2G\mu}\right)^{1/2}\left(\frac{4}{3}\pi\rho\right)^{-1/2}. \tag{2}$$

This would result in an inverse mass segregation where the more massive stars are in low-density regions, in direct opposition to observations. Another potential problem with a turbulently driven origin for the IMF is that simulations of such clouds shows that only a small subset of the generated cores are actually bound, and that the masses of these cores is approximately the mean Jeans mass of the cloud (Clark & Bonnell 2004). Furthermore, these bound cores commonly fragment to form multiple systems. There is therefore no one-to-one mapping of the pre-stellar core mass distribution to the stellar IMF.

Instead, we turn to models of accretion in a clustered environment to produce the observed initial mass function. Star formation is a dynamical process where most stars form in a clustered ennvironment (Lada & Lada 2003; Clarke, Bonnell & Hillenbrand 2000). In such an environment, stars and gas move in their combined potential on timescales comparable to the formation time of individual stars. Furthermore, the initial fragmentation of a molecular cloud is very inefficient (eg., Motte et al. 1998), such that the youngest clusters are dominated by their gas content. In such an environment, gas accretion can contribute significantly to the final mass of a star.

Stellar clusters are found to be mass segregated even from the youngest ages. The location of massive stars in the cores of clusters cannot be explained by dynamical mass segregation as the systems are too young (Bonnell & Davies 1998). A Jeans mass argument also fails as the Jeans mass in the core should be lower then elsewhere in the cluster. Mass segregation is a natural outcome of competitive accretion due to the gas inflow to the centre of the cluster potential.

2 Accretion in stellar clusters: two regimes

In a series of numerical experiments , we investigated the dynamics of accretion in gas-dominated stellar clusters (Bonnell et al. 1997, 2001a). In the initial studies of accretion in small stellar clusters, we found that the gas accretion was highly non-uniform with a few stars accreting significantly more than the rest. This occurred as the gas flowed down to the core of the cluster and was there accreted by the increasingly most-massive star. Other, less massive stars were ejected from the cluster and had their accretion halted (see also Bate, Bonnell & Bromm 2002). In a follow-up study investigating accretion in clusters of 100 stars, we discovered two different physical regimes (Bonnell et al. 2001a) resulting in different accretion radii, $R_{\rm acc}$, for the mass accretion rate

$$M_{\rm acc} = \rho v \pi R_{\rm acc}^2, \tag{3}$$

where ρ is the local gas density and v is the relative velocity of the gas. Firstly, in the gas dominated phase of the cluster, tides limit the accretion as the relative velocity between the stars and gas is low. The tidal radius, due to the star's position in cluster potential,

$$R_{\rm tidal} \approx 0.5 \left(\frac{M_*}{M_{\rm enc}}\right)^{\frac{1}{3}} R_*, \tag{4}$$

is then smaller than the traditional Bondi-Hoyle radius and determines the accretion rate. Accretion in this regime naturally results in a mass segregated cluster as the accretion rates are highest in the cluster core.

Once accretion has increased the mass of the stars, and consequently decreased the gas mass present, the stars begin to dominate the stellar potential and thus virialise. This occurs first in the core of the cluster where higher-mass stars form due to the higher accretion rates there.The relative velocity between the gas and stars is then large and thus the Bondi-Hoyle radius,

$$R_{\rm BH} = 2GM_*/(v^2 + c_s^2), \tag{5}$$

becomes smaller than the tidal radius and determines the accretion rates.

3 Resultant IMFs

We can use the above formulation of the accretion rates, with a simple model for the stellar cluster in the two physical regimes, in order to derive the resultant mass functions (Bonnell et al. 2001b). The primary difference is the power of the stellar mass in the accretion rate equation, $M_*^{2/3}$ for tidal-accretion and M_*^2 for Bondi-Hoyle accretion. Starting from a gas rich cluster with equal stellar masses, tidal accretion results in higher accretion rates in the centre of the cluster where the gas density is highest. This results in a spread of stellar mass and a mass segregated

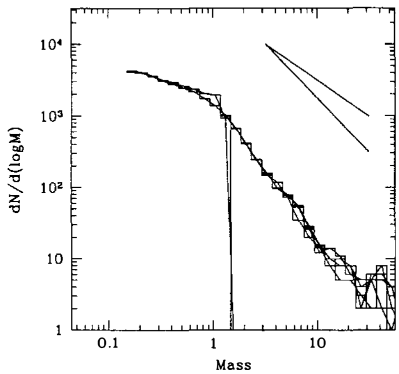

Figure 2: The IMF that results from competitive accretion in a model cluster. the two power-law IMF results from a combination of tidal accretion for low-mass stars and Bondi-Hoyle accretion for high-mass stars (BCBP 2001).

cluster. The lower dependency of the accretion rate on the stellar mass results in a fairly shallow IMF of the form (where Salpeter is $\gamma = -2.35$)

$$dN/dM_* \propto M_*^{-3/2}. \tag{6}$$

Once the cluster core enters the stellar dominated regime where Bondi-Hoyle accretion occurs, the higher dependency of the accretion rate on the stellar mass results in a steeper mass spectrum. Zinnecker (1982) first showed how a Bondi-Hoyle type accretion results in a $\gamma = -2$ IMF. In a more developed model of accretion into the core of a cluster with a pre-existing mass segregation, the resultant IMF is of the form

$$dN/dM_* \propto M_*^{-5/2}. \tag{7}$$

This steeper IMF applies only to those stars that accrete the bulk of their mass in the stellar dominated regime, ie. the high-mass stars in the core of the cluster (see Figure 2).

4 The formation of stellar clusters

In order to asses the role of accretion in determining the IMF, we need to consider self-consistent models for the formation of the cluster. We followed the fragmentation of a 1000 $M_\odot$ cloud with a 0.5 pc radius (Bonnell, Bate & Vine 2003). The cloud is initially supported by turbulence which decays on the cloud's crossing time. As the turbulence decays, it generates filamentary structure which act as the seeds for the subsequent fragmentation. The cluster forms in a hierarchical manner with many subclusters forming before eventually merging into one larger cluster. In all 419 stars form in 5×10^5 years (Figure 3). The simulation produces a field star IMF with a shallow slope for low-mass stars steepening to a Salpeter-like slope for high-mass stars (Figure 4). The stars all form with low masses and accrete up to their final masses. The stars that are in the centres of the subclusters accrete more gas and thus become higher-mass stars.

A careful dissection of the origin of the more massive stars reveals the importance of competitive accretion in setting the IMF. the Lagrangian nature of the SPH simulations allows us

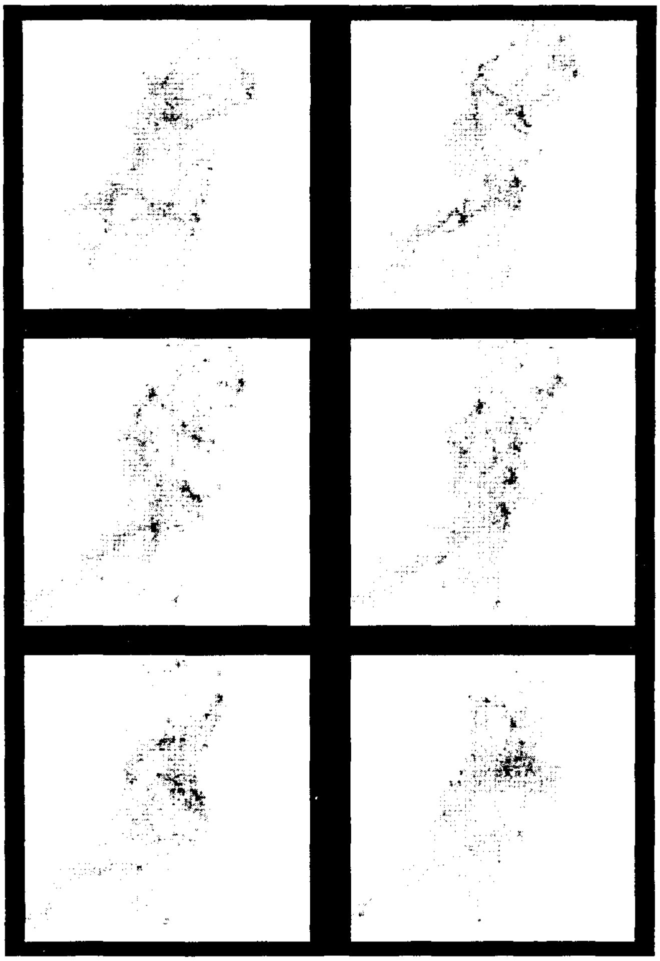

Figure 3: The evolution of a 1000 $M_{\odot}$ cloud that fragments to form 419 stars (Bonnell, Bate & Vine 2003).

to trace the mass from which a star forms. We can therefore distribute this mass as being in one of three categories: 1) The original fragment which formed the star; 2) A contiguous envelope around the fragment until we reach the next forming star; and 3) mass which originates beyond the forming group or cluster of stars. Figure 5 shows the three contributions to the final stellar mass of the 419 stars (Bonnell, Vine & Bate 2004). We see that the initial fragment mass is generally around $0.5 M_{\odot}$ and fails to account for both high-mass and low-mass stars. The contiguous envelope does a better job as it accounts for subfragmention into lower-mass stars. It still fails to explain the mass of higher-mass stars. We are thus left with accretion from beyond the forming protocluster in order to explain the existence of higher-mass stars. Thus, high-mass stars are formed due to competive accretion of gas that *infalls* into the stellar cluster.

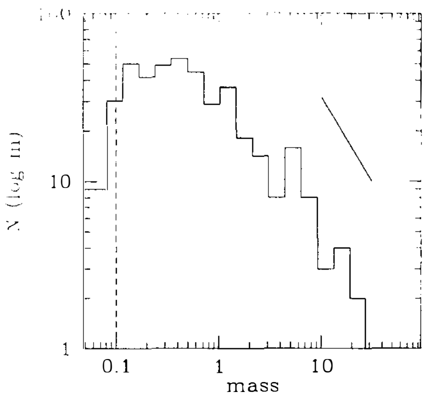

Figure 4: The IMF that results from a numerical simulation of the fragmentation of a turbuelnt cloud and the formation of a stellar cluster containing 419 stars. The comparison slope is for a $\gamma = -2$ IMF (BBV 2003).

5 Massive stars and cluster formation

We have seen above that the formation of massive stars is due to the infall of gas into a stellar cluster and the subsequent competitive accretion inside the cluster. in addition to gas, newly formed stars also infall into the cluster, increasing the number of stars, and hence the stellar densities. Investigating the evolution of the individual clusters, we find a correlation in the richness of the cluster and the mass of the most massive star therein (Figure 6). This can be understood in the following way. Given an effective initial efficiency of fragmentation, for every star that falls into the cluster a certain amount of gas also enters the cluster. This gas joins the common reservoir from which the most massive star takes the largest share in this competitive environment. Thus, the mass of the most massive star increases as the cluster grows in numbers of stars. We thus have a prediction from this model that there should exist a strong correlation between the mass of the most massive star and the number of stars in the cluster (Figure 6, Bonnell, Vine & Bate 2004). There is a similar correlation of the total stellar mass in a cluster with the mass of the most massive star (Bonnell, Vine & Bate 2004). In fact, this relation

$$M_{max} \propto M_{tot}^{\frac{2}{3}}, \tag{8}$$

is just telling us that each cluster is producing an IMF

Another outcome of competitive accretion in stellar clusters is that it increases the stellar density. This occurs as the mass loading increases the binding energy of the cluster. Even if significant momentum is also accreted, the effect is to force the cluster to contract and reviralise. This increases the stellar density. In the simulation of Bonnell, Bate & Vine (2003), stellar densities of the order of 10^6 to 10^8 stars pc^{-3} were reached in the cores of the clusters. In fact, even these high densities are lower-limits due to the gravitational softenning used. The high stellar densities may have some drastic outcomes as stellar collisions can then become a viable alternative to accretion as the formation mechanism of massive stars (Bonnell, Bate & Zinnecker 1998). This can circumvent any problem with accretion and radiation pressure from high-mass stars.

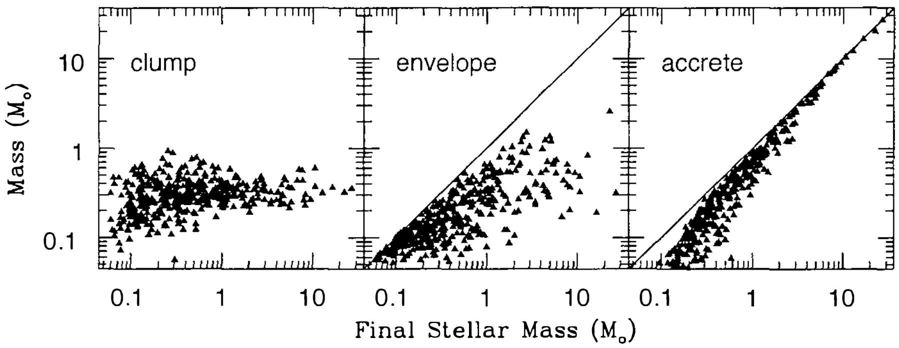

Figure 5: The relation between fragment mass (left) mass in a contiguous envelope (middle) and mass accreted from beyond the cluster (right) is plotted against final stellar mass. High-mass stars attain their mass due to competitive accretion of gas infalling into the stellar cluster (Bonnell, Vine & Bate 2004).

6 What is the role of the Jeans mass?

The IMF has a further parameter which it is important to understand. This is the 'knee' where the slope changes from the shallower one at lower masses to a steeper one for the higher mass stars. One possibility is that this reflects the Jeans mass of the prestellar system. We saw above that the average fragment mass in which stars form is ≈ 0.5 $M_\odot$ while the initial Jeans mass is $= 1M_\odot$. Thie Jeans mass is therefore important at setting the scale of the initial fragmentation.

In order to test this we reran the above simulation of 1000 $M_\odot$ but with a Jeans mass of $5M_\odot$. The resultant IMF, shown in Figure 7, is fairly shallow up to masses of $\approx 5 - 10M_\odot$, corresponding roughly to the Jeans mass. In Figure 4 we see that the slope of the IMF becomes steeper at $\approx 1M_\odot$, the Jeans mass in this simulation. We can thus deduce that the Jeans mass helps set the *knee* in the IMF, with lower masses determined by fragmentation and the tidal shearing of nearby stars, while higher-masses are determined by accretion in a clustered environment.

7 Conclusions

Competiitve accretion is a simple physical model that can explain the origin of the initial mass function. It relies on gravitational competition for gas in a clustered environment. This occurs via a tidal competition in regions where the gas dominates the gravitational potential as the relative star-gas velocities are then low. In this case, the accretors need not have any large-scale motion as it is the tidal field which limits and hence sets the mass. In contrast, in stellar dominated potentials that occur in the core of dense young clusters, the stars virialise and have large velocities relative to the infalling gas. The accretion is then decided by Bondi-Hoyle type accretion. the higher dependency of the accretion rate on the accretor's mass (m^2) results in a much steeper IMF which approaches the Salpeter value of $\gamma = -2.35$.

It is probably even more important for any model of the IMF to have secondary characteristics that can be compared to observations. Competitive accretion naturally results in a mass segregated system as the higher mass stars form in the cores of cluster due to the higher

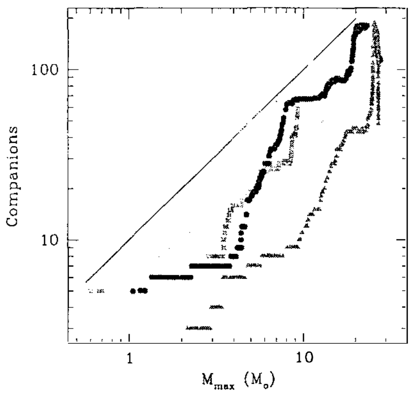

Figure 6: The number of stars in a subcluster is plotted against the mass of the most massive star therein(BVB 2004).

accretion rates there. Furthermore, competitive accretion predicts that massive star formation is intrinsically linked to the formation of a stellar cluster and that few, if any, massive stars should form in isolation.

8 Acknowledgments

Some of the simulations reported here were performed with the UK's Astrophysical Fluid facility, UKAFF.

1. Adams, F.C., Fatuzzo, M., 1996, ApJ, 464, 256
2. Bate, M. R., Bonnell, I. A., Bromm, V. 2002, MNRAS, 336, 705
3. Bonnell, I. A., Bate, M. R., Clarke, C. J., & Pringle, J. E., 1997, MNRAS, 285, 201
4. Bonnell, I. A., Bate, M. R., Clarke, C. J., & Pringle, J. E., 2001, MNRAS, 323, 785
5. Bonnell, I. A., Bate, M. R., & Vine, S. G. 2003, MNRAS, 343,413
6. Bonnell, I. A., Bate, M. R., & Zinnecker, H., 1998, MNRAS, 298, 93
7. Bonnell, I. A., Clarke, C. J., Bate, M. R., & Pringle, J. E., 1997, MNRAS, 324, 573
8. Bonnell, I. A., Davies, M. B., 1998, MNRAS, 295, 691
9. Bonnell, I. A., Vine, S. G., & Bate, M. R. 2004, MNRAS, 349, 735
10. Clark, P. C., Bonnell, I.A., MNRAS, submitted
11. Clarke, C. J., Bonnell, I. A., Hillenbrand, L. A., 2000, PPIV, Mannings, Boss & Russell eds, p 151
12. Coppin, K. E. K., Greaves, J. S., Jenness, T., & Holland, W. S. 2000, A&A, 356, 1031
13. Elmegreen, B., 1997, ApJ, 486, 944
14. Lada C. J., Lada, E. 2003, ARA&A, 41, 57
15. Larson, R.B., 1985, MNRAS, 214, 379
16. Larson, R.B., 1992, MNRAS, 256, 641
17. Meyer, M., Adams, F.C., Hillenbrand, L.A., Carpenter, J.M., Larson, R.B., 2000, PPIV, Mannings, Boss & Russell eds, p 121
18. Motte, F., Andre, P., & Neri, R. 1998, A&A, 336, 150
19. Padoan, P., & Nordlund, A., 2002, ApJ, 576, 870

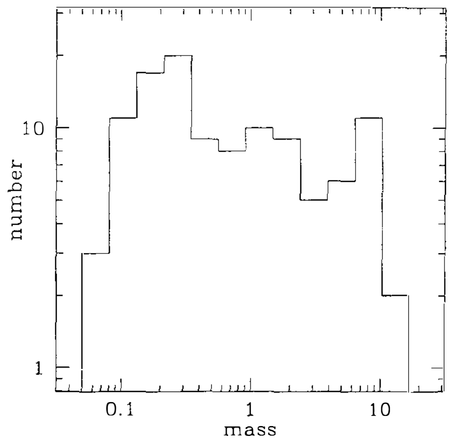

Figure 7: The IMF that results from a fragmentation of a 1000 $M_\odot$ cloud where the Jeans mass is 5 $M_\odot$..

20. Salpeter, E. E. 1955, ApJ, 123, 666
21. Silk, J., 1995, ApJ, 438, L41
22. Zinnecker, H. 1982, New York Academy Sciences Annals, 395, 226

"Portrait of youth with white frisbees"

A PHOTOMETRIC STUDY OF THE YOUNG CLUSTER COLLINDER 359

N. LODIEU (1), J. BOUVIER (2) & M. J. McCAUGHREAN (1)

(1) Astrophysikalisches Institut Potsdam, An der Sternwarte 16, 14482 Potsdam, Germany
(2) Laboratoire d'Astrophysique de Grenoble, BP 53, 38041 Grenoble Cédex, France

We present the first deep optical wide-field imaging survey of the young open cluster Collinder 359, complemented by near-infrared follow-up observations. We have surveyed 1.6 square degree in the cluster in the I and z filters with the CFH12K on the Canada-France-Hawaii 3.6-m telescope down to completeness and detection limits in both filters of 22.0 and 24.0, respectively. Based on their location in the optical $(I,I-z)$ colour-magnitude diagram, we have extracted new cluster member candidates in Collinder 359 spanning 1.3–0.04 $M_{\odot}$, assuming an age of 80 Myr and a distance of 500 pc for the cluster. We have derived the cluster luminosity and mass functions using the latest evolutionary models from the Lyon group: the best fit to the slope of the cluster mass function, when expressed as the mass spectrum, is $\alpha = 0.30 \pm 0.20$ over the 0.55–0.035 $M_{\odot}$ mass range. The derived slope appears flatter than the estimates in the Pleiades and α Per open clusters.

Keywords: Open clusters and associations: individual: Collinder 359 — Stars: low-mass, brown dwarfs — Stars: luminosity function, mass function — Techniques: photometric

1 The young open cluster Collinder 359

The young open cluster Collinder 359 (= Melotte 186) was selected as a pre-main-sequence open cluster within the framework of a CFHT Key Programme to study the sensitivity of the low-mass stellar and substellar IMF to time and environment. The cluster is located in the Ophiuchus constellation around the supergiant 67 Oph. Collinder 359 was relatively unstudied and very little literature is available about it: in particular, no modern optical survey exists of the cluster core.

The cluster was first seen on the Franklin-Adams Charts Plates and described by Melotte in 1915 [21] as a large scattered group of bright stars around 67 Oph, covering an area of about 6 square degrees. In his catalogue of open clusters, Collinder (1931)[9] described the cluster as a group of about 15 stars with no appreciable concentration on the sky and no well-defined outline. A list of probable candidates was given in Collinder's paper, along with coordinates, magnitudes, and spectral types. The membership of these objects was, however, not well established and more than half of them were later rejected by Van't Veer (1980)[30] and Rucinski (1987)[25]. Based on isochrone fitting, the distance of the cluster was estimated between 200 and 300 parsecs while the parallax measurements from HIPPARCOS suggested a distance of approximately 270 pc[15]. A recent analysis of the cluster by Kharchenko et al. (2004, personal communication) derived a much larger distance of 650 pc, based on a larger number of objects included in the HIPPARCOS and Tycho 2 catalogues. The age of the cluster has previously been estimated as 30 Myr[31], as confirmed by Kharchenko et al. (2004).

2 The optical wide-field survey

A Canada-France-Hawaii Telescope Key Programme (30 nights over 2 years) centred on wide-field optical imaging of young, intermediate-age, and older open clusters was carried out within the framework of the European Research Training Network "The Formation and Evolution of Young Stellar Clusters", to examine the sensitivity of the low-mass stellar and substellar IMF to time and environment. The survey was conducted with a large-CCD mosaic camera (CFH12K) in the I and z filters down to detection and completeness limits of $I = 24.0$ and 22.0, respectively.

Five CFH12K frames were obtained on 18 and 20 June 2002 in Collinder 359 in the I and z filters, covering a total area of 1.6 square degrees in the cluster. Fields A, B, C, and D were covered on 18 June 2002 under photometric conditions with seeing ~ 0.8 arcsec. The final field, field E, was observed on 20 June 2002 under non-photometric conditions. Three sets of exposures were taken for each field-of-view: short, medium, and long exposures with integration times of 2, 30, and about 900 seconds, respectively. The long exposures were exposed 3×300 and 3×360 seconds in the I and z filter, respectively.

The initial data reduction was provided by the Elixir pipeline, including bias subtraction, flat-fielding, correction for scattered light in both filters, combining the dithered frames in case of long exposures, and astrometric calibration. Zero-points were also provided by the pipeline from a repeated monitoring of several standard stars. The photometry was extracted with the SExtractor package coupled with a PSF fitting routine (kindly provided by E. Bertin[6]).

3 Identification of cluster member candidates

Photometry has been extracted in the I and z filters, allowing us to draw a colour-magnitude diagram (I, $I-z$) shown in Figure 1. To take into account the uncertainties in the age and the distance of the cluster, we have selected all objects located to the right of the combined NextGen+Dusty isochrones from the Lyon group[4,8], assuming a distance of 650 pc and an age of 80 Myr for the cluster. This value of the age takes into account the possibility of older ages as suggested by the lithium test applied to the Pleiades[26], α Per[27], and IC2391[2]. We have examined each cluster member candidate by eye both in the I and z images to reject extended objects, blended sources, and detections affected by bad pixels or bad columns. We have extracted a total of 1033 candidates ranging from $I = 12.0$ to $I = 22.5$ over 1.6 square degree area surveyed in Collinder 359. The new candidates are displayed as filled circles in Figure 1 and span masses between 1.3 and 0.04 $M_\odot$ according to the tracks.

We have also cross-correlated our sample of optically-selected candidates with the 2MASS database. All objects brighter than $I = 17$ have a 2MASS counterpart, and, therefore, near-infrared magnitudes. In addition, we have obtained K'-band photometry with the infrared

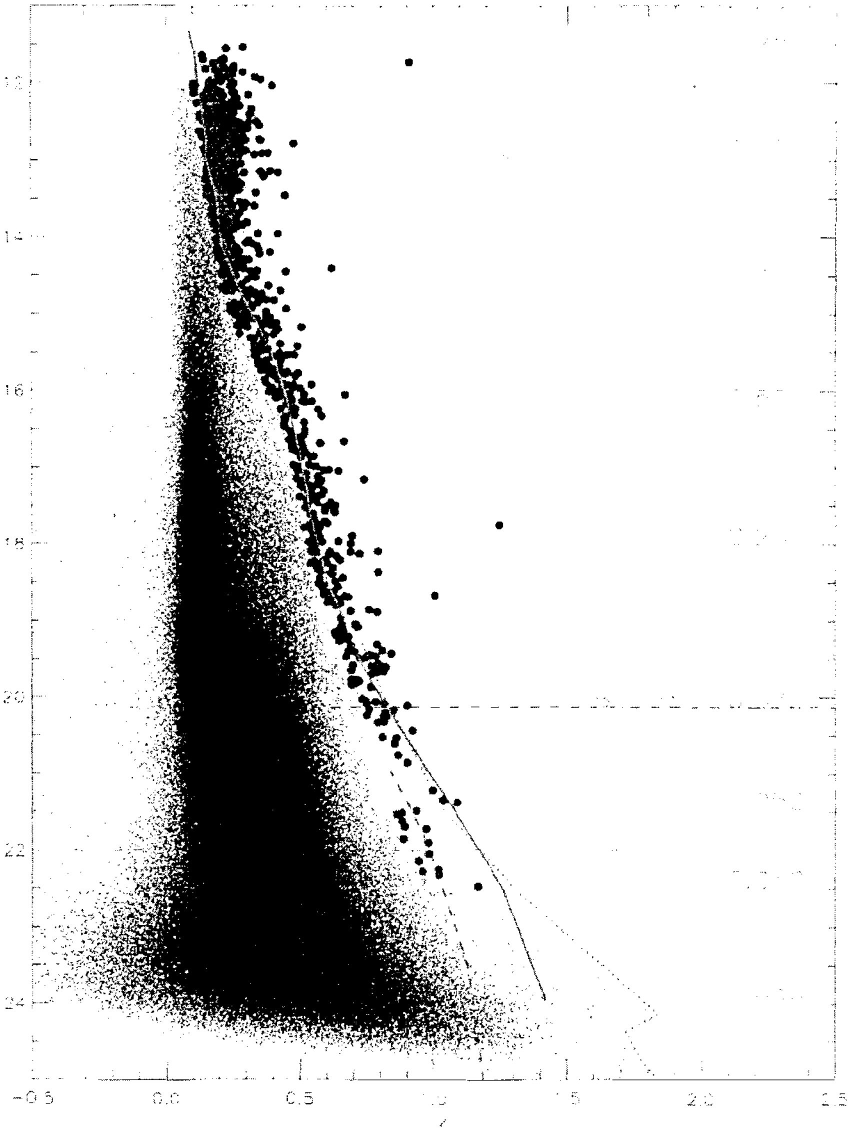

Figure 1: Colour-magnitude diagram (I, $I-z$) for the intermediate-age open cluster Collinder 359 over the full 1.6 square degree area surveyed by the CFH12K camera. The large filled dots are all optically-selected cluster member candidates spanning 1.3–0.04 $M_{\odot}$. Overplotted are NextGen (solid line; Baraffe et al. 1998) the Dusty (dashed line; Chabrier et al. 2000) and the Cond (dotted line; Chabrier et al. 2000) isochrones for 80 Myr, assuming a distance of 500 pc for the cluster. The dashed line at $I \sim 20$ indicates the stellar/substellar boundary at 0.075 $M_{\odot}$. The mass scale (in solar masses) is given on the right side of the graph. A reddening vector of $A_V = 1$ is indicated for comparison purposes. The open triangles depicts candidates with proper motion consistent with cluster membership.

camera (CFHTIR) on the CFH 3.6-m telescope to probe the contamination at and below the substellar limit ($I \sim 20$). This procedure rejected some objects exhibiting bluer colours than cluster members in the optical-to-infrared colour-magnitude diagram.

We have used our optical survey in Collinder 359 complemented by near-infrared photometry to address the issue regarding the uncertainties on the age and the distance of the cluster.

First, we have followed the approach applied to the α Per cluster by Stauffer et al. (2003). By comparing the location of the supergiant 67 Oph in the colour-magnitude diagram (M_V, $B-V$) with theoretical solar metallicity isochrones including moderate overshoot [11], we have inferred an age of 60 ± 20 Myr for Collinder 359.

Second, we have cross-correlated our list of candidates with the latest version of the USNO CCD Astrograph Catalog [32] which provides proper motion for a large number of candidates. We have retained probable member candidates with photometric and proper motion measurements consistent with cluster membership. The location of these candidates in the colour-magnitude diagram suggested a most likely age of 80 Myr and a distance of 500 pc.

4 The cluster luminosity function

We have derived the cluster luminosity function using the list of candidates extracted from the colour-magnitude diagram, assuming an age of 80 Myr and a distance of 500 pc for Collinder 359 (Figure 2). The luminosity function is drawn from all probable candidates whose optical and near-infrared photometry are consistent with cluster membership.

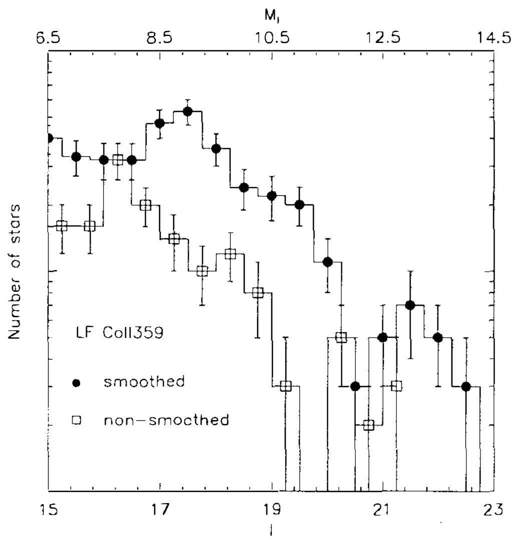

Figure 2: The cluster luminosity function drawn for the candidates selected to the right of the isochrones, assuming an age of 80 Myr and a distance of 500 pc for Collinder 359. The open squares represent the number of stars per bin of 0.5 magnitude whereas the filled circles indicate the number of stars in a 1.0 magnitude bin with an interval of 0.5 magnitudes. Poisson errors are indicated by vertical lines.

We have employed two approaches to derive the cluster luminosity function. The first approach consisted in counting the number of stars per bin of 0.5 mag (open squares in Figure 2). The second approach "smoothed" the luminosity function to better characterise the faint end, i.e. we have counted the number of stars per interval of 1.0 magnitude by step of 0.5 magnitude (filled circles in Figure 2). Both methods yielded similar cluster luminosity functions.

The optical colour-magnitude diagram (Figure 1) is suggestive of a large contamination at the high-mass end ($M \geq 0.6\,M_\odot$) as the cluster sequence merges with field stars. As a consequence, we are unable at present to derive reliable luminosity and mass functions for Collinder 359 for masses larger than $0.6\,M_\odot$. Additional follow-up observations such as optical spectroscopy are mandatory to estimate the level of contamination in this mass range.

Two features are seen in the cluster luminosity function (Figure 2). First, a peak at $I = 17.0$–17.5 mag ($M_I = 8.5$–9.0 mag) corresponding to $M \sim 0.30\,M_\odot$. Comparable peaks are seen in different clusters at different magnitudes, including NGC2516 (150 Myr; $M_I = 11$,[13]), M35 (150–200 Myr; $M_I = 9$,[1]), and α Per (90 Myr; $M_I = 10$,[3]) but its origin is currently unknown. Second, a dip around $I = 20.5$ mag ($M \sim 0.070\,M_\odot$) is present in the cluster luminosity function and clearly detected in the colour-magnitude diagram (Figure 1) well above our completeness limit. This feature is comparable to the gap seen in the α Per luminosity function at $M_I = 12.5$[3]. This dip is detected both in the field[24] and in young clusters, including σ Orionis[5], the Trapezium Cluster[16], IC348[17], the Pleiades[12], and IC 2391[2]. This feature might originate from the formation of large dust grains at low temperatures around spectral types M7–M8[12].

5 The cluster mass function

We have converted the luminosity function into a mass function using the evolutionary models from the Lyon group, assuming an age of 80 Myr and a distance of 500 pc for the cluster.

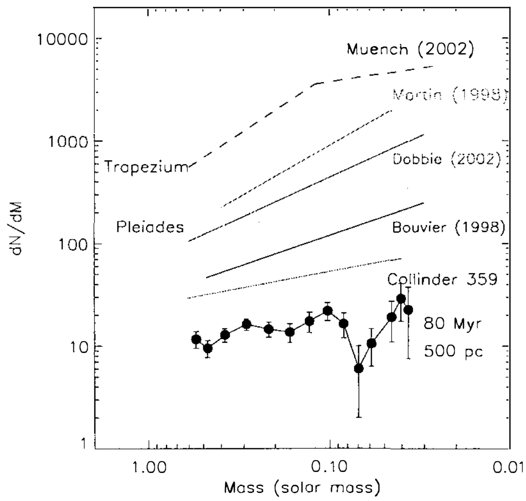

Figure 3: The cluster mass function assuming an age of 80 Myr and a distance of 500 pc for Collinder 359. The cluster mass function (filled circles) is compared with the mass functions derived for the Pleiades (0.5–1.0; Bouvier et al. 1998; Martin et al 1998; Tej et al. 2002; Dobbie et al. 2002; Moraux et al. 2003) and the Trapezium Cluster (0.27 in the 0.12–0.025 mass range; Muench et al. 2002).

The cluster mass function exhibit a slow steepening from $0.6\,M_\odot$ down to our completeness limit at about $0.040\,M_\odot$. The best linear fit to the mass function in Collinder 359 is obtained for an index $\alpha = 0.30 \pm 0.2$ in the 0.60–0.04 $M_\odot$ mass range, when expressed as the mass spectrum

$dN/dM \propto M^{-\alpha}$ (solid line in Figure 3). This estimate appears flatter than the ones in the Pleiades ($\alpha = 0.6 \pm 0.1$; [22]) and in α Per ($\alpha = 0.59 \pm 0.05$; [3]) over the same mass range. Furthermore, a dip occurs around 0.070 $M_\odot$ in the mass function, likely due to the dearth of objects with spectral types of M7–M8 objects [12], at the age and distance of the cluster.

This optical survey of Collinder 359 constitutes a first step in the study of the cluster. Near-infrared imaging and low-resolution optical spectroscopy of the selected cluster member candidates is underway to refine the determination of the cluster mass function.

Acknowledgements

This work was supported by the European Research Training Network entitled "The Formation and Evolution of Young Stellar Clusters" (HPRN-CT-2000-00155), through funding to NL and the "Young Local Universe" meeting.

References

1. Barrado y Navascués, D. *et al.* 2001, ApJ, 546, 1006
2. Barrado y Navascués, D. *et al.* 2001, ApJS, 134, 103
3. Barrado y Navascués, D. *et al.* 2002, A&A, 395, 813
4. Baraffe, I., Chabrier, G., Allard, F., & Hauschildt, P. H. 1998, A&A, 337, 403
5. Béjar, V. J. S. *et al.* 2001, ApJ, 556, 830
6. Bertin, E. and Arnouts, S. 1996, A&AS, 117, 393
7. Bouvier, J. *et al.* 1998, A&A, 336, 490
8. Chabrier, G., Baraffe, I., Allard, F., & Hauschildt, P. H. 2000, ApJ, 542, 464
9. Collinder, P. 1931, Annals of the Observatory of Lund, 2, 1
10. Dobbie, P. D. *et al.* 2002, MNRAS, 335, 687
11. Girardi, L. *et al.* 2002, A&A, 391, 195
12. Jameson, R. F., Dobbie, P. D., Hodgkin, S. T., & Pinfield, D. J. 2002, MNRAS, 335, 853
13. Jeffries, R. D., Thurston, M. R. & Hambly, N. C., 2001, A&A, 375, 863
14. Kharchenko, N. *et al.* 2004, in preparation
15. Loktin, A. V. & Beshenov, G. V. 2001, 27, 386
16. Lucas, P. W. and Roche, P. F. 2000, MNRAS, 314, 858
17. Luhman, K. L. 1999, ApJ, 525, 466
18. Luhman, K. L. *et al.* 2003a, ApJ, 590, 348
19. Luhman, K. L. *et al.* 2003b, ApJ, 593, 1093
20. Martín, E. L., Zapatero Osorio, M. R. & Rebolo, R. 1998 ASP Conf. Ser. 134: *Brown Dwarfs and Extrasolar Planets*, p507
21. Melotte, P. J. 1915, Mem Ras, 60, 175
22. Moraux, E., Bouvier, J., Stauffer, J. R., & Cuillandre, J.-C. 2003, A&A, 400, 891
23. Muench, A. A., Lada, E. A., Lada, C. J., & Alves, J. 2002, ApJ, 573, 366
24. Reid, I. N. and Cruz, K. L. 2002, AJ, 123, 2806
25. Rucinski, S. M. 1987, PASP, 99, 487
26. Stauffer, J. R. *et al.* 1998, ApJL, 499, 219
27. Stauffer, J. R. *et al.* 1999, ApJ, 527, 219
28. Stauffer, J. R. *et al.* 2003, in *Brown Dwarfs*, ed. E. L. Martín (IAU 211), p163–170
29. Tej, A., Sahu, K. C., Chandrasekhar, T., & Ashok, N. M. 2002, ApJ, 578, 523
30. Van't-Veer, F. 1980, Acta Astronomica, 30, 381
31. Wielen, R. 1971, A&A, 13, 309
32. Zacharias, N. *et al.* 2003, VizieR Online Data Catalog

BINARY STAR FORMATION FROM ROTATIONAL FRAGMENTATION

D. A. HUBBER & A. P. WHITWORTH

School of Physics and Astronomy, 5 The Parade, Cardiff, CF24 3YB, U.K.

We consider a model of binary star formation in which a rotating core collapses, bounces and undergoes ring fragmentation producing a small cluster of $\mathcal{N}$ protostars (where $\mathcal{N} < 7$). We follow the dynamical evolution using an $\mathcal{N}$-body code, and perform many realisations to obtain statistically robust distributions for the various stellar and binary parameters. This model can reproduce the observed distributions of eccentricity and multiplicity, as well as the IMF. The width of the binary period distribution can also be explained by this model, provided the amount of rotation in star forming cores covers a wide logarithmic range.

Keywords : binaries : general - methods : N-body simulations - methods : statistical - stars : formation

1 Introduction and Observations

One of the main constraints on star formation theory is to reproduce the observed statistics of binary stars, in particular the binary period distribution. Duquennoy & Mayor (1991; hereafter DM91) have made observations of a complete sample of G-dwarf (i.e. solar mass) primaries in the solar neighbourhood and determined the various binary parameters. They find that the period distribution can be well fitted by a log-normal, i.e.

$$\frac{d\mathcal{N}}{d\log P_d} = \exp\left(\frac{-(\log P_d - \overline{\log P_d})^2}{2\sigma^2_{\log P}}\right) \tag{1}$$

where P_d is the period in days, $\overline{\log P_d} = 4.8$, and $\sigma_{\log P}$=2.3. They also observe that nearly 60% of all the G-dwarves in their sample are in multiple systems. These two observations indicate not only that binary stars are more common than single stars, but that they must form on a wide range of scales, corresponding to nearly ten orders of magnitude in period. The high multiplicty of young stellar objects (e.g. Reipurth & Zinnecker 1993) implies that stars are born in multiple systems, not as isolated single stars that pair-up later.

Molecular cores are believed to collapse under gravity and form stars. Since the majority of binary separations ($\sim$ 100AU) are much smaller than the typical size of a star forming core ($\sim$ 0.1pc), it is presumed that multiple systems form when cores fragment into more than one component rather than forming a single star. In this work, we consider what happens if rotationally induced fragmentation is the dominant binary formation mechanism (e.g. Bonnell & Bate 1994,Cha & Whitworth 2003). We investigate this model because (a) it is simple to describe with few free parameters, and (b) observations suggest that cores may be rotating. Goodman et al. (1993; hereafter G93) measured the velocity profiles of 43 cores and found that 29 of them had a significant velocity gradient. If we interpret the velocity gradient as a signature of rotation, this suggests that most cores have some degree of bulk rotation.

We presume that a core with a small degree of rotation will form a disk, which overshoots centrifugal support and bounces, forming a dense ring. We further presume this ring fragments producing a small cluster of $\mathcal{N}$ protostars. We model these protostars as point masses and use an $\mathcal{N}$-body code to follow their dynamical evolution. Initially, we run dimensionless simulations of the model and scale them later using the observed distributions of core parameters. We can thus obtain statistical distributions of the various binary parameters and compare them with the observations. We use $\mathcal{N}$-body methods rather than hydrodynamical codes, because we can then run many realisations and obtain well-constrained statistical distributions of the various parameters (see also Sterzik & Durisen 1998, Sterzik & Durisen 2003)

2 Outline of model and initial conditions

Here we discuss setting up the inital conditions for the dimensionless simulations. We consider a rotating pre-stellar core with mass M_c of initial radius R_i, and having an initial value of the ratio of rotational to gravitational potential energy, β_i, which is less than unity. If the core collapses conserving angular momentum, then $\beta \propto R^{-1}$. We assume that the point of rotationally induced fragmentation is when $\beta \sim 1$, and thus the radius of the ring is $R_{\rm f} \sim \beta_{\rm i} R_{\rm i}$. We assume that the ring fragments into $\mathcal{N}$ proto-stars, where $\mathcal{N}$ is a free parameter. We draw the stellar masses at random from a log-normal distribution

$$\frac{d\mathcal{N}}{d\log m} = \frac{\mathcal{N}}{(2\pi)^{\frac{1}{2}}\sigma^2_{\log m}} \exp\left(\frac{-(\log m)^2}{2\sigma^2_{\log m}}\right) \tag{2}$$

where the standard deviation $\sigma_{\log m}$ is also a free parameter. We rescale the masses in each cluster so that the total system mass is equal to unity.

$$\sum_{n=1}^{n=\mathcal{N}} \{m_n\} \ = \ 1 \tag{3}$$

Before fragmentation, the ring is assumed to have uniform line density. Therefore, the protostars are distributed round the ring so that each protostar occupies a fraction of the circumference proportional to its mass. The angular segment of the material from which the n^{th} protostar forms is

$$\Delta\theta_n = \frac{2\pi m_n}{M_c}. \tag{4}$$

Hence, in circular polar co-ordinates, we can put $\theta_1 = 0$ and

$$\theta_n = \theta_{n-1} + \tfrac{1}{2}\left(\Delta\theta_{n-1} + \Delta\theta_n\right), \quad n = 2, 3, ., \mathcal{N}. \tag{5}$$

The stars are placed at the centre of mass of the material from which they formed, i.e. at a radius from the centre of the ring

$$r_n = R_f \left(\frac{M_c}{m_n \pi}\right) sin\left(\frac{m_n \pi}{M_c}\right). \tag{6}$$

The n^{th} protostar has circular speed

$$v_n = V\left(\frac{M_c}{m_n\pi}\right) sin\left(\frac{m_n\pi}{M_c}\right) \tag{7}$$

where V is scaled so that the total system energy is virialised. It should be noted that scaling the velocities in this way means that not all the angular momentum of the initial core goes into the orbital motion of the protostars. The remaining angular momentum must go into spin of the individual stars and their attendent discs.

For any system with $\mathcal{N} > 2$, the motion is chaotic and must be followed using an N-body code. The cluster will eject stars dynamically until it reaches a stable or quasi-stable state. We evolve each system for about 1000 crossing times to ensure that the vast majority of systems have dissolved. In general, a statistical ensemble of simulations produces a variety of end-states, such as binaries, triples, quadruples and ejected singles. We record the various final binary parameters, i.e. the multiplicity, the orbital eccentricity, the component mass-ratio $q \equiv m_2/m_1$, the orbital semi-major-axis and the orbital period. To obtain good statistics for the distributions, we follow many realisations. We use an adapted version of NBODY3 written by Aarseth (1999). NBODY3 uses sophisticated regularisation techniques to accurately integrate the dynamical motion and identify binaries and other multiple systems.

3 Dimensionless simulations

We initially perform dimensionless simulations of the cluster, so $R_f = 1$ and $M_c = 1$. This allows us to scale the results to any core size, as discussed later. We measure the dimensionless separation (the ratio of semi-major-axis to ring radius), and the dimensionless period (the ratio of orbital to ring period) as well as the eccentricity and multiplicity. We have 2 free parameters to investigate, $\mathcal{N}$ and $\sigma_{\log m}$. We choose the values $\mathcal{N} = 3, 4, 5$ & 6, and $\sigma_{\log m} = 0.2, 0.4$ & 0.6.

Period distribution - The dimensionless period distribution has approximately log-normal form, although it is asymmetric with a tail stretching to longer-periods. The width of the distribution ranges from $\sim 0.1 - 0.5$ for different values of $\mathcal{N}$ and $\sigma_{\log m}$. First, if we fix $\sigma_{\log m}$ and increase $\mathcal{N}$, the period distribution shifts to shorter periods and becomes broader. Second, if we fix $\mathcal{N}$ and increase $\sigma_{\log m}$, the period distribution shifts to longer periods and is also somewhat broader. The width is more strongly controlled by the value of $\mathcal{N}$ than the value of $\sigma_{\log m}$.

Eccentricity - The observed eccentricity distribution can be approximated by the form $d\mathcal{N}/de = 2e$. The simulations tend to produce too many high eccentricity binaries compared to the observations. Increasing either $\mathcal{N}$ or $\sigma_{\log m}$ increases the proportion of low eccentricity binaries, although there still tends to be an excess of very high ($e > 0.95$) binaries.

Mass ratio - The observed mass-ratio distribution has a large fraction of low-q systems (i.e. $q \leq 0.3$) for G-dwarf primaries. This can only be reproduced if $\sigma_{\log m}$ is high enough ($\sigma_{\log m} > 0.4$).

4 Convolving with the core mass spectrum (CMS)

Motte et al. (2001) have measured the CMS in Orion B and fitted it using a two-part power law with a knee at $1M_\odot$, i.e.

$$\psi = \frac{d\mathcal{N}}{dM_c} = \begin{cases} k_1 M_c^{-1.5}, & 0.5M_\odot \leq M_c \leq 1.0M_\odot; \\ k_2 M_c^{-2.5}, & 1.0M_\odot \leq M_c \leq 10.0M_\odot. \end{cases} \tag{8}$$

Other observations have shown similar forms to Equation 8. We now convolve the dimensionless simulations with this CMS.

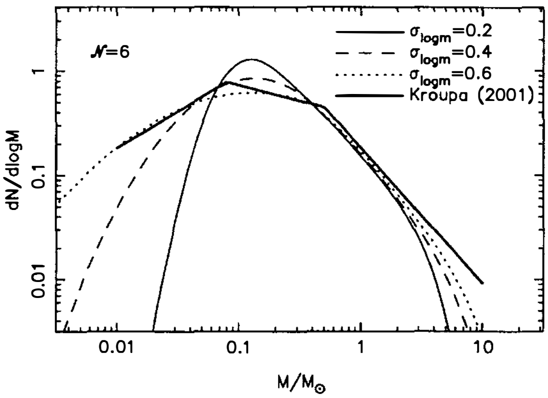

Figure 1: The IMF generated in our model for $\mathcal{N} = 6$ and $\sigma_{\log m} = 0.2, 0.4$ & 0.6. Shown also for comparison is the Kroupa IMF (2001) as a 4-part power law.

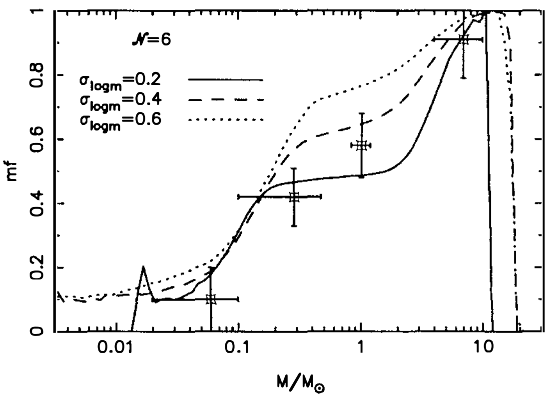

Figure 2: The multiplicity frequency generated in our model for $\mathcal{N} = 6$ and $\sigma_{\log m} = 0.2, 0.4$ & 0.6. Some observational points for the multiplicity frequency have been added (see Section 4)

The resultant IMF - We obtain resultant IMF's for all combinations of $\mathcal{N}$ and $\sigma_{\log m}$, and compare them to the Kroupa IMF (2001), which is represented by a 4-part power law. Figure 1 shows the resultant IMF for $\mathcal{N} = 6$ and $\sigma_{\log m} = 0.2, 0.4$ & 0.6. The shape of the IMF is strongly dependent on $\sigma_{\log m}$. For low $\sigma_{\log m}$, the form of the IMF is similar to the CMS, but as $\sigma_{\log m}$ increases, the overall shape becomes broader. We find a good fit to the IMF with relatively high $\sigma_{\log m}$ (> 0.4) and $\mathcal{N} > 4$.

Multiplicity - We define the multiplicity frequency, $\mathrm{mf}(m)$ as the fraction of systems with primary mass m., which are multiple, i.e.

$$\mathrm{mf}(m) = \frac{B(m) + T(m) + Q(m)}{S(m) + B(m) + T(m) + Q(m)} \tag{9}$$

where $S(m)$, $B(m)$, $T(m)$ and $Q(m)$ are the number of single, binary, triple and quadruple systems with primary mass m. The multiplicity frequency has been determined observationally for several mass-ranges. The four we use for comparison with our results (c.f. Sterzik & Durisen 2003) are 0.10 ± 0.10 for $0.01 M_\odot \leq M \leq 0.08 M_\odot$ (Martín et al. 2000), 0.42 ± 0.09 for $0.08 M_\odot \leq M \leq 0.47 M_\odot$ (Fisher & Marcy 1992), 0.58 ± 0.10 for $0.84 M_\odot \leq M \leq 1.20 M_\odot$ (DM91) and

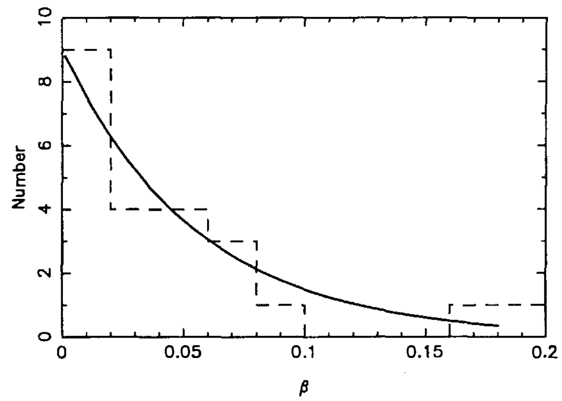

Figure 3: Inferred values of β for cores (Goodman et al 1993). Also shown is a simple functional fit, Equation 11

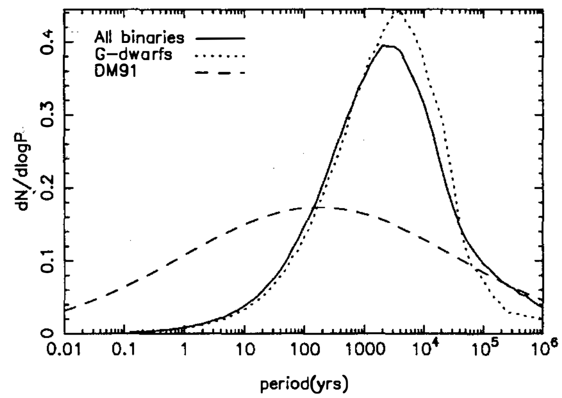

Figure 4: Period distribution for $\mathcal{N} = 6$ and $\sigma_{\log m} = 0.4$ convolved over both the CMS and β-distribution for all binaries and for G-dwarves only. DM91 is shown for comparison.

0.91 ± 0.12 for $4.0M_\odot \leq M \leq 10.0M_\odot$ (Shatsky & Tokovinin 2002).

The results of the model show a similar trend to the observations, i.e. **mf** is very low for low-mass brown-dwarves, steadily increases with increasing m, and reaches approximately unity at around $8M_\odot$. If we fix $\sigma_{\log m}$ and increase $\mathcal{N}$, the multiplicity generally decreases for all m. If we fix $\mathcal{N}$ and increase $\sigma_{\log m}$, the multiplicity increases at almost all m.

5 Convolving with the distribution of core radii

To scale the periods and semi-major axes of the binaries, we must know the physical radius of the ring, R_f. If we assume that $R_f \sim \beta_i R_i$ as discussed in Section 2, and that the initial core radii obey Larson's scaling relations (c.f. Larson 1981, Myers 1983), then

$$R_f = \begin{cases} 400AU \left(\frac{\beta_i}{0.02}\right)\left(\frac{M_c}{M_\odot}\right), & M_c < M_\odot; \\ 400AU \left(\frac{\beta_i}{0.02}\right)\left(\frac{M_c}{M_\odot}\right)^{\frac{1}{2}}, & M_c > M_\odot. \end{cases} \tag{10}$$

The physical separation of a binary is thus given by $a = R_f\xi$ where ξ is the dimensionless separation. The period is then given by Keplers third law.

Since $R_f = R_f(M_c, \beta_i)$, we convolve the dimensionless distribution over both the CMS and the distribution of β_i-values. We use a simple analytical fit to the observed β distribution (G93)

$$\frac{d\mathcal{N}}{d\beta} = \beta_0^{-1} \exp - \frac{\beta}{\beta_0} \tag{11}$$

where β_0 is a constant. $\beta_0 = 0.056$ gives a good fit to the observations. Figure 4 shows the overall period distribution for our best set of parameters. $\mathcal{N} = 0.6$ and $\sigma_{\log m} = 0.4$ gives a reasonable fit to the observed distributions of e,q and **mf**. Convolving with the β_i-distribution of Equation 11 we obtain a period distribution with standard deviation $\sigma_{\log P} = 0.94$ (see Figure 4). This is significantly less than the standard deviation obtained by DM91 for G-dwarf primaries, $\sigma_{\log P} = 2.3$.

6 Discussion

Although this simple model ignores much of the detailed physics of star formation (e.g. accretion), it can explain many of the observations of binary stars. In general the model faithfully reproduces the observed IMF and the observed distributions of eccentricity and mass-ratio, if $\mathcal{N}$ and $\sigma_{\log m}$ are relatively high ($\mathcal{N} \sim 5-6$, $\sigma_{\log m} \sim 0.4-0.6$). The observed distribution of multiplicity frequency suggests somewhat lower values of $\sigma_{\log m}$ ($\sim 0.2-0.4$). Therefore the optimum fit to the observations is $\mathcal{N} \sim 5-6$ and $\sigma_{\log m} \sim 0.4$. However the distribution of periods produced by this model, although broad ($\sigma_{\log P} \sim 1$) is not as broad as that observed by DM91 ($\sigma_{\log P} = 2.3$). Since the observations of velocity gradients in cores by G93 do not constrain the β-distribution that well, there is scope for investigating different forms of the β-distribution. A large logarithmic range of β values may explain the period distribution.

Acknowledgments

We thank Simon Goodwin for helpful discussions and Sverre Aarseth for help with NBODY3.

References

1. Aarseth, S. J. 1999, PASP, 111, 1333
2. Bonnell, I. A. & Bate, M. R. 1994, A&A, 271, 999
3. Cha, S.-H. & Whitworth, A. P. 2003, MNRAS, 340, 91
4. Duquennoy, A. & Mayor, M. 1991, A&A, 248, 485
5. Fischer, D. A. & Marcy, M. 1992, ApJ, 396, 178
6. Goodman, A. A., Benson, P. J., Fuller, G. A. & Myers, P.C. 1993, ApJ, 406, 528
7. Kroupa, P. 2001, MNRAS, 322, 231
8. Larson, R., B. 1981, MNRAS, 194, 809
9. Martín, E. L., Brandner, W., Bouvier, J. et al. 2000, ApJ,543, 299
10. Myers, P. C. 1983, ApJ, 1983, 2
11. Reipurth, B. & Zinnecker, H. 1993, A&A, 278
12. Shatsky, N. & Tokovinin, A. 2002, A&A, 382, 92
13. Sterzik, M. F. & Durisen, R. H. 1998, A&A, 339, 95
14. Sterzik, M. F. & Durisen, R. H. 2003, A&A, 400, 1031

IMPULSIVELY TRIGGERED STAR FORMATION

A.P. WHITWORTH
School of Physics & Astronomy, Cardiff University, 5 The Parade, Cardiff CF24 3YB, Wales, UK.

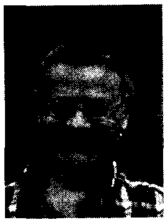

I review several different modes of impulsively triggered star formation, starting with star formation in turbulent molecular clouds and the origin of (i) the core mass function and (ii) the scaling relations between mass, radius and velocity dispersion. This leads to the identification of a critical ram pressure for triggering rapid star formation, and a reappraisal of the minimum mass for opacity-limited star formation. I also discuss star formation triggered by expanding nebulae (HII regions, stellar-wind bubbles and supernova remnants) and star formation triggered by a sudden increase in external pressure, including the formation of brown dwarves and planetary-mass objects by photo-erosion of pre-existing prestellar cores. I conclude by describing simulations of interactions between protostellar discs in dense small-N clusters, and note that such interactions are an efficient means of creating low-mass companions.

Keywords: ISM kinematics and hydrodynamics – Instabilities – Stars: formation

1 Introduction

In this contribution, I shall adopt the viewpoint that many (perhaps most) of the dominant modes of star formation in the Universe are impulsively triggered (e.g. Whitworth et al. 1996), and that star-forming molecular clouds spawn stars on a dynamical time-scale. This picture is usually referred to as 'star formation in a crossing time' (Elmegreen 2000). In this picture, molecular clouds are turbulent, because when they form they do not have sufficient time to relax to a quiescent state. Star formation occurs only in those places where two (or more) turbulent elements, having sufficient mass and density, collide with sufficient ram pressure to create a gravitationally unstable dense star-forming core. Therefore, in Section 2, I will review the gravitational fragmentation of a layer formed by the collision of two turbulent elements. In Section 3, I will develop a theory for the origin of the clump mass spectrum, based on gravitational fragmentation. In Section 4, I will derive a critical pressure for impulsively triggered star formation to proceed rapidly, based on the requirement that the shock compressed gas must be able to cool by coupling thermally to the dust. In Section 5, I will revisit the question of opacity limited fragmentation and the minimum mass for star formation, and show that one-shot layer fragmentation can deliver significantly lower-mass fragments ($\sim 0.003 M_\odot$) than conventional hierarchical fragmentation. In Section 6, I will discuss the fragmentation of shells swept up by expanding nebulae, as a means of generating star-forming clumps, and briefly mention a model of Sharples 104 which I am developing with Deharveng and colleagues. In Section 7, I will describe some work with Hennebelle on the collapse of cores which are subjected to an increase in external pressure, and compare the results with observation. In Section 8, I will present some work with Zinnecker in which we have shown that free-floating brown dwarves and planetary-mass objects can be formed rather easily when cores are overrun by an HII region and stripped down by photo-erosion. Finally, in Section 9, I will describe briefly some simulations of interactions between protostars and protostellar discs, which show that such interactions are an efficient way of generating low-mass companions.

2 Fragmentation of a shock-compressed layer

The fragmentation of a shock-compressed layer is one of the fundamental microphysical processes in a turbulent, star-forming cloud. The simplest case to consider is where two identical flows of gas, each with density $\rho_{\rm O}$, collide at relative velocity $2v_{\rm O}$. A shocked layer is formed, with isotropic velocity dispersion $\sigma_{\rm S}$ and density $\rho_{\rm S} \sim \rho_{\rm O}(v_{\rm O}/\sigma_{\rm S})^2$. The layer is contained by the ram-pressure $P_{\rm RAM} = \rho_{\rm O} v_{\rm O}^2$ of the material which continues to flow in from either side, *and not by self-gravity.* Consequently, until it fragments, the layer is close to equilibrium, and has a flat density profile. It fragments while it is still acquiring mass from the two colliding flows.

At their inception, the fastest-growing fragments are shaped like oblate spheroids, with their short dimension z parallel to the inflowing flux of matter, and their long dimension r in the plane of the layer. The time at which the layer starts to fragment non-linearly, and the initial radius, initial thickness and initial mass of the fastest-growing fragments, are given by

$$\begin{aligned} t_{\rm FRAG} &= \left[\frac{\sigma_{\rm S}}{G\,\rho_{\rm O}\,v_{\rm O}}\right]^{1/2}; & r_{\rm FRAG} &= \left[\frac{\sigma_{\rm S}^3}{G\,\rho_{\rm O}\,v_{\rm O}}\right]^{1/2}; \\ m_{\rm FRAG} &= \left[\frac{\sigma_{\rm S}^7}{G^3\,\rho_{\rm O}\,v_{\rm O}}\right]^{1/2}; & z_{\rm FRAG} &= \left[\frac{\sigma_{\rm S}^5}{G\,\rho_{\rm O}\,v_{\rm O}^3}\right]^{1/2} \end{aligned} \tag{1}$$

(Whitworth et al. 1994a,b). It is important to note that these expressions are not the same as those for conventional Jeans fragmentation of an extended 3-dimensional medium having the shocked density, $\rho_{\rm S} \sim \rho_{\rm O}(v_{\rm O}/\sigma_{\rm S})^2$. If we introduce the Mach number of the shock, $\mathcal{M} \equiv v_{\rm O}/\sigma_{\rm S}$, then the initial mass and the initial radius ($m_{\rm FRAG}$, $r_{\rm FRAG}$) are larger by a factor $\mathcal{M}^{1/2}$, and the thickness ($z_{\rm FRAG}$) is smaller by the same factor; hence the ratio of the initial radius to the initial thickness (i.e. the initial edge-on aspect ratio of a fragment) is $r/z \sim \mathcal{M}$.

The equations above have been confirmed by numerical simulations (e.g. Chapman et al. 1992, Pongracic et al. 1992). In general the shock compressed layer at first breaks up into a network of intersecting filaments, and then into prestellar cores along the filaments. The separation between adjacent filaments, and between adjacent cores on a filament, is of order $r_{\rm FRAG}$, as given above. This pattern of fragmentation has the effect that the prestellar cores tend to accrete most of their mass from along the filament from which they formed. Since in general the two colliding flows are not perfectly aligned, the shock-compressed layer has a net angular momentum, which causes it to tumble. Consequently the filaments in the layer are also tumbling, and as a core accretes from a filament it is spun up until it fragments to produce multiple star systems (Turner et al. 1995, Whitworth et al. 1995).

3 Larson's scaling relations and the clump mass spectrum

We can now use the phenomenology of layer fragmentation to explain Larson's scaling relations (Larson 1981) and the origin of the clump mass spectrum. In their simplest form, Larson's scaling relations give the radius, R, and internal velocity dispersion, σ, of a clump having mass M – and hence also the mean density, ρ, and dynamical time-scale, t, of the clump – in terms of simple power laws:

$$\begin{aligned} R(M) &\simeq R_\bullet\,(M/M_\bullet)^{\alpha}\,; & \rho(M) &\simeq \rho_\bullet\,(M/M_\bullet)^{1-3\alpha}\,; \\ \sigma(M) &\simeq \sigma_\bullet\,(M/M_\bullet)^{\beta}\,; & t(M) &\simeq t_\bullet\,(M/M_\bullet)^{\alpha-\beta}\,, \end{aligned} \tag{2}$$

where $(R_\bullet, M_\bullet, \rho_\bullet, \sigma_\bullet, t_\bullet)$ are reference values. Similarly, the clump mass spectrum can be approximated by a power law,

$$\begin{aligned} \mathcal{N}_M\,dM &\simeq K\,M^{-\gamma}\,dM\,, \\ \mathcal{M}_M\,dM &\simeq K\,M^{1-\gamma}\,dM \;\equiv\; K\,M^{2-\gamma}\,d\ell n[M]\,, \end{aligned} \tag{3}$$

where $\mathcal{N}_M\,dM$ is the number of clumps having mass in the interval $(M, M+dM)$ and $\mathcal{M}_M\,dM$ is the total amount of mass in clumps having mass in the same interval.

Star formation removes clumps from the low-mass end of this spectrum, but since the overall rate of star formation is slow, the net transfer of mass down the mass spectrum must also be slow. Either the transfer is one-way (from diffuse high-mass clumps to dense low-mass star-forming clumps) and proceeds very slowly at a rate equal to the rate of star formation, or the transfer is two-way and in approximate statistical equilibrium with almost as much mass being transferred up the spectrum by merging as down the spectrum by fragmentation. Either way, the mass spectrum can only be maintained if the mass in equal logarithmic mass bins is proportional to the dynamical time-scale. Combining Eqns. 2 and 3, we obtain the approximate constraint:

$$2-\gamma \simeq \alpha-\beta \qquad \longrightarrow \qquad \gamma \simeq 2-\alpha+\beta\,. \tag{4}$$

At the high-mass end of the clump mass spectrum, the clumps are supported mainly by turbulence (i.e. the line-widths are non-thermal), and the internal velocity dispersion decreases with decreasing mass. Therefore we can envisage an hierarchy of clumps within clumps, such that a clump of mass M contains subclumps of mass fM, and these in turn contain subsubclumps of mass f^2M. The properties of the clumps, subclumps and subsubclumps in this hierarchy are tabulated below

	clump	subclump	subsubclump
Mass	M	fM	f^2M
Velocity dispersion	σ	$f^{\beta}\sigma$	$f^{2\beta}\sigma$
Mean density	ρ	$f^{1-3\alpha}\rho$	$f^{2-6\alpha}\rho$

Thus, subclumps of mass fM having mean density $f^{1-3\alpha}\rho$ typically collide at velocity σ (i.e. the internal velocity dispersion of their parent clump) and the resulting shock-compressed layer typically fragments into subsubclunps of mass f^2M having internal velocity dispersion $f^{2\beta}\sigma$. We can therefore substitute $m_{\rm FRAG} \to f^2M$, $\sigma_{\rm S} \to f^{2\beta}\sigma(M)$, $\rho_{\rm O} \to f^{1-3\alpha}\rho(M)$ and $v_{\rm O} \to \sigma(M)$ in Eqn. 1, to obtain

$$f^{14\beta+3\alpha-5}\left(\frac{M}{M_\bullet}\right)^{6\beta+3\alpha-3} = \frac{G^3\,M_\bullet^2\,\rho_\bullet}{\sigma_\bullet^6}\,. \tag{5}$$

Since this must be true for any f and any M, both the exponents on the lefthand side of Eqn. 5 must be zero, which in combination with Eqn. 4 gives

$$\text{FOR TURBULENT HIGH-MASS CLUMPS:} \qquad \alpha \simeq \frac{1}{2}\,, \quad \beta \simeq \frac{1}{4}\,, \quad \gamma \simeq \frac{7}{4} \tag{6}$$

(cf. Williams et al. 1994). Additionally, the righthand side of Eqn. 5 must equal unity, so possible reference values are $M_\bullet = M_\odot$, $\rho_\bullet = 4 \times 10^{-20}\,\mathrm{g\,cm^{-3}}$ (corresponding to $n_{H_2} = 10^4\,H_2\,\mathrm{cm^{-3}}$), $\sigma_\bullet = 0.2\,\mathrm{km\,s^{-1}}$ (corresponding to the isothermal sound speed in molecular gas at temperature $T = 10\,\mathrm{K}$), $R_\bullet = 0.08\,\mathrm{pc}$, and $t_\bullet = 0.4\,\mathrm{Myr}$.

At the low-mass end of the clump mass spectrum, the clumps are supported mainly by thermal pressure, and – within a factor of 1.5 – the temperature is $T_\bullet = 10\,\mathrm{K}$, so the isothermal sound speed is $a_\bullet = 0.2\,\mathrm{km\,s^{-1}}$. (The gas cannot readily cool below the cosmic microwave background at $T_{CMB} \sim 3$ K, and efficient cooling by molecular line emission and dust emission keeps the temperature close to 10K.) Hence $R \simeq GM/a_\bullet^2 \propto M^1$ and $\sigma \simeq a_\bullet \propto M^0$, giving

$$\text{FOR THERMAL LOW-MASS CLUMPS:} \qquad \alpha \simeq 1, \quad \beta \simeq 0, \quad \gamma \simeq 1. \tag{7}$$

Consequently there is a knee in the clump mass function around $M_\bullet \sim M_\odot$, where the switch occurs between the high-mass regime (where core support is dominated by turbulence and $\gamma \simeq 1.75$) and the low-mass regime (where core support is dominated by thermal pressure and $\gamma \simeq 1$). We emphasize that this result presumes an approximately steady statistical equilibrium. If there were a sudden increase in external pressure, this would presumably perturb this equilibrium, driving matter preferentially down to lower masses (and ultimately to protostellar collapse) and thereby steepening the clump mass function somewhat.

4 The critical pressure for rapid star formation

A critical issue in the fragmentation of shock compressed layers is the ability of the shocked gas to cool radiatively. Indeed, gravitational fragmentation requires better than isothermal cooling across the shock, as first demonstrated by Stone (1970). This requirement cannot be satisfied by line cooling. It requires the full bandwidth afforded when the gas couples thermally to the dust and the dust then emits continuum radiation. Therefore a critical condition for the fragments of a shock-compressed layer to collapse and form stars is that the time-scale for the gas to couple thermally to the dust, t_{COUPLE}, should be less than the freefall time t_{FF}. Assuming that the velocity dispersion in the shock compressed layer is the same as the isothermal sound speed ($\sigma_S \simeq a_S$), and so the density is $\rho_S \simeq \rho_O (v_O/a_S)^2$ (where v_O is the velocity with which matter flows into the shock), the time-scale for the gas to couple thermally to the dust is

$$t_{COUPLE} \simeq \frac{(2\pi)^{1/2}\, r_D\, \rho_D}{Z_D\, \rho_S\, a_S} \left(\frac{a_T^2 + a_S^2}{a_T^2} \right). \tag{8}$$

Here $r_D \sim 10^{-5}$ cm is the radius of a representative (spherical) dust grain, $\rho_D \sim 3\,\mathrm{g\,cm^{-3}}$ is the density of the solid material from which dust grains are made, and $Z_D \sim 0.01$ is the fraction by mass of dust in the protostellar matter. The term in brackets on the lefthand side of the equation represents the inverse of the thermal accomodation coefficient. This term is approximately unity for $a_S < a_T$, which with $a_T \sim 1\,\mathrm{km\,s^{-1}}$ corresponds to $T_S < 300\,\mathrm{K}$; for higher temperatures the thermal accommodation coefficient decreases approximately as T^{-1}, but we will be mainly concerned with the low temperature regime where thermal accommodation is efficient.

If we now require that $t_{COUPLE} \lesssim t_{FF} = (3\pi/32G\rho_S)^{1/2}$, we obtain

$$P_S \equiv \rho_S\, a_S^2 \gtrsim P_{COUPLE} \simeq \frac{64\,G}{3} \left[\frac{r_D\, \rho_D}{Z_D} \right]^2 \simeq 10^5\,\mathrm{cm^{-3}\,K}\,k_B\,, \tag{9}$$

where k_B is the Boltzmann constant. We emphasize two important aspects of this result. (i) Since in our model of dynamically triggered star formation $P_S = \rho_S a_S^2 = P_{RAM} = \rho_O v_O^2$, this is in effect a threshold for the ram pressure which will trigger rapid star formation in a turbulent cloud. (ii) $10^5\,\mathrm{cm^{-3}\,K}\,k_B$ is typical of the turbulent pressures found in star-forming molecular clouds; for a self-gravitating cloud, it corresponds to a critical surface-density

$$\Sigma_{\rm COUPLE} \;\simeq\; \left(\frac{P_{\rm COUPLE}}{G}\right)^{1/2} \;\simeq\; 1.4\times10^{-2}\,\mathrm{g\,cm^{-2}}\,,$$

or equivalently to a critical column-density $N_{\rm H_2} \simeq 4\times10^{21}\,\mathrm{H_2\,cm^{-2}}$.

5 The minimum mass for star formation

The minimum mass for star formation is normally attributed to opacity limited 3-dimensional hierarchical fragmentation, as first described by Hoyle (1953). In this picture, a protocluster cloud contracts under gravity, and as long as the gas can cool efficiently – i.e. as long as the gas remains isothermal – the Jeans mass decreases with increasing density and so the cloud can break up into subclouds, and the subclouds can break up into subsubclouds, and so on until the initial cloud is broken up into many small prestellar cores. The process of hierarchical fragmentation halts rather suddenly when the fragments become so dense and opaque that they can no longer cool efficiently, the Jeans mass no longer decreases with increasing density, and fragmentation then ceases. An elegant analysis by Rees (1976) shows that the minimum mass for 3-dimensional hierarchical fragmentation is given by

$$M_{\rm MIN} \;\simeq\; \frac{m^3_{\rm PLANCK}}{\bar{m}^2}\left(\frac{a}{c}\right)^{1/2} \;\propto\; T^{1/4}\,\bar{m}^{-9/4}\,, \tag{10}$$

where $m_{\rm PLANCK} \equiv (hc/G)^{1/2} \simeq 5.5\times10^{-5}\,$g is the Planck mass, $\bar{m} \simeq 4\times10^{-24}\,$g is the mean gas-particle mass, a is the isothermal sound speed, and c is the speed of light. A more detailed analysis by Silk (1977) gives a value of order $0.015M_\odot$ for contemporary (Population I) star formation in the solar vicinity ($Z \simeq Z_\odot$).

However, there are problems with this picture. Hierarchical fragmentation is never observed in numerical simulations, and there is no evidence for its occuring in nature. The reason for this probably has to do with the following factors. (i) The time-scale on which a subcloud contracts is always longer than the time-scale on which its parent cloud is contracting. Therefore neighbouring subclouds tend to be merged by the overall contraction of the parent cloud, before they can condense out as separate entities. Permanent fragmentation is therefore unlikely – unless nonlinear perturbations are applied at the outset (i.e. 'turbulence' is invoked, e.g. Goodwin et al. 2004a, 2004b), but even then the fragmentation is not noticeably hierarchical. (ii) Isolated subclouds are likely to grow by accretion as they contract. Thus, even if a subcloud starts out with a mass just exceeding the local Jeans mass, its mass will have increased by a large factor before its density contrast with the background becomes significant.

Given these problems with hierarchical fragmentation, and in the light of the hypothesis that star formation regions may be very dynamical, Boyd & Whitworth (2004) have considered whether the opacity limit gives a different minimum mass when applied to one-shot 2-dimensional fragmentation of a shock-compressed layer. As in Section 2, we consider a shock compressed layer formed by the collision of two idenitical streams having pre-shock density $\rho_{\rm O}$ and relative velocity $2v_{\rm O}$; we again assume that the velocity dispersion in the shock compressed layer is the same as the isothermal sound speed ($\sigma_{\rm S} \simeq a_{\rm S}$), and the unperturbed shocked density is therefore $\rho_{\rm S} \simeq \rho_{\rm O}(v_{\rm O}/a_{\rm S})^2$. Proto-fragments are modelled as spheroids with initial half-thickness $z_{\rm I}$ equal to the half-thickness of the layer. The initial radius $r_{\rm I}$ is chosen by identifying the fastest growing fragment. Fragmentation occurs whilst the layer continues to grow, and the opacity limit is set by the requirement that the heating rate,

$$\mathcal{H} \;\simeq\; -P\,\frac{dV}{dt} + r^2\,\rho_{\rm O}\,v_{\rm O}\left(v_{\rm O}^2 - \dot{r}^2\right), \tag{11}$$

must not exceed the maximum possible radiative cooling rate,

$$\mathcal{C} \simeq r^2 \sigma_{\rm SB} T_{\rm S}^4 . \tag{12}$$

The first term on the righthand side of Eqn. 11 is the rate at which the internal energy of the fragment is increased by compressional work. The second term is rate at which energy is dissipated in the shock where the inflowing material is decelerated, minus the energy used to accelerate this material up to the speed with which the fragment is condensing laterally. Typically these two terms are comparable. Adopting $a_{\rm S} = 0.2\,{\rm km\,s^{-1}}$ (corresponding to molecular gas, $\bar{m} \simeq 4 \times 10^{-24}\,{\rm g}$, at $T_{\rm S} = 10{\rm K}$), we find

$$M_{\rm MIN} \simeq 0.0027 M_\odot . \tag{13}$$

Figure 1 shows the region of the $(\rho_{\rm O}, v_{\rm O})$-plane in which the minimum mass is less than $0.005 M_\odot$. We see that there is a wide range of values ($5 \times 10^{-18}\,{\rm g\,cm^{-3}} \lesssim \rho_{\rm O} \lesssim 2 \times 10^{-15}\,{\rm g\,cm^{-3}}$ and $0.6\,{\rm km\,s^{-1}} \lesssim v_{\rm O} \lesssim 6\,{\rm km\,s^{-1}}$) over which very low mass fragments can be created by the fragmentation of shock-compressed layers.

We note that this is a conservative estimate for the minimum mass, since the immediate post-shock gas is much hotter than $T_{\rm S} = 10\,{\rm K}$, and therefore the energy dissipated in the accretion shock is radiated at higher temperature – hence more efficiently – than the PdV work. We also note that this is a more realistic derivation of the minimum mass than the standard derivation of the minimum mass for 3-dimensional hierarchical fragmentation, on two important counts. (i) It takes account of competition with other scales of fragmentation. Here the minimum mass is required to be the fastest condensing mass-scale. (It is a well-known property of layer fragmentation that there is a finite fragmentation scale which condenses out faster than all others.) (ii) The analysis takes account of continuing accretion during condensation. For example the minimum mass fragment with $M_{\rm FINAL} = 0.0027 M_\odot$ starts out with $M_{\rm INITIAL} = 0.0011 M_\odot$ (Boyd & Whitworth 2004).

6 The fragmentation of shells swept up by expanding nebulae

There are other channels for impulsively triggered star formation. For example, on large scales star formation occurs in shells swept up by expanding nebulae, i.e. expanding HII regions, stellar wind bubbles and supernova remnants. This is the basis of sequential self-propagating star formation. If an HII region, stellar wind bubble or supernova remnant is excited by a large cluster of recently-formed stars, it can lead to a burst of star formation of such violence that the interstellar medium is restructured on scales comparable with the host galaxy. In such cases it is necessary to include the effect of galactic rotation (Jungwiert & Palous, 1994). However, the basic mechanism of fragmentation is essentially the same as for layer fragmentation.

As an example, we consider a stellar wind bubble driven by a star (or stars) whose wind is steady and isotropic and has mechanical luminosity $L_{\rm WIND} \equiv \dot{M}_{\rm WIND} v_{\rm WIND}^2 / 2$, where $\dot{M}_{\rm WIND}$ is the mass loss rate and $v_{\rm WIND}$ is the speed of the wind. We suppose that the ambient interstellar medium is static with uniform density $\rho_{\rm O}$ and that this gas is swept up into a thin dense shell at the edge of the bubble; the swept-up gas in the shell has isothermal sound speed $a_{\rm S}$. The spherically symmetric expansion of the bubble can then be approximate by a similarity solution $R_{\rm SHELL} \sim (L_{\rm WIND} t^3 / \rho_{\rm O})^{1/5}$. Non-linear fragmentation of the shell occurs at time $t_{\rm FRAG}$ when the shell has radius $R_{\rm FRAG}$, where

$$t_{\rm FRAG} \simeq \left[\frac{a_{\rm S}^5}{G^5 \rho_{\rm O}^4 L_{\rm WIND}} \right]^{1/8} , \qquad R_{\rm FRAG} \simeq \left[\frac{L_{\rm WIND}\, a_{\rm S}^3}{G^3 \rho_{\rm O}^4} \right]^{1/8} . \tag{14}$$

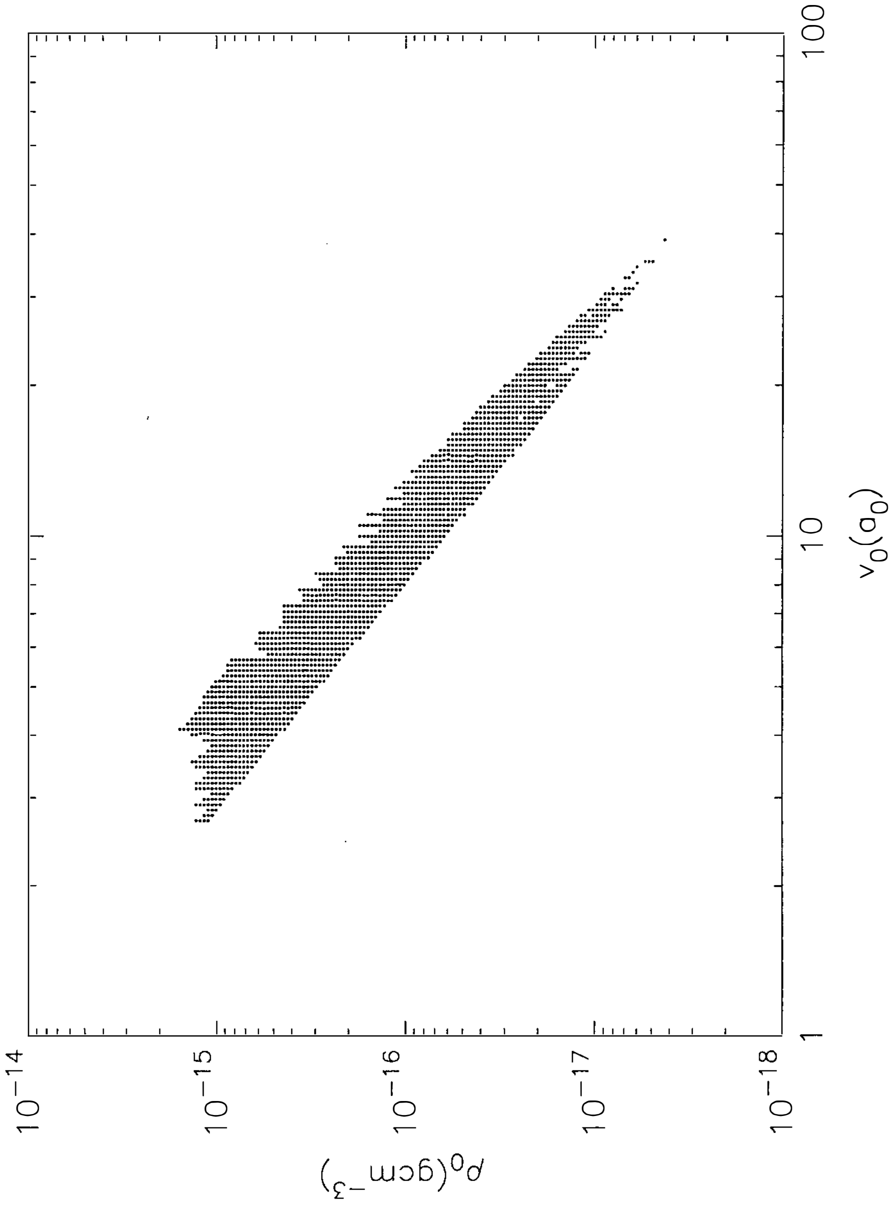

Figure 1: We assume that two streams of gas with uniform density ρ_o collide at relative speed $2v_o$, and that the resulting shock-compressed layer has isothermal sound speed $a_o = 0.2\,\mathrm{km\,s^{-1}}$. The shaded region of the $(\ell og_{10}[\rho_o/\mathrm{g\,cm^{-3}}], \ell og_{10}[v_o/\bullet_{\rm s}])$-plane is the locus of conditions where the fastest-condensing fragment in the shock-compressed layer has mass less than $0.005M_{\bullet}$. The scalloped edge to the locus arises because sometimes an initially small fragment bounces in the z direction and therefore increases rather rapidly in mass, as it advances to meet the inflow; consequently its final mass depends on the phase and duration of the bounce.

The mass and initial radius of the fastest condensing fragments are then

$$m_{\rm FRAG} \simeq \left[\frac{a_{\rm S}^{29}}{G^{13}\,\rho_{\rm O}^{4}\,L_{\rm WIND}}\right]^{1/8}, \qquad r_{\rm FRAG} \simeq \left[\frac{a_{\rm S}^{13}}{G^{5}\,\rho_{\rm O}^{4}\,L_{\rm WIND}}\right]^{1/8} \tag{15}$$

(Whitworth & Francis 2002). We note that these results are not very sensitive to the assumption of a uniform background density. In other words, they still hold if there is a density gradient in the ambient interstellar medium so that only a partial shell forms. They are also evidently not very sensitive to $L_{\rm WIND}$, except that we must have

$$L_{\rm WIND} > 3\times 10^{4}\,\frac{a_{\rm S}^{5}}{G} \simeq 10^{3}\,L_{\odot}\left(\frac{a_{\rm S}}{\rm km\,s^{-1}}\right)^{5}, \tag{16}$$

otherwise the expansion of the shell stalls, due to the gravity of the accumulated mass, before it fragments. The shell can still fragment after it stalls, but the fragments are then comparable is size to the radius of the shell, and their mass is essentially the same as the Jeans mass in the undisturbed background medium.

With Deharveng and Lefloch I am currently trying to model Sharples 104. This is a spherically symmetric HII region with four molecular fragments distributed evenly around its rim; one of the fragments contains an embedded young star cluster (Deharveng et al. 2003). In our model, a star cluster forms at the centre of a molecular cloud and excites an HII region which then expands, sweeping up a dense shell of gas which eventually breaks up into the four molecular fragments we see today. The model is constrained to fit the observed output of ionizing photons ($\dot{\mathcal{N}}_{\rm LyC}$), the mass and diameter of the HII region ($M_{\rm HII}$,$d_{\rm HII}$), the mass of molecular gas in the four fragments, the fact that there are just four fragments, and the lack of molecular gas on the line of sight through the centre of the HII region (Whitworth et al. 2004).

7 Pre-existing cores subjected to a sudden increase in internal pressure

Another type of impulsively triggered star formation occurs when a pre-existing core is subjected to a sudden increase in pressure. In the simplest case, we consider a stable Bonnor-Ebert sphere, contained by an external pressure $P_{\rm EXT}$, and then we increase $P_{\rm EXT}$ on a time-scale shorter than, or comparable with, the sound-crossing time (Hennebelle et al. 2003). This has the effect of driving a compression wave into the core. The compression wave leaves in its wake a subsonic and approximately uniform inward velocity field, similar to what is inferred from the asymmetric double-peaked molecular-line profiles seen in L1544 and other prestellar cores (e.g. Tafalla et al. 1998, Williams et al. 1999, Lee et al. 1999, 2001, Gregersen et al. 2000). When the compression wave reaches the centre, it is reflected as an expansion wave, and a protostar is formed. The protostar grows by accretion, at first quite rapidly ($\gtrsim 10^{-5}M_{\odot}\,{\rm yr}^{-1}$) and then less rapidly ($\lesssim 10^{-6}M_{\odot}\,{\rm yr}^{-1}$). This pattern of initially rapid and then decreasing accretion accords well with observations of Class 0 and Class I sources. (Class 0 sources are relatively rare, and their outflows are powerful, implying a short-lived period of rapid accretion. Class I sources are more frequent and have weaker outflows, implying a longer-lived period of slower accretion.)

In these spherically symmetric simulations, only a single central protostar is formed. However, if a little rotation is added (Hennebelle et al. 2004), the result is usually a small-N multiple. For small β (initial ratio of rotational to gravitational energy), the large-scale flows are the same as in the non-rotating case, but then a disc forms around the central primary protostar and the disc fragments to form secondary protostars. The disc tends to be more unstable – in the sense that it spawns more secondary protostars – if β is larger or the rate of compression is higher. This is because, as β is increased, more matter is deposited in the outer parts of the circum-primary disc; and as the rate of compression is increased, the matter is deposited in the outer parts of the disc more rapidly and at higher density. All these factors contribute to making the disc unstable against gravitational fragmentation. For very high β and very rapid compression, there is no central primary protostar. Instead fragmentation occurs via the formation of a ring.

We are now trying to model specific sources (see Hennebelle in this volume).

8 Forming free-floating brown dwarves and planetary-mass objects by photo-erosion

One way in which the pressure acting on a pre-existing core might be increased is if the surrounding gas is suddenly ionized. With Zinnecker (Whitworth & Zinnecker 2004) I have developed a semi-analytic model for a pre-existing core which is overrun by an HII region. We have shown that this could be a very efficient way of forming free-floating brown dwarves and/or planetary-mass objects. As soon as the surroundings of the core are ionized, the increase in external pressure drives a compression wave into the core. When this compression wave impinges on the centre of the core a protostar forms there and starts to grow by accretion. At the same time, the compression wave is reflected as an expansion wave and propagates outwards, leaving in its wake an approximately freefall velocity field, which feeds the accretion flow onto the growing central protostar. Whilst all this is going on, an ionization front eats into the core, eroding its outer layers. The final mass of the central protostar is determined by the moment at which the inward propagating ionization front encounters the outward propagating expansion wave. Soon after that moment, the kinetic energy of the newly ionized gas flowing off the ionization front becomes less than its binding energy to the central protostar, and photo-erosion ceases. To a good approximation the final protostellar mass is given by

$$M_{\rm FINAL} \simeq 0.012 M_\odot \left(\frac{a_{\rm I}}{\rm km\,s^{-1}}\right)^6 \left(\frac{\dot{\mathcal{N}}_{\rm LyC}}{10^{50}\,\rm s^{-1}}\right)^{-1/3} \left(\frac{n_{\rm O}}{10^3\,\rm cm^{-3}}\right)^{-1/3}, \tag{17}$$

where $a_{\rm I}$ is the isothermal sound speed in the neutral gas of the core, $\dot{\mathcal{N}}_{\rm LyC}$ is the rate at which the central OB star (or stars) emit hydrogen-ionizing photons, and $n_{\rm O}$ is the density in the ambient HII region. There is evidently a wide swathe of parameter space in which free-floating brown dwarves and planetary-mass objects can be formed by this process – provided there are suitable cores pre-existing in the vicinity of an OB star when it switches on its ionizing output. This is illustrated on Fig. 2.

9 Forming low-mass companions and free-floating objects in interactions between protostellar discs

Another mechanism for forming low-mass objects impulsively involves violent interactions between protostellar discs. Most protostars are surrounded by accretion discs when they first form, and initially these discs are likely to be quite massive (i.e. disc mass comparable to the mass of the central protostar) and quite extended (radius $\gtrsim$ 100 AU). At the same time, it appears that about 40% of stars are born in binaries with separations less than $\sim$ 200 AU; and numerical simulations suggest that collapsing cores fragment when they reach the density $\rho_{\rm CRIT} \sim 10^{-13}\,\rm cm^{-3}$ at which the gas switches from approximate isothermality to approximate adiabaticity, i.e. fragmentation occurs on scales $\sim (M_\odot/\rho_{\rm CRIT})^{1/3} \sim 100$ AU. Therefore it seems inevitable that protostellar discs will experience violent interactions with other protostellar discs, and with naked protostars. Indeed, such interactions are probably an essential element in the birth of a small-N subcluster from a star-forming core.

With Watkins, Boffin Bhattal and Francis (Boffin et al. 1998, Watkins et al. 1998a,b) I have simulated a large ensemble of such interactions. In order to treat the gas as isothermal, we consider a $1M_\odot$ disc with radius 1000 AU around a $1M_\odot$ protostar. We limit the approach orbit

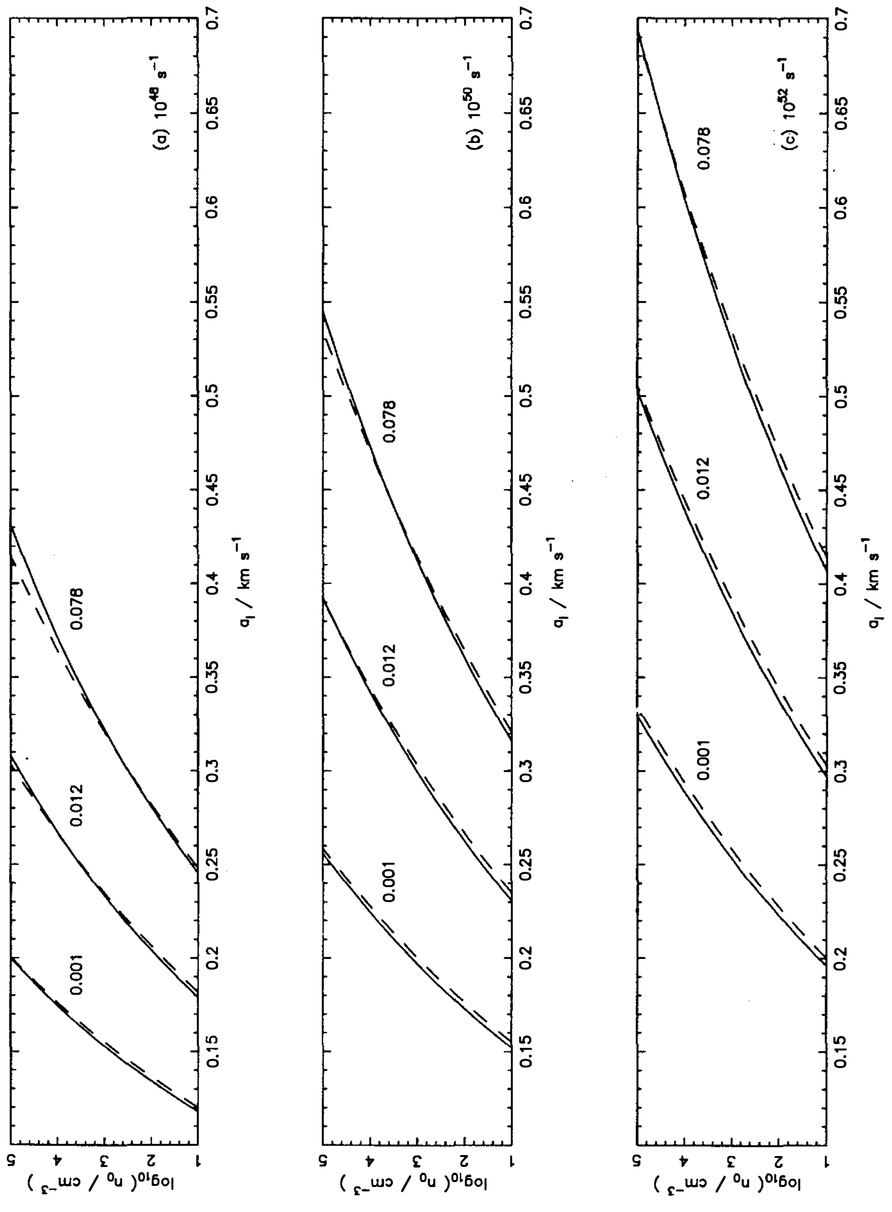

Figure 2: For (a) $\dot{\mathcal{N}}_{\rm Lyc} = 10^{48}\,{\rm s}^{-1}$, (b) $\dot{\mathcal{N}}_{\rm Lyc} = 10^{50}\,{\rm s}^{-1}$, and (c) $\dot{\mathcal{N}}_{\rm Lyc} = 10^{52}\,{\rm s}^{-1}$, the solid lines show the loci on the $(a_{\rm I}, \ell og_{10}[n_{\rm O}])$-plane where free-floating objects of mass $0.001M_\odot$, $0.012M_\odot$ and $0.078M_\odot$ can form due to photo-erosion of pre-existing cores. The dashed lines show the predictions of the approximate Eqn. 17.

to the parabolic case, but we sample all the different possibilities for the relative orientation of the spins and the orbit, and many different periastra. In general we find interactions to be very efficient in triggering disc fragmentation, and hence the formation of additional low-mass protostars. More violent encounters (i.e. encounters with smaller periastra) are more effective in this regard, but even distant 'tidal' encounters lead to fragmentation. Encounters in which the spin and orbital angular momenta are aligned are also somewhat more effective, but even with random alignments of the spins relative to the orbit the mechanism still appears to be effective in triggering disc fragmentation. On average an encounter leads to the formation of ~ 2.4 additional protostars if the spins are aligned with the orbit, and ~ 1.2 additional protostars if the spins are random. Most of these new protostars remain bound to the initial protostars, and in this case they acquire their own discs and continue to grow by accretion – as long as there is a supply of accretable material and they can compete effectively for it. The rest of the newly-formed protostars are ejected dynamically, and these are normally discless (i.e. low-mass Weak-Lined T Tauri stars).

The critical parameter in these simulations appears to be the viscosity. If we use the viscosity parametrization of Shakura & Sunyaev (1973), the masses of the additional protostars are concentrated in the range $0.010 - 0.100 M_\odot$ (i.e. brown dwarves) for $\alpha_{\rm SS} \simeq 10^{-2}$, and in the range $0.001 - 0.010 M_\odot$ (i.e. planetary-mass objects) for $\alpha_{\rm SS} \simeq 10^{-3}$. In view of the brown-dwarf desert, and the relative abundance of exo-planets, this might be interpreted as evidence for the lower value of $\alpha_{\rm SS} \simeq 10^{-3}$. This is, however, very speculative.

10 Conclusions

We have shown that there are many different possible modes of impulsively triggered star formation, and that these modes seem likely to make a significant contribution to the star formation in the Universe. Impulsively triggered modes of star formation have a number of advantages over more spontaneous – and therefore more quasistatic – modes (for instance star formation which is regulated by the loss of magnetic flux through ambipolar diffusion). In particular, (i) impulsive triggers have the potential to co-ordinate star formation across a large region of space, and thereby to explain the approximate co-evality of star formation in clusters. (ii) By launching matter directly into the non-linear regime of instability against fragmentation, impulsive triggers promote the formation of multiple systems, and of multiple systems having a wide range of parameters (mass ratios, separations and eccentricities). Impulsive triggering would seem to be an essential element of sequential self-propagating star formation and of starbursts, but it is probably also important even in more quiescent star formation regions like Taurus (e.g. Hartmann et al. 2002). In contrast, spontaneous, quiescent modes of star formation have difficulty explaining the approximatre co-evality of star formation across extended star clusters, the frequency of multiple star systems and their wide range of parameters, and the time-scales for the different phases of star formation (as inferred from the statistics of the different classes of prestellar core and protostar).

Acknowledgments

I gratefully acknowledge the support of the EC for the Research Training Network on *The Formation and Evolution of Young Stellar Clusters* (HPRN-CT-2000-00155), and many collaborations, in particular those with with Henri Boffin, Douglas Boyd, Lise Deharveng, Simon Goodwin, Patrick Hennebelle, and Hans Zinnecker.

References

1. Boffin HMJ, Watkins SJ, Bhattal AS, Francis N, Whitworth AP, 1998, MNRAS, 300, 1189
2. Boyd DFA, Whitworth AP, 2004, submitted to A&A
3. Chapman SJ, Pongracic H, Disney MJ, Nelson AH, Turner JA, Whitworth AP, 1992, Nature, 359, 207
4. Deharveng L, Lefloch B, Zavagno A, Caplan J, Whitworth AP, Nadeau D, Martin S, 2003, A&A, 408, L25
5. Deharveng L, Lefloch B, Zavagno A, Caplan J, Whitworth AP, Nadeau D, Martin S, 2004, in preparation
6. Elmegreen BG, 2000, ApJ, 530, 277
7. Goodwin SP, Ward-Thompson D, Whitworth AP, 2004a, A&A, 414, 633
8. Goodwin SP, Ward-Thompson D, Whitworth AP, 2004b, A&A, 419, 543
9. Gregersen EM, Evans NJII, Mardones D, Myers PC, 2000, ApJ, 533, 440
10. Hartmann L, Ballesteros-Paredes J, Bergin EA, 2002, ApJ, 562, 852
11. Hennebelle P, Whitworth AP, Gladwin PP, André P, 2003, MNRAS, 340, 670
12. Hennebelle P, Whitworth AP, Cha, SH, Goodwin SP, 2004, MNRAS, 348, 687
13. Hoyle F, 1953, ApJ, 118, 513
14. Jungwiert B, Palous J, 1994, A&A, 287, 55
15. Larson RB, 1981, MNRAS, 194, 809
16. Lee CW, Myers PC, Tafalla M, 1999, ApJ, 526, 788
17. Lee CW, Myers PC, Tafalla M, 2001, ApJSS, 136, 703
18. Pongracic H, Chapman SJ, Davies JR, Disney MJ, Nelson AH, Whitworth AP, 1992, MNRAS, 256, 291
19. Rees MJ, 1976, MNRAS, 176, 483
20. Silk, JI, 1977, ApJ, 214 152
21. Stone ME, 1970, ApJ, 159, 293
22. Stutzki J, Güsten R, 1990, ApJ, 356, 513
23. Tafalla M, Mardones D, Myers PC, Caselli P, Bachiller R, Benson PJ, 1998, ApJ, 504, 900
24. Turner JA, Chapman SJ, Bhattal AS, Disney MJ, Pongracic H, Whitworth AP, 1995, MNRAS, 277, 705
25. Watkins SJ, Bhattal AS, Boffin HMJ, Francis N, Whitworth AP, 1998a, MNRAS, 300, 1205
26. Watkins SJ, Bhattal AS, Boffin HMJ, Francis N, Whitworth AP, 1998b, MNRAS, 300, 1214
27. Whitworth AP, Bhattal AS, Chapman SJ, Disney MJ, Turner JA, 1994a, A&A, 290, 421
28. Whitworth AP, Bhattal AS, Chapman SJ, Disney MJ, Turner JA, 1994b, MNRAS, 268, 291
29. Whitworth AP, Bhattal AS, Francis N, Watkins SJ, 1996, MNRAS, 283, 1061
30. Whitworth AP, Chapman SJ, Bhattal AS, Disney MJ, Pongracic H, Turner JA, 1995, MNRAS, 277, 727
31. Whitworth AP, Deharveng L, Lefloch B, Zavagno A, Caplan J, Nadeau D, Martin S, 2004, in preparation
32. Whitworth AP, Francis N, 2002, MNRAS, 329, 641
33. Whitworth AP, Zinnecker H, 2004, submitted to A&A
34. Williams JP, Myers PC, Wilner DJ, Di Francesco J, 1999, ApJ, 513, L61
35. Williams JP, de Geus EJ, Blitz L, 1994, ApJ, 428, 693

S Ori 70: still a strong cluster planet candidate

E.L. Martín (1)

(1) Instituto de Astrofísica de Canarias
Avda. Vía Láctea, E-38200 La Laguna, Spain

In this paper I show that the coolest σOrionis cluster planet S Ori 70 is still a strong candidate member despite recent claims by Burgasser et al. that it could be a brown dwarf interloper. The main point of my argument is that the colors of S Ori 70 are significantly different to those of field dwarfs. This object has in fact the reddest $H-K$ color of all known T dwarfs, a clear indication of low gravity according to all published models. In a $J-H$ versus $H-K$ diagram, S Ori 70 lies in the region where models of ultracool dwarfs predict that low gravity objects should be located. I conclude that S Ori 70 is still a strong candidate member of the σOrionis open cluster. I briefly discuss additional observational tests that can be carried out with existing facilities to verify the σOrionis membership of this cluster planet candidate.

Keywords: stars: very low mass stars and brown dwarfs.

1 Introduction

The term brown dwarf (BD) refers to objects with masses below the limit for stable hydrogen fusion in stellar interiors. For solar composition, this limit was calculated to be 0.08 $M_\odot$ by Kumar (1963) and Hayashi & Nakano (1963). Modern calculations have changed the value of this boundary only slightly. For example, Baraffe et al. (1998) give 0.072 $M_\odot$ for solar metallicity.

There is no consensus in the community about the minimum mass of brown dwarfs (Boss et al. 2003). Some argue for the deuterium burning limit at 13 Jupiter masses (for solar composition). Some prefer a limit at around 10 Jupiter masses, where there appears to be a sharp rise in the number of extrasolar planets detected by high-precision radial velocity surveys around main-sequence stars. Finally, it has also been proposed to use a limit at 5 Jupiter masses where the mass-radius relationship of substellar objects changes its sign. In this paper we continue to use the deuterium limit as the mass boundary between brown dwarfs and planets because we do not have any strong reason to change the nomenclature adopted in our previous papers.

Another term used in this paper is that of ultracool dwarf, which refers to small objects with very cool effective temperatures. Since 1997, two new ultracool spectral classes have been adopted to extend the classical OBAFGKM system into cooler temperatures. The L dwarfs are characterized by weak or absent TiO bands, and very broad NaI and KI lines in the optical spectrum (Martín et al. 1997, 1999; Kirkpatrick et al. 1999, 2000). The T dwarfs are characterized by methane bands in the near-infrared spectra (Oppenheimer et al. 1995; Burgasser et al. 2002; Geballe et al. 2002). Current estimates of the temperatures of ultracool dwarfs range from about 2400 K to 1400 K for L dwarfs, and from 1400 K to 700 K for T dwarfs (Basri et al. 2000; Vrba et al. 2004).

Most of the known ultracool dwarfs have been identified in the general field by the wide area surveys 2MASS and SDSS. These objects consist of a mixed population of very low-mass stars, brown dwarfs and free-floating planets formed in different star-formation events during the lifetime of the Milky Way. Their individual ages, chemical compositions and masses are not known. Our best chance to study a population of ultracool dwarfs of known age, chemical composition, and uniform distance is to find them in open clusters where the stellar populations are well characterized. Two of the first brown dwarfs identified were located in the Pleiades open cluster (PPl 15 and Teide 1, Stauffer et al. 1994; Basri et al. 1996; Rebolo et al. 1995). Now, we know several dozens of bona fide brown dwarfs in the Pleiades and in other open clusters.

The σOrionis open cluster has been a region where our group has concentrated many efforts to reveal the substellar population (see Zapatero Osorio et al. 2003 for a recent review). It offers several advantages: (1) It is young (3-8 Myr) and, thus, the substellar objects are relatively bright and hot (Béjar et al. 2001), but not so young that the theoretical models cannot be reliably used to obtain masses (Baraffe et al. 2001). (2) It has very little extinction (Lee 1968), probably because the parental cloud has been blown away by the O-type star at the center of the cluster. (3) It is relatively nearby (distance 350 pc). (4) It is moderately rich and dense. Béjar et al. (2004, in preparation) estimate a peak central density of 0.2 members per square arcminute.

So far the coolest and faintest candidate member that we have found in the σOrionis cluster is the T dwarf candidate S Ori 70 (Zapatero Osorio et al. 2002). It was found in a pencil-beam deep mini-survey of only 55 square arcminutes with a sensitivity of 21 magnitude in the J and H-bands carried out with the 4.2-meter William Herschel Telescope in the Observatorio del Roque de los Muchachos. Follow-up near-infrared photometry and low-resolution spectroscopy were obtained with NIRC at the 10-meter Keck I telescope. The photometry is summarized in Table 1, together with the data for field T dwarfs of similar spectral type obtained from the literature. A mid-resolution spectrum in the K-band obtained with NIRSPEC on Keck II was presented in Martín & Zapatero Osorio (2003). We have claimed that both the NIRC and the NIRSPEC spectra are best fitted with synthetic spectra with low gravity (log g=3.5), which is consistent with membership in the σOrionis open cluster. We have estimated a mass of 3 Jupiter masses for an age of 3 Myr, making S Ori 70 the least massive object observed directly outside the solar system.

2 A critique of Burgasser et al.'s paper

Burgasser et al. (2004) have carried out an independent analysis of our Keck NIRC and NIRSPEC data of S Ori 70. We sent them our raw and reduced spectra. Burgasser et al. reprocessed our spectra using their own software and found the same results as us for S Ori 70 but not for the comparison object 2MASS J055919-1404. Apparently, our NIRSPEC data reduction for the 2MASS comparison object was incorrect, and it turned out to be a field star rather than a T dwarf.

Table 1: Comparison of photometric data of field T4-T8 dwarfs with S Ori 70

Name	SpT	J	$J-H$	$H-K$	Ref.
2MASS 2254+3123	T4	15.01±0.03	0.06±0.04	-0.08±0.04	K04
SDSS 0000+2554	T4.5	14.73±0.05	-0.01±0.06	-0.08±0.04	K04
SDSS 0207+0000	T4.5	16.63±0.05	-0.03±0.07	0.04±0.07	L02
SDSS 0926+5847	T4.5	15.47±0.03	0.05±0.04	-0.08±0.04	L02
2MASS 0559-1404	T4.5	13.57±0.03	-0.07±0.04	-0.09±0.04	L02
SDSS 0742+2055	T5	15.60±0.03	-0.35±0.04	-0.11±0.04	K04
SDSS 0830+0128	T5.5	15.99±0.03	-0.18±0.04	-0.21±0.04	K04
SDSS 0741+2351	T5.5	15.87±0.03	-0.25±0.06	0.00±0.07	K04
2MASS 2339+1352	T5.5	15.81±0.03	-0.19±0.04	-0.17±0.04	K04
SOri70	T5.5	20.28±0.10	-0.14±0.15	0.64±0.25	MZO02
Gl 229B	T6	14.33±0.05	-0.02±0.07	-0.07±0.07	L99
SDSS 1231+0847	T6	15.14±0.03	-0.26±0.04	-0.06±0.04	K04
SDSS 2124+0100	T6	15.88±0.03	-0.24±0.04	0.05±0.04	K04
2MASS 0937+2931	T6	14.29±0.03	-0.38±0.04	-0.72±0.04	K04
2MASS 1225-2739	T6	14.88±0.03	-0.29±0.04	-0.11±0.04	L02
SDSS 1110+0116	T6	16.12±0.05	-0.10±0.07	0.17±0.07	L02
2MASS 1047+2124	T6.5	15.46±0.03	-0.37±0.04	-0.37±0.04	K04
SDSS 1758+4633	T7	15.86±0.03	-0.34±0.04	0.08±0.04	K04
2MASS 1217-0311	T8	15.56±0.03	-0.42±0.04	0.06±0.04	L02
Gl 570D	T8	15.33±0.05	0.05±0.10	0.01±0.19	B00
2MASS 0727+1710	T8	15.19±0.03	-0.48±0.04	-0.02±0.04	K04

Burgasser et al. compared the spectra of S Ori 70 with spectra of field T brown dwarfs (bdTs) obtained by them, and claimed to find a good match between our object and old brown dwarfs. In their Figure 2, they showed a comparison of their reduction of our NIRSPEC spectrum of S Ori 70 and their NIRSPEC spectrum of the field bdT7 2MASS1553+1532. In their Figure 4, they showed a comparison of our NIRC spectrum of S Ori 70 with their NIRC spectrum of the field bdT6.5 2MASS1047+2124. From these comparisons they claimed that S Ori 70 is a field brown dwarf that coincidentally lies in the line of sight of the cluster. If the interpretation of Burgasser et al. is correct, S Ori 70 should be at a distance of only 75 to 100 pc, instead of 350 pc.

We note that contrary to the claims of Burgasser et al., there are significant differences between S Ori 70 and field T dwarfs. The KI doublet at 1.25 microns is stronger in S Ori 70 than in 2MASS1553+1532, the pseudocontinuum bump between 1.57 and 1.62 microns is narrower in SOri70 than in 2MASS1047+2124, and the pseudocontinuum bump between 2.0 and 2.2 microns is higher and redder in SOri70 than in 2MASS1047+2124. All these three features are consistent with the model predictions for gravity effects as also noted by Lucas et al. (2001) in their analysis of infrared spectra of L dwarfs in the Trapezium cluster and by Knapp et al. (2004) in their analysis of field T dwarfs. Burgasser et al. neglected to comment on the NIRC spectra mis-matches between SOri70 and field T dwarfs, and dismissed the detection of the KI doublet because the NIRSPEC spectrum is too noisy.

Knapp et al. (2004) have proposed that the spread of $H-K$ colors observed in field T dwarfs could be due to differences in gravities, expected for a sample of brown dwarfs with a wide range of ages and masses. The models indicate that objects with red H-K colors have low gravities due to weaker pressure-induced H_2 absorption in the K-band. This effect was first predicted by Saumon et al. (1996), and can also be noticed in the models published by Allard et al. (2001). It seems to be a robust prediction of all models. In Figure 1, I display a color-color diagram comparing the position of S Ori 70 with that of field T4-T8 dwarfs. The S Ori 70 photometry was calibrated in the same system as that of Leggett et al. (2002). The plot includes six bdTs with photometry from Leggett et al. (2002). The MKO system used by Knapp et al. (2004) is very close to the Leggett et al. system, and hence I have made no corrections. I also show the models used by Knapp et al. Full explanation of these cloudless models can be found in Marley et al. (2002). All the field bdT objects are located in the region where the models give gravities in the range log g=4.0-5.5, consistent with their presumed old ages. S Ori 70, on the other hand, is located outside the locus of the field bdTs, even taking into account the photometric error bars. Its red $H-K$ color indicates lower gravity than the field objects according to the models. In fact, Martín & Zapatero Osorio (2003) derived log g=3.5 for S Ori 70, which implies a mass of 3 Jupiters. The red $H-K$ color cannot be due to interstellar reddening because extinction is very low in this line of sight, and because reddening would also affect the $J-H$ color.

3 Where do we go from here?

The differences in colors and spectral energy distribution between SOri70 and field bdTs strongly suggest that S Ori 70 has lower gravity, consistent with young age and low mass. We conclude that, despite Burgasser's claims, S Ori 70 is still a strong cluster planet candidate. Nevertheless, more data is necessary to improve our understanding of this object and to confirm its cluster membership in σ Orionis. In this section, I discuss future observations that will provide crucial information about S Ori 70.

- **The proper motion:** Zapatero Osorio et al. (2002) compared images with a 3 year baseline of the field around S Ori 70. They placed an upper limit of 0.1 arcsec per year on the proper motion of S Ori 70. If S Ori 70 is a bdT at 75-100 pc, the proper motion should be about 0.05 arcsec per year. The last images of S Ori 70 were obtained at Keck I on December 2001. We plan to obtain new images in winter 2004 in order to improve the limit on the proper motion of S Ori 70 by a factor of two. Unfortunately, proposals to obtain accurate astrometry of S Ori 70 with HST in Cycles 11, 12 and 13 have not been successful.

- **The KI near-infrared lines:** The detection of the KI doublet at 1.25 microns reported by Martín & Zapatero Osorio (2003) needs to be confirmed with higher signal to noise ratio. A proposal to reobserve S Ori 70 with Keck/NIRSPEC was rejected by the NASA TAC given "the extensive study of S Ori 70 by Burgasser and his colleagues". In this paper we have shown that the Burgasser et al. study did not provide the final word on the nature of this object, and that S Ori 70 clearly deserves further investigation.

- **The spectral energy distribution (SED):** The SED coverage of S Ori 70 is still incomplete and the error bars in the photometry should be reduced. A proposal to obtain the JH spectrum with Keck/NIRC, and to improve the HK spectrum was rejected by the NASA TAC. A proposal to obtain mid-infrared photometry with SIRTF/IRAC was also turned down. We plan to insist on applying for telescope time to observe S Ori 70 so that we can obtain an excellent SED of this benchmark cluster planet, which can be a reference for future studies of planetary-mass objects in star-forming regions and young open clusters. In parallel with more detailed observations of S Ori 70, there should also be theoretical efforts to improve the synthetic spectra of T dwarfs. The best fit of the J-band NIRSPEC spectrum found by Martín & Zapatero Osorio (2003) has a T_{eff}=1,100 K,

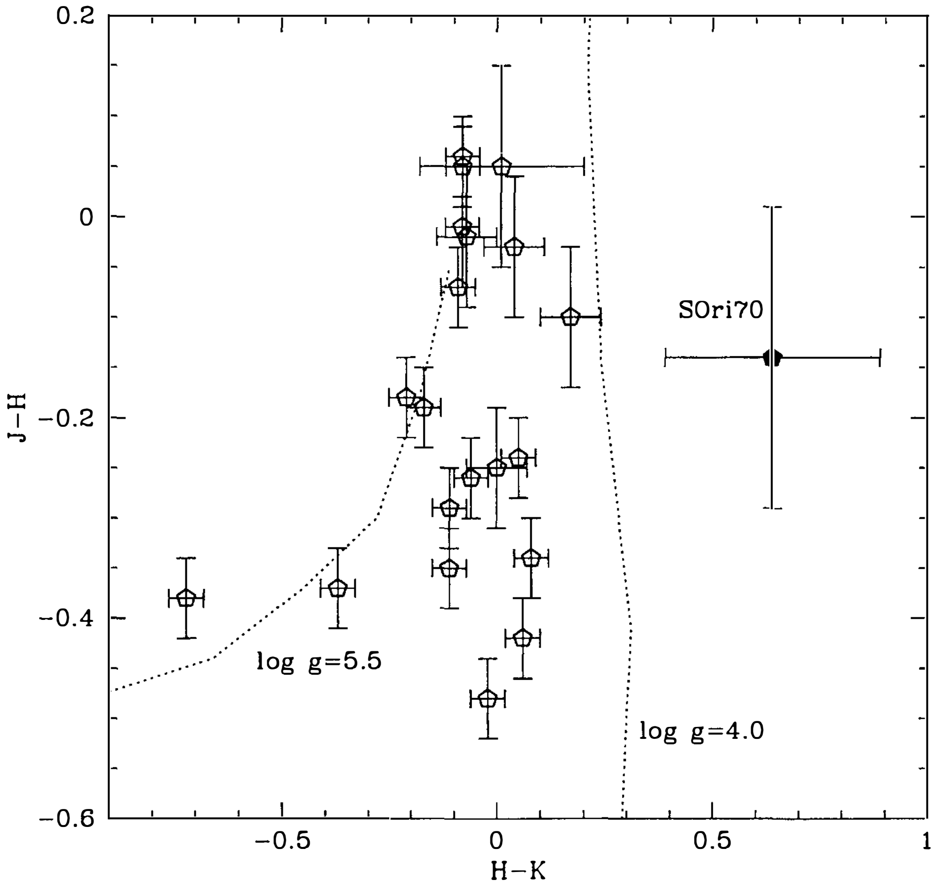

Figure 1: Comparison of S Ori 70 with field bdT4-T8 objects. Theoretical models from Marley et al. (2002) are also shown with dotted lines for two different gravities. Note that S Ori 70 is located in a region outside the locus of field T dwarfs, consistent with having lower surface gravity. All the known field T dwarfs are bracketed by the models.

significantly hotter than the best fit of the HK NIRC spectrum for T_{eff}=800 K obtained by Zapatero Osorio et al. (2002). Burgasser et al. (2004) correctly pointed out this inconsistency in the comparison of observations with theory and also showed that this fitting technique provides gravities that are too low for bdT7-bdT8 field objects. However, the gravities obtained from the models are reasonable for bdT6 field objects, which is closer to the spectral type of S Ori 70.

Last but not least, I would like to note that our efforts to find more cluster planets similar to S Ori 70 have met with poor weather in several observatories (Calar Alto, Canarics, Hawaii and Paranal). We do not have a reliable database to search for these objects yet. Nevertheless, we have found a few candidates that await spectroscopic observations. I showed one of them at the Moriond meeting, a possible planetary mass companion to an M dwarf member in the σOrionis open cluster. Follow-up observations of these objects with several telescopes are planned. Stay tuned!

Acknowledgments

Partial funding for attending this conference was provided by a grant from the RTN network "The Formation and Evolution of Young Stellar Clusters" led by Mark McCaughrean. Adam Burgasser, Jose Antonio Caballero, David Barrado y Navascués and Maria Rosa Zapatero Osorio provided useful comments that helped to improve the manuscript. Mark Marley sent a computer readable version of the models used in Figure 1.

References

1. Allard, F., Hauschildt, P.H., Alexander, D.R. et al. 2001, ApJ, 556, 357
2. Baraffe, I., Chabrier, G., Allard, F., & Hauschildt, P.H. 1998, A&A, 337, 403
3. Basri, G., Marcy, G.W., Graham, J.R. 1996, ApJ, 458, 600
4. Béjar, V.J.S., Martín, E.L., Zapatero Osorio, M.R., et al. 2001, ApJ, 556, 830
5. Burgasser, A.J., Kirkpatrick, J.D., Cutri, R.M., et al. 2000, ApJ, 531, L57
6. Burgasser, A.J., Kirkpatrick, J.D., McGovern, M.R. et al. 2004, ApJ, 604, 827
7. Hayashi, C., & Nakano, T. 1963, Progr. Theor. Phys., 30, 460
8. Kirkpatrick, J.D., Reid, N.I., Liebert, J. et al. 1999, ApJ, 519, 802
9. Kirkpatrick, J.D., Reid, N.I., Liebert, J. et al. 2000, AJ, 120, 447
10. Knapp, G.R., Leggett, S.K., Fan, X. et al. 2004, AJ, 127, 3553
11. Kumar, S. S. 1963, ApJ, 137, 1121
12. Leggett, S.K., Toomey, D.W., Geballe, T.R., Brown, R.H. 1999, ApJ, 517, L139
13. Leggett, S.K., Golimowski, D.A., Fan, X. et al. 2002, ApJ, 564, 452
14. Lee, T.A. 1968, ApJ, 152, 913
15. Lucas, P.W., Roche, P.F., Allard, F., & Hauschildt, P.H. 2001, MNRAS, 326, 695
16. Marley, M.S., Seager, S., Saumon, D. et al. 2002, ApJ, 568, 335
17. Martín, E.L., Basri, G., Delfosse, X., Forveille, T. 1997, A&A, 327, L29
18. Martín, E.L., Delfosse, X., Basri, G. et al. 1999, AJ, 118, 2466
19. Martín, E.L. & Zapatero Osorio, M.R. 2003, ApJ, 593, L113
20. Rebolo, R., Zapatero Osorio, M.R., & Martín, E.L. 1995, Nature, 377, 129
21. Saumon, D., Hubbard, W.B., Burrows, A. et al. 1996, ApJ, 460, 993
22. Stauffer, J.R., Hamilton, D., & Probst, R.G. 1994, AJ, 108, 155
23. Vrba, F.J., Henden, A.A., Luginbuhi, C.B. et al. 2004, AJ, 127, 2948
24. Zapatero Osorio, M.R., Béjar, V.J.S., Martín, E.L. et al. 2002, ApJ, 578, 536
25. Zapatero Osorio, M.R., Béjar, V.J.S., et al. 2003, in IAU Symposium 211: Brown Dwarfs.

FORMATION AND PROGENITORS OF MASSIVE STARS

R. Chini, V. Hoffmeister, M. Nielbock

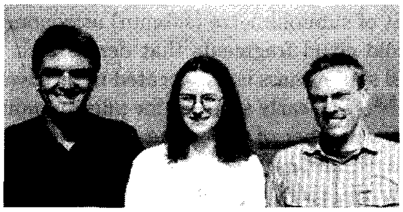

Astronomisches Institut der Ruhr-Universität Bochum,
44780 Bochum, Germany

Earliest stages of massive stars - though difficult to observe - gain increasing interest in observational astronomy due to the advent of new technical developments. To address the question of progenitors, an overview on recent millimetre surveys is given. Particularly, regions with of methanol masers - which are regarded as signposts for massive star formation - harbour sources of different evolutionary stages as witnessed by various combinations of infrared, millimetre and radio emitting objects within the same volume. Certainly, better spatial resolution is required to disentangle the individual sources and to probe their evolutionary stage. The question of formation, i.e. the debate of accretion vs. collision, is reviewed by analysing the most prominent massive protostar candidates and by zooming into a recently discovered source within M 17. Here, a deeply embedded infrared object is surrounded by a huge flared rotating disk; all evidence collected so far points toward a massive protostar that is currently born through disk accretion.

Keywords: Stars: formation, ISM: jets and outflows

1 Introduction

The formation of stars is one of the great miracles in astrophysics. Nevertheless, the birth of low-mass stars has been investigated in great detail during the last decades and it looks that both theory and observation have agreed on a common scenario: stars form from dense clumps in molecular clouds by accretion of material from an envelope and - at later stages - from a disk. The formation process of massive stars is considerably more difficult in all aspects: i) Massive star formation involves large outflows, winds and radiation pressure, which makes it hard to believe that it is simply a scaled-up version of the low-mass formation scenario (e.g. Wolfire & Cassinelli 1987) [1]. ii) Our theoretical understanding and the current computational capabilities are far from a proper treatment of all processes that contribute to the interaction between radiation, gas and dust. Nevertheless, recent model calculations indicate that the formation by accretion from a massive circumstellar disc onto a central protostar might be feasible (Norberg & Maeder 2000, Yorke & Sonnhalter 2002)[2,3]. Given that most massive stars are found in stellar clusters and associations, Bonnell, Bate & Zinnecker (1998)[4] have suggested an alternative scenario where the coalescence of low- to medium-mass protostars leads to the formation of massive stars. iii) Observationally, massive stars are rare and their birth places are usually rather distant. Because their formation occurs on short time scales, the probability of catching a birth in the act is extremely low. Despite of the mentioned obstacles, a variety of observational evidence for massive star formation has been recognised during recent years. In the first part of this review, the latest attempts of finding progenitors of high-mass stars are described while the second part deals with the question whether there is unique signature for accretion with massive stars.

2 Progenitors of high-mass stars

Without doubt, it is the merit of submillimetre (submm) astronomy to have discovered the first true protostars, i.e. dense, cold cloud fragments that derive their luminosity by accretion and where the majority of the final stellar mass is still located in an envelope and/or disk (e.g. André et al. 1993, Chini et al. 1993)[5,6]. The early searches for pure submm emitting massive protostars were less successful although a number of pre-stellar cloud cores could be found which might at some later stage may collapse into high-mass stars (e.g. Mezger et al. 1988)[7]. The reason for this failure is likely due to the short evolutionary times scales of massive pre-stellar cores: high-mass stars reach the main sequence, form (ultra-)compact HII regions and develop ionised winds before all of the material in the envelope has fallen in.

Obviously, the aim is to find high-mass protostars before they form ultracompact HII regions (UC HIIs). One of the most promising strategies is to study regions with maser emission. While OH masers appear to be associated with HII regions, H_2O (collisional pumping) and CH_3OH (radiative pumping) masers seem to occur with early stages, when molecular outflows produce shocks within dense and warm gas. As a consequence a number of millimetre (mm) surveys have been performed (e.g. Beuther et al. 2002a, Sridharan et al. 2002)[8,9]. A recent attempt in this field has been performed by Nielbock et al. (in prep.): Based on a radio continuum and methanol maser survey near southern UC HIIs (Walsh et al. 1998)[10], a subsample of 37 infrared and radio-quiet maser sites have been observed at 1.2 mm. All investigated regions contain a wealth of new mm sources, many of which are neither coinciding with UC HII regions nor masers. As it is well established that high-mass stars tend to be embedded in stellar clusters and associations, it seems that this agglomeration is already introduced at an early stage of formation, at least on large scales.

We separated the sources into 4 different groups according to their spectral properties at IR, mm and radio wavelengths; in addition, we calculated the 1.2 mm luminosity $L_{1.2}$ for every mm source. The groups comprise the following objects: UCHIIs and radio continuum sources (group A), masers without radio continuum emission and not classified as UCHIIs (group B), infrared sources detected by IRAS or MSX without being associated with masers, UCHIIs or radio continuum emission (group C), and finally pure mm sources (group D).

Group A sources are equally distributed between $1 < L_{1.2}\,[\mathrm{L}_\odot] < 10$, and contain the five most luminous objects of the entire sample with $L_{1.2} > 20\,\mathrm{L}_\odot$. This is obviously due to the content of young massive stars that ionise and densify their immediate surroundings. The mm continuum flux might be contaminated by free-free emission. Group B sources are also fairly equally distributed below $10\,\mathrm{L}_\odot$, while only two objects are slightly more luminous. It is likely that this group represents the immediate predecessors of the UCHIIs. Group C only populates the low luminosity regime significantly below $10\,L_\odot$. The IR emission points toward the presence of relatively warm and compact sources which could be evolving pre-main sequence (PMS) stars

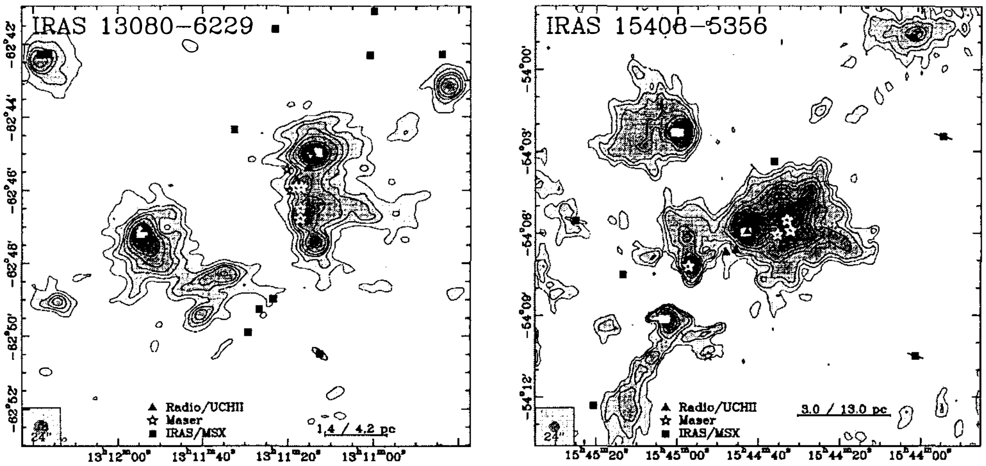

Figure 1: Composite images of methanol maser regions around the IRAS sources 13080-6229 and 15408-5356 mapped at 1.2 mm; known masers are marked by a star. The images display the typical, highly structured regions with lots of embedded compact sources.

- probably of low mass - or accreting massive protostars. Group D sources strongly peak at luminosities below $1\,L_\odot$. These objects probably either contain young low-mass protostars or starless clouds. This suggests that high and low-mass stars are forming in a common area.

Fig. 1 shows that the potential regions of high mass star formation are extremely confused and that the various sources (IR, mm, UCHIIs, masers) appear right next to each other. Given that the distance is uncertain in many cases, the absolute luminosity is not unique; furthermore, due to the low spatial resolution of the FIR data the source of luminosity remains questionable. Finally, one has to be aware of the fact, that the linear sizes of many mm cores is of the order of $0.1 - 1$ pc which is comparable to galactic HII regions and clusters.

3 Accretion vs. collision

As mentioned in the beginning, there is an ongoing debate about the formation scenario of massive stars. While the collision idea cannot be verified observationally, the accretion hypothesis can in principle be checked by searching for massive stars with disks. Bipolar molecular outflows are a spectacular manifestation of ongoing star formation and are probably intensely related to the accretion process. They provide a mechanism for accretion disks to shed angular momentum thereby permitting matter in the disk to migrate to the central protostar. Therefore, the period of intense mass loss coincides with the accretion phase of the protostar and is believed to occur over a large stellar mass range. Among others, Shepherd & Churchwell (1996) [11] showed that bipolar outflows are very common also in regions of massive star formation. Moreover the relation between bolometric luminosity of the protostar and the mechanical luminosity of the flow, its momentum flux, and its mass outflow rate smoothly extends from low-mass stars (Cabrit & Bertout 1992) [12] into the high-mass regime. Beuther et al. (2002b) [13] corroborated qualitatively this result but showed simultaneously that the mass entrainment rates are not a unique function of the embedded luminosity. A general problem with these statistical studies is the distance uncertainty with many of the sources and the question whether the observed IRAS luminosity is due to a single object or a cluster of stars.

There are small number of well investigated candidates which are regarded as massive young stellar objects (YSOs) being associated with disks and/or outflows; if true these cases would indicate that high-mass star formation is indeed a continuous extension of the well-known low-mass accretion. Without aiming at completeness some of the most famous templates will be reviewed briefly by discriminating between firm observational evidence and - sometimes far reaching - interpretation.

3.1 Outflow sources

S 106 Historically, the first, spectacular massive outflow source was S 106; this bipolar HII region is excited by an O7 - O9 ZAMS star (Gehrz et al. 1983) [14] called S 106 IR. The bipolar structure of the ionised gas was explained in terms of a slight asymmetry in the density distribution of a mass loss envelope (Felli et al. 1984a) [15]. The two lobes are separated by a dark lane which was initially interpreted as a large-scale molecular disk. However, Stutzki et al. (1982) [16], Barsony et al. (1989) [17] and Schneider et al. (2002) [18] falsified this suggestion and concluded that there is no molecular gas disk in S 106.

HH 80-81 Marti et al. (1993) [19] investigated the Herbig-Haro complex HH 80-81 where a compact radio continuum source, H_2O maser emission and the bright infrared object IRAS 18162-2048 point toward massive star formation within the region. Placed at a distance of 1.7 kpc the IRAS luminosity implies the presence of a $1.7 \cdot 10^4 L_\odot$ star or a cluster of stars (Aspin & Geballe 1992) [20]. Assuming that this luminosity is due to a single ZAMS star it would be a B0 and would create ionisation far in excess of that observed. There is a highly collimated outflow but no disk.

G9.62+0.19 G9.62+0.19 is a well-studied region of massive star formation with a number of extended, compact and ultracompact HII regions. Hofner et al. (2001a) [21] detected a high-velocity molecular outflow and concluded from the mass and energetics of the outflowing gas that a luminous central object must be the driving source in the region. Again, there is no direct evidence for an accretion disk and the driving candidate cannot be assigned uniquely.

IRAS 20126+4104 IRAS 20126+4104 is another massive YSO. With a bolometric luminosity corresponding to a ZAMS spectral type of about B0, the absence of strong radio continuum emission indicates that IRAS 20126+4104 is likely in an evolutionary stage prior to that of an ultracompact HII region. A bipolar jet/outflow is centred on a dense gas clump oriented perpendicular to the flow. However, there are multiple jets suggesting multiplicity of the central source. Likewise, only limits on the presence of an accretion disk can be given (Hofner et al. 2001b) [22].

HW2 The star forming region Cepheus A contains three embedded YSOs (Curiel et al. 2002) [23] as well as a bubble of expanding water masers. It was suggested that one of these radio continuum sources is the embedded YSO powering the water maser structure, but its nature is still unknown. Since this source appears unresolved in the 7 mm map, the size of the HII region or the protostellar disk (and/or envelope) is below 30 AU. HW2 may actually be a small cluster of YSOs in formation.

3.2 Disk candidates

While the above examples do only provide evidence for outflows there are also some objects where "accretion disks" have been claimed.

G192.16-3.82 The largest circumstellar disk hitherto quoted has a diameter of 130 AU and is associated with the potential massive protostar G192.16-3.82 (Shepherd et al. 2001) [24]; this is about the size of the disks detected around low-luminosity protostars. Looking into detail, the central mass of $8-18\,M_\odot$ is derived indirectly from the CO mass outflow and from the luminosity of an IRAS source which includes everything: stellar, accretion and outflow luminosity. Both conversions into a spectral type and then into a stellar mass include large uncertainties and assume a ZAMS relationship between L_{bol} and T_{eff} that may not hold for YSOs. Likewise, the mass estimates for the disk are uncertain due to contamination by free-free emission; the disk mass could be even lower than $3\,M_\odot$ if the emission is partially due to ionised gas. Finally, there is the question of multiple stars. From models of the radio emission Shepherd et al. (2001) [24] conclude that the protostar is a binary system. In addition, they state with respect to the spectral type B2 that this designation represents an upper limit, because lower mass stars in a cluster may also contribute to dust heating.

IRc2-I The high-mass protostar IRc2-I in the BN/KL region in Orion has been claimed to have disk of 80 AU (Plambeck et al. 1990) [25]; Wright et al. (1995) [26] even talk of 1000 AU. In contrast, Greenhill et al. (1998) [27] show that the SiO emission of IRc2-I within 60 AU is not due to a disk but that the region is dominated by a conical bipolar outflow, rather than the expected disk. A slower outflow, close to the equatorial plane of the protostellar system, extends to radii of 1000 AU and contradicts the disk interpretation by Wright et al. (1995) [26].

NGC 7538 S-a This potential massive YSO close to a site of OH and H2O masers is embedded in an elongated cloud core (Sandell et al. 2003) [28]. The mm continuum has revealed a resolved elliptical source of about 14" × 8" while the line emission yields a source size of 11" × 7" at the position of the OH and H2O masers. The velocity gradient along the major axis of the elliptical source is interpreted as a rotating disk. Though the molecular line studies indicate both rotation and outflow, the velocity structure of the entire system is extremely confused and there is no direct evidence for a disk. The luminosity of the source of $2 \cdot 10^4\,L_\odot$ has been determined from data at 57, 100 and 1000 μm and corresponds to regions of 30", 55" and 60", respectively, with a positional accuracy of 15". Thus, the FIR observations do not have enough spatial resolution or positional accuracy to confirm that the luminosity originates from the OH/H_2O masers.

Orion 114-426 The largest silhouette disk so far is known as Orion 114-426 (McCaughrean et al. 1998) [29] and has a diameter of about 1000 AU and a mass of $\geq 5 \times 10^{-4}\,M_\odot$; however, its central star is likely a low-mass object of about $1.5\,M_\odot$ rather than a massive protostar.

To summarise, all above candidates - apart from Orion 114-426 - provide only indirect evidence for a disk and all of them do not show a direct signature for ongoing accretion. Furthermore, it is highly uncertain whether the observed outflows originate from a massive protostar or from low-mass companions. Likewise, the inferred luminosities which are mainly based on large-beam FIR data and/or CO outflows may originate from single stars and/or clusters. Thus, although there is growing evidence that massive stars are associated with outflows that probably originate from an accretion process through a disk there is not a single clear-cut case so far to uniquely support the accretion scenario for high-mass stars.

3.3 The first massive accretion disk?

In the following, the most recent example for the formation of a massive protostar through disk accretion is described. It has been discovered by Chini et al. (2004) [30] and comprises all constituents expected from a massive protostellar source: i) a uniquely defined central source, ii)

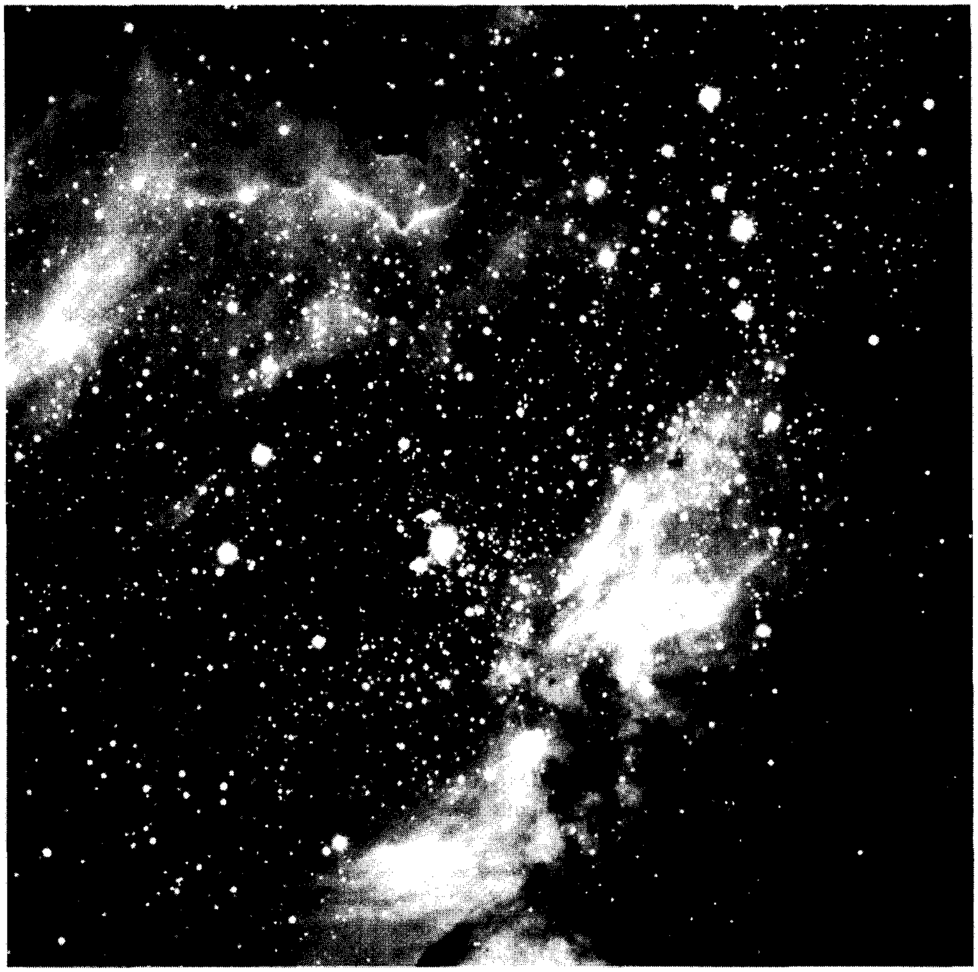

Figure 2: JHK mosaic of the young cluster in M 17; the massive disk is embedded in the interface between the HII region and the molecular cloud in the SW.

a massive flared rotating disk, iii) spectral evidence for accretion, iv) a bipolar reflection nebula, and v) a bipolar jet.

Looking into the cradle

The Omega nebula or M 17 is one of the most prominent star forming regions in our Galaxy at a distance of 2.2 kpc (Chini & Wargau 1998) [31]. Fig. 2 shows part of a three-colour infrared mosaic of the area which was the initial observation leading to our investigation. It shows a dense cluster of young stars embedded in clouds of gas and dust. M 17 is extremely young as witnessed by the presence of several high-mass stars which ionise the surrounding hydrogen gas; the total energy output of these stars is almost 10^7 $L_\odot$. Adjacent to its south-western edge, there is a huge cloud of molecular gas which is believed to become a site of future star formation. The interface between the HII region and the molecular cloud is the locus where the radio emission as well as the infrared emission of the area attain their maximum (Felli et al. 1984b) [32]. Nevertheless, despite many attempts no stellar object could be identified to be responsible for this emission. Therefore, it is believed that the radio and infrared emission is not due to an individual stellar source, but rather is the result of a collision between the expanding HII region and the molecular cloud; this leads to a density and temperature enhancement of the interstellar medium and thus to an increase in emission from the boundary layer.

Chini et al. (2004) [30] have recently investigated this interface between the HII region and the molecular cloud by means of unprecedented deep infrared imaging between 1.2 and 2.2 μm in order to penetrate the dust and to search for newly forming high-mass stars. Due the sensitivity of these measurements more than 50 magnitudes of visual extinction became transparent and the faint nebular emission of the HII region could shine through the south-western molecular cloud. Close to the radio and infrared emission peaks a tremendous opaque silhouette appears against the nebular background associated with an hourglass shaped nebula and surrounded by a larger disrupting dust envelope. As outlined in the following, this system complies perfectly with theoretical predictions for a newly forming high mass star surrounded by a huge accretion disk and accompanied by an energetic bipolar mass outflow.

The accretion disk

The most obvious morphological components of the system are two triangular shaped dust lanes that become visible at infrared wavelengths. Fig. 3 is a JHK image showing the silhouette of a flared disk, seen nearly edge-on, and a bipolar nebula. With a radius of about 10.000 AU it is by far the largest circumstellar disk ever detected. Its orientation is parallel to the interface between the HII region and the molecular cloud, indicating that large scale motions and density gradients may have influenced the formation of the disk. When going from the centre towards its outer edges the disk widens substantially. Using the background nebular light as a homogenous source of illumination, the extinction and thus the column density of interstellar matter within the disk can be determined at each point along the line of sight. This analysis reveals three morphological details: starting from a central hole of $4 \cdot 10^{15}$ cm radius, a dense inner torus extends up to $r \sim 3.8 \cdot 10^{16}$ cm and widens with increasing radius from $z \sim 7.9 \cdot 10^{15}$ to $1.8 \cdot 10^{16}$ cm. Further out a flared disk dominates the optical depth extending up to $r \sim 9.9 \cdot 10^{16}$ cm with a thickness z from $1.8 \cdot 10^{16}$ to $4.1 \cdot 10^{16}$ cm. An outer envelope can be traced to about $r \sim 5.3 \cdot 10^{17}$ cm with $1.0 \cdot 10^{17} < z\,[\mathrm{cm}] < 4.0 \cdot 10^{17}$.

The maximum column density of hydrogen inferred from the optical depth at 2.2 μm is $\sim 6 \cdot 10^{22}$ atoms cm^{-2}. Adopting normal interstellar dust properties, this value can be converted into a dust mass; using 140 as a recent number for the gas-to-dust ratio we obtain about 6 $M_\odot$ for the gas inside the inner disk. However, both assumptions of normal dust properties and a normal gas-to-dust ratio may be far from the true conditions in such an extreme environment.

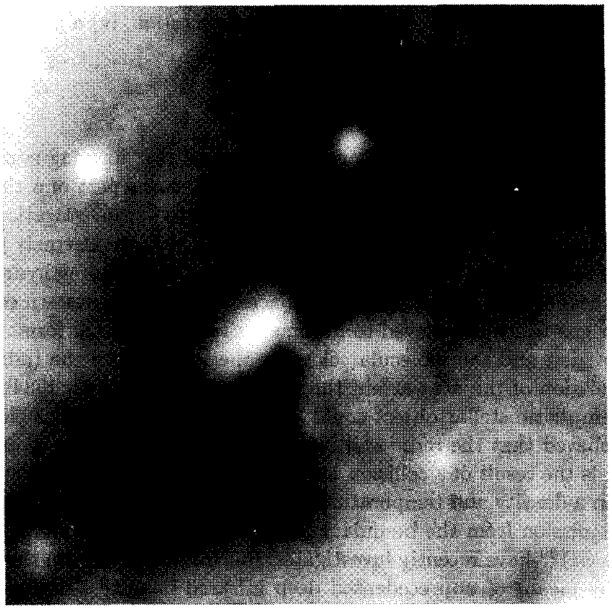

Figure 3: Composite JHK image showing the disk morphology and the associated bipolar nebula.

Further physical properties concerning the mass and the kinematics of the disk and its surroundings have be obtained from mm observations. ^{13}CO data indicate that the disk/envelope system slowly rotates with its north-western part approaching the observer. A velocity shift of 1.7 km/s corresponding to a velocity gradient of about 11 km/s/pc is present over an extent of 30.800 AU. Adopting an abundance ratio of 43 between ^{12}CO and ^{13}CO and a conversion factor of $N_{H_2} = 2.3 \cdot 10^{20}\,\mathrm{cm}^{-2}$ per K km/s to derive H_2 column densities from the velocity integrated ^{12}CO intensities a conservative lower limit for the disk mass of 110 solar masses is obtained. Several effects will increase the true disk mass: i) All observed lines are more (^{12}CO) or less (^{13}CO, C^{18}O) optically thick. ii) The CO lines may be partly photo-dissociated. iii) The above conversion factor is more compatible with regions of low densities ($n_H \sim 200\,\mathrm{cm}^{-3}$) and low temperatures ($T \sim 10\,\mathrm{K}$) and thus may not be applicable in a hot dense core environment of a massive star, or in an externally heated and compressed cloud edge such as the M 17 ionisation front. Given that the conversion factor varies with $\sqrt{n}/T$, the disk mass could increase by a factor of three when using $n_H \sim 10^5\,\mathrm{cm}^{-3}$, as suggested by the column densities from the optical depth at 2.2 μm and assuming a temperature of $T \sim 100\,\mathrm{K}$.

The bipolar nebula and the jets

A sequence of images from 0.4 to 2.2 μm (Chini et al. 2004) [30] depicts a second morphological structure - an hourglass-shaped nebula perpendicular to the plane of the disk where the two lobes show different wavelength dependent intensities. The fact that optical light is detectable throughout the huge amount of foreground extinction can only be explained if the emission is - at least partly - due to reflected light scattered by dust grains. In this case, the extinction which increases roughly inversely with wavelength is compensated by the effect of scattering which varies as λ^{-4}. The nebular light seems to originate from two separate components, a diffuse extended shimmer and a more compact emission in the central region.

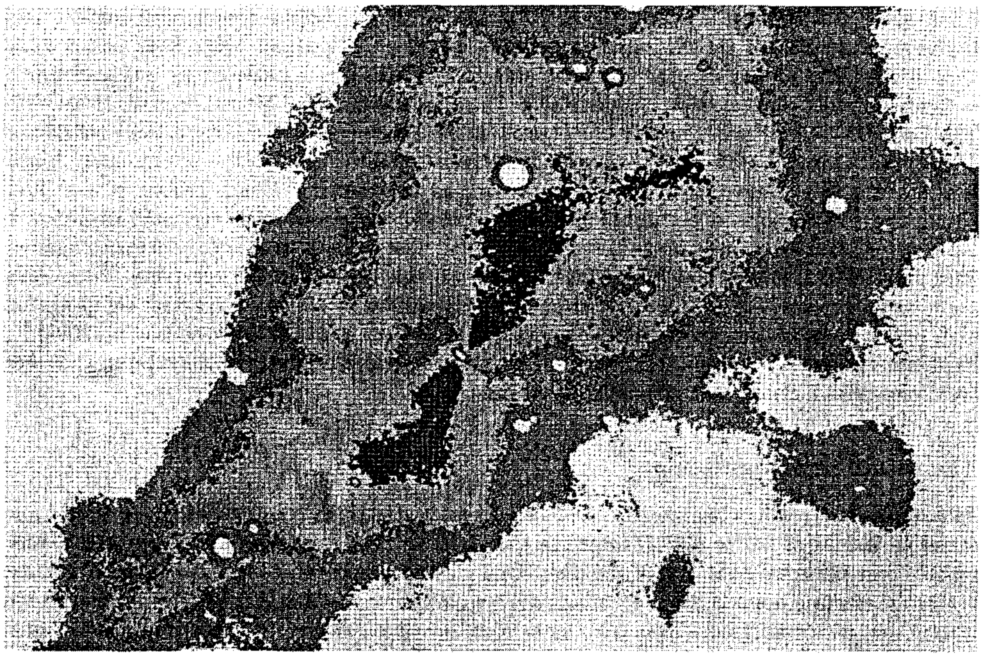

Figure 4: Contrast-enhanced 2.2 μm NACO image that shows the inner disk (blue) and the bipolar jet (red).

Firstly, the diffuse emission - particularly prominent at optical wavelengths - is symmetric and seems to mark the walls of an hourglass shaped cavity. It extends at least up to $5 \cdot 10^{1}7$ cm above the plane of the disk towards both sides with a maximum width of about the same size. The origin of this emission is probably due to scattered light from the walls of the cavities that have been cleared by an energetic mass outflow. From the fact that the NE lobe becomes brighter with increasing wavelength while the intensity of the SW lobe remains almost constant we conclude that the former suffers from more extinction. This suggests a slight inclination of the disk with respect to the line of sight which hides the NE lobe partly behind the disk. Vice versa one is facing the disk slightly from below and thus are looking into the SW cavity. The hourglass morphology of the SW cavity is supported by two curved dusty ejecta that end in typical bow-shocks as a result of their interaction with the ambient medium. This picture is further corroborated by CO data which also trace the walls of both cavities.

Secondly, there is a more compact emission at both sides of the innermost disk. Both blobs show a strong wavelength dependence. with the western one being bright in the optical and almost vanishing in the infrared; at about 1 μm the clumps are of equal intensity and attain simultaneously their maximum brightness. Beyond 1 μm the eastern blob becomes stronger by 10% at J and K and by 40% at H. This is in contrast to what one would expect from the pure extinction which is higher along the eastern line of sight due to the inclination of the disk. It is likely that there are intrinsic intensity differences between the two features which may either be caused by an asymmetric outflow or by line emission, particularly in the $H-$band. The eastern outflow shows a pronounced morphology; it seems to originate close to the central object and resembles an precessing jet that turns over shortly after leaving the innermost region; farther out the orientation of the flow axis is almost parallel to the disk plane. The much fainter western flow is more diffuse and has an angle of about 45° with respect to the disk plane (Fig. 4).

A spectrum between 0.4 and 0.9μm (Chini et al. 2004) [30] that covers both cavities and the flows is dominated by the emission lines of Hα, the CaII triplet 8498, 8542 and 8662Å, and HeI 6678Å. In the case of low-mass stars these lines are considered as unquestionable evidence for an ongoing accretion process (e.g. Hartmann et al. 1994, Muzerolle et al. 1998) [33,34]. The CaII triplet was also shown to be a product of disk accretion for both a large sample of TTauri and Herbig Ae/Be stars (Hamann & Persson 1992) [35]. The Hα line is extremely broad and shows a deep blue-shifted absorption as well as an inverse P Cygni profile; blue-shifted absorption components in permitted lines are typically associated with accretion disk-driven outflows (Muzerolle et al. 1998, Calvet 1997) [34,36]. The same is true for forbidden emission lines such as [O I] 6300Å and [S II] 6731Å which are also present in the spectrum. Numerous permitted and forbidden Fe II lines which are velocity-shifted by 120 km/s are clear signposts for high velocity dissociative shocks with velocities of more than 50 km/s (Muzerolle et al. 2001) [37]. In summary, there is a typical TTauri spectrum from two 30.000 AU nebular lobes that are associated with a flared disk of 10.000 AU radius.

The nature of the protostar

At the disk centre where one expects the newly forming star there is a relatively compact 2.2 μm emission feature of 240 × 450 AU which is too small to host a cluster. Its major axis differs by 15° from the rotational axis of the disk. One may speculate whether this elongated feature marks the starting point of the precessing massive outflow or whether it originates from a binary system that is currently born from a common accretion disk. Given that there is only a K−band brightness for this central object its absolute luminosity is highly uncertain. From extinction values of neighbouring stars it is likely that the disk is deeply embedded in the molecular cloud behind a visual extinction of about 50 magnitudes. The dust within the disk produces another contribution of about 60 magnitudes toward its centre which makes it impossible to obtain any optical information about the protostellar accreting object. Assuming that the central emission is due to direct stellar light an absolute infrared brightness of $K \sim -2.5$ mag is derived. This would correspond to a main sequence star of about 20 $M_\odot$ and a temperature of 35.000 K. An independent mass estimate from dynamical considerations, concerning the rotation of the molecular disk, yields a mass of about 15 $M_\odot$ for the central gravitational object. Due to the fact that the accretion process is still active, and that the gas reservoir of the disk still allows for a substantial mass gain, it is likely that in the present case a massive protostar is on its way to become an O-type star. Theoretical calculations show that an initial gas cloud of 60 to 120 $M_\odot$ evolves into a star between 33 and 43 $M_\odot$ while the remaining mass is rejected into the interstellar medium (Yorke & Sonnhalter 2002) [3].

All presented evidence point toward a massive star that is currently forming via accretion through a disk while the associated energetic mass outflow disrupts the surrounding environment and rejects part of the accreted material into the ambient medium. The observations show - for the very first time - all theoretically predicted ingredients of the star formation process directly and simultaneously in a single object and therefore improve our current understanding of such an event tremendously. The schematic picture of Fig. 5 summaries the individual components as revealed by the different observing techniques and complies perfectly with recent magneto-centrifugal disk/wind models (Hartigan et al. 1995, Hirose et al. 1997) [38,39]. A central protostar - maybe even a binary system - is surrounded by a flared, slowly rotating disk from which it accretes mass along a reconnected magnetospheric field. A considerable fraction of the transferred mass is accelerated from the polar regions of the protostar/disk interface into opposite directions along the open stellar magnetic field. This reconnection-driven jet is further accelerated magneto-centrifugally due to stellar rotation and excavates the ambient medium. Eventually, a bipolar high-velocity neutral wind forms an hourglass like cavity which reflects light from the

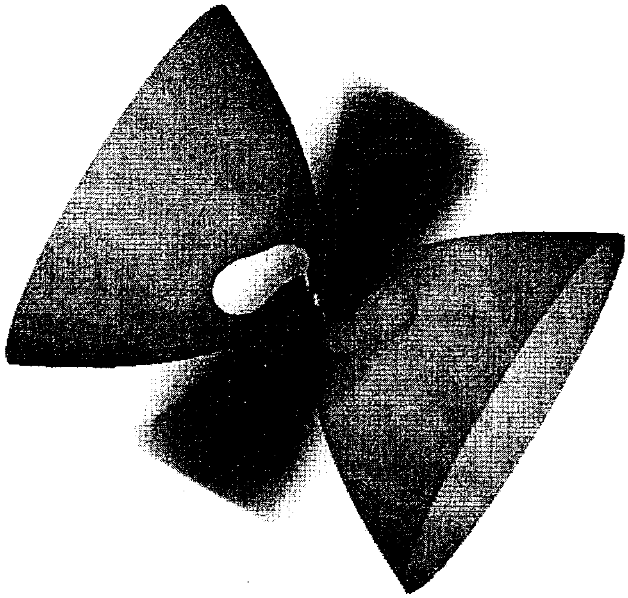

Figure 5: Model of the source outlining the disk (black) seen under an aspect angle of 15°, two nebular hourglass shaped lobes and two precessing jets.

very inner regions of the system. Further out this neutral wind drives the observed molecular bipolar flow.

4 Summary

This review has focused on progenitors of massive stars, i.e. on evolutionary stages between massive pre-stellar cores and UC HIIs. It looks that the current submm/FIR surveys are likely to detect proto-clusters rather than protostars. Though valuable for a first glimpse of where massive star formation occurs in our Galaxy, these surveys will have to be refined by future missions with higher spatial resolution. Some of individual well-known massive protostellar candidates have been reviewed. While there is ample evidence for energetic mass outflows the driving sources are difficult to identify; likewise, their luminosity is highly uncertain - partly due to confusion, partly due to missing photometric data. Nevertheless, the mass and energetics of the outflowing gas point toward luminous central objects as driving sources. The new disk in M 17 seems to be a promising case in favour of the accretion scenario. It is the largest and most massive disk that could be directly observed with sub-arcsecond spatial resolution. Follow-up observations are definitely required to constrain the mass and the luminosity of the forming star.

Acknowledgments

This work is based on data collected at the European Southern Observatory, La Silla and Paranal, Chile and at the IRAM Plateau de Bure Interferometer, Grenoble, France. The project is partly funded by the Nordrhein-Westfälische Akademie der Wissenschaften.

References

1. Wolfire, M. & Cassinelli, J. 1987, ApJ, 319, 850
2. Norberg, P. & Maeder, A. 2000, AA, 359, 1025
3. Yorke, H. & Sonnhalter, C. 2002, ApJ, 569, 846
4. Bonnell, I.A., Bate, M.R., Zinnecker, H. 1998, MNRAS, 298, 93
5. André, P., Ward-Thompson, D., Barsony, M. 1993, ApJ, 406, 122
6. Chini, R. et al. 1993, AA, 272, L5
7. Mezger, P.G., Chini, R., Kreysa, E., Wink, J.E., Salter, C.J. 1988, AA, 191, 44
8. Beuther, H., Schilke, P., Sridharan, T.K., Menten, K.M., Walmsley, C.M., Wyrowski, F. 2002, AA, 390, 289
9. Sridharan, T.K., Beuther, H., Schilke, P., Menten, K.M., Wyrowski, F. 2002, ApJ, 566, 931
10. Walsh, A.J., Burton, M.G., Hyland, A.R., Robinson, G. 1998, MNRAS, 301, 640
11. Shepherd, D.S. & Churchwell, E. 1996, ApJ, 472, 225
12. Cabrit, S. & Bertout, C. 1992, AA, 261, 274
13. Beuther, H., Schilke, P., Sridharan, T. K., Menten, K. M., Walmsley, C. M., Wyrowski, F. 2002, AA, 383, 892
14. Gehrz, R.D., Grasdalen, G.L., Castelaz, M., Gullixson, C., Mozurkewich, D., Hackwell, J.A. 1982, ApJ, 254, 550
15. Felli, M., Massi, M., Staude, H.J., Reddmann, T., Eiroa, C., Hefele, H., Neckel, T., Panagia, N. 1984a, AA, 135, 216
16. Stutzki, J., Ungerechts, H., Winnewisser, G. 1982, AA, 111, 201
17. Barsony, M., Scoville, N. Z., Bally, J., Claussen, M.J. 1989, ApJ, 346, L93
18. Schneider, N., Simon, R., Kramer, C., Stutzki, J., Bontemps, S. 2002, AA, 384, 225
19. Marti, J., Rodriguez, L., Reipurth, B. 1993, ApJ, 416, 208
20. Aspin, C. & Geballe, T.R. 1992, AA, 266, 219
21. Hofner, P., Wiesemeyer, H., Henning, T. 2001a, ApJ, 549, 425
22. Hofner, P., Cesaroni, R., Rodriguez, L.F., Marti, J. 2001b, BAAS, 33, 1419
23. Curiel, S. et al. 2002, AbJ, 564, L35
24. Shepherd, D., Claussen, M., Kurtz, S. 2001, Sience, 292, 1513
25. Plambeck, R. L., Wright, M. C. H., Carlstrom, J. E. 1990, ApJ, 348, L65
26. Wright, M.C.H., Plambeck, R.L., Mundy, L. G., Looney, L.W. 1995, ApJ, 455, L185
27. Greenhill, L., Gwinn, C., Schwartz, C., Moran, J., Diamond, P., 1998, Nature, 396, 650
28. Sandell, G., Wright, M., Forster, J. 2003, ApJ 590, L45
29. McCaughrean, M.J. et al. 1998, ApJ, 492, L157
30. Chini, R., Hoffmeister, V.H., Kimeswenger, S., Nielbock, M., Nürnberger, D., Schmidtobreick, L., Sterzik, L. 2004, Nature, 429, 155
31. Chini, R. & Wargau, W. 1998, AA, 329, 161
32. Felli, M., Churchwell, E., Massi, M. 1984b, AA, 136, 53
33. Hartmann, L., Hewett, R., Calvet, N. 1994, ApJ, 426, 669
34. Muzerolle, J., Hartmann, L., Calvet, N. 1998, AJ, 116, 455
35. Hamann, F. & Persson, S. 1992, ApJS, 82, 285
36. Calvet, N. 1997, IAU Symposium 182, 417
37. Muzerolle, J., Calvet, N., Hartmann, L. 2001, ApJ, 550, 994
38. Hartigan, P., Edwards, S., Ghandour, L. 1995, ApJ, 452, 736
39. Hirose, S., Uchida, Y., Shibata, K., Matsumoto, R. 1997, PASJ, 49, 193

THE TIMESCALE AND MODE OF STAR FORMATION IN CLUSTERS

JONATHAN C. TAN

Princeton University Observatory, Princeton, NJ 08544, USA

I discuss two questions about the origin of star clusters: How long does the process take? What is the mode of individual star formation? I argue that observations of Galactic star-forming regions, particularly the Orion Nebula Cluster (ONC), indicate that cluster formation often takes several Myr, which is *many* local dynamical timescales. Individual stars and binaries, including massive stars, appear to form from the collapse of gas cores.

Keywords: stars: formation — stars: pre-main sequence — open clusters and associations

1 The Timescale for Star Cluster Formation

In this section I ask: how long, in terms of dynamical timescales, does star cluster formation take? In the next, I consider how gas joins individual stars, forming in a cluster — is it from the collapse of pre-existing gas *cores* with masses that help determine the final stellar mass, or from the sweeping-up of gas, initially unbound to the protostar? I try to derive answers from an interpretation of observational data and then discuss the implications for theoretical models.

Star clusters are born from the densest gas *clumps* in giant molecular clouds (GMCs). We can measure how long this takes, from the beginning to end of star formation, in terms of the number of free-fall timescales, $t_{\rm ff} = (3\pi/32)(G\rho)^{-1/2}$ or the number of dynamical-crossing timescales $t_{\rm dyn} = R/\sigma = 1.1(G\rho)^{-1/2}$, where σ is the 1D velocity dispersion given by $\sigma^2 = \alpha_{\rm vir}GM/(5R)$ with the observed virial parameter $\alpha_{\rm vir} \sim 1$ (McKee & Tan 2003). In this case $t_{\rm ff} = 0.50t_{\rm dyn}$.

The formation timescale is an important overall constraint for theoretical models. It also determines how much dynamical relaxation occurs during formation. For N equal mass stars the relaxation time is $t_{\rm relax} \simeq 0.1N/(\ln N)t_{\rm dyn}$, i.e. about 14 crossing timescales for $N = 1000$. Using numerical experiments, Bonnell & Davies (1998) found that the mass segregation time (of clusters with mass-independent initial velocity dispersions) was similar to the relaxation time.

To evaluate the free-fall and dynamical-crossing timescales requires a choice of density and/or scale, but in reality density varies with scale. Gas clumps have approximately power-law density profiles with $\rho \propto r^{-k_\rho}$; $k_\rho \simeq 1.5-1.8$ (e.g. Mueller et al. 2002). The stellar distributions of young clusters are also usually centrally concentrated; e.g. Hillenbrand & Hartmann (1998) fit King models to the ONC. Allowing for a 50% formation efficiency, Elmegreen (2000) estimated the density in the proto-ONC as $n_{\rm H} = 1.2 \times 10^5\ {\rm cm}^{-3}$, so $t_{\rm ff} = 1.25 \times 10^5$ yr and $t_{\rm dyn} = 2.5 \times 10^5$ yr. This applies where the present stellar density is $2 \times 10^3\ M_\odot\ {\rm pc}^{-3}$, i.e. about 0.3-0.4 pc from the center. Bonnell & Davies (1998) estimated a half-mass radius of 0.5 pc, and using $\sigma = 2.5{\rm km\ s}^{-1}$ derived $t_{\rm dyn} \simeq 2 \times 10^5$ yr (note, they define a crossing time $2R/\sigma$, i.e. 4×10^5 yr).

These estimates are based on the present spatial distribution of matter, even if allowing for a formation efficiency. We expect that the initial distribution was probably more extended, since self-gravity and the decay of turbulent support should lead to contraction, at least in the early stages of formation. However, feedback from star formation could maintain turbulence (Norman & Silk 1980; see below). Also, dispersal of gas leads to the expansion of the cluster (Hills 1980).

To measure the actual formation time, a common method is to find the age spread of individual cluster members; for young clusters this is only practical for lower-mass stars that have a pre-main-sequence phase once they have finished accreting (high-mass stars reach the main sequence while still accreting). Observed positions in the Hertzsprung-Russell (HR) diagram are compared to theoretical models of evolution (e.g. Palla & Stahler 1999, hereafter PS99). Modeling uncertainties include the choice of deuterium abundance; D burning swells accreting protostars, so raising the "birthline" where they appear on the HR diagram (Stahler 1988). A relatively high value of [D/H]$= 2.5 \times 10^{-5}$ was adopted by PS99. Increasing the accretion rate also raises the birthline. PS99 used constant rates of $10^{-5}\,M_\odot\,{\rm yr}^{-1}$, which may be smaller than expected in the high pressure environments of forming clusters (McKee & Tan 2003). Finally the birthline is also influenced by the geometry of accretion (PS99 assumed spherical as opposed to disk accretion), since this affects the energetics of the gas just before it joins the stellar surface (Hartmann 2003). Fortunately, as the initial contraction from the birthline is quite rapid, the birthline position mostly affects age determinations $\lesssim 1$ Myr old. The ages of older stars tend to be estimated more robustly. Uncertainties also become larger at the lowest stellar masses.

The observables for each star are luminosity and surface temperature. Some stars are likely to be unresolved binaries, which must be allowed for (e.g. PS99). The surface temperatures and luminosities of a substantial fraction of ONC stars have been measured (Hillenbrand 1997). This sample is biased against very embedded sources and low-mass stars ($\lesssim 0.4 M_\odot$). Patchy extinction introduces errors. Some systematic errors are evident as the high-mass zero age main sequence lies above the theoretical expectation by 0.3 dex in luminosity (or below by 0.05 dex in temperature). If these effects also operate at lower masses, then ages would be underestimated.

PS99 could estimate ages of 258 stars with masses $0.4 < m_*/M_\odot < 6.0$ from Hillenbrand's (1997) sample. The lower limit of this range was set because of incompleteness at $L_* \simeq 0.1\ L_\odot$, the predicted luminosity of a 10 Myr old $0.4\,M_\odot$ star. However, given that the model uncertainties are largest at these low masses, and given possible observational systematic uncertainties, the sample may not be complete at 0.4 $M_\odot$ to ages of only several Myr. The large numbers of stars at these low masses increases the potential importance of incompleteness in the lowest mass bin. When divided into different mass intervals, the lowest mass bin with mean mass of $\bar{m}_* = 0.56\ M_\odot$, does appear to be different from the next two bins with $\bar{m}_* = 1.0, 1.8\ M_\odot$.

Assuming a complete sample, PS99 found: 82 stars aged 0-1 Myr, 57 aged 1-2 Myr, 34 aged 2-3 Myr, 17 aged 3-4 Myr, 8 aged 4-5 Myr, 8 aged 5-6 Myr, 8 aged 6-7 Myr, and 6 aged 7-10 Myr. Hartmann (2003) has argued that the oldest ages ($\sim$ 10 Myr) may be due to a problem of foreground contamination. As described above, birthline uncertainties mostly affect the youngest ages ($\lesssim$ 1 Myr). We conclude that a significant fraction of the stars are as old as 3 Myr, and that this is a lower limit to $t_{\rm form}$ since star formation is still continuing in the cluster.

An independent method of dating the cluster comes from the identification of a dynamical ejection event of 4 massive stars (a binary and two singles) that appear to have originated from the ONC about 2.5 Myr ago (Hoogerwerf, de Bruijne & de Zeeuw 2001). The central value of the time since this ejection event is about 2.3 Myr in the analysis of Hoogerwerf et al. (2001); however, if the cluster's distance of about 450 pc is adopted, then the best estimate for the age is 2.5 Myr. The identification is based upon the fact that the extrapolation of the motion of the center of mass of the four stars from the ejection event to the present day, leads to a predicted position coincident with the ONC (uncertainties are a couple of pc). These results imply that 2.5 Myr ago the ONC was already a rich cluster containing at least four stars of spectral type earlier than O9/B0. Before this the stars had to form and have enough time to find and eject each other in a close interaction. Thus the estimate of 2.5 Myr is again a lower limit to $t_{\rm form}$.

Taken together, the above results lead us to conclude, with some confidence, that the formation timescale for the cluster is $t_{\rm form} \geq 3$ Myr. This is $\geq$12 (24) dynamical-crossing (free-fall) timescales, as estimated at the conditions considered by Elmegreen (2000) (see above). This age corresponds to a free-fall timescale for densities of $n_{\rm H} = 210\,{\rm cm}^{-3}$, much smaller than the mean density of the ONC region. The dynamical ejection event implies that a dense stellar cluster existed 2.5 Myr ago, i.e. that the densities have not changed appreciably during this time, and the ONC has taken many ($\gtrsim 10$) dynamical-crossing times to form.

How does this result compare to what is know from other star-forming regions? Forbes (1996) did not find evidence for an age spread in NGC 6531, but the analysis was insensitive to timescales shorter than at least 3 Myr. Hodapp & Deane (1993) analyzed L1641, placing twelve stars in an HR diagram: ten are spread in age from 0-2 Myr and two are about 6 Myr old. The conclusions that can be drawn from this cluster are limited due to the small sample, lack of correction for binarity, and use of relatively old pre-main-sequence tracks. Palla & Stahler (2000) presented what is so far the most extensive and systematic analysis of young clusters and associations (in addition to the ONC, they consider Taurus-Auriga, Lupus, Chamaeleon, ρ Ophiuchi, Upper Scorpius, IC 348 and NGC 2264). From these results we again conclude that $t_{\rm form} \gtrsim 3$ Myr. These systems exhibit a large range of stellar densities, mostly extending to lower values than the ONC, so that this timescale does not correspond to as many dynamical-crossing timescales as in the case of the ONC. Siess, Forestini & Dougados (1997) and Belikov et al. (1998) concluded that the age spread in the Pleiades was $\sim$ 30 Myr around a mean value of about 100 Myr. If true, then this is the largest measured formation time of local clusters.

If the formation time is many dynamical timescales, then there should be virialized and heavily embedded clusters at early stages in their evolution (most clusters analyzed with the HR diagram method are by necessity optically revealed and probably nearing the end of star formation). This population of embedded clusters probably corresponds to the population of hot molecular clumps observed in sub-mm continuum and molecular lines (e.g. Mueller et al. 2002; Shirley et al. 2003). Indeed most of the CS line maps of Shirley et al. (2003) have morphologies consistent with quasi-spherical virialized distributions. The clumps have typical masses $M \sim 100 - 10^4\,M_\odot$, diameters $\sim$ 1 pc and surface densities $\Sigma \sim 1\,{\rm g\,cm}^{-2}$.

Relatively slow, almost quasi-static evolution of the star-forming clump, contrasts with some theories and models of star formation that take only one or a few crossing times (e.g. Elmegreen 2000; Bonnell & Bate 2002). One theoretical motivation for such fast timescales has been the rapid decay of turbulence: even in a strongly magnetized medium, the kinetic energy associated with supersonic turbulence decays with a half-life of just over a signal crossing timescale (Stone, Ostriker, & Gammie 1998). Thus a long formation time requires that the turbulence observed in star-forming clumps is maintained by energy input, most likely from protostellar outflows and the overall contraction of the clump. In fact the energy requirements are quite modest; the energy dissipation rate of virialized clumps (with $k_\rho = 3/2$ and mean surface density $\Sigma = M/(\pi R^2)$) that lose half their kinetic energy in one dynamical crossing time, $t_{\rm dyn}$ is $21(M/4000M_\odot)^{5/4}\Sigma^{5/4}\,L_\odot$. Even very inefficient coupling of protostellar outflows to the gas allows turbulence to be maintained. The initial kinetic energy of outflows is expected to be about half of the total energy release associated with accretion (e.g. Shu et al. 2000), but much of this is dissipated in shocks as gas is swept-up. The collimated nature of the flows also means that a lot of energy escapes from the star-forming region. Nevertheless, even if only 1% of the outflow energy generates turbulence in the clump, then the cluster can form leisurely in 20 dynamical-crossing times and still maintain its turbulent support[a]. This inefficiency of star formation is consistent with some numerical simulations of self-gravitating, unmagnetized gas with driven turbulence (Vázquez-Semadeni, Ballesteros-Paredes, & Klessen 2003).

Note that while the observed age spreads of clusters imply formation times long compared to the local dynamical timescale of the clump, these times are about equal to the dynamical timescale of the larger scale GMCs, in which clumps are embedded. Hartmann, Ballesteros-Paredes, & Bergin (2001) used this fact to argue that GMCs are transient objects, which would be true if GMCs did not have a long period of quiescence before star formation and if they were destroyed quickly once the stars had formed. However, the star formation in most GMCs is spatially localized, so that most of the mass is quiescent, and it is not clear that most newly formed star clusters are able to destroy their parental clouds. The observational study of Leisawitz, Bash & Thaddeus (1989) found that open star clusters older than about $\sim$ 10 Myr were not associated with molecular clouds, which is consistent either with post-star-formation cloud lifetimes shorter than this age or with relative velocities of star clusters and their parent clouds of about 10 km s^{-1}, as might arise from photoionization feedback (Williams & McKee 1997).

One traditional objection to longer formation timescales has been the idea that once massive stars are formed in a cluster, they would very rapidly disperse the gas with their ionizing radiation and stellar winds. Observational evidence suggests that massive stars are not always the last stars to form in their clusters (e.g. Hoogerwerf et al. 2001). Tan & McKee (2001; 2004) found that the turbulent, clumpy, and self-gravitating nature of gas led to much slower dispersal times, compared to a uniform medium. A single O star producing 10^{49} H-ionizing photons s^{-1} was unable to disperse the gas in a 4000 $M_\odot$ clump with a density comparable to the proto-ONC. If the gas in the clump was allowed to form stars at a rate such that 50% of the initial mass would be turned into stars in 15 $t_{\rm dyn}$ and the feedback from this star formation was accounted for, then the gas was dispersed in about 2 Myr (about 10 $t_{\rm dyn}$). The dynamical ejection of massive stars from clusters, which was not included in the above calculations, would increase the dispersal timescale. We have seen that such an ejection occurred in the ONC 2.5 Myr ago. It also appears to be happening at the present epoch with the ejection of the Becklin-Neugebauer (BN) object and $\Theta^1 C$, the most massive star in the cluster (Plambeck et al. 1995; Tan 2004a).

A 3 Myr formation time for the ONC has implications for how much mass segregation has occurred, which bears upon the question of whether massive stars tend to form preferentially in the centers of clusters. This time corresponds to about 8 diameter crossing times at the half mass radius of 0.5 pc, which is the unit of time used in the study of Bonnell & Davies (1998). If the 30 most massive stars are initially placed at the half-mass radius, $r_{1/2}$, then after this time the median location of the 6 most massive stars has migrated in to only $0.15 r_{1/2}$. However, the effects of gradual formation and the presence of gas need to be accounted for before detailed comparison is made to the present-day ONC stellar distribution.

2 The Mode of Star Formation in Star Clusters

The paradigm of star formation from initially quasi-hydrostatic gas cores (e.g. Shu, Adams, & Lizano 1987) has faced the challenges of competitive accretion and dynamical interactions

[a]This calculation assumes 50% star formation efficiency, a turbulent decay half-life of 1 $t_{\rm dyn}$, a Salpeter initial mass function (IMF) from 0.1 to 120 $M_\odot$, protostellar sizes based on the model of McKee & Tan (2003), outflow mechanical luminosity of $Gm_*\dot{m}_*/(2r_*)$, and a coupling efficiency of 0.01. The formation time that maintains turbulent support is then $t_{\rm form} = \eta_{\rm dyn} t_{\rm dyn}$ with $\eta_{\rm dyn} = 21(M/4000 M_\odot)^{-1/2}\Sigma^{-1/2}$.

when applied to star formation, particularly of high-mass stars, in nascent star clusters (e.g. Bonnell, Bate, & Zinnecker 1998; Stahler, Palla, & Ho 2000). For example, the smooth-particle-hydrodynamics (SPH) simulations of Bonnell, Bate and collaborators are characterized by a much more chaotic evolution in which long-lived cores are not readily apparent. Bonnell, Vine, & Bate 2004 showed that the most massive star at the end of their simulation had gained mass that was initially very widely distributed. However, cores (both starless and with embedded protostars) are observed in real proto-clusters (e.g. Testi & Sargent 1998; Motte et al. 2001; Li, Goldsmith, & Menten 2003; Beuther & Schilke 2004), and even have an IMF that, although uncertain, is similar to that of stars. Part of the resolution of this discrepancy may lie in the methodology of the numerical simulations: these do not yet include magnetic fields or feedback from forming stars; the equation of state is isothermal; the SPH method uses a softening length for each particle so does not resolve features smaller than this scale, particularly shocks; and protostars are modeled as sink particles that form when a mass of $\geq 0.1\,M_\odot$ happens to be self-gravitating, sub-virial and at a density $n_{\rm H_2} \geq 3.1 \times 10^8\ {\rm cm}^{-3}$. One example of where the SPH technique may fail is the problem of the rate of Bondi-Hoyle accretion, which is how most of the stellar mass is acquired in the above simulations. In this process gas is gravitationally focused by a passing star so that streamlines collide, shock and dissipate their energy. It occurs on scales unresolved by the present SPH techniques. Eulerian grid simulations, including adaptive mesh refinement of small scale structures, have been used to simulate the interaction of sink particles with surrounding turbulent gas: the accretion rate is much smaller than the classical analytic estimate of accretion from a uniform medium (Krumholz, McKee, & Klein, in prep.).

In spite of recent progress in the observations of high-mass star-forming regions, the mode of massive star formation remains controversial. There is as yet no clear-cut example of a massive protostar for which the accretion disk and core are readily identified. One difficulty is the uncertainty in the expected properties of such disks and cores. McKee & Tan (2003) described the properties of virialized cores in pressure equilibrium with their high-pressure proto-cluster surroundings, and calculated the evolution of the protostars that form from them. Tan (2004b) compared these models to observations of the Orion Hot Core in the Kleinmann-Low region of the ONC, concluding that the picture of massive star formation from the collapse of massive cores was supported. Here we highlight the main points of this argument.

The total luminosity of the Kleinmann-Low region is about $10^5\,L_\odot$, and the orientation of the polarization vectors of 3.8 μm emission suggest that much of this comes from a very localized region close to the center of a dense and hot molecular core, known as the Orion Hot Core (Werner, Dinnerstein, & Capps 1983). Thermal emission from dust in this structure is also seen at 450 μm and it has a radius of $\sim$0.05 pc (Wright et al. 1992), about that expected for an initially 60 $M_\odot$ core. If about half of the total luminosity of the region comes from a single protostar, then it would have a mass of about 20 $M_\odot$ (McKee & Tan 2003), so, allowing for accretion inefficiencies due to outflows, the core is about half way through its collapse. If the initial ratio of rotational to gravitational energy is about 2%, as is typical for low-mass cores (Goodman et al. 1993), then the expected size of the accretion disk is about 1000 AU. This corresponds to the size of the region of SiO (v=0) maser emission seen by Wright et al. (1995). If the velocity gradient across this structure is interpreted as being due to Keplerian motion of a disk, then the central mass is about 30 $M_\odot$. The orientation of the disk is perpendicular to the larger scale molecular outflow that is ejected to the NW and SE of this region (e.g. Chernin & Wright 1996). At the center of the SiO (v=0) emission is a thermal radio source, known as "I" (e.g. Menten & Reid 1995). It is elongated perpendicular to the disk (Menten & Reid, in preparation), i.e. parallel to the outflow. In particular, the major axis aligns very closely with the direction towards Herbig-Haro objects to the NW that show blue-shifted velocities of up to 400 km s^{-1} (Taylor et al. 1986). Allowing for flow geometry, this corresponds to a total velocity of 1000 km s^{-1}, which is the expected initial outflow velocity from a $\sim 20 - 30\,M_\odot$ protostar, i.e. about its escape speed. The thermal radio source is likely due to ionized gas: the massive protostar is only able to ionize a small patch of its outflow, which is dense enough to confine the radiation, except along the rotation axis. These "outflow-confined" HII regions have been considered by Tan & McKee (2003): the models explain the elongation and radio spectrum of source "I". In summary, there are many independent pieces of evidence that corroborate a model of star formation involving collapse of a massive core to an accretion disk, which then feeds a massive ($\sim 20\ M_{\odot}$) protostar, driving a powerful outflow in the process. No individual piece of evidence is conclusive, but in their totality a remarkably consistent picture emerges.

The situation is, of course, somewhat more complicated than the above description. There are a few other protostars and outflows in the region, but these seem to have quite modest luminosities and their apparent proximity to the Orion Hot Core may be due to projection effects. If there is a physically close second protostar, then this may indicate that the core is collapsing to form a binary, a relatively minor extension of the basic model. In addition, the collapse of the core is probably perturbed by other cluster members; e.g., the BN object made a close projected passage to source "I" about 500 yr ago (Tan 2004a). On smaller scales of several tens of AU from the center of source "I", SiO (v=1) maser emission is seen with a morphology approximately in the shape of an X, stretched along the NW-SE axis (Greenhill et al. 2003). The densities and temperatures required for excitation are similar to those expected in the inner part of the outflow (Tan & McKee 2003), but the velocity structure has also been interpreted as evidence for a disk aligned along this NW-SE axis (Greenhill et al. 2003), which would be incompatible with the above model. The small velocity differences ($\sim$ tens $\mathrm{km\,s^{-1}}$) in the maser spots are hard to understand in the context of an outflow from a massive star that should have much faster speeds, although the radial velocity range surveyed so far is only $\sim 100\ \mathrm{km\,s^{-1}}$. Further observations of these features would be very useful to help resolve this issue.

Acknowledgments

I thank organizers of this meeting. This work benefited from helpful discussions with L. Blitz, I. Bonnell, L. Greenhill, M. Krumholz, C. McKee, P. Padoan, F. Palla, & J. Stone. I am supported by a Princeton Spitzer-Cotsen fellowship & NASA grant NAG5-10811.

References

1. Belikov, A.N., Hirte, S., Meusinger, H., Piskunov, A., & Schilbach E. 1998, A&A, 332,575
2. Beuther, H., & Schilke, P. 2004, Science, 303, 1167
3. Bonnell, I. A., & Bate, M. R. 2002, MNRAS, 336, 659
4. Bonnell, I. A., Bate, M. R., & Zinnecker, H. 1998, MNRAS, 298, 93
5. Bonnell, I. A., & Davies, M. B. 1998, MNRAS, 295, 691
6. Bonnell, I. A., Vine, S. G., & Bate, M. R., 2004, MNRAS, 349, 735
7. Chernin, L. M., & Wright, M. C. H. 1996, ApJ, 467, 676
8. Elmegreen, B. G. 2000, ApJ, 530, 277
9. Forbes, D. 1996, AJ, 112, 1073
10. Goodman, A. A., Benson, P. J., Fuller, G. A., & Myers, P. C. 1993, ApJ, 406, 528
11. Greenhill, L. J., Reid, M. J., Reid, M. J., Chandler, C. J., et al. 2003, IAU Symp. 221, Star Formation at High Angular Resolution, eds.Burton et al., ASP,(astro-ph/0309334)
12. Hartmann, L. 2003, ApJ, 585, 398
13. Hartmann, L., Ballesteros-Paredes, J., & Bergin, E. A. 2001, 562, 852
14. Hillenbrand, L. A. 1997, AJ, 113, 1733
15. Hillenbrand, L. A., & Hartmann, L. W. 1998, ApJ, 492, 540
16. Hills, J. G. 1980, ApJ, 235, 986

17. Hodapp, K-W, & Deane, J. 1993, ApJS, 88, 119
18. Hoogerwerf, R., de Bruijne, J. H. J., & de Zeeuw, P. T. 2001, A&A, 365, 49
19. Leisawitz, D., Bash, F. N. & Thaddeus, P. 1989, ApJS, 70, 731
20. Li, D., Goldsmith, P. F., & Menten, K. 2003, ApJ, 587, 262
21. McKee, C. F. & Tan, J. C. 2003, ApJ, 585, 850
22. Menten, K. M. & Reid, M. J. 1995, ApJL, 445, L157
23. Motte, F., André, P., Ward-Thompson, D., & Bontemps, S. 2001, A&A, 372, L41
24. Mueller, K. E., Shirley, Y. L., Evans, N. J. II, Jacobson, H. R. 2002, ApJS, 143, 469
25. Norman, C., & Silk, J. 1980, ApJ, 238, 158
26. Palla, F., & Stahler, S. W. 1999, ApJ, 525, 722 (PS99)
27. Palla, F., & Stahler, S. W. 2000, ApJ, 255, 270
28. Plambeck, R. L., Wright, M. C. H., Mundy, L. G., & Looney, L. W. 1995, ApJ, 455, L189
29. Shirley, Y. L., Evans, N. J., Young, K. E., Knez, C. & Jaffe, D. T. 2003, ApJS, 149, 375
30. Shu, F. H., Adams, F. C., & Lizano, S. 1987, Ann. Rev Astron. & Astrophys., 25, 23
31. Shu, F. H., Najita, J., Shang, H., Li, Z.-H. 2000, in Protostars & Planets IV, eds. V. Mannings, A. Boss, & S. Russell, U. of Arizona, 789
32. Siess, L., Forestini, M., & Dougados, C. 1997, A&A, 324, 556
33. Stahler, S. W. 1988, ApJ, 332, 804
34. Stahler, S. W., Palla, F., & Ho, P. T. P. 2000, in Protostars & Planets IV, eds. V. Mannings, A. Boss & S. Russell, U. of Arizona, 327
35. Stone, J. M., Ostriker, E. C., & Gammie, C. F. 1998, ApJL, 508, L99
36. Tan, J. C. 2004a, ApJL, 607, L47
37. Tan, J. C. 2004b, in Star Formation in the ISM, eds. Adams et al., ASP,(astro-ph/0310724)
38. Tan, J. C., & McKee, C. F. 2001, in Starburst Galaxies: Near and Far, eds. L. Tacconi & D. Lutz, Springer-Verlag, 188 (astro-ph/0012005)
39. Tan, J. C., & McKee, C. F. 2003, IAU Symp. 221, Star Formation at High Angular Resolution, eds. Burton, Jayawardhana, & Bourke, ASP(astro-ph/0309139)
40. Tan, J. C., & McKee, C. F. 2004, in Formation and Evolution of Young Massive Clusters, eds. H. J. G. L. M. Lamers, A. Nota and L. Smith, ASP, in press (astro-ph/0403498)
41. Taylor, K., Dyson, J. E., Axon, D. J., & Hughes, S. 1986, MNRAS, 221, 155
42. Testi, L., & Sargent, A. I. 1998, ApJ, 508, L91
43. Vázquez-Semadeni, E., Ballesteros-Paredes, J., & Klessen, R. S. 2003, ApJL, 585, L131
44. Werner, M. W., Capps, R. W., & Dinerstein, H. L. 1983, ApJL, 265, L13
45. Williams, J. P., & McKee, C. F. 1997, ApJ, 476, 166
46. Wright, M. C. H., Plambeck, R.L., Mundy, L.G., & Looney, L.W. 1995, ApJL, 455,L185
47. Wright, M. C. H., Sandell, G., Wilner, D. J., & Plambeck, R. L. 1992, ApJ, 393, 225

Mont Blanc mountains as seen from Val d'Aosta

THE LOWER IMF OF BLANCO 1 AND SIMILAR AGE OPEN CLUSTERS

E. MORAUX (1), J. BOUVIER (2)

(1) Institute of Astronomy, Cambridge, CB3 0HA, UK
(2) Laboratoire d'Astrophysique de Grenoble, BP 53X, 38041 Grenoble Cedex, France

We report new estimate for the lower Blanco 1 mass function across the stellar/substellar boundary. We find that it is well represented by a single power-law $dn/dm \propto m^{-0.58\pm0.10}$ between $0.03M_\odot$ and $0.5M_\odot$. Over a larger mass domain, however, the mass function is better fitted by a log-normal distribution. We compare this result to the mass functions of two other young open clusters having a similar age ($\sim$ 100 Myr), the Pleiades and NGC 2516.

Keywords: Stars: low-mass, brown dwarfs – Stars: luminosity function, mass function – open clusters and associations: individual: Blanco 1 – open clusters and associations: general

1 Introduction

Since the first brown dwarf discovery in 1995 (Nakajima et al. 1995; Rebolo et al. 1995), new perspectives have opened regarding the formation of condensed objects in molecular clouds. Today more than one thousand brown dwarfs (BDs) are known but their mode of formation is still controversial and the theoretical framework describing the stellar and substellar formation process(es) is far from being satisfactory. How do brown dwarfs form ? Is there a lower mass limit for an object to be formed ? A way to tackle these questions is to determine the mass spectrum resulting from the stellar formation process, i.e. the initial mass function (IMF), down to the substellar regime.

Young nearby open clusters are ideal environments for such a purpose. Their members constitute an uniform population in terms of distance and age, the extinction is usually low, and their youth ensures that brown dwarfs are still bright enough for being easily detected. Moreover, the rich stellar populations of the nearest open clusters complement the recent discoveries of cluster brown dwarfs to yield a complete mass function from the substellar domain up to massive stars.

We therefore looked at the substellar population in young open clusters of similar age ($\sim$ 100 Myr) in order to estimate their mass function (MF) and start to investigate the IMF dependance on environmental conditions. In this contribution, we present the results obtained from the CFHT wide-field survey of Blanco 1 (Section 2) and the estimates of the lower mass function of other similar age open clusters (Section 3). We then briefly discuss.......

2 The Blanco 1 cluster

The Blanco 1 open cluster ($\alpha_{J2000} = 0^h04^m24^s$, $\delta_{J2000} = -29^d56.4'$) is located close to the ζ Sculptoris star at a distance of $\sim$ 260 pc (Robichon et al. 1999) and has an age of 90 ± 25 Myr (Panagi & O'Dell 1997). About 200 stellar members spread over 1.5 deg. (Hawkings & Favata 1998) are known and its very low mass star and brown dwarf population is still unexplored

In September 1999 and December 2000 we conducted deep wide field photometric surveys with the CFH12K camera in the I and z-band to look for brown dwarfs in the Blanco 1 open cluster. We mapped $\sim$2.5 sq.deg., i.e. 75% of the cluster, from the center to the external regions, and the detection limit is around $I = 24$. We selected all the low mass star and brown dwarf candidates on the basis of their location in the $(I, I-z)$ colour-magnitude diagram (CMD) compared to the location of the cluster zero age main sequence predicted by theoretical models (NEXTGEN models from Baraffe et al. 1998, and DUSTY models from Chabrier et al. 2000). We thus identified 56 brown dwarf candidates down to $\sim 30 M_{Jup}$ (see Fig. 1).

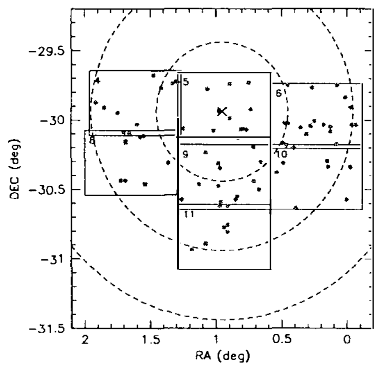

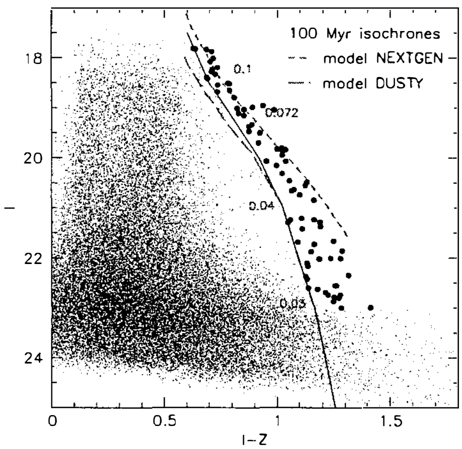

Figure 1: *Left panel :* Area of the sky covered by the CFHT 1999 and 2000 Blanco 1 surveys. Each rectangle corresponds to one CFH12K field. The small cross represents the cluster center and the dashed circles have a radius of 0.5, 1 and 1.5 degrees respectively. Filled dots show the location of detected very low mass star and brown dwarf candidates. ***Right panel :*** (I, I-z) CMD for all stellar-like objects identified in our survey. The 100 Myr NEXTGEN isochrone from Baraffe et al. (1998) and DUSTY isochrone from Chabrier et al. (2000) shifted to the distance of Blanco 1 are shown as a short-dashed line and a long-dashed line labelled with mass (in $M_\odot$ unit) respectively. The thin solid line represents our empirical selection. All redder objects (large dots) have been identified as very low mass star and brown dwarfs candidates. (from Moraux 2003)

However, one of the major shortcomings of this photometric selection is the contamination by sources which may lie in the same region of the CMD. While a fraction of these selected objects must be true cluster members, others are merely unrelated older and more massive late-type field dwarfs in the line of sight. To assess the cluster membership of the brown dwarf candidates, we obtained K-band photometry for most of them with SOFI on the ESO/NTT. The study of their location in the $(I, I-K)$ CMD allowed us to weed out some of the contaminants (see Fig. 2, left). We also obtained optical spectroscopy with FORS2 at the VLT to study some gravity features such as the Na doublet (see Fig. 2, right)

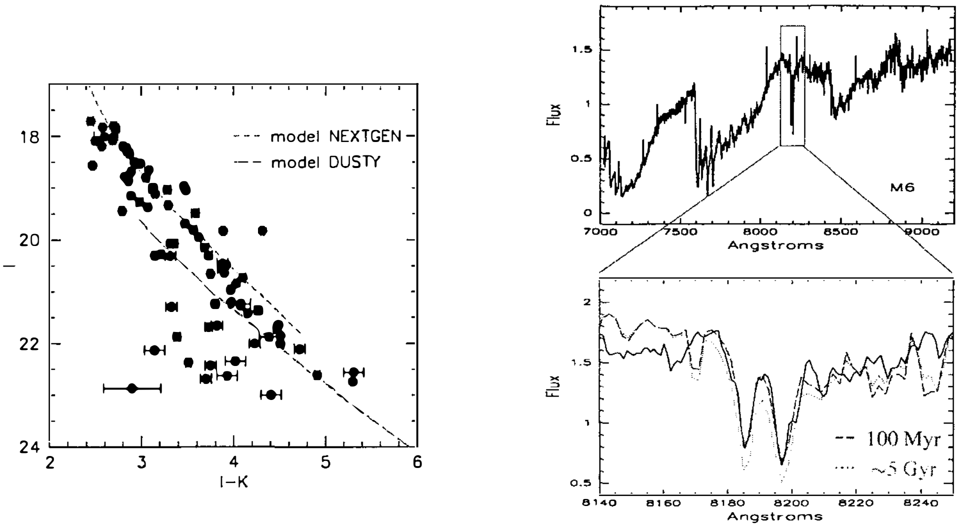

Figure 2: *Left panel:* $(I, I - K)$ CMD of the Blanco 1 very low mass star and brown dwarf candidates. As in Fig 1, the 100 Myr NEXTGEN and DUSTY isochrones are shown. All the objects 0.2 mag bluer than these isochrones have been rejected. *Right panel:* Optical spectrum of a brown dwarf candidate obtained with FORS2 at the VLT (top) with a zoom on the gravity sensitive Na doublet. Three spectra are shown on this zoom: the Blanco 1 candidate spectrum (solid line), and two field dwarfs spectra obtained in the same conditions and having the same M6 spectral type. One of these two has about the same age than Blanco 1 (296A, dashed line) while the other one (GJ 866, dotted line) belongs to the old disk population. The older is a dwarf, the larger is its surface gravity and the larger is the equivalent width of the Na doublet at a given spectral type. The Blanco 1 candidate has a Na equivalent width similar to this of the young field dwarf and is therefore a genuine brown dwarf member.

in order to distinguish between young cluster's brown dwarfs and field dwarfs (Martín et al. 1999).

After this confirmation step, the luminosity function is then converted into a mass function (MF) using the I magnitude-mass relationship from Baraffe et al. (1998) for low mass stars and Chabrier et al. (2000) for brown dwarfs. The derived Blanco 1 system's MF (i.e. binaries are not resolved) across the stellar/substellar boundary is shown in Figure 3. It is reasonably well-fitted by a single power-law $dn/dm \propto m^{-0.58\pm0.10}$ over more than one decade in mass, from 0.03 to $0.5 M_\odot$

3 The lower IMF of similar age open clusters

Blanco 1 is located at a very high galactic latitude ($b \sim -79$ deg.), has a low stellar density and is metal-rich ([Fe/H]=+0.14; Jeffries & James 1999). These peculiarities make Blanco 1 very interesting to compare to other open clusters to test the dependance of the IMF on environmental conditions.

We studied two other clusters having about the same age ($\sim$ 100 Myr) but different properties of metallicity and density, the Pleiades and NGC 2516. The Pleiades cluster has a solar metallicity and contains about $\sim$ 1000 stellar members (Pinfield et al. 1998). Its age is about 120 Myr (Stauffer et al. 1998). NGC 2516 is a bit older ($\sim$ 150 Myr), richer – it contains about 2000 stars – and may be metal-poor.

Their system MFs have been derived from optical CMDs and corrected from field contaminants in a similar fashion as for Blanco 1 (see above) over a mass range extending from low mass stars down to $0.03 M_\odot$ for the Pleiades (Moraux et al. 2003) and down to the stellar/substellar limit for NGC 2516 being further away. When approximated by a power-law, the slope of the MF over this restricted mass range is similar for the various clusters, with a power-law index $\alpha \simeq -0.5\pm0.1$ within uncertainties. We

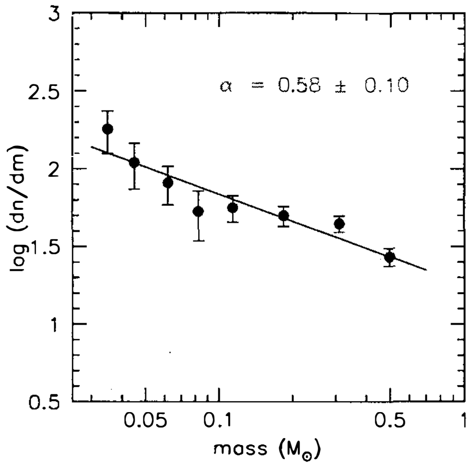

Figure 3: The Blanco 1 system's mass function across the stellar/substellar boundary. Note that all the data points are derived from the same surveys, using short exposures for the stellar domain and long exposures for the substellar regime. This provides a consistent determination of the slope of the cluster's mass function in the mass range from 0.030 to $0.4 M_\odot$. The data points are fitted by a power law $dn/dm \propto m^{-\alpha}$ with an index $\alpha = 0.58 \pm 0.10$.

used data from Pilliteri et al. 2003 for Blanco 1, from the Prosser and Stauffer database for the Pleiades and from Jeffries at al. 2001 for NGC 2516 to extend our MF estimates in the stellar domain up to a few solar masses. The mass functions are shown Fig. 4.

Pending the resolution of the uncertainties on these results (mainly related to small number statistics and shown as Poisson error bars), there is presently no evidence for signifi cant differences in the mass function between these clusters, regardless of the metallicity or the stellar density. They are all relatively well fi tted by a log-normal distribution

$$\xi(\log m) = \frac{dn}{d\log m} \propto \exp\left[-\frac{(\log m - \log m_0)^2}{2\sigma^2}\right] \tag{1}$$

with $m_0 \sim 0.2 - 0.3 M_\odot$ and $\sigma \sim 0.5$ over the entire mass range. The galactic disk mass function for systems from Chabrier (2003) is shown for comparison and is also very similar. This result suggests that there is a caracteristic system mass m_0 linked to the stellar formation process which does not seem to depend much on environmental conditions. If we look more closely at Fig. 4, we can notice that m_0 is different for each cluster as for the fi eld but it is not clear yet that this is a real effect or if it is only the reflect of uncertainties, due for example to the models used in the mass determination for different metallicity.

In the substellar domain the Blanco 1 and Pleiades MFs have a very similar behaviour and show in particular the same dip around $0.05 - 0.07 M_\odot$ corresponding to a M7-M8 spectral type. Such a feature was also found in the Trapezium cluster by Muench et al. (2002) for the same spectral type (i.e. $m \sim 0.03 - 0.05 M_\odot$ at a few Myr) and has been interpreted by Dobbie et al. (2002) as evidence for a sharp change in the shape of the luminosity-mass relationship due to the onset of dust formation in the upper atmosphere around $T_{eff} \sim 1800$ K. The mass of brown dwarfs with spectral type later than M7-M8 may thus be underestimated by current theoretical models leading to an apparent drop of the MF in this domain. The fact that this feature is seen in the MF of several clusters with different ages at the same spectral type and not at the same mass tends to favour this interpretation.

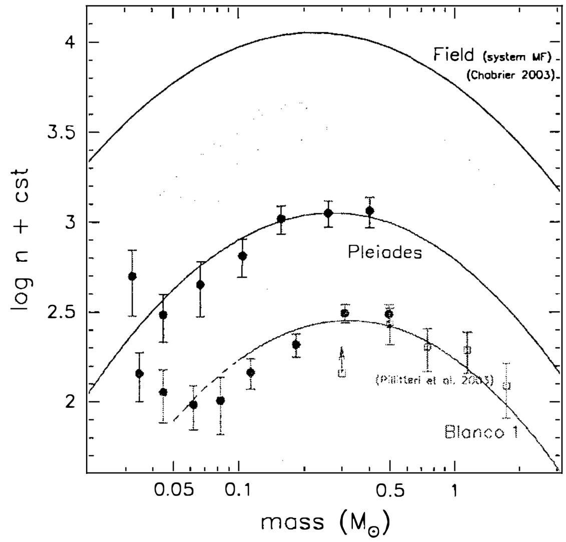

Figure 4: The mass function of young open clusters represented as the number of objects per logarithmic mass units over the mass range extending from $2M_\odot$ down to $0.03M_\odot$. In this representation Salpeter's slope is 1.35. For each cluster, the large dots represents our data points and the solid line is the log-normal fit. A constant has been added to each MF for clarity. The estimate of the field mass function by Chabrier (2003) is shown for comparison.

4 Conclusions

Deep wide-fi eld photometric surveys of brown dwarfs in the Blanco 1 young open clusters allowed us to estimate its mass function across the stellar/subtellar boundary. We found that it can be approximated by a power-law $dn/dm \propto m^{-\alpha}$ with an exponent $\alpha = -0.58 \pm 0.10$ over the mass range 0.03-0.6 $M_\odot$, and by a log-normal distribution

$$\frac{dn}{d\log m} \propto \exp\left[-\frac{(\log m - \log m_0)^2}{2\sigma^2}\right] \tag{2}$$

with $m_0 \sim 0.3M_\odot$ and $\sigma \sim 0.5$ over the entire mass range. Estimates of the mass function of two other clusters (the Pleiades, NGC 2516) having about the same age than Blanco 1 ($\sim$ 100 Myr) suggest that there is no appreciable differences in the shape of the MF between the various clusters, regardless of their precise age, metallicity or richness. The shape of the Galactic disk MF is also similar to these results. This suggest that there is a characteristic system mass $m_0 \sim 0.2 - 0.3$ issued from the star formation process which does not depend much on the environmental conditions.

Acknowledgments

The authors have been funded by the FP5 EC-RTN *"The formation and evolution of young open clusters"* to come to this Moriond meeting.

References

1. Baraffe, I., Chabrier, G., Allard, F., Hauschildt, P.H. 1998, A&A, 337, 403

2. Chabrier, G., Baraffe, I., Allard, F., Hauschildt, P.H. 2000, ApJ, 542, 464
3. Chabrier 2003, PASP, 115, 703
4. Dobbie, P.D., Pinfi eld, D.J., Jameson, R.F., & Hodgkin, S.T. 2002, MNRAS, 335, L79
5. Hawkins, G.W. & Favata, F. 1998, AAS, 193, 6707
6. Jeffries, R. D. & James, D. J. 1999, ApJ, 511, 218
7. Jeffries, R. D., Thurston, M.R., Hambly, N.C., 2001, A&A, 375, 863
8. Martín, E. L., Delfosse, X., Basri, G., Goldman, B., Forveille, T., & Zapatero Osorio, M. R. 1999, AJ, 118, 2466
9. Moraux, E., Bouvier, J., Stauffer, J.R., Cuillandre, J.-C. 2003, A&A, 400, 891
10. Moraux, E. 2003, PhD thesis, Grenoble University
11. Muench, A.A., Lada, E.A., Lada, C.J., Alves, J., 2002, ApJ, 573, 366
12. Nakajima, T., Oppenheimer, B.R., Kulkarni, S.R., Golimowski, D.A., Matthews, K., Durrance, S.T., 1995, Nature, 378, 463
13. Panagi, P.M. & O'Dell, M.A. 1997, A&AS, 121, 213
14. Pillitteri, I., Micela, G., Sciortino, S., & Favata, F. 2003, A&A, 399, 919
15. Pinfi eld, D.J., Jameson, R.F., & Hodgkin, S.T. 1998, MNRAS, 299, 955
16. Rebolo, R., Zapatero-Osorio, M.R., Martín, E.L., 1995, Nature, 377, 129
17. Robichon, N., Arenou, F., Mermilliod, J.-C., & Turon, C. 1999, A&A, 345, 471
18. Stauffer, J. R., Schultz, G., & Kirkpatrick J. D. 1998, ApJ, 499, L199

INTERMEDIATE LUMINOSITY YSOs IN THE S235A-B STAR FORMING REGION

F. MASSI (1), M. FELLI (1), R. CESARONI (1)
(1) INAF - Osservatorio Astrofisico di Arcetri
Largo E. Fermi 5, 50125 Firenze, Italy

We present new high-resolution radio, millimetric and submillimetric observations towards the water maser lying in between the nebulosities S235A and S235B. A warm (30 K) compact (< 0.1 pc) molecular and dust core has been found peaking at the maser position, which appears to host the driving sources of 2 almost perpendicular outflows traced by HCO^+. One of these is associated with an intermediate-mass protostar embedded within the gas. More uncertain is the signature of a circumstellar disk possibly detected in $C^{34}S$ at the centre of the most prominent outflow.

Keywords: HII regions – circumstellar matter – ISM: S235 – Stars: formation – Radio continuum: ISM – Submillimeter.

1 Introduction

1.1 Intermediate-mass star formation

While the physical processes driving the formation of low mass stars (< 2 M$_\odot$) are believed to be reasonably well known, many problems still affect the theoretical picture concerning the growth of high-mass stars (> 10 M$_\odot$). In particular, accretion at relatively low rates (10^{-4}–10^{-6} M$_\odot$ yrs^{-1}) causes protostars to enter the ZAMS already at masses as large as ~ 10 M$_\odot$. At this stage, the radiation emitted by such massive objects is able to reverse the infall, stopping the accretion. Two scenarios have been proposed to circumvent these difficulties: i) accretion at higher rates through circumstellar disks (for an updated discussion, see Cesaroni 2004), and ii) mass growth by coalescence of smaller stars. The intermediate-mass regime (2–10 M$_\odot$) may represent a benchmark for studying the onset of the conditions leading to massive star formation. In this regime, a pre-main sequence phase is believed to exist, represented by the Herbig Ae/Be

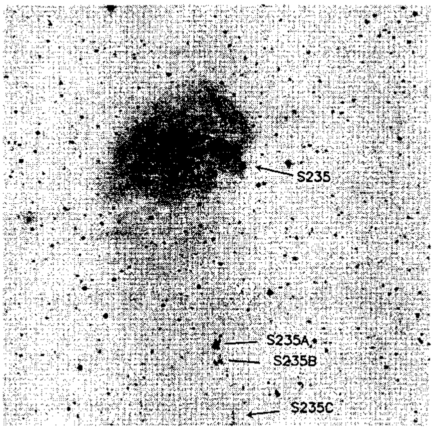

Figure 1: Optical image (DSS) of a $20' \times 20'$ region around S235. The main nebulosities are labelled. North is up, east is left.

class of stars. Very young objects of this kind have been found, e. g., in the Vela Molecular Ridge (Massi et al. 2003). We are hereby presenting a rare example of intermediate-mass stars likely to be in a still earlier evolutionary stage, probably the intermediate-mass analogue of the low-mass Class 0 sources.

1.2 Outline of the S235 region

The sky area towards $\alpha(2000)$ =05:40:53 $\delta(2000)$ =35:41:49 displays a number of interesting star formation sites in different evolutionary stages. Figure 1 shows a large scale view of the region at optical wavelengths. The largest nebulosity is S235, an evolved HII region studied in the radio continuum by Israel & Felli (1978). Southward of S235, there appear a pair of small patches of diffuse emission ($\sim 1'$ apart), named S235A and S235B. The former is a more compact, less evolved HII region (Israel & Felli 1978), whereas the latter is a strong emitting source in hydrogen lines (Hα, Brγ). Felli et al. (1997) found strong NIR continuum emission from S235B; the lack of cm emission suggests that it is an ionized expanding envelope around a young star rather than a compact HII region. An embedded young star cluster in the region S235A-B was also unveiled by the NIR observations of Felli et al. (1997). The southernmost small patch of diffuse emission, named S235C, was identified as a small HII region by Israel & Felli (1978).

Single dish observations were successful in revealing maser activity towards S235A-B; in particular, the region hosts H_2O (Henkel et al. 1986, Comoretto et al. 1990), methanol (Nakano & Yoshida 1986, Haschick et al. 1990) and SiO (Harju et al. 1990) masers. These are clear signposts of recent star formation. Subsequent high resolution radio observations with the VLA (Tofani 1995) showed that the H_2O maser is actually unrelated with either S235A or S235B, lying in between them (at the coordinates given above). No compact HII regions (UCHIIs) were detected close to the maser. Line observations in molecular tracers of high density gas (Cesaroni et al. 1999) revealed that the H_2O maser is located at the centre of a high-density small diameter molecular core peaking just between S235A and B. In the following, we focus on this small region, presenting the results of new high-resolution mm and cm observations. Following Nakano & Yoshida (1986), we assume a distance of 1.8 kpc.

Table 1: List of transitions observed with the Plateau de Bure interferometer.

Line	Frequency	Spectral resolution
	(MHz)	(km s^{-1})
3.3 mm continuum	90494	$\sim$ 16
HCO^+(1–0)	89189	$\sim$ 0.5
CH_3CN(5–4)	91987	$\sim$ 1
1.2 mm continuum^b	242631	$\sim$ 6
$C^{34}S$(5–4)	241016	$\sim$ 0.4
H_2CS 7(1-6)–6(1,5)	244048	$\sim$ 6
SO_2 14(0,14)–13(1,13)	244254	$\sim$ 0.4

2 New observations

Interferometric observations were carried out on November 22, 1997 and March 25, 1998 in the CD configuration of the IRAM array at Plateau de Bure, France. The observed tracers are listed in Table 1. This configuration led to synthesized beams (HPBW) of $\sim$ 5" at 3.3 mm and $\sim$ 2" at 1.2 mm. The phase centre corresponds to the water maser position. Submillimeter observations (at 450 and 850 μm) were carried out with SCUBA on the JCMT (Mauna Kea, Hawaii) on October 24, 2000. They were retrieved from the public archive at the CADC. Details of the instrumental parameters and data reduction are given in Felli et. al. (2004).

These new data have been recently complemented with interferometric radio observations at 1.3 and 3.6 cm with the VLA performed on February 26, 2004. The array was set in the C configuration, yielding synthesized beamwidths (HPBW) of 0.9" at 1.3 cm and 2.3" at 3.6 cm. The achieved sensitivity is $\sim$ 0.03 mJy/beam (1 r.m.s.) at 1.3 cm.

3 Results

3.1 The molecular core

An almost unresolved dust compact core was detected towards the water maser, almost exactly peaking at its position, in the 3.3- and 1.2-mm continuum (see Fig. 2a). At the higher resolution of the 1.2-mm map, the core diameter is 3", slightly larger than the beam size. A tail-like structure protruding to the south is apparent in the 3.3-mm map, but also barely discernible in the 1.2-mm one. S235A is detected at 3.3-mm, confirming that most of the radio-continuum emission comes from the ionized gas within the HII region. Yet, S235B has not been detected. The flux densities of the core are 20 and 245 mJy at 3.3 and 1.2 mm, yielding a spectral index of 2.5. But when measured towards the tail, the flux densities result in a spectral index of $\sim$ 0.6.

The compact core is visible in all molecular transitions, roughly centred at $V_{LSR} \sim 17$ km s^{-1}, although the emission of HCO^+(1–0) exhibits a more complex morphology. In particular, a second compact component, blue-shifted with respect to the core, is located a few arcsec south of the water maser. This one has no counterparts in the mm continuum, and is detected only in CH_3CN, beside HCO^+, indicating either that the dust temperature there is much lower, or that the abundance of HCO^+ and CH_3CN is much higher than in the northern mm component (hereafter, the mm core).

The gas temperature in the mm core was derived from the CH_3CN(5–4), $K = 0, 1, 2, 3$

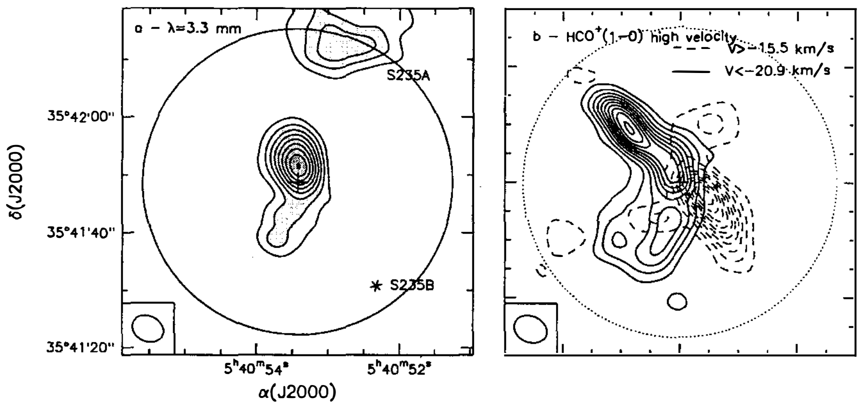

Figure 2: **a** The 3.3 mm map. Contour levels range from 1 (3σ) to 9 by 1 mJy/beam. **b** The HCO^+ otflows. Contour levels range from 10 to 100 by 10 mJy/beam.(red lobe, dashed) and 6 to 60 by 6 mJy/beam (blue lobe, full line). The water maser location is marked by a cross, the dotted circle defines the primary beam HPW. The synthesized beam is shown in the lower left box.

Table 2: Physical parameters of the mm core as derived from the different molecular transitions.

Line	Source diameter	LTE mass	Mean volume density	Virial mass
	(pc)	($M_\odot$)	(cm^{-3})	($M_\odot$)
HCO^+(1–0)	0.1	31	9×10^5	58
CH_3CN(5–4)	0.06	2.3	3×10^5	53
$C^{34}S$(5–4)	0.03	7	7×10^6	7

lines through the rotational diagram method, which assumes that all energy levels of CH_3CN are populated according to local thermodynamic equilibrium (LTE) with a single excitation temperature. This yields a value of ~ 30 K.

The mass of the mm core was obtained using two different methods. From the molecular lines intensity assuming LTE and a suitable abundance, and from the molecular lines width and source size by means of the virial theorem. Core mass, size and density (as derived from the different molecular transitions) are listed in Table 2. A more detailed discussion can be found in Felli et al. (2004).

3.2 The molecular outflows

The HCO^+(1–0) map clearly shows two outflows roughly centred at the mm core (Fig. 2b): a more collimated one aligned in a NE-SW direction, and a fainter one in a NNW-SSE direction coinciding with the mm tail visible in Fig. 2a. This clearly indicates that multiple star formation is in progress within the core, or the occurrence of multiple outflow episode.

The coincidence of the mm tail with a molecular bipolar structure indicates that it is tracing a jet. In particular, the small spectral index measured towards the tail suggests that the continuum

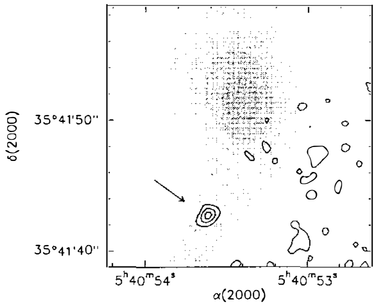

Figure 3: The 3.3 mm map (greyscale) overlaid with the 1.3 cm radio-continuum emission map. Contour levels range from 0.1 to 0.4 by 0.1 mJy/beam.

Table 3: Physical parameters of the outflows.

Outflow component	Time scale	Mass	Mechanical luminosity
	(yrs)	($M_\odot$)	($L_\odot$)
NE-SW blue lobe	14700	3	1.9
NE-SW red lobe	< 5400	6	> 1.7
NNW-SSE blue lobe	15000	3	0.3
NNW-SSE red lobe	20000	1	0.05

emission is originated in a thermal jet. This view is confirmed by the VLA map in the 1.3-cm continuum emission: a compact radio source is found within the mm tail (see Fig. 3). The physical parameters of the 2 outflows derived from the HCO^+ observations are listed in Table 3.

3.3 The embedded protostars

In order to estimate the properties of the protostar(s) embedded in the core, we attempted to constrain the bolometric luminosity by using the mm, sub-mm and FIR (IRAS) observations. In the MIR and FIR, the emission is overwhelmingly dominated by S235A and B. Furthermore, the resolution of the IRAS data is too low to allow to separate the emission of the mm core from that of S235A. At sub-mm wavelengths the mm core is instead the main detected feature. The estimated temperature and the mm and sub-mm flux measurements allow us to construct the SED of the mm core, yielding a bolometric luminosity of $\sim 10^3$ $L_\odot$.

The bolometric luminosity derived from the core SED has to be compared with the bolometric luminosity expected for the embedded protostar according to other measured physical parameters of the gas. Using the relation between outflow mass loss rate and driving star luminosity given in Churchwell (1997), we estimate the latter to be 3400 $L_\odot$ for the NE-SW outflow and 170 $L_\odot$ for the NNW-SSW outflow. If we assume that the mm core is heated by a central star, in the case of gas spherical symmetry, a temperature of 30 K requires from 220 up to 2700 $L_\odot$ (Felli et al. 2004). Within the uncertainties, it is clear that the gas is heated by an intermediate-mass protostars. In fact, note that a ZAMS star of 6 $M_\odot$ has $\sim$ 1000 $L_\odot$, whereas a protostar of the same mass has $\sim$ 3100 $L_\odot$.

In summary, we find that the NE-SW outflow is driven by an intermediate-mass protostar embedded in the mm core, whereas the less powerful NNW-SSW outflow is driven by a much less massive (proto)star, possibly related to the blue-shifted molecular component seen in HCO^+.

3.4 A circumstellar disk?

Collimated outflows are believed to be associated with circumstellar disks, so we tried to find out possible evidence of disk-like structures around the embedded protostars by studying the gas kinematics through the emission of the high-density tracer $C^{34}S$ which has been observed at a higher angular resolution than HCO^+. Actually, by mapping the blue and the red end of the emission we found an offset of $\sim$ 3.5" along an axis perpendicular to the NE-SW outflow. The maximum velocity difference is $\sim$ 5 km s^{-1}. If taken at face value, this would imply a disk $\sim$ 3000 AU in radius with a dynamical mass $\geq$ 22 $M_\odot$ (Felli et al. 2004). The lower limit is due to the unknown disk inclination. The gas mass derived from the mm continuum emission is $\sim$ 16 $M_\odot$; if it is assumed to be dominated by the matter in the disk, there are > 6 $M_\odot$ left for the mass of the central star. This compares well with what found on the previous section.

Acknowledgments

IRAM is supported by INSU/CNRS (France), MPG (Germany) and IGN (Spain). The JCMT is operated by the Joint Astronomy Centre in Hilo, Hawaii on behalf of the parent organizations PPARC in the United Kingdom, the National Research Council of Canada and The Netherlands Organization for Scientific Research. The National Radio Astronomy Observatory, operating the VLA, is a facility of the National Science Foundation operated under cooperative agreement by Associated Universities, Inc.

References

1. Cesaroni, R., *et al.* 1999, A&AS, 136, 333
2. Cesaroni, R. 2004, AP&SS, in press
3. Churchwell, E. 1997, in *Herbig-Haro Flows and the Birth of Low Mass Stars*, ed. B. Reipurth & C. Bertout (Kluwer Academic Publishers, Dordrecht), p. 525
4. Comoretto, G., *et al.* 1990, A&AS, 84, 179
5. Harju, J., *et al.* 1998, A&AS, 132, 211
6. Haschick, A. D., *et al.* 1990, ApJ, 354, 556
7. Henkel, C., *et al.* 1986, A&A, 165, 197
8. Israel, F. P., & Felli, M. 1978, A&A, 63, 325
9. Nakano, N., & Yoshida, S. 1986, PASJ, 38, 531
10. Felli, M., *et al.* 1997, A&A, 320, 594
11. Felli, M., *et al.* 2004, A&A, 420, 553
12. Massi, F., *et al.* 2003, A&A, 399, 147
13. Tofani, G., *et al.* 1995, A&AS, 112, 299

THE CYGNUS X REGION - A MULTI WAVELENGTH VIEW

J. KNÖDLSEDER

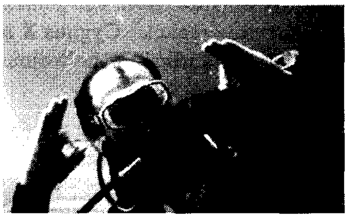

Centre d'Étude Spatiale des Rayonnements, 9, avenue Colonel-Roche, B.P. 4346, 31028 Toulouse Cedex 4, FRANCE

The Cygnus X region is one of the most nearby massive star forming regions within our Galaxy, recognised by prominent emission throughout the entire electromagnetic spectrum, from radio to gamma-ray waves. This paper reviews our current knowledge about this region by describing its multi-wavelength characteristics. Particular emphasis will be given to the central stellar cluster Cyg OB2 that dominates the energetics and kinematics in the area. The cluster is also believed to be an active site of nucleosynthesis, as traced by the observation of the 1809 keV gamma-ray line, attributed to radioactive decay of ^{26}Al. New observations obtained by the SPI telescope onboard the INTEGRAL gamma-ray observatory will be presented that corroborate this hypothesis, and that for the first time allow to measure the kinematics of the gas in the hot Cygnus X superbubble.

Keywords: H II regions – ISM: bubbles – Open clusters and associations: Cyg OB2 – nucleosynthesis

1 Introduction

Massive star forming regions are impressive building blocks of active galaxies. They provide large amounts of UV photons leading to the ionisation of the interstellar medium (ISM), observable in the radio and microwave domains, and visible through Hα recombination line emission. They are important sources of interstellar dust heating, leading to ubiquitous infrared emission. The strong winds of their massive stars and the subsequent supernova explosions release considerable amounts of kinetic energy, creating a rarified hot ($\sim 10^6$ K) superbubble emitting in the X-ray domain; its cavity may eventually be discerned from H I and CO observations of interstellar gas. Massive star forming regions are potential sources of cosmic-ray particle acceleration, observable by radio synchrotron emission and high-energy gamma-ray emission. Their massive stars synthesize considerable amounts of fresh heavy nuclei that are released either by the stellar winds or the subsequent supernova explosions, and that contribute to the chemical enrichment of the host galaxy. Nucleosynthesis products may be traced by co-produced radioactive isotopes that are observable through their characteristic gamma-ray line emission.

Studying massive star forming regions in a single waveband provides certainly interesting clues on their characteristics; yet a comprehensive understanding of the phenomenon requires a rigorous multi-wavelength approach. I present in this paper a multi-wavelength view of the Cygnus X region, one of the most nearby galactic massive star forming regions, at a distance of ~ 1.4 kpc. Cygnus X lies in the galactic plane at longitudes $\sim 80°$, making it a fairly well isolated source on the sky. Yet, foreground dust obscuration produces substantial extinction of parts of the region, preventing thus a comprehensive survey in the visible and soft X-ray bands. Eventually, a spiral arm structure seen tangentially over distances $\sim 1-4$ kpc may also be present in this area of the sky, yet highly uncertain distance estimates make it difficult to assess the reality of this feature. In any case, most massive stars in Cygnus X, and in particular the young massive cluster Cyg OB2, are situated at about the same distance (~ 1.4 kpc), suggesting a physical relation of the objects in the region.

The proximity of Cygnus X and its isolation from the galactic ridge makes it a brilliant test case for understanding massive star forming regions. Cygnus X is like a *Rosetta stone* of massive star formation, enabling a profound understanding of the various processes at work and of their interplay.

2 Cygnus OB2

Cyg OB2, originally classified as OB association, is one of the most massive star clusters known in our Galaxy. It is situated at galactic coordinates $(l, b) \sim (80°, 1°)$ with an angular diameter of 2° (50 pc at the distance of Cyg OB2), right at the heart of the Cygnus X region.[16] Foreground dust obscuration sheds parts of the cluster in the visible waveband, requiring infrared observations for a complete census. Such a census has been obtained using the 2MASS survey, which revealed a total of 120 ± 20 O star members and suggests a total cluster mass of $(4-10) \times 10^4$ $M_\odot$.[16] A synthetic plot of the stellar distribution in the area is shown in Fig. 1.

Near-infrared spectroscopic observations support these findings.[6,12] Distance estimates to Cyg OB2 were generally situated around 1.7 kpc, yet the recent revision of the O-star effective temperature scale suggest a smaller value of 1.4 kpc.[12] The cluster age has been estimated from isochrone fitting to $3-4$ Myr[15], where the age range may reflect a non-coeval star forming event. The total Lyman continuum luminosity of the stars has been estimated to 10^{51} ph s^{-1}, their mechanical luminosity amounts to a few 10^{39} erg s^{-1}.[15,18] Obviously, with such high luminosities, Cyg OB2 should leave a clear imprint on the interstellar surroundings.

Cyg OB2 houses some of the hottest and most luminous stars known in our Galaxy. Among the members is a O3 If* star, three Wolf-Rayet stars, and two LBV candidates. Since spectroscopic measurements are still incomplete for the cluster, these numbers present probably lower limits to the population of extremely massive and evolved objects.

3 The Cygnus X region

3.1 Radio emission

The Cygnus X region has been named by Piddington & Minnett (1952) who were the first to observe an extended source of radio emission in the constellation of Cygnus. Cygnus X is composed of numerous individual H II regions[9] with distances estimated between $1.2-2.4$ kpc.[8] In addition to these point-like sources, a component of diffuse thermal radio emission has been identified that constitutes $\gtrsim 50\%$ of the emission in Cygnus X.[24]

Figure 2 presents a two-colour radio image of the region. Thermal emission appears blueish

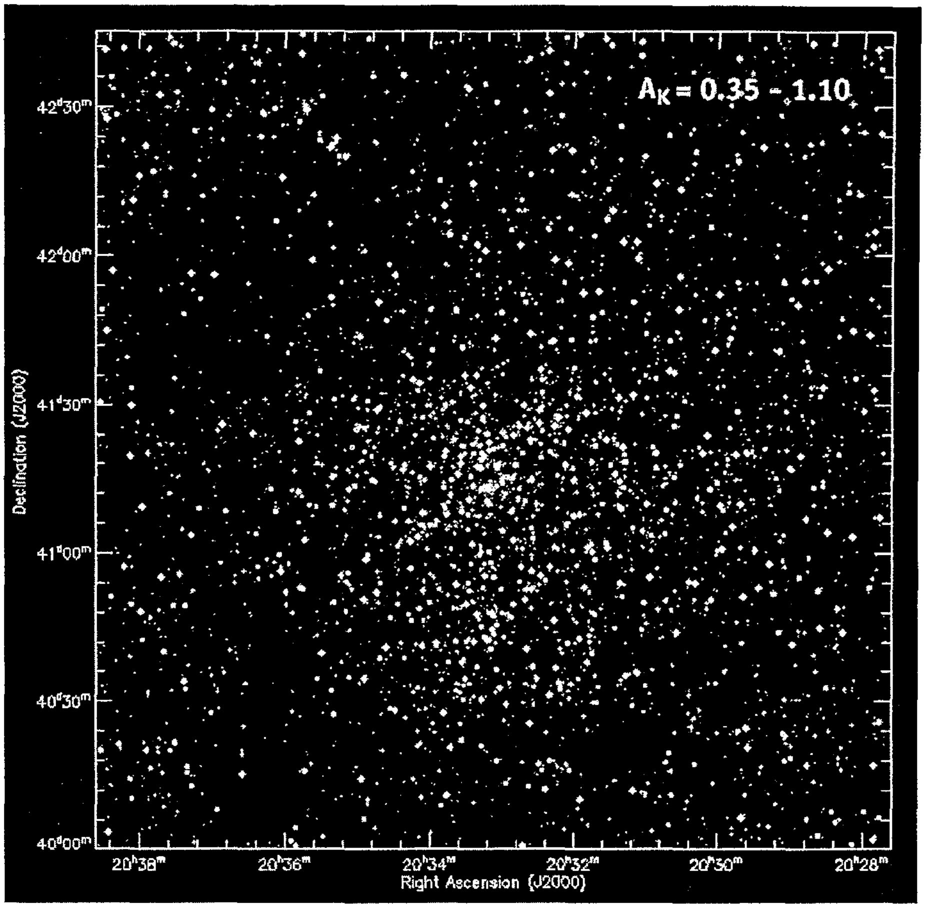

Figure 1: Synthetic absorption free plot of the stellar density distribution in the Cyg OB2 area based on 2MASS data. Stars in the absorption band $A_K = 0.35 - 1.1$ mag are shown as symbols with brightness proportional to the absolute (reddening corrected) K band magnitude.

while non-thermal (i.e. synchrotron emission) appears reddish in this representation. The dominance of thermal emission is obvious, as well as the presence of ubiquitous diffuse emission with embedded compact and ultra-compact H II regions. Only little synchrotron emission is present, such as the circular feature near $(l, b) \sim (78°, 2°)$ which corresponds to the γ Cygni supernova remnant. Apparently, the radio emission originates mainly from the ionisation of the interstellar medium; the supernova activity seems rather low. These facts suggest that the Cygnus X region is very young, probably not older than 4 Myr.[15]

Véron (1965) has suggested that Cygnus X is a single giant H II region powered by Cyg OB2, yet the identification of individual H II regions with their exciting stars in Cygnus X indicates that there are also other ionising sources in the area. About 50% of the ionising luminosity in Cygnus X comes from Cyg OB2, the rest is provided by massive stars that are found in the surrounding associations and clusters.[15] Using typical values for electron temperature and density of H II regions ($T_e = 6000$ K and $n_e = 10$ cm^{-3}, respectively), the ionising power of Cyg OB2 alone would lead to a Strömgren sphere of 60 pc in radius, corresponding to an angular diameter

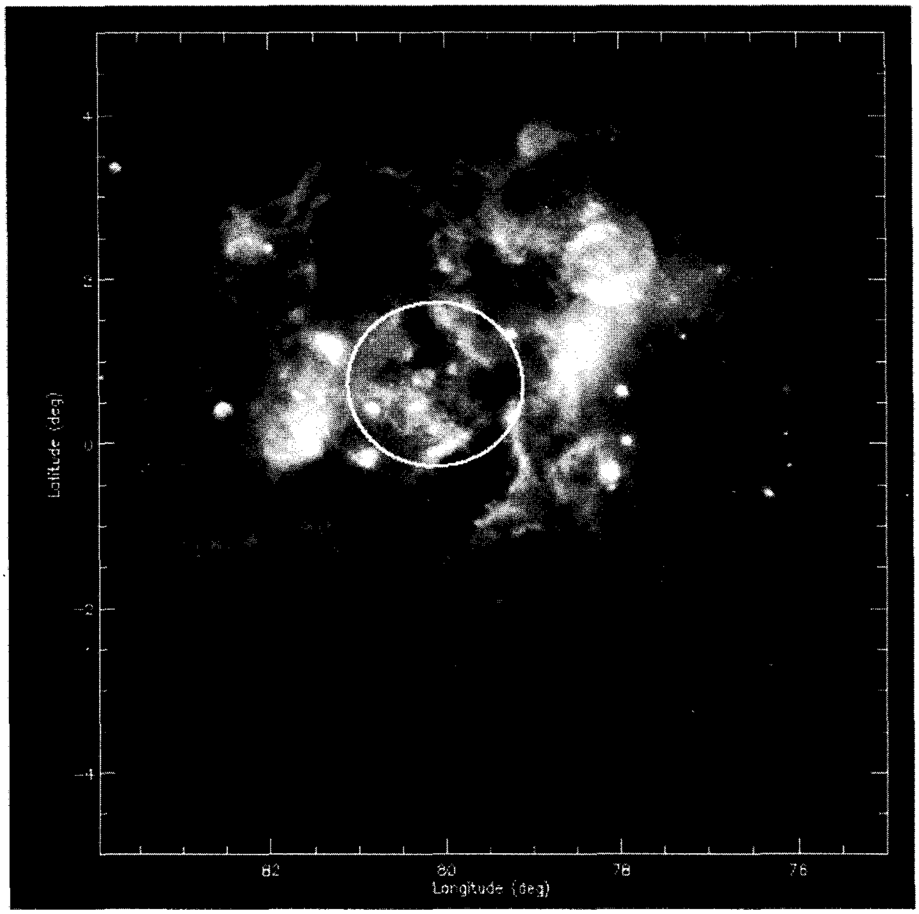

Figure 2: DRAO 74 cm (red) and 21 cm (blue) composite of radio emission from the Cygnus X region. Thermal emission appears blueish while non-thermal (i.e. synchrotron emission) appears reddish in this representation. The Cyg OB2 association, represented by the white circle, is located near the centre of the Cygnus X region.

of 5° at the distance of the cluster. This diameter is in good agreement with the observed extent of the diffuse thermal radio component in Cygnus X, supporting the idea that this emission component represents a giant H II region that is powered by Cyg OB2.

3.2 Infrared emission

The mid- and far-infrared image of Cygnus X shows striking similarities with the radio emission: a diffuse emission structure with embedded point-like sources (cf. Fig. 3). The infrared spectrum becomes harder (as illustrated by the blueish colour) towards the centre of Cygnus X, probably as a result of dust heating by the massive stars of the embedded Cyg OB2 association. Around Cyg OB2, a large number of point-like sources is detected, that have been identified as either embedded early-type stars or star clusters, or young stellar objects (YSO).[19] Many of them are associated to the compact and ultra-compact H II regions that are observed in thermal radio continuum emission.

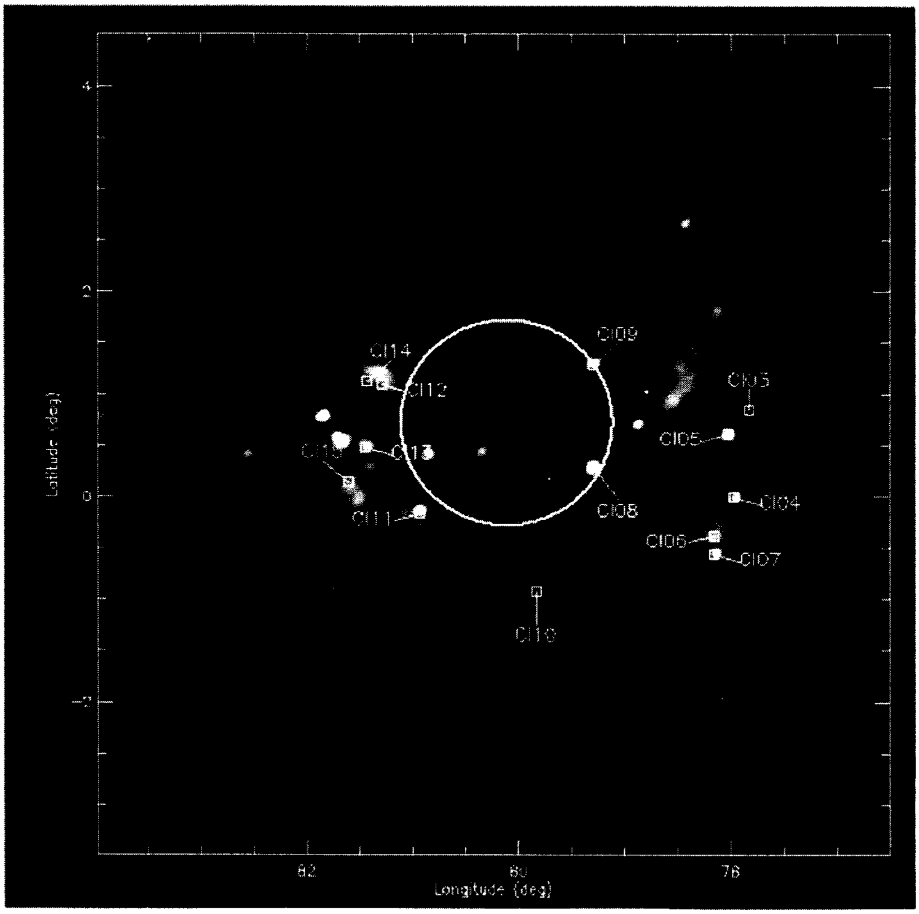

Figure 3: IRAS three-colour composite of the Cygnus X region (red: 100 μm, yellow: 60 μm, blue: 25 μm). The central region, heated by the Cyg OB2 cluster appears blue, while the surrounding colder medium shows up as reddish emission. Bright spots coincide generally with embedded star clusters (labelled according to the catalogue of embedded star clusters given by Le Duigou & Knödlseder, 2002).

Le Duigou & Knödlseder (2002) have searched 2MASS near-infrared data for possible embedded star clusters in the area and found 15 such objects. Although no detailed age information is available for these objects, their embedded nature suggests a fairly small age ($\sim$ 1Myr). In addition, their location at the outskirts of Cyg OB2 indicates a triggered star formation event, as result of the expansion of a superbubble around Cyg OB2 that has compressed the ambient ISM.

Such a superbubble has been searched for by several authors in interstellar gas maps of the region (H I and CO)[14,13,10,18], yet velocity crowding makes the identification of interstellar bubbles difficult in the Cygnus area. Assuming that the Cyg OB2 association injects kinetic energy into the ISM since $\sim$ 2 Myr, and assuming an initial density of 100 cm^{-3} (in agreement with measurements of immersed molecular clumps in Cyg OB2)[11], a superbubble with a radius of 63 pc should have been created by the association, with an actual bubble shell velocity of 19 km s^{-1}.[18] At the distance of Cyg OB2, the superbubble should have an apparent diameter of

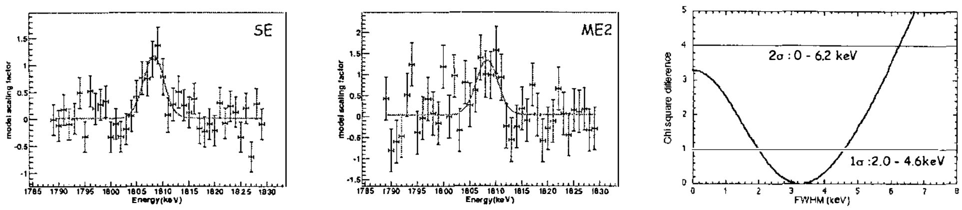

Figure 4: 1809 keV gamma-ray line emission spectra obtained from observations using the SPI telescope aboard the INTEGRAL gamma-ray observatory. The left panel shows the spectrum for single-detector events (SE), the mid panel shows the spectrum for double-detector events (ME2) (SE and ME2 refer to two different event types that are registered by the SPI telescope; the detection of the signal at the same level in both event types is a valuable internal consistency check of the complex data analysis; the information of both event types is added to achieve the maximum sensitivity of the SPI telescope). The right panel illustrates the χ^2 statistics of a gaussian shaped line profile fit as function of the astrophysical line width. At the 1σ level, a line broadening of 3.3 ± 1.3 keV (FWHM) is suggested by the data, while the line is compatible with an unbroadened line at the 2σ level.

5°, comparable to the estimated size of the Strömgren sphere, and comparable to the location of the embedded star clusters that may have formed in the compressed ISM surrounding the bubble.

3.3 The Cygnus X-ray superbubble

The Cygnus X-ray superbubble has been discovered by Cash et al. (1980) as an incomplete ring of soft X-ray emission 13° × 18° in diameter surrounding the Cygnus X region. The morphology of the X-ray emission is shaped by heavy foreground extinction due to the Great Cygnus Rift, and the underlying source could in reality present a nearly uniform emission morphology.[5,22] The origin of the Cygnus X-ray superbubble is still subject to debate, and the protagonists split into two groups who either suggest a single superbubble formed by Cyg OB2[5,1] or a superposition of sources aligned along the local spiral arm.[4,22] Probably, the truth lies between these extreme positions: a substantial fraction of the X-ray emission may indeed arise from shock heating due to the combined stellar winds of Cyg OB2, while other objects along the line of sight my also contribute to the emission.

3.4 Gamma-ray emission from Cygnus X

Prominent 1809 keV gamma-ray line emission has been reported from the Cygnus X region based on observations of the COMPTEL telescope.[7,21] The 1809 keV gamma-ray line arises from the decay of ^{26}Al, a radioactive isotope with a mean lifetime of about one million years. ^{26}Al is mainly produced during the core hydrogen burning phase in massive stars, and is subsequently ejected by stellar winds (in particular during the LBV and Wolf-Rayet phases) and/or supernova explosions. The presence of ^{26}Al in the Cygnus region is again a clear indicator of extensive mass loss by massive ($M > 20 M_\odot$) stars in this area.

The recently launched INTEGRAL gamma-ray observatory, equipped with the high-resolution gamma-ray spectrometer SPI, observed the Cygnus X region during the performance verification phase end of 2002. Figure 4 shows the spectra that have been obtained. The flux integrated over the area $l = [73°, 93°]$ and $b = [-7°, 7°]$ in the line amounts to $(7.2 \pm 1.8) \times 10^{-5}$ ph cm^{-2}s^{-1}. The energy of the line is measured to 1808.4 ± 0.3 keV, compatible with the ^{26}Al decay energy of 1808.65 keV. The line appears broadened, with a gaussian FWHM of 3.3 ± 1.3 keV, yet the statistical confidence of this measurement is still relatively modest.

SPI provided also valuable information on the morphology of the 1809 keV emission. Figure 5 illustrates that the emission is extended, with a most likely value of 5° FWHM assuming a

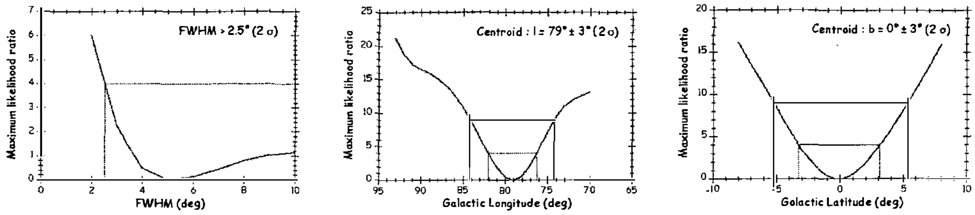

Figure 5: Morphology constraints on the distribution of 1809 keV gamma-ray line emission in Cygnus X, obtained from SPI/INTEGRAL data using the Maximum Likelihood Ratio test (MLR). The left panel illustrates the dependence of the MLR as function on the extension of the emission, assuming a 2d-gaussian shaped intensity distribution centred on galactic longitude/latitude of 80°/0° (the abscissa shows the FWHM of the 2d-gaussian). The source is extended by more than 2.5° at the 2σ significance level, an optimum extension of 5° is suggested. The mid panel show the dependence of the MLR on galactic longitude, assuming a 2d-gaussian shaped intensity distribution of FWHM= 5° at galactic latitudes of 0°. The emission is located at galactic longitude 79° ± 3° (2σ confidence level). The right panel show the dependence of the MLR on galactic latitude, assuming a 2d-gaussian shaped intensity distribution of FWHM= 5° at galactic longitude of 79°. The emission is located in the galactic plane at latitude 0° ± 3° (2σ confidence level). 2σ and 3σ confidence limits are indicated as violet and blue lines, respectively.

gaussian shaped emission. The emission is located at galactic longitude 79° ± 3° and latitude 0° ± 3°. Extension and location are fully compatible with the morphology of the Cygnus X region, and in particular, with the location of the Cyg OB2 cluster.

Using an evolutionary synthesis model, Knödlseder et al. (2002) have suggested that Cyg OB2 is indeed the dominant ^{26}Al source in the Cygnus X region. Yet, actual nucleosynthesis models underestimate the 1809 keV line flux by roughly a factor of 2. Possibly, the neglection of stellar rotation, which plays a crucial role for the evolution of massive stars, may explain this discrepancy.[15]

The SPI measurement provide for the first time an estimate of the intrinsic width of the 1809 keV line in Cygnus X. The measured width corresponds to a Doppler broadening of 550 ± 210 km s^{-1} (FWHM). This translates into expansion velocities of 170-380 km s^{-1} if a thin expanding shell is assumed, or to 240-550 km s^{-1} for a homologously expanding bubble. Obviously, these values significantly exceed expectations (see above), hence it seems unlikely that the gamma-ray data trace expansion motions. Yet, turbulent motions in hot superbubbles can reach velocities of a few 100 km s^{-1} (De Avillez, these proceedings), and the ^{26}Al ejecta may eventually follow these motions. Hence, the gamma-ray observations may provide a direct measure of the turbulent motions in the hot Cygnus X superbubble. However, more observations of Cygnus X are required to confirm this hypothesis, by providing more stringent informations on the ^{26}Al line profile.

4 Conclusions

Multi-wavelength observations reveal that Cygnus X that is a textbook case of a massive star forming region. Its massive (O-type) star population is catalogued using optical and near-infrared photometric and spectroscopic observations, unveiling a young massive central cluster (Cyg OB2), surrounded by even younger embedded star clusters. The youth of Cyg OB2 explains the apparent absence of supernova remnants and the presence of ubiquitous diffuse thermal radio emission, produced by the ionising UV radiation of its O-star members. The observations suggest that the combined stellar winds of the massive Cyg OB2 members have blown a superbubble of ~ 100 pc in diameter into the ISM, compressing the surrounding gas, leading to triggered star formation near the bubble shell. The superbubble is filled with hot rarified gas that gives rise to soft X-ray emission. The massive stars also ejected already a significant amount of nucleosynthesis products into the bubble, as traced by the 1809 keV gamma-ray line from radioactive ^{26}Al decay. The 1809 keV line shape indicates turbulent velocities of a few 100 km s^{-1} within the bubble that may help to accelerate cosmic rays in this region. The recent discovery of a TeV gamma-ray source in Cyg OB2 together with the presence of an unidentified EGRET gamma-ray source may be a further indication of present cosmic-ray acceleration in Cygnus X.[3]

References

1. Abbott, D.C., Bieging, J.H., & Churchwell, E. 1981, ApJ, 250, 645
2. Aharonian, F.A., et al. 2002, A&A, 393, 73
3. Benaglia, P., Romero, G.E., Stevens, I.R., & Torres, D.F. 2001, A&A, 366, 605
4. Bochkarev, N.G., & Sitnik, T.G. 1985, Ap&SS, 108, 237
5. Cash, W., et al. 1980, ApJ, 238, L71
6. Comerón, F., et al. 2002, A&A, 389, 874
7. Del Rio, E., et al. 1996, A&A, 315, 237
8. Dickel, H.R., Wendker, H., & Bieritz, J.H. 1969, A&A, 1, 270
9. Downes, D., & Rinehart, R. 1968, ApJ, 144, 937
10. Gosachinskii, I.V., Lozinskaya, T.A., & Pravdikova, V.V. 1999, Astron. Reports, 43, 391
11. Gredel, R., & Münch, G. 1994, A&A, 285, 640
12. Hanson, M.M. 2003, ApJ, 597, 957
13. Heiles, C. 1979, ApJ 229, 533
14. Kaftan-Kassim, M.A. 1961, ApJ, 133, 821
15. Knödlseder, et al. 2002, A&A, 390, 945
16. Knödlseder, J. 2000, A&A, 360, 539
17. Le Duigou, J.-M., & Knödlseder, J. 2002, A&A, 392, 869
18. Lozinskaya, T.A., Pravdikova, V.V., & Finoguenov, A.V. 2002, Astron. Letters, 28, 223
19. Odenwald, S.F. 1989, AJ, 97, 801
20. Piddington, J.H., & Minnett, H.C. 1952, Aust. J. Sci. Res., 17, 1952
21. Plüschke, S. 2001, PhD thesis, Technical University, Munich
22. Uyaniker, B., et al. 2001, A&A, 371, 675
23. Véron, P. 1965, Annales d'Astrophysique, 28, 391
24. Wendker, H.J. 1970, A&A, 4, 378

High-mass star formation seen through methanol masers

V. Minier

Service d'Astrophysique DAPNIA/DSM/CEA
91191 Gif-sur-Yvette, France

Recent radio and millimetre surveys in the Milky Way have revealed a close relationship between methanol masers and the early stages of high-mass (> 8 $M_\odot$) star formation. These masers are bright (10-1000 Jy) radio molecular lines with narrow linewidths (0.5 km s^{-1}), require high gas density (> 10^5 cm^{-3}) and temperature (>100 K) conditions, and arise from small (1-100 AU) masing molecular clouds. Radio, millimetre and IR observations toward maser sites have shown that they coincide with protoclusters of massive YSOs within complexes of high-mass star formation. Interestingly, methanol masers are not detected in regions forming less massive stars such as rho-Ophiuchus. About 520 methanol maser sites have been detected in the Galactic plane, which give an insight of the distribution of the high-mass star-forming regions. These masers are also excellent tools to probe the star-forming cores at scales of 1-100 AU. They trace disk-like structures and are also seen in outflows associated with high-mass YSOs. I shall review recent results on methanol masers and star formation, including their Galactic distribution and detailed studies of star-forming clusters.

Keywords: masers — stars: formation — circumstellar matter

1 Introduction

High-mass stars[a] are pivotal objects in the evolution of galaxies and perhaps in the early stages (z=50 to 10) of the Universe and galaxy formation. Their energetic impact on the parent galaxy is extremely violent through stellar winds driven by strong radiation ($10^4 - 10^6$ $L_\odot$), outflows ($\sim 10^{-5} - 10^{-3}$ $M_\odot$ yr^{-1}) and supernova explosion.

High-mass stars also play a major role in the chemical evolution of galaxies and more generally in the whole process of star formation. During their short lives they actively participate in the heating of the molecular clouds and in the enrichment of the interstellar medium in heavy

[a]They have a mass in the range 8-100 $M_\odot$ and a spectral type earlier than B3.

atomic (between C and Fe) and molecular (e.g. CH_3OH) elements through stellar yields, hot molecular chemistries in the protostellar envelopes, mass-losses and supernova explosions; their strong ionising winds disrupt their parent cloud, re-shape their neighbourhood and probably trigger the formation of new stars and maybe new solar systems.

In consequence, massive star formation (MSF) is an unavoidable and constant feature in the life of galaxies. A good knowledge of high-mass star formation and evolution process is crucial to a complete understanding of the dynamics, luminosity and metallicity of galaxies.

2 Methanol masers: tracers of high-mass star-forming regions

Massive stars are born in very obscured regions, far away from us and within dense (proto)stellar clusters. For these reasons, the study of the earliest phases of massive star formation requires the use of high angular resolution tools and cold gas/dust probes. Methanol masers and (sub)millimetre continuum emission satisfy these requirements.

Interstellar masers are potentially excellent tools to identify massive young stellar objects (YSOs) because they are powerful and arise from very compact regions whose absolute positions can be measured with an accuracy of a few milliarcseconds (mas) using VLBI techniques. 6.7 and 12.2 GHz methanol masers have for instance proved to be remarkable probes for hunting down young massive stars. They often coincide with hyper compact HII regions and hot molecular cores, i.e. before the HII region phase. Whether all the 6.7 GHz (and 12.2 GHz) methanol masers are exclusively associated with high-mass (M > 8 $M_\odot$) star formation is currently a matter of debate.

Despite their original detection toward sites of high-mass star formation (e.g. giant molecular clouds, IRAS colour selected point sources, HII regions), more and more methanol maser sources are found *not* associated with any traditional signpost of high-mass star formation (e.g. Ellingsen et al. 1996; Szymczak et al. 2002). This tendency is confirmed at higher angular resolution. ATCA (Phillips et al. 1998; Walsh et al. 1998) and VLBI (Minier et al. 2001) observations have revealed that the very large majority (up to 80%) of methanol masers, originally thought to be coincident with IRAS colour selected point sources and ultra-compact HII (UC HII) regions, are indeed separated from them by more than 10^4 AU[b]. These sources are often referred to as *isolated* methanol masers to distinguish them from those closely associated with radio continuum and far infrared IRAS point sources. These isolated methanol masers are, however, always coincident with (sub)millimetre continuum emission from massive (> 20 $M_\odot$) and luminous (> 10^3 $L_\odot$) molecular clumps (Pestalozzi et al. 2002; Walsh et al. 2003, Minier et al. 2004 & Fig. 1).

This led to two hypotheses on the nature of methanol maser sites. Methanol masers may be signposts of high-mass protostars that have not yet significantly ionised their environment (Walsh et al. 1998). This is supported by VLBI work for a subset of methanol maser sources (Minier et al. 2001). Alternatively, methanol masers may be signposts of weakly or non-ionising young stars (Phillips et al. 1998), i.e. intermediate-mass ($3 < M < 8$ $M_\odot$) or low-mass ($M < 3$ $M_\odot$) young stellar objects (YSOs). This second scenario is supported by mid-IR observations (De Buizer et al. 2000). In both hypotheses, the methanol masers would not have any strong (i.e. > 10 mJy) radio emission counterpart.

Complementary spectral line observations might confirm the MSF hypothesis. Preliminary results from a molecular line survey with the Mopra millimetre-wave telescope suggest that isolated methanol masers are possibly associated with hot molecular cores (HMCs) (Purcell et al. 2004), which are presumed to be the sites where massive protostars evolve to form an ionising ZAMS star (Kurtz et al. 2000). The intense and complex chemistry, the temperature (some 100 K) and the density ($\geq 10^7$ cm^{-3}) of these HMCs would provide suitable conditions for methanol masers to arise (see Sect. 3).

[b] 10^4 AU is the typical size of hot molecular cores and protostellar envelopes

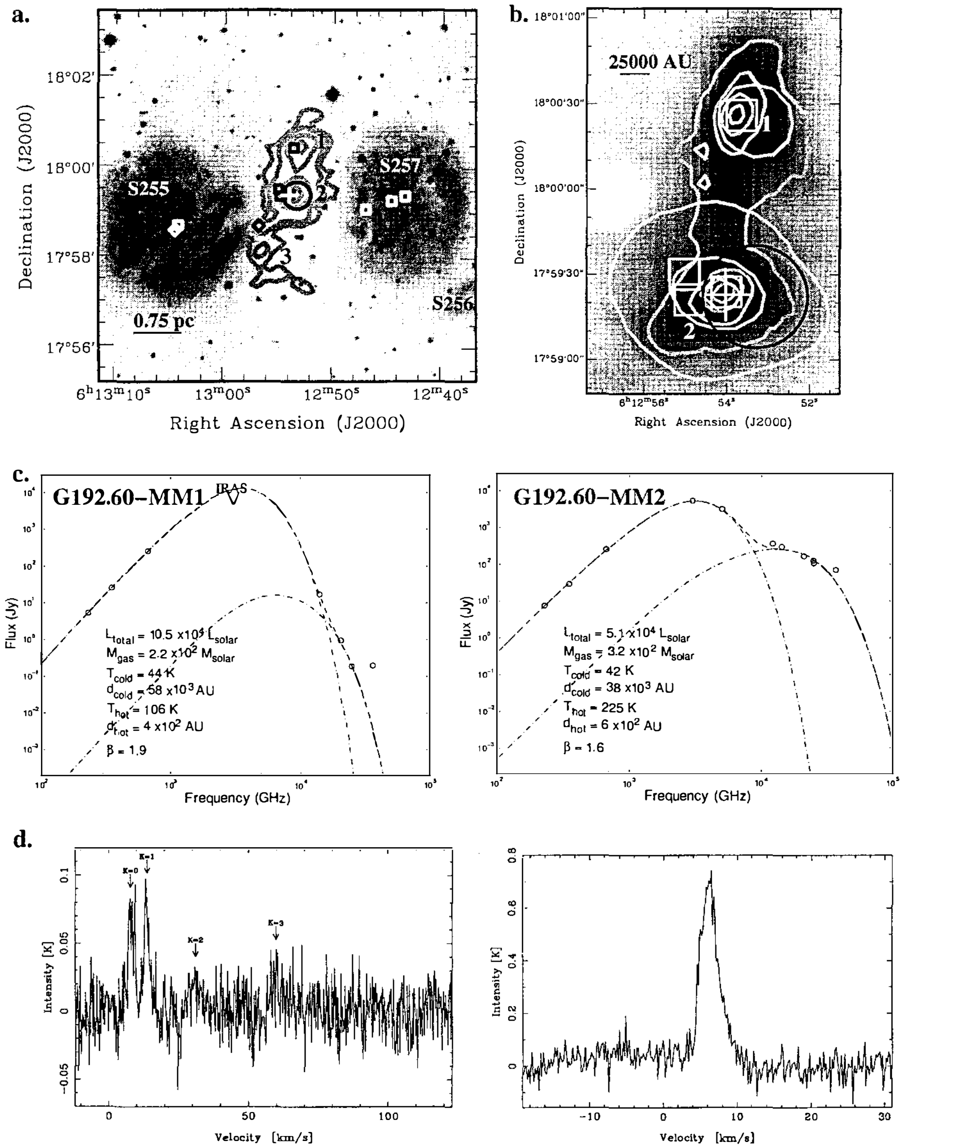

Figure 1: G 192.60-0.05 (S255IR). **a.** Optical image (grey scale) of the neighbourhood of G 192.60-0.05. The grey contours represent the 1.3-mm continuum emission imaged by SIMBA (10, 20, 50 and 90% of peak flux). The cross represents the position of the methanol masers, the squares are the radio continuum sites, the diamond is a recombination line site and the large circle shows the position of the IRAS source. The methanol maser source is not coincident with any visible object or optically visible HII region but it is associated with a strong mm source. **b.** Close-up of the mm sources 1 and 2. 850-μm SCUBA (grey scale), 450-μm SCUBA (grey contours; 25, 45, 65 and 85% of peak flux) and 21-μm MSX (white contours; 5, 45 and 85% of peak flux) images. The mm sources 1 and 2 are also seen with SCUBA and MSX. **c.** SEDs of mm sources 1 and 2. The IRAS icon shows the IRAS 100-μm flux level. **d.** CH_3CN and $C^{18}O$ line spectra. Minier et al. (2004).

Finally, recent ATCA observations by Minier et al. (2003) might indicate an exclusive association between methanol masers and massive star-forming regions following a nil detection rate of masers toward regions of low-mass star formation.

All these elements tend to demonstrate that methanol masers trace an early stage of MSF and give us insights on the Galactic distribution of high-mass star-forming regions. Whether methanol masers trace embedded massive protostars or suitable conditions nearby a site of MSF remains an open question.

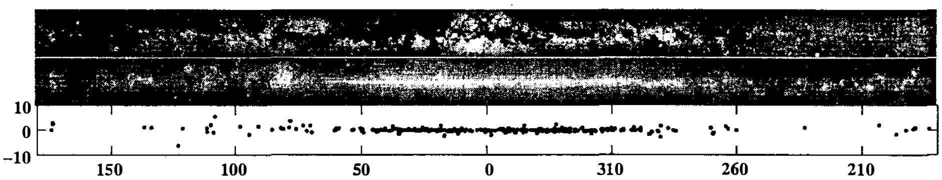

Figure 2: The Galactic plane seen at optical (top frame), far infrared (middle frame) wavelengths and using 6.7 GHz methanol maser as a probe (bottom frame). The optical and FIR images are from the NASA Multiwavelength Milky Way poster. The methanol maser distribution has been produced with all the methanol maser positions published in the literature and compiled by Pestalozzi & Minier (2004).

3 Physical conditions for methanol masers

The prevalent model for 6.7 GHz methanol masers is the Sobolev-Deguchi model (Sobolev & Deguchi 1994; Sobolev et al. 1997). This model has recently been further refined to examine in detail the large number of methanol maser transitions observed in NGC6334F and G345.01+1.79 (Cragg et al. 2001) and W3(OH) (Sutton et al. 2001). The model of Sobolev et al. (1997) is the only one which has been able to reproduce the high brightness temperatures ($> 10^{12}$ K) observed toward strong methanol maser sources. This model has approximately ten free parameters, with the most important in terms of producing strong methanol masers being the gas temperature, the dust temperature, the density and the methanol column density. The model requires the temperature of the gas producing the masers to be moderately cool ($\sim$ 30 K), with a hydrogen number density in the range of 10^6 - 10^8 cm^{-3}. In addition a nearby region of warm ($>$ 175 K) dust is necessary to produce the sub-millimetre and FIR photons required to create the population inversion and a methanol column density of $\sim 5\times 10^{17}$ cm^{-2} is needed to account for the observed brightness temperatures. The parameter values required to produce strong masers are in broad agreement with the observed physical conditions in high-mass star formation regions, but have yet to be rigorously tested through complementary observations (e.g. Ellingsen et al. 2003). However, it is currently the best framework we have for evaluating and understanding the physical conditions required to produce methanol masers.

Comparing the physical conditions which have been observed in class 0 and class I low-mass YSOs and (pre)protostellar condensations with the parameters of the Sobolev-Deguchi model which produce strong masers, the non-detection toward these sources is not surprising. Although methanol is relatively abundant in the environment of class 0 protostars (Goldsmith et al. 1999; Garay et al. 2002), the mechanism for releasing methanol molecules from dust grains differs from that seen in the protostellar envelope of high-mass YSOs. In the heated envelope of high-mass YSOs ($L_*\sim10^5$ $L_\odot$), the dust temperature (T_d) is expected to be greater than 90 K at 1000 AU from the centre (van Dishoeck & Blake 1998). At T_d > 90 K CH_3OH and H_2O completely evaporate from the icy dust grains. Hence, a dust temperature T_d > 100 K plays a dual role in producing methanol masers, it is required to release methanol from the dust grains and also to provide pump photons for the population inversion.

In contrast, molecular line observations of low-mass YSOs locate the thermal methanol emission between 500 to 3000 AU from the core centre (van Dishoeck & Blake 1998 and references therein; Bachiller et al. 1998; Garay et al. 2002). At distances beyond 100 AU, equation 2 of Motte & André (2001) shows that T_d < 90 K for low-mass stars (< 3 $M_\odot$). So methanol in low-mass YSO environments has to separate from dust grains by other means than evaporation. The coincidence of methanol emission with outflows in low-mass star-forming regions (Bachiller et al. 1998; Garay et al. 2002) suggests that methanol is released from the icy dust grain mantles through grain-grain collisions in shocked layers. These conditions (T_d << 175 K and collisions) would appear to preclude any strong methanol maser action according to the Sobolev-Deguchi model.

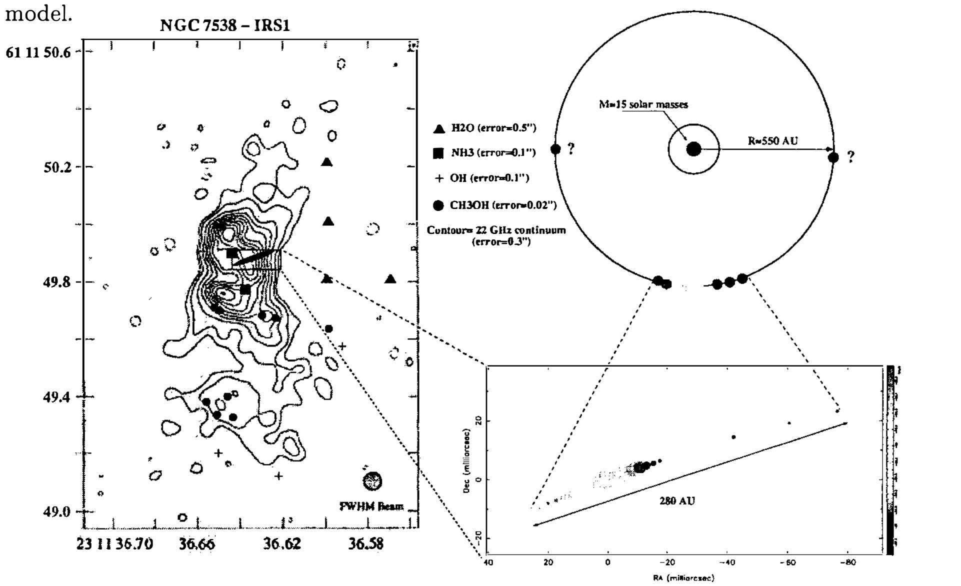

Figure 3: Left: 6.7 GHz methanol maser distribution (Minier et al. 2000) in NGC 7538-IRS1 overlaid on the 22 GHz radio continuum emission (contours) that traces a north-south ionised outflow. Masers are associated with clumps in the radio outflow and with a linear structure. Right: Masers partially tracing an edge-on circumstellar disk in NGC 7538-IRS1. The colour scale indicates the velocity. The dot size is proportional to the intensity of the maser component. From radio continuum observations, the exciting star responsible for the central ionised region coincident with the maser site could be a O9.5 star, having a mass of ~15 $M_\odot$. Using the linear velocity gradient along the maser line, the derived radius of the Keplerian disk is 550 AU which is larger than the measured half-diameter of the line of masers. Masers are probably seen in front of the star, but no maser is detected on the edge of the disk.

4 Protostellar disks

VLBI observations of 6.7 and 12.2 GHz methanol masers in 10 star-forming regions have revealed that the masers trace elongated morphologies and exhibit linear velocity gradients along them (Minier et al. 2000). These linear structures have lengths of 50 to 1300 AU. They are consistent with circumstellar disks. Assuming that we see the whole diameter of a Keplerian disk then we derive sub-solar central masses in general. However, it is possible that we only see masers in a fraction of the disk which lies in front of a young massive star (Fig. 3). Assuming that the Keplerian disks have diameters of 1000 AU, then the derived enclosed masses vary from 1 to 75 $M_\odot$. Other models such as accelerating outflows could explain the linear structures.

5 Conclusions

Methanol masers are the signposts of protoclusters of massive YSOs in a younger stage than those discovered using radio emission from (UC) HII regions; moreover, methanol masers within these clusters indicate the position of young massive stars and provide information on kinematics and dynamics within the protostellar cores. With 520 methanol masers detected, there are potentially 520 sites of massive star formation, mainly in the Southern sky, with precise positions to be studied with ALMA.

Acknowledgments

The author acknowledges support from the EC RTN on "The Formation and Evolution of Young Stellar Clusters" (HPRN-CT-2000-00155).

References

1. Bachiller, R., Codella, C., Colomer, F., Liechti, S., & Walmsley, C.M. 1998, A&A, 335, 266
2. Cragg D.M., Sobolev A.M., Ellingsen S.P., Caswell, J.L., Godfrey, P.D. & Dodson, R.G. 2001, MNRAS, 323, 939
3. De Buizer, J.M., Piña, R.K., & Telesco, C.M. ApJS 130, 437
4. Ellingsen, S. P., von Bibra, M. L., McCulloch, P.M., et al. 1996, MNRAS, 280, 378
5. Ellingsen, S. P., Cragg, D.M., Minier, V., Muller, E., & Godfrey, P.D., MNRAS, 344, 73
6. Garay, G., Mardones, D., Rodriguez, L.F., Caselli, P., & Bourke, T.L. 2002, ApJ, 567, 980
7. Goldsmith, P.F., Langer, W.D., & Velusamy, T. 1999, ApJ, 519, L173
8. Kurtz, S., Cesaroni, R., Churchwell, E., Hofner, P., & Walmsley, M. 2000, In: Mannings V., Boss A.P., Russell S. S. (eds.) Protostars and Planets IV. University of Arizona Press, p. 299
9. Minier, V., Booth, R.S., & Conway, J.E. 2000, A&A, 362, 1093
10. Minier, V., Conway, J.E., & Booth, R.S. 2001, A&A, 369, 278
11. Minier, V., Booth, R.S., & Conway, J.E. 2002, A&A, 383, 614
12. Minier, V., Ellingsen, S.P., Norris, R.P., & Booth, R.S. 2003, A&A, 403, 1095
13. Minier, V., Burton, M.G., Hill, T., Pestalozzi, M.R., et al. 2004, A&A, submitted
14. Motte, F., & André, P. A&A, 365, 440, 2001a
15. Pestalozzi, M.R., Humphreys, E.M., & Booth, R.S. 2002, A&A, 384, L15
16. Pestalozzi, M.R. & Minier, V. 2004, A&A, in revision
17. Phillips C.J., Norris R.P., Ellingsen S.P., & McCulloch P.M. 1998, MNRAS 300, 1131
18. Purcell, C.R., Burton, M.G., Hunt, M., Minier, V., & Hill, T. 2004, In: Star Formation at High Angular Resolution, IAU, Symposium 221, in press
19. Sobolev A.M. & Deguchi, S. 1994, A&A 291, 569
20. Sobolev A.M., Cragg D.M., & Godfrey P.D. 1997a, A&A 324, 211
21. Sutton, E.C., Sobolev, A.M., Ellingsen, S.P., Cragg, D.M., Mehringer, D.M., Ostrovskii, A.B. & Godfrey, P.D. 2001, ApJ 554, 173
22. Szymczak, M., Kus, A. J., Hrynek, G., Kepa, A., & Pazderski, E. 2002, A&A, 392, 277
23. van Dishoeck, E.F., & Blake, G.A. 1998, ARA&A, 36, 317
24. Walsh, A.J., Burton, M.G., Hyland, A.R., & Robinson, G. 1998, MNRAS, 301, 640
25. Walsh A.J., Macdonald, G.H., Alvey, N.D.S., Burton, M.G., & Lee, J-K. 2003, A&A, 410, 597

ROTATING DISKS IN HIGH-MASS YOUNG STELLAR OBJECTS: G24.78+0.08 and G31.41+0.31

M.T. BELTRÁN (1), R. CESARONI (1), R. NERI (2), C. CODELLA (3), R.S. FURUYA (4), L. TESTI (1), L. OLMI (3)

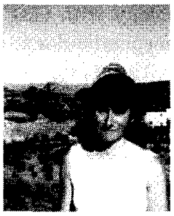

(1) Osservatorio Astrofisico di Arcetri, Largo E. Fermi 5, I-50125 Firenze, Italy
(2) IRAM, 300 Rue de la Piscine, F-38406 Saint Martin d'Hères, France
(3) Istituto di Radioastronomia, CNR, Largo E. Fermi 5, I-50125 Firenze, Italy
(4) Division of Physics and Astronomy, CALTECH, Pasadena, CA 91125, USA

We report on the detection of four rotating massive disks in two regions of high-mass star formation. The disks are perpendicular to known bipolar outflows and turn out to be unstable but long lived. We infer that accretion onto the embedded (proto)stars must proceed through the disks with rates of $\sim 10^{-2}$ $M_{\odot}$ yr^{-1}.

Keywords: Stars: formation – Radio lines: ISM – ISM: molecules – ISM: individual (G24.78+0.08, G31.41+0.31)

1 Introduction

The formation of massive stars represents a puzzle from a theoretical point of view. Unlike their low-mass counterparts, they are believed to reach the zero-age main sequence still deeply embedded in their parental cores: in particular, Palla & Stahler (1993) [21] predict that this occurs for stellar masses in excess of 8 $M_{\odot}$. Once the star has ignited hydrogen burning, further accretion should be inhibited by radiation pressure and powerful stellar winds, with the consequence that stars more massive than 8 $M_{\odot}$ should not exist. Two formation scenarios have been proposed to solve this paradox: non-spherical accretion (Yorke & Sonnhalter 2002) [26] and merging of lower mass stars (Bonnell, Bate, & Zinnecker 1998) [6]. Discriminating between these two models represents a challenging observational goal.

In this context, the detection of disks would strongly favour the accretion scenario, since random encounters between merging stars are not expected to lead to axially symmetric structures. On the contrary, conservation of angular momentum is bound to cause flattening and rotation of the infalling material, thus producing disk-like bodies. Indeed, circumstellar disks have been detected in low-mass stars and found to undergo Keplerian rotation (Simon, Dutrey, & Guilloteau 2000)[24]. Similar evidence has been found in a few high-mass young stellar objects (YSOs), but in most cases the angular resolution was insufficient to assess the presence of a disk unambiguously. In conclusion, only few bona fide examples are known (see Cesaroni 2002)[10] and all of these are associated with moderately massive stars (B1-B0). This is not sufficient to understand the role of disks in the formation of even more massive stars and establish the relevance of accretion to this process.

With this in mind, we have decided to perform a search for disks in a limited number of high-mass YSOs. For this purpose, we have selected two luminous objects with typical signposts of massive star formation such as water masers and ultracompact (UC) HII regions. The first, G31.41+0.31 (hereafter G31), is a well studied hot core located at 7.9 kpc (Olmi et al. 1996b[20]; Cesaroni et al. 1998[8]), where preliminary evidence of a rotating massive disk oriented perpendicularly to a bipolar outflow has been reported in Cesaroni et al. (1994)[7]. The other, G24.78+0.08 (hereafter G24), is a cluster of massive (proto)stars with a distance of 7.7 kpc, where recently Furuya et al. (2002)[14] have detected a pair of cores, each of these associated with a compact bipolar outflow. By analogy with G31 the expectation is that also in this case the cores could contain rotating disks perpendicular to the flow axes.

On the basis of previous experience with this type of objects (see, e.g., Cesaroni et al. 1999)[9], CH_3CN has been used as disk tracer. This is a low-abundance molecule which is excited in very dense regions. Therefore, searching for disks requires not only high angular resolution, but also great sensitivity given the faintness of the lines observed. In order to achieve these goals, we have used the Plateau de Bure interferometer (PdBI) at 1.4 mm in the most extended configuration. The main goal of our study was the discovery of rotating disks associated with massive YSOs deeply embedded in dense, compact cores. This was achieved searching for well defined *velocity gradients* in the cores, *perpendicular to molecular outflows* powered by the YSOs, as illustrated in the next sections.

2 Observations

We carried out observations in the 1.4 mm continuum and CH_3CN(12–11) line emission with the PdBI on 2003 March 16. The inner hole in the (u,v) plane has a radius of 15 $k\lambda$. Line data have been smoothed to a spectral resolution of 0.5 km s^{-1} and channel maps were created with natural weighting, attaining a resolution of $1.2'' \times 0.5''$ (full width at half power of the synthesized beam) and a sensitivity of 40–50 mJy/beam/channel (1σ RMS). For the continuum map the resolution and sensitivity are $1.2'' \times 0.5''$ and 4–6 mJy/beam, respectively.

In the following, we further analyze previous CS(3–2) observations obtained with the Nobeyama Millimeter Array (NMA) by Cesaroni et al. (2003)[11], to whom we refer for technical details.

3 Structure of the cores

The region G31 consists of a hot core, detected in various high-energy lines (Olmi, Cesaroni, & Walmsley 1996a)[19] located at the center of a bipolar outflow, at $\sim 5''$ from an UC HII region (Cesaroni et al. 1998)[8]. On the other hand, G24 is more complex, as it contains four distinct objects (see Fig. 1 of Furuya et al. 2002)[14]: two of these, G24 A and G24 C, are massive cores associated with two bipolar outflows and represent the target of the present study.

A picture of the G24 A and G31 cores is given in Fig. 1, where overlays of the 1.4 mm continuum and integrated CH_3CN(12–11) line emission are shown (Beltrán et al. 2004a)[4]. Note that no map is shown for G24 C because no CH_3CN(12–11) line emission has been detected with the PdBI. However, the 1.4 mm continuum flux is consistent with the extrapolation of the

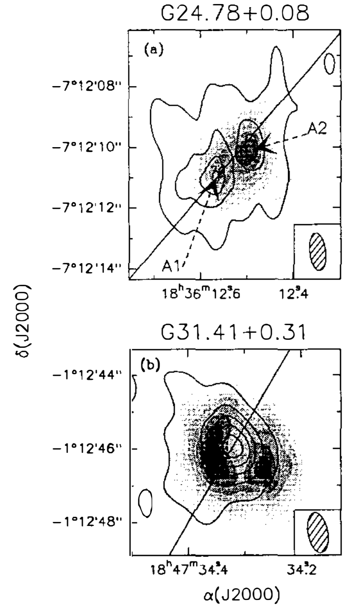

Figure 1: **Upper panel**: Overlay of the 1.4 mm continuum contour map on the grey scale image obtained integrating the $CH_3CN(12–11)$ emission under the K = 0, 1, and 2 components for G24 . Contour levels range from 0.02 to 0.2 in steps of 0.06 Jy beam^{-1}. Greyscale levels range from 0.1 to 1.00 in steps of 0.18 Jy beam^{-1}. The straight line represents the axis of the bipolar outflow. The synthesized beam is shown in the lower right-hand corner. **Lower panel**: same as upper panel for G31. Contour levels range from 0.08 to 1.28 in steps of 0.3 Jy beam^{-1}. Greyscale levels range from 0.1 to 0.82 in steps of 0.12 Jy beam^{-1} (Beltrán et al. 2004a).

spectral energy distribution presented by Furuya et al. (2002) [14], thus confirming the existence of such core. Very likely the fact that G24 C is detected in the $CH_3CN(8–7)$ transitions (Furuya et al. 2002) [14], but not in the (12–11) is due to this core being significantly colder than G24 A (see Codella et al. 1997) [12], which makes it difficult to detect high energy lines.

When observed with sub-arcsec resolution, G24 A is resolved into two separate cores. This is evident both in the 1.4 mm continuum and line maps. In the following we shall refer to these cores as G24 A1 (the one to the SE) and G24 A2 (the one to the NW). The former lies slightly closer to the geometrical center of the bipolar outflow reported by Furuya et al. (2002), but the small separation between the cores and the fact that they are aligned along the outflow axis make it difficult to establish whether the outflow is indeed associated with G24 A1; in the following we arbitrarily assume that this is the case. The conclusions derived in our study are independent of the association of the outflow with either of the cores. Noticeably, G24 A1 coincides with an unresolved UC HII region detected by Codella, Testi, & Cesaroni (1997), whereas no free-free emission is reported toward G24 A2. To determine whether this is an effect of different evolutionary stages of the two cores requires a detailed comparison of their physical properties which we postpone to a forthcoming paper.

The appearance of G31 is even more intriguing: while the 1.4 mm continuum seems to trace a roughly spherical core, the CH_3CN map reveals a toroidal structure with the dip centered at the position of the continuum peak (Fig. 1). This suggests that either the CH_3CN abundance drops dramatically in the central region of the core, due to a temperature increase toward the center (in agreement with the findings of Olmi et al. 1996b), or the temperature near to the embedded source is so high that the ground level states of CH_3CN are under populated. Interestingly, the two peaks of the CH_3CN emission are roughly symmetric with respect to the axis of the outflow observed by Olmi et al. (1996b), suggesting a physical connection between the toroid and the flow. Such a connection will become more evident when considering the velocity field in the cores.

4 Kinematics of the cores

An obvious way to analyze the velocity field in the cores is to produce maps of the line peak velocity obtained with Gaussian fits. Since multiple CH_3CN K-components are simultaneously observed in the same intermediate-frequency bandwidth, it is possible to improve the accuracy of the fit by fitting all lines together, assuming identical widths and fixing their separations to the laboratory values (see, e.g., Olmi et al. 1993) [18]. Such a fit has been made in each point where CH_3CN emission is detected. The maps of the LSR velocity for the G24 A1, G24 A2, and G31 cores can be seen in Figs. 2c, 2d, and 2e. The same method could not be applied to G24 C because the CH_3CN(12–11) line emission is not detected toward this core in our PdBI observations, while the spectral resolution used for the CH_3CN(8–7) transition by Furuya et al. (2002) [14] was too poor (16 km s^{-1}). Hence, we have re-analyzed the CS(3–2) data by Cesaroni et al. (2003) [11], as the CS emission line was much stronger and observed with sufficient spectral resolution (0.5 km s^{-1}). In this case the line profile deviates significantly from a Gaussian, presenting prominent emission in the red wing. Therefore we preferred to estimate the velocity from the first moment computed over a velocity interval including only the peak of the emission, from 108 to 116 km s^{-1}, rather than from a Gaussian fit. The resulting V_{LSR} map is shown in Fig. 2a (Beltrán et al. 2004a) [4].

The first conclusion that can be drawn from this figure is that all cores show clear velocity gradients, with V_{LSR} increasing steadily along well defined directions. We examine three possible explanations for such gradients: expansion, infall, or rotation. The first can be ruled out as the velocity gradient should be maximum in the same direction as the molecular outflow, which is clearly not the case (see Figs. 2b and 2e). Spherical infall is also impossible, because self-absorption would shift the peak velocity toward lower values at the core center, whereas we observe a steady velocity increase along a well defined direction (see Figs. 2a, 2c, 2d, and 2e). The fact that such a direction is perpendicular to the outflow axis strongly favours the rotation hypothesis: this is exactly what one expects if the core is rotating about the axis of the corresponding outflow. This behaviour might be mimicked also by two distinct cores with different V_{LSR} and too close to be resolved by our observations: the velocity gradient would be a consequence of line emission from the two cores observed in the same instrumental beam. However, we believe this to be very unlikely. In fact, at least in the case of G31, the angular separation between the regions emitting at the maximum and minimum velocities is definitely greater than the beam size.

In conclusion, we believe that the most plausible explanation for the kinematics of G24 and G31 is that **the cores have toroidal structures undergoing rotation about the corresponding outflow axis**. Hereafter, we shall refer to these simply as **disks**, although one has to keep in mind that these are very different from the geometrically thin circumstellar disks seen in low-mass YSOs.

5 Nature of the G24 and G31 disks

The major question raised by our results is whether the disks are stable entities. In Table 1 we give a few disk parameters, among which the mass of the cores, M_{gas}, and the dynamical mass, M_{dyn}, needed for equilibrium (Beltrán et al. 2004a) [4]. The former was estimated from the millimeter continuum emission assuming a mass opacity of $\simeq 0.02$ cm^{-2} g^{-1} at 1.4 mm for

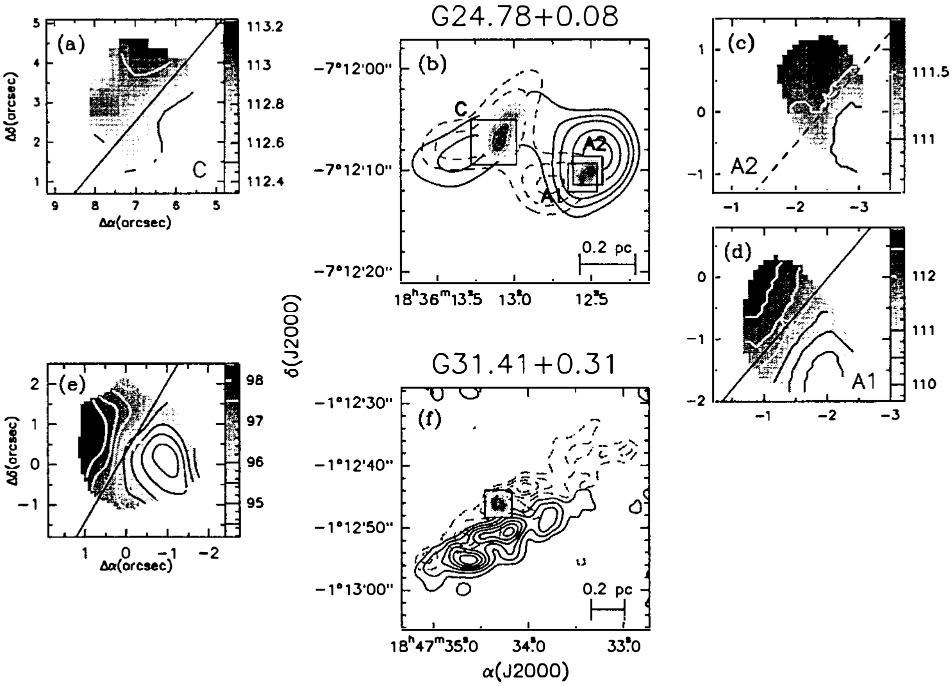

Figure 2: **a.** Map of the first moment of the CS(3–2) line observed by Cesaroni et al. (2003) toward G24 C. The straight line represents the outflow axis. The star indicates the peak of the mm continuum emission. **b.** Comparison between the bipolar outflows observed by Furuya et al. (2002), the $CH_3CN(12–11)$ line emission mapped by us toward G24 A1 and G24 A2, and the CS(3–2) line map from Furuya et al. (2002) toward G24 C. Contour levels for $CH_3CN(12–11)$ are the same as in Fig. 1, while for CS(3–2) contour levels range from 0.4 to 0.8 in steps of 0.1 Jy beam^{-1} km s^{-1}. **c.** Map of the $CH_3CN(12–11)$ line peak velocity toward G24 A2 obtained with a Gaussian fit. The dashed line indicates the direction of the outflow, arbitrarily associated with G24 A1 (see text). **d.** Same as c for G24 A1. **e.** Same as c for G31. Note that for this case the direction of the outflow has been obtained connecting the peaks of the blue and red lobes. **f.** Comparison between the bipolar outflow observed by Olmi et al. (1996b) and the $CH_3CN(12–11)$ line emission map toward G31. Contour levels for $CH_3CN(12–11)$ are the same as in Fig. 1 (Beltrán et al. 2004a).

Table 1: Parameters of disks and outflows in G24 and G31.

Core	T (K)	R (pc)	$v_{\rm rot}$ (km s^{-1})	$M_{\rm dyn}$ ($M_\odot$)	$M_{\rm gas}$ ($M_\odot$)	$t_{\rm ff}$ (yr)	$t_{\rm acc}$ (yr)	$t_{\rm out}$ (yr)	$\dot M_{\rm acc}$[a] ($M_\odot$yr^{-1})	$\dot M_{\rm out}$ ($M_\odot$yr^{-1})
G24 A1	87[b]	0.02	1.50	23	130	4×10^3	7×10^3	2×10^4 [c]	2×10^{-2}	5×10^{-4} [c]
G24 A2	87[b]	0.02	0.75	4	80	3×10^3	1×10^4	—	8×10^{-3}	—
G24 C	30[b]	0.04	0.50	5	250	9×10^3	4×10^4	2×10^4 [c]	6×10^{-3}	5×10^{-4} [c]
G31	230[d]	0.04	2.10	87	490	6×10^3	1×10^4	2×10^5 [d]	5×10^{-2}	4×10^{-4} [d]

[a] Computed assuming $v_{\rm in}$=$v_{\rm rot}$.
[b] From Codella et al. (1997) [12].
[c] From Furuya et al. (2002) [14].
[d] From Olmi et al. (1996b) [20].

a gas-to-dust ratio of 100 (see, e.g., André, Ward-Thompson, & Barsony 2000) [3], and the temperatures listed in Table 1; the latter was computed assuming equilibrium between centrifugal and gravitational forces from the expression $M_{\rm dyn} = v_{\rm rot}^2\, R/G \sin^2 i$, where $v_{\rm rot}$ is the rotation velocity, R is the radius of the disk, and i is the inclination angle of the disk assumed to be 45°. $M_{\rm gas}$ is much larger than $M_{\rm dyn}$, suggesting that the disks may be unstable. In principle, magnetic fields could stabilize the disks, but this would require a few 20–40 mG, values too large to be plausible even in regions as dense as 10^8 cm^{-3} (see Fig. 1 of Crutcher 1999) [13]. Therefore, the disks must be transient structures with lifetimes of the order of the free-fall time, $t_{\rm ff}$, also listed in Table 1. Another estimate of the disks lifetime, $t_{\rm acc}$, can be derived from the ratio between the disk mass, $M_{\rm gas}$, and the accretion rate. The latter is computed from the expression $\dot M_{\rm acc} = 2\pi\Sigma R v_{\rm in}$ where $\Sigma = M_{\rm gas}/\pi R^2$ is the surface density and $v_{\rm in}$ is the infall velocity, which has been assumed to be equal to the rotation velocity following Allen, Li, & Shu (2003) [2]. As one can see from Table 1, $t_{\rm ff}$ is very close to $t_{\rm acc}$, and both agree within a factor $\leq$4 with the outflow age, $t_{\rm out}$, derived from the data of Olmi et al. (1996b) [20] and Furuya et al. (2002) [14]. Note that $t_{\rm out}$ is to be multiplied by $\cot\theta$ to correct for the (unknown) inclination angle θ of the flow with respect to the line of sight. We believe that θ cannot differ significantly from 45° otherwise blue- and red-shifted emission would mix up in the plane of the sky (for $\theta \simeq 90^\circ$) or along the line of sight through the center (for $\theta \simeq 0^\circ$): this implies a correction factor of order unity. The correction factors for $\theta = 30^\circ$ and 60° would be 1.7 and 0.6 respectively.

In conclusion, the lifetime of the disks seems to be of order of 10^4 yr. Such a short lifetime should imply 10 times less disks than UC HII regions, which are supposed to live 10^5 yr (Wood & Churchwell 1989) [25]. Although it is obviously impossible to confirm this estimate on a statistical ground, disks appear to be an ubiquitous phenomenon in massive star forming regions, as we have detected 4 of them in 2 regions only. Therefore, it seems unlikely that disks are 10 times less numerous than UC HII regions. This implies a significantly longer lifetime than $\sim 10^4$ yr, which in turn means that disks must be fed by a larger scale reservoir of material at a rate comparable to $\dot M_{\rm acc} \simeq 10^{-2}\ M_\odot$ yr^{-1}. Accretion rates that large have been estimated by Fontani et al. (2002) [15] for the parsec-scale clumps where high-mass star formation is observed.

If the disk lifetime is comparable to that of UC HII regions, then the total accreted mass should result in $\dot M_{\rm acc} \times 10\, t_{\rm ff} \simeq 10^{-2} \times 10^5 = 10^3\ M_\odot$ of stars, too large a value for a single star, but acceptable if the infalling gas is accreting onto a cluster of stars. Indeed, this resembles the situation in the Orion cluster (Palla & Stahler 1999) [22], where only <7% of the mass in stars (>600 $M_\odot$) is contained in the most massive star of the cluster ($\sim$40 $M_\odot$).

6 Temperature gradient in G31

The averaged CH_3CN emission for low K-components toward G31 shows a toroidal geometry with the higher K-components emission and the dust emission filling the central gap and peak-

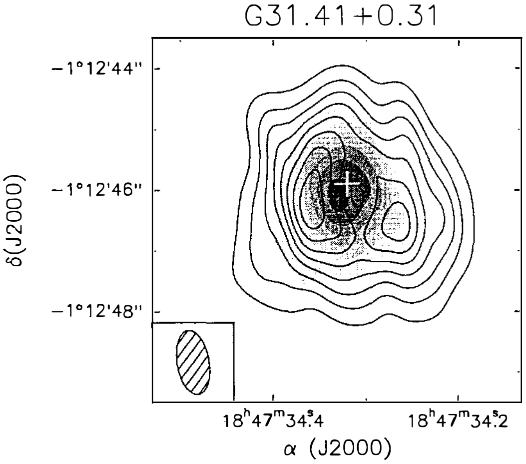

Figure 3: Overlay of the PdBI averaged CH_3CN (J=12→11) emission under the K = 0, 1, and 2 components (*contours*) and the emission under K = 8 (*greyscale*) toward G31.41+0.31. Contour levels range from 0.1 to 0.94 in steps of 0.12 Jy beam^{-1}. Greyscale levels range from 0.1 to 0.70 in steps of 0.12 Jy beam^{-1} km s^{-1}. The synthesized beam is shown in the lower left-hand corner. The white cross marks the position of the 1.4 mm continu um emission peak (Beltrán et al. 2004b).

ing at the center of the torus (see Fig. 1 and 3). This suggests that the CH_3CN gas is not entirely depleted at the center of the core and distributed in a toroidal structure surrounding the embedded YSO, but there is gas also close to the center. We found that the CH_3CN column density is higher toward the center of the core, so that cannot be explained in terms of a lack of CH_3CN molecules toward the center. Thus, the most plausible explanation for this geometry is an increase of the temperature toward the center, which implies the existence of a temperature gradient in the core. In this case, the temperature at the center of the core should be so high that states with higher excitation energies, such as K = 8, are more easily excited and populated than low-K states, that is, with lower energies (see Fig. 3). In order to check for the existence of such a temperature gradient, we computed a map of the rotational temperature, $T_{\rm rot}$, and the total methyl cyanide column density, $N_{\rm CH_3CN}$, in the core by fitting the Boltzman plots at each position. The fits were performed by means of the rotation diagram (RD) method (which assumes that the molecular levels are populated according to LTE conditions at a single temperature $T_{\rm rot}$) to the $CH_3{}^{13}CN$ K=1, 2, 3, 4, 5, and 6 components. Figure 4 shows the resulting $T_{\rm rot}$ map, as well as the $N_{\rm CH_3CN}$ map, derived with the same method, overlaid on the integrated $CH_3{}^{13}CN$ (J=12→11) emission under the $K = 1 + 2$ components (Beltrán et al. 2004b) [5]. This figure clearly confirms that the temperature at the center of the core is very high ($\sim$ 350 K), while the temperature in the outer regions is lower ($T_{\rm rot} \sim$ 150 K). This is consistent with the findings of Cesaroni et al. (1998) [8] who have detected a decrease of the NH_3 (4,4) brightness temperature, which is interpreted as a temperature gradient in the core.

7 Modeling the velocity field

As already discussed in § 4, we have detected clear velocity gradients in the G31 and G24 cores by simultaneously fitting multiple CH_3CN (J=12→11) K-components at each position where CH_3CN is detected. This velocity gradient is orientated perpendicularly to the molecular outflows detected in the regions, and the most plausible explanation is that the core is undergoing

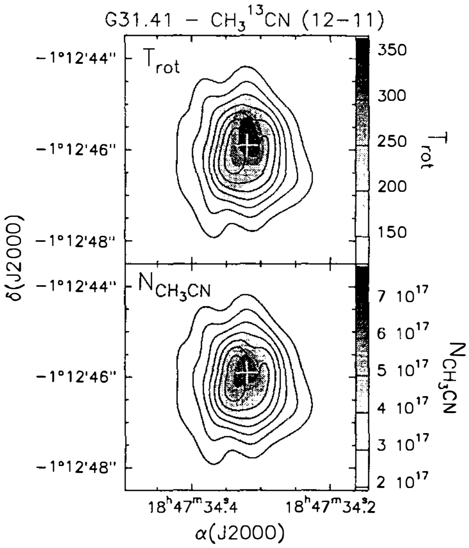

Figure 4: Overlay of the PdBI $CH_3{}^{13}CN$ (J=12→11) emission averaged under the K = 1 and 2 components (*contours*) on the T_{rot} map (*top panel*) and the N_{CH_3CN} map (*bottom panel*) in greyscale, derived by fitting the Boltzmann pl ots at each position, toward G31.41+0.31. The contour levels range from 0.1 to 0.82 Jy beam^{-1} in steps of0.12 Jy beam^{-1}. Greyscale levels range from 100 to 350 K by 50 K (*top panel*), and from 2 to 7×10^{17} cm^{-2} by 1 × 10^{17} cm^{-2} (*bottom panel*). The white cross marks the position of the 1.4 mm continuum emission peak (Beltrán et al. 2004b).

rotation about the outflow axis. As already mentioned, the sizes and masses of these rotating structures make them remarkably different from the geometrically thin circumstellar disks seen in low-mass YSOs, where the mass of the disk is significantly less than that of the star. Thus, these structures rather resemble thick toroids and it is tempting to interpret them as "circumcluster" disks: in other words, one would expect that such massive toroids host not just a single massive star, but a whole cluster.

The kinematics of the gas toward the core of G31, and core A1 in G24 can be seen in the position-velocity (PV) cuts done of the CH_3CN (J=12→11) K = 3 emission along a direction roughly perpendicular to the outflow axis (Figs. 5 and 6). We modeled the CH_3CN emission assuming that the emission arises from a rotating disk seen edge-on by the observer. We computed the models by adopting a power law dependence on the distance from the core center for the velocity ($v \propto R^{\gamma}$), the density ($\rho \propto R^{-p}$), and the temperature ($T \propto R^{-q}$) of the emitting gas. The radiative transfer equation along the line of sight was solved for a given column density and line width. The models were finally convolved with a circular Gaussian beam to mimic the PdBI observations, and the synthetic PV diagrams were computed along the projected major axis of the toroid. The parameters of the models are the inner and outer radius of the toroid, $R_{\rm inn}$ and $R_{\rm out}$, respectively, the CH_3CN peak column density, the line width, the power-law index p of the density, the temperature at the outer radius, $T_{\rm out}$, the power-law index q of the temperature, and the rotation velocity measured at the edge of the toroid, $v_{\rm rot}$.

The initial guesses for the input parameters, such as the size of the toroid or the rotation velocity, were derived from the observations. Regarding the velocity field, the mass of the toroid is so huge that the rotation cannot be Keplerian, because in Keplerian rotation the mass of the disk must be less than that of the star. Thus, we modeled the velocity field as a rigid rotator. According to recent theoretical models (Galli et al. 1991) [16], discriminating between constant

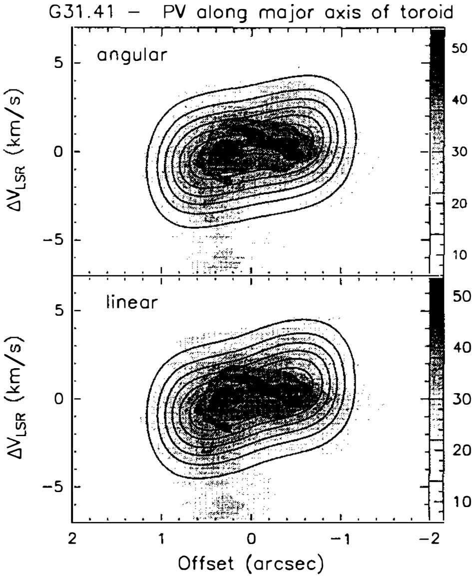

Figure 5: Overlay of the PV plot of the CH_3CN (J=12→11) K = 3 emission (*greyscale*) along the major axis of the toroid (P.A. ~ 20°) in G31.41+0.31, and the synthetic emission PV plot of a model (*contours*) with constant angular velocity (*top panel*), and with constant rotation velocity (*bottom panel*). The contour levels range from 6 to 54 Jy beam^{-1} in steps of 8 Jy beam^{-1} (Beltrán et al. 2004b).

rotation velocity and constant angular velocity should help to assess whether magnetic braking plays a crucial role during the process of disk, and hence, star formation. Thus, we considered models with two different velocity fields: one with a constant rotation velocity v = constant ($\gamma = 0$), and one with a constant angular velocity $v \propto R$ ($\gamma = 1$). According to accretion disks theory, for geometrically thin disks the dependence of the temperature on the radius is $T \propto R^{-3/4}$ (Pringle 1981) [23], both for "passive" and "active" disks. The heating is provided by the central star in the former ones, while the latter are internally heated by viscosity. Thus, we assumed a temperature power law $T \propto R^{-3/4}$. Regarding the density distribution, we adopted typical power-law indices p ranging from 1 to 2 (Adams, Lada, & Shu 1987) [1].

The observed and synthetic PV diagrams for both scenarios, constant rotation velocity and constant angular velocity, can be seen in Figs. 5 and 6 (Beltrán et al. 2004b) [5]. As one may see, it is not possible to distinguish between constant rotation or constant angular velocity, because both velocity fields fit the data reasonably well. For G31, only the models with a temperature gradient ($T \propto R^{-3/4}$) can fit the observed PV plots and reproduce the " inner hole" seen in the data. On the other hand, the data may be fitted equally well by models with or without a density gradient. For the sake of simplicity we adopted constant density. The best fit was obtained for $T_{\rm out} \sim 100$ K, $v_{\rm rot} \sim 1.7$ km s^{-1}, $R_{\rm out} \sim 1.7''$ (~ 13400 AU), and $R_{\rm inn} \sim 0.17''$ (~ 1350 AU), which is roughly the separation between two sources detected at 7 mm (Hofner, private communication). The values of $v_{\rm rot}$ and $R_{\rm out}$ are consistent with those derived directly from the velocity gradient and the 1.4 mm continuum emission at 50% of the peak, respectively (see Table 1).

For core A1 in G24, we computed models with and without temperature gradients, and both provided a satisfactory fit to the data. Also in this case we adopted a temperature distribution $T \propto R^{-3/4}$ for the models. The best fit was achieved for $p = 1$, $T_{\rm out} \sim 100$ K, $v_{\rm rot} \sim 2$ km s^{-1},

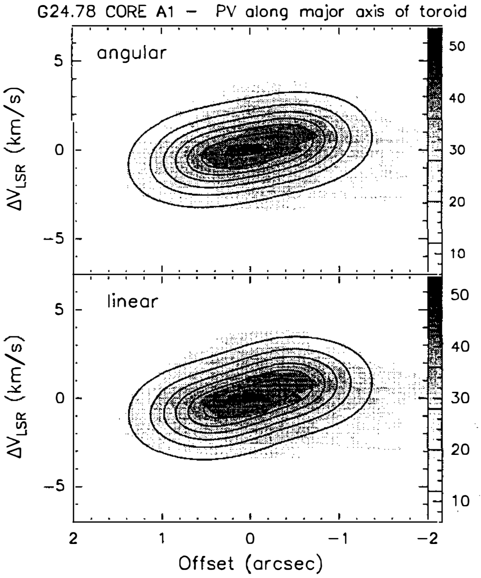

Figure 6: Same as Fig. 5 for core A1 in G24.78+0.08. PV cut along a P.A. $\sim 40°$. The contour levels range from 4 to 52 Jy beam^{-1} in steps of 8 Jy beam^{-1} (Beltrán et al. 2004b).

$R_{\rm out} \sim 1''$ ($\sim$ 7700 AU), and $R_{\rm inn} \sim 0.3''$ ($\sim$ 2300 AU), which is the size of the HII region at 1.3 cm at the 3σ emission level (Beltrán et al. 2004b) [5]. The $R_{\rm out}$ derived from the model is roughly twice the value measured from the 1.4 mm continuum emission at 50% of the peak (see Table 1).

8 Conclusions

The main finding of our study is that we have detected rotating disks associated with high-mass YSOs. This result strongly suggests that non-spherical accretion is a viable mechanism to form high-mass stars. Only a larger number of observations may confirm this conclusion on a statistical ground, thus assessing that disks are a natural product of the star formation process also for early-type stars.

References

1. Adams, F. C., Lada, C. J., & Shu, F. H. 1987, ApJ, 312, 788
2. Allen, A., Li, Z.-Y., & Shu, F. H. 2003, ApJ, 599, 363
3. André, P., Ward-Thompson, D., & Barsony, M. 2000, in Protostars and Planets IV, ed. V. Mannings, A. Boss, & S. Russell (Tucson: Univ. Arizona Press), 59
4. Beltrán, M.T., Cesaroni, R., Neri, R., Codella, C., Furuya, R. S., Testi, L., & Olmi, L. 2004a, Ap.J, 601, L187
5. Beltrán, M.T. 2004b, in preparation
6. Bonnell, I. A., Bate, M. R., & Zinnecker, H. 1998, MNRAS, 298, 93
7. Cesaroni, R., Olmi, L., Walmsley, C. M., Churchwell, E., & Hofner, P. 1994, ApJ, 435, L137
8. Cesaroni, R., Hofner, P., Walmsley, C. M., & Churchwell, E. 1998, A&A, 331, 709

9. Cesaroni, R., Felli, M., Jenness, T. et al. 1999, A&A, 345, 949
10. Cesaroni, R. 2002, Highlights of Astronomy, 12, 156
11. Cesaroni, R., Codella, C., Furuya, R. S., & Testi, L. 2003, A&A, 401, 227
12. Codella, C., Testi, L., & Cesaroni, R. 1997, A&A, 325, 282
13. Crutcher, R. M. 1999, ApJ, 520, 706
14. Furuya, R. S., Cesaroni, R., Codella, C. et al. 2002, A&A, 390, L1
15. Fontani, F., Cesaroni, R., Caselli, P., & Olmi, L. 2002, A&A, 389, 603
16. Galli, D., Shu, F. H., Laughlin, G., & Lizano, S. 1991, ApJ, 551, 36
17. Hildebrand, R. H. 1983, QJRAS, 24, 267
18. Olmi, L., Cesaroni, R., & Walmsley, C. M. 1993, A&A, 276, 489
19. Olmi, L., Cesaroni, R., & Walmsley, C. M. 1996a, A&A, 307, 599
20. Olmi, L., Cesaroni, R., Neri, R., & Walmsley, C. M. 1996b, A&A, 315, 565
21. Palla, F., & Stahler, S. W. 1993, ApJ, 418, 414
22. Palla, F., & Stahler, S. W. 1999, ApJ, 525, 772
23. Pringle, J. E. 1981, ARA&A, 19, 137
24. Simon, M., Dutrey, A., & Guilloteau, S. 2000, ApJ, 545, 1034
25. Wood, D. O. S., & Churchwell, E. 1989, ApJS, 69, 831
26. Yorke, H. W., & Sonnhalter, C. 2002, ApJ, 569, 846

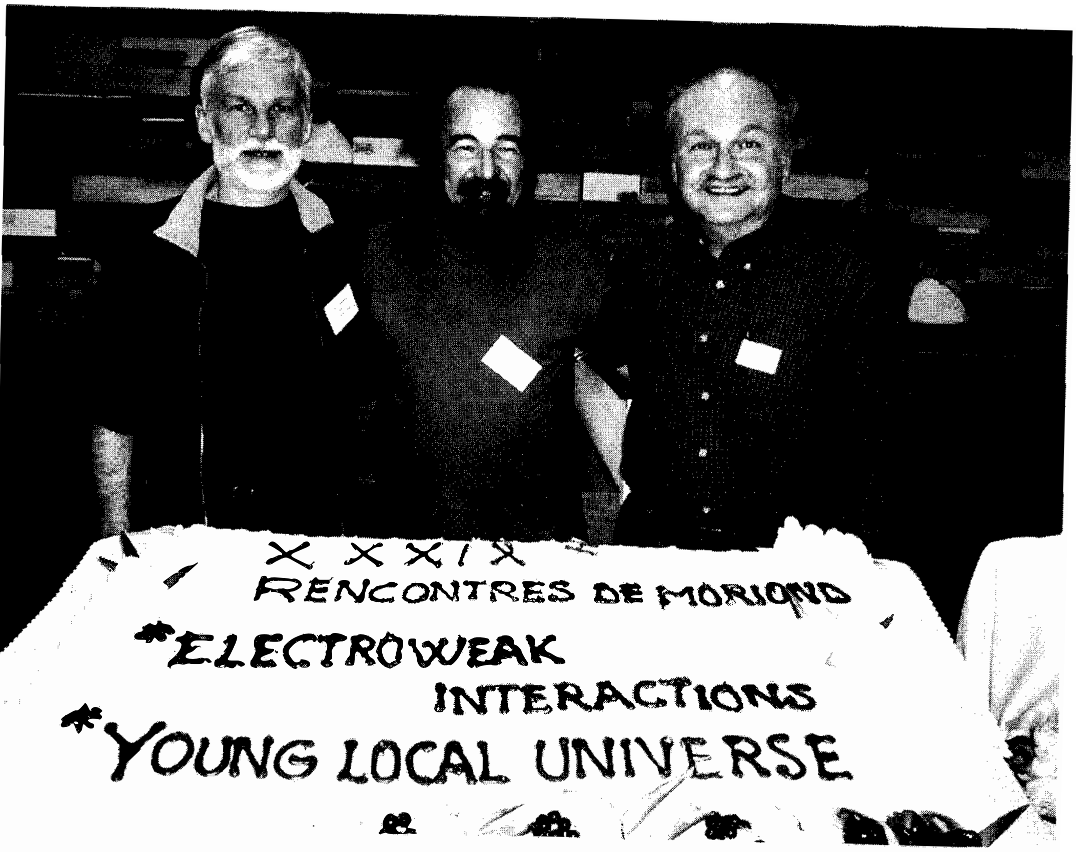

Strange Attractors

Part 2

Initial conditions for star formation and environmental effects

MOLECULAR CLOUDS AND THEIR STRUCTURES IN THE ANDROMEDA GALAXY

S. MULLER[1,2]
M. GUÉLIN[2], H. UNGERECHTS[3], N. NEININGER[4], R. LUCAS[2], R. WIELEBINSKI[5]
[1]*Institute of Astronomy and Astrophysics, Academia Sinica, P.O. Box 23-141, Taipei, 106 Taiwan*
[2]*Institut de Radioastronomie Millimétrique, 300, rue de la piscine, F-38406 St Martin d'Hères, France*
[3]*Instituto de Radioastronomia Millimétrica, Avenida Divina Pastora 7, E-18012 Granada, Spain*
[4]*Radioastronomisches Institut der Universität Bonn, Auf dem Hügel 71, D-53121 Bonn, Germany*
[5]*Max-Planck-Institut für Radioastronomie, Auf dem Hügel 69, D-53121 Bonn, Germany*

We present the distribution and physical properties of the giant molecular clouds in the Andromeda galaxy (M31) as derived from observations of the CO molecule emission with the IRAM 30m telescope (Pico Veleta, Spain) and the Plateau de Bure Interferometer (PdBI, France). Not only is M31 the closest spiral galaxy, which allows to study the interstellar medium at molecular clouds scale with current mm interferometers (1" corresponds to 4 pc), but its distance is also very accurately known (D = 780 ± 17 kpc, that is to say 5 % uncertainty !) which allows reliable measurements of physical properties such as sizes and luminosities. Adding to this, and unlike in the case of Galactic molecular clouds, there are no distance ambiguities, and the line of sight is free from intervening material. We therefore have access to both global and local views, which is essential in interstellar medium studies from large scales (spiral pattern) down to the small scales of star formation sites (molecular clouds).

Keywords: Galaxies: spiral, ISM; ISM: molecular clouds

1 Introduction

Studying the formation, properties and evolution of giant molecular clouds in nearby galaxies is essential to understand the required conditions for the star formation processes. Why and how stars form is still one the hottest topic of modern astronomy and at least generated quite a lot of discussions during this week in La Thuile. While Galactic star forming regions offer lots of details, the nearby galaxies still are more than interesting candidates, since they provide the opportunity to study the star formation in different environments and physical conditions (metallicity, temperature, density, excitation ...).

In the Milky Way, the properties of molecular clouds have since a long time been studied with single dish antennas (see for example Solomon *et al.* 1987, Dame *et al.* 2001). However, in this case, we face problems of distance uncertainties and intervening material, which make things difficult to disentangle and prevent to estimate physical parameters precisely. One particular issue concerns the determination of the mass of the molecular gas. While in principle several other methods can be used to trace the molecular gas (thin lines of CO isotopomers, dust thermal emission, dust extinction), one mostly relies on observations of the $^{12}C^{16}O$(1-0) line.

Although H_2 is by far the most abundant molecule, it has no permanent dipole moment so that H_2 emission is mostly undetectable in the interstellar medium. Therefore, one has to turn towards other tracers of the molecular gas. After H_2, CO is the most abundant molecule, with an abundance ratio $[CO/H_2] \sim 10^{-4}$. Empirically, the mass of the molecular gas is found to be proportional to the integrated intensity of the optically thick $^{12}C^{16}O$(1-0) line with a CO to H_2 conversion factor $\mathcal{X}$. A standard value $\mathcal{X} = 1 - 4$ (in units of 10^{20} cm^{-2} K^{-1} km^{-1} s) is commonly used in practice (Sanders *et al.* 1984, Solomon *et al.* 1987, Strong *et al.* 1988, Digel *et al.* 1995, Strong & Mattox 1996), despite the fact that $\mathcal{X}$ may vary from one galaxy to the other according to density, temperature and metallicity of the gas (Maloney & Black 1988).

In external galaxies, the study of the interstellar medium at a few parsecs resolution is still at its early ages, although some recent work has made significant breakthroughs in M31, M33 and LMC (see contributions from Blitz and Fukui, this conference, for the 2 latest). However, they are still limited to our very closest neighbours.

This contribution aims to present the molecular gas in the Andromeda galaxy. It is divided into three parts. First, we will present the global distribution of the molecular gas. Then, we will discuss the physical properties of the molecular clouds and complexes, with some emphasis on their masses. The last part will deal with some kinematic issues.

2 Distribution of the molecular gas

2.1 Overall distribution

The global overview of the molecular gas distribution in the disk of the Andromeda galaxy can be seen on Fig.1. These observations have been carried out with the IRAM 30m in the CO(1-0) line at 115 GHz (Neininger *et al.* 1998, Nieten *et al.* 2004, Guélin *et al.* 2000 and 2004). The whole galactic disk has been mapped in on-the-fly observing mode recording more than 1.5 millions spectra. To date, it is the deepest and more detailed survey of the molecular disk in M31: the resolution is 23" (90 pc) and the sensitivity reaches 30 mK for 2.6 km/s velocity channels. The CO(1-0) emission peaks at 1.5 K. In addition, some fields of about 10' x 10' in size have been observed in the CO(2-1) transition.

The main properties of the molecular gas distribution in the disk of M31 can be summarized as follows:

- the CO emission shows spiral arms and filamentary structures, matching dust absorption lanes. Nieten *et al.* 2004 have successfully fitted a simple spiral pattern with 2 logarithmic trailing arms and constant pitch angle.

- at smaller scales ($\sim 100 - 300$ pc) the CO emission appears patchy and can be decomposed into giant molecular complexes (GMC).

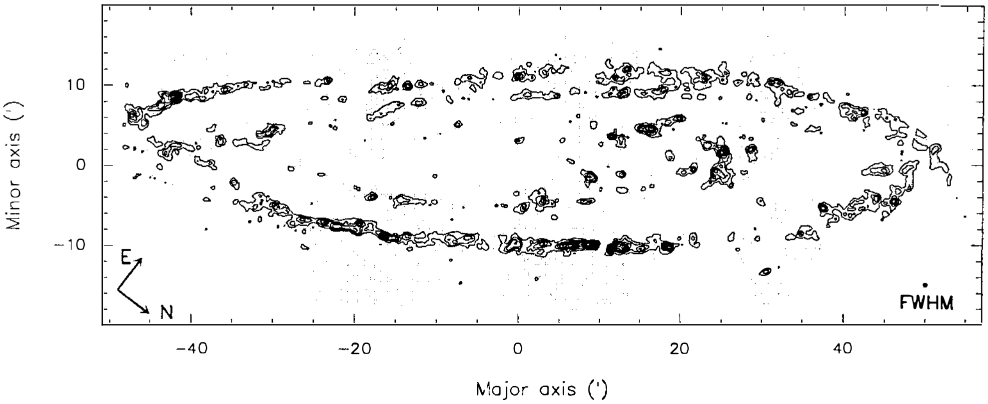

Figure 1: CO(1-0) integrated emission of the disk of M31 as mapped with the IRAM 30m telescope. Contours are every 2.5 K.km/s (main beam brightness temperature). The overall pattern draws a spiral arm structure.

- the spiral arms appear much thinner (< 400 pc) and better defined in CO than in HI.

- the arm to interarm contrast of the molecular gas is much higher than seen in atomic gas (up to 20 compared to $\sim 3-5$ for atomic gas). This implies that molecular clouds should be short-lived structures, forming and being destroyed rather quickly with timescales of $\sim 10^7$ yr.

- the CO emission is essentially weak towards the inner 3 kpc ($I_{CO(1-0)} < 0.4$ K.km/s).

- the total mass of molecular gas is estimated to be $2-3\ 10^8\ M_\odot$, that is to say $\sim 1/15^{th}$ of the mass of atomic gas in M31 (adopting the HI mass from Cram *et al.* 1980) or about $1/4^{th}$ of the total mass of molecular gas in the Milky Way (adopting the H_2 mass from Bronfman *et al.* 1988).

2.2 Molecular fraction

Using the HI (from WSRT, Brinks & Shane 1984) and CO maps smoothed to the same resolution (36"x 24", major axis to the North), one can produce the map of the molecular fraction f_{mol}, defined as:

$$f_{mol} = \frac{2\mathcal{N}(H_2)}{\mathcal{N}(HI) + 2\mathcal{N}(H_2)} = \frac{2\mathcal{X} I_{CO(1-0)}}{\mathcal{N}(HI) + 2\mathcal{X} I_{CO(1-0)}}$$

Here, we used a value of $\mathcal{X} = 2$. We stress that the HI might be overestimated compared to CO due to the contribution of the warp in the line of sight.

Fig.2 shows the resulting map of the molecular fraction and its dependance on galactocentric radius. f_{mol} decreases regularly from center to periphery (note that there is almost no HI emission at the center). In the inner 4 kpc disk, the gas is mostly molecular, while in the outer disk > 5 kpc, the atomic gas is dominant. As expected, the molecular fraction appears to be higher in the central part of the spiral arms, where the gas is more dense. This effect is particularly obvious in the bottom left part (SW arm).

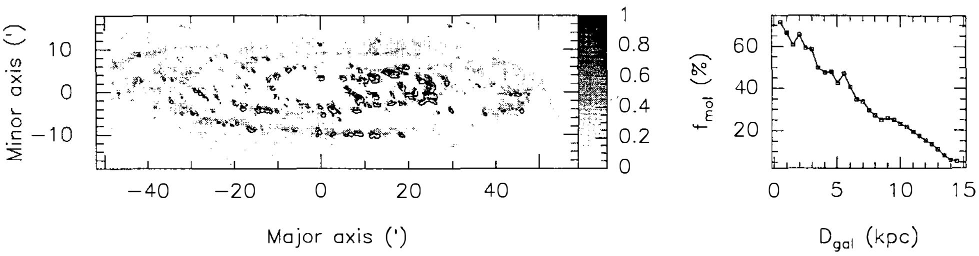

Figure 2: Molecular fraction f_{mol}. Left: Map of f_{mol} obtained from HI (Brinks & Shane 1984) and CO(1-0) (IRAM 30m) smoothed to the same resolution of 36" x 24". Contours at 50 %. Right: Molecular fraction f_{mol} as a function of galactocentric radius D_{gal}.

3 Physical properties and mass of the molecular clouds

We have decomposed the CO emission data cube into 3D Gaussian structures (position – velocity) using the *Gaussclump* algorithm (Stutzki *et al.* 1990, Kramer *et al.* 1998). For each decomposed cloud, we obtain the position, velocity, size, velocity dispersion and peak intensity, allowing us to study the statistical properties of these molecular clouds. In total, we decomposed:

- 300 clouds in the whole disk observed in CO(1-0) with the 30m at $\sim$ 90 pc resolution.
- 50 clouds in the smaller fields observed in CO(2-1) with the 30m at $\sim$ 45 pc resolution.
- 30 clouds observed in the different fields observed with PdBI at $<$ 15 pc resolution.

3.1 Size and velocity dispersions

Fig.3 (left side) presents histograms of the distribution in size and velocity dispersion of the Gaussian structures decomposed by *Gaussclump.* The size is defined as the width R_g in the Gaussian expression $I_{CO} \propto \exp(-r^2/R_g^2)$. R_g can be expressed as the FWHM of the Gaussian shape: $R_g = \frac{FWHM}{4\log 2}$. Typically, the size R_g of the complexes ranges from 50 to 150 pc. At higher angular resolution, those complexes can be resolved into several substructures of scale $\sim$ 10 pc. Velocity dispersions ΔV are FWHM. They mainly range from 4 to 10 km/s according to the size scale. We did not find any obvious relation between size and velocity width. From the ratio of size over line width, we derived dynamical timescales of $\sim 10^7$ yr.

3.2 Mass spectrum

Comparing the mass spectra of molecular clouds in different galaxies could be very important for understanding star formation mechanisms and feedback. Stars form from molecular clouds, so that one naturally expects that the properties of molecular clouds affect the star formation. On the other hand, massive stars certainly affect the molecular clouds in return. Thus, molecular clouds populations should differ between normal galaxies and starbursts.

From observations so far, it appears that the mass spectra of molecular clouds follow a power law distribution: $dN/dM = A\ M^{-\alpha}$. According to the value of the spectral index α, most of the mass is distributed in massive, if $\alpha < 2$ or small clouds, if $\alpha > 2$. Fig.3 (right side) shows the mass spectrum for the molecular complexes and clouds in M31. The masses are derived from the CO integrated intensity, using a conversion factor $\mathcal{X} = 1$. Changing this value does not affect the value of the spectral index, it just shifts the mass limits. To combine 30m and PdBI data, we have adjusted the relative normalization constant A.

Tab.1 lists the spectral indexes derived in the few galaxies where a sufficient number of

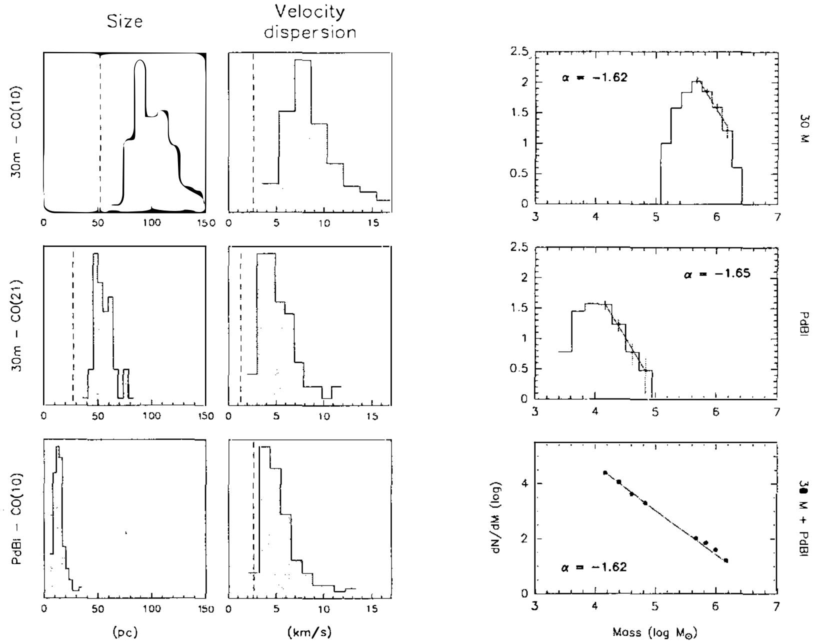

Figure 3: Properties of the molecular clouds and complexes in M31. Left: Histograms of the distributions in size and velocity dispersion of the clouds observed with the 30m in CO(1-0) (upper), CO(2-1) (middle) and with the PdBI in CO(1-0) (bottom). The vertical dashed line indicates the beam resolution and channel width. Right: Mass spectrum for the molecular complexes from the 30m map (upper), from the PdBI fields (middle) and both sets combined (bottom). Masses are estimated from CO(1-0) line integrated intensities.

molecular clouds have been identified allowing to establish a mass spectrum (one preferably needs $\sim$ 50 or more clouds). While results are very similar for the Milky Way and M31, with α = 1.5 and 1.6 respectively, the spectral indexes are higher for the Large Magellanic Cloud (1.9, but still < 2) and especially for M33, where the situation is reversed ($\alpha > 2$) and most of the molecular mass appears to be distributed in low mass clouds. In the case of the Antennae, which is a merging pair of galaxies undergoing starburst activity, there is a population of very massive supergiant molecular complexes with mass 2 or 3 orders of magnitude higher than in the Milky Way or M31.

Nevertheless, it is worth to notice that mass spectra may be biaised by sensitivity and/or resolution effects, preventing to detect low mass clouds. For interferometric observations also, missing short spacings can affect size and flux estimations, thus masses and spectral indexes.

3.3 Mass from virial theorem applied to individual clouds

Assuming a molecular cloud to be in a stationary state, isolated and self-gravitationally bound, one can apply the virial theorem, which states that:

$$2\mathcal{T} + \mathcal{W} = 0$$

where $\mathcal{T}$ is the kinetic energy of the cloud and $\mathcal{W}$ its gravitational energy. To derive this expression, magnetic fields and pressure effects are assumed to be negligible. Writing further with analytic expressions of $\mathcal{T}$ and $\mathcal{W}$, we obtain the widely used relationship between mass $\mathcal{M}_{vir}$, size R and velocity dispersion ΔV of the cloud:

	α	Mass range	References
M31	**1.6**	$\mathbf{10^4 - 10^6}$ $\mathbf{M_\odot}$	Muller 2003
MW	1.5	$10^5 - 10^6$ $M_\odot$	Solomon *et al.* 1987
MW	1.6 – 1.8	$10^{-4} - 10^4$ $M_\odot$	Kramer *et al.* 1998
M33	2.6 ± 0.3	$10^5 - 10^6$ $M_\odot$	Engargiola *et al.* 2003 & Blitz this conference
LMC	1.9 ± 0.1	$8\ 10^4 - 3\ 10^6$ $M_\odot$	Fukui *et al.* 2001 and this conference
Antennae	1.4 ± 0.1	$5\ 10^6 - 9\ 10^8$ $M_\odot$	Wilson *et al.* 2003

Table 1: Power law index values of mass spectra for different galaxies.

$$\mathcal{M}_{vir} = k\ R\ \Delta V^2$$

The constant k is fixed by the density distribution (McLaren *et al.* 1988 and Ungerechts *et al.* 2000) and can vary accordingly by a factor of ~ 2. In the case of a power law density distribution $\rho(r) \propto \mathrm{r}^{-n}$, one has to fix a truncation radius in order to let the mass converge (this value is completely arbitrary). For this reason also, indexes n are limited in the range $0 < \mathrm{n} < 3$. On the other hand, a Gaussian density distribution ($\rho(\mathrm{r}) \propto \exp(-r^2/R_g^2)$) naturally leads to a converging mass. Although power law density distribution coefficients are commonly used in the literature, we adopted here the choice of a Gaussian density distribution to calculate the virial mass $\mathcal{M}_{vir}$ as:

$$\mathcal{M}_{vir}(M_\odot) \ = \ 315\ \frac{R_g}{pc}\ \left(\frac{\Delta V}{km/s}\right)^2 \tag{1}$$

Using the clouds properties as decomposed by *Gaussclump*, we applied this virial analysis to M31 clouds in order to calibrate a value of the conversion factor. The results are presented in Fig.4, where we compare the mass derived form the virial theorem and the mass estimated from the CO integrated intensity.

This calibration of the conversion factor leads to values of $\mathcal{X}$ between 4 and 8, that is to say 2 to 4 times higher than the Galactic conversion factor. We stress out that the virial mass is usually overestimated, due to overestimation of sizes and velocity dispersions by lack of resolution. Adding to this, it is also possible that clouds are not virialized, again leading to overestimate the virial mass.

In the following section, we propose another method based on the virial theorem, giving conversion factors similar to the Galactic value.

3.4 Virial theorem applied to a system of gravitationally bound point-like particles

Besides the application of the virial theorem to individual clouds (§*3.3*), we have adopted a second approach, aiming to apply the virial theorem to a group of gravitationally bound clouds. Within one given molecular complex, resolved clouds are now considered as point like particles, their relative positions and velocities tracing the gravitational field and therefore the mass. This "ballistic" method is usually applied to groups of galaxies (see for example Heisler *et al.* 1985). In this picture, the virial theorem leads to the following expression:

$$\mathcal{M}_{dyn} \ = \ \frac{3\pi N}{2G} \frac{\sum_i \langle V_{zi}^2 \rangle}{\sum_{i<j} \left\langle \frac{1}{R_{\perp,ij}} \right\rangle} \tag{2}$$

where $\mathcal{M}_{dyn}$ is the total dynamical mass of the system, N the number of particles, $R_{\perp,ij}$ the relative distance between particle i and j (projected in the plane of the sky) and V_{zi} the radial velocity of the particle i (projected in the line of sight).

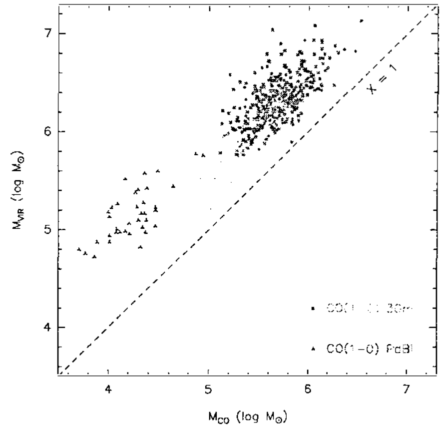

Figure 4: Calibration of the conversion factor using the virial theorem applied on individal clouds. This diagram shows for each cloud the virial mass (M_{vir}) plotted versus the mass derived from the CO integrated luminosity (M_{CO}). This latest is calculated assuming $\mathcal{X} = 1$, which is represented by the dashed line. Changing the value of the conversion factor is equivalent to shift all the points horizontally.

We have applied this formalism to 3 different molecular complexes, which have been observed with the PdBI at angular resolution of few arcseconds.

Complex	Position	D_{gal} (kpc)	R_g (pc)	ΔV (km/s)	$\mathcal{M}_{vir}$ (10^6 $M_\odot$)	$\mathcal{M}_{dyn}$ (10^6 $M_\odot$)	$\mathcal{X}$
D153	(-18' ; -4')	5.8	94	8.1	2.0	0.9	1
INT	(30' ; -4.5')	8.2	108	12.3	5.2	1.1	2.6
D84	(-16.5' ; -8.7')	9.8	94	16.4	8.0	3.7	2.6

Table 2: Results for 3 different complexes observed with the PdBI. Positions refer to the center of the galaxy, major axis and minor axis; D_{gal} is the galactocentric radius; R_g and ΔV correspond to the size and the velocity width of the complex respectively; $\mathcal{M}_{vir}$ is the virial mass, derived from Eq.1; $\mathcal{M}_{dyn}$ is the dynamical mass, derived from Eq.2; $\mathcal{X}$ is the conversion factor calibrated from the comparison of $\mathcal{M}_{dyn}$ and the mass estimated from the CO(1-0) integrated intensity (in units of 10^{20} cm^{-2} K^{-1} km^{-1} s).

- D84 is the brightest peak of emission in the molecular disk. It is quite compact, although its velocity dispersion is relatively high.

- D153 (Fig.5) appears as a very well isolated and compact complex and presents a narrow line profile ($\sim$ 8 km/s), therefore it apparently fullfills the application criteria of the virial theorem.

- INT is one of the rare interarm clouds that can be seen on the CO map. It also appears very isolated. One particular fact concerning this interarm complex is that the CO emission appears to be more diffuse than for the 2 other complexes discussed here.

Results are summarized in Tab.2. They are different from the value derived with the first application of the virial theorem as indicated in the previous paragraph. However, this method does not suffer from overestimating the sizes or velocity dispersions, and thus should give more reliable results. The application of this ballistic method to complexes at different galactocentric radii nicely offers the possiblity to probe the evolution of the conversion factor through the disk.

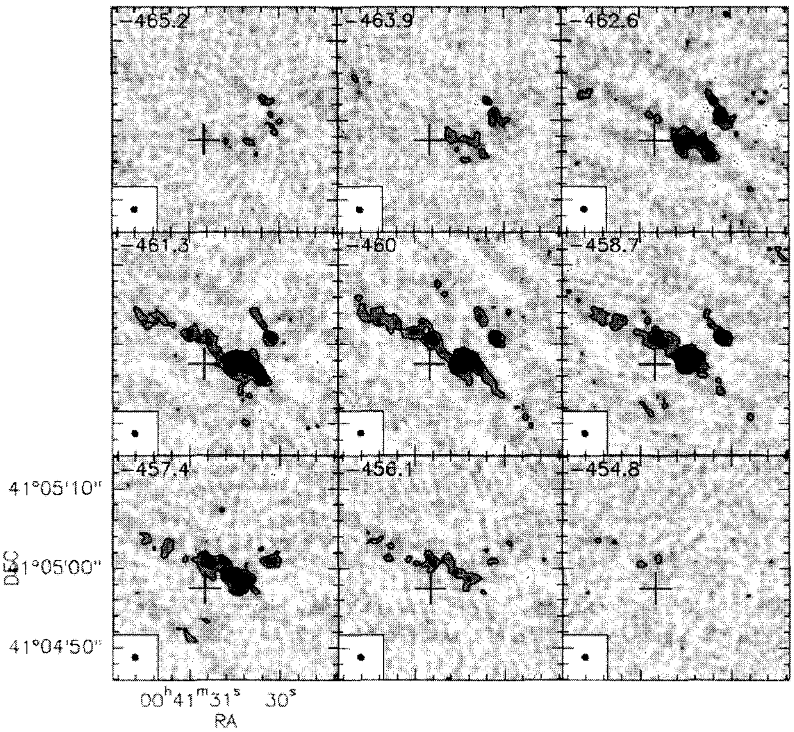

Figure 5: Channel map of the cloud D153, observed with the PdBI in the CO(2-1) line. The beam resolution is 0.8" - corresponding to $\sim$ 3 pc - and is indicated in the small square box for each channel. Contour levels are every 2 K or 50 mJy/beam.

4 Kinematics: multi-peaked profiles

The velocity field within the disk can be interpreted to first order by a flat rotation curve derived from HI (Brinks & Shane 1984). CO lines allow to trace the gas kinematic closer to the center, where the gas is mostly molecular.

In the case of M31, some spectra show multi-peaked profiles, spread over the whole disk of the galaxy (Fig.6). The typical interval between velocity components is 10 – 20 km/s but separations as wide as 40 km/s can be found. Most of the multi-peaked profiles ($\sim$ 90 %) are double peaks, while the few others show 3 or 4 distinct peaks.

The region D47 (Fig.7 for 30m spectra & Fig.8 for PdBI channel map) illustrates particularly well the situation: at the same position, molecular emission is found with velocity components separated by $\sim$ 40 km/s. One has to realize that in the case of the Milky Way, these observations would be interpreted as different molecular clouds in the line of sight, belonging to different spiral arms. This explanation is not consistent in the case of M31; we review the possible scenarios:

- it cannot be due to velocity gradient within the beam of the telescope since they are < 15 km/s / 30m beam. In the case of D47 observed with the PdBI (Fig.8), one also can see several velocity components, whereas the velocity gradient in the beam is minimal.

- in HI, such profiles are imputed to the warp, but the corresponding CO emission is not

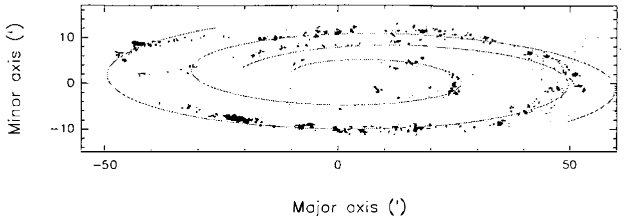

Figure 6: Distribution of multi peaked profiles over the disk of M31. All the points correspond to a 30m spectrum showing at least a double peaked structure. The spiral pattern is the fit proposed by Nieten *et al.* 2004.

detected: either the molecular disk does not extend to large galactocentric radii or the CO emission is below our sensitivity limit. Nevertheless, intensities of multiple peaks are comparable, whereas we would expect weaker emission form presumably outer disk components.

- positions of multi-peaked profiles are not tightly correlated with star forming regions or OB associations, although the expansion of HII regions could account for such motions of the gas.

- the effect could be due to the thickness of the molecular disk, (a 100 pc thick disk could account for $\sim$ 10 km/s velocity difference due to projection effects). Indeed, Dame & Thaddeus (1994) detected emission up to 200 pc above the Galactic plane but the CO emission is 30 times weaker than within the inner plane.

- finally, density waves through the disk could be responsible for this fact. According to this theory (Lin & Shu 1964) aiming to explain spiral structures, a density wave compresses the gas, forming spiral arms with enhanced density, and leading to large scale star formation within the disk. Close to the spiral arms, the gas may have non circular streaming motions and could be shocked. In the case of M31, the molecular clouds seems to be *accelerated* compared to the HI velocity field, providing good evidence for this explanation.

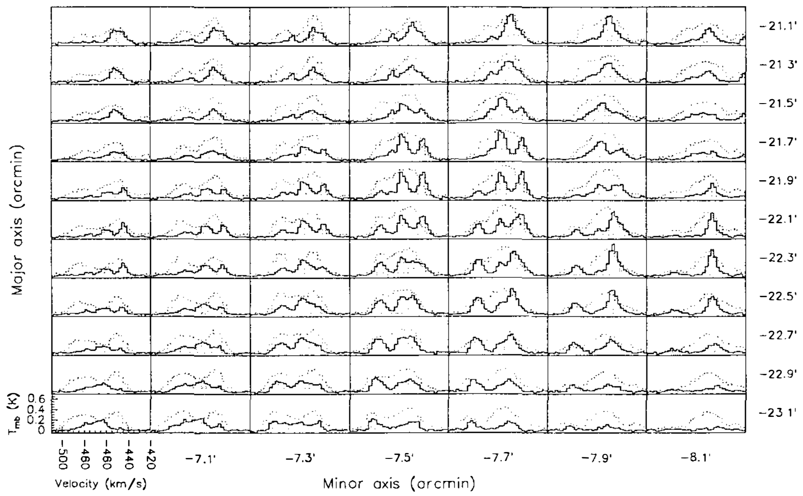

Figure 7: Multi peaked profiles around the region D47. The filled spectra correspond to the CO(1-0) line observed with the IRAM 30m, while the dashed spectra correspond to HI from WSRT (Brinks & Shane 1984).

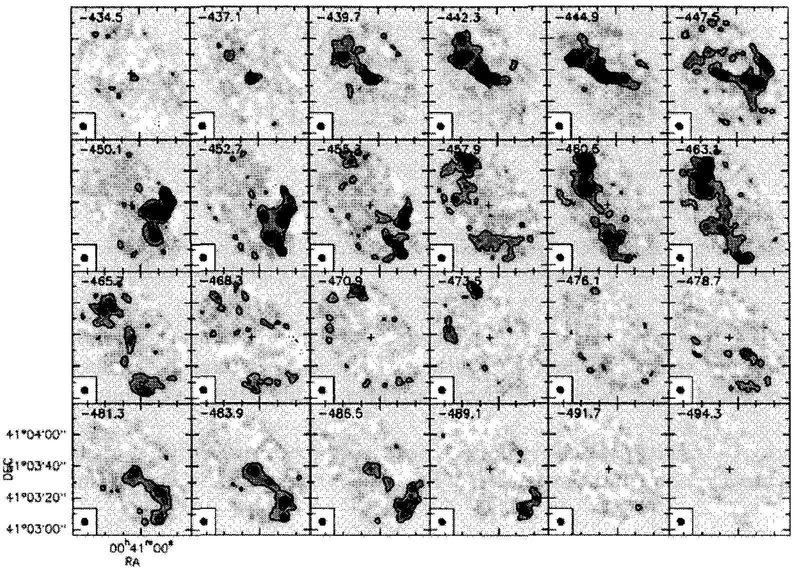

Figure 8: Channel map of the region D47, observed with the PdBI in the CO(1-0) line with a 2 fields mosaic. The beam resolution is 4.48" x 3.85" (PA=-142 °), one velocity channel corresponds to 2.6 km/s. Contour levels are every 100 mJy/beam or 0.54 K. The short spacings from the 30m have been included. One can see multi peaks emission at the very center of the field, with a velocity interval of about 40 km/s.

Conclusion

We present the distribution of the molecular gas in the disk of the Andromeda galaxy. The physical properties of the molecular clouds are discussed and they appear to be very similar to the Galactic molecular clouds. We propose two different methods based on the virial theorem to estimate the mass of the molecular gas. The first approach is based on the application of the virial theorem to individual clouds and complexes. It may suffer from resolution effects, therefore overestimating the virial masses. The second method lies on the application of the virial theorem to a complex of resolved clouds, which we consider as point-like particles, tracing the dynamical mass of the whole complex. This last method allows us to derive conversion factors $\mathcal{X} \sim 1 - 2.6$, rather similar to the Galactic value. M31 molecular clouds follow a power law mass spectrum, with spectral index $\alpha = 1.6$, indicating that most of the molecular mass is actually distributed in massive clouds. Finally we adress the problem presented by multi-peaked profiles in CO spectra, which could be due either to the thickness of the molecular disk, to the expansion of HII regions or to streaming motions induced by a density wave.

References

1. Brinks E. & Shane W.W. 1984, A&A Supp. 55, 179
2. Bronfman L., Cohen R.S., Alvarez H., May J. & Thaddeus P. 1988 ApJ 324, 248
3. Cram T.R., Roberts M.S. & Whitehurst R.N. 1980 A&A Supp. 40, 215
4. Dame T.M., Hartmann D. & Thaddeus P. 2001 ApJ 547, 792
5. Dame T.M. & Thaddeus P. 1994 ApJ 436, L173
6. Digel S.W., Hunter S.D. & Mukherjee R. 1995 ApJ 441, 270
7. Engargiola G., Plambeck R.L., Rosolowsky E. & Blitz L. 2003 ApJ Supp. 149, 343

8. Fukui Y., Mizuno N., Yamaguchi R., Mizuno A., & Onishi T. 2001 PASJ 53, 41
9. Guélin M., Muller S., Nieten C. *et al.* 2004 in "The dense ISM in galaxies", Springer-Verlag, Eds. Pfalzner S. *et al.* p.121
10. Guélin M., Nieten C., Neininger N., Muller S., Lucas R., Ungerechts H. & Wielebinski R. 2000 in "The interstellar medium in M31 and M33", Proceedings 232. WE-Heraeus Seminar, Bad Honnef, Germany p.15
11. Heisler J., Tremaine S. & Bahcall J.N. 1985 ApJ 298, 8
12. Kramer C., Stutzki J., Rohrig R. & Corneliussen U. 1998 A&A 329, 249
13. Lin C.C. & Shu F.H. 1964 ApJ 140, 646
14. MacLaren I., Richardson K.M. & Wolfendale A.W. 1988 ApJ 333, 821
15. Maloney P. & Black J.H., 1988, ApJ, 325, 389
16. Muller S. 2003 PhD Thesis, Grenoble
17. Neininger N., Guélin M., Ungerechts H., Lucas R. & Wielebinski R. 1998 Nature 395, 871
18. Nieten *et al.* 2004 submitted to A&A
19. Sanders D. B., Solomon P. M. & Scoville, N. Z. 1984 ApJ 276, 182
20. Solomon P.M., Rivolo A.R. & Yahil A. 1987 ApJ 319, 730
21. Strong A., Bloemen J., Dame, T., Grenier I., Hermsen W., Lebrun F., Nyman L.-A., Pollock A. & Thaddeus P. 1988 A&A 201, 1
22. Strong A. & Mattox, J. 1996 A&A 308, 21
23. Stutzki J. & R.Güsten R. 1990 ApJ 356, 513
24. Ungerechts H., Umbanhowar P. & Thaddeus P. 2000 ApJ 537, 221
25. Wilson C.D., Scoville N., Madden S.C. & Charmandaris V. 2003 ApJ 599, 1049

Acknowledgments

We would like to thank our colleagues at the Pico Veleta and Plateau de Burė observatories who make this work possible. Part of this study was made in the frame of SM's PhD thesis at IRAM Grenoble. SM wishes to thank all the people there for their kind help and encouragement, with a special mention to Bure's staff. SM also deeply thank the organizers of this conference for giving the opportunity to present this work.

On the behalf of the Chairman…

GIANT MOLECULAR CLOUDS AND STAR FORMATION IN THE MAGELLANIC SYSTEM

Y. FUKUI

Department of Astrophysics, Nagoya University, Chikusa-ku, Nagoya 464-8602, Japan

It is widely accepted that almost all giant molecular clouds are forming massive stars actively as evidenced by observations of the solar vicinity. New mm-wave CO observations of the Large Magellanic Cloud(=LMC) however have revealed that nearly 40 % of the giant molecular clouds in the LMC show no signs of massive star formation, remaining starless apparently. This suggests that the timescale of star formation is considerably longer in the LMC than that in the Milky Way. We propose a hypothesis that the lower heavy element abundance in the LMC is the primary cause of this retarded star formation via higher inonization degree and lower molecular cooling. We also suggest a possible connection of the retarded star formation to the formation of populous clusters="mini globulars".

keywords :galaxies: Local Group — galaxies: Magellanic Clouds — galaxies: star clusters — globular clusters: general — ISM: molecules — magnetic fields

1 Introduction

Most of the stars are formed in giant molecular clouds (="GMCs" hereafter). It is therefore of vital importance to understand star formation processes in GMCs in our continuing efforts to elucidate galaxy evolution (e.g., Elmegreen 2002). It has been widely accepted that almost all the giant molecular clouds are forming massive stars actively as indicated by accompanying HII regions and/or OB associations in addition to a number of young low-mass stars (Dame et al. 1987; Blitz 1991 and references therein). The Orion A cloud is one of the best examples of this kind(e.g., Genzel & Stutzki 1989) and there are many more star-forming GMCs including M17(e.g., Lada 1976), Orion B(e.g., Lada, Bally, & Stark 1991; Aoyama et al. 2001), Rossete Nebula(e.g., Blitz et al. 1986), W3/W4/W5(e.g., Heyer & Terebey 1998), η Carinae(e.g., de Graauw et al. 1981; Grabelsky et al. 1988) etc. There is only one known GMC which lacks signs of massive star formation in the solar neighbourhood, i.e., the Maddalena's cloud (Maddalena

& Thaddeus 1985) and the reason for this may be either that it is at a very young stage prior to massive star formation (Maddalena & Thaddeus 1985) or that it is in a late stage after active star formation (Lee, Snell, & Dickman 1994). Our current understanding is thus that GMCs consist almost exclusively of a single population, i.e., star-forming GMCs.

It is here to be noted that spatially resolved GMCs studied so far in terms of star formation are limited to the solar vicinity, within a few kpcs of the sun at most, because of heavy contamination and/or obscuration in the galactic disk. In order to better understand GMCs and star formation, we should undoubtedly extend a survey for GMCs into nearby galaxies.

CO observations toward the Local Group galaxies have been mostly limited in the northern sky (e.g., Tacconi & Young 1987; Wilson & Scoville 1990; Ohta et al. 1992; Ohta et al. 1993; Wilson 1995; Neininger et al. 1998; Taylor, Kobulnicky, & Skillman 1998; Loinard et al. 1999), although spatial resolutions and sensitivity high enough to resolve GMCs are achieved only with the largest mm-wave dishes or interferometers for the M31 group at $\sim$ 800 kpc (Neininger et al. 1998; Engargiola et al. 2003). This large distance however rearn how star formation is taking place in the individual GMCs (e.g., Engargiola et al. 2003 for M33).

In the southern sky, SEST was used to observe CO in the Magellanic Clouds extensively, and several % of the galaxy were mapped for GMCs (e.g., Johansson et al. 1998). A significant progress has been achieved by a CO $J=1$–0 survey covering fully the Large Magellanic Cloud (= LMC) made with a 4m mm/sub-mm wave telescope NANTEN. This has provided an opportunity to study a flux-limited sample of 55 GMCs at a spatial resolution of 40 pc, well below a typical size of a GMC, ~100 pc (Fukui et al. 1999, Paper I hereafter; Mizuno et al. 2001b). Intriguingly enough, the authors showed in Paper I that there are a significant fraction of starless GMCs, more than one fourth, that exhibit no sign of massive star formation based on a spatial correlation of GMCs with HII regions and young stellar clusters in the LMC. If this is correct, the properties of the GMCs may be quite different in terms of star formation between the Milky Way and the LMC. The CO survey in Paper I has a sensitivity equivalent to molecular column density of 2.7×10^{21} cm^{-2} where an X factor, 9×10^{20} cm^{-2} [K km s^{-1}]$^{-1}$, is adopted. We should note that this relatively high column density limit may lead to underestimate the cloud size, resulting in missing signs of star formation. It is therefore desirable to improve the sensitivity of CO observations equivalent to molecular column density as low as $\sim 10^{21}$ cm^{-2}, similar to the studies of Galactic GMCs (Dame, Hartmann, & Thaddeus 2001), in order to corroborate "starless GMC".

We, NANTEN team, have performed newly a CO survey of the LMC more sensitive than that in Paper I. In this contribution we present and discuss these new CO results and their implications on the evolution of GMCs.

2 New CO survey of the LMC

The LMC is the nearest neighbour to our own and is actively forming stars as populous clusters (Hodge 1960) or OB associations as well as HII regions. It is the most suitable target to make a detailed comprehensive study of GMCs, since it is located at 50 kpc from the Sun, 16 times closer than the M31 group, and is nearly face-on, allowing us to unambiguously identify young objects associated with GMCs. The new survey in the 2.6mm $J = 1$–0 rotational emission of CO has used NANTEN, a 4m mm/sub-mm wave telescope located in Las Campanas, Chile, and has achieved a sensitivity by a factor of $\sim$ 3 better than that in Paper I, equivalent to $N(H_2)\sim 1.0 \times 10^{21}$ cm^{-2} (see Fukui et al. 2001 & Yamaguchi et al. 2001a for more details of observations). It covered the whole extent of the LMC and has revealed distributions of 270 GMCs with 29000 observed positions (Figure 1). I have chosen 168 GMCs among the 270, for which reliable estimates of physical quantities are available. The mass of the 168 GMCs ranges from $8 \times 10^4 M_\odot$ to $3 \times 10^6 M_\odot$ (Fukui et al. 2001).

3 Star formation in GMCs

3.1 Starless GMCs as a common population

We have used the present sample of 168 GMCs to learn how star formation is taking place by comparing the GMC distributions with optical signposts of star formation including young stellar clusters (Bica et al. 1996) and HII regions (Davies, Elliott, & Meaburn 1976, Kennicutt & Hodge 1986). We note that the detection limit of HII regions is quite low, $L(\mathrm{H}\alpha) \sim 2 \times 10^{36}$ergs s^{-1}, corresponding to one fourth of that of Orion Nebula. This allows reliable assignments of the optical signposts to individual GMCs as already demonstrated in Paper I and by Yamaguchi et al. (2001b).

Figure 2 shows the distributions of projected separations of HII regions and stellar clusters from the nearest GMC. This clearly indicates that the youngest clusters of an age smaller than 10 Myrs, i.e., SWB0 (Bica et al. 1996), and the HII regions are sharply peaked within 100 pc of a GMC exhibiting strong spatial correlations. This provides enough evidence for the GMCs as natal clouds of these young objects. On the other hand, the older clusters, SWB1($\tau > 10$ Myr) or later, show much weaker or no correlation, as is consistent with the rapid cloud dissipation after cluster formation (Paper I).

We shall identify a GMC to be starless if there are no HII regions or youngest clusters (SWB0) within the lowest contour of the NANTEN survey. As a result, we have identified 64 GMCs to be starless (see Table 1).

Table 1: Association of GMCs with young clusters and HII regions

GMC Population	Association	Number of GMCs (ratio %)			
		LMC		SMC[a]	
I	No association	64	(38 %)	13	(50 %)
IIa	Only with HII regions	66	(39 %)		
IIb	With HII regions and clusters[b]	38[c]	(23 %)	13	(50 %)
	Total	168		26	

a GMCs with virial masses ranging from $6 \times 10^4 M_\odot$ to $9 \times 10^5 M_\odot$ observed by NANTEN (Mizuno et al. 2001a).

b Those clasified as SWB 0 by Bica et al. (1996) are considered here.

c One of the clouds is associated with a young cluster, SL 785 (SWB 0), but with no HII regions cataloged. Nevertheless, a careful examination of DSS (R) and ESO (R) platesshows a compact nebula toward the cloud.

In case of the Milky Way, all the HII regions associated with GMCs are located well inside the CO contours of GMCs (see e.g, the Rosette GMC in Blitz 1991). We are confident that the present way is to give a secure lower limit to the fraction of starless GMCs, since the beam-size effect tends to make the cloud area greater than seen at higher resolution.

It was shown in Paper I that the GMCs are classified into three groups based on a sample of 55 GMCs whose mass ranges from $2 \times 10^5 M_\odot$ to $3 \times 10^6 M_\odot$; 1) starless GMCs, 2) those with small HII regions whose Hα luminosity is less than 10^{37} erg s^{-1}, and 3) those with stellar clusters and large HII regions of Hα luminosity greater than 10^{37} erg s^{-1}. We find that the present results confirm the validity of this classification. We have also confirmed that there is no significant difference in physical parameters including mass, CO linewidth, and size among the three groups as is consistent with Paper I.

We shall hereafter use *GMC Population* defined as follows; GMC Population I stands for "starless GMCs", and GMC Population II stands for "massive-star-forming GMCs". GMC population II may be further divided into two, GMC Population IIa = with only HII regions, and GMC Population IIb = with HII regions and clusters. Table 1 provides a summary of these. The fraction of GMC Population I is 38 %, while those of GMC Populations IIa and IIb are 39 % and 23 %, respectively. It is also shown in Table 1 that in the Small Magellanic Cloud (=SMC) the fraction of GMC Population I is even higher, ~ 50 % (Mizuno et al. 2001a). Figure 3 shows CO distributions of typical GMCs of the three Populations superposed on optical pictures.

3.2 Are they really starless?

We first examine if the starless GMCs are not an artifact.

In the Milky Way, almost all the GMCs in the solar neighborhood, within ~ 2 kpc, are known to be forming massive stars. This indicates that any visual extinction in a GMC is not able to veil HII regions or young stars. The reason for this is rather obvious; first, the HII regions create a cavity into the natal GMCs, a well known phenomenon referred to as "Champagne model" (e.g., Tenorio-Tagle 1979). Second, GMCs are highly filamentary as seen in Orion A and others (e.g., Bally et al. 1987; Nagahama et al. 1998) and such a distribution favors disclosing HII regions toward any direction.

A similar situation likely holds in the LMC that is face-on, 1)because the GMCs in the LMC also show filamentary distributions at higher resolutions (e.g., Israel et al. 2003), and 2)because the cavity should be more easily formed due to the less UV extinction (Koornneef 1982) combined with higher UV intensity (Israel et al. 1986) in the LMC than in the Milky Way.

We therefore conclude that the starless GMCs are not an artifact of observations and that a significant portion of the GMCs, ~ 40 %, in the LMC are not forming massive stars.

4 Evolution of the GMCs

In Paper I, the authors estimated the lifetime of a GMC as ~ 10 Myrs by using the flux limited sample of 55 GMCs as well as clusters at a more evolved phase represented by highly-dissipated smaller cloudlets surrounding clusters (see Yamaguchi et al. 2001b).

An evolutionary scheme of GMCs has been depicted elsewhere for the Milky Way (see e.g., Figure 1 in Lada 1987), where the cloud evolution begins with a stage with only low-mass star formation followed by active formation of massive stars as manifested by HII regions and OB associations. What is actually observed in the solar vicinity is that the stage with only low-mass-star formation is very rare, with only one known possible case, Maddalena's cloud. This indicates the GMCs in the solar vicinity has been continuously forming massive stars almost immediately since its formation (Blitz 1991).

This rapid formation of massive stars in the Milky Way is in a marked contrast with the starless GMCs that are so common in the LMC. By adopting the lifetime of GMC, ~10 Myrs, in Paper I, I estimate the starless stage has a time scale of ~ 4 Myrs as 40 % of 10 Myrs.

5 Discussion

I discuss the implications of starless GMCs in the LMC.

An idea that immediately occurs to explain starless GMCs is that the timescale in star formation and/or cloud contraction is significantly longer in the LMC than in the Milky Way. I propose here that a higher ionization degree in a GMC is the primary cause of the retarded star formation in the LMC.

The ionization degree in a molecular cloud is likely determined by the far-ultraviolet (FUV) photons of stellar radiation fields (McKee 1989; Nozawa et al. 1991). In the LMC, the FUV flux is several times higher (Israel 1986) and the dust extinction is smaller by a factor of 3–4 for a given gaseous column density (Koornneef 1982). Thus, the ionization degree in molecular gas should become roughly ten times higher. Since the time scale of the diffusion of magnetic field is propotional to the ionization degree (Spitzer 1978), it seems likely that contraction of cloud is effectively retarded by magnetic field. In addition, the cooling rate via molecular and dust emission is likely smaller by a factor of 3–4 in the LMC than in the Milkey Way, further helping to slow down star formation. Higher ionization degree and smaller cooling rate are basically the consequences of lower metalicity in the LMC (Dufour 1984) and are likely responsible for the retarded star formation.

We may be able to test this hypothesis by observing GMCs in other regions with different metalicities to see if the timescale of massive star formation is dependent on metalicity. At the moment, one of the testable galaxies is the SMC which has ten times lower metalicity than the Milky Way (e.g., Dufour 1984). Table 1 indeed suggests that there may be more starless GMCs in the SMC, while the total star formation rate is much less compared to the LMC, making the statistics poorer in the SMC. Another possibility is M 33 whose metalicity is similar to the Milky Way. In this spiral galaxy GMC Population II seems dominant ($\geq$ 75 %), while the existence of GMC Population I is not yet confirmed (Engargiola et al. 2003). We need to wait new instruments with even higher resolution at mm/sub-mm wavelengths including ALMA which will allow us to reach resolved GMCs in more distant galaxies.

Another region of interest is the Ophiuchus region (not the ρ Oph main cloud alone but the more extended region in the north, see Nozawa et al. 1991) in the Milky Way where the FUV radiation is roughly ten times higher than the average due to the Sco OB2 association (Figure 3). According to Nozawa et al. (1991), the molecular complex in the Oph north region, consisting of 23 ^{13}CO clouds, has a total mass of 4000 $M_{\odot}$, which is similar to that of the Taurus cloud complex (Mizuno et al.1995). Star formation in these clouds is, however, very rare and the star formation efficiency defined as the ratio of the stellar mass divided by the total system mass is less than $\sim$0.3 %, much smaller than that in Taurus or the average value of the Galactic disk molecular clouds, a few %. On the other hand, the ρ Oph main cloud having a total extinction of 50 mag is characterized by an unusually high star formation efficiency greater than $\sim$ 20 % , and a gravitationally bound, dense stellar cluster of $\sim$ 1000 stars may be forming there (e.g., Wilking & Lada 1983).

I suggest that the Ophiuchus region may represent a miniature of the LMC; the inoization degree is significantly higher than the average in the Milky Way due to the massive stars in Sco OB2 and most of the clouds having typical extinction of several mag are not allowed to form stars quickly owing to the higher ionization degree. But, once a cloud can accumulate molecular gas to achieve an extinction high enough to effectively shield FUV radiation, star formation can occur at a high efficiency. It is only the ρ Oph main cloud that is forming a star cluster unusually actively and this cloud exhibits the highest extinction and highest concentration of the molecular gas within a volume of $\sim$ 1 pc radius in the Ophichus region. It is possible to analogize that the starless GMCs and populous clusters in the LMC correspond to the clouds of low star formation and the ρ Oph cluster, respectively, in the Ophiuchus region. The GMCs in the LMC having less metallicity than in the Milky Way are than expected to exhibit the same trend at a more enhanced level of forming even richer stellar clusters as is seen in the LMC.

An alternative idea to explain starless GMC is that the GMCs in the LMC are of very recent formation, a situation possibly similar to the Maddalena's clouds. It is well known that the LMC has a number of supershells expanding to accumulate the interstellar matter (Meaburn 1980; Oey 1996; Kim et al. 1999). Yamaguchi et al. (2001a) investigated the possible correlation between GMCs and supergiant shells and conclude that one third of GMCs may be located towards the shell boundaries, suggesting that a significant number of GMCs may have been formed under the triggering by expanding shells. The spatial distribution of the starless GMCs are however fairly random, showing little correlation with supergiant shells. It seems therefore more likely that the difference in the heavy element abundance by a factor of 3–4 is the primary cause of the retarded star formation in the LMC.

Finally, I shall comment on a possible link between starless GMCs and the populous stellar clusters, "mini-globulars" including $\sim$ 10000 stars in the LMC (Hodge 1960); detailed plots of the number of stars in clusters are found in Kumai, Basu, & Fujimoto (1993) and Hunter et al. (2003). It is tempting to speculate that populous clusters and the starless GMCs are intimatedly linked with each other because GMCs are formation sites of populous clusters (Paper I). A possible explanation is that the longer timescale of star formation allows the formation of proto-cluster molecular condensations of a few pc radius as massive as $10^5 M_{\odot}$, which can lead to form populous clusters. This will never happen in the Milky Way because of the rapid star formation immediately after formation of proto-cluster molecular condensations (referred to as "hot cores") having mass of $10^3 M_{\odot}$ (e.g., Shirley et al. 2003). Massive and compact proto-cluster molecular condensations of $10^5 M_{\odot}$ should be detectable with ALMA within several years.

6 acknowledgments

The NANTEN project is based on a mutual agreement between Nagoya University and the Carnegie Institution of Washington (CIW). I greatly appreciate the hospitality of all the staff members of the Las Campanas Observatory of CIW. I am thankful to many Japanese public donors and companies who contributed to the realization of the project. This work is financially supported in part by a Grant-in-Aid for Scientific Research from the Ministry of Education, Culture, Sports, Science and Technology of Japan (No. 15071203) and from JSPS (No. 14102003).

1. Aoyama, H., Mizuno, N., Yamamoto, H., Onishi, T., Mizuno, A., & Fukui, Y. 2001, PASJ, 53, 1053
2. Bally, J., Langer, W. D., Stark, A. A., & Wilson, R. W. 1987, ApJ, 312, L45
3. Bica, E., Claria, J. J., Dottori, H., Santos, J. F. C. Jr., & Piatti, A. E., 1996, ApJS, 102, 57
4. Blitz, L. 1991, in The Physics of Star Formation and Early Stellar Evolution, ed. C. J. Lada & N. D. Kylafis (Dordrecht: Kluwer), 3
5. Blitz, L. & Stark, A. A. 1986, APJ, 300, L89
6. Dame, T. M., Ungerechts, H., Cohen, R. S., de Geus, E. J., Grenier, I. A., May, J., Murphy, D. C., Nyman, L. A., & Thaddeus, P. 1987, APJ, 322, 706
7. Dame, T., M., Hartmann, D., & Thaddeus, APJ, 2001, 547, 792
8. Davies, R. D., Elliott, K. H., & Meaburn, J. 1976, MmRAS, 81, 89
9. de Graauw, T., Lidholm, S., Fitton, B., Beckman, J., Israel, F. P., Nieuwenhuijzen, H., Vermue, J. 1981, A&A, 102, 257
10. Dufour, R. J. 1984, in Structure and Evolution of the Magellanic Clouds, ed. S. van den Bergh & K. S. de Boer (Dordrecht: Reidel Publishing Co.) 353
11. Elmegreen, B. G. 2002, ApJ, 577, 206
12. Engargiola, G., Plambeck, R. L, Rosolowsky, E., & Blitz, L. 2003 ApJS, 149, 343 Fukui, Y. 2002, in Modes of Star
13. Fukui, Y., Mizuno, N., Yamaguchi, R., Mizuno, A., Onishi, T., Ogawa, H., Yonekura, Y., Kawamura, A., Tachihara, K., Xiao, K., et al. 1999, PASJ, 51, 745 (Paper I)
14. Fukui, Y., Mizuno, N., Yamaguchi, R., Mizuno, A., Onishi, T. 2001, PASJ, 53L, 41
15. Genzel. R, & Stutzki, J. 1989, ARA&A, 27, 41
16. Grabelsky, D. A., Cohen, R. S., Bronfman, L., & Thaddeus, P. 1988, ApJ, 331, 181

17. Heyer, M. & Terebey, S. 1998, ApJ, 502, 265
18. Hodge, P. 1960, ApJ, 131, 351
19. Hunter, D. A., Elmegreen, B. G., Dupuy, T. J., & Mortonson, M. 2003, AJ, 126, 1836
20. Israel, F. P., de Graauw, Th., van de Stadt, H., & de Vries, C. P. 1986, ApJ, 303, 186
21. Israel, F. P., Johhansson, L. E. B, Rubio, M., Garay, G., de Graauw, Th., Booth, R. S., Boulanger, F., Kutner, M. L., Lequeux, J., Nyman, L.-A. 2003, A&A, 406, 817
22. Johansson, L. E. B., Greve, A., Booth, R. S., Boulanger, F., Garay, G., Graauw, Th. de, Israel, F. P., Kutner, M. L., Lequeux, J., Murphy, D. C., Nyman, L.-A., & Rubio, M. 1998, A&A, 331, 857
23. Kennicutt, R. C., Jr., & Hodge, P. W. 1986, ApJ, 306, 130
24. Kim, S., Dopita, M. A., Staveley-Smith, L., & Bessel, M. S. 1999, AJ, 118, 2797
25. Koornneef, J. 1982, A&A, 107, 247
26. Kumai, Y. Basu, B., & Fujimoto, M. 1993, ApJ, 404, 144
27. Lada, C. J. 1976, ApJS, 32, 603
28. Lada, C. J. 1987, in Star Forming Regions, IAUS 115, (Dordrecht: D. Reidel Publishing Co), 1
29. Lada, E. A., Bally, J., & Stark, A. A. 1991, ApJ, 368, 432
30. Lee, Y., Snell, R. L., & Dickman, R. D. 1994, ApJ, 432, 167
31. Loinard, L., Dame, T., Heyer, M. H., Lequeux, J., & Thaddeus, P. 1999, A&A, 351, 1087
32. McKee, C. F. 1989, ApJ, 345, 782
33. Maddalena, R. J. & Thaddeus, P. 1985, ApJ, 294, 231
34. Meaburn, J. 1980, MNRAS, 192, 365
35. Mizuno,A., Onishi, T., Yonekura, Y., Nagahama, T., Ogawa, H., Fukui, Y. 1995, ApJ, 445, L161
36. Mizuno, N., Rubio, M., Mizuno, A., Yamaguchi, R., Onishi, T., Fukui, Y. 2001a, PASJ, 53, L45
37. Mizuno, N., Yamaguchi, R., Mizuno, A., Rubio, M., Abe, R., Saito, H., Onishi, T., Yonekura, Y., Yamaguchi, N., Ogawa, H., Fukui, Y. 2001b, PASJ, 53, 971
38. Nagahama, T., Mizuno, A., Ogawa, H., Fukui, Y. 1998, AJ, 116, 336
39. Neininger, N., Guelin, M., Ungerechts, H., Lucas, R., & Wieleninski, R. 1998, Nature, 395, 871
40. Nozawa, G., Mizuno, A., Teshima, Y., Ogawa, H., & Fukui, Y. 1991, ApJS, 77, 647
41. Oey, M. S. 1996, ApJ, 467, 666
42. Ohta, K., Sasaki, M., Yamada, T., Saito, M., & Nakai, N. 1992, PASJ, 44, 585
43. Ohta, K., Tomita, A., Saito, M., Sasaki, M., & Nakai, N. 1993, PASJ, 45L, 21
44. Shirley, Y. L., Evans, N. J. II, Young, K. E., Knez, C., & Jaffe, D. T. 2003, ApJs, 149, 375
45. Spitzer, L. Jr.1978, Physical Processes in the Interstellar Medium (New York: Wiley Interscience)
46. Tacconi, L. J., & Young, J. S. 1987, ApJ, 322, 681
47. Taylor, C. L., Kobulnicky, H., A., & Slillman, E. D. 1998, AJ, 116, 2746
48. Tenorio-Tagle, G. 1979, A&A, 71, 59
49. Wilking, B., A., Lada, C., J. 1983, ApJ, 274, 698
50. Wilson, C. D. 1995, ApJ, 448, L97
51. Wilson, C. D., & Scoville, N. 1990, ApJ, 363, 435
52. Yamaguchi, R., Mizuno, N., Onishi, T., Mizuno, A., Fukui, Y. 2001a, PASJ, 53, 959
53. Yamaguchi, R., Mizuno, N., Mizuno, A., Rubio, M., Abe, R.,Saito, H., Moriguchi, Y., Matsunaga, L., Onishi, T., Yonekura, Y., Fukui, Y. 2001b, PASJ, 53, 985

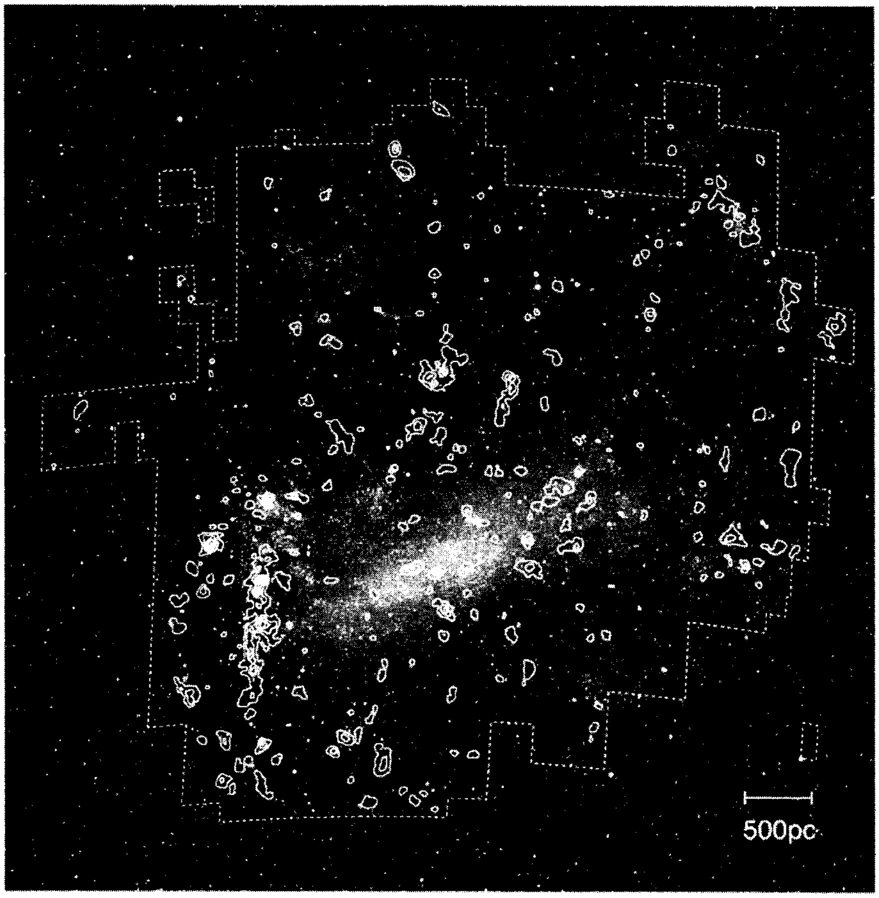

Figure 1: CO (J = 1–0) velocity-integrated intensity map of the LMC superposed on an optical image. The contour levels begin at 1.2 K km s^{-1} (= 3σ noise level), and increase in steps of 2.4 K km s^{-1}. The broken lines indicate the observed area.

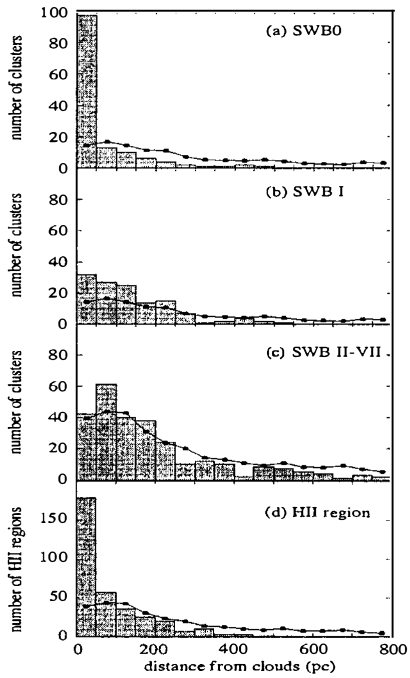

Figure 2: Histograms of the projected distance of the clusters with the age of (a) $\tau < 10$ Myr (SWB 0), (b) 10 Myr $< \tau < 30$ Myr (SWB I), and (c) 30 Myr $< \tau$ (SWB II to SWB VII) (Bica et al. 1996) to the nearest GMCs. The bottom pannel (d) shows the projected distance of the HII regions (Davies et al. 1976) to the GMCs. The lines represent the frequency distribution of the clusters or HII regions if the same number of objects are distributed at random, respectively.

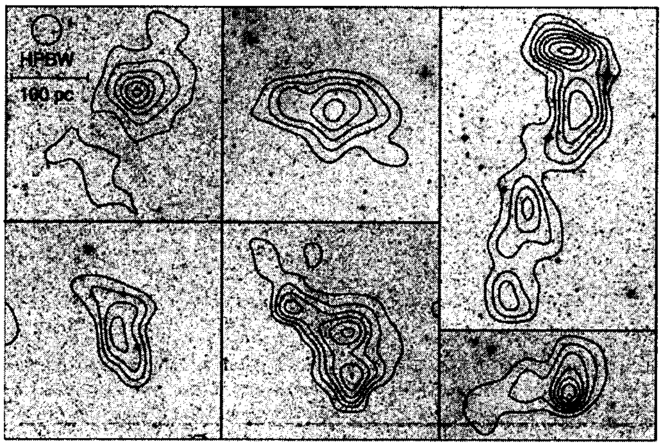

Figure 3: Examples of GMCs in (a) GMC Population I, (b) GMC Population IIa, and (c) GMC Population IIb. Each panel shows a velocity-integrated intensity of CO emission superposed on DSS (R) plate, respectively. Contour levels are from 1.2 K km s^{-1} with intervals of 1.2 K km s^{-1}.

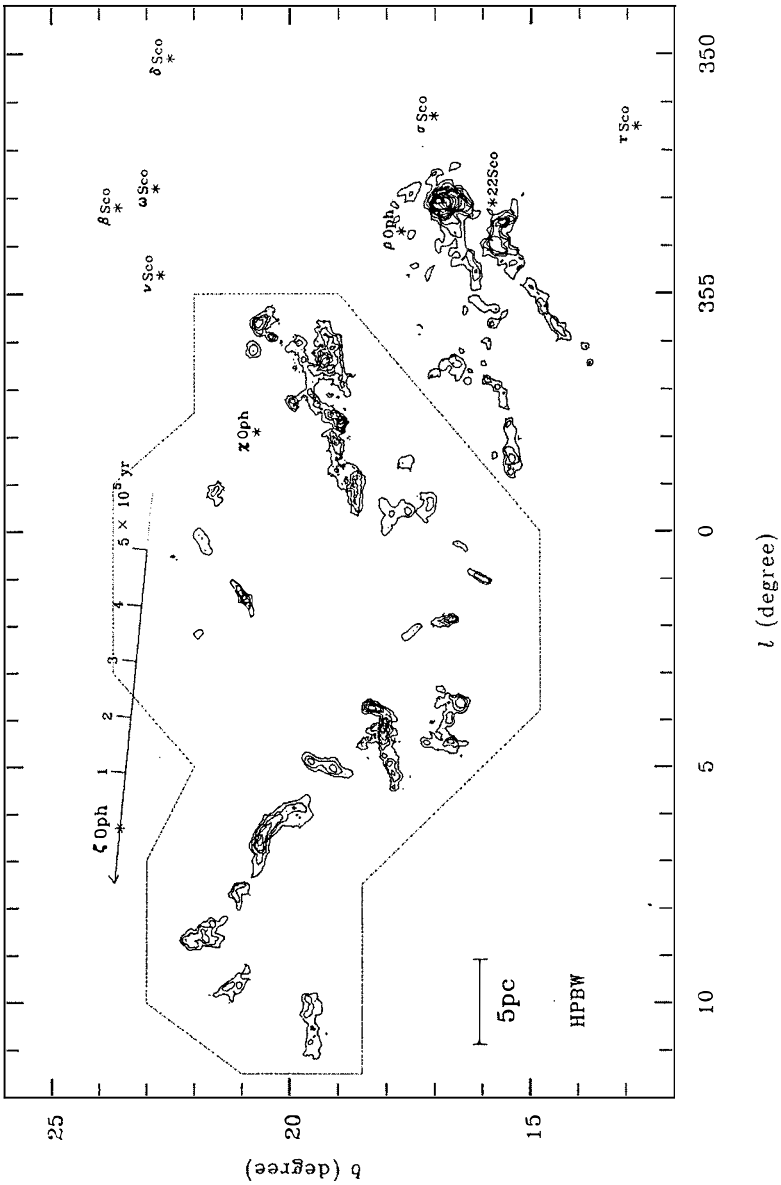

Figure 4: Overall distribution of the $^{13}CO(J{=}1\text{-}0)$ integrated intensity as a contour map, along line with the position of ζ Oph, its path, and the positions of the early-B-type stars of Sco OB2. Contours are every 1.8 K km s^{-1} from 1.8 K km s^{-1} as the lowest level. This figure is taken from Figure 3 in Nozawa(1991).

A DYNAMICAL STUDY OF THE NGC2264 CLUSTER-FORMING CLUMPS

N. PERETTO (1), P. ANDRÉ (1), A. BELLOCHE (2)

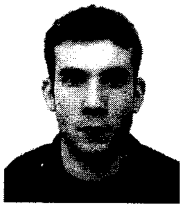

(1) Service d'Astrophysique, CEA Saclay
Orme des merisiers, 91191 Gif-sur-Yvette, France
(2) MPIfR, Bonn, Germany

We discuss the results of a millimeter study of the two cluster-forming clumps NGC2264-C and NGC2264-D in the Mon OB1 cloud complex. Based on 1.3mm dust continuum maps, we detect a total of 27 protostellar condensations whose masses range from ~1 to ~15 $M_\odot$. Our molecular line observations confirm that the central filamentary region of NGC2264-C is in a state of global collapse. We also find evidence for a strong dynamical interaction of at least two massive condensations at the center of NGC2264-C.

Keywords: star: formation; star: kinematics; ISM: dust; ISM: molecules

1 Introduction

Until recently, molecular clouds and dense cores were understood as objects in near hydrostatic equilibrium, evolving quasi-statically in a magnetically controlled medium (e.g., Shu et al., 1987). More recently, a new scenario has emerged, according to which clouds are viewed as very dynamic structures in which turbulence plays a key role. In the latter scenario, a molecular cloud, as well as its dense cores, result from turbulent density fluctuations of gas (e.g., Klessen & Burkert, 2000). The static magnetic field plays little role and most of the star-forming objects are out of equilibrium (Ballesteros-Paredes et al. 2003). Determining which of these two pictures dominates in real molecular clouds is still an open issue.
Since the dynamical properties of star-forming clumps differ markedly in the two pictures, (sub)millimeter studies of the kinematics of prestellar condensations and Class 0 protostars (cf André et al. 2000) can provide powerful observational tests. In an effort to improve our knowledge of the kinematics of proto-clusters and constrain theoretical models of clustered

star formation, we carried out a combination of millimeter dust continuum and molecular line observation of the NGC2264 cluster-forming region, located in the Mon OB1 molecular cloud complex (d~ 800 pc). NGC 2264 is a very active star-forming cloud with more than 360 near-IR YSOs detected (Lada et al. 1993). In the southern part of NGC2264, two IRAS sources, IRS1 and IRS2, are associated with CO molecular flows (Margulis et al. 1988), called NGC2264C and NGC2264D, respectively. Molecular line (Wolf-chase et al. 1995) and dust continuum (Ward-Thompson et al. 2000; Williams & Garland 2002) observations revealed two massive cluster-forming clumps at the positions of these outflows. Detailed observations on the vicinity of IRS1 show objects at different stages of evolution: pre-main-sequence stars (Thompson et al. 1998) and prestellar cores/protostars (Nakano et al. 2003; Schreyer et al. 2003). In NGC2264D, an intermediate mass Class 0 protostar was identified by Wolf-Chase et al. (2003). Previous kinematic studies of NGC2264C revealed a very complex velocity structure (Krügel et al. 1987; Nakano et al. 2003) including the global collapse of the entire clump (Williams & Garland 2002). However, these studies focused on a much smaller region and/or had much lower angular resolution than the observations reported here.

2 Millimeter Observations

In December 2000, we performed 1.3mm dust continuum observations with the IRAM 30 m telescope using the MAMBO 37 channel bolometer array, on Pico Veleta, Spain. Eleven on-the-fly maps were obtained covering a total area of $\sim$ 400 arcmin^2 with a final mean rms noise of 7 mJy/11"-beam. In March and May 2002 we performed follow-up molecular line observations of N_2H^+(1-0), HCO^+(3-2), $H^{13}CO^+$, CS, $C^{34}S$, using either the HERA camera or SIS detectors depending on wavelength. For the majority of the lines we took on-the-fly maps over large areas, following the location of the 1.3mm dust continuum emission.

3 Dust continuum mapping at 1.3mm

Our 1.3 mm dust continuum mapping confirms the presence of two distinct clumps, NGC2264-C and NGC2264-D (see Fig.1) which follow the CS(2-1) integrated intensity map of Wolf-chase et al. (1995). NGC2264C and NGC2264D do not have the same morphology: NGC2264C is denser and more compact than NGC2264D (cf Fig.1). To search for protostellar condensations within NGC2264C and NGC2264D, we have developed a systematic method based on a combination of the multi-resolution software of Starck et al. (1995) and the Gaussian fitting code of Stutzki & Güsten (1990), Gaussclump (kindly provided by C.Kramer). The first step is to select an upper scale, i.e. ScUp, beyond which we consider that the dust emission arises from the ambient cloud rather than from prestellar/protostellar sources. We set ScUp=20" ($\sim$0.1pc), corresponding to the physical diameter of structures called 'dense cores' in ρ-Oph by MAN98. The multi-resolution wavelet analysis allows us to remove all emission structures arising from spatial scales greater than ScUp (see Fig.1). Then, we apply Gaussclump on the resulting image (Stutzki & Güsten, 1990) to detect all condensations above the 5σ threshold (i.e. 35 mJy/beam here). In this way, we identify 27 sources : 12 in NGC2264C and 15 in NGC2264D (cf Fig.1), 14 of which are new dust continuum detections.

Assuming optically thin dust emission at 1.3mm, and adopting a dust temperature of 15K and dust mass opacity κ_{dust} = 0.005 cm^{-2}.g^{-1} (cf MAN98), we infer a total mass of gas $\sim$ 1000 $M_\odot$ for Clump C and $\sim$ 900 $M_\odot$ for Clump D, corresponding to a mean volume density of 1.8×10^4 cm^{-3} and to 1.5×10^4 cm^{-3}, respectively. We find $< N_{H_2} >_{beam}\sim 17\times10^{22}$ cm^{-2} for NGC2264C and $< N_{H_2} >_{beam}\sim 9\times10^{22}$ cm^{-2} for NGC2264D. The 27 condensations have deconvolved sizes ranging from < 0.02 pc to 0.12 pc, masses ranging from $\sim$ 1 to $\sim$ 15 $M_\odot$,

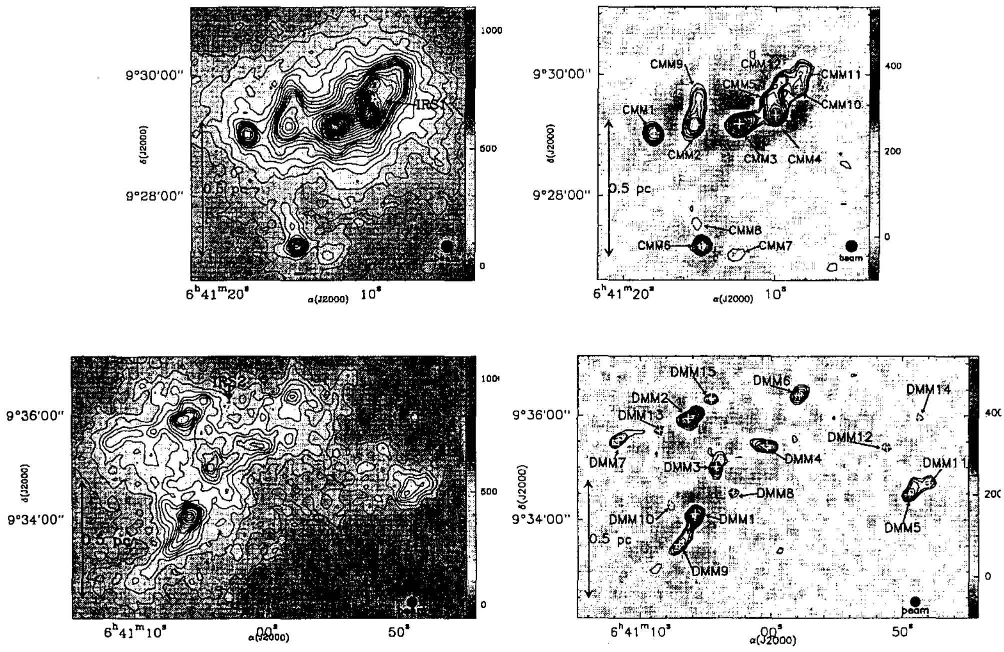

Figure 1: (left): 1.3mm dust continuum maps of NGC2264C (top) and NGC2264D (bottom). The white open star corresponds to the positions of IRSl and IRS2. (right): Background subtracted 1.3mm dust continuum images of NGC2264C (top) and NGC2264D (bottom), obtained from the addition of all wavelet planes corresponding to spatial scales smaller than ScUp=20". The white crosses mark the condensations detected with Gaussclump.

and volume density ranging from $\sim 1\times10^5$ to $> 3\times10^7$ cm^{-3}. The most massive condensation is CMM3 which is located at the center of NGC2264-C.

4 Molecular line observations

4.1 Results

Each hyperfine N_2H^+(1-0) spectrum is fitted using the CLASS reduction package from IRAM. From each spectrum, we measure, by Doppler shift, the average velocity along the corresponding line-of-sight and the FWHM linewidth, ΔV. For each clump we can thus estimate the systemic velocity V_{sys}, the 3D velocity dispersion of the gas, σ_{3D}, calculated assuming isotropical motions, and the mean FWHM linewidth, $<\Delta V>$. We find $\sigma_{3D} \sim 1.3$ km.s^{-1} and $<\Delta V> = 1.4$ km.s^{-1} for both clumps, $V_{sys} = 7.6$ km.s^{-1} in Clump C and $V_{sys} = 5.5$ km.s^{-1} in Clump D. Although our N_2H^+(1-0) on-the-fly maps contain more than 1000 spectra, only the spectra associated with the densest parts of the clumps (i.e. corresponding to condensations) have sufficient signal to noise to calculate V_{LSR} and ΔV. Thus, the velocity dispersion σ_{3D} quoted above refers only to the condensations. Our observations provide little information on the velocity dispersion of the surrounding gas on larger scales.

Our observations of optically thick molecular lines (e.g. HCO^+(3-2), CS(3-2)) confirm the presence of infalling motions on large scales in NGC2264C (Williams & Garland 2002). Our mapping in optically thin molecular lines (i.e. N_2H^+(1-0), $H^{13}CO^+$(1-0)) reveals a remarkable unknown velocity structure. Fig.2 shows the position-velocity diagram observed in N_2H^+(1-

0) along an East-West (i.e. EW) axis going through CMM2, CMM3 and CMM4 (see Fig.2). We note two distinct velocity components, associated with CMM2 and CMM4 respectively, both extending over more than 50" (i.e. ~0.2 pc). These two structures form a sharp velocity discontinuity $\sim$ 2 km.s^{-1} in amplitude at the position of CMM3. Fig.2 (right) shows the contours of the N_2H^+(101-012) high velocity component (associated with CMM2) and the low velocity component (associated with CMM4), overlaid with the 1.3mm dust continuum map of the central part of NGC2264C. The two velocity components are overlapping at the position of CMM3.

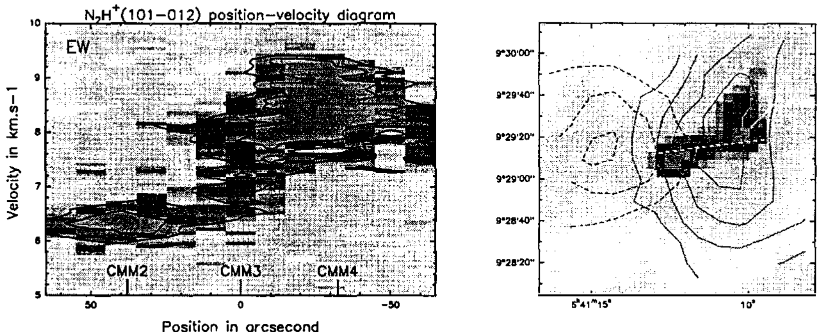

Figure 2: (left): N_2H^+(101-012) position-velocity diagram along an East-West axis going through CMM2, CMM3, and CMM4 (cf the right panel). The positions of CMM2, CMM3, and CMM4 are indicated on the x axis. (right) : 1.3mm continuum (grey scale) of the central part of NGC2264C overlaid on contours of the N_2H^+(1-0) emission integrated from 5 to 7 km.s^{-1} (solid contours) and from 8 to 10 km.s^{-1} (dashed contours). The East-West axis along which the position-velocity diagram was taken is shown as a white dashed line.

4.2 Analysis

Global crossing time vs. local evolutionary timescale

The velocity dispersion estimates allow us to infer a crossing time for the condensations within the clumps. Adopting a diameter of ~1 pc for NGC2264C and ~1.25 pc for NGC2264D, we find a crossing time $t_{cross} \sim 9 \times 10^5$ yr for Clump D and $\sim 7 \times 10^5$ yr for Clump C. The condensations we detect at 1.3mm are not seen in the IR and are likely to be either prestellar cores or Class 0 protostars. A rough estimate of their lifetime is provided by their free-fall time which is $< 1\times10^5$yr, based on the volume densities estimated in § 3. This suggests the condensations will evolve into PMS objects before any interaction can take place.

A strong dynamical interaction at the center of NGC2264-C

The velocity discontinuity observed in the innermost part of NGC2264C (Fig.2) cannot be explained by a purely rotational effect. Indeed, at the position of CMM3, which is the center of the system, we observe both the high and low velocity components without observing the intermediate velocity which should be stronger than the others. Moreover, the rotational curve expected for differential rotation is characterized by a S shape (Belloche et al. 2002) rather than a sharp discontinuity as observed. In order to account for this velocity structure, we have modelled the central region of NGC2264C as a cylindrical filament centered on CMM3 (see Fig.3). The system is collapsing toward its center of mass (CMM3), so that the two sides of the filament (CMM2 and CMM4) are moving toward each other. The long axis is not in the plane of the sky but inclined by 45^o to the line-of-sight (see Fig.3). When probing the kinematics of such structure, an observer would see a sharp velocity discontinuity at the center of the filament.

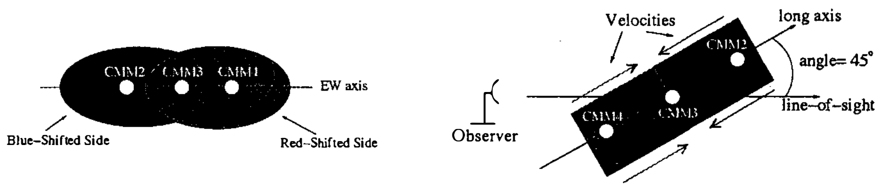

Figure 3: Schematic view of the proposed scenario for NGC2264C. (left): View of the filament projected on the plane of the sky (as seen by an oberver). The redshifted part (light grey) and the blueshifted part (dark grey) are shown as well as the inner three condensations (filled white circles). (right): Transverse view of the filament. The symbols are the same as in the left panel.

To test this scenario we have performed radiative transfer simulations, calculating the populations of the rotational energy levels of CS, $C^{34}S$, HCO^+ and $H^{13}CO^+$, using a 1D Monte-Carlo code (cf Bernes 1979). We integrate the line emission along the line-of-sight using the radiative transfer code MAPYSO (cf Belloche et al. 2002) in a 2D mode. Several parameters are fixed as inputs to the code. The velocity profile is set to reproduce a collapsing filament along its long axis. The density profile is consistent with the observed intensity profile of NGC2264C, i.e., $\rho \sim r^{-1.4}$, where r is the radius from CMM3. The CS and $C^{34}S$ abundance profiles are the same, and take depletion into account in the region where the density is higher than $\sim 10^5$ cm^{-3} (Tafalla al. 2002). The kinetic temperature profile is taken to be $T_k(r) = ((T_0(\frac{r}{r_0})^{-0.4})^4 + T_1^4)^{0.25}$ with T_0=60 K, r_0=200 AU and T_1=15 K. This temperature profile is consistent with a central heating source radiating in an optically thin medium, and reaches a colder background temperature of 15K at large radii. We also include a non-thermal velocity dispersion component, σ_{NT}=1.1 km.s^{-1}, in agreement with the N_2H^+(1-0) linewidths observed in NGC2264C.

In Fig.4, we compare the synthetic spectra calculated in this way along the EW axis with the observed spectra in the CS(3-2), $C^{34}S$(3-2), $C^{34}S$(5-4), HCO^+(3-2) and $H^{13}CO^+$(3-2) lines. The (0",0") position corresponds to CMM3. The agreement between the simulations and the observations is very encouraging given the simplicity of our model. The central dips are well reproduced, the linewidths and the positions of the peaks as well. On the West side we see that the simulated spectra are not strong enough. This is due to our 1D temperature profile which underestimates the kinetic temperature at the position of the luminous IR source IRS1. It is noteworthy that such a model manages to reverse the asymmetry of the self-absorbed spectra (cf. Fig.4) without any outward velocity component in it. The asymmetry reversal is a consequence of the particular geometry of the model. Of course this does not mean that outflows do not play a role in shaping the spectra, but given the complexity of the velocity field in NGC2264C (outflows, collapse onto individual protostars, global collapse) the observed spectra result from a mixture of all of these velocity components and reveal primarily the dominant one at each location.

5 Discussion : An interaction in the innermost part of NGC2264C

As already pointed out in § 4, the two sides of the NGC2264C filament, associated with CMM2 and CMM4, respectively, are interacting at the position of CMM3. The velocity profile used in our radiative transfer fit (cf Fig.4) allows us to infer a dynamical time $t_{dyn} \sim 1.5\times10^5$ yr for this interaction, corresponding to the time needed by CMM2 and CMM4 to get to the position of CMM3. This dynamical time is shorter than the crossing time calculated in § 4.2, and is more comparable to the free-fall time of the individual condensations. We conclude that the observed dynamical interaction may play a role in defining the final masses of the objects located at the center of NGC2264C. We can also estimate the rate at which matter flows toward

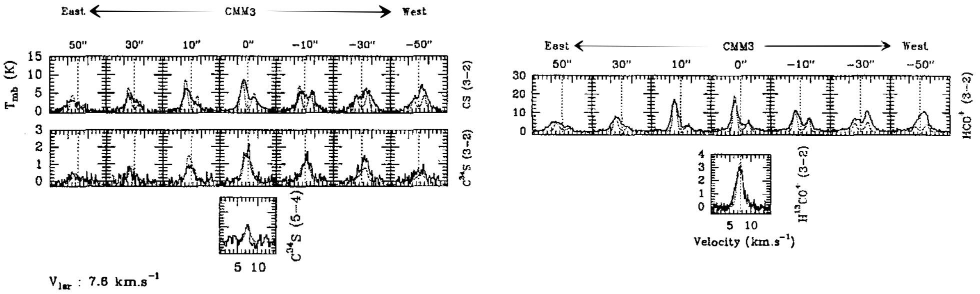

Figure 4: Observed (black) and simulated (light grey) spectra in the central part of NGC2264C for: (left): CS(3-2), $C^{34}S$(3-2), $C^{34}S$(5-4), and for: (right): HCO^+(3-2) and $H^{13}CO^+$(3-2). The simulated spectra were obtained using the radiative transfer code MAPYSO in a 2D cylindrical geometry. Relevant parameters are given in § 4. The observed spectra were taken along an East-West axis going through CMM2, CMM3 and CMM4 (see Fig.3 and Fig.2). The 0" position corresponds to CMM3.

the center of the filament, $\dot{M}_{inf}$. Using n_{mean}=1×10^5 cm^{-3}, V_{inf}=1.2 $km.s^{-1}$, and a filament radius of 0.2 pc, we find that $\dot{M}_{inf} \sim 3\times10^{-3}$ $M_\odot.yr^{-1}$. Although, $\dot{M}_{inf}$ differs in nature from a standard protostellar accretion rate, it is interesting to compare its value to the accretion rate needed by models of high-mass star formation. According to Mc Kee & Tan (2002) an accretion rate $\dot{M}_{acc} \sim 1\times10^{-3}$ $M_\odot.yr^{-1}$ is sufficient to overcome radiation pressure during the formation process of a massive star. We may thus be witnessing a very early phase of the formation of a high-mass star at the center of NGC2264C.

References

1. André, P., Ward-Thompson, D., Barsony, M., 2000, in Protostars and Planets IV, p. 59
2. Ballesteros-Paredes, J., Klessen, R., Vasquez-Semadeni, E., 2003, Apj, 592, 188
3. Belloche, A., André, P., Despois, D., Blinder, S., 2002, A&A, 393, 927
4. Bontemps, S. *et al.*, 2001, A&A, 372, 173
5. Klessen, R. & Burkert, A., 2000, ApJS, 128, 287
6. Krügel, E., Guesten, R., Schulz, A., Thum, C., 1987, A&A, 185, 283
7. Lada, C., Young, E., Greene, T., 1993, ApJ, 408, 471
8. Margulis, M., Lada, C., Snell, R., 1988, ApJ, 333, 316
9. Mc Kee, C. & Tan, J., 2002, Nature, 416, 59
10. Motte, F., André, P., & Neri, 1998, A&A, 336, 150 (MAN98)
11. Nakano, M., Sugitani, K., Morita, K., 2003, PASJ, 55, 321
12. Schreyer, K., Stecklum, B., Linz, A., Henning, T., 2003, ApJ, 599, 335
13. Shu, F., Adams, F., Lizano, S., 1987, ARA&A, 25, 23
14. Starck, J-L., Bijaoui, A. & Murtagh, F., 1995, in CVIP: Graphical Models and Image Processing, 57, 5, 420
15. Stutski, J., & Güsten, R., 1990, ApJ, 356, 513
16. Tafalla, M. *et al.*, 2002, ApJ, 569, 81
17. Ward-Thompson, D., Zylka, R., Mezger, P., Sievers, A., 2000, A&A, 355, 1122
18. Williams, J., & Garland, C., 2002, ApJ, 568, 259
19. Wolf-Chase, G., Walker, C., Lada, C., 1995, ApJ, 442, 197
20. Wolf-Chase, G., Moriarty-Schieven, G., Fich, M., Barsony, M., 2003, MNRAS, 344, 809

DUST TEMPERATURES IN ASYMMETRIC PRESTELLAR CORES

D. STAMATELLOS & A. P. WHITWORTH

School of Physics & Astronomy, Cardiff University
5 The Parade, Cardiff CF24 3YB, Wales, UK

We present 2D Monte Carlo radiative transfer simulations of flattened prestellar cores. We argue the importance of observing prestellar cores near the peak of their emission spectra, and we point out observable characteristic features on isophotal maps of asymmetric cores at FIR wavelengths that are indicative of the cores' density and temperature structure. These features are on scales 1/5 to 1/3 of the overall core size, and so high resolution observations are needed to observe them. Finally, we discuss the importance of determining the temperatures of prestellar cores with high accuracy.

Keywords: Stars: formation – ISM: clouds-structure-dust – Methods: numerical – Radiative transfer

1 Introduction

Prestellar cores are condensations in molecular clouds that are on the verge of collapse or already collapsing. Their study is important for constraining the initial conditions for star formation (see André et al. 2000). Prestellar cores have typical sizes 2000 – 15000 AU, and typical masses $0.05 - 10\ \mathrm{M}_{\odot}$. They are cold with typical dust temperatures 7 – 20 K. Their density profiles tend to be flat in the centre and to fall off as r^{-n} ($n = 2 - 4$) in the envelope. Many authors have used Bonnor-Ebert (BE) spheres to represent prestellar cores (e.g. Alves et al. 2001). However, studies of the shapes of cores indicate that they are best described as triaxial ellipsoids, and they are close to being oblate spheroids (Goodwin et al. 2002). Additionally, numerical simulations of the collapse of turbulent molecular clouds indicate that prestellar cores are transient, non-spherical systems, which when projected onto the plane of sky appear to mimic BE spheres (Ballesteros-Paredes et al. 2004). Information about prestellar cores comes from molecular line observations (e.g. NH_3, CO), but also from continuum observations, where cores are seen in emission (FIR, submm and mm) or absorption (NIR). In this paper, we focus on modelling the continuum emission of prestellar cores.

2 Asymmetric models of prestellar cores

We use 2D models to represent slightly asymmetric prestellar cores (see Stamatellos et al. 2004). Our goal is to capture generically the different features we might hope to detect on the isophotal maps of such cores. We use a Plummer-like density profile (Plummer 1915), that is modified to include azimuthally symmetric departures from spherical symmetry. This profile is simple and captures the basic observed characteristics of prestellar cores. Here, we present a model of a slightly flattened core (disk-like asymmetry; Fig. 1, left), with density profile

$$n(r,\theta) = n_0 \left[1 + A\left(\frac{r}{r_0}\right)^2 \sin^p(\theta)\right]\left[1 + \left(\frac{r}{r_0}\right)^2\right]^{-(\eta+2)/2}, \quad (1)$$

where n_0 is the density at the centre of the core, and r_0 is the extent of the central region in which the density is approximately uniform. The parameter A determines the equatorial-to-polar optical depth ratio e, i.e. the maximum optical depth from the centre to the surface of the core ($\theta = 90°$), divided by the minimum optical depth from the centre to the surface of the core ($\theta = 0°$ and $\theta = 180°$). The parameter p determines how rapidly the optical depth from the centre to the surface rises with increasing θ, i.e. going from the north pole at $\theta = 0°$ to the equator at $\theta = 90°$. We assume that the core has a spherical boundary at radius $R_{\rm core} = 2 \times 10^4$ AU, and $n_0 = 10^6\,{\rm cm}^{-3}$, $r_0 = 2 \times 10^3$ AU, $\eta = 2$, $p = 4$, and $e = 2.5$. The simulations are performed using PHAETHON, a 3D Monte Carlo radiative transfer code (Stamatellos & Whitworth 2003).

3 Dust temperature profiles

The dust temperature (Fig. 1, right) drops from around 17 K at the edge of the core to 7 K at the centre of the core (also see Zucconi et al. 2001; Evans et al. 2001; Stamatellos & Whitworth 2003). We find that the dust temperature inside a core with disk-like asymmetry is θ dependent, similar to the results of Zucconi et al. (2001) and Gonçalves et al. (2004). As expected, the equator of the core is colder than the poles. The difference in temperature between two points having the same distance r from the centre of the core but with different polar angles θ, is larger for more asymmetric cores (see Stamatellos et al. 2004). This temperature difference will affect the appearance of the core at wavelengths shorter than or near the core peak emission.

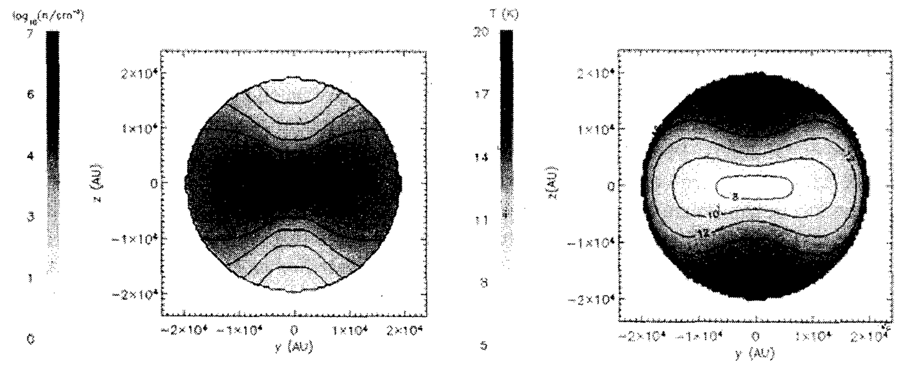

Figure 1: **Left:** Density on the $x = 0$ plane for a flattened asymmetric core with equatorial-to-polar optical depth ratio $e = 2.5$ and $p = 4$. We plot isopycnic contours every $10^{0.5}{\rm cm}^{-3}$. The central contour corresponds to $n = 10^{5.5}{\rm cm}^{-3}$. **Right:** Temperature on the $x = 0$ plane for the same model, calculated with a Monte Carlo RT simulation. We plot isothermal contours from 8 to 18 K, every 2 K.

4 SEDs and isophotal maps

The SED of the slightly asymmetric core we examine, is the same at any viewing angle, because the core is optically thin to the radiation it emits (FIR and longer wavelengths). However, the isophotal maps do depend on the observer's viewing angle. Additionally, they depend on the wavelength of observation. PHAETHON calculates images at any wavelength, and therefore provides a useful tool for direct comparison with observations, e.g. at MIR (ISOCAM), FIR (ISOPHOT) and submm/mm (SCUBA, IRAM) wavelengths. We focus on wavelengths near the peak of the core emission (150-250 μm; we choose 200 μm as a representative wavelength). At 200 μm the core appearance depends both on its temperature and its column density in the observer's direction. This interplay between core temperature and column density along the line of sight results in characteristic features on the images of the cores (see Fig. 2). Such features include (i) the two intensity minima at almost symmetric positions relative to the centre of the core, on the image at 30°, and (ii) the two intensity maxima, again at symmetric positions relative to the centre of the core, on the image at 90°.

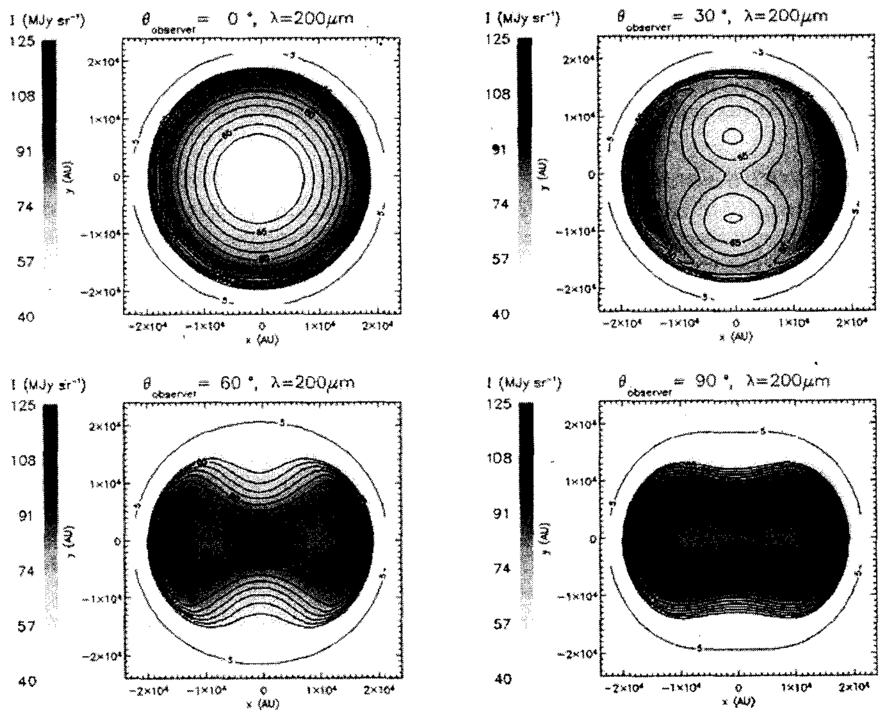

Figure 2: Isophotal maps at viewing angles 0°, 30° 60° and 90°, for a flattened prestellar core with e = 2.5 and p = 4 at 200 μm. We plot an isophotal contour at 5 MJy sr^{-1} and then from 60 to 110 MJy sr^{-1}, every 5 MJy sr^{-1}. There are characteristic symmetric features due to core temperature and orientation with respect to the observer. (We note the axes (x, y) refer to the plane of sky as seen by the observer).

We conclude that isophotal maps at 200 μm contain detailed information, and sensitive, high resolution observations at 200 μm are helpful in constraining the core density and temperature structure and the orientation of the core with respect to the observer. In Fig. 3, left, we present a perpendicular cut (at $x = 0$) of the core images shown in Fig. 2. We also plot the beam size of the ISOPHOT C-200 camera (90″, or 9000 AU for a core at 100 pc) and the beam size of the

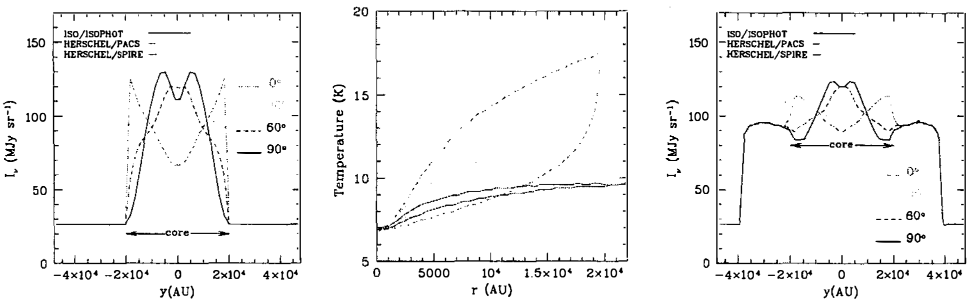

Figure 3: **Left:** A perpendicular cut through the centre of the core images presented in Fig. 2 (but also including the background radiation field). We also plot the beam size of ISOPHOT and the beam size of the upcoming *Herschel* PACS/SPIRE (assuming a core distance of 100 pc). **Centre:** The effect of the parent cloud on cores. Temperature profiles of a non-embedded core (dashed lines), and of a core at the centre of an ambient cloud with $A_V = 4$ (dotted lines), and $A_V = 13$ (solid lines). The upper curve of each set of lines corresponds to the direction towards the pole of the core ($\theta = 0°$), and the bottom curve to the direction towards the core equator ($\theta = 90°$). The difference between the two curves is indicative of the temperature gradient. The core is colder when it is inside a thicker parent cloud, and the temperature gradient within the core is smaller. **Right:** Same as on the left, but for a core embedded in a molecular cloud with visual extinction $A_V = 4$. The characteristic features at different viewing angles are weaker than in the case of a non-embedded core, but still observable.

upcoming (2007) *Herschel* (13″or 1300 AU for the 170 μm band of PACS; 17″or 1700 AU for the 250 μm band of SPIRE). ISOPHOT's resolution is probably not good enough to detect the features mentioned above. Indeed, a search in the Kirk (2002) sample of ISOPHOT observations (also see Ward-Thompson et al. 2002) does not reveal any cores with such distinctive features. However, *Herschel* should, in principle, be able to detect such features in the future.

5 The effect of the parent cloud

Cores are generally embedded in molecular clouds, with visual optical depths ranging from 2-10 (e.g. in Taurus) up to 40 (e.g. in ρ Oph). Due to the ambient cloud the radiation incident on a core embedded in the cloud is reduced in the UV and optical, and enhanced in the FIR and submm (Mathis et al. 1983). Previous radiative transfer calculations of spherical cores embedded at the centre of an ambient cloud (Stamatellos & Whitworth 2003), have shown that embedded cores are colder ($T < 12$ K) and that the temperature gradients inside these cores are smaller than in non-embedded cores.

Here, we examine the same core as before when it is embedded in a uniform density ambient cloud with different visual extinctions A_V. The ambient cloud is illuminated by the interstellar radiation field. Relative to the non-embedded core, the core embedded in an ambient cloud with $A_V = 4$ is colder and has lower temperature gradient (Fig. 3, centre). The isophotal maps are similar to those of the non-embedded core, but the characteristic features are less pronounced. This is because the temperature gradient inside the core is smaller when the core is embedded. In Fig. 3, right, we present a perpendicular cut through the centre of the embedded core image. It is evident that the features are quite weak, but they have the same size as in the non-embedded core (Fig. 3, left), and they should be detectable with *Herschel*, given an estimated rms sensitivity better than $\sim 1 - 3$ MJy sr^{-1} at 170-250 μm.

Thus, continuum observations near the peak of the core emission can be used to obtain information about the core density and temperature structure and orientation, even if the core is very embedded ($A_V \sim 10$).

6 Application: Modelling L1544

We model L1544 (core distance $D = 140$ pc) using a slightly flattened density profile ($e = 2$ and $p = 4$). Our goal is to fit the SCUBA 850 μm image (Fig. 4, left), the SED data points (Fig. 4, right), and to calculate the temperature profile in the core. To fit the observational data we choose the asymmetry parameter e, based on the 850 μm image of the core. Then we vary the mass of the core (by adjusting the central core density and the core flattening radius), so as to fit the submm and mm SED data. Finally, we vary the extinction through the ambient cloud in order to fit the FIR SED data.

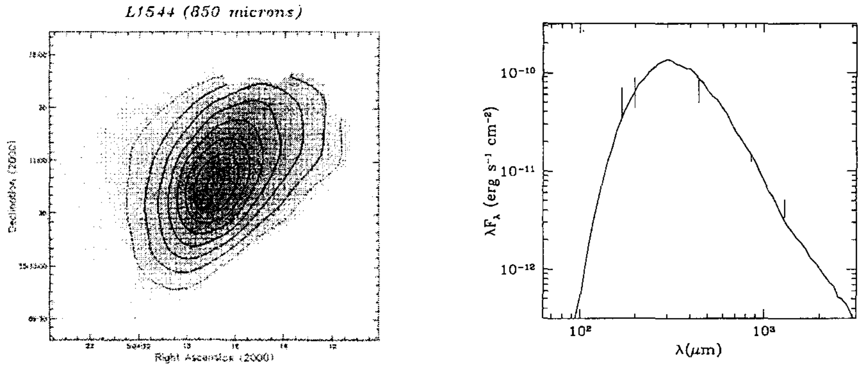

Figure 4: **Left:** 850 μm SCUBA image of L1544 (from Kirk 2002). **Right:** SED of the core. The line corresponds to the model, and the points to the observed SED (data taken from Kirk 2002).

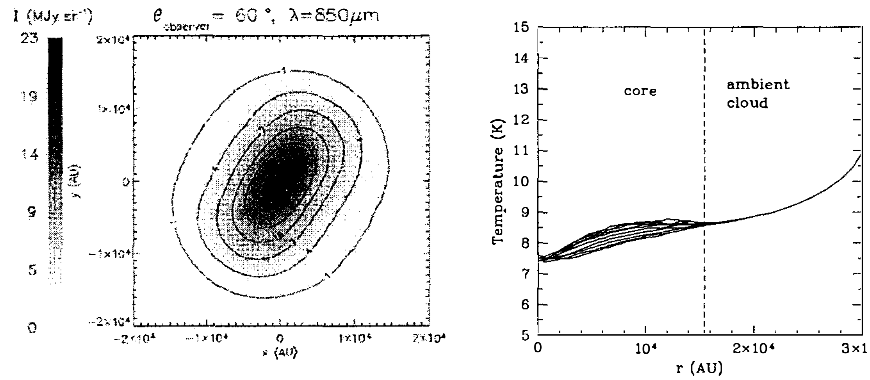

Figure 5: **Left:** 850 μm isophotal map of the model. The core is viewed at an angle $\theta = 60°$. **Right:** Dust temperature profile of the core and the immediate ambient cloud. Different lines correspond to different directions (from $\theta = 0°$, upper line, to $\theta = 90°$, bottom line).

The best-fit model is obtained using central density $n_0 = 3.4 \times 10^5\,\mathrm{cm}^{-3}$, inner flattening radius $r_0 = 0.015\,\mathrm{pc}$, core extent $R_{\rm core} = 0.075\,\mathrm{pc}$, and an ambient cloud of visual extinction $A_V^{\rm cloud} = 23.7$. These values are in good agreement with observations of L1544 (e.g. Ward-Thompson et al. 2002, Kirk et al. 2004). The calculated luminosity emitted from the core is $L_{\rm core} = 0.10\ \mathrm{L}_\odot$, in agreement with observations (Kirk 2002). The model fits the SED data very well (Fig. 4, right). The model also reproduces reasonably well the central region of the L1544 850 μm map (cf. Figs 4 and 5, left). However, it does not reproduce the asymmetries in the outer parts of the core, which are signatures of triaxiality.

The temperature at the edge of the core is $T_{\mathrm{edge}} = 8.7$ K and at the centre $T_{\mathrm{centre}} = 7.5$ K (Fig. 5, left). The dust temperature we calculate with the model is lower by $2-3$ K than the temperature estimated by Kirk (2002) using FIR (90, 170 and 200 μm) ISOPHOT observations ($T_{\mathrm{iso}} = 10.2^{+0.5}_{-0.4}$ K). However, ISO observations have difficulty distinguishing the core from the ambient cloud, and thus this larger temperature may be due to the presence of the hotter ambient cloud in the observing beam. As a result of overestimating the dust temperature, the core mass calculated by Kirk (2002) is underestimated. The core mass is $M_{\mathrm{core}} \propto F_\lambda/(B_\lambda(T_{\mathrm{dust}})\kappa_\lambda)$ (e.g. André et al. 1999), where F_λ is the flux at a submm or mm wavelength, and κ_λ is the assumed dust opacity per unit mass. If the core temperature is overestimated by 2 K (10 K instead of 8 K) then using the 850 μm flux the core mass is underestimated by a factor of 1.6 ($B_{850\mu\mathrm{m}}(10\mathrm{K}) = 1.6 \times B_{850\mu\mathrm{m}}(8\mathrm{K})$). The core mass of the model is $M = 2.5$ $\mathrm{M}_\odot$ which is similar to what Kirk et al. (2002) calculated ($M_{\mathrm{iso}}^{850\mu\mathrm{m}} = 2.5 \pm 1$). However, we note that Kirk uses a dust opacity $\kappa_{850\mu m} = 0.01$ cm^{2}g^{-1}, which is smaller by a factor of 2 than the dust opacity we use ($\kappa_{850\mu m} = 0.02$ cm^{2}g^{-1}). Thus, to consistently compare the mass we need to divide the Kirk (2002) value by 2.

We conclude that accurate estimates of core temperatures are important when calculating core masses from submm and mm observations, since e.g. overestimating temperatures by even just 1-2 K can lead to underestimating core masses by a factor of 2.

7 Conclusions

Far-infrared continuum maps of prestellar cores reflect both the column density and temperature field along the line of sight, and thus contain complementary information to the mm continuum maps that mainly trace column density. The radiative transfer models presented here show that the effect of the combined dust temperature and column density along the line of sight is to produce characteristic features in the FIR intensity maps. These features are useful for constraining the conditions in prestellar cores, and are expected to be present in cores with high enough temperature gradients ($\sim$2 K).

Acknowledgements

We acknowledge help from the EC Research Training Network "The Formation and Evolution of Young Stellar Clusters" (HPRN-CT-2000-00155). We also thank P. André for useful comments.

References

1. Alves, J., Lada, C. J., & Lada, E. A. 2001, Nature, 409, 159
2. André, P., Ward-Thompson, D., & Barsony, M. 2000, Protostars and Planets IV, 59
3. Ballesteros-Paredes, J., Klessen, R. S., & Vázquez-Semadeni, E. 2003, ApJ, 592, 188
4. Evans, N. J., Rawlings, J. M. C., Shirley, Y. L., & Mundy, L. G. 2001, ApJ, 557, 193
5. Gonçalves, J., Galli, D., & Walmsley, M. 2004, A&A, 415, 617
6. Goodwin, S. P., Ward-Thompson, D., & Whitworth, A. P., 2002, MNRAS, 330, 769
7. Kirk, J., Ph.D. Thesis, Cardiff University, 2002
8. Kirk, J., et al. 2004, in preparation
9. Plummer, H. C., 1915, MNRAS, 76, 107
10. Stamatellos, D. & Whitworth, A. P. 2003, A&A, 407, 941
11. Stamatellos, D. & Whitworth, A. P., André, P., Ward-Thompson 2003, A&A, in press
12. Ward-Thompson, D., André, P., & Kirk, J. M. 2002, MNRAS, 329, 257
13. Zucconi, A., Walmsley, C. M., & Galli, D. 2001, A&A, 376, 650

ISOLATED STAR FORMATION IN BOK GLOBULES

R. LAUNHARDT

Max Planck Institute for Astronomy, Königstuhl 17, 69117 Heidelberg, Germany

Because of their isolated location and simple structure, the dense cores of nearby Bok globules are ideal laboratories to study in detail the process of low-mass star formation. In this paper we describe the general characteristics of Bok globules and summarize our current knowledge of the properties of their star-forming cores. In particular we discuss radial density profiles, evolutionary effects, multiplicity, magnetic fields, kinematic properties like rotation and turbulence, star-formation efficiency, and the overall energy balance.

Keywords: Stars: formation – ISM: clouds – ISM: magnetic fields

1 Introduction

Different aspects of star formation can be studied on different size scales and in different environments. The large-scale distribution of star-forming regions and the relation between molecular cloud life cycles, galactic spiral density waves, and star formation can be studied by observing nearby galaxies. The stellar initial mass function, which is needed to interpret these data, is usually derived from rich young stellar clusters in our own Galaxy. Dense star-forming dark cloud complexes like, e.g., the ρ Oph cloud are the places to study the relation between molecular clump mass spectra, turbulence, and star-formation. And finally, nearby isolated Bok globules are the best places to study in detail the initial properties of individual star-forming cores, their chemical evolution, kinematic structure, and the physics of collapse and fragmentation. However, one has to keep in mind that some of the results may be typical only for the isolated mode of star formation and may not be applicable to dense and clustered star-forming regions.

Bok globules are small, simply-structured, relatively isolated molecular clouds that often contain only one single star-forming core (e.g. Clemens & Barvainis 1988; Bourke et al. 1995). Figure 1 shows optical/NIR images of three "typical" nearby Bok globules together with contours of the thermal submm/mm dust emission from the dense star-forming cores. Table 1 summarizes the average general properties of typical Bok globules and their star-forming cores.

Although they are the most simple star-forming molecular clouds, most globules deviate considerably from spherical geometry. They are often cometary or irregularly shaped. The dense star-forming cores are often not located at the center of the globule, but in cometary-shaped globules located closer to the sharper rim ("head" side). Pre-protostellar cores often appear to be fragmentary and filamentary. However, the protostellar cores and envelopes of Class I YSOs are more spherically symmetric, which can be understood as a result of the gravitational collapse of the inner dense $R \sim 5000$ AU region.

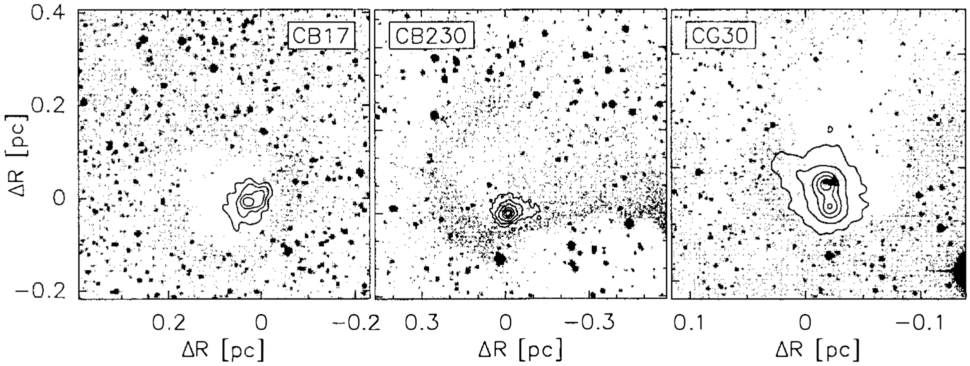

Figure 1: Optical/NIR images of "typical" nearby Bok globules ($D = 200 \ldots 400$ pc). Contours of the thermal mm dust emission mark the dense star-forming cores. Axis labeling in pc refers to the distance of the globules.

Table 1: Average general properties of Bok globules and their dense cores.

	Globule	Dense core
Mass	5 - 50 $M_\odot$	1 - 5 $M_\odot$
Radius	0.1 – 1 pc	$\sim$ 0.05 pc (10,000 AU)
Density	($10^3\,cm^{-3}$)	$10^6\,cm^{-3}$
Temperature	(15 K)	10 K
Line widths	0.5 – 2 $km\,s^{-1}$	0.4 – 0.7 $km\,s^{-1}$

2 Properties of the star-forming cores

2.1 Pre-protostellar cores

Based on submillimeter and millimeter dust continuum maps, models of isolated pre-protostellar cores in Taurus and in Bok globules have been derived by a number of authors (e.g., Ward-Thompson et al. 1994, 1999:, Evans et al. 2001; Launhardt et al. in prep.). Despite different modeling approaches, all authors derive some common features. Isolated pre-protostellar cores appear to have an inner flat-density core of radius few hundred to few thousand AU and central densities of one to a few $10^6\,cm^{-3}$, an outer radial density profile that approaches $n_H \propto R^{-2}$, a well-defined outer cut-off radius at $\sim 2 \times 10^4$ AU, and total mass between 2 and 5 $M_\odot$. Typical masses inside $R < 5000$ AU are of order 0.5 – 1 $M_\odot$, i.e., ~20% of the total core mass. Typical dust temperatures are 6 – 10 K in the inner core and 10 – 15 K towards the outer edge, which is due to external heating by the interstellar radiation field (e.g., Evans et al. 2001).

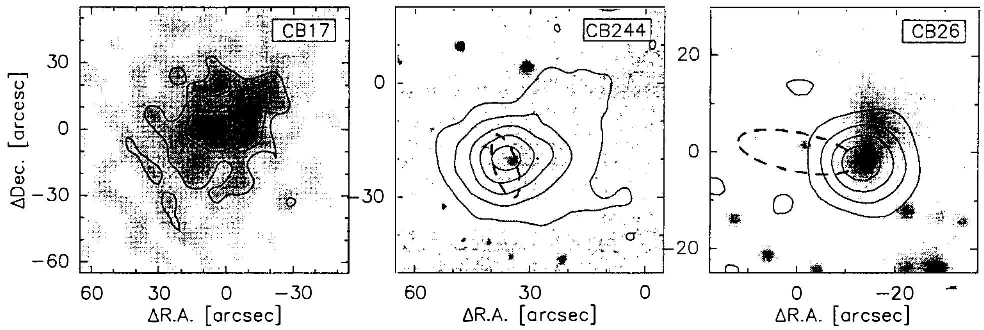

Figure 2: Millimeter dust continuum images of **a)** a pre-protostellar core (CB 17), **b)** a Class 0 protostellar core (CB 244, contours overlayed on a K-band image), and **d)** a disk-dominated Class I YSO (CB 26, contours overlayed on a K-band image; Launhardt & Sargent 2001). Dashed ellipses show IRAS point sources.

Figure 2a shows a 1.3 mm dust continuum map one such core (CB 17, Launhardt et al. in prep.). As this map shows and as already mentioned by Ward-Thompson et al. (1999), most pre-protostellar cores are far from being spherically symmetric; they typically have a rather filamentary structure and in some cases the flat inner cores seem to be fragmented. Evans et al. (2001) find that the large-scale morphology of many pre-protostellar cores can also be well-modeled by Bonnor-Ebert spheres with different degrees of central concentration, which could be an evolutionary effect. However, the filamentary structure and the turbulent nature of the outer envelopes (Falgarone et al. 1998; Park et al. 2004) make the assumption of an ideal Bonnor-Ebert gas sphere somewhat doubtful. For the same reason, radial density profiles should be taken with caution since models are usually fitted to circularly averaged emission profiles.

2.2 Class 0 protostellar cores

Isolated Class 0 protostellar cores have been observed in the submm/mm dust continuum emission and modeled by, e.g., Motte & André (2001), Shirley et al. (2002), and Launhardt et al. (in prep.). Molecular outflows have been mapped by, e.g., Yun & Clemens (1994). We have derived radial density profiles (and mean dust temperatures) for a number cores by fitting beam-convolved ray-traced core models to multi-wavelengths submm/mm dust emission maps (see Figs 3 and 4). The results compare well to those derived by other authors.

Isolated protostellar cores have a higher central mass concentration ($\frac{M_{5000\,\mathrm{AU}}}{M_{\mathrm{tot}}} \approx 0.4$) and appear to be more spherically symmetric than pre-protostellar cores. Their envelopes have a power-law radial density gradient of $n_{\mathrm{H}} \propto R^{-2\ldots-1.8}$ and a well-defined outer radius at $\sim 1\ldots2\times10^4$ AU. Densities inside $R < 3000-4000$ AU are up to more than two orders of magnitude higher than in pre-protostellar cores. Total masses are comparable to those of pre-protostellar cores, i.e., $2-5\,\mathrm{M}_\odot$. At their very center, higher dust temperatures and embedded accretion disks add additional dust emission, leading to strongly centrally peaked submm/mm continuum images. Envelope dust temperatures are comparable to those in pre-protostellar cores, which means that the embedded low-mass protostars usually do not considerably contribute much heating to the envelope. Although the average power-law index of the outer radial density profile resembles that of an isothermal sphere, no inner turn-over to shallower profiles ($p = 1.5$) could be confirmed in most sources, like predicted by the "standard" inside-out collapse model (Shu 1977). However, due to the limited angular resolution of most studies and the often unresolved and unknown contribution from an embedded accretion disk, this conclusion needs to be confirmed by detailed analysis of combined single-dish and interferometer data.

Cores in dense and clustered star-forming regions are expected to have different properties than isolated cores due to different environmental conditions like, e.g., better shielding from the external radiation field, differences in external pressure and turbulent environment, and effects of competitive accretion. Indeed, Johnstone et al. (2000) find smaller outer cutoff radii and smaller degrees of central condensation for cores in the ρ Ophiuchi molecular cloud.

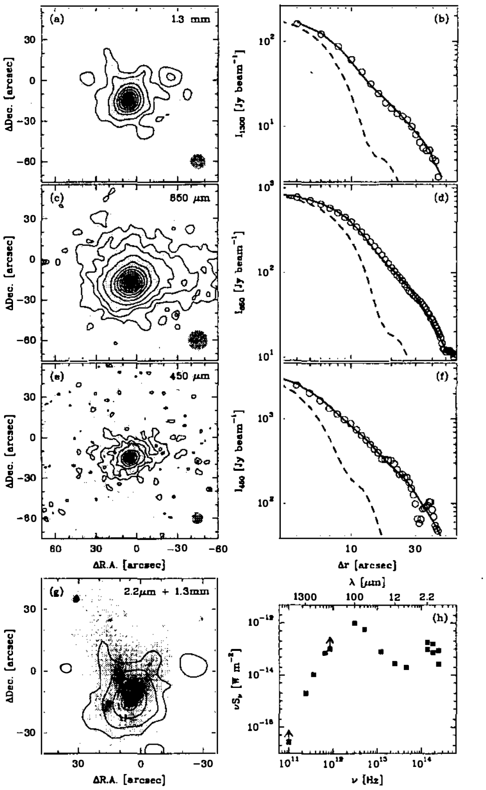

Figure 3: Submm/mm dust continuum maps and K-band image (lower left) of CB 230 (Class 0/I transition object). Observed and modeled radial emission profiles together with the beam profiles are shown in the right panels. SED at lower right. (Launhardt et al. in prep.)

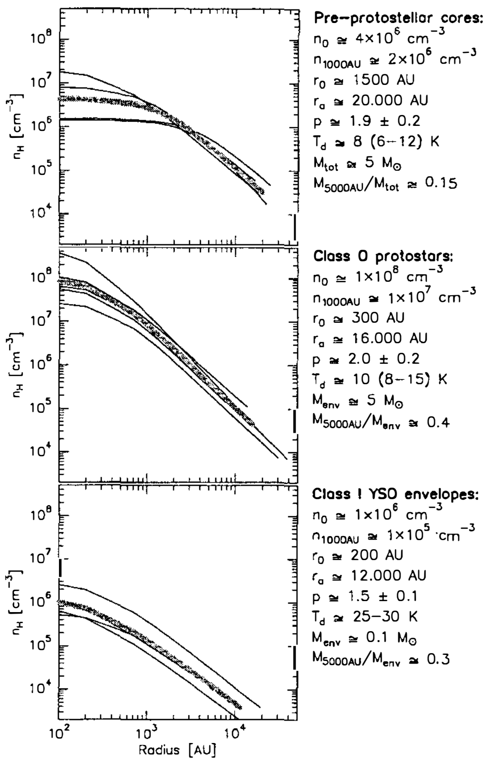

Figure 4: Radial density profiles of the form $n(r) = \frac{n_0}{\left(1+\frac{r}{r_0}\right)^p}$ for isolated pre-protostellar cores, Class 0 protostars, and Class I YSO envelopes, derived from model fits to the multi-wavelengths submm/mm dust emission maps. Thick grey curves show the averaged profiles. Central point sources in Class 0 and I (accretion disks) are not included. (Launhardt et al. in prep.)

2.3 Class I YSO envelopes

Class I sources are often also called "protostars", but we think of them rather as deeply embedded YSO's in an evolved, decelerated accretion stage with remnant envelopes. In contrast to Class 0 protostars, the mm continuum emission from the immediate circumstellar environment is dominated by an accretion disk rather than a dense infalling envelope. Systematic studies of the extended envelopes around Class I YSOs have been performed by, e.g., Young et al. (2003)

and Launhardt et al. (in prep.). The extended envelopes around isolated Class I YSOs have shallower density profiles ($p \approx 1.5$), lower densities ($n_{1000\mathrm{AU}} \approx 10^5\,\mathrm{cm}^{-3}$), higher dust temperatures (25–30 K), and much lower total masses ($\langle M_{\mathrm{env}} \rangle \approx 0.1\,\mathrm{M}_\odot$) than pre-protostellar and protostellar cores. Outer radii are about 10^4 AU. Depending on the viewing angle, the central star can be visible at NIR wavelengths, or the NIR emission is dominated by either scattered light from the outflow lobes or by shock-excited line emission from jets.

3 Multiplicity and efficiency of star formation

Although one would naively expect that simple isolated globules form one star each at their center, detailed studies in recent years showed that about 75% of star-forming cores in globules appear to be multiple on size scales between 500 AU (smallest observed scales) and 20000 AU (0.1 pc) (Launhardt 2003). This number includes true binary protostars (e.g., L 723 VLA 2, Launhardt et al. in prep.), embedded multiple YSOs (e.g., CB 230, Launhardt 2001), as well as multiple dense cores in a globule (e.g., CB 244) (see Fig. 5). While wide double cores like in CB 244 may not have formed by protostellar fragmentation nor may they lead to the formation of physical binary stars, high-resolution observations like for L 273, that would reveal binary protostars formed by fragmentation of a single protostellar core, do exist only for a handful of sources. This shows that even in isolated simple Bok globules star formation and fragmentation/multiplicity are inherently coupled, although exact numbers for the multiplicity rate cannot be given yet.

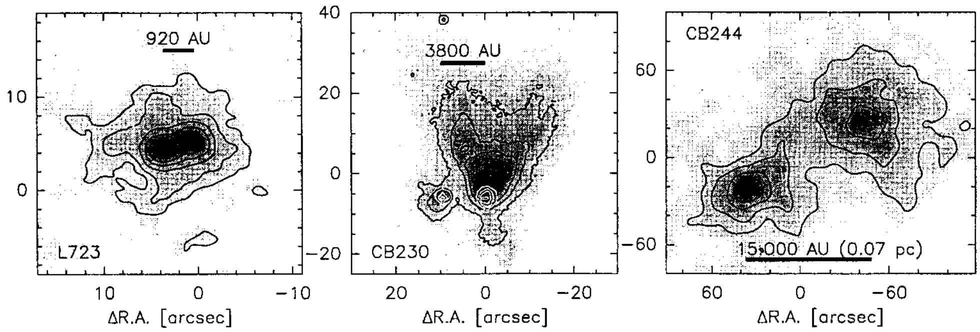

Figure 5: Isolated star formation and multiplicity: Left: 3 mm dust continuum image of L 723 VLA 2, showing a binary protostar with a projected separation of 920 AU. Middle: NIR image of CB 230 with 6.7 μm contours (white) superimposed, showing the two deeply embedded YSOs with a projected separation of ~3800 AU. Right: 1.3 mm dust continuum image of the wide double core in the globule CB 244. The SE core is a Class 0 protostar, the NW core is of pre-protostellar nature.

It is often assumed that in the process of star formation, the mass of a clump or dense core is more or less completely transformed into stars. However, the average total mass in low-mass isolated pre-protostellar and protostellar cores ($R_\mathrm{a} \sim 1-2\times10^4$ AU) is about 5 $\mathrm{M}_\odot$. The typical mass within $R < 5000$ AU of a protostellar core (the assumed total size of the collapse region) is about 2 $\mathrm{M}_\odot$. The typical mass of stars that already have formed in globules is rather unknown. However, for the Class I YSO in CB 26, Launhardt & Sargent (2001) derive a mass of 0.3 $\mathrm{M}_\odot$ for the central star from the rotation curve of the circumstellar disk. Luminosities of stars with 12 μm IRAS PSC fluxes that are located within the projected boundaries of nearby Bok globules are typically 1 – 2 $\mathrm{L}_\odot$ (Launhardt 1996). Assuming an age of one to a few million years, this luminosity would indicate a stellar mass between 0.5 and 1 $\mathrm{M}_\odot$. Since these masses are also typical for stars formed in the isolated mode in the Taurus cloud, it is safe to assume that the typical final stellar mass of a star or binary pair formed in an isolated low-mass core with the above properties is in the range $0.3 - 1\,M_{\odot}$. The efficiency whith which the mass of a cloud core is transformed into stellar mass would then be $6 - 20\%$ for the entire dense core ($R_a \sim 10^4$ AU) or $15 - 50\%$ of the mass included in the inner $R < 5000$ AU in a protostellar core.

4 Magnetic fields

Magnetic fields play a crucial role in star formation although it remains unclear at which stage (clump formation, fragmentation, protostellar collapse) and under which environmental conditions (isolated star formation vs. clustered mode in large and dense molecular clouds) turbulence or magnetic fields are the dominant force. Ward-Thompson et al. (2000), Henning et al. (2001), Wolf et al. (2003), and Crutcher et al. (2004) have obtained submillimeter dust emission polarization maps of a number of isolated prestellar and protostellar cores, i.e., of the dense and smooth inner cores, not the turbulent outer envelopes (see examples in Fig. 6). In most sources, the large-scale magnetic field structure appears to be well-ordered. By applying the Chandrasekhar-Fermi method, they estimate the mean magnetic field strengths in the plane of the sky for each source (dense cores only). Average magnetic field strength are $B \sim 125 \pm 40\,\mu$G in pre-protostellar cores and $\sim 170 \pm 50\,\mu$G in protostellar cores. Magnetic field strengths in the outer envelopes are much less-constrained. For the globule B 1, Goodman et al. (1989) measured $\sim 27\,\mu$G. Note however, that these are only order-of-magnitude estimates and the uncertainties are rather large.

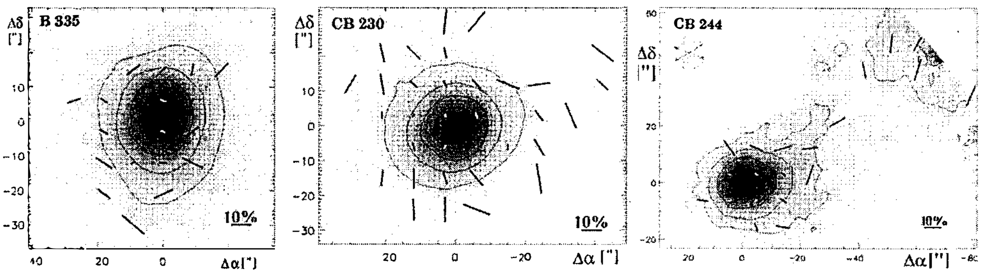

Figure 6: SCUBA images at 850 μm of B 335, CB 230, and CB 244, with polarization vectors superimposed. The polarization maps are used to derive the strengths and mean direction of the magnetic fields in these protostellar cores (from Wolf et al. 2003).

5 Distribution and evolution of angular momentum

Bok globules, like all celestial objects, have non-zero angular momentum and rotate. However, other sources of stochastic and systematic motion like, e.g., turbulence on different size scales, outflows, infall, and shearing can complicate the interpretation of velocity fields derived from molecular emission lines. Goodman et al. (1993) and Kane & Clemens (1997) have analyzed velocity fields and rotation curves of Bok globules and isolated cores in Taurus. They find that most clouds / cloud cores are rotating in approximate solid-body motion with specific angular momenta scaling with cloud size (i.e., approximate conservation of angular velocity) and being consideralby larger than that of T Tauri binary systems. However, stars do not form from the entire cloud, but only from the dense inner $R \approx 5000$ AU part of the cores that undergoes dynamical gravitational collapse and decouples from the rest of the cloud. Detailed kinematic studies of pre-protostellar cores (e.g., IRAM04191, Belloche et al. 2002; CB 17, Launhardt et al. in prep.) and binary protostellar cores (e.g., CB 230, Launhardt 2001, 2003, see Fig. 7) show

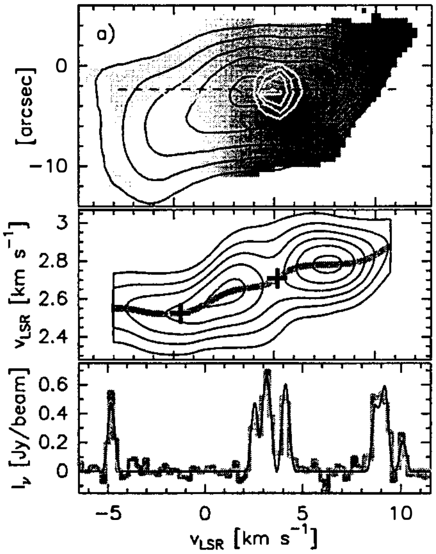

Figure 7: Kinematic structure of the protostellar double core in CB 230. Top: integrated N_2H^+ map (black contours) and mean velocity map (grey-scale, white to black: 2.4 to 2.9 km s^{-1}). White contours show the embedded MIR sources observed with ISOCAM. Center: position-velocity diagram along the dashed line in top panel. Bottom: $N_2H^+(1\text{–}0)$ spectrum and fit (Launhardt 2000).

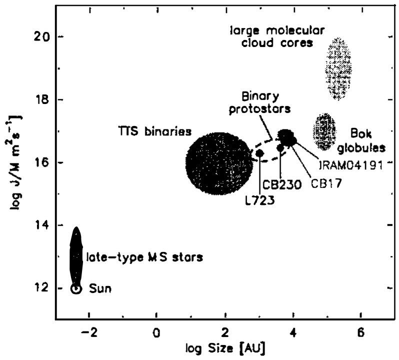

Figure 8: Specific angular momentum vs. size scale for different astronomical sources, from large molecular cloud cores to MS stars. CB 17 (Launhardt et al. in prep) and IRAM 04191 (Belloche & André 2004) are pre-protostellar cores. Binary protostars from Launhardt (2003).

that on size scales below $R \approx 5000$ AU, angular momenta do not scale (or scale only weakly) with size (i.e., angular momentum is conserved). The (specific) angular momentum of prestellar and protostellar cores on these size scales is comparable or only a factor of few larger than that of typical T Tauri binary systems (see Fig. 8). In the context that most protostellar cores are assumed to fragment and form binary stars, this means that most of the angular momentum contained in the collapse region is transormed into orbital angular momentum of the resulting stellar binary system.

6 Energy balance

Here, we attempt to estimate the contribution of different terms to the total energy balance of "typical" (average) isolated low-mass pre-protosteller and protostellar cores. Table 2 summarizes the basic (simplified) equations and the estimated numbers for the thermal, turbulent, rotational kinetic, magnetic, and gravitational potential energy content for the inner 5000 AU and the entire source of both pre-protostellar and protostellar cores. We assume average total gass masses and temperatures listed in Table 2 and radial density profiles of $\rho \propto R^{-1}$ in the inner 5000 AU of pre-protosteller cores and $\rho \propto R^{-2}$ everywhere else.

At the given temperatures, thermal FWHM line widths for a mean particle of mass $2.33 \times m_{\rm H}$ are in the range $\Delta v_{\rm therm} = \sqrt{8 \ln 2}\sqrt{\frac{kT}{2.33\,m_{\rm H}}} = 0.4 - 0.5\,{\rm km\,s^{-1}}$. Observed FWHM widths of optically thin N_2H^+ and NH_3 lines (tracing dense gas in the cores) towards isolated pre-protostellar and protostellar cores (where not strongly affected by outflow or systematic infall motions) are in the range $0.35 - 0.4\,{\rm km\,s^{-1}}$ (e.g., Benson & Myers 1989; Benson et al. 1998).

Table 2: Energy balance of globule cores

Term	Equation$^{(a)}$	—— Pre-protostellar ——		—— Class 0 ——	
		$R \leq 5000$ AU ($M = 1\,M_\odot$) ($T = 8$ K)	$R \leq 20000$ AU ($M = 5\,M_\odot$) ($T = 12$ K)	$R \leq 5000$ AU ($M = 2\,M_\odot$) ($T = 10$ K)	$R \leq 16000$ AU ($M = 5\,M_\odot$) ($T = 12$ K)
$E_{\rm therm}$	$\frac{3}{2} M \frac{kT}{\mu m_{\rm H}}$	4×10^{34} J	3×10^{35} J	1×10^{35} J	3×10^{35} J
$E_{\rm turb}$	$\frac{3}{2} M \langle v_{\rm x}^2 \rangle$	2×10^{34} J	3×10^{35} J	6×10^{34} J	4×10^{35} J
$E_{\rm rot}$	$\frac{\alpha_{\rm rot}}{2} M R^2 \omega^2$ $^{(b)}$	1.5×10^{33} J	2.5×10^{33} J	2×10^{34} J	3×10^{34} J
$E_{\rm mag}$	$\frac{1}{6} R^3 B^2$	1×10^{35} J	4×10^{35} J	2×10^{35} J	4×10^{35} J
$-E_{\rm grav}$	$\alpha_{\rm vir} M^2 R^{-1} G$ $^{(c)}$	2.4×10^{35} J	2×10^{36} J	1.4×10^{36} J	2.8×10^{36} J

$^{(a)}$ Approximation for an ideal gas sphere of radius R, mass M, and temperature T. Furthermore, $\mu = 2.33$ is the mean molecular weight, $m_{\rm H}$ is the mass of an hydrogen atom, k is the Boltzman constant, $\langle v_{\rm x}^2 \rangle$ is the mean quadratic one-dimensional turbulent velocity dispersion of the gas (related to the FWHM line width by $\sqrt{\langle v_{\rm x}^2 \rangle} = \frac{\Delta v_{\rm turb}}{\sqrt{8 \ln 2}}$), ω is the rotational angular velocity of the cloud core (assuming solid-body rotation), B is the average magnetic field strength, and G is the gravitational constant.
$^{(b)}$ $\alpha_{\rm rot} = \frac{2}{5+2p}$, where p is the radial density power-law index (see Fig. 4). $^{(c)}$ $\alpha_{\rm vir} = \frac{3-p}{5-2p}$.

Fuller & Myers (1992) and others report mean $C^{18}O$ line widths tracing core and envelope) of $0.4 - 0.5\,{\rm km\,s^{-1}}$ for starless cores and $0.5 - 0.7\,{\rm km\,s^{-1}}$ for protostellar cores. Neglecting possible contributions from systematic mass motions, turbulent contributions to FWHM line widths are then $\Delta v_{\rm NT} \approx 0.35\,{\rm km\,s^{-1}}$ for the inner 5000 AU in both pre-protostellar and protostellar cores and $\approx 0.4 - 0.6\,{\rm km\,s^{-1}}$ in the outer envelopes.

The numbers for the thermal and turbulent energy content calculated from these estimates show that in the inner 5000 AU of both pre-protostellar and protostellar cores thermal contributions slightly outweight turbulence, while in the outer envelopes turbulence appears to dominate (see Table 2). This is consistent with Falgarone et al. (1998), Park et al. (2004), and others who find that the outer envelopes of starless cores are clumpy and turbulent, while the inner cores appear to be more quiet and smooth with a power-law density distribution. Rotational kinetic energies derived from measured rotation curves (see Sect. 5) appear to be much lower than thermal and turbulent contributions. The magnetic energy content derived from measured magnetic field strengths (Sect. 4) appears to be larger than the other contributions, implying that magnetic fields play an important role in supporting the dense cores against gravitational collapse or at least delaying the collpase. However, the uncertainties in magnetic field strength and mean core radius are rather large and the dependence is strongly non-linear, so that this statement should be taken with caution.

When we apply the equilibrium viral theorem $2\,[E_{\rm th} + E_{\rm turb} + E_{\rm rot}] + E_{\rm mag} + E_{\rm grav} = 0$, we find that pre-protostellar cores are close to virial equilibrium, while Class 0 protostellar cores (in particular the inner 5000 AU) are significantly supercritical (by a factor of 2 – 2.5).

7 Summary

Dense cores of nearby isolated Bok globules are ideal laboratories to study in detail the process of low-mass star formation. However, one has to keep in mind that some of the results may be typical only for the isolated mode of star formation and may not be directly applicable to dense and clustered star-forming regions. The main results can be summarized as follows:

1. Many Bok globules with typical total gas masses $5 - 50\,M_\odot$ and sizes $0.1 - 1$ pc contain dense cores and form stars of typical mass $0.3 - 1\,M_\odot$. The dense cores typically contain $10 - 20\%$ of the total mass in the globule and have sizes of $10000 - 20000$ AU. It is still under debate if smaller globules with less-prominent cores can form lower-mass stars or even substellar objects.

2. Most globules are slightly cometary or irregularly shaped and have the dense core located closer to the sharper rim ("head" side).

3. Pre-protostellar cores often appear filamentary and have very irregular and relatively turbulent outer envelopes. Mean radial density profiles in the inner few thousand AU are rather flat and approach R^{-2} further out.

4. Class 0 protostellar cores have a higher central mass concentration and appear to be more spherically symmetric than pre-protostellar cores. Their envelopes have a power-law radial density gradient of $n_H \propto R^{-2}$ and a well-defined outer radius at $\sim 1.5 \times 10^4$ AU. Most observations have not found a turn-over to shallower density profiles in the inner expected collapse region.

5. Most star-forming cores in globules appear to be multiple on size scales between 500 AU and 20000 AU. While some globules contain initially separate dense cores that collapse and evolve independently, many cores appear to fragment in the process of protostellar collapse and form binary or multiple stellar systems.

6. The (specific) angular momentum contained in the inner ≈ 5000 AU of isolated protostellar cores is comparable or only a factor of few larger than that of typical T Tauri binary systems, i.e. most of the angular momentum contained in the collapse region is transormed into orbital angular momentum of the resulting stellar binary systems.

7. Only about $6-20\%$ of the mass of a dense core ($R < 20000$ AU) is transformed into stars. For the inner $R < 5000$ AU of protostellar cores, this efficiency goes up to $15-50\%$.

8. Typical magnetic field strength are $B \sim 125\,\mu$G in pre-protostellar cores, $\sim 170\,\mu$G in protostellar cores, and $\sim 30\,\mu$G in the outer envelopes. However, the uncertailnties are rather large.

9. Although numbers for the magnetic field strengths are somewhat uncertain, the main support against gravitational collapse of the dense inner cores appears to come from magnetic fields, followed by thermal pressure. Only in the outer envelopes turbulent support becomes equally important. Rotational kinetic energies are about one order of magnitude lower than other contributions. Pre-protostellar cores are close to virial equilibrium, while Class 0 protostellar cores (in particular the inner 5000 AU) are significantly supercritical.

Acknowledgments

I wish to thank Th. Henning, T. Khanzadyan, S. Wolf, D. Ward-Thompson, R. Zylka, T. Bourke, A. Sargent, H. Zinnecker, Y. Pavluchenkov, and L. V. Tóth who all contributetd in one way or the other to the work on which this review is based. I also want to thank P. André, A. Burkert, and M. Smith for helpful discussions.

References

1. Belloche, A., André, P., Despois, D., & Blinder, S. 2002, A&A, 393, 927
2. Benson, P. J. & Myers, P. C. 1989, ApJS, 71, 89
3. Benson, P. J., Caselli, P., & Myers, P. C. 1998, ApJ, 506, 743
4. Bourke, T. L., Hyland, A. R., & Robinson, G. 1995, MNRAS, 276, 1052 (BHR)
5. Clemens, D. P. & Barvainis, R. 1988, ApJS, 68, 257 (CB)
6. Crutcher, R. M., Nutter, D. J., Ward-Thompson, D., & Kirk, J. M. 2004, ApJ, 600, 279
7. Evans, N. J., Rawlings, J. M. C., Shirley, Y. L., & Mundy, L. G. 2001, ApJ, 557, 193
8. Falgarone, E., Panis, J.-F., Heithausen, A., Perault, M., Stutzki, J., Puget, J.-L., & Bensch, F. 1998, A&A, 331, 669
9. Fuller, G. A. & Myers, P. C. 1992, ApJ, 384, 523
10. Goodman, A. A., Crutcher, R. M., Heiles, C., Myers, P. C., & Troland, T. H. 1989, ApJ, 338, L61
11. Goodman, A. A., Benson, P. J., Fuller, G. A., & Myers, P. C. 1993, ApJ, 406, 528
12. Johnstone, D., Wilson, C. D., Moriarty-Schieven, G., Joncas, G., Smith, G., Gregersen, E., & Fich, M. 2000, ApJ, 545, 327
13. Henning, T., Wolf, S., Launhardt, R., & Waters, R. 2001, ApJ, 561, 871
14. Kane, B. D. & Clemens, D. P. 1997, AJ, 113, 1799
15. Launhardt, R. 1996, Ph.D. Thesis, University of Jena
16. Launhardt, R. 2001, IAU Symposium, 200, 117
17. Launhardt, R. 2003, IAU Symposium, 221, 140
18. Launhardt, R. & Sargent, A. I. 2001, ApJ, 562, L173
19. Motte, F. & André, P. 2001, A&A, 365, 440
20. Park, Y., Lee, C. W., & Myers, P. C. 2004, ApJS, 152, 81
21. Shirley, Y. L., Evans, N. J., & Rawlings, J. M. C. 2002, ApJ, 575, 337
22. Shu, F. H. 1977, ApJ, 214, 488
23. Ward-Thompson, D., Scott, P. F., Hills, R. E., & André, P. 1994, MNRAS, 268, 276
24. Ward-Thompson, D., Motte, F., & André, P. 1999, MNRAS, 305, 143
25. Ward-Thompson, D., Kirk, J. M., Crutcher, R. M., Greaves, J. S., Holland, W. S., & André, P. 2000, ApJ, 537, L135
26. Wolf, S., Launhardt, R., & Henning, T. 2003, ApJ, 592, 233
27. Young, C. H., Shirley, Y. L., Evans, N. J., & Rawlings, J. M. C. 2003, ApJS, 145, 111
28. Yun, J. L. & Clemens, D. P. 1994, ApJS, 92, 145

MAGNETIC FIELDS IN MOLECULAR CLOUD CORES

SHANTANU BASU

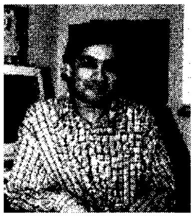

Department of Physics and Astronomy, University of Western Ontario, London, Ontario N6A 3K7, Canada

Observations of magnetic field strengths imply that molecular cloud fragments are individually close to being in a magnetically critical state, even though both magnetic field and column density measurements range over two orders of magnitude. The turbulent pressure also approximately balances the self-gravitational pressure. These results together mean that the one-dimensional velocity dispersion σ_v is proportional to the mean Alfvén speed of a cloud V_A. Global models of MHD turbulence in a molecular cloud show that this correlation is naturally satisfied for a range of different driving strengths of the turbulence. For example, an increase of turbulent driving causes a cloud expansion which also increases V_A. Clouds are in a time averaged balance but exhibit large oscillatory motions, particularly in their outer rarefied regions. We also discuss models of gravitational fragmentation in a sheet-like region in which turbulence has already dissipated, including the effects of magnetic fields and ion-neutral friction. Clouds with near-critical mass-to-flux ratios lead to subsonic infall within cores, consistent with some recent observations of motions in starless cores. Conversely, significantly supercritical clouds are expected to produce extended supersonic infall.

Keywords: ISM: clouds - ISM: magnetic fields - MHD - stars: formation - turbulence

1 Magnetic field data

When discussing magnetic fields in molecular clouds, a useful starting point is to look at the confirmed detections of magnetic field strength using the Zeeman effect. Other methods using measurements of polarized emission and the Chandrasekhar-Fermi method are just beginning to be applied to molecular clouds, but are characterized by larger uncertainties. We look at data encompassing 15 confirmed detections compiled by Crutcher (1999), one more detection (in L1544) by Crutcher & Troland (2000), and one (in RCW38) by Bourke et al. (2001). The last one does not have a density estimate, so is used only in Fig. 1a below. It emerges that the data satisfy two independent correlations, as first noted by Myers & Goodman (1988) from data available at that time. We cast these correlations in the following manner.

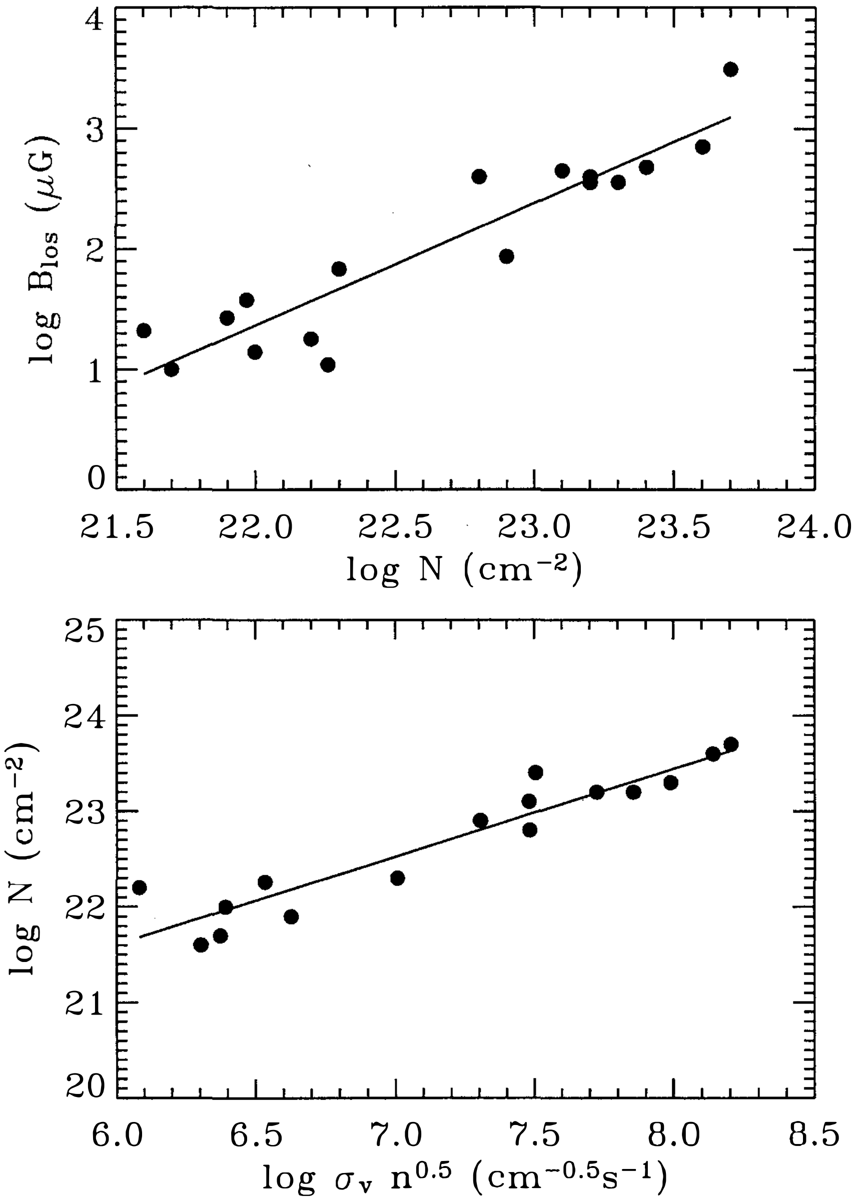

Figure 1: *Top*: Plot of $\log B_{\rm los}$ versus $\log N$ for the sample of 17 clouds with confirmed magnetic field detections (see text). The solid line is a least squares best fit to the data. *Bottom*: Plot of $\log N$ versus $\log \sigma_v n^{0.5}$ for the same sample of clouds (minus RCW38). The solid line is a least squares best fit to the data.

Figure 1a shows that there is a clear correlation between $B_{\rm los}$, the line-of-sight component of the magnetic field that is measurable by the Zeeman effect, and the column density N (by definition also a line-of-sight value), in over two orders of magnitude variation in each quantity. This is expected from the relation

$$\frac{\Sigma}{B} \equiv \mu\,(2\pi G^{1/2})^{-1} \tag{1}$$

(where $\Sigma = mN$, in which m is the mean molecular mass) if the dimensionless mass-to-flux ratio μ, measured in units of the critical value $(2\pi G^{1/2})^{-1}$ (Nakano & Nakamura 1978), is approximately constant from cloud to cloud. The solid line is the least squares best-fit to $\log B_{\rm los}$ versus $\log N$. It has an estimated slope 1.02 ± 0.10, consistent with the expected slope of unity. The average measured mass-to-flux ratio is $\langle \mu_{\rm los}\rangle = \langle \Sigma/B_{\rm los}\rangle \times 2\pi G^{1/2} = 3.25$. Since the measured field $B_{\rm los}$ is related to the full magnetic field strength B by $B_{\rm los} = B\cos\theta$, then if the magnetic fields have a random set of inclinations θ to the line-of-sight, we would expect that $\langle B\rangle = 2\langle B_{\rm los}\rangle$. Assuming that N is the same for all lines of sight, we then expect the average total mass-to-flux ratio to be $\langle\mu\rangle = \langle\Sigma/B\rangle \times 2\pi G^{1/2} = 1/2\langle\mu_{\rm los}\rangle = 1.63$. We also note that if the clouds are preferentially flattened along the magnetic field direction, the column density parallel to the magnetic field $N_\parallel = N\cos\theta$. Since $N_\parallel$ is the relevant column density for calculating the mass-to-flux ratio, in this case we get $\langle\mu\rangle = \langle\Sigma_\parallel/B\rangle \times 2\pi G^{1/2} = 1/3\langle\mu_{\rm los}\rangle = 1.08$, using an angle-averaging process (see Crutcher 1999). All in all, it is a remarkable feature that molecular clouds are so close to a magnetically *critical* state over a wide range of observed length scales and densities.

A second correlation is between the self-gravitational pressure at the midplane of a cloud and the internal turbulent pressure. One may imagine that a cloud settles into such a state by establishing approximate force balance along magnetic field lines. In this case, we expect

$$\rho_0\,\sigma_v^2 = \frac{\pi}{2} G\,\Sigma^2, \tag{2}$$

where ρ_0 is the density at the midplane, and σ_v is the total (thermal and non-thermal) one-dimensional velocity dispersion. We have assumed that the effect of confining external pressure is small compared to the self-gravitational pressure. Since the mean density ρ may be related to ρ_0 by some multiplicative constant, we expect that

$$N \propto \sigma_v n^{1/2}, \tag{3}$$

where $n = \rho/m$ is the mean number density. Figure 1b shows that this relation is indeed valid for our cloud sample. The least squares best-fit yields a slope 0.92 ± 0.09, again consistent with unity. We note in passing that equation (3) is the generalized form of the well-known linewidth-size relation for molecular clouds; if $N \propto nR \approx$ constant (unlike this sample) for a sample of clouds of different radii R, then $\sigma_v \propto n^{-1/2} \propto R^{1/2}$.

Since $B \propto N$ and $N \propto \sigma_v n^{1/2}$, it is clear that we expect

$$B \propto \sigma_v n^{1/2}. \tag{4}$$

Figure 2 shows this correlation from the data using $B_{\rm los}$ instead of B. This relation is equivalent to $\sigma_v \propto V_{\rm A}$, where $V_{\rm A} \equiv B/\sqrt{4\pi\rho}$ is the mean Alfvén speed of the cloud, calculated using the mean density ρ. Our best fit (solid line) yields a slope 1.03 ± 0.09. The average ratio $\langle\sigma_v/V_{\rm A}\rangle = 0.54$, if we again use $\langle B\rangle = 2\langle B_{\rm los}\rangle$.

It is also interesting to note here that derived relation $\sigma_v \propto V_{\rm A}$ does *not* necessarily imply that the turbulence consists of Alfvénic motions. We have only assumed a near critical mass-to-flux ratio and any unspecified turbulent motions. The relationship is a reflection of the

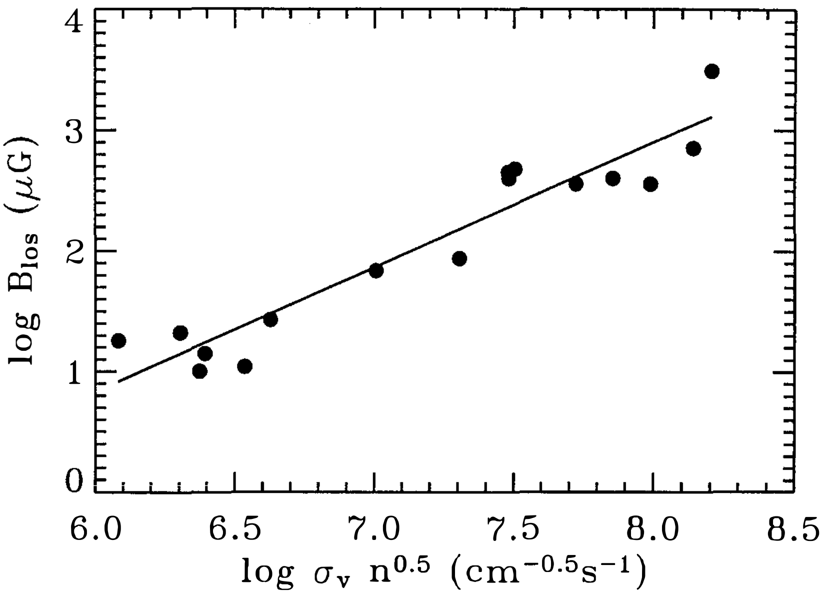

Figure 2: Plot of $\log B_{\rm los}$ versus $\log \sigma_v n^{1/2}$ for the same clouds as in Fig. 1b. The solid line is the least squares best fit.

global properties of a cloud, and follows from the virial relations (Myers & Goodman 1988). Indeed, Alfvén waves alone might lead to material motions that are significantly sub-Alfvénic. For example, linear Alfvén waves obey the relation $\delta v = V_{\rm A}\delta B/B$, where δv and δB are the amplitudes of fluctuations in the material speed and magnetic field, respectively. Thus we see that $\delta v \ll V_{\rm A}$ if $\delta B/B \ll 1$.

2 A Model for MHD Turbulence

Kudoh & Basu (2003) have presented a numerical model of MHD turbulence in a stratified, bounded, one-dimensional cloud. The model is 1.5 dimensional, meaning that vector quantities have both y and z components, but can only vary in the z-direction. It is a *global* model of turbulence, in contrast to a *local* periodic box numerical model. In this model, the cloud stratification can be modeled, and the mean cloud density ρ can change with time.

The model initial condition is a hydrostatic equilibrium between thermal pressure and self-gravity in a cloud that is bounded by an external high temperature medium. The initial state of the cloud is a truncated (at about $z = 3H_0$) Spitzer equilibrium density profile $\rho(z) = \rho_0 \,\mathrm{sech}^2(z/H_0)$, in which $H_0 = c_{s0}/\sqrt{2\pi G\rho_0}$ and c_{s0} is the isothermal sound speed of the cloud. Isothermality is maintained for each Lagrangian fluid element. A sinusoidal driving force of dimensionless amplitude $\tilde{a}_d$ (see Kudoh & Basu 2003 for details) is introduced near the midplane of the cloud and the dynamical evolution of the vertical structure of the cloud is followed. The cloud is characterized by a critical mass-to-flux ratio ($\mu = 1$). Figure 3 shows the time evolution of the density presented by Kudoh & Basu (2003). The density plots at various times are stacked with time increasing upward in uniform increments of $0.2t_0$, where $t_0 = H_0/c_{s0}$. Because the driving force increases linearly with time up to $t = 10t_0$, the density changes gradually at

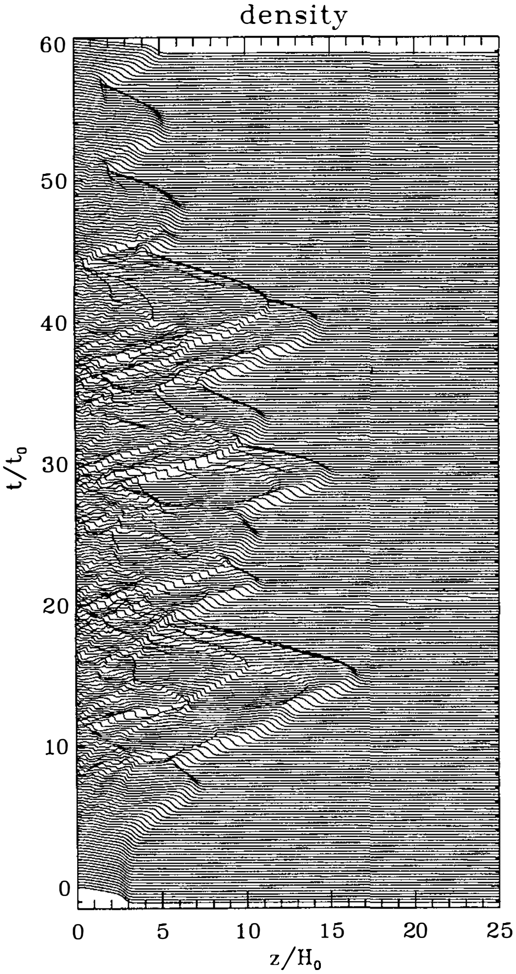

Figure 3: Time evolution of the density in a global model of MHD turbulence (Kudoh & Basu 2003). The density versus z/H_0 at various times are stacked with time, with time increasing upwards in uniform increments of $0.2t_0$.

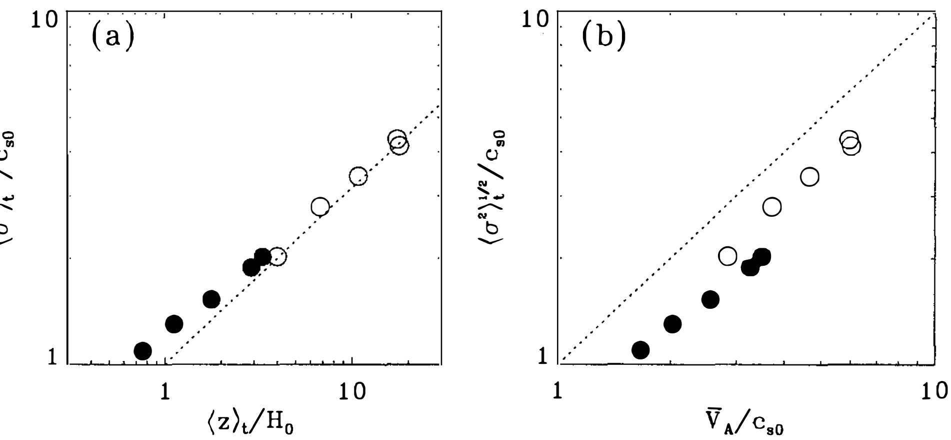

Figure 4: Global properties of an ensemble of clouds with different turbulent driving strengths $\tilde{a}_d$. (a) Time averaged velocity dispersions $\langle\sigma^2\rangle_t^{1/2}$ of different Lagrangian fluid elements for different $\tilde{a}_d$, as a function of time averaged positions $\langle z\rangle_t^{0.5}$. The open circles correspond to Lagrangian fluid elements whose initial positions are $z/H_0 = 2.51$, close to the cloud edge. The filled circles correspond to Lagrangian fluid elements whose initial positions are $z/H_0 = 0.61$, approximately the cloud half-mass position. The dotted line is the relation $\langle\sigma^2\rangle_t^{1/2} = \langle z\rangle_t^{0.5}$. (b) $\langle\sigma^2\rangle_t^{1/2}$ versus mean Alfvén speed $V_A \equiv B/\sqrt{4\pi\rho}$, where ρ is the average density. The dotted line shows $\langle\sigma^2\rangle_t^{1/2} = V_A$. All quantities are normalized to the isothermal sound speed c_{s0} in the cloud.

first. After $t = 10t_0$, the density structure shows many shock waves propagating in the cloud, and significant upward and downward motions of the outer portion of the cloud, including the temperature transition region. After terminating the driving force at $t = 40t_0$, the shock waves are dissipated in the cloud and the transition region moves back toward the initial position, although it is still oscillating. A stronger driving force (larger $\tilde{a}_d$) causes a larger turbulent velocity, which results in a more dynamic evolution of the molecular cloud, including stronger shock waves, and larger excursions of the cloud boundary.

Figure 4a shows the time averaged velocity dispersions $\langle\sigma^2\rangle_t^{1/2}$ of different Lagrangian fluid elements for different strengths of the driving force, as a function of the time averaged height $\langle z\rangle_t$. The open circles correspond to Lagrangian fluid elements close to the cloud edge, while the filled circles represent fluid elements near the half-mass position of the cloud. Each circle corresponds to a different value of $\tilde{a}_d$, with increasing $\tilde{a}_d$ generally resulting in increasing $\langle z\rangle_t$. The dotted line shows

$$\langle\sigma^2\rangle_t^{1/2} \propto \langle z\rangle_t^{0.5}, \tag{5}$$

and reveals that the model clouds are in a time-averaged equilibrium state. The relation is also consistent with the well-known observational linewidth-size relation of molecular clouds (e.g., Larson 1981; Solomon et al. 1987).

Figure 4b plots $\langle\sigma^2\rangle_t^{1/2}$ versus the mean Alfvén speed V_A for individual Lagrangian fluid elements. The dotted line shows

$$\langle\sigma^2\rangle_t^{1/2} \propto V_A, \tag{6}$$

and reveals that the simulations result in a good correlation between $\langle\sigma^2\rangle_t^{1/2}$ and $V_A \equiv B_0/\sqrt{4\pi\rho}$, where $\rho = \Sigma/(2\langle z\rangle_t)$ is the mean density and Σ is the column density for each Lagrangian element having mean position $\langle z\rangle_t$. This relation is essentially the same as the observational correlation $B \propto \sigma_v n^{1/2}$ presented in § 1.

It is worth noting here that the motions inside the cloud are overall slightly sub-Alfvénic, and highly sub-Alfvénic in the rarefied envelopes of the stratified clouds, where the local Alfvén speed can be very high. Furthermore, very strong driving *fails* to produce super-Alfvénic motions, due to the ability of the cloud to expand and lower its density, thus increasing $V_{\rm A}$. A natural time-averaged balance is always established in which $\sigma_v \approx 0.5 V_{\rm A}$; both σ_v and $V_{\rm A}$ are variable quantities, unlike in a periodic box simulation where they may be held fixed.

3 Fragmentation of a Magnetized Cloud

Basu & Ciolek (2004) have modeled the evolution of a two-dimensional region perpendicular to the mean magnetic field direction, using the thin-disk approximation. This is a non-ideal MHD simulation which includes the effect of ambipolar diffusion (ion-neutral drift), in a region that is partially ionized by cosmic rays. Physically, this model is complementary to that of Kudoh & Basu (2003) in that it models the other two dimensions (perpendicular to the mean magnetic field), in a sub-region of a cloud where turbulence has largely dissipated. Ion-neutral friction is also expected to be more efficient in subregions of clouds where the background ultraviolet starlight cannot penetrate (McKee 1989), and the ionization fraction is therefore much lower. Indeed, MHD turbulent motions may also be preferentially damped in regions with lower ionization fraction (e.g., Myers & Lazarian 1998). The two-dimensional computational domain is modeled with periodic boundary conditions and has an initially uniform column density $\Sigma_{\rm n}$ ("n" denotes neutrals) and vertical magnetic field B_z. Small white-noise perturbations are added to both quantities in order to initiate evolution.

Figure 5 shows the contours of $\Sigma_{\rm n}/\Sigma_{\rm n,0}$ and the velocity vectors for a model with critical initial mass-to-flux ratio ($\mu_0 = 1$), at a time when the maximum value of $\Sigma_{\rm n}/\Sigma_{\rm n,0} \approx 10$. The time is $t = 133.9\, t_0$, where $t_0 = c_{\rm s}/(2\pi G \Sigma_{\rm n,0}) = 2.38 \times 10^5$ yr for an initial volume density $n_{\rm n,0} = 3 \times 10^3$ cm^{-3}. Star formation is expected to occur very shortly afterward in the peaks due to the very short dynamical times in those regions, which are now magnetically supercritical. Although it takes a significant time $\approx 3 \times 10^7$ yr for the peaks to evolve into the runaway phase, it is worth noting that nonlinear perturbations would result in lesser times. The contours of mass-to-flux ratio $\mu(x,y) = \Sigma_{\rm n}(x,y)/B_z(x,y) \times 2\pi G^{1/2}$ (now nonuniform due to ion-neutral drift) also reveal that regions with $\Sigma_{\rm n}/\Sigma_{\rm n,0} > 1$ are typically supercritical while regions with $\Sigma_{\rm n}/\Sigma_{\rm n,0} < 1$ are typically subcritical (Basu & Ciolek 2004). This means that ambipolar diffusion leads to flux redistribution that naturally creates *both* supercritical and subcritical regions in a cloud that is critical ($\mu_0 = 1$) overall. A distinguishing characteristic of the critical model is that the infall motions are *subsonic*, both inside the core and outside, with maximum values $\approx 0.5 c_{\rm s} \approx 0.1$ km s^{-1} found within the cores. This is consistent with detected infall motions in some starless cores, specifically in L1544 (Tafalla et al. 1998; Williams et al. 1999). The core shapes are mildly non-circular in the plane, and triaxial when height Z consistent with vertical force balance is calculated. However, the triaxial shapes are closer to oblate than prolate since the x- and y- extents are roughly comparable and both much greater than the extent in the z-direction.

Figure 6 shows the contours of $\Sigma_{\rm n}/\Sigma_{\rm n,0}$ and the velocity vectors for a model with $\mu_0 = 2$, i.e., significantly supercritical initially. The distinguishing characteristics of this model are the relatively short time ($t = 17.6\, t_0 \approx 4 \times 10^6$ yr) required to reach a maximum $\Sigma_{\rm n}/\Sigma_{\rm n,0} \approx 10$, the supersonic infall motions within cores, and the more elongated triaxial shapes of the cores. Note that the velocity vectors in Fig. 6 have the same normalization as in Fig. 5. The extended supersonic infall (on scales $\lesssim 0.1$ pc) provides an observationally distinguishable difference between clouds being critical or significantly supercritical.

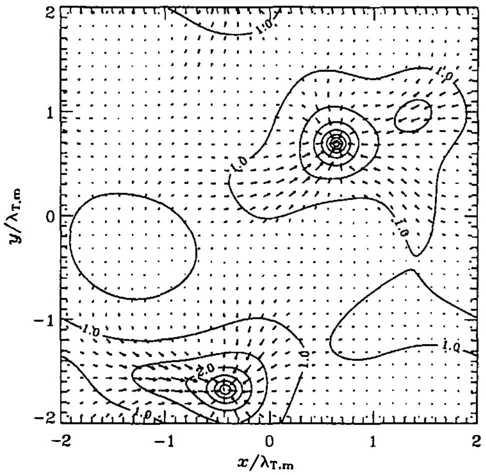

Figure 5: Fragmentation in the critical model ($\mu_0 = 1$) of Basu & Ciolek (2004). The data are shown when the maximum column density $\approx 10\,\Sigma_{n,0}$. Lines represent contours of normalized column density $\Sigma_n(x,y)/\Sigma_{n,0}$, spaced in multiplicative increments of $2^{1/2}$, i.e., [0.7,1.0,1.4,2,2.8,...]. Also shown are velocity vectors of the neutrals; the distance between tips of vectors corresponds to a speed $0.5\,c_s$. The positions x and y are normalized to $\lambda_{T,m}$, the wavelength of maximum growth rate for linear perturbations in a nonmagnetic sheet.

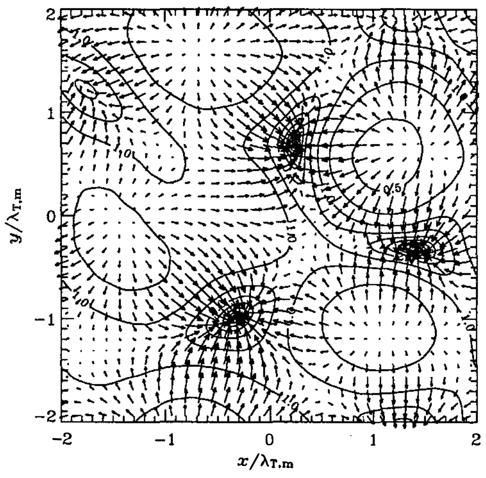

Figure 6: Fragmentation in a supercritical model ($\mu_0 = 2$) of Basu & Ciolek (2004). The data are shown when the maximum column density $\approx 10\,\Sigma_{n,0}$. Lines represent contours of normalized column density $\Sigma_n(x,y)/\Sigma_{n,0}$, spaced in multiplicative increments of $2^{1/2}$. Also shown are velocity vectors of the neutrals; they have the same normalization as in Fig. 5. Note the significantly more rapid motions in this case.

4 Discussion and Conclusions

We have seen that any cloud that has a balance of self-gravitational pressure and turbulent pressure, and also has a large-scale magnetic field such that $\mu \sim 1$ will satisfy the relation $B \propto \sigma_v n^{1/2}$ ($\sigma \propto V_{\rm A}$). Observed cloud fragments satisfy this correlation very well. Numerical experiments (Kudoh & Basu 2003) modeling the global effects of internal MHD turbulence show that clouds evolve in an oscillatory fashion (with the outer parts making the largest excursions) but satisfy the above correlation in a time-averaged sense. The temporal averaging in that model may also be akin to a spatial averaging through many layers of cloud material along the line of sight. We emphasize that the observations and numerical simulations imply that clouds can readjust to *any* level of internal turbulence in such a way that σ_v and $V_{\rm A}$ come into approximate balance (specifically $\sigma_v \approx 0.5 V_{\rm A}$). Unlike the sound speed $c_{\rm s}$ in an isothermal cloud, the mean Alfvén speed $V_{\rm A}$ in a self-gravitating cloud is not a fixed quantity, and varies in space and time, as the cloud expands and contracts.

Molecular cloud fragments seem to represent an ensemble of objects with varying levels of turbulent support, but which have a near-critical mass-to-flux ratio. The data has sometimes been suggested to be consistent with the relation $B \propto n^{1/2}$. Such a relation is expected for the contraction of a cloud that is flattened along the magnetic field direction, if flux-freezing holds. It is roughly satisfied by the data (see Crutcher 1999) given that σ_v only varies by one order of magnitude while B and n have much larger variations. However, as shown by Basu (2000), the correlation is much better for $B \propto \sigma_v n^{1/2}$. We believe that the proper interpretation is that the cloud fragments all have near-critical mass-to-flux ratio and varying levels of internal turbulence. These clouds do not represent a direct evolutionary sequence since the sizes and masses of the objects differ by many orders of magnitude, e.g., the sizes range from 22.0 pc down to 0.02 pc, and masses from $\sim 10^6$ $M_\odot$ down to ~ 1 $M_\odot$!

In regions where turbulence has largely dissipated, one may expect a gravitational fragmentation process regulated by (non-ideal) MHD effects, as modeled by Basu & Ciolek (2004). We note that the non-turbulent models also satisfy $\sigma_v \sim V_{\rm A}$, where $\sigma_v = c_{\rm s}$ in this case, since it is essentially thermal pressure which balances the gravitational pressure along field lines. We have found that the fragmentation process of a significantly supercritical cloud may be ruled out in the context of current star formation in e.g., the Taurus molecular cloud, due to the lack of observed supersonic infall (Tafalla et al. 1998; Williams et al. 1999). Velocity fields provide an interesting distinguishing characteristic of various levels of magnetic support. Cloud core shapes are invariably triaxial, and closer to oblate rather than prolate. The observed distribution of cloud core shapes, which imply triaxial but more nearly oblate objects (Jones, Basu, & Dubinski 2001) can be naturally understood using these kind of models, although more complete models will need to be truly three-dimensional and include internal turbulent support. The critical model of Basu & Ciolek (2004) also shows that flux and mass redistribution naturally creates both supercritical regions and subcritical envelopes. Mass redistribution in flux tubes is a key feature of gravitationally driven ambipolar diffusion, as emphasized long ago by Mouschovias (1978). Detailed targeted observations of the inter-core medium are necessary in order to identify the putative subcritical envelopes. All in all, the outcome of gravitational fragmentation in a non-ideal MHD environment in which $\mu \approx 1$ may hold many surprises. We are just beginning to explore the rich physics of such systems.

Looking forward, we must grapple with several key questions about the role of the magnetic field and star formation in general. Are the triaxial shapes of cores an important factor in binary or multiple system formation? This will require high-resolution MHD simulations of nonaxisymmetric cores. Do the different rates of infall in subcritical, critical, and supercritical clouds actually affect the final outcome? We have heard at this meeting that star formation in many environments (e.g., starbursts) can be quite efficient. Perhaps supercritical fragmentation was important in the past history of the Galaxy and in external galaxies, while the relatively inefficient current day star formation in the Galaxy is the result of critical or subcritical fragmentation. We need to quantify to what extent a subcritical or critical cloud can limit star formation through subcritical envelopes which have an inability or lack of available time to form stars. Simulations which go much further ahead in time, and include the feedback effect of the first generation of stars, can answer these questions. At this point, we are not sure to what extent stellar masses are determined by (1) a finite mass reservoir due to envelopes supported by magnetic and/or turbulent support, and/or (2) feedback from outflows. Future observations and numerical models should resolve this issue.

Acknowledgments

I thank Glenn Ciolek, Takahiro Kudoh, Eduard Vorobyov, and James Wurster for their collaborative work and many stimulating discussions. I am also very appreciative of the organizers for a most thought-provoking and enjoyable meeting. This work was supported by the Natural Sciences and Engineering Research Council (NSERC) of Canada.

References

1. Basu, S. 2000, ApJ, 540, L103
2. Basu, S., & Ciolek, G. E. 2004, ApJ, 607, L39
3. Bourke, T. L., Myers, P. C., Robinson, G., & Hyland, A. R. 2001, ApJ, 554, 916
4. Crutcher, R. M. 1999, ApJ, 520, 706
5. Crutcher, R. M., & Troland, T. H. 2000, ApJ, 537, L139
6. Jones, C. E., Basu, S., & Dubinski, J. 2001, ApJ, 551, 387
7. Kudoh, T., & Basu, S. 2003, ApJ, 595, 842
8. Larson, R. B. 1981, MNRAS, 194, 809
9. McKee, C. F. 1989, ApJ, 345, 782
10. Mouschovias, T. Ch. 1978, in Protostars & Planets, ed. T. Gehrels (Tucson: Univ. Arizona), 209
11. Myers, P. C., & Goodman, A. A. 1988, ApJ, 326, L27
12. Myers, P. C., & Lazarian, A. 1998, ApJ, 507, L157
13. Nakano, T., & Nakamura, T. 1978, PASJ, 30, 671
14. Solomon, P. C, Rivolo, A. R., Barrett, J., & Yahil, A. 1987, ApJ, 319, 730
15. Tafalla, M., Mardones, D., Myers, P. C., Caselli, P., Bachiller, R., & Benson, P. J. 1998, ApJ, 504, 900
16. Williams, J. P., Myers, P. C., Wilner, D. J., & DiFrancesco, J. 1999, ApJ, 513, L61

The Average Magnetic Field Strength in Star–Forming Clouds

P. PADOAN (1), R. JIMENEZ (2), M. JUVELA (3), Å. NORDLUND (4)
(1) Department of Physics, University of California, San Diego, La Jolla, CA 92093-0424, USA
(2) Department of Physics and Astronomy, University of Pennsylvania, Philadelphia, PA 19104, USA
(3) Helsinki University Observatory, Tähtitorninmäki, P.O.Box 14, SF-00014 University of Helsinki, Finland
(4) Copenhagen Astronomical Observatory, NBI, DK–2100, Copenhagen, Denmark

The magnetic field strength in molecular clouds is a fundamental quantity for theories of star formation. It is estimated by Zeeman splitting measurements in a few dense molecular cores, but its volume–averaged value within large molecular clouds (over several parsecs) is still uncertain. In this work we provide a new method to constrain the average magnetic field strength in molecular clouds. We compare the power spectrum of gas density of molecular clouds with that of two 350^3 numerical simulations of supersonic MHD turbulence. The numerical simulation with approximate equipartition of kinetic and magnetic energies (model A) yields the column density power spectrum $P(k) \propto k^{-2.25\pm0.01}$, the super–Alfvénic simulation (model B) $P(k) \propto k^{-2.71\pm0.01}$. The column density power spectrum of the Perseus, Taurus and Rosetta molecular cloud complexes is found to be well approximated by a power law, $P_o(k) \propto k^{-a}$, with $a = 2.74 \pm 0.07$, 2.74 ± 0.08 and 2.76 ± 0.08 respectively. We conclude that the observations are consistent with the presence of super–Alfvénic turbulence in molecular clouds (model B) while model A is inconsistent with the observations.

Keywords: turbulence – ISM: kinematics and dynamics – radio astronomy: interstellar: lines

1 Introduction

The volume–averaged magnetic field strength in molecular clouds has never been measured directly. Zeeman splitting has been detected only from a few dense molecular cloud cores, where emission lines from molecules such as OH and CN are observed (Crutcher, 1999; Bourke et al., 2001). Dense cores fill only a small fraction of the volume of molecular clouds. Therefore, the magnetic field strength averaged over the molecular cloud volume cannot be directly inferred from its value in the cores. This is true especially if the magnetic field strength has a very intermittent distribution and is correlated with the gas density, as suggested by Padoan & Nordlund (1999).

Estimates of magnetic field strength in molecular clouds have been inferred from the dispersion in the polarization angle (e.g. Myers & Goodman, 1991; Chrysostomou et al., 1994; Lai et al., 2001; Matthews & Wilson, 2002; Lai et al., 2002) as originally suggested by Davis (1951) and Chandrasekhar & Fermi (1953). This method was tested in numerical simulations of MHD turbulence by Ostriker et al. (2001), Padoan et al. (2001) and Heitsch et al. (2001). The relative motion of ions and neutral molecules, as manifested by a comparison of their spectral lines, has also been used to estimate the magnetic field strength in molecular clouds (Houde et al., 2000, 2002).

In this work we present a new way to constrain the average magnetic field strength in molecular clouds, based on the density power spectrum. In § 2 we show numerical simulations of supersonic MHD turbulence with different magnetic field strength yield different power spectra of gas density. The power spectrum is then computed from maps of molecular clouds in § 3. We find that only a rather low value for the average magnetic field strength, leading to super-Alfvénic turbulence, is consistent with the observations. Conclusions are summarized in § 4.

The density power spectrum depends on the rms sonic Mach number of the turbulence, M_S (the ratio of the rms flow velocity and the sound speed). In this work we use only simulations with $M_S \approx 10$ because that is the approximate value in the molecular cloud complexes we have studied. We do not study the dependence of the power spectrum on the value of M_S. In general, smaller values of M_S yield steeper density power spectra than the $M_S \approx 10$ models (this was verified with a set of simulations that will be presented elsewhere). Turbulent flows with $M_S \ll 1$, for example, are expected to generate a Kolmogorov density power spectrum, proportional to $k^{-11/3}$. This slope is comparable with the electron density power spectrum on very small scale estimated from scintillation studies (Armstrong et al., 1995). HI surveys of our galaxy and the Magellanic Clouds (Crovisier & Dickey, 1983; Elmegreen et al., 2001; Stanimirović & Lazarian, 2001; Dickey et al., 2001) produced power spectra with slope intermediate between the present results in molecular clouds and the scintillation studies.

2 Power Spectrum of Gas Density in Supersonic MHD Turbulence

In order to study the power spectrum of gas density, we have run two simulations of driven supersonic MHD turbulence with rms sonic Mach number $M_S \approx 10$ and isothermal equation of state. We have solved the three dimensional compressible MHD equations in a staggered mesh with 350^3 computational cells and periodic boundary conditions. The initial magnetic and density fields are uniform. The flow is driven by an external large scale random and solenoidal force, correlated at the largest scale turn-over time. The time derivative of the random force is generated in Fourier space, with power only in the range of wavenumbers $1 \leq k\,L_{\rm mesh}/2\,\pi \leq 2$. The initial velocity field is proportional to the initial force, with an rms amplitude of approximately 50% of its relaxed value. Details about the numerical method are given in Padoan & Nordlund (1999).

We have run the simulations for five dynamical times. The dynamical time is here defined as $t_{\rm d} = L_{\rm mesh}/(2\,u)$, where u is the rms flow velocity. We choose this definition of dynamical time because the flow is forced up to wavenumber $k = 4\pi/L_{\rm mesh}$ and therefore the largest turbulent scale is approximately $L_{\rm mesh}/2$.

We characterize the simulations based on the relative importance of magnetic and dynamic (turbulent) pressure. The pressure ratio is defined as $P_{\rm m}/P_{\rm d} = \langle B^2\rangle/[8\pi\,\langle\rho u^2\rangle]$, averaging over the computational volume and over the last four dynamical times. In the first simulation (model A) the statistically relaxed pressure ratio is $P_{\rm m}/P_{\rm d} \approx 0.65 \pm 0.05$ (approximate equipartition of magnetic and kinetic energies). In the second simulation (model B), the ratio is $P_{\rm m}/P_{\rm d} \approx 0.09 \pm 0.01$ (kinetic energy of the turbulence approximately five times larger than magnetic energy). The standard deviation of approximately 10% in the pressure ratio of models A and B is due primarily to time fluctuations of the random force.

Power spectra have been computed for 18 times over the last four dynamical times (the small scale portions of these power spectra are statistically independent because the dynamical time decreases with spatial scale). The slopes are computed from a least square fit of the time-averaged power spectra plotted in Figure 1. We find that the power spectrum of the density field

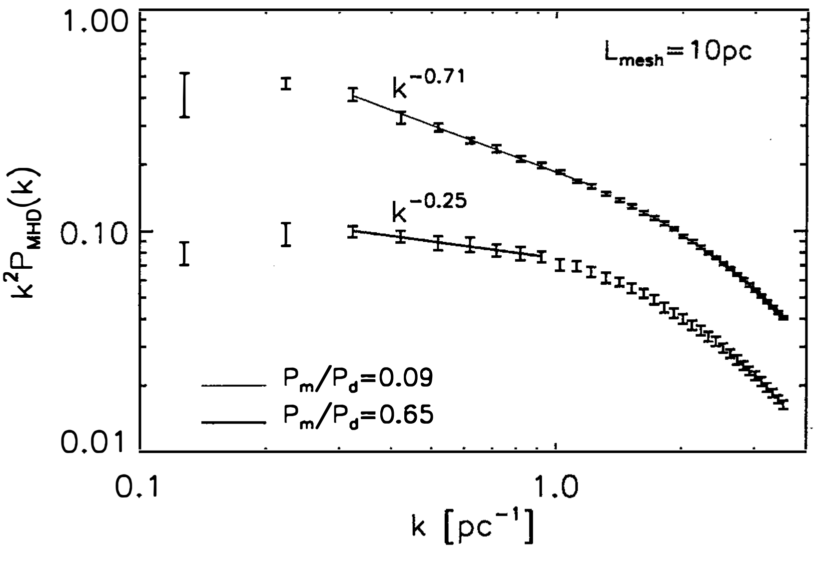

Figure 1: Time-averaged density power spectra of model B (upper plot), and model A (lower plot). The solid lines are least square fits in the range 0.3–0.9 pc^{-1} for model A and 0.3–1.2 pc^{-1} for model B, assuming a mesh size $L_{\rm mesh} = 10$ pc.

is sensitive to the pressure ratio (or the average magnetic field strength). The power spectrum of the three dimensional (3D) density field is $P(k) \propto k^{-2.25\pm0.01}$ in the equipartition run (model A) and $P(k) \propto k^{-2.70\pm0.01}$ in the super–Alfvénic case (model B).

In isotropic turbulence the power spectrum of the projected density is the same as the power spectrum of the 3D density field (not necessarily in the presence of a mean magnetic field or in real molecular clouds). We have verified this in our numerical data. We have also verified that the power spectrum of the projected density does not depend on the direction of projection relative to the direction of the mean magnetic field. However, our results are based on the power spectra of the 3D density field and not of the projected density, because the statistical sample size is reduced by the projection (larger noise in 2D power spectra than in 3D ones).

3 Power Spectrum of Column Density in Molecular Clouds

The distribution of column density in molecular clouds can be estimated from maps of the J=1-0 ^{13}CO emission line. In this work we use J=1-0 ^{13}CO maps of the Perseus (Padoan et al., 1999), Taurus (Mizuno et al., 1995) and Rosetta (Heyer & et al., 2003) molecular cloud complexes and find the power spectrum of projected density in these regions is well approximated by a power law, $P_{\rm o}(k) \propto k^{-a_{\rm o}}$.

The value of the gas column density inferred from the J=1-0 ^{13}CO maps depends on the distribution of ^{13}CO abundance and J=1-0 ^{13}CO excitation temperature, $T_{\rm ex}$. The column density can be estimated using the LTE method (Dickman, 1978; Harjunpää & Mattila, 1996; Padoan et al., 1998a). In the LTE method the value of $T_{\rm ex}$ along each line of sight is assumed to be constant and is estimated using the observed peak temperature, $T_{\rm r} = T_{\rm p}$, of an optically

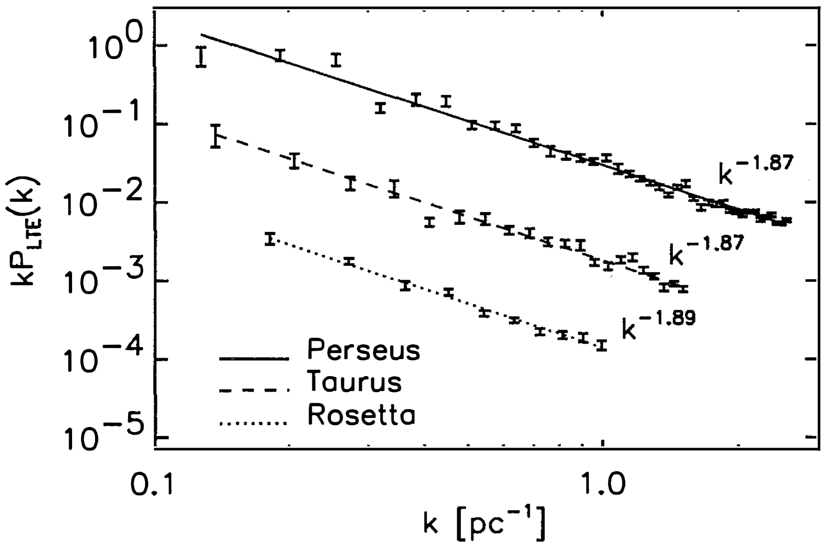

Figure 2: Power spectra of three molecular cloud complexes. The power spectra are computed from images of column density obtained with the LTE method applied to maps of the J=1-0 ^{13}CO emission line.

thick line ($\tau \gg 1$) in the equation:

$$T_r = [J(T_{ex}) - J(T_{bg})](1 - e^{-\tau}) \tag{1}$$

where $T_{bg} = 2.7$ K is the background temperature, and the function $J(T)$ is defined as:

$$J(T) = \frac{T_0}{\exp(T_0/T) - 1} \tag{2}$$

with $T_0 = h\nu_{10}/k$ and ν_{10} is the frequency of the J=1-0 ^{13}CO transition. The J=1-0 ^{12}CO transition, when available, is generally used as the optically thick line to estimate the value of T_{ex}. For the present analysis we apply the LTE method using only the J=1-0 ^{13}CO line because ^{12}CO maps are not available to us. This line is optically thick only in the brightest regions of the maps used in the present work. The value of T_{ex} can be estimated from the J=1-0 ^{13}CO line only in those regions. Therefore, we use the peak temperature of this line over the whole map to estimate the value of T_{ex} as outlined above. This single value of T_{ex} is used for all map positions (the effect of this assumption is addressed below with radiative transfer calculations). Finally, the ^{13}CO column density is given by:

$$N_{LTE} = 6.39 \times 10^{14}\, Q\, \frac{\Sigma_v \tau(v) \Delta v}{1 - e^{-T_0/T_{ex}}} \tag{3}$$

where $\tau(v)$ is the optical depth in the velocity channel corresponding to the velocity v and is estimated from equation (1) using the estimated value of T_{ex} and the radiation temperature $T_r(v)$ given by the observed line profile. Δv is the width of the velocity channels in the observations, expressed in km/s, and the partition function Q is assumed to be a constant over the map so its value is not required as it does not affect the slope of the density power spectrum.

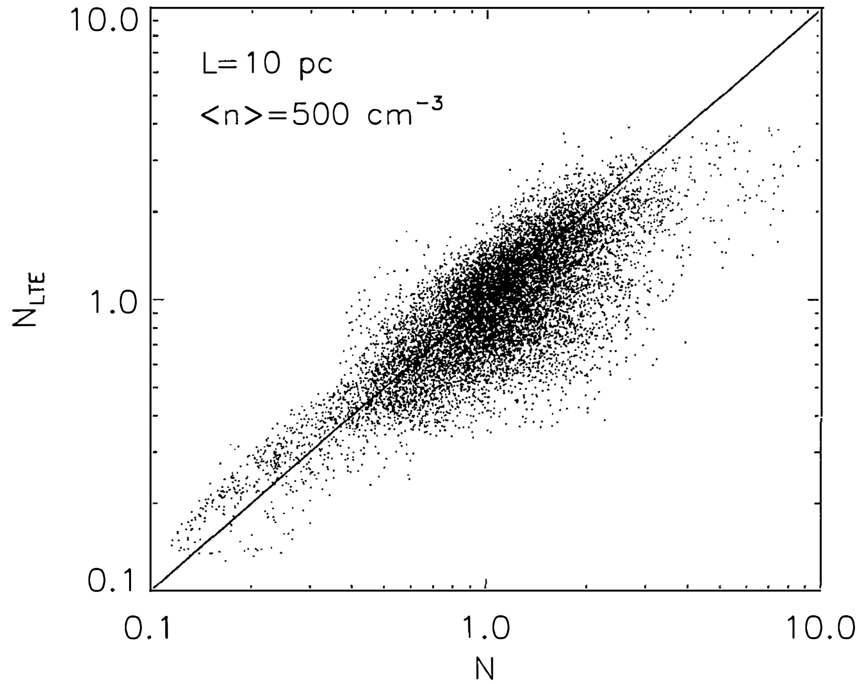

Figure 3: Scatter plot of column density estimated with the LTE method applied to a synthetic map of the J=1-0 ^{13}CO emission line versus the column density in the MHD data cube used to compute the synthetic spectra.

Column density maps of the Perseus, Taurus and Rosetta regions have been computed from the observed J=1-0 ^{13}CO spectral maps with this simplified LTE method. Their power spectra are plotted in Figure 2. They are shown to be well approximated by power laws over one decade or more in wavenumber, $P_o(k) \propto k^{-a_o}$, with $a_o \approx 2.87 \pm 0.04$ for Perseus, $a_o \approx 2.87 \pm 0.06$ for Taurus and $a_o \approx 2.89 \pm 0.06$ for Rosetta.

In order to estimate the effect of assuming constant Q and T_{ex}, the simplified LTE method for estimating the gas column density has been applied to synthetic spectra. Assuming a uniform ^{13}CO abundance, synthetic spectral maps of the J=1-0 ^{13}CO line have been computed with a 3D non–LTE Monte Carlo radiative transfer code (Juvela, 1997) as described in Padoan et al. (1998b). The radiative transfer is computed through the density and velocity field of two snapshots of model B (at 3 and 4 dynamical times), regridded to a resolution of 175^3, assuming average density $\langle n \rangle$ = 500 cm^{-3} and mesh size L_{mesh} = 10 pc. The 3D distribution of kinetic temperature is computed self–consistently as part of the radiative transfer solution, from the balance of cosmic ray heating and molecular and atomic cooling. We have assumed a cosmic ray hydrogen ionization rate of 2×10^{-17} s^{-1} and heating of 8 eV per ionization.

Six maps of 175×175 synthetic J=1-0 ^{13}CO lines are obtained in this way, corresponding to three orthogonal directions of projection of the two 3D snapshots. The simplified LTE method is then applied to these six synthetic spectral maps and the estimated column density is compared with the actual column density in the original snapshots of model B. The result for one of the maps is plotted in Figure 3. Figure 3 shows the estimated column density, $N_{\rm LTE}$, is roughly proportional to the true column density, but tends to saturate at large column density values. This is due both to the low gas temperature and to the J=1-0 ^{13}CO line saturation in the densest regions. The power spectra of the column density field estimated from the synthetic spectral map, $P_{\rm LTE}(k) \propto k^{-a_{\rm LTE}}$, are then compared with the power spectra computed directly from the projections of the original MHD data cube, $P_{\rm MHD}(k) \propto k^{-a_{\rm MHD}}$.

We find that $P_{\rm LTE}(k)$ is generally steeper than $P_{\rm MHD}(k)$. This is primarily due to the decreased emission from the densest regions due to their low gas temperature and to the saturation of the J=1-0 ^{13}CO line. The difference is $a_{\rm LTE} - a_{\rm MHD} = 0.13 \pm 0.06$. If this correction is applied to the observed molecular cloud complexes, the corrected power spectrum has a slope $a = 2.74 \pm 0.07$ for Perseus, $a = 2.74 \pm 0.08$ for Taurus and $a = 2.76 \pm 0.08$ for . At the 1 σ level, model B is consistent with these molecular cloud complex power spectra, while the power spectrum of model A is inconsistent with the observations with virtually 100% confidence (7 σ).

Variations in ^{13}CO abundance may affect the estimated column density. However, significant CO depletion is expected only above 10 magnitudes of visual extinction and the CO abundance should drop only below 1-2 magnitudes. Most of the gas mass in molecular cloud complexes emits at values of visual extinction between 1 and 10 mag. Therefore, the effect of gas temperature variations estimated above should be more important than the neglected effect of variations in ^{13}CO abundance.

4 Conclusions

The average magnetic field strength in molecular clouds cannot be measured directly. However, it can be inferred from observational data due to its effect on the gas dynamics. In this work we have found the power spectrum of the density field is a sensitive diagnostic of the magnetic field strength. Numerical simulations of supersonic MHD turbulence with rms sonic Mach number $M_{\rm S} \approx 10$ develop a power law power spectrum of gas density, $P_{\rm MHD}(k) \propto k^{-a_{\rm MHD}}$. The value of the power law exponent is $a_{\rm MHD} = 2.25 \pm 0.01$ when the flow rms velocity is comparable to the Alfvén velocity and $a_{\rm MHD} = 2.71 \pm 0.01$ in the super–Alfvénic simulation.

The density power spectrum can be measured also in molecular cloud complexes, for example using J=1-0 ^{13}CO maps. However, the column density (and its power spectrum) estimated using only the J=1-0 ^{13}CO line and the LTE method are biased by a number of uncertainties. The most significant uncertainties are the 3D distribution of the gas kinetic temperature in the molecular cloud complexes and the saturation of the J=1-0 ^{13}CO line in very dense regions. We have investigated the effect of these uncertainties in the density power spectrum using synthetic J=1-0 ^{13}CO spectral maps computed with a non–LTE Monte Carlo radiative transfer code. The 3D equilibrium temperature distribution is computed self–consistently as part of the radiative transfer solution by balancing cosmic ray heating with molecular and atomic cooling. The correct power spectrum slope, $a_{\rm MHD}$, is found to be smaller than the slope estimated with the LTE method, $a_{\rm LTE}$, with $a_{\rm MHD} = a_{\rm LTE} - 0.13 \pm 0.06$.

With this correction, the power spectrum slope is $a = 2.74 \pm 0.07$ for Perseus,$a = 2.74 \pm 0.08$ for Taurus and $a = 2.76 \pm 0.08$ for Rosetta. The super–Alfvénic model is consistent with this result, while the model with rms flow velocity comparable to the Alfvén velocity is ruled out by the observations. This is yet another indication that super–Alfvénic turbulence provides a good description of molecular cloud dynamics. As first proposed by Padoan & Nordlund (1997, 1999), the average magnetic field strength in molecular clouds may be much smaller than required to support them against the gravitational collapse. Evidence of super–Alfvénic turbulence was also found recently by Troland and Heiles (2001) in HI clouds.

Acknowledgments

MJ acknowledges the support from the Academy of Finland Grants no. 174854 and 175068. Computing time was provided by the Danish Center for Scientific Computing.

References

Armstrong, J. W., Rickett, B. J., & Spangler, S. R. 1995, ApJ, 443, 209

Bourke, T., Myers, P., Robinson, G., & Hyland, H. 2001, ApJ

Chandrasekhar, S. & Fermi, E. 1953, ApJ, 118, 113

Chrysostomou, A., Hough, J. H., Burton, M. G., & Tamura, M. 1994, MNRAAS, 268, 325

Crovisier, J. & Dickey, J. M. 1983, A&A, 122, 282

Crutcher, R. M. 1999, ApJ, 520, 706

Davis, L. 1951, Physical Review, 81, 890

Dickey, J. M., McClure-Griffiths, N. M., Stanimirović, S., Gaensler, B. M., & Green, A. J. 2001, ApJ, 561, 264

Dickman, R. L. 1978, ApJS, 37, 407

Elmegreen, B. G., Kim, S., & Staveley-Smith, L. 2001, ApJ, 548, 749

Harjunpää, P. & Mattila, K. 1996, A&A, 305, 920

Heitsch, F., Zweibel, E. G., Mac Low, M., Li, P., & Norman, M. L. 2001, ApJ, 561, 800

Heyer, M. H. & et al. 2003, in preparation

Houde, M., Bastien, P., Dotson, J. L., Dowell, C. D., Hildebrand, R. H., Peng, R., Phillips, T. G., Vaillancourt, J. E., & Yoshida, H. 2002, ApJ, 569, 803

Houde, M., Bastien, P., Peng, R., Phillips, T. G., & Yoshida, H. 2000, ApJ, 536, 857

Juvela, M. 1997, A& A, 322, 943

Lai, S., Crutcher, R. M., Girart, J. M., & Rao, R. 2001, ApJ, 561, 864

—. 2002, ApJ, 566, 925

Matthews, B. C. & Wilson, C. D. 2002, ApJ, 574, 822

Mizuno, A., Onishi, T., Yonekura, Y., Nagahama, T., Ogawa, H., & Fukui, Y. 1995, ApJL, 445, L161

Myers, P. C. & Goodman, A. A. 1991, ApJ, 373, 509

Ostriker, E. C., Stone, J. M., & Gammie, C. F. 2001, ApJ, 546, 980

Padoan, P., Bally, J., Billawala, Y., Juvela, M., & Nordlund, Å. 1999, ApJ, 525, 318

Padoan, P., Goodman, A., Draine, B. T., Juvela, M., Nordlund, Å., & Rögnvaldsson, Ö. E. 2001, ApJ, 559, 1005

Padoan, P., Juvela, M., Bally, J., & Nordlund, Å. 1998a, ApJ, in press

—. 1998b, ApJ, 504, 300

Padoan, P. & Nordlund, Å. 1997, astro-ph/9706176

—. 1999, ApJ, 526, 279

Stanimirović, S. & Lazarian, A. 2001, ApJL, 551, L53

Troland, T. H. & Heiles, C. 2001, American Astronomical Society Meeting, 198, 0

Impulsively triggered collapse of Prestellar corės

P. Hennebelle (1), A. Belloche (2), P. André (3), S. Goodwin (4), A. Whitworth (4)

(1) Ecole normale supérieure and Observatoire de Paris
24 rue Lhomond 75005 Paris, France
(2) Max-Planck-Institut für radiastronomie, Auf dem Hügel 69, 53121 Bonn, Germany
(3) Commissariat à l'énergie atomique, Orme les merisiers 91191 Gif sur Yvette
(4) Cardiff University, PO box 913, 5 the Parade, Cardiff CF24 3YB, Wales UK

We have investigated the collapse of low-mass, isothermal, molecular cores which are subjected to an increase in external pressure. If the external pressure increases very slowly, the core approaches instability quite quasi-statically. However, for fast compressions, a compression wave is driven into the core (Hennebelle et al. 2003) and the collapse occurs dynamically. Quantitative comparisons with observational velocity and density profiles are presented for a very young protostellar core belonging to Taurus (IRAM04191) and for a protostellar core belonging to Perseus (IRAS4A). It is found that slow compression is required in order to match the first one whereas very rapid compression appears necessary to reproduce the second one.

Keywords: gravitation, hydrodynamics, accretion, accretion disks, stars: formation, ISM: clouds, ISM: kinematics and dynamics

1 Introduction

In a recent study, Hennebelle et al. (2003, 2004) have investigated the possibility that the collapse of low-mass isothermal molecular cores may be driven from the outside by an increase in external pressure $P_{\rm ext}$.

This model seems to reproduce many of the key features observed in nearby star forming cores, viz. (i) During the pre-stellar phase, the density profile is approximately flat in the centre (ii) For slow to moderate compression rates, subsonic infall velocities develop in the outer parts of the core, during the prestellar phase (iii) During the Class 0 phase, subsonic velocities persist in the outer parts of the core and transsonic velocities develop in the inner parts ($r \simeq 2000$ AU). (iv) There is an initial short phase of rapid accretion onto the central protostar (the Class 0 phase), followed by a longer phase of slower accretion (the Class I phase).

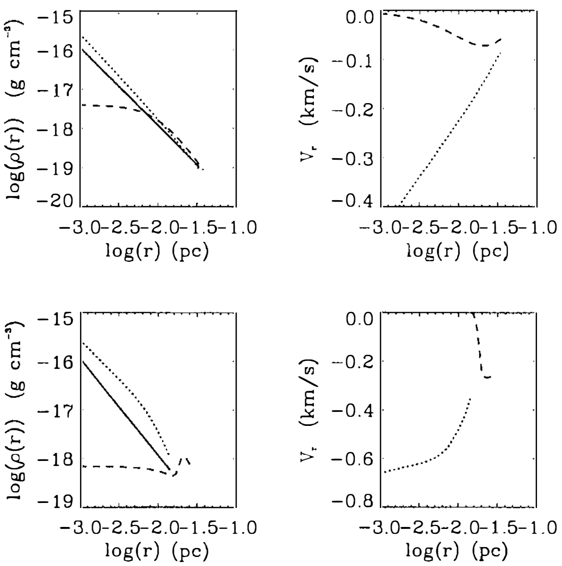

Figure 1: Density and radial Velocity for a slow compression (upper panels) and for a fast compression (lower panels). The solid line is the density of the singular isothermal sphere. The dashed lines correspond to the prestellar phase and represent time $t = 0.5$ Myr for the slow compression and time $t = 0.1$ Myr for the fast compression. The dotted lines correspond to the class 0 phase (very close to the protostar formation) and represent time $t = 0.567$ Myr for the slow compression and time $t = 0.145$ Myr for the fast compression.

Here we present results for a rotating core subjected to a slow, and fast increase in external pressure. We show and discuss the equatorial density and radial velocity profiles both during the prestellar phase and the class 0 phase for non rotating and for rotating clouds. We then undergo a comparison with 2 young class 0 objects, IRAM04191 belonging to the Taurus molecular cloud and IRAS4A belonging to the Perseus molecular cloud.

The simulations are performed using a Smoothed Particle Hydrodynamical code. At the start of a simulation, low mass cores (1 $M_\odot$) are modelled as slowly rotating ($\beta = E_{rot}/E_{grav} = 2\%$) truncated equilibrium isothermal spheres ($T = 10$ K, $\xi = 6$), contained by a hot rarefied external medium. The particles belonging to the cloud, the internal particles, experience hydrodynamical and gravity forces whereas particles belonging to the external medium experience only hydrodynamical forces. We use 100,000 internal particles and 100,000 external particles. To avoid infinitely large density in the centre a barotropic equation of state is used. The external pressure increases according to the simple law: $P_{\rm ext} = P_0 + \dot{P}t$ and we define $\phi = (P/\dot{P})/(R_c/C_s)$, the compression rapidity (R_c is the cloud radius and $C_s \simeq 0.19$ km/s the sound speed).

2 Influence of compression and rotation on the cloud profiles

2.1 Density and velocity profiles of slowly and fastly compressed clouds

Fig. 1 displays the density and the velocity fields in the slow compression case, $\phi = 3$ (upper panels) and in the fast compression case, $\phi = 0.03$ (lower panels). The solid line is the density of the singular isothermal sphere (SIS), the dashed and the dotted lines represent timesteps belonging respectively to the prestellar and class 0 phase.

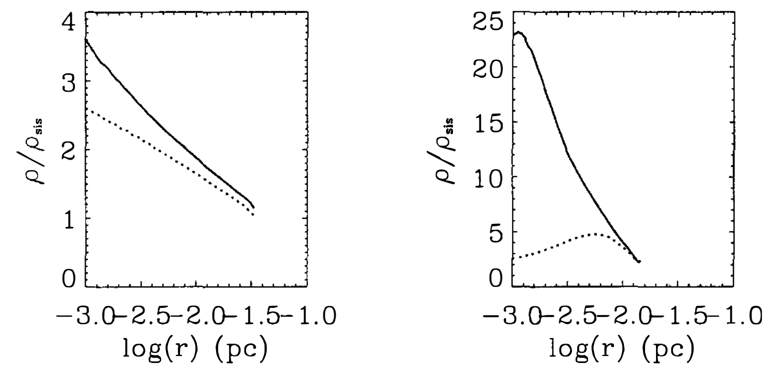

Figure 2: Ratio between the equatorial density and the density of the SIS for a slow compression and a rapid compression at time close to the formation of the protostar. Dotted line : without rotation. Full line: with an initial rotation (initially one has $E_{rot}/E_{grav} = 0.02$).

In the slow compression case the cloud contraction stays subsonic during almost all the prestellar phase and the density profile remains very similar to a Bonnor-Ebert sphere (dashed line of upper panel). During the class 0 phase (dotted line of upper panels), the infall velocity remains subsonic in the outer parts of the core and becomes supersonic in the inner parts. In the outer parts of the core, the density during the class 0 phase is rather close to the density of the SIS. It is slightly higher in the inner parts. The fact that the density profile of this collapsing core is close to an equilibrium configuration (Bonnor-Ebert sphere and SIS) is a simple consequence of the infall velocity being subsonic in most of the core implying that the core is not violently out of equilibrium.

In the fast compression case a strong compression wave is launched inwards (dashed lines of lower panels) so that the density at the edge is higher than the central density. The radial velocity is supersonic (about 1.5-2 times the sound speed). During the class 0 phase, the density profile is not far from an r^{-2} law but it is 2.5 to 5 times higher than the density of the SIS (depending on the radius).

These features are qualitatively in good agreement with cores belonging to Taurus for the slow compression case and with the core IRAS4A belonging to the Perseus cloud for the fast compression case. A detailed comparaison will be presented in Sect.3.

2.2 Equatorial density profile of a rotating cloud

Fig. 2 displays the ratio between the equatorial density and the density of the SIS at a timestep close to the protostar formation. The left panel corresponds to the slow compression case and the second one to the fast compression. The dotted lines correspond to the non rotating cloud whereas the full lines correspond to a cloud which is initially in solid body rotation and has a rotational energy equal initially to 2% of the gravitational energy.

It is seen that because of the centrifugal force that provides an extra support to the cloud, the equatorial density is higher for the rotating cloud than for the non rotating one. This effect is stronger near the centre of the cloud and for the large compression for which the cloud is strongly squeezed. In both cases this is because that due to the angular momentum conservation, the rotation speed is large.

These effects are qualitatively reproduced by the simple semi-analytical model developed by

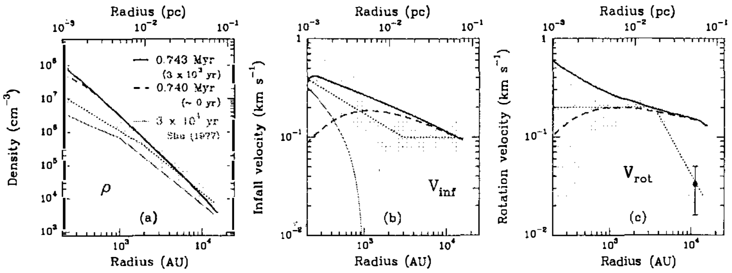

Figure 3: Comparison between the young protostar IRAM04191 and the model ($\beta = 5\%, \phi = 3$, see text). The shaded areas show the domains of density (panel a), radial velocity (panel b) and rotation velocity (panel c) where models match the observations reasonably well. The 2 blue curves display 2 time steps of the model. The red curve displays one timestep of the SIS collapse (Shu 1977)

Hennebelle et al. (2004). With the assumption that the density profile is approximately an r^{-2} power law, it can be shown that by the time of the protostar formation the equatorial density can be reasonnably approximated by:

$$\rho(r, z=0) \;=\; \delta\, \rho_{\rm SIS}(r) \;=\; \frac{\delta C_s^2}{2\pi G r^2}\,, \tag{1}$$

$$\delta \;\simeq\; \left(\frac{P_{\rm ext}}{P_0}\right)^{1/3} \left(1 + \frac{v_\theta^2}{2C_s^2}\right)\,. \tag{2}$$

where $P_0 \sim C_s^8/G^3 M_c^2$, $P_{\rm ext}$ is the external pressure and v_θ is the azimuthal velocity. The agreement is good for slow compression (see Hennebelle et al. 2004) but less accurate for fast compression.

3 Comparison with observations

We have undertaken the detailed comparison between the compression models and 2 sources. The first one, IRAM04191 belongs to the Taurus molecular cloud and presents subsonic infall motions (Belloche et al. 2002) and the second one IRAS4A belongs to the Perseus molecular cloud and undergoes supersonic infall motions (Di Francesco et al. 2001).

3.1 Comparison with IRAM04191

We compare in Fig. 3 the physical properties of a model with slow compression ($\Phi = 3$, $\beta = 5\%$, close to the model shown in Fig. 1) with the physical properties of the IRAM04191 protostellar envelope deduced from millimeter observations and radiative transfer modelling by Belloche et al. (2002). IRAM04191 is the youngest Class 0 protostar in the Taurus molecular cloud. It is associated with a highly collimated outflow and a prominent envelope undergoing both extended infall (panel *b* of Fig. 3) and fast, differential rotation (panel *c*). The shaded areas show the domains of density (panel *a*), infall velocity (panel *b*) and rotation velocity (panel *c*) estimated with our radiative transfer modelling, where models match the observations reasonably well. The blue curves show the density, infall velocity and rotation velocity in the equatorial plane of the hydrodynamical simulation with slow compression, at 2 timesteps close to the formation of the protostar (t = 0.740 and 0.743 Myr after the start of the simulation). The red curve shows the density and velocity of the SIS self-similar collapse (Shu 77) at t = 0.03 Myr after the formation of the protostar.

It is seen that the self-similar collapse of the SIS is not in good agreement with the observation. The main difference is due to the fact that the infall velocity in the model vanishes in

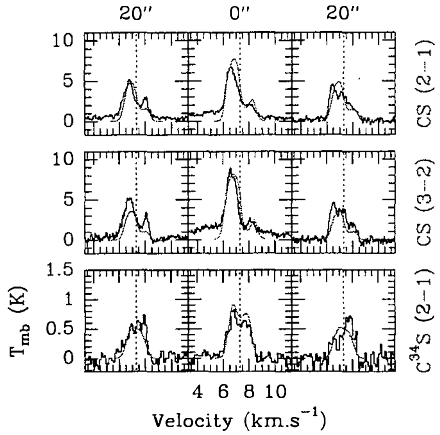

Figure 4: Comparison between the observational spectra of IRAS4A (black) and the synthetic spectra calculated from our simulation (red) for the 3 molecular lines $C^{34}S$ (2-1), CS (3-2) and CS (2-1).

the outer part of the core. On the contrary a reasonable agreement is obtained between the observational data and the slowly compressed isothermal Bonnor-Ebert sphere for times between $\simeq 0.74$ and 0.743 Myr.

This comparison suggests that an age less than 3000 yr is required to match the infall velocity profile and the inner part of the rotation velocity profile deduced from the observations. This upper limit is 2-3 times smaller than the dynamical timescale of the outflow (André et al. 1999).

However, the model does not reproduce the steep decrease of the rotation velocity in the outer part of the envelope (panel *c*), which could result from a loss of angular momentum produced by magnetic braking (see Belloche et al. 2002). The magnetic field could also slow down the collapse (see Basu & Mouschovias 1995): a good match with the observations could then be obtained with a slightly more evolved model.

3.2 Comparison with IRAS4A

We have also carried out a comparison with the class 0 protostar IRAS4A in the NGC1333 molecular cloud. This source presents supersonic infall motions as well as rapid rotation (Di Francesco et al. 2001). It has also a density which is roughly proportional to r^{-2} but which is about 10 times the density of the SIS (Motte & André 2001). As mentioned previously, this accords qualitatively well with the fast compression model which presents simultaneously rapid infall motions, rapid rotation (the initial rotation being amplified by the strong squeezing) and large density.

In order to perform a quantitative comparison with the model ($\phi = 0.03$, $\beta = 2\%$) we have calculated the synthetic spectra in the molecular lines $C^{34}S$ (2-1), CS (3-2) and CS (2-1) using the radiative transfer code which is described in Belloche et al. (2002). The comparison is displayed in Fig. 4. The synthetic spectra match the observations reasonably well toward the center: the position of the dips and the asymmetry of the CS(2-1) and CS(3-2) optically thick spectra, and the shape of the $C^{34}S$(2-1) low opacity spectrum are well reproduced. This model, with a mass infall rate of 1.1×10^{-4} $M_\odot$ yr^{-1} at 2000 AU, is also in good agreement with the result of Di Francesco et al. (2001).

4 Conclusion

We have investigated the collapse of a prestellar core which is squeezed by an external pressure. When the compression occurs slowly compared to the internal sound crossing time, the infall velocity remains subsonic during all the prestellar phase whereas the density profile is close to the equilibrium solutions of the Bonnor-Ebert spheres. During the class 0 phase, the infall motions are supersonic in the inner parts and remain subsonic in the outer parts, the density profile being close to the density of the SIS. When the compression is strong a compression wave is launched inwards. The infall velocity is supersonic and the density is few times higher than the density of the equilibrium solutions. Because of the centrifugal support, the equatorial density of the rotating cloud is few times larger than the density of the non rotating cloud particularly in the inner parts of the cloud or when the compression is fast.

We present quantitative comparisons between the models and the 2 young class 0 objects, IRAM04191 belonging to the Taurus molecular cloud and IRAS4A belonging to the Perseus molecular cloud.

We find that IRAM04191 can be reasonnably reproduced by a slowly compressed rotating core except for the rotation profile in the outer parts which is incompatible with the cloud being initially in solid body rotation and the conservation of the angular momentum. It is worth noting that IRAM04191 is also in reasonnable agreement with the fastest models of clouds controled by ambipolar diffusion (Basu & Mouschovias 1995, Ciolek & Basu 2000). Indeed it turns out that the slowest hydrodynamical models, described first by Foster & Chevalier (1993), are not very different from the fastest models controled by ambipolar diffusion. Therefore careful comparisons need to be pursued in order to descriminate between the different collapse models.

We find that the spectra in 3 molecular lines of IRAS4A are well reproduced by the synthetic spectra calculated for a very fastly compressed rotating model. This source presents supersonic infall, rapid rotation and large density. All these features appear naturally in the fast compression model.

These 2 comparisons and relatively good agreements suggest that the external pressure is an important parameter for the dense core evolution and that it may vary significantly from one cloud to another.

References

1. André P., Motte F., Bacmann A., 1999, A&A, 513L, 57
2. Basu S., Mouschovias T., 1995, ApJ, 423, 271
3. Belloche A., André P., Despois D., Blinder S., 2002, A&A, 393, 927
4. Ciolek G. E., Basu S., 2000, ApJ, 529, 925
5. Di Francesco J., Myers P. C., Wilner D. J., Ohashi N., Mardones D., 2001, ApJ, 562, 770
6. Hennebelle P., Whitworth A. P., Gladwin P. P., André P., 2003, MNRAS, 340, 870
7. Hennebelle P., Whitworth A. P., Cha S., Goodwin S., 2004, MNRAS 348, 687
8. Foster P. N., Chevalier R. A., 1993, ApJ, 416, 303
9. Motte F., André P., 2001, A&A 365, 440
10. Shu F., 1977, ApJ, 214, 488

Part 3

Feedback effects from massive stars

Galactic and Extragalactic Bubbles

D. BREITSCHWERDT (1), M.A. DE AVILLEZ (1,2), M.J. FREYBERG (3)
(1) Institut für Astronomie, Universität Wien, Türkenschanzstraße 17, A-1180 Wien, Austria
(2) Department of Mathematics, University of Évora, R. Romão Ramalho 59, 7000 Évora, Portugal
(3) MPI für extraterrestrische Physik, Giessenbachstraße 1, D-85748 Garching, Germany

The observational and theoretical state of Galactic and extragalactic bubbles are reviewed. Observations of superbubbles are discussed, with some emphasis on nearby bubbles such as the Local Bubble (LB) and the Loop I superbubble (LI). Analytical bubble theory is revisited, and similarity solutions, including the time-dependent energy input by supernova explosions according to a Galactic initial mass function (IMF), are studied. Since the agreement with observations is not convincing in case of the LB, we present high resolution 3D AMR simulations of the LB and LI in an inhomogeneous background medium. It is demonstrated that both the morphology and recently published FUSE data on OVI absorption line column densities can be well understood, if the LB is the result of about 20 supernova explosions from a moving group, and the LB age is about 14.7 Myrs.

Keywords: ISM: general - ISM: evolution - ISM: bubbles - Galaxies: ISM - X-rays: ISM

1 Introduction

The term "bubble" in science is not well defined. A convenient operational definition could be that of a closed two-dimensional surface in three-space, separating two media of different (physical) properties, with lower density inside than outside. Consequently there exists a vast range of topics in the literature from electron bubbles in superfluid helium to bubbles in avalanches. In astrophysics, interstellar bubbles are an already classical subject in ISM research, and seem to have experienced a renaissance each time a new process for significant energy injection has been found. After the discovery of the Stroemgren (1939) sphere, generated by stellar Lyman continuum photons, it became clear that the rise in temperature in the HII region, T_{II}, with respect to the neutral ambient medium, T_I, would imply a strong pressure imbalance of the order $\sim T_{II}/T_I$, and thus a shock wave would be driven outwards (Oort 1954). The major effect is the growth of the HII region in size due to the decrease in electron density n_e inside and hence in recombination rate ($\propto n_e^2$), allowing stellar photons to propagate further out. The net result is a bubble filled with low density ionized gas. Another, even more powerful energy injection mechanism emerged after the discovery of P Cygni profiles in stellar spectra (Morton 1967), revealing the existence of hypersonic stellar winds smashing into the ISM at speeds of ~ 2000 km/s and a canonical mass loss rate of $10^{-6}\, M_\odot$/yr, or even higher for Wolf-Rayet stars. Like in the case of the solar wind this leads to a two-shock structure, separated by a contact discontinuity that isolates the wind from the ISM material, but is in reality unstable to perturbations and allows mixing and mass loading of the stellar wind flow. Observationally, these bubbles can be detected in X-rays, since the temperature behind the inner termination shock rises according to mass and momentum conservation (energy conservation for a monatomic gas does not give any new information) to $T \approx \frac{3}{32}\bar{m}\frac{V_w^2}{k_B} = 5.4 \times 10^7$ K, neglecting ambient thermal pressure with respect to ram pressure. Under these conditions radiative cooling of the bubble is negligible, and the bubbles are in their so-called energy driven phase. Adiabatic cooling due to $p - dV$ work on the surrounding medium, however, is significant. Sweeping up and compressing ISM gas slows down the outer shock, which can eventually suffer severe radiative losses, as the downstream density is considerably higher than behind the stellar wind termination shock. Moreover the dense outer shell (or part of it) is photoionized and thus well observable in the optical. Diffuse soft X-ray emission from stellar wind bubbles has been observed from NGC 6888 with ASCA SIS (Wrigge et al. 1998) and from S 308 with XMM-*Newton* EPIC pn (Chu et al. 2003), revealing temperatures of 1.5×10^6 K and 8×10^6 K for NGC 6888, and 1.1×10^6 K, for S 308. As we shall see, mass loading must play an important rôle for decreasing the temperature thereby enhancing the cooling and thus the X-ray emissivity.

Already 70 years ago, Baade & Zwicky (1934) suggested that stellar core collapse resulting in a neutron star could release a sufficient amount of gravitational energy to power a supernova (SN) explosion. The effect of the kinetic energy of 10^{51} erg, which is only $\sim$ 1% of the released neutrino energy, is dramatic. After a free expansion phase, in which a shell with mass similar to the ejecta mass is swept up, the pressure difference between shocked ISM and ejecta drives a reverse shock into the supernova remnant (SNR), reheating the ejecta as it propagates inwards. The transfer of energy to the ISM is now determined by the adiabatic Sedov-Taylor phase, lasting several ten thousands of years until the cooling time of the outer shock becomes less than the dynamical time scale, and the SNR enters the radiative phase before eventually merging with the ISM. The widespread OVI line in the ISM is thought to be the signature of old SNRs.

Young star clusters, like the four million years old NGC 2244 exciting the Rosette Nebula, can blow holes into the emission nebulae by the *combined* action of several stellar winds. Since the discoveries of huge HI shells, so-called supershells, either in the Milky Way (e.g. Heiles 1979, 1980) or in M 31 (Brinks & Shane 1984), or by direct observation of huge X-ray emitting cavities (e.g. Cash et al. 1980) in the Orion, Eridanus or Cygnus regions, it is understood that O- and B-stars in concert can create *superbubbles* (SBs). Although stellar winds are the initial contributors over the first few million years, it is obvious that SN explosions dwarf their energy input over the SB life time of a few tens of million years. The SBs range in sizes from a few tens to a few hundreds of parsecs. The most prominent ones are undoubtedly the Local Bubble (LB), in which our solar system is immersed, and which is still not well understood, and the adjacent Loop I SB (LI); both will be discussed in some detail in this review. Extreme examples of bubbles with respect to their energy input on galactic scales are those driven by (nuclear) starbursts - often called superwinds -, which in case of NGC 3079 (Cecil et al. 2002) show clear signatures of an outflowing bubble both with Chandra and HST. Although driven by star formation processes, but for lack of space, we will discuss neither planetary nebulae, which exhibit a prominent white dwarf blown wind bubble, nor pulsar wind bubbles driven by energetic particles, nor bipolar outflows and jets, which show some additional features such as Mach disks. Why is it important to study bubbles? Apart from being interesting astrophysical objects, they are part of the interstellar matter cycle, enriching the ISM with metals, and, most importantly, they are the major energy sources of the ISM, controlling its structure and evolution, with SNRs and SBs being the major contributors.

In Section 2 we present some recent observations of the LB and the LI SB, taken in X-rays and in HI. Then, in Section 3 some analytical work, mainly similarity solutions, and their limitations are discussed, and in Section 4 numerical high resolution simulations of the LB and LI are shown, finishing off with our conclusions in Section 5.

2 Observation of nearby superbubbles

Since we want to describe bubbles in the *young local universe*, the closest examples are undoubtedly the LB, in which our solar system is immersed, and the neighbouring LI SB, whose outer shell is most likely in contact with the LB shell (cf. Egger & Aschenbach 1995). The centre of the LI bubble is approximately 250 pc away, and the bubble radius is about 170 pc. Its proximity is most impressively seen in a ROSAT All Sky Survey (RASS) multispectral image (Freyberg & Egger 1999), which shows it as the largest coherent X-ray structure in the sky (see Fig. 1), centred roughly on the Galactic Centre direction and covering a solid angle of $7/6\,\pi$ (Breitschwerdt et al. 1996). Although the existence of local X-ray emission was realized already

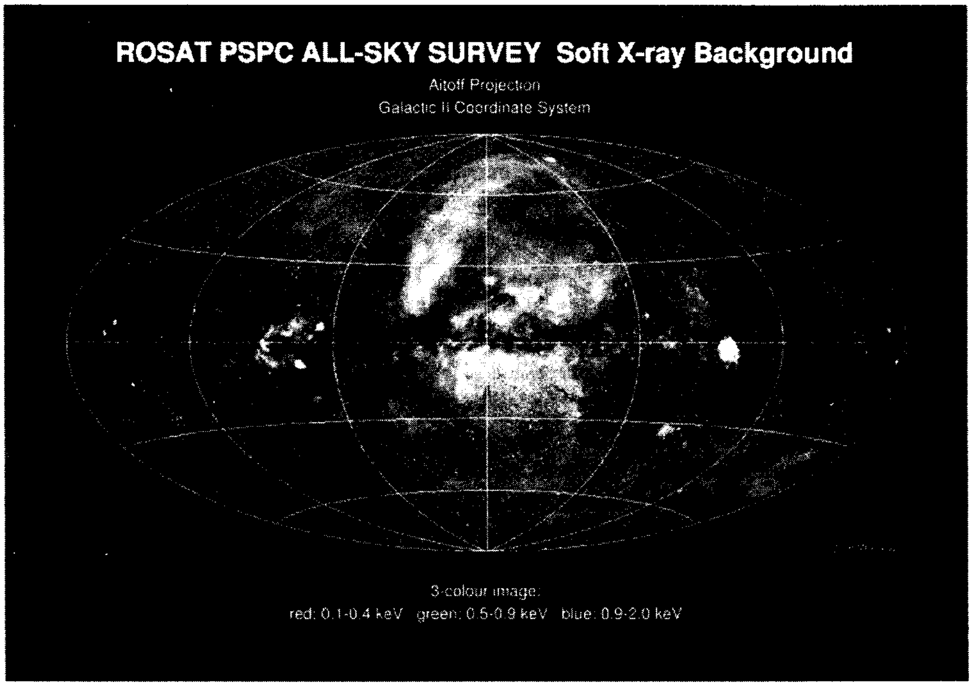

Figure 1: Multispectral X-ray view of the soft X-ray background as seen by the ROSAT PSPC. The RGB image covers three energy bands (1/4, 3/4 and 1.5 keV, respectively), and is shown in galactic coordinates in Aitoff-Hammer projection. The Galactic Centre is at $l = 0°$ with longitudes increasing to the left. The Loop I bubble lies in the direction of the Galactic Centre and is the largest coherent X-ray structure in the sky. The North Polar Spur stretching from $(l, b) = (30°, 15°)$ to $(300°, 80°)$ is clearly visible. Since we are located inside the Local Bubble, we can observe its X-ray emission from all directions. The picture is taken from Freyberg & Egger (1999).

soon after the observation of the diffuse soft X-ray background (SXRB) (Bowyer et al. 1968), the idea received considerable support by HI observations, revealing a local *cavity* (e.g. Frisch & York, 1983). The simplest explanation is given by the so-called "displacement" or Local Hot Bubble model (Sanders et al., 1977; Tanaka & Bleeker, 1977), in which it is assumed that the solar system is immersed in a bubble of diffuse hot plasma in collisional ionization equilibrium, that displaces HI, and has an average radius of 100 pc. More recent observations of the Local Cavity (see Fig. 2), using NaI as a sensitive tracer of HI (Lallement et al. 2003), show a more complex 3D structure of the hydrogen deficient hole in the Galactic disk, as well as a clear indication of opening up into the halo like a chimney. As a natural result, also the X-ray brightness of the bubble will vary with direction, especially if entrained clouds are shocked and

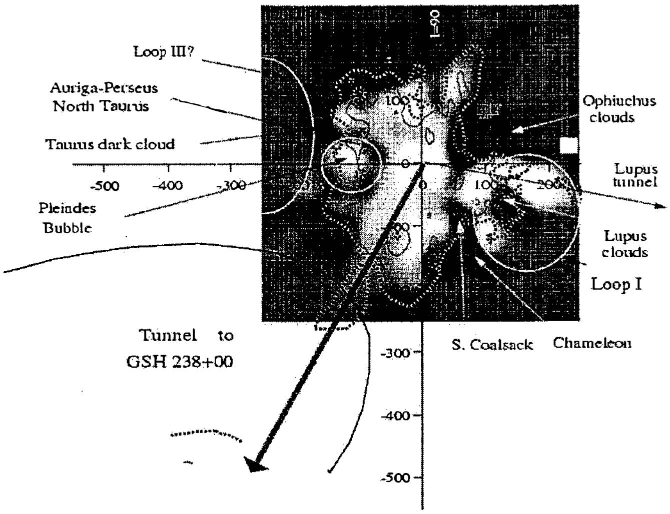

Figure 2: Projection of the Local Cavity onto the Galactic plane inferred from NaI absorption line studies by Lallement et al. (2003), using sightlines to 1005 stars with known Hipparcos parallaxes. The grey scale represents the density contrast with white being low and dark high densities. The dashed lines give the contours of NaI equivalent widths of 20 and 50mÅ, respectively, with 20 mÅ corresponding to log(NaI) = 11.0 or $N_H \approx 2 \times 10^{19}\,\mathrm{cm}^{-2}$. The existence of a shell in most directions is clearly seen, since the small difference between the contours indicates a steep gradient.

evaporated. Indeed, observations of the SXRB exhibit a distinct patchiness in emission, as has been reported from ROSAT PSPC observations (Snowden et al. 2000), and more recently by a mosaic of observations of the Ophiuchus cloud (Mendes et al. 2005), which was used to shadow the SXRB and thus allow to disentangle cloud fore- and background emission. The absorbing column density in direction to the Ophiuchus cloud, which is a well-known star forming region at a distance of 150 pc in direction of the Galactic Centre, contains up to $10^{22}\mathrm{cm}^{-2}$ H atoms, efficiently blocking out background radiation up to 1 keV. This is demonstrated nicely by a deep shadow in diffuse X-rays, which correlates very well with the IRAS 100 μ contours (s. Fig. 3). Our analysis of the spectral composition of the fore- and background radiation (s. Fig. 4) shows convincingly that the major fraction of the emission below 0.3 keV (most likely unresolved carbon lines) is generated in the foreground. In addition we observe a significant local fraction of oxygen lines (OVII and OVIII) between 0.5 and 0.7 keV, as well as lines between 0.7-0.9 keV (probably iron). These results give strong observational evidence that the gas inside the LB is *not* in collisional ionization equilibrium, in disagreement with the classical Local Hot Bubble model. A small fraction of the foreground emission stems also from LI. However, Fig. 4 shows that the off-cloud spectrum contains iron lines, which are absent in the on-cloud spectrum. Therefore the excitation temperature in the LI SB must be significantly higher than in the LB, allowing to disentangle spectrally the respective contributions. This is not surprising as LI is still an active SB in contrast to the LB, as we shall see in section 4.

The spectral interpretation of the SXRB is far from trivial. First of all it is at present unclear to what extent different sources contribute. These are: (i) diffuse local emission from the LB (and possibly the LI SB, although its major component has a distinctly higher temperature), (ii) diffuse Galactic emission from the hot ISM (and other SBs) and unresolved point sources (e.g. X-ray binaries), (iii) a diffuse Galactic halo component (presumably from the Galactic

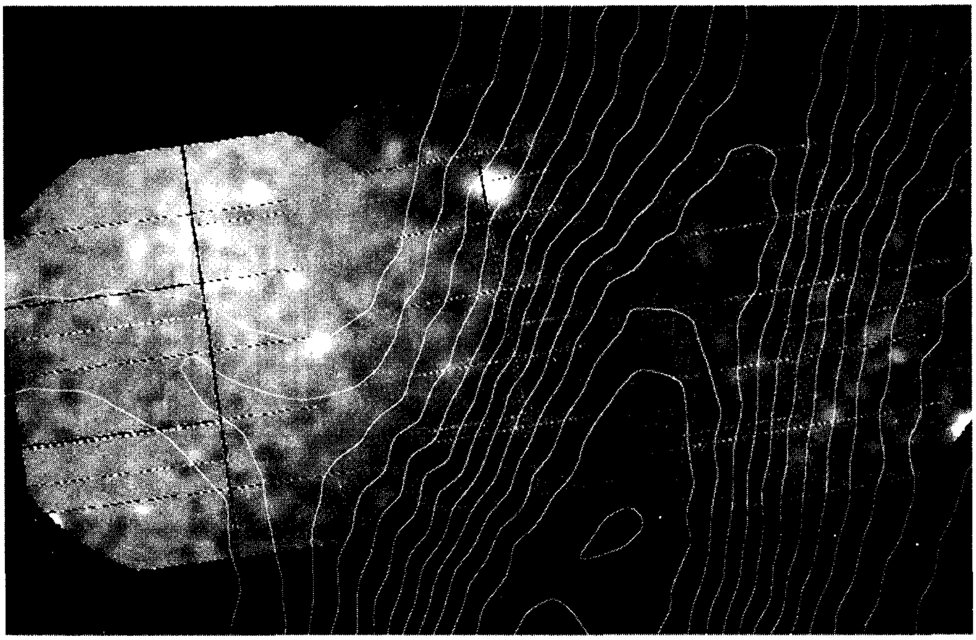

Figure 3: Three individual pointings of the Ophiuchus molecular cloud merged into one EPIC-pn image, showing the first X-ray shadow detected with XMM-*Newton*, in the energy range $0.5 - 0.9$ keV. There is an excellent anticorrelation between soft X-ray emission and the overlaid IRAS $100\,\mu$ contours (green). The color coding represents the X-ray intensity with white being the maximum.

fountain/wind), (iv) a diffuse extragalactic component (thought to consist of the WHIM = Warm Hot Intergalactic Medium and unresolved point sources). Shadowing the darkest regions of the Milky Way, i.e. nearby Bok globules with extinctions of $A_V \sim 30 - 50$ mag, give unmistakably in case of Barnard 68 *two temperature components* of the local emission (and thus *inconsistent* with the standard Local Hot Bubble model!): $kT_1 \approx 0.14 \pm 0.04$ keV, and $T_2 \approx 0.20 \pm 0.06$ keV (Freyberg et al. 2004). How is this possible? Several (not mutually exclusive) explanations have to be further investigated: (i) the LB is an old SB emitting X-rays from a gas not in ionization equilibrium (cf. Breitschwerdt & Schmutzler 1994) thus mimicking a multi-temperature plasma, (ii) there is a significant contribution from heliospheric plasma which undergoes charge exchange reactions with highly ionized solar wind atoms (Lallement 2004). At present it is unclear what the quantitative contribution of the latter process is (values $\leq 75\%$ in the disk and $\leq 50\%$ in the halo have been advocated). Such a very local emission should in principle exhibit seasonal variations. We have obtained two exposures of the Ophiuchus cloud, which partially overlap and are 6 months apart. The differences in emission measure and the spectrum are within the noise level. Although this is no counterargument it does not support the hypothesis of a substantial time-dependent variation of the heliospheric contribution. Further studies are needed to pin down this crucial component.

3 Analytical treatment of superbubble (SB) evolution

The dynamics of SBs has been worked out analytically by McCray & Kafatos (1987), based on earlier work by Pikel'ner (1968), Dyson & deVries (1972), Weaver et al. (1977) on stellar winds.

A basic principle, which is used in aerodynamics for constructing models in the wind channel,

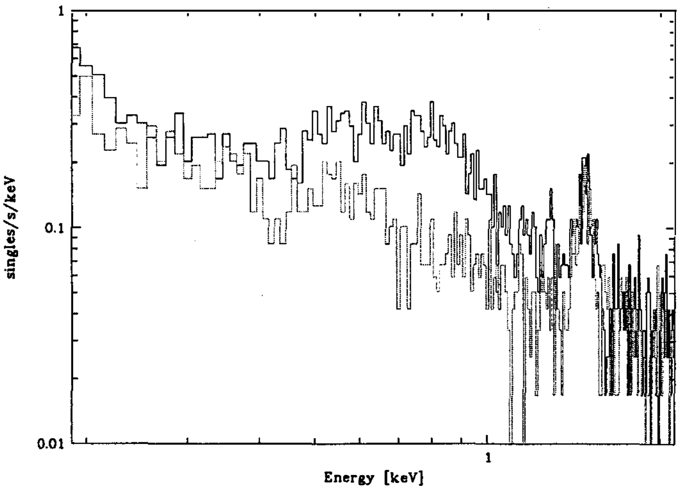

Figure 4: Spectrum of the soft X-ray background towards the Ophiuchus cloud. We have analyzed XMM-*Newton* EPIC pn data from two pointings of 20 ksec exposure each. Emission line complexes are clearly distinguishable at 0.5–0.7, ~ 0.9 keV, and to a minor extent at ~ 0.3 keV. The on-cloud pointing (red) contains mainly contributions from the Local Bubble, while the off-cloud observation has significant contributions from the ambient Loop I superbubble, as can be seen from the substantial amount of emission at 0.8 – 0.9 keV. This can be attributed to iron line complexes, indicating a higher plasma temperature in Loop I than in the Local Bubble.

is the scaling of hydrodynamic flows if there are no specific length or time scales entering the problem. Strictly speaking this is never fulfilled, because there are always boundary layers or time-dependent changes in the flow, but for studying the large-scale asymptotic behaviour of the flow this ansatz works remarkably well. If we e.g. neglect the initial switch-on phase of a SB, if we assume that the stellar source region is much smaller than the bubble, and if the discontinuous energy supply during the SN explosion phase can be approximated by a continuous injection of mass, momentum and energy, then *similarity solutions* are reasonably well applicable.

Mathematically speaking, the transformation to a similarity variable $\xi = (r/A)t^{-\alpha}$, projects the family of solutions of a PDE system to a one-dimensional family, with all hydrodynamic variables depending only on the dimensionless similarity variable ξ. A flow is said to be self-similar if its properties at any point x_1 and instance of time t_1 can be recovered by a similarity transformation at some other point in spacetime (x_0, t_0). The exponent α can already be derived from dimensional analysis. The physical quantities determining the SB dynamics are the energy injection rate, $L_{\rm SB}$, (with mass and momentum injection being negligible with respect to the shell mass and momentum during the energy driven phase) and the ambient density, ρ_0. Note that it is implicitly assumed that the pressure of the ambient medium can be neglected with respect to the interior pressure of the bubble. This is certainly valid until the shock becomes weak, in which case counterpressure has to be included. Then, $\xi = (L_{\rm SB}/\rho_0)^{-1/5}\,rt^{-3/5}$, is the only possibility to form a dimensionless quantity. Using this similarity variable, it is now possible to construct the complete flow solutions in terms of variables $u'(\xi), \rho'(\xi)$ and $P'(\xi)$, obeying matching conditions for boundaries in the flow at which these variables change discontinuously, like at the termination shock (where the "wind" ejecta are decelerated), the contact discontinuity (separating the wind from the ISM flow), and the outer shock (propagating into the ISM). The integration of the resulting ODE system is a straightforward but tedious exercise that can be carried out with the help of an integral, representing the conservation of the total energy of the system. We can simplify the procedure considerably by making a few additional, but well justified, assumptions about the flow in the different regions. Firstly, the ejecta gas, having a high kinetic energy, is compressed and heated by the strong termination shock, converting 3/4 of its initial bulk motion into heat. Therefore the temperature and the speed of sound in this bubble region are so high, that radiative cooling can be neglected and the pressure remains uniform for long time. On the other hand the pressure in the swept-up shell is also uniform due to its thinness, or in more physical terms, because the sound crossing time is much less than the dynamical time scale. This is because the outer shock can cool efficiently, as the ISM density is orders of magnitude higher than the ejecta gas density, if the latter one is assumed to be smoothly distributed. In essence, we are allowed to assume spatially constant density and pressure in the wind bubble and the shell, respectively.

As it turns out, the assumption of constant energy injection rate $L_{\rm SB}$ can be relaxed without violating the similarity argument. In reality we are dealing with an OB association, in which the stars are distributed according to some initial mass function (IMF) given by $\Gamma = \frac{d\log\zeta(\log m)}{d\log m}$; ζ denotes the number of stars per unit logarithmic mass interval per unit area with $\Gamma = -1.1 \pm 0.1$ for stars in Galactic OB associations with masses in excess of 7 $M_\odot$ (Massey et al. 1995). This translates into a number $N(m)\,dm$ of stars in the mass interval $(m, m + dm)$ (calibrated for some mass interval $N_0 = N(m_0)$), i.e. $N(m)dm = N_0 \left(\frac{m}{m_0}\right)^{\Gamma-1} dm$. It can be transformed into a time sequence, if we express the stellar mass by its main sequence life time, $\tau_{\rm ms}$. For stars within the mass range $7M_\odot \leq m \leq 30\,M_\odot$ this can be empirically approximated by $\tau_{\rm ms} = 3 \times 10^7\,(m/[10M_\odot])^{-\eta}$ yr (Stothers 1972), with $\eta = 1.6$. Since this defines m as a function of time τ, implicitly assuming that the energy input can be described as a continuous process, we obtain $m(\tau) = {\rm M}_\odot\,\left(\frac{\tau}{C}\right)^{-1/\eta}$, with $C = 3.762 \times 10^{16}$ s.

Let then $L_{\rm SB}(t)$ be the energy input per unit time due to a number of successive SN explosions with a constant energy input of $E_{\rm SN} = 10^{51}$ erg each, so that the cumulative number of SNe between stellar masses m and $m_{\rm max}$ reads

$$\tilde{N}_{\rm SN}(m) = \int_m^{\rm mmax} N(m')dm' = \frac{N_0 m_0}{\Gamma}\left[\left(\frac{m'}{m_0}\right)^{\Gamma}\right]_m^{\rm mmax} . \tag{1}$$

Then we have

$$L_{\rm SB} = \frac{d}{dt}(\tilde{N}_{\rm SN}E_{\rm SN}) = E_{\rm SN}\frac{d\tilde{N}_{\rm SN}}{dt} = E_{\rm SN}\frac{d\tilde{N}_{\rm SN}}{dm}\frac{dm}{d\tau}\frac{d\tau}{dt} \tag{2}$$

$$= \frac{N_0 E_{\rm SN} M_\odot K^{1-\Gamma}}{\eta C}\left(\frac{\tau_0 + t}{C}\right)^{-(\Gamma/\eta+1)}, \tag{3}$$

using the previous equations, and putting $m_0 = K\,M_\odot$. Since $\tau = t + \tau_0$, where t is the time elapsed since the first explosion, i.e. $\tau_0 = \tau_{\rm MS}(m_{\rm max})$, we have $d\tau/dt = 1$. With the above values for Γ and η, we obtain the useful formula $L_{\rm SB} = L_0\,t_7^\delta$, where $\delta = -(\Gamma/\eta + 1) = -0.3125$ and $t_7 = t/10^7$ yr. L_0 depends on the richness of the stellar cluster. Thus we see that, depending on the stellar IMF, the energy input rate by SN explosions is a mildly decreasing function of time. Although the number of core collapse SNe increases as the higher masses of the cluster become depopulated, the increasing time interval between explosions more than compensates this effect.

If the ambient medium is further assumed to have a constant ambient density, or one which varies with distance like $\rho \propto r^{-\beta}$, in which case the similarity variable has to be transformed to $\alpha = 3/(5-\beta)$, the system can be cast into the following form:

$$M_{\rm sh}(r) = \int_0^r \rho(r')d^3r', \quad E_{\rm th}(r) = 1/(\gamma-1)\int_0^r p(r')d^3r' . \tag{4}$$

and the energy input is shared between kinetic and thermal energy. Using $\gamma = 5/3$ for the ratio of specific heats, observing that the bubble pressure P_b remains uniform, and applying spherical symmetry, conservation of momentum and energy

$$\frac{d}{dt}(M_{\rm sh}\dot{R}_b) = 4\pi R_b^2 P_b\,, \quad \frac{dE_{\rm th}}{dt} = L_{\rm SB}(t) - 4\pi R_b^2 \dot{R}_b P_b\,, \tag{5}$$

yields the solution

$$R_b = At^\alpha\,; \quad \alpha = \frac{\delta+3}{5-\beta}\,, \tag{6}$$

$$A = \left\{\frac{(5-\beta)^3(3-\beta)}{(7\delta-\beta-\delta\beta+11)(4\delta+7-\delta\beta-2\beta)}\right\}^{1/(5-\beta)} \times \left\{\frac{L_0}{2\pi(\delta+3)\rho_0}\right\}^{1/(5-\beta)}\,. \tag{7}$$

Since the swept-up shell is usually thin, the bubble and shell radius can be treated as equal during the energy driven phase and are denoted by R_b. The similarity variable in the case considered here is given by $\alpha = (2 - \Gamma/\eta)/(5-\beta)$. For simplicity, the ambient density is assumed to be constant ($\beta = 0$), although, as we shall see in our numerical simulations, this assumption becomes increasingly worse with time. On scales of ten parsec, the ISM cannot be assumed to be homogeneous any more. As the cold and warm neutral media are observed to be rather filamentary in structure, high pressure flows will be channelled through regions of low density and pressure. It should be mentioned here, that it is not only the pressure difference between the bubble and the ambient medium that determines the expansion, as it is sometimes argued, but also the *inertia* of the shell is a crucial factor (see Eq. 5). Therefore mass loading of the flow is an important factor. Unfortunately, some convenient assumptions, like e.g. the bubble behaves isobaric, do not hold any more. Pittard et al. (2001a,b) have shown that similarity flow can be maintained provided the mass loading rate scales as $\dot{\rho} \propto r^{(5-7\beta)/3}$ in case of conductive evaporation or $\dot{\rho} \propto r^{(-2\beta-5)/3}$ for hydrodynamic mixing according to the Bernoulli effect. It was assumed that in the former case clumps passed through the outer shock as it expanded into a clumpy medium and evaporated in the hot bubble, whereas in the latter case the clumps were thought to be ejected by the central source itself. Here it is possible for strong mass loading that the wind flow is slowed down considerably due to mass pick-up, and in the extreme case even a termination shock transition can be avoided.

Berghöfer & Breitschwerdt (2002) have studied the evolution of the LB under the assumption that 20 SNe from the Pleiades moving subgroup B1 exploded according to their main sequence life times with masses between 20 and 10 $M_\odot$. Using the above similarity solutions, the radius and the expansion velocity of the bubble evolve as

$$R_b = 251\left(\frac{2\times10^{-24}{\rm g/cm^3}}{\rho_0}\right)^{1/5} t_7^{0.5375}\,{\rm pc}\,, \dot{R}_b = 13.22\left(\frac{2\times10^{-24}{\rm g/cm^3}}{\rho_0}\right)^{1/5} t_7^{-0.4625}\,{\rm km/s}\,. \tag{8}$$

As a result of a decreasing energy input rate the exponent in the expansion law of the radius, $\alpha = 43/80 = 0.5375$, in Eq. (8) is between a Sedov ($\mu = 0.4$) and a stellar wind ($\mu = 0.6$) type solution. Thus the present radius of the LB will be 289 pc and 158 pc and its velocity is 11.7 km/s and 6.4 km/s, if the ambient density is $\rho_0 = 2\times10^{-24}$ g/cm^3 and $\rho_0 = 4\times10^{-23}$ g/cm^3, respectively (for details see Berghöfer & Breitschwerdt 2002). In the latter case the value of the ambient density would correspond roughly to that of the cold neutral medium. There are several reasons why we may have overestimated the size of the LB in the similarity solutions above. Firstly, the mass inside the bubble is significantly higher than the pure ejecta mass, as can be inferred from the ROSAT X-ray emission measures; when assuming bubble parameters of $R_b = 100$ pc and $n_b = 5\times10^{-3}$ cm^{-3} (e.g. Snowden et al. 1990) a mass of at least 600 $M_\odot$ is derived, and using non-equilibrium ionization plasma models (Breitschwerdt & Schmutzler 1994) it is even more than a factor of five higher. The contribution of ejecta is only of the order of 100 $M_\odot$, and the bulk of the bubble mass is therefore due to hydrodynamic mixing of shell material, heat conduction between shell and bubble and evaporation of entrained clouds; hence the flow must be mass-loaded. The net effect is to reduce the amount of specific energy per unit mass, because the material mixed in is essentially cold, thus increasing the rate of radiative cooling. Secondly, the stellar association has probably been surrounded by a molecular cloud with a density in excess of $n_0 = 100\,\mathrm{cm}^{-3}$ with subsequent break-out of the bubble and dispersal of the parent cloud (Breitschwerdt et al. 1996). Thirdly, the number of SN explosions could be less; here we have assumed that all 20 SNe have occurred inside the LB. This need not be the case as the subgroup B1 does not move through the centre of the LB. ROSAT PSPC observations have revealed an annular shadow centered toward the direction ($l_{\mathrm{II}} = 335°$, $b_{\mathrm{II}} = 0°$), which has been interpreted as an interaction between the LB and the neighbouring LI SB (Egger & Aschenbach 1995). The trajectory of the cluster B1 may have partly crossed the LI region. Alternatively and more likely, part of the thermal energy might have been liberated into the Galactic halo, since there is some evidence that the LB is open toward the North Galactic Pole (see Lallement et al. 2003). It should also be mentioned that due to small number statistics the true number of SNe can vary by a factor of 2. Finally, although there is no stringent evidence, it would be very unusual, if the LB would not be bounded by a magnetic field, whose tension and pressure forces would decrease the size of the LB.

Given these uncertainties and the fact that the simple analytic model discussed above can only be considered as an upper limit, the direct comparison with observations is not convincing. The bubble radius and shell velocity are rather insensitive to the energy input rate and the ambient density (due to the power of 1/5) and therefore not well constrained, but depend more sensitively on the expansion time scale. Thus we can only assert with some confidence that the age of the LB should be between $1 - 2 \times 10^7$ yr.

The most serious drawback of analytical solutions in general and of similarity solutions in particular, is the assumption of homogeneity of the ambient medium on scales exceeding about 10 pc. To see this, consider the area coverage of the disk by hot gas, which is $\xi_{\mathrm{SN}} \sim \nu_0/2\,\tau_{\mathrm{SN}}\,(R_{\mathrm{SN}}/R_{\mathrm{gal}})^2 \approx 0.67$ due to SNe, and $\xi_{\mathrm{SB}} \sim \nu_0/2\,\tau_{\mathrm{SB}}\,(R_{\mathrm{SB}}/R_{\mathrm{gal}})^2 \approx 0.9$ due to SBs, respectively, assuming that half of the explosions go off randomly, and half in a clustered fashion within a star forming disk of 10 kpc radius and a disk SN rate of $\nu_0 = 2$ per century. Here we used the final SN radius according to McKee & Ostriker (1977), being $R_{\mathrm{SN}} \approx 55$ pc after $\tau_{\mathrm{SN}} \approx 2.2 \times 10^6$ yr and the SB radius from the paper of McCray & Kafatos (1987) of $R_{\mathrm{SB}} \approx 212$ pc after $\tau_{\mathrm{SB}} \approx 10^7$ yr, for a typical cluster with 50 OB stars. The overturning rate of a typical patch of ISM will then roughly be between 3.4×10^6 yr and 1.1×10^7 yr for SNe and SBs, respectively. Since we did not take into account overlapping of remnants and bubbles these values are lower limits. As will be shown in the next section, a roughly constant star formation rate and hence SN rate for a Galactic initial mass function (IMF) will lead to an ISM background medium that is highly irregular in density and temperature (and even pressure variations within an order of magnitude are observed) and it bears a high level of turbulence.

4 Numerical simulations of the Local Bubble (LB) and Loop I (LI) evolution

We have performed high resolution 3D simulations of the Galactic disk and halo (Avillez & Breitschwerdt 2004, 2005; see also this volume) on a grid of $1\,\mathrm{kpc} \times 1\,\mathrm{kpc}$ in the plane and $z = \pm 10\,\mathrm{kpc}$ perpendicular to it. Using AMR technique, we obtained resolution of scales down to 1.25 pc for MHD, and 0.625 pc for pure hydrodynamical (HD) runs. These simulations, which revealed many new features of the ISM, e.g. low volume filling factor of hot gas in the disk, establishment of the fountain flow even in the presence of a disk parallel magnetic field, more than half of the mass in classical thermally unstable regions, serve as a *realistic background* *medium* for the expansion of the LB and the LI SB. We took data cubes of HD runs and picked up a site with enough mass to form the 81 stars, with masses, M_*, between 7 and 31 $M_\odot$,

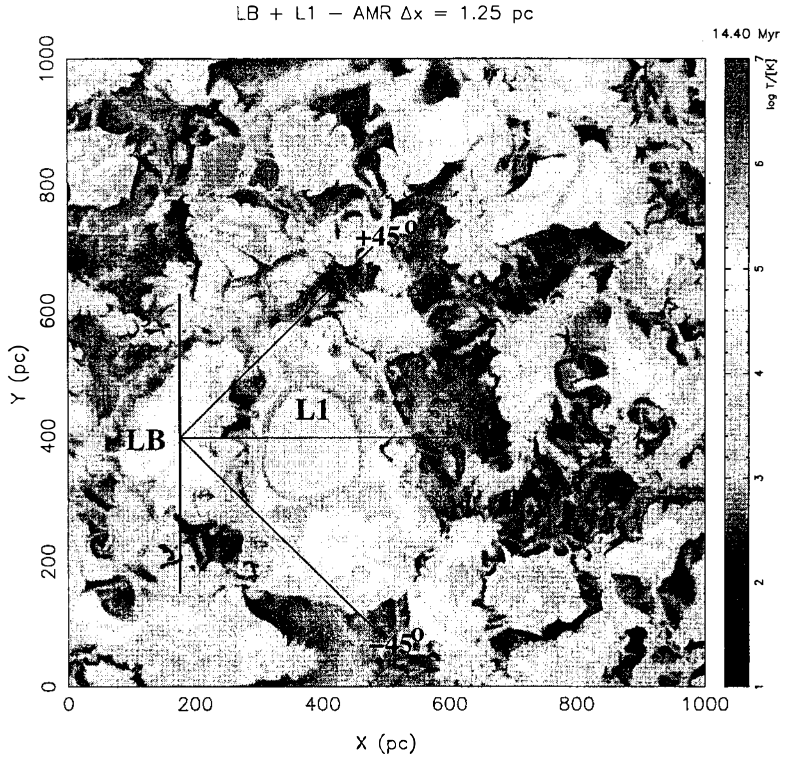

Figure 5: Temperature map (cut through Galactic plane) of a 3D Local Bubble simulation, 14.4 Myr after the first explosion; LB is centered at (175, 400) pc and Loop I at (375, 400) pc.

that represent the Sco-Cen cluster inside the LI SB; 39 massive stars with $14 \leq M_* \leq 31\,M_\odot$ have already exploded, generating the LI cavity. At present the Sco-Cen cluster (arbitrarily located at (375, 400) pc has 42 stars to explode within the next 13 Myrs). We followed the trajectory of the moving subgroup B1 of Pleiades (see Berghöfer & Breitschwerdt 2002), whose SNe in the LB went off along a path crossing the solar neighbourhood. As a result, we observe that the locally enhanced SN rates produce coherent LB and LI structures (due to ongoing star formation) within a highly disturbed background medium (see Fig. 5). The successive explosions heat and pressurize the LB, which at first looks smooth, but develops internal temperature and density structure at later stages. After 14 Myr the 20 SNe that occurred inside the LB fill a volume roughly corresponding to the present day size (see Fig. 5, bubbles are labelled by LB and L1). The cavity is still bounded by an outer shell, which exhibits holes due to Rayleigh-Taylor instabilities, as has been predicted analytically by Breitschwerdt et al. (2000), and it will start to fragment in ~ 3 Myr from now. It has been argued that a crucial test of any LB model is the column density of the interstellar ion OVI (Cox 2004), whose discovery back in the 70's led to the establishment of the hot intercloud medium. So far all models have failed to reproduce the fairly low OVI-value, most recently measured with FUSE (Oegerle et al. 2004), to be $N_{\mathrm{OVI}} \simeq 7 \times 10^{12}$ cm^{-2}. To compare this with our simulations we have calculated the average and maximum column densities of OVI, i.e., $\langle \mathrm{N(OVI)} \rangle$ and $\mathrm{N_{max}(OVI)}$ along 91 lines of sight (LOS) extending

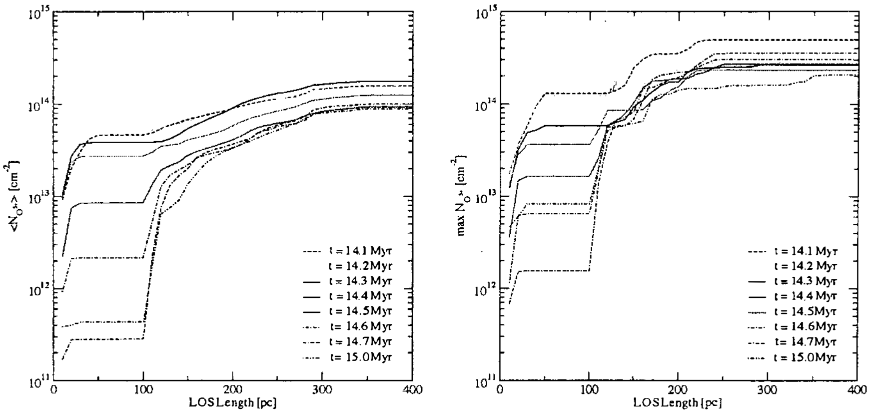

Figure 6: OVI column density averaged over angles (left panel) indicated in Fig. 5 and maximum column density (right panel) as a function of LOS path length at $14.1 \leq t \leq 15$ Myr of Local and Loop I bubbles evolution.

from the Sun and crossing LI from an angle of -45 deg to $+45$ deg (s. Fig. 5). Within the LB (i.e., for a LOS length $l_{LOS} \leq 100$ pc) $\langle N(\mathrm{OVI})\rangle$ and $N_{max}(\mathrm{OVI})$ decrease steeply from 5×10^{13} to 3×10^{11} cm^{-2} and from 1.2×10^{14} to 1.5×10^{12} cm^{-2}, respectively, for $14.1 \leq t \leq 15$ Myr (Fig. 6), because no further SN explosions occur and recombination is taking place. For LOS sampling gas from outside the LB (i.e., $l_{LOS} > 100$ pc) $\langle N(\mathrm{OVI})\rangle > 6\times10^{12}$ and $N_{max}(\mathrm{OVI}) > 5\times10^{13}$ cm^{-2}. We have made histograms of column densities obtained in the 91 LOS for $t = 14.5$ and 14.6 Myr, which show that for $t = 14.6$ Myr all the LOS have column densities smaller than $10^{12.9}$ cm^{-2}, while for $t = 14.5$ Myr 67% of the lines have column densities smaller than 10^{13} cm^{-2} and in particular 49% of the lines have $N(\mathrm{OVI}) \leq 7.9\times10^{12}$ cm^{-2}. Noting that in the present model at 14.5 Myr the OVI column densities are smaller than 1.7×10^{13} cm^{-2} and $\langle N(\mathrm{OVI})\rangle = 8.5\times10^{12}$ cm^{-2} (see the respective lines in both panels of Fig. 6), we are thus able to reproduce the measured $\langle N(\mathrm{OVI})\rangle$ values, provided that the age of the LB is $\sim 14.7^{+0.5}_{-0.2}$ Myrs.

5 Conclusions

Galactic and extragalactic interstellar bubbles are still an active area of research. Despite the widespread belief that HII regions, SNRs, stellar wind bubbles and superbubbles are fully understood in theory, it has to be emphasized that *real bubbles*, observed in the Galaxy, such as the Local or LI superbubbles, or in external galaxies, such as in the LMC, are often poorly fitted by standard similarity solutions. The reason lies in the inapplicability of major assumptions, e.g., that the ISM is homogeneous, and that the bubbles are either in an energy or momentum conserving phase. High resolution 3D simulations in a highly structured and turbulent background medium offer a much better description and include physical processes such as mass loading and turbulent mixing on a fundamental level. Although this drains heavily on computer resources, the increased precision of observations in the near future will warrant such an effort.

Acknowledgments

DB would like to thank Thierry Montmerle and Almas Chalabaev for their excellent organization, for financial help and patience with the manuscript. It was a great pleasure to be in La Thuile. He also thanks Verena Baumgartner for proofreading of the text.

References

1. Avillez, M.A., Breitschwerdt, D. 2004, A&A 425, 899
2. Avillez, M.A., Breitschwerdt, D. 2005, A&A (in press)
3. Baade, W., Zwicky, F. 1934, Proc. Nat. Acad. Sci. 20, 254
4. Berghöfer, T.W., Breitschwerdt, D., 2002, A&A 390, 299
5. Bowyer, S., Field, G.B., Mack, J.E. 1968, Nature 217, 32
6. Breitschwerdt, D., Egger, R., Freyberg, M.J. 2000, A&A 361, 303
7. Breitschwerdt, D., Egger, R., Freyberg, M.J., Frisch, P.C., Vallerga, J. 1996, SSRv 78, 183
8. Breitschwerdt D., Schmutzler T. 1994, Nature 371, 774
9. Brinks, E., Shane, W.W. 1984, ApJS 55, 179
10. Cash, W., et al. 1980, ApJ 238, L71
11. Cecil, G., Bland-Hawthorn, J., Veilleux, S. 2002, ApJ 576, 745
12. Chu, Y.-H., et al. 2003, ApJ 599, 1189
13. Cox, D.P. 2004, Ap&SS, 289, 469
14. Dyson, J.E., de Vries, J. 1972, A&A 20, 223
15. Egger, R.J., Aschenbach, B., A&A 294, L25
16. Freyberg, M.J., Breitschwerdt, D., Alves, J. 2004, Mem. de la Soc. Astron. Ital. 75, 509
17. Freyberg, M.J., Egger, R.J. 1999, in *Highlights in X-ray Astronomy*, eds. B. Aschenbach, M.J. Freyberg, MPE-Report 272, 278
18. Frisch, P.C., York, D.G. 1983, ApJ 271, L59
19. Heiles, C. 1979, ApJ 229, 533
20. Heiles, C. 1980, ApJ 235, 833
21. Lallement, R. 2004, A&A 418, 143
22. Lallement, R., Welsh, B.Y., Vergely, J.L., Crifo, F., Sfeir, D. 2003, A&A 411, 447
23. Massey, P., Johnson, K.E., Degioia-Eastwood, K. 1995, ApJ 454, 151
24. McCray, R., Kafatos, M. 1987, ApJ 317, 190
25. McKee, C.F., Ostriker, J.P. 1977, ApJ 218, 148
26. Mendes, P., Freyberg, M.J., Breitschwerdt, D. 2005, A&A (in preparation)
27. Morton, D.C. 1967, ApJ 147, 1017
28. Oegerle, W. R., et al. 2004, ApJ (submitted), [astro-ph/0411065]
29. Oort, J.H. 1954, Bull. of the Astron. Society of the Netherlands, vol. 12, No. 455, 177
30. Pikel'ner, S.B. 1968, Astrophys. Lett. 2, 97
31. Pittard, J.M., Hartquist, T.W., Dyson, J.E. 2001, A&A 373, 1043
32. Sanders, W.T., Kraushaar, W.L., Nousek, J.A., Fried, P.M. 1977, ApJ 217, L87
33. Snowden, S.L., Cox, D.P., McCammon, D., Sanders, W.T. 1990, ApJ 354, 211
34. Snowden, S.L., Freyberg, M.J., Kuntz, K.D., Sanders, W.T. 2000, ApJS 128, 171
35. Stothers, R. 1972, ApJ 175, 431
36. Stroemgren, B. 1939, ApJ 89, 526
37. Tanaka, Y., Bleeker, J.A.M. 1977, SSRv 20, 815
38. Weaver, R., Castor, J., McCray, R., Shapiro, P., Moore, R. 1977, ApJ 218, 377
39. Wrigge, M., Chu, Y.-H., Magnier, E.A., Kamata, Y. 1998, in *The Local Bubble and Beyond*, eds. D. Breitschwerdt, M.J. Freyberg, J. Trümper, LNP 506, p. 425

Disk-Halo-Disk Circulation and the Evolution of the ISM - 3D HD and MHD Adaptive Mesh Refinement Simulations

M.A. de Avillez (1,2), D. Breitschwerdt (2)
(1) Department of Mathematics, University of Évora, R. Romão Ramalho 59, 7000 Évora, Portugal
(2) Institut für Astronomie, Universität Wien, Türkenschanzstr. 17, A-1180 Wien, Austria

State of the art models of the ISM use adaptive mesh refinement to capture small scale structures, by refining on the fly those regions of the grid where density and pressure gradients occur, keeping at the same time the existing resolution in the other regions. With this technique it became possible to study the ISM in star-forming galaxies in a global way by following matter circulation between stars and the interstellar gas, and, in particular the energy input by random and clustered supernova explosions, which determine the dynamical and chemical evolution of the ISM, and hence of the galaxy as a whole. In this paper we review the conditions for a self-consistent modelling of the ISM and present the results from the latest developments in the 3D HD/MHD global models of the ISM. Special emphasis is put on the effects of the magnetic field with respect to the volume and mass fractions of the different ISM "phases", the relative importance of ram, thermal and magnetic pressures, and whether the field can prevent matter transport from the disk into the halo. The simulations were performed on a grid with a square area of 1 kpc^2, centered on the solar circle, extending ± 10 kpc perpendicular to the galactic disk with a resolution as high as 1.25 pc. The run time scale was 400 Myr, sufficiently long to avoid memory effects of the initial setup, and to allow for a global dynamical equilibrium to be reached in case of a constant energy input rate.

Keywords: magneto-hydrodynamics – galaxies: ISM – galaxies: kinematics and dynamics – Galaxy: disk – Galaxy: evolution – ISM: bubbles – ISM: general – ISM: kinematics and dynamics – ISM: structure

1 Introduction

So far our understanding of the evolution of the ISM has been scanty, because of the inherent nonlinearity of all the processes involved. Analytic ISM models, which tried to explain the distribution of the ISM gas into various thermally stable "phases" such as the pioneering work by, e.g., Field (1965), Field et al. (1969), Cox & Smith (1974), and McKee & Ostriker (1977), can at most be regarded as exploratory. Noticeable progress was only possible by the development of sophisticated numerical codes, adequate computing power, and precision input data by observations. Only very recently, by the rapid evolution of telescope and detector technology, as well as the availability of large numbers of parallel processors, we are in the fortunate situation to follow in detail the evolution of the ISM on the global scale taking into account the disk-halo-disk circulation in three dimensions (the first models using 2D grids were developed by Rosen & Bregman 1995).

In this paper we discusss the most important numerical prerequisites for a realistic and self-consistent modelling of the ISM (Section 2), followed by a brief summary of the latest 3D disk-halo-disk circulation simulations (Section 3). Section 4 discusses model testing and finally, in Section 5 a few final remarks are presented.

2 Modelling of the ISM

The key to a realistic description of the ISM is the use of the apropriate dimensionality, grid coverage, the highest possible spatial resolution, and a realistic input of the basic physical processes with appropriate boundary and initial conditions. All this coupled to the appropriate tools for the included physics, which are sophisticated HD and MHD codes capable of tracking non-linear and small scale structures, solving the Riemann problem between neighbouring cells without introducing large artificial viscosity and guarantee the conservation of $\nabla \cdot \mathrm{B} = 0$ in case magnetic fields are included. These simulations are considered to provide a reliable description of the ISM providing the memory of the initial conditions and evolution has been lost and the models used in these runs have been tested against observations in the local ISM and in particular within the Local Bubble (Cox 2004; Breitschwerdt & Cox 2004, see also Breitschwerdt et al. in this volume).

Dimensionality is of crucial importance as it determines the dynamics (and the turbulence) of the flow with/without magnetic fields. For example, the idea that a disk parallel magnetic field could suppress break-out and outflow into the halo was mainly based on 2D simulations carried out in the last 15 years, owing to computing power limitations. It is obvious, that in 2D-MHD, the flow perpendicular to the magnetic field lines (and hence to the galactic plane) is subject to opposing magnetic tension forces. In 3D however, field lines can be pushed aside and holes and channels can be punched into the gas and field, allowing pressurized flow to circumvent *ever increasing tension and pressure forces* in z-direction.

This behaviour requires that the **grid coverage** in the $z-$direction must be large enough to accomodate the outflows, whose upper height above the Galactic plane can be estimated by calculating the flow time, τ_f, that the gas needs to travel to the critical point of the flow in a steady-state (see Kahn 1981). This is the characteristic distance from which information in a thermally driven flow can be communicated back to the sources. Then $\tau_f \sim r_c/c_s$, where r_c and c_s are the location of the critical point and the speed of sound, respectively. For spherical geometry, the critical point can be simply obtained from the steady state fluid equations, $r_c \sim GM_{gal}/(2c_s^2)$, which yields with a Milky Way mass of $M_{gal} \approx 4 \times 10^{11}\,\mathrm{M}_\odot$ a distance $r_c \approx 31.3$ kpc for an isothermal gas at $T = 2 \times 10^6$ K (corresponding to a sound speed of $1.67 \times 10^7\,\mathrm{cm\,s^{-1}}$), and thus $\tau_f \sim 180$ Myr as an upper limit for the flow time. For comparison, the radiative cooling time of the gas at a typical density of $n = 2 \times 10^{-3}\,\mathrm{cm^{-3}}$ is roughly $\tau_c \sim 3k_BT/(n\Lambda) \approx 155$ Myr for a standard collisional ionization equilibrium cooling function $\Lambda = 8.5 \times 10^{-23}$ erg cm^3 s^{-1} of gas with cosmic abundances. This value is apparently of the same order as the flow time, ensuring that the flow will not only cool by adiabatic expansion, but also radiatively, thus giving rise to the fountain return flow, which is the part of the outflow that loses pressure support from below and therefore cannot escape. Note that r_c is the maximum extension of the fountain flow in steady state. Thus, the lack of such an extended z-grid inhibits the disk-halo-disk circulation of matter, which otherwise would return gas to the disk sometime later, with noticeable effects for the dynamical evolution there. The loss of matter may be compensated by some injection of mass by means of rather artificial **boundary conditions** imposed into the upper and bottom faces of the grid.

The **resolution** adopted in a simulation results from a compromise between the available computing resources and the minimum scale required to handle appropriately the physical processes involved in the system under study. For instance in the ISM simulations high resolutions are required due to the formation of small scale structures, resulting from instabilities in the flows, in particular from thermal instabilities and condensations as a result of radiative cooling. The amount of cooling may be substantially increased if the resolution is high enough to trace regions of high compression by shocks, rather than smearing them out over larger cells, and thereby wiping out density peaks. Radiative cooling as a nonlinear process can become more efficient, since high density regions contribute more to the energy loss rate than low density regions can compensate by an accordingly lower rate. Since cooling is most efficient for dense gas, the cool phase is affected most. In addition, the spatial resolution of shear layers and contact surfaces, gives rise to an increased level of turbulence and a larger number of mixing layers. The latter is most important, because it allows for a faster mixing between parcels of gas with different temperatures (conduction or diffusion processes being of second order and hence inherently slow in nature). The small scale mixing is promoted by numerical rather than molecular diffusion, and therefore, the time scales for mixing in the different phases to occur is somewhat smaller (because it happens on larger scales) than those predicted by molecular diffusion theory (e.g., Avillez & Mac Low 2002). However, turbulent diffusion, as a consequence of the onset of turbulence due to shear flows, will be most efficient.

A necessary, but not sufficient, condition on **convergence** of the simulations is that by increasing the resolution (normally by doubling it a few times) global properties, such as volume filling factors, history of minimum temperature and maximum density, mass distribution with time, etc, do not change significantly. When the numerical solutions, with the increase in resolution, have a small discrepancy of a few percent then one can safely conclude that the simulations converge for the physical processes included. For further discussion see Avillez & Breitschwerdt (2004).

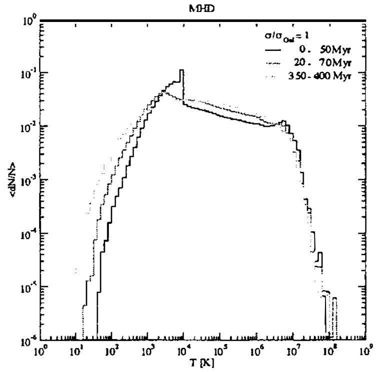

Figure 1: Averaged volume-weighted temperature histogram for a MHD global ISM simulation over the periods of 0-50 Myr (black), 20-70 Myr (red) and 350-400 Myr (green) calculated using 51 snapshots taken at time intervals 1 Myr. The resolution of the finest AMR level is 1.25 pc.

The initial evolution of a system imprints its signature in the averaged histograms of time evolved variables until the nonlinear processes developing during this time wipe out the signature of the initial conditions. In the case of global models as the ones discussed below, the initial evolution imprint is still seen after 70 Myr of evolution of a magnetized ISM (Fig. 1, which shows averaged volume weighted histograms of the temperature over the periods of 0-50, 20-70 and 350-400 Myr for an MHD run with the Galactic SN rate and a finest AMR resolution of 1.25 pc). This imprint is also seen in corresponding histograms of HD simulations (Avillez & Breitschwerdt 2004).

3 Results from the Latest HD and MHD Simulations of a Disk-halo-disk Circulation System

Taking into account the above considerations we carried out high resolution (using adaptive mesh refinement with finer resolutions ranging from 0.625 to 2.5 pc and coarse grid resolution of 10 pc) three-dimensional kpc-scale HD and MHD simulations of the ISM including the disk-halo-disk circulation with a grid centred on the solar circle and extending from $z = -10$ to 10 kpc with a square disk area of 1 kpc^2. The basic processes included are the gravitational field provided by the stars in the disk, radiative cooling assuming an optically thin gas in collisional ionization equilibrium, uniform heating due to starlight varying with z, supernovae (with a canonical explosion energy of 10^{51} erg) types Ia (with scale height, distribution and rate taken

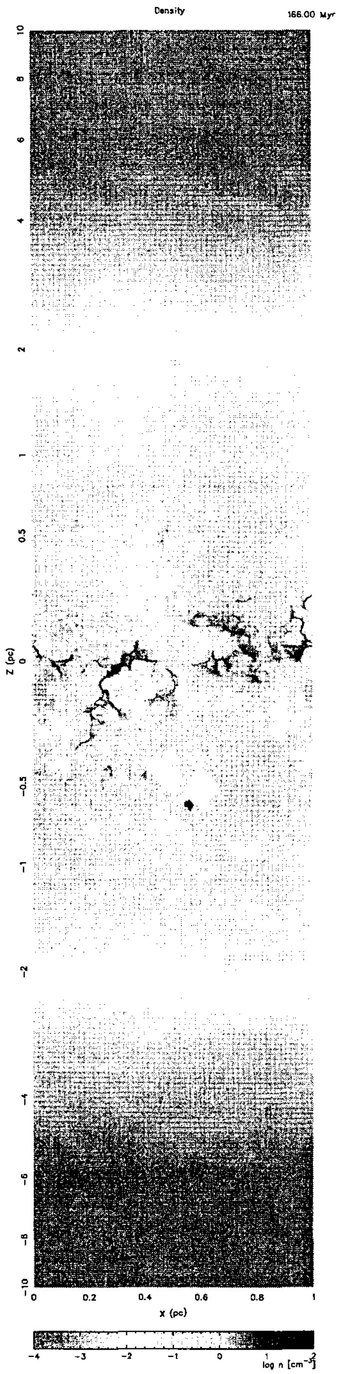

Figure 2: Slice through the 3D data set showing the vertical (perpendicular to the midplane) distribution of the density at time 166 Myr.

from the literature) and Ib and II, whose formation, and spatial location is calculated self-consistently by determining the number and masses and main sequence lifetimes of the OB stars formed in regions with $n \geq 10$ cm^{-3}, T$\leq$ 100 K, respectively, and $\nabla \cdot \vec{v} < 0$, where $\vec{v}$ is the gas velocity. Some $40-50\%$ of the stars (these are mainly the stars with masses $\leq 11M_\odot$) explode in the field (the rest in associations) and have an average scale height of ~ 90 pc. The mean total rate per unit volume of occurrence of SNe in these simulations is 18 kpc^{-3} Myr^{-1}, a value similar to the observed one. In the case of the MHD run the ISM is pervaded by a magnetic field with a total strength of $\simeq 4.45$ μG resulting from unform and random components with mean values of 3.25 and 3.1 μG, respectively.

3.1 Global Evolution

The simulations depart from an hydrostatic setup of the disk and halo gas which does not hold for long as a result of the lack of equilibrium between gravity and (thermal, kinetic and turbulent) pressure during the "switch-on phase" of SN activity. As a consequence the gas in the upper and lower parts of the grid collapses onto the midplane, leaving low density material behind. However, in the MHD run it takes a longer time for the gas to descend towards the disk and the complete collapse into the midplane is prevented by the opposing magnetic pressure and tension forces. As soon as enough SNe have gone off in the disk building up the required pressure support, a thick frothy disk is formed overlayed by a hot halo. The thick gas disk is feeded and supported by the motions of the hot gas warmed up by randomly distributed SNe which rises buoyantly and eventually breaks through into the halo. Transport into the halo is not prevented, although the escape of the gas takes a few tens of Myr to occur in the MHD run – somewhat longer than in the pure hydrodynamical case. The crucial point is that the huge thermal overpressure due to combined SN explosions can sweep the magnetic field into dense filaments and punch holes into the extended warm and ionized layers allowing the setup of pressure release valves, after which there is no way from keeping the hot over-pressured plasma to follow the pressure and density gradient into the halo.

Fig. 2 shows the density distribution in the plane perpendicular to the Galactic midplane at time 166 Myr. Red/blue in the colour scale refers to lowest/highest density (or highest/lowest temperature). The $z-$scale above 0.5 and below -0.5 kpc is shrunk (in order to fit the paper size) and thus, the distribution of the labels is not uniform. The image shows the presence of a wiggly thin disk of cold gas overlayed by a frothy thick disk (punctured by chimneys and crossed by hot buoyant ascending gas) composed of neutral (light blue), with a scale height of $\sim$ 180 pc, and ionized (greenish) gas with a scale height of 1 kpc. These distributions reproduce those described in Dickey & Lockman (1990) and Reynolds (1987), respectively. The upper parts of the thick ionized disk form the disk-halo interface located around 2 kpc above and below the midplane, where a large scale fountain is set up by hot ionized gas, injected there either from gas streaming out of the thick disk or directly from superbubbles in the disk underneath, escaping in a turbulent convective flow. The corresponding magnetic field maps, presented in Avillez & Breitschwerdt (2005), show the presence of a thin magnetized disk overlayed by Parker-like loops (produced without cosmic rays), magnetic islands, and clouds wrapped in field lines moving downwards. There is also cold gas descending along the Parker loops.

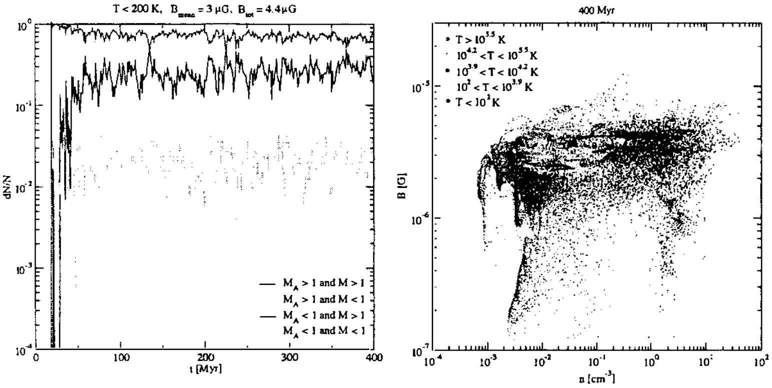

Figure 3: *Left panel:* History of the cold (T $\leq$ 200 K) gas fraction that is super/sub-alfvénic (denoted by M_A > *or* < 1) and super/sub-sonic (denoted by M > *or* < 1). As it can be seen the less than 10^{-2}% of cold gas has $M_A > 1$ and $M < 1$. *Right panel:* Scatter plot of B versus n for $T \leq 10^2$ (black), $10^2 < T \leq 10^{3.9}$ (grey), $10^{3.9} < T \leq 10^{4.2}$ (blue), $10^{4.2} < T \leq 10^{5.5}$ K (green), and $T > 10^{5.5}$ K (red) regimes at 400 Myr of disk evolution. The points in the plot are sampled at intervals of four points in each direction.

3.2 Shock Compressed Layers

The highest density gas with $T \leq 10^2$ K is confined to shocked compressed layers that form in regions where several large scale streams of convergent flow (driven by SNe) occur. The compressed regions, which have on average lifetimes of a few free-fall times, are filamentary in structure, tend to be aligned with the local field and are associated with the highest field strengths (in the MHD run), while in the HD runs there is no preferable orientation of the filaments. The formation time of these structures depends on how much mass is carried by the convergent flows, how strong the compression and what the rate of cooling of the regions under pressure are. During the dynamical equilibrium evolution on average 70% of the cold ($T \leq 200$ K) gas is subalfvénic and supersonic, while only 1-5% is subalfvénic and subsonic, the remaining fraction of the gas has $M_A > 1$ and $M > 1$ (Fig. 3). This means that although in the ISM the majority of the cold gas is supersonic and subalfvenic there is a considerable fraction ($\langle dN/N \rangle \simeq 30\%$) of the gas where the mean magnetic pressure is dynamically low, i.e., $M_A > 1$.

3.3 Field Dependence with Density

After the global dynamical equilibrium has been set up the magnetic field shows a high variability (which decreases towards higher gas densities spanning two orders of magnitude from 0.1 to 15

μG; see Fig. 3) and it is *largely uncorrelated with the density.* The spreading in the field strength increases with temperature, being largest for the hot ($T > 10^{5.5}$ K) and smallest (with almost an order of magnitude variation from 0.8 to 6 μG) for the cold ($T \leq 200$ K) gas. The large scatter in the field strength for the *same* density, seen in Fig. 3, suggests that the field is being driven by the inertial motions, rather than it being the agent determining the motions. In the latter case the field would not be strongly distorted, and it would direct the motions predominantly along the field lines. In ideal MHD field diffusion is negligible, and the coupling between matter and field should be perfect (we are of course aware of numerical diffusion which weakens the argument at sufficiently small scales). Therefore gas compression is correlated with field compression, except for strictly parallel flow.

3.4 Driving Forces in the ISM

The relative importance of the driving pressures, i.e., thermal (P_{th}), ram (P_{ram}) and magnetic (P_{mag}), in the ISM varies with increasing temperature (Fig. 4). For $T \leq 150$ K $P_{th} << P_{ram} < P_{mag}$ indicating that the gas is dominated by the Lorentz $\vec{j} \times \vec{B}$ force, and the magnetic field determines the motion of the fluid, while for $T \geq 10^{5.5}$ K thermal pressure dominates. At the intermediate temperatures ram pressure determines the dynamics of the flow, and therefore, the magnetic pressure does not act as a significant restoring force (see Passot & Vázquez-Semadeni 2003) as it was already suggested by the lack of correlation between the field strength and the density. It is also noteworthy that in this temperature range ($150 - 10^{5.5}$ K) the weighted magnetic pressure is roughly constant (suggesting that the magnetic and thermal pressures are largely independent, whereas both thermal and ram pressures undergo large variations in this temperature interval.

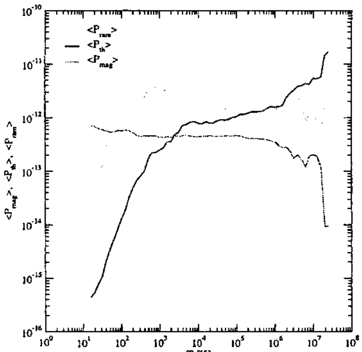

Figure 4: Average $\langle P_{ram} \rangle$ (green), $\langle P_{th} \rangle$ (black), and $\langle P_{mag} \rangle$ (red) as function of the temperature (in the simulated disk $|z| \leq 250$ pc) averaged over temperature bins of $\Delta \log T = 0.1$ K between 350 and 400 Myr.

3.5 The Chandrasekhar-Fermi Law

As ram pressure fluctuations in the ISM dominate over the other pressures a perfect correlation between the field and density following the classical scaling law $B \sim \rho^{\alpha}$ is not expected, with $\alpha = 1/2$, according to the Chandrasekhar-Fermi (CF) model (1953), but a broad distribution of B versus ρ. Although in general $0 \leq \alpha \leq 1$ would be expected, it should be noted that in reality heating and cooling processes, and even magnetic reconnection could induce further changes, making the correlation rather complex. It should be kept in mind that in CF it was assumed that the field is distorted by turbulent motions that were subalfvénic, whereas in our simulations in addition both supersonic and superalfvénic motions can occur, leading to strong MHD shocks. In other words, according to the CF model, the turbulent velocity is directly proportional to the Alfvén speed, which in a SN driven ISM need not be the case.

3.6 Pressure Distributions and Fluctuations

The pressure coverage of three orders of magnitude, for volume fractions of $dN/N \geq 10^{-2}$, seen in the averaged (over the period 350-400 Myr) volume weighted histograms of P_{th} (Fig. 5) is similar for the magnetized and unmagnetized ISM runs, although the power law fits to their profiles have different negative slopes: 2.6 and 1.5, respectively. These results are indicative of the large fluctuations in thermal pressure between different temperature regimes, suggesting that there are no real "phases", i.e., co-existing thermodynamic regimes with different density and temperature but in pressure equilibrium (see also Avillez & Breitschwerdt 2004, 2005; Mac Low et al. 2005).

3.7 Volume Weighted Histograms

A comparison between the averaged (over the time 350 through 400 Myr) volume weighted histograms of the density and temperature of the magnetized and unmagnetized disk gas shows differences that include the (i) decrease/increase by an almost order of magnitude in the histograms density/temperature coverage, (ii) change in the relative weight of the dominant temperature regimes (in the density histograms) and consequently (iii) changes in the pronounced bimodality of the total density and temperature histograms. This latter effect is most noticeable in the temperature PDFs (see Fig. 1). In effect, while the temperature PDF of the HD run has a bimodal structure (as it has two peaks: one at 2000 K and another around 10^6 K), in the MHD run the decrease/increase in importance of the $10^{3.9} < T \leq 10^{4.2}$ K/$10^{4.2} < T \leq 10^{5.5}$ K leads to the reduction/increase of the occupation fraction of these regimes and therefore to a change of the histogram structure appearing it to be unimodal. This variation of the intermediate region appears to be an effect of the presence of the magnetic field, with the smoothing effect being less pronounced for lower field strengths in the disk.

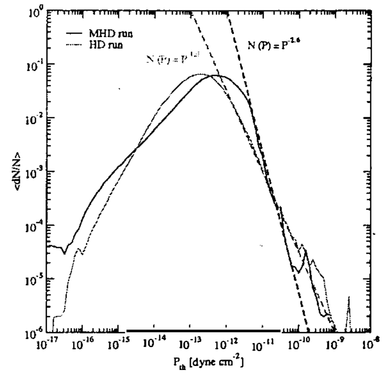

Figure 5: Averaged thermal pressure distribution in the simulated disk ($|z| \leq 250$ pc) for the MHD (black) and HD (red) runs. These pdfs are calculated by using 51 snapshots taken between 350 and 400 Myr with a time interval of 1 Myr. The right side of the histograms is overlayed with a straight dashed line corresponding to power laws with negative slopes 1.5 and 2.6.

3.8 Volume Filling Factors

During most of the history ($t > 100$ Myr) of ISM evolution the occupation (f_V) fractions of the different thermal regimes have an almost constant distribution, varying around their mean values (cf. Table 1; see also Avillez 2000; Avillez & Breitschwerdt 2004, 2005). The thermally stable regimes with $T \leq 200$ K and $10^{3.9} < T \leq 10^{4.2}$ K have similar occupation fractions of $\sim 5\%$ and $\sim 10\%$, respectively, in both runs, while the hot gas has an increase from $\sim 17\%$ in the HD run to $\sim 20\%$ in the MHD case. By far the disk volume is occupied by gas in the thermally unstable regimes at $200 < T \leq 10^{3.9}$ and $10^{4.2} < T \leq 10^{5.5}$ K with similar occupation fractions $\sim 30\%$ in the MHD run, while in the HD run these regimes occupy 46% and 22%, respectively, of the disk volume.

These results indicate that the presence of the magnetic field, which may inhibit the breakout of an individual remnant, but certainly not the high-pressure flow resulting from supernova explosions in concert within an OB association, only leads to a slight increase in the occupation fraction of the hot gas in the disk. The reason is that the volume filling factor of the hot gas increases slightly is because magnetic tension forces help to confine bubbles and Lorentz forces obstruct mixing with cooler gas. It is plausible to assume that, similarly to what seen in HD simulations with different star forming rates, there is a correlation between the filling factor of the hot gas and the rate at which SN occur, since higher rates will produce more hot plasma which, as we have shown here, is not magnetically controlled.

Table 1: Summary of the average values of volume filling factors, mass fractions and root mean square velocities of the disk gas at the different thermal regimes for the HD and MHD runs (from Avillez & Breitschwerdt 2005).

T	$\langle f_V\rangle^a$ [%]		$\langle f_M\rangle^b$ [%]		$\langle v_{rms}\rangle^c$	
[K]	HD	MHD	HD	MHD	HD	MHD
< 200 K	5	6	44.2	39.9	7	10
$200 - 10^{3.9}$	46	29	49.0	43.7	15	15
$10^{3.9} - 10^{4.2}$	10	11	4.4	8.5	25	21
$10^{4.2} - 10^{5.5}$	22	33	2.0	7.4	39	28
$> 10^{5.5}$	17	21	0.3	0.5	70	55

^{a} volume filling factor.

^{b} Mass fraction.

^{c} Root mean square velocity in units of km s^{-1}.

3.9 ISM Mass Fractions and Warm Neutral Medium Mass

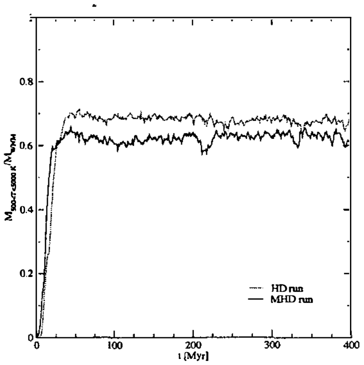

Figure 6: History of the fraction of mass of the WNM gas having $500 < T \leq 5000$ K in the disk for the HD (red) and MHD (black) runs.

Most of the disk mass is found in the $T \leq 10^{3.9}$ K gas, with the cold ($T \leq 200$ K) and thermally unstable gases ($200 < T \leq 10^{3.9}$ K) harbouring on average 80 and $\sim 90\%$ of the disk mass in the MHD and HD runs (Table 1), with the cold regime enclosing $\sim 40\%$ of the disk mass. The remaining ISM mass is distributed between the other temperature regimes with the $10^{3.9} < T \leq 10^{4.2}$ K and $10^{4.2} < T \leq 10^{5.5}$ K regimes enclosing a total of only $\sim 7\%$ and $\sim 16\%$ of mass in the HD and MHD runs, respectively, and the hot gas enclosing $< 1\%$ of the disk mass in both runs. In both runs, 60-70% of the warm neutral mass ($500 < T \leq 8000$ K) is contained in the $500 \leq T \leq 5000$ K temperature range (bottom panel of Fig. 6).

This latter result is strongly supported by interferometric (Kalberla et al. 1985) and optical/UV absorption-line measurements (Spitzer & Fitzpatrick 1995, Fitzpatrick & Spitzer 1997), which indicate that a large fraction ($\sim 63\%$) of the warm neutral medium (WNM) is in the unstable range $500 < T < 5000$ K. Moreover 21 cm line observations (Heiles 2001; Heiles & Troland 2003) provide a lower limit of 48% for the WNM gas in this unstable regime. Direct numerical simulations of the nonlinear development of the thermal instability under ISM conditions with radiative cooling and background heating discussed in Gazol et al. (2001) and Kritsuk & Norman (2002) show that about 60% of the system mass is in the thermally unstable regime. However, it is unclear from their simulations what the time evolution of this mass fraction (which is shown in the figure for $t > 100$ Myr) is and what explicitly the origin of the unstable gas is. These authors suggest that ensuing turbulence is capable of replenishing gas in the thermally unstable regime by constantly stirring up the ISM. We have carried out detailed numerical studies of the stability of the ISM gas phases (Avillez & Breitschwerdt 2005a), and verified the hypothesis that SN driven turbulence is capable of replenishing fast cooling gas in classically unstable regimes. In effect, turbulence as a diffusion process can prevent thermal runaway on small scales. That is, turbulence has a stabilizing effect thereby inhibiting local condensation modes.The turbulent viscosity $\nu_{\rm turb} \sim Re\,\nu_{\rm mol}$ can be orders of magnitude above the molecular viscosity, with Re being the Reynolds number of the flow. What happens physically then, is that with increasing eddy wavenumber $k = 2\pi/\lambda$, the eddy crossing time $\tau_{\rm eddy} \sim \lambda/\Delta u$ (with Δu being the turbulent velocity fluctuation amplitude) becomes shorter than the cooling time $\tau_{\rm cool} \sim 3k_BT/(n\Lambda(T))$, where $\Lambda(T)$ is the interstellar cooling function. Although not strictly applicable here, it is instructive to see that in case of incompressible turbulence following a Kolmogoroff scaling law, where the energy dissipation rate is given by $\varepsilon \sim \rho\Delta u^3/\lambda$, we obtain a lower cut-off in wavelength, where thermal instability becomes inhibited, if

$$\begin{aligned} \lambda &< \left(\frac{3k_B\bar{m}}{\Lambda_0}\right)^{3/2} \varepsilon^{1/2}\,\frac{T^{3/4}}{\rho^2} \\ &\approx 1.4210^{19}\,\mathrm{cm}\,, \end{aligned} \tag{1}$$

taking $\varepsilon \sim 10^{-26}\,\mathrm{erg\,cm^{-3}\,s^{-1}}$ for SN energy injection; a simple cooling law for the warm neutral medium of $\Lambda(T) = \Lambda_0 T^{1/2}$ has been adopted, with $\Lambda_0 \approx 1.9 \times 10^{-27}\,\mathrm{erg\,cm^3\,s^{-1}\,K^{-1/2}}$ (taken from the cooling curve of Dalgarno & McCray 1972) for a WNM of a density of $n = 0.3\,\mathrm{cm}^{-3}$, a temperature of $T = 1000$ K, and a low degree of ionization $x \approx 0.01$. Therefore rough numerical estimates are typically of the order of parsecs, consistent with our numerical resolution. In fact, the critical wavelength λ varies with temperature, degree of ionization and hence cooling; for the WNM we find quite a large range of values from $10^{17} - 10^{20}$ cm, according to Eq. (1).

3.10 Turbulent Velocities

The root mean square velocity, $\mathrm{V_{rms}}$, which is a measure of the disordered motion of the gas, increases with temperature (see Table 1) in the MHD and HD runs. The average rms velocity ($\langle \mathrm{V_{rms}} \rangle$) in the last 100 Myr of evolution has large fluctuations in the different thermal regimes in the HD run, which are reduced due to the presence of the magnetic field. These velocities agree remarkably well with the observed rms velocities discussed by Kulkarni & Fich (1985). The near constancy of the rms velocity with time indicates the presence of a dynamical equilibrium, with random motions, i.e. thermal and turbulent pressures adding to the total pressures, provided that the energy injection rate remains constant on a global scale.

4 Testing the Model

Although the above mentioned results are in good agreement with present day observations of the ISM and other numerical experiments, though these have more a local character, one can trace the quality of the present model by applying it to the dynamics and evolution of the Local Bubble, powered by the explosions of 19 SNe in the last 14 Myr (Berghöfer & Breitschwerdt 2002; Fuchs et al. 2005), and trace its OVI content that has been observed using Copernicus and FUSE. While standard Local Bubble (LB) models fail to reproduce the observed low OVI absorption column density (Shelton & Cox 1994; for a recent discussion see Breitschwerdt & Cox 2004), the present model when applied to the study of the dynamics and evolution of the Local and Loop I bubbles predicts column densities $< 1.7 \times 10^{13}$ cm^{-2} towards Loop I with a mean value of $\leq 8.5 \times 10^{12}$ cm^{-2} (for details see Breitschwerdt et al. these proceedings) in agreement with the mean column density of 7×10^{12} cm^{-2} inferred from analysis of FUSE absorption line data in the Local ISM (Oegerle et al. 2004).

5 Final Remarks

The present simulations still neglect an important component of the ISM, i.e., high energy particles, which are known to be in rough energy equipartition *locally* with the magnetic field, the thermal and the turbulent gas in the ISM. The presence of CRs and magnetic fields in galactic halos is well known and documented by many observations of synchrotron radiation generated by the electron component. The fraction of cosmic rays that dominates their total energy is of Galactic origin and can be generated in SN remnants via the diffusive shock acceleration mechanism to energies up to 10^{15} eV (for original papers see Krymski et al. 1977, Axford et al. 1977, Bell 1978, Blandford & Ostriker 1978, for a review Drury 1983, for more recent calculations see Berezhko 1996). The propagation of these particles generates MHD waves due to the streaming instability (e.g. Kulsrud & Pearce 1969) and thereby enhances the turbulence in the ISM. In addition, self-excited MHD waves will lead to a dynamical coupling between the cosmic rays and the outflowing fountain gas, which will enable part of it to leave the galaxy as a galactic wind (Breitschwerdt et al. 1991, 1993, Dorfi & Breitschwerdt 2005). Furthermore, as the cosmic rays act as a weightless fluid, not subject to radiative cooling, they can bulge out magnetic field lines through buoyancy forces. Such an inflation of the field will inevitably lead to a Parker type instability, and once it becomes nonlinear, it will break up the field into a substantial component parallel to the flow (Kamaya et al. 1996), thus facilitating gas outflow into the halo. We are currently performing ISM simulations including the CR component.

In the dynamical picture of the ISM emerging from our simulations, thermal pressure gradients dominate mainly in the neighbourhood of SNe. These events drive motions whose ram pressures overwhelm the mean thermal pressure (away from the energy sources) and the magnetic pressure by a large factor. The magnetic field is dynamically important at low temperatures, apart from also weakening gas compression in MHD shocks and thereby lowering the energy dissipation rate. The thermal pressure of the freshly shock heated gas exceeds the magnetic pressure by usually more than an order of magnitude and the B-field can therefore not prevent the flow from rising perpendicular to the galactic plane. Thus hot gas is fed into the galactic fountain at almost a similar rate than without field (Avillez & Breitschwerdt 2004, 2005).

However, the circulation of gas between the disk and halo is a dynamic process, which involves a flow time scale, that can be much shorter than any of the microphysical time scales due to ionization and recombination. The gas escaping into the halo has an initial temperature well in excess of 10^6 K, where the assumption of collisional ionization equilibrium (CIE) is approximately valid. This means that the rate of ionizations per unit volume through collisions between ions and electrons equals the rate of recombinations per unit volume. As the hot plasma expands away from the disk it will cool adiabatically thereby reducing its temperature and density. It has been shown (Breitschwerdt & Schmutzler 1999) that recombination of highly ionised species lags behind and occurs mainly at considerable heights from the disk. In the case of the X-ray halo of NGC 3029, spectral fitting has shown that an outflow model based on non-equilibrium ionization (NEI) effects gives an excellent agreement with observations (see Breitschwerdt 2003).

Acknowledgments

MA would like to thank the SOC and Thierry Montmerle and Almas Chalabaev for the invitation and financial help to attend this excellent conference.

References

1. Avillez, M. A. 2000, MNRAS, 315, 479

2. Avillez, M. A., & Mac Low, M.-M. 2002, ApJ, 581, 1047
3. Avillez, M. A., & Breitschwerdt, D. 2004, A&A, 425, 899
4. Avillez, M. A., & Breitschwerdt, D. 2005a, A&A, in press
5. Avillez, M. A., & Breitschwerdt, D. 2005b, ApJ, in preparation
6. Axford, W.I., Leer, E., & Skadron, G. 1977, in Proc. 15th Int. Cosmic Ray Conf. (Plodiv) 11, 132
7. Bell, A. R. 1978, MNRAS, 182, 147
8. Berezhko, E. G. 1996, APh 5, 367
9. Berghöfer, T., & Breitschwerdt, D. 2002, A&A, 390, 299
10. Blandford, R. D., & Ostriker, J. P. 1978, ApJ, 221, 29
11. Breitschwerdt, D., McKenzie, J.F., & Völk, H.J. 1991, A&A 245, 79
12. Breitschwerdt, D., McKenzie, J.F., & Völk, H.J. 1993, A&A 269, 54
13. Breitschwerdt D.,& Schmutzler T. 1999, A&A, 347, 650
14. Breitschwerdt D. 2003, RMxAA (Serie de Conferencias), 15, 311
15. Breitschwerdt, D., & Cox, D. P. 2004, in "How does the Galaxy Work?", eds. E. Alfaro, E. Perez, & J. Franco, Kluwer (Dordrecht), p. 391
16. Chandrasekhar, S., & Fermi, E. 1953, ApJ, 118, 113
17. Cox, D. P., & Smith, B. W. 1974, ApJ, 189, L105
18. Cox, D. P. 2004, in "From Observations to Self-consistent Modelling of the ISM in Galaxies", eds. M. A. de Avillez, & D. Breitschwerdt, Kluwer (Dordrecht), p.
19. Dalgarno, A., & McCray, R. A. 1972, ARA&A, 10, 375
20. Dickey, J. M., & Lockman, F. J. 1990, ARA&A, 28, 215
21. Dorfi, E.A., Breitschwerdt, D. 2005, A&A (in preparation)
22. Drury, L. O'C. 1983, Rep. Prog. Phys. 46, 973
23. Field, G. B. 1965, ApJ, 142, 531
24. Field, G. B., Goldsmith, D. W., & Habing, H. J. 1969, ApJ, 155, L149
25. Fitzpatrick, E. L., & Spitzer, L. 1997, ApJ, 475, 623
26. Fuchs, B., Breitschwerdt, d., Dettbarn, C., & Flynn, C. 2005, MNRAS, in preparation
27. Gazol, A., Vázquez-Semadeni, E., Sanchez-Salcedo, J., & Scalo, J. 2001, ApJ, 557, 121
28. Heiles, C. 2001, ApJ, 551, L105
29. Heiles, C., & Troland, T. H. 2003, ApJ, 586, 1067
30. Kalberla, P. M. W., Schwarz, U. J., & Goss, W. M. 1985, A&A, 144, 27
31. Kamaya, H., Mineshige, S., Shibata, K., & Matsumoto, R. 1996, ApJ, 458, L25
32. Kahn, F. D. 1981, in "Investigating the Universe", ed. F.D. Kahn, Reidel (Dordrecht), p. 1.
33. Kritsuk, A., & Norman, M. L. 2002, ApJ, 580, L51
34. Krymsky, G. F. 1977, Dokl. Nauk. SSR 234, 1306, (Engl. trans. Sov. Phys. Dokl. 23, 327)
35. Kulsrud, R. M., & Pearce, W. D. 1969, ApJ, 156, 445
36. Mac Low, M.-M., Balsara, D., Kim, J., & Avillez, M. A. 2004, ApJ, in revision [astro-ph/0410734]
37. McKee, C. F., Ostriker, J. P. 1977, ApJ 218, 148
38. Oegerle, W. R., E. B. Jenkins, E. B., Shelton, R. L., Bowen, D. V., & Chayer, P. 2005, ApJ, Submitted [astro-ph/0411065]
39. Passot, T., Vázquez-Semadeni, E. 2003, A&A, 398, 845
40. Reynolds R. J. 1987, ApJ, 323, 118
41. Rosen A., & Bregman, J. N. 1995, ApJ, 440, 634
42. Shelton, R., & Cox, D. P. 1994, ApJ, 434, 599
43. Spitzer, L., & Fitzpatrick, E. L., 1995, 445, 196

A fine sense of Equilibrium

FEEDBACK AND THE INITIAL MASS FUNCTION

Joseph Silk
Astrophysics, Department of Physics, University of Oxford
Oxford OX1 3RH UK

I describe a turbulence-inspired model for the stellar initial mass function which includes feedback and self-regulation via protostellar outflows. A new aspect of the model provides predictions of the star formation rate in molecular clouds and gas complexes. A similar approach is discussed for self-regulation on kiloparsec scales via supernova input, and an expression is presented for the global star formation rate that depends on the turbulent pressure of the interstellar medium.

Keywords: star formation-galaxies-turbulence

Introduction

The turbulence paradigm seems to be increasingly accepted in star formation theory. The dissipation time of the observed supersonic turbulence especially in giant molecular clouds (GMCs) is less than the cloud lifetime, demonstrating that cloud support is by turbulent pressure. Implications include the consequences that molecular clouds on all scales are short-lived and hence that large-scale star formation is relatively inefficient. This corresponds to what is observed: about 0.1-1 percent of a GMC is in stars, and the dynamical time-scale of a GMC is $10^6 - 10^7$ yr, giving consistency with the global star formation rate of the Milky Way galaxy, that requires about 10 percent efficiency of conversion of gas to stars over a galactic rotation time. On small scales, such as cloud cores, supersonic turbulence is still present, although less dominant, and one generally observes a much higher efficiency of star formation. The efficiency for star clusters embedded in molecular clouds, which have ages less than 5×10^6 yr, is 10-30 % (Lada and Lada 2003). Presumably an important difference is that self-gravity plays a prominent role on these scales. The turbulence drivers are not well understood. Possible sources include external drivers (galactic rotation, Parker instability, OB wind/SN-driven super-bubbles) as well as internal sources (protostellar jets and outflows, gravitational collapse), and the turbulence is likely to be multi-scale, controlled both by cascades and inverse cascades.

I will focus here mostly on protostellar outflows on small scales, although I will also discuss supernova input on larger scales, as sources of interstellar turbulence. The aim will be to demonstrate that outflow-generated turbulence allows self-regulation of star formation via control of the accretion rate. A GMC is viewed as a network of overlapping, interacting protostellar-driven outflows. This leads to simple derivations of the IMF and of the star formation rate.

Similar ideas are implicit in models of competitive accretion by turbulent fragments (Bonnell, Vine and Bate 2004). The idea of a network of interacting wind-driven shells is a manifestation of the fragmentation models developed by Klessen and collaborators, in which colliding, supersonic flows shock, dissipate and produce dense gravitationally unstable cores (Klessen, Heitsch and MacLow 2000; Burkert 2003).

1 Observational issues

Substantial churning of molecular clouds by protostellar outflows is a common phenomenon. Observations of some cloud complexes such as Circinus, Orion and NGC 1333 support the idea that protostellar outflows drive the observed turbulence (Yu, Bally and Devine 1997; Bally et al. 1999; Bally and Reipurth 2001; Sandell and Knee 2001). Quantitatively, such flows seem to be an important source of turbulence. One may estimate the outflow strength as (e.g., Konigl 2003)

$$\dot{M}_{wind} \sim (r_d/r_A)^2 \dot{M}_{acc} \sim 0.1 \dot{M}_{acc} \sim 0.1 v_{amb}^3/G,$$

where the wind velocity is of order 100 km/s, and $v_{amb} \sim 0.3 - 3\mathrm{km\,s^{-1}}$. In general, one expects that $v_{wind} >> v_{amb}$. Moreover, outflow momenta accumulate since typical outflow durations are $t_{wind} \sim 10^5$yr, so that the cloud lifetime $t_{dyn} >> t_{wind}$. Hence one wind outflow event per forming star ejecting 10 percent of its mass can, on the average, balance the accretion momentum in a typical cloud core that forms stars at $\sim$ 10% efficiency.

An important issue is the extent to which the outflows are localised. Observed jets suggest that some outflows deposit energy far from the dense cores, but this inference cannot easily be generalised since it is likely to be highly biased by extinction. Jets may be ubiquitous, but could still be unstable enough to drive bipolar outflows and mostly deposit their energy in and near dense cores. Protostellar outflows are a possible source of the observed molecular cloud turbulence, and the only one that is actually observed in situ. The relevant driving scales cover a wide range, and may well yield the observed, apparently scale-free cloud turbulence.

The projected density profiles of some dense cores are well fit by a pressure-confined self-gravitating isothermal sphere (Alves, Lada and Lada 2002). Others require supercritical cores undergoing subsonic collapse (Harvey et al. 2003). Magnetic support offers one explanation of the initial conditions, with magnetically supercritical cores surrounded by subcritical envelopes. However the core profiles can also, more debatably, be reproduced as supersonic turbulence-compressed eddies (Ballesteros-Paredes, Klessen and Vazquez-Semadini 2003).

2 IMF Theory

There are many explanations that yield a power-law IMF, $mdN/dm = Am^{-x}$, with $x \approx 4/3$, the Salpeter value. However it is harder to account for the interesting physics embedded in $A(p, t...)$, which determines the star formation rate and efficiency. It is likely that molecular clouds are controlled by feedback. Protostellar outflows feed the turbulence which controls ambient pressure, which in turn regulates core formation. Pressure support includes magnetic fields. There are different views about the details of self-regulation, depending on the relative roles of magnetic and gravitational support versus turbulent compression. Collapse of the supercritical cores into protostellar disks might drive outflows that levitate the envelopes, thereby limiting core masses (Shu et al 2003). Ambipolar diffusion and magnetic reconnection would be controlled by the turbulence, thereby setting the mass scale of cores (Basu & Ciolek 2004). The outflows should cumulatively set the ambient pressure that in turn controls both core masses and the accretion rate at which cores can grow (Silk 1995).

Consider a simple model for a spherically symmetric outflow into a uniform medium that drives a shock-compressed shell until either the shell encounters another expanding shell or until pressure balance with the ambient medium is achieved. At this point, the shell breaks up into blobs confined by ram or by turbulent pressure, with the relevent turbulent velocity being that of the shell at break-up.

Now the shell radius is $R = \left(\dot{M}_{wind}v_w/\rho_a\right)^{1/4} t^{1/2} \Rightarrow R \propto v^{-1}, \quad t \propto v^{-2}$. Here $v = dR/dt$ is the shell velocity. The protostellar outflows generate a network of interacting shells that form clumps with a velocity distribution:

$$N(> v) = 4\pi R^3 t \dot{N}_* = \left(\dot{M}_{wind}v_w/\rho_a\right)^2 v^{-5}\dot{N}_*.$$

To convert to a mass function, I combine this expression for the velocity distribution of clumps with the relation between mass m and turbulent velocity (identified with v) for a clump: $m = v^3G^{-3/2}(v/B)$ for magnetically supercritical cores or $m = v^3G^{-3/2}(vp^{-1/2})$ for gravitationally supercritical Bonnor-Ebert cores. Now B scaling suggests $B \overset{\propto}{\sim} v \Rightarrow \epsilon = 3$ (c.f. Shu et al. 2003). Alternatively, scaling from Larson's laws yields $\rightarrow \rho \overset{\propto}{\sim} v^{-2} \Rightarrow \epsilon = 4$. If I instead generalise the wind-driven, approximately momentum-conserving, shell evolution to $R \propto t^\delta$, the IMF can now be written in the form $\rightarrow mdN/dm \propto m^{-x}$ with $x = \frac{3\delta+1}{\epsilon(1-\delta)}$ where $R \propto t^\delta$ and $m \propto v^\epsilon$. One finally obtains the following values for x: $x = 5/3$ if $\delta = 1/2$; $x = 4/3$ if $\delta = 3/7$ $(\epsilon = 3)$, and $x = 5/4$ if $\delta = 1/2$; $x = 4/3$ if $\delta = 13/25$ $(\epsilon = 4)$. There seems to be little difficulty in obtaining a Salpeter-like IMF.

However in practice, the IMF is not a simple power-law in mass. It may be described by a combination of three different power-laws: $x = -2/3$ over 0.01 to 0.1 $M_\odot$; $x = 1/3$ over 0.1 to 1 $M_\odot$; $x = 4/3$ over 1 to 100 $M_\odot$ (Kroupa 2002). A scale of around 0.3 $M_\odot$ must therefore be built into the theory. One clue may come from the fact that the observed IMF is similar to the mass function of dense clumps in cold clouds, at least on scales above $\sim 0.3M_\odot$ (Motte et al. 2001).

3 Feedback

I now describe an approach that yields the normalisation of the IMF, and in particular its time-dependence. The idea is that the network of interacting shells must self-regulate, in that star formation provides both the source of momentum that drives the shells, and is itself controlled by the cumulative pressure that enhances clump collapse. I introduce porosity as the parameter that controls self-regulation, via the overlap of outflows. I define porosity as $Q = 4\pi R_{max}^3 \dot{N}_* t_{max}$. Now for self-regulation, I expect that $Q \sim 1$. One may rewrite the IMF as

$$mdN/dm = Q(m_a/m)^x$$

where $m_a = v_a^3 G^{-3/2}(v_a/B_a)$ or $m_a = v_a^4 G^{-3/2} p_a^{-1/2}$. Now with $Q \sim 1$, one can expect self-regulation. However in addition, one must require self-gravity to avoid clump disruption. This allows the possibility of either negative or positive feedback.

The predicted IMF is $mdN/dm = Am^{-x}$. The preceding argument yields A. More generally with regard to x, if $R_{wind} \propto t^\delta$ and $m_{clump} \propto v^3$, we obtain $\delta = 2/5, 3/7, 1/2 \rightarrow x = 2/3, 4/3, 5/3$. The principal new result is the self-regulation ansatz that yields A. We infer that $A \propto Q$ where porosity Q can be written as $f_{\text{low density phase}} = 1 - e^{-Q}$. The IMF slope is in accordance with observations for plausible choices of parameters. Of course numerical simulations in 3-D are needed to make a more definitive calculation of the IMF in the context of the present model.

Nevertheless, there is one encouraging outcome. Turbulent feedback seems to be significant for stars of mass $\gtrsim 0.3M_\odot$. This is an observed fact, and is attributed to detailed models that generally invoke magnetically-driven accretion disk outflows and jets. Of course even sub-stellar objects display outflows but the outflow rates are dynamically unimportant for the parent cloud (e.g., Barrado et al. 2004). Such a hypothesis could help explain why a feedback explanation of the IMF naturally selects a characteristic mass of $\sim 0.3M_\odot$. As the stellar mass increases, negative feedback mediates the numbers of more massive clumps and stars. The numbers of increasingly massive stars fall off according to the power-law derived here.

4 Summary of IMF results

There are 3 crucial components to star formation phenomenology. These are the initial stellar mass function or IMF, the star formation efficiency or SFE, and the star formation rate or SFR. The outflow-driven turbulence model predicts these quantities, provided we can identify the mass of a star with $m = \mu v^3 G^{-3/2} \rho^{-1/2}$, where $\mu = p^{1/2}/B$ or 1, for either magnetically or pressure-supported clouds. One then finds that, above the feedback scale, the IMF is

$$mdN/dm \propto Q(v_a/v)^5 = f\mu\rho_a Q {m_a}^{2/3} m^{-5/3}.$$

Here f is a constant of order unity.

The SFR is

$$\dot{n}_* = \frac{Q}{R_a^3 t_a} = Q v_a^{\frac{3\delta+1}{1-\delta}} \left(\frac{\rho_a}{\dot{M}_{wind} v_w}\right)^{\frac{1}{1-\delta}} \propto \frac{Q\rho_a^2}{v_a}.$$

In the final expression, I set $\delta = 1/2$ and $\dot{M}_{wind} = 0.1 v_a^3/G$. The SFR $\overset{\propto}{\sim} \rho_a^2$. This means that the SFR accelerates as the cloud evolves and contracts. The enhanced dissipation from outflows most likely results in the increase of turbulent density in the cloud, at least until sufficiently massive stars form whose energetic ouflows, winds and eventual explosions blow the cloud apart. Evidence for accelerating star formation in many nearby star-forming regions, based on pre-main-sequence evolutionary tracks, is presented by Palla and Stahler (2000). This suggests that a ministarburst is a common phenomenon.

The SFE is

$$\frac{m^*_{char}\dot{n}_* t_{dyn}}{\rho_a} \sim \frac{m^*_{char}\dot{n}_*}{G^{1/2}\rho_a^{3/2}} \propto \frac{Q\rho_a^{1/2}}{v_a}.$$

This scaling gives an SFE that is $\sim 10 - 100$ times larger in cores than in a GMC, more or less as is observed.

There are a number of unresolved issues. The scale-free nature of the observed turbulence in molecular clouds is suggestive of a cascade. Normally these proceed from large to small scales. With internal protostellar sources, an inverse cascade must be invoked, such as could arise via injection of turbulence associated with jet-driven helical magnetic fields. Alternatively, the wide range of jet and outflow scales suggests that the driving scale may largely be erased.

Efficient thermal accretion onto low protostellar mass cores coupled with protostellar outflows and turbulent fragmentation, for which $M_J^{turb} \sim \mathcal{M}^2 M_J^{therm}$ (Padoan and Nordlund 2002), will help to imprint the characteristic stellar mass scale. This suggests that magnetic fields, insofar as they regulate and drive outflows, are likely to play an important role in setting the characteristic stellar mass scale. Moreover, regions of enhanced turbulence, such as would be associated with star formation induced by merging galaxies, could plausibly have a increased feedback scale and hence a top-heavy IMF.

5 A theory for kiloparsec-scale outflows

I now show that a porosity formulation of outflows can also lead to a large-scale burst of star formation. Rather than consider molecular cloud regions, where the physics is more complex, I discuss a more global environment where the physics can be simplified but the essential ingredient of interacting outflows remains. Consider a larger-scale version of self-regulated feedback. I model a cubic kiloparsec of the interstellar medium, which contains atomic and molecular gas clouds and ongoing star formation. I assume that the dominant energy and momentum to the multiphase interstellar medium is via supernovae. One expects self-regulation to lead to a situation in which the porosity $Q \sim 1$. The porosity is initially small, but increases as outflows and bubbles develop. If it is too large, I argue that molecular clouds are disrupted and the galaxy blows much of the gas out of the disk, e.g. via fountains into the halo. Star formation is quenched until the gas cools and resupplies the cold gas reservoir in the disk. Whether the gas leaves in a wind is not clear; this may occur for dwarf galaxy starbursts, but cannot happen for Milky-Way type galaxies as long as the supernova rates are those assumed to apply in the recent past. I further speculate that the feedback is initially positive, in a normal galaxy. The outflows drive up the pressure of the ambient gas which enhances the star formation rate by accelerating collapse of molecular clouds. The feedback eventually is negative in dwarf galaxies, once a wind develops. In more massive galaxies, the ensuing starburst is only limited by the gas supply.

To develop a simple model, I make the following ansatz. The porosity may be defined by

$$Q \sim (SN\, bubble\, rate) \times (maximum\, bubble\, 4\text{-}volume)$$
$$\propto (star\ formation\ rate) \times \left(turbulent\ pressure^{-1.4}\right).$$

Expansion of a supernova remnant is limited by the ambient pressure, when it can be described as a radiation pressure-driven snowplow with $R_a^3 t_a \propto p_{turb}^{1.4}$ (Cioffi et al. 1988). Hence the star formation rate may be taken to be $\propto Q p_{turb}^{1.4}$, and by introducing a new parameter ϵ may also be written as $\epsilon \times$ *rotation rate* $\times$ *gas density*. What is in effect the global star formation efficiency is now given by $\epsilon \equiv \left(\frac{\sigma_{gas}}{\sigma_f}\right)^{2.7}$, where $\sigma_f \approx 20\mathrm{kms}^{-1}\left(\mathrm{E_{SN}}/10^{51}\right)^{1.27}(200\mathrm{M_\odot}/\mathrm{m_{SN}})$. We expect positive feedback at high gas turbulent velocities. High resolution numerical simulations of a multiphase medium demonstrate that a starburst is generated, and that the porosity formalism describes the star formation rate (Slyz et al. 2004). The porosity formulation yields a star formation rate that gives a remarkably good fit to the numerical results. The positive feedback arises from the implementation of the derived star formation law with star formation rate proportional to turbulent gas pressure. Pressure enhancements are mostly due to shocked gas. It is interesting to note that a star formation law which favours shock dissipation can more readily account for the spatial extent of star formation as modelled for interacting galaxies (Barnes 2004) than can an expression in which the star formation rate is only a function of gas density (as in the Schmidt-Kennicutt law).

Porosity may therefore regulate star formation, on the physical grounds that porosity can be neither too large nor too small. If it is too small, the rate of massive star formation (and death) accelerates until the porosity increases. If the porosity is too large the cloud is blown apart via a wind and loses its gas reservoir. To make the concept of a porosity-driven wind more precise, I write the disk outflow rate as the product of the star formation rate, the hot gas volume filling factor, and the cold gas mass loading factor. If the hot gas filling factor $1 - e^{-Q}$ (Q is porosity) is of order 50%, then this suggests that the outflow rate is of order the star formation rate. I emphasize that such a result is plausible but only qualitative: it has yet to be numerically simulated in a sufficiently large box.

One infers that the metal-enriched mass ejected in a wind is generically of order the mass in stars formed. This is similar to what is observed for nearby starbursting dwarf galaxies (e.g. NGC 1569: Martin, Kobulnicky and Heckman 2002). Observations suggest that massive galaxies should have had massive winds in the past, in order both to account for the observed baryonic mass and the galaxy luminosity function (Benson et al. 2003), although theory has difficulty in rising to this challenge. It is clear that, energetically, with conventional supernova rates, one cannot drive winds from massive or even Milky Way-like galaxies (Springel and Hernquist 2003). The situation is very different for dwarfs, where supernova input suffices to drive vigorous winds, although even in these cases geometric considerations are important (MacLow and Ferrara 1999).

Simulations in a multiphase medium currently lack sufficient resolution to adequately treat such instabilities as Rayleigh-Taylor and Kelvin-Helmholtz, that will respectively enhance the porosity and the wind loading. The highest resolution simulations to date (Slyz et al. 2004) of a multiphase medium already show that SN energy input efficiency is considerably underestimated by failure to have adequate resolution to track the motions of OB stars from their birth sites in dense clouds before they explode.

It is likely therefore that feedback may occur considerably beyond the scales hitherto estimated (Dekel and Silk 1986), possibly extending to the galactic (stellar) mass scale of about $3 \times 10^{10} M_\odot$, only above which the star formation efficiency is inferred to be approximately constant (Kauffmann et al. 2003).

Whether even more refined and detailed hydrodynamical simulations can be consistent with the requirement of substantial early gas loss from massive galaxies is uncertain (Silk 2003). One simply lacks the energy input. Instead, recourse must be made either to an early top-heavy IMF or outflows from a quasar phase that coincided with the epoch of bulge formation, A top-heavy IMF is motivated by the earlier derivation of an IMF driven by turbulent feedback. The case for an early quasar phase during galaxy bulge formation is motivated by the empirical bulge-supermassive black hole correlation, high quasar metallicities and SMBH growth times (Dietrich and Hamann 2004). Yet another option is an enhanced early rate of hypernovae in starbursts, as suggested by the interpretation of the peculiar abundances found in the starburst galaxy M82 (Umeda et al. 2002).

While all of these enhanced sources of energy and momentum are likely to play some role in forming galaxies, it is intriguing to note that early reionisation, in concordance with requirements from CMB measurements by the WMAP satellite, can also be accomplished by the first of these hypotheses which can simultaneously account for chemical evolution of the metal-poor IGM and the abundance ratios observed in extreme metal-poor halo stars (Daigne et al. 2004). Moreover, a top-heavy IMF, if identified with luminous starbursts, can also account for the faint sub-millimetre galaxy counts (Baugh et al. 2004) and the chemical abundances in the enriched intracluster medium (Nagashima et al. 2004).

References

1. Alves, J., Lada, C. and Lada, E. 2001, Nature, 409, 159
2. Ballesteros-Paredes, J. Klessen, R. and Vazquez-Semadini, E. 2003, ApJ, 592, 188
3. Bally, J. et al. 1999, AJ, 117, 410
4. Bally, J. and Reipurth, B. 2001, ApJ, 546, 299
5. Barnes, J. 2004, MNRAS, 350, 798
6. Barrado y Navascus, D., Mohanty, S. and Jayawardhana, R. 2004, ApJ, 604, 284
7. Basu, S. and Ciolek, G. 2004, ApJ, 607, L39
8. Baugh, C. et al. 2004, astro-ph/0406069
9. Benson, A. et al. 2003, ApJ, 599, 38
10. Bonnell, I., Vine, S. and Bate, M. 2004, MNRAS, 349, 735
11. Burkert, A. 2003, astro-ph/0404015
12. Cioffi, D., McKee, C. and Bertschinger, E. 1988, ApJ, 334, 252
13. Daigne, F. et al. 2004, A&A, submitted
14. Dekel, A. & Silk, J. 1986, ApJ, 303, 39
15. Dietrich, M. and Hamann, F. 2004, ApJ, 611, 761
16. Harvey, D. et al. 2003, ApJ, 598,1112
17. Kauffmann, G. et al. 2003, MNRAS, 341, 54
18. Klessen, R., Heitsch, F. and MacLow, M. 2000, ApJ, 535, 887.
19. Konigl, A. 2003, astro-ph/0312287
20. Kroupa, P. 2002, Science, 295, 82
21. Lada, C. and Lada, E. 2003, ARA&A, 41, 57
22. Martin, C., Kobulnicky, H. and Heckman, T. 2002, ApJ, 574, 663
23. MacLow, M. and Ferrara, A. 1999, ApJ, 513, 142

24. Motte, F. et al. 2001, A&A, 372L, 41
25. Nagashima, M. et al. 2004, astro-ph/0408529
26. Palla, F. and and Stahler, S. 2000, ApJ, 540, 255.
27. Padoan, P. and Nordlund, A. 2002, ApJ, 576, 870
28. Sandell, G. and Knee, L. 2001, ApJ, 546, L49
29. Shu, F. et al 2003, astro-ph/0311426
30. Silk,J. 1995, ApJ, 438, L41
31. Silk,J. 2003, MNRAS, 343, 249
32. Slyz, A. et al. 2004, MNRAS, submitted.
33. Springel, V. and Hernquist, L. 2003, MNRAS, 339, 289
34. Umeda, H. et al. 2002, ApJ, 578, 855
35. Yu, K., Bally, J. and Devine, D. 1997, ApJ, 485, L45
36. Yu, K. et al. 2000, AJ, 120, 1974

Classes

The Gould Belt, star formation, and the local interstellar medium

Isabelle A. Grenier

AIM, Service d'Astrophysique, CEA Saclay, 91191 Gif/Yvette, France

The history of the local medium, within a few hundred parsecs, is dominated by the evolution of the Gould Belt. The event that triggered this star-forming region and molded the gas distribution is still unknown. Its orientation and extent are reasonably well determined and its expansion matches the space and velocity distributions of many large HI and H_2 clouds within half a kiloparsec. The present rim coincides with most of the nearby OB associations, but their mean velocity does not seem to be related to the Belt expansion. The Belt age is uncertain by a factor of 2 because of the discrepancy found between the dynamical timescale (20 to 30 Myr) and the stellar ages (30 to 60 Myr). The stellar content is derived from kinematic studies for massive stars and from X-ray observations for young solar-mass ones. Whether star formation is active along the rim or spread over a larger fraction of the disc is debated. The Belt flatness and its tilt remain very difficult to interpret. Various scenarii involve the impact of a high-velocity cloud, a cascade of supernovae, the dissolution of a rotating system, or the braking of a supercloud entering the spiral arm. Because of the enhanced star formation, the Belt supernova rate over the past few million years has been 3 to 4 times larger than the local Galactic rate. The corresponding pulsars may be responsible for the population of unknown γ-ray sources associated with the Belt. The higher rate also implies an enhanced cosmic-ray production locally.

Keywords: Galaxy: solar neighbourhood, stars: early-type, stars: supernovae, stars: pulsars, ISM: kinematics and dynamics, Gamma rays: observations

1 The Belt geometry

Many stars have formed locally over the past few 10^7 years in a surprisingly flat and inclined disc named the Gould Belt. The Sun happens to be crossing this structure. The asymmetry about the Galactic plane of the the bright-star distribution was first pointed out by Sir John Herschel [26] in 1847 and studied in 1874 by Benjamin A. Gould[20] who determined the Belt orientation with respect to the Galactic plane. From the decomposition of the spatial distributions of the two intersecting discs in the *Hipparcos* data[43], Torra et al. found that 60 to 66% of the massive stars with ages < 60 Myr and distances < 600 pc belong to the Belt. This fraction significantly decreases to 42-44% for ages between 60 and 90 Myr. In terms of spectral types, 44% and 36% of the O-B2.5 and O-B9.5 stars within 1 kpc are respectively linked to the Belt [6].

Significant changes in the Oort constants with stellar age within 600 pc reflect the Belt kinematical influence. A nearly pure differential Galactic rotation is found for the old stars (> 90 Myr) whereas the younger ones exhibit a marked decrease in A and a large negative B value that suggests that the whole system is rotating[29,43]. A positive K term, indicative of expansion, is measured for stars younger than 30 Myr. These peculiarities remain after removing the Sco-Cen and Ori OB1 associations from the sample, so stars outside these famous clusters along the Belt rim participate to the unusual kinematics. The true velocity field may, however, be more complex than the Oort constants would suggest. There is a systematic gradient in the vertical velocities of the young stars along the Galactic plane [8] and the ascending node longitude for vertical oscillation is $337° \pm 20°$ instead of $296° \pm 2°$ for the Belt orientation [35].

Whereas the massive-star content has been extensively studied, less is known about the low-mass star production. Young (30–80 Myr old) Lithium-rich solar-mass stars show up as X-ray sources because of their active coronae. Even though the X-ray horizon is limited by interstellar absorption to 150-300 pc for sources with luminosities of $(0.3 - 3)10^{23}$ W typical of young late-type stars, such stellar sources in the ROSAT All-Sky Survey nicely trace the Belt in the sky [25].

The Gould Belt also contains interstellar clouds and has been early associated with an expanding HI ring [28]. The fact that dark clouds participate to the expansion was recognized 20 years later [42]. Famous H_2 complexes, such as Orion, Ophiuchus, and Lupus, have long been related to the Belt, but more recently mapped complexes, such as Aquila Rift, Cepheus, Cassiopeia, Perseus, and Vela appear to be part of the expanding shell as well [35].

The present size of the gas shell was first estimated by comparing the radial velocities in the Lindblad HI ring with the 2D expansion of a shock wave inside the Galactic plane [32], then with the 3D expansion of a superbubble in a uniform medium [31]. The dynamical evolution has been revisited to allow 3D expansion in a non uniform medium and to compare with the location and motion of all the nearby HI and H_2 clouds [35]. An inclined cylindrical shock wave, with thickness H, has been used. It sweeps momentum from the ambient medium where the gas density varies with altitude above the Galactic plane according to the 90, 225, and 400 pc scale heights that describe the HI layer [14], and to the 74 pc scale height of the local CO gas [12]. Because of the Galactic differential rotation, the circular section of the Belt rapidly evolves into an elliptical one which precesses with time. The rim slightly takes an hourglass shape from its faster expansion in the more rarefied medium at high altitude. The Belt further warps and falls back in the Galactic gravitational potential. A density gradient with Galactocentric distance has little effect on the evolution. The sequence that best matches the present location and longitude-latitude-velocity distribution of all the nearby HI and CO clouds at $|b| > 5°$ is displayed in Figure 1. The current Belt geometry is close to that depicted in the 30 Myr plot and the last plot illustrates the Belt in 10-15 Myr from now.

The dimensions [35] that best fit the cloud data are a height H of 60 pc and semi-major axes $a = 354 \pm 5$ pc and $b = 232 \pm 5$ pc, in good agreement with the sizes derived from the sole HI data for the expansion of a 2D ring[32] (360×210 pc) or a 3D superbubble in a uniform medium[31] (341×267 pc). The present inclination of $17.2° \pm 0.3°$ to the Galactic plane nicely compares with the latest stellar estimates ($16° - 22°$ for massive stars younger than 60 Myr[43] and $17.5° - 18.3°$ for O-B stars [6]). The larger inclination of $27.5° \pm 1°$ indicated by the young solar-mass stars is biased by the dominant Sco-Cen associations within the X-ray visibility horizon [25]. The current Belt centre is found at 104 ± 4 pc from the Sun, toward $l = 180° \pm 2°$, so the Sun is nearly half way to the rim. The ascending node longitude $l_\Omega = 296.1° \pm 2.0°$ is 10° higher than the values obtained from the massive and young low-mass stars[43,25], possibly reflecting the time-lag

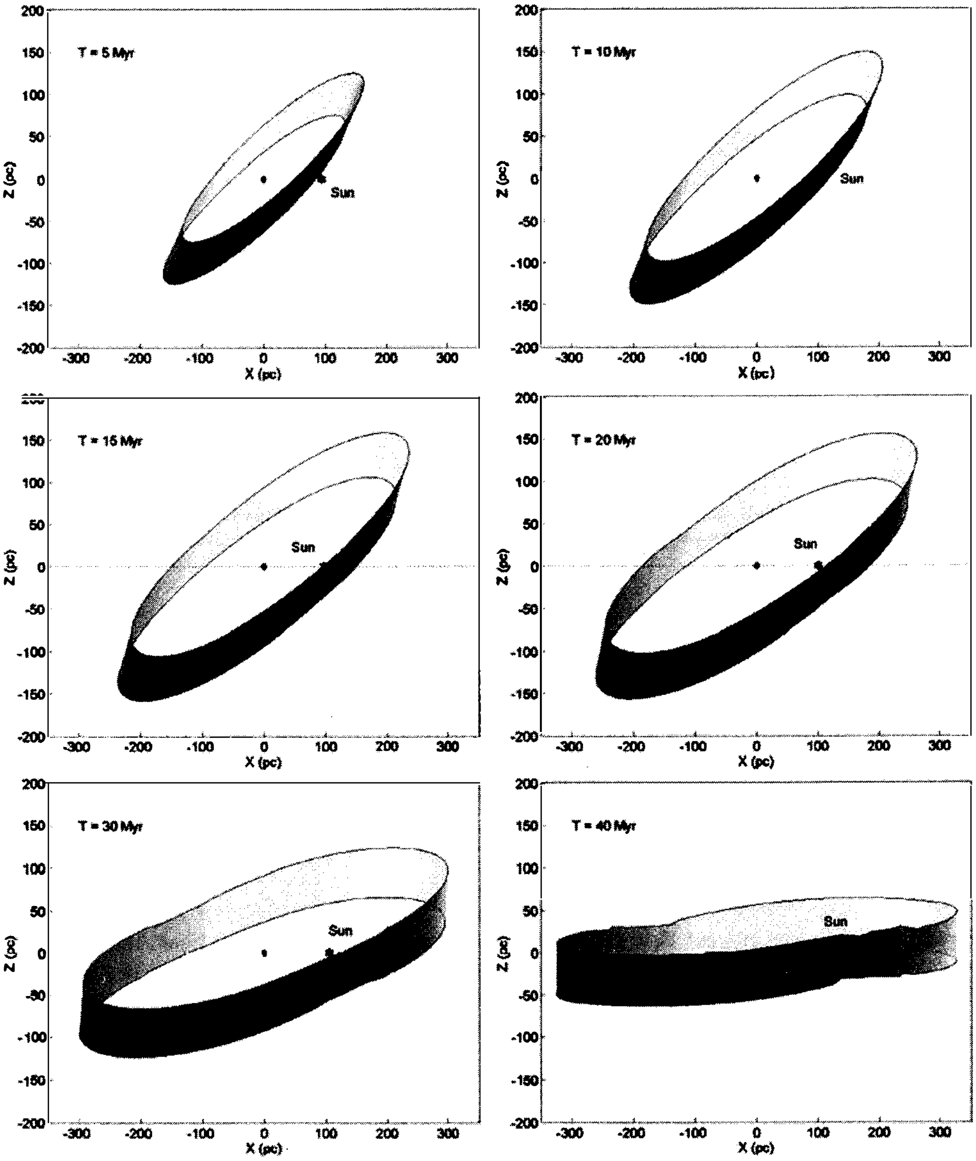

Figure 1: The Gould Belt evolution as seen at different epochs after the outburst, in a plane perpendicular to the Galactic plane, centred on the Belt centre. The x axis points to the Galactic centre and the location of the Sun, nearly half way to the rim, is marked by an asterisk.

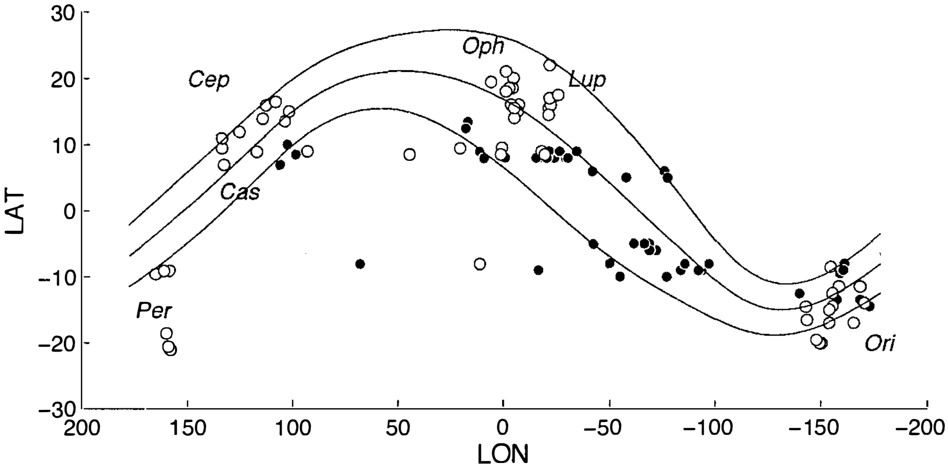

Figure 2: Galactic longitude and latitude distribution of the nearby HI and H_2 clouds at $|b| > 5°$ and the trace of the 60-pc-thick disc of the Belt across the sky. The Belt angular extent is larger near Ophiuchus where the rim is closer to the Sun.

between stellar birth and the slowly precessing rim.

The Belt position and orientation differ from previous estimates because of the use of *Hipparcos* distance information and of major H_2 complexes in the second quadrant. They had not been firmly associated with the Belt before, but their direction, distance, and velocity appear to be quite consistent with the modelled Belt and with the HI Lindblad ring [35]. In fact, nearly all the local H_2 complexes at $|b| > 5°$ seem to participate to the shell, except the very nearby Taurus and R CrA clouds that are well inside the Belt, and the Chamaeleon clouds that belong to the Local Arm. Figure 2 shows the Belt trace across the sky with respect to the clouds.

2 Star-formation in the Belt

Figure 3 displays the current Belt geometry with respect to the OB associations, the positions of which are known from *Hipparcos* measurements [13]. It nicely coincides with most of them, but for Col 121 and Cep OB2 that clearly lie outside the Belt, and for Lac OB1 that is too far on the wrong side of the Galactic plane. The total swept-up mass in the evolved cylindrical shell amounts to $2.4\ 10^5\ M_\odot$. The mass accumulated over the past few Myr varies with longitude and is lowest in the $35° < l < 100°$ and $-155° < l < -110°$ sectors which are indeed free of major cloud complexes and OB associations near the rim. There is, however, no convincing relation between the mean velocity field of the individual OB associations and the shell expansion [35].

The column-densities of active X-ray stars show a marked excess over the Galactic population that varies with longitude [25]. It extends to the 300 pc visibility horizon in the $195° - 285°$ interval, and to the remote edge at 170 pc of the Sco-Cen associations in the $285° - 15°$ quadrant. It disappears in the $15° - 105°$ interval, and is hardly visible out to 150 pc in the $105° - 195°$ quadrant, once the very nearby Hyades and Pleiades groups are subtracted. The lack of active star formation within 50 pc is due to the Local Bubble. These distributions indicate that stellar formation is not only active along the Belt rim, but also 100 pc or so inward, i.e. over a significant, yet poorly constrained, radial extent. This picture is consistent with the spatial distribution of massive stars in the 3rd and 4th Galactic quadrants. Yet, as for the young X-ray stars, no ring-like enhancement is seen in the 1st and 2nd quadrants even though the OB star

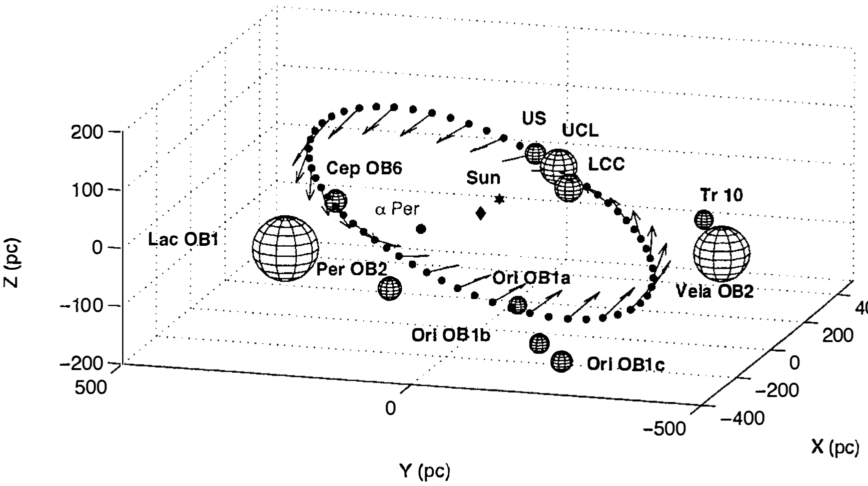

Figure 3: 3D view of the present Gould Belt and its velocity field with respect to the local standard of rest. The local OB associations are marked as spheres. The diamond notes the location of the Belt centre and the star that of the Sun.

visibility reaches quite beyond the Belt edge.

3 The Belt age and origin

The Belt dynamical ages agree reasonably well for the different types of outburts (26.4 $\pm$ 0.4 Myr for the 3D cylindrical shock wave [35], 23 and 15.5 Myr for a superbubble expansion with and without internal pressure [31]), but they are notably smaller than that derived from the stars (30-60 Myr for photometric ages [11,43], 30-80 Myr from X-ray activity [25], and 34 ± 3 Myr from stellar dynamics [8]). The former are sensitive to the local gas density estimates, the latter to the separation of the Belt and Galactic populations and to the photometric age accuracy. To reduce this discrepancy, one may explore the influence of stellar rotation which can lower age estimates by 30 to 50 %, particularly for high rotators such as OB stars [16].

The required initial kinetic energy of (1.0 ± 0.1) 10^{45} J in the 3D cylindrical shock wave [35] is comparable, but 60% higher than that needed in the 2D model[32] because of the extra work used to expand against the Galactic gravitational pull in the early phases. An equivalent energy of 6 10^{44} J is required for a superbubble expansion in a 3 times lower interstellar density, but against ambient pressure [31]. This energy deposit is typical of multiple, rapidly succeeding supernovae inside a young stellar cluster. It is also typical of a hypernova powering a collimated γ-ray burst event, or of the potential energy of high-velocity clouds falling on the Galactic disc [9,10].

Preserving the structural coherence of the Belt stellar system over a large fraction of the vertical oscillation and expansion timescales is challenging. Pure expansion models cannot reproduce the stellar data. A system initially rotating as a solid body can remain flat and tilted in the Galactic gravitational potential if it is initially inclined [8]. The angular momentum of the parent cloud would therefore not be perpendicular to the Galactic plane. The dissolution of such a self-gravitating rotating stellar system may explain the persistence of a flat expanding disc [30].

The Belt formation is still a puzzle. Its flatness and tilt remain very difficult to interpret. Various scenarii involve the oblique impact of a high-velocity cloud on the Galactic disc [9,10] or a cascade of supernova explosions (see [38] for a review). The former naturally provides some inclination, the gas expansion, and it is consistent with the measured Oort constants. For instance [9,10], a 500 pc size, 10^{-2} M$\odot$ pc^{-3} cloud, falling at 100 km/s from the northern halo and from inside the solar circle, could have created the Gould Belt and the Monoceros R2 complex. Recent MHD simulations of an oblique impact, however, show that the hole punched in the Galactic disc and the lateral compression waves are strongly driven by the vertical density gradient, perpendicular to the Galactic plane, so getting a global inclination for the star-forming disc should be carefully investigated (J. Franco, private communication). On the other hand, the expanding shock wave from an explosive event or a rapid series of explosions [32,35] can match the space and velocity distribution of the gas if an initial asymmetry provides a large inclination. Whether a γ-ray burst event would apply is being investigated. Whether subsequent supernovae or stellar winds inside the Belt keep powering its expansion at later stages is an open question. Injecting energy gradually would accelerate the Belt expansion and further increase the age discrepancy ($R \propto t^{3/4}$ instead of $R \propto t^{1/3}$ in a uniform medium [35]), as well as reduce its eccentricity. The stellar orbits emerging from an expanding superbubble [31] can reproduce the velocity field of the nearby O-B5.5 stars and of the HI Lindblad ring only if the stars from the Pleiades group are removed, suggesting that two independent events have formed the Pleiades and the Belt. Alternatively, a 2 10^7 M$\odot$, 400 pc size supercloud has been proposed as the common precursor of the Sirius supercluster, the Gould Belt and the Local Arm [33]. The braking and compression of the supercloud while entering a spiral arm would have produced the latter two while the stellar cluster, unaffected by friction, would have moved on, away from the gas system. The supercloud angular momentum being concentrated at large radii, the inner regions would collapse into a flattened disc, precursor of the Gould Belt, whereas the ejection of the outer parts into a super-ring would form a precursor of the Local Arm.

Whatever triggered the Belt and its expansion has so deeply influenced the local interstellar medium, in particular the pressure gradient, that the Local Bubble cavity, or rather the Local Chimney, has opened up to the halo along an axis perpendicular to the Belt disc [27]. The chimney also notably opens toward more intermediate- and high-velocity clouds than other regions of the halo. It has been suggested that these clouds formed from material ejected by the initial Belt burst and they now fall back onto the Galactic disc [32,45]. The lack of cold HI and the presence of intermediate-velocity clouds at high latitude in the 2nd quadrant could be the signature of an explosive event that took place 35 myr ago near the α Per association [37].

4 The Belt supernovae and cosmic rays

During its evolution, the Belt has produced massive stars, therefore supernovae, in excess of the local Galactic rate. Explosions should have lately occurred from the first generations of massive stars born in the Belt. In the next few tens of Myr, 340 ± 30 stars [6] with masses > 8 M$_\odot$ will explode and their maximum lifetime implies a crude minimum rate > 35 collapses Myr^{-1} kpc^{-2}. In comparison, a Galactic rate of 20 events Myr^{-1} kpc^{-2} is inferred at the solar circle from the distribution of stars in the Galaxy and from the average frequency of $2.5^{+0.8}_{-0.4}$ events per century for all types of supernovae in the Galaxy [41], ~ 85 % of which arise from the core collapse of a massive star. This value reasonably agrees with the 29 progenitors Myr^{-1} kpc^{-2} found with masses > 8 M$_\odot$ within 1 kpc from the Sun [41], in particular given the enhanced yield from the Belt inside this region. A rate can be inferred for the recent past from the current Belt stellar content as a function of mass, given the Γ index of the initial mass spectrum ($dN/dM \propto M^{\Gamma-1}$), lifetime estimates for stars with solar metallicity, a constant birth rate for simplicity, a conservative mass threshold for collapse of 8 M$_\odot$, and a Belt age of 40 Myr consistent with the stellar estimates. The observed star counts [11] imply a supernova frequency of 20 to 27 supernovae per Myr in the entire Belt [23]. This rate falls to 17 to 20 supernovae per Myr using revised star counts [6]. The uncertainty stems from that in the star counts and Belt age and, mostly, from the large uncertainty in the Γ index between -2.0 and -1.1 at large mass. Using a size of 354×232 pc, the corresponding rate of 65 to 78 Myr^{-1} kpc^{-2} is 3 to 4 times the local Galactic one and is valid for the past few Myr. This rate stresses how actively the local medium has been heated and enriched by supernova remnants as well as irradiated by cosmic rays.

The rate is consistent with the existence of four 0.1–1 Myr old radio loops [3], the Local Bubble, and possibly the Vela supernova remnant near the rim. Vela Junior, alias RX J0852.0-4622 or G266.2-1.2, may be as close as 200 pc to be young enough to power the possible COMPTEL detection[44] of ^{44}Ti decay lines. The interstellar absorption of the X-ray emission, however, suggests a distance [40] of 1–2 kpc, so a confirmation of the 68, 78, and 1157 keV lines by INTEGRAL is eagerly awaited. RCW 114, alias G343.0-6.0, may be a nearby evolved remnant, well into its radiative phase, that has expanded in a rather dense medium. Maps of the interstellar density do show a cavity 200 pc away in this direction, near the Belt rim [27].

Supernova shock waves are generally proposed as the sources of cosmic rays up to 10^{15} eV (see [15] for a review). The detection of synchrotron X-rays from various remnants (Cas A, SN 1006, G347.3-0.5, Tycho) lends further support to the diffusive acceleration of electrons up to tens of TeV. Direct observational evidence for the acceleration of ions is still searched for, but the indirect evidence becomes compelling [2]. The Belt rate is globally consistent with the power of 2.3 10^{44} J Myr^{-1} kpc^{-2} required to maintain the local cosmic-ray density [4] for a standard supernova-to-cosmic-ray energy conversion efficiency of a few percent [15]. However, the cosmic-ray spectrum should vary with source proximity in space and time. The fluctuations are particularly strong for the electrons above 50 GeV for which the synchrotron and inverse Compton radiative timescale is short, so they diffuse no further than several hundred parsecs from their accelerator. Adding the contributions from sources in the Galactic disc and in the Belt, with the respective rates quoted above, the average electrum spectrum at Earth turns to be only slightly harder with the Belt than without [36], with a spectral index increase of 0.07 above 50 GeV. Yet, the currently measured spectrum may not be representative of the average, nor should it be uniform in the local interstellar medium. It should correlate with that in the nearby Ophiuchus and Taurus clouds, but not much with the spectrum in more remote places like Orion, Cepheus, Perseus, and Monoceros [36]. The power per supernova required to sustain the local electron spectrum is reduced by 40 % when including the Belt, compared to a pure Galactic disc production. Cosmic-ray protons and primary nuclei do not suffer serious radiative losses, but the source clustering in the Belt also leads to an increased cosmic-ray density locally, to large fluctuations about the average, and to a slight softening of the average spectrum because the higher-energy particles diffuse away faster [5].

5 γ-ray sources and pulsars in the Belt

New facets of the Gould Belt activity have been brought to light at high energy with the discovery of a population of γ-ray sources associated with it [23,17]. These sources are part of the $\sim$ 130 unidentified γ-ray sources seen above 100 MeV by the EGRET telescope on board the late Compton Gamma-Ray Observatory [19]. A subset of 35 to 40 of these sources [24], among the steadiest, is gathering at medium latitude ($3° < |b| < 30°$) along the characteristic trace of the Gould Belt (see figure 4). The source distribution is significantly better correlated with the Belt than with other Galactic structures likely to display sources at medium latitude [23], such as a homogeneous spherical Galactic halo, or the local Galactic disc (with any scale height), or the 400 pc-thick disc of radio pulsars. This should come as no surprise since there is clear evidence, close to the Galactic plane, that unidentified γ-ray sources are linked to star-forming sites. What is puzzling, however, is that most of the sources lack conspicuous radio or X-ray counterparts despite their proximity. Whatever powers the γ-ray source emits most of its radiative energy in γ rays. No clear picture has emerged yet as to the nature of these objects, but neutron star

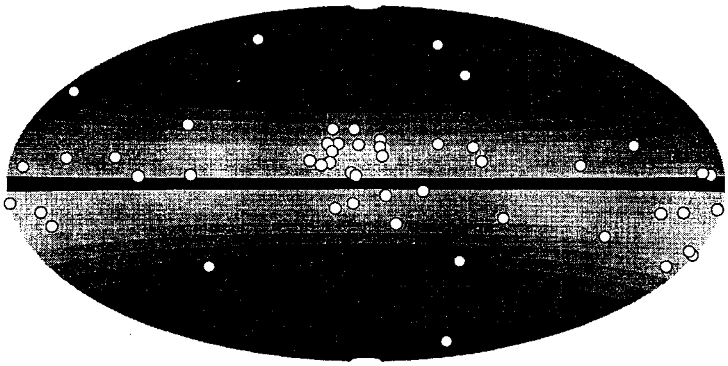

Figure 4: Spatial distribution, in Galactic coordinates, of the 50 unidentified persistent EGRET sources $|b| > 3°$. The grey scale traces the column-density of local young stars (< B3), convolved with the EGRET exposure.

activity appears as a promising prospect. Other possibilities are unlikely [23]. The sources are too bright in γ rays to be unresolved gas clumps irradiated by the local cosmic-ray flux. The required mass of $\sim 10^4$ $M_\odot$ at 500 pc cannot have escaped the radio and IR surveys, even when considering radio beam dilution from unresolved clouds. Nor can they be slow, old neutron stars, wandering in the interstellar medium and accreting gas from a dense cloud for they would be 10^{2-3} times too rare and the maximum Bondi-Hoyle accretion power of $\sim 2\ 10^{25}$ W that can be drawn from the surrounding HII region is 10 times too low. The accretion power reached for slowly spinning, highly magnetized neutron stars moving at 200–400 km s^{-1} in the intercloud medium (10^{-3} H cm^{-3}), though increased by Kelvin-Helmholtz instabilities in the shocked gas, is also orders of magnitude too low. Isolated accreting black holes are even more rare and compact objects accreting from a stellar companion, as well as microquasars, would shine too brightly in X rays [39]. No source coincides with any of the numerous O Belt stars despite their highly supersonic winds with kinetic powers of 10^{28-29} W. Nearby supernova remnants would appear as extended γ-ray sources. Therefore, only pulsars are left as promising candidates even though the present models for pulsed emission predict too few of them.

13 radio pulsars from the ATNF catalogue are found with distances < 1.5 kpc and age < 2 Myr, but they are too few and too fast to show a correlation with the inclined Belt or with the Galactic plane. The narrow radio beams from many more may miss the Earth. Two young and energetic radio pulsars, Geminga and PSR B0656+14, are born inside the Belt, 0.35 and 0.11 Myr ago, respectively. The younger Vela pulsar exploded 11 kyr ago near the rim. Geminga and Vela are both conspicuous γ-ray pulsars and the detection of the third one above 100 MeV awaits confirmation. Geminga stands out as a unique example of a radio-quiet γ-ray pulsar. It is the intrinsically faintest γ-ray pulsar observed so far, but equally faint sources would have been easily detected anywhere inside or around the Belt if their radiation beam swept by us. How the luminosity evolves at older ages is model dependent. Population synthesis studies have been performed, both to provide information on the likelihood that these unidentified sources be radio-quiet γ-ray pulsars and to study the pulsar population born in the Belt.

Pulsars are produced in the simulations with a constant birth rate of 1–1.4 per century over the past billion years in the Galactic disc and of 20–24 per Myr in the expanding Gould Belt. They evolve in the Galactic potential to the present time. Their initial period and magnetic field distributions are chosen to fit the $P - \dot{P}$ diagram of a thousand radio pulsars. Their radio and γ-ray beams evolve with their spin-down luminosity, $\dot{E}_{sd}$, as they get old. The slot-gap and outer-gap models [21,7] for pulsed emission predict similar luminosity evolutions ($L_\gamma \propto \dot{E}_{sd}^{0.5}$ and $L_\gamma \propto \dot{E}_{sd}^{0.38}$, respectively). The beam apertures greatly differ in the two cases because of their different origins in the open magnetosphere. Radiation is produced in the slot gap in funnel-like beams deep inside the magnetosphere, above the polar caps, whereas the outer-gap fan-like beams originate near the light cylinder. It appears that the characteristic spatial signature of the Belt is preserved over several Myr despite its expansion, the rapid pulsar migration [1], and the blending with the Galactic pulsar population [34,18].

The results [21,7] show that 4 slot-gap and 5 outer-gap radio-loud γ-ray pulsars of Belt origin should have been detected by EGRET, in reasonable agreement with the 2 or 3 detections. An extra 5 or 15 radio-quiet ones should appear as unidentified sources. The 3 times larger prediction of the outer gap model results from the much wider beam that can be seen at large angles. In both cases, Belt pulsars remain detectable for EGRET up to 2 Myr of age, i. e. much longer than for the more distant pulsars in the Galactic disc. With more detections with the future GLAST satellite, to be launched in 2007, the ratio of radio-loud to radio-quiet γ-ray pulsars will be an important clue to discriminate between pulsar models. Yet, both models fail to explain the number of sources associated with the Belt. The same conclusion is reached using a different scheme that yields an upper limit to the pulsar contribution at mid latitudes for a minimal choice of assumptions, namely that the beam geometry shrinks with age as the open magnetosphere and that the γ-ray luminosity scales with the spin-down power as for the known γ-ray pulsars [18]. A total of 19 Belt γ-ray pulsars is obtained by fitting the spatial and flux distributions of all the unidentified EGRET sources near and away from the Galactic plane, without any radio population constraints. So, the origin of most of the unidentified Belt sources remains a puzzle.

Finding the Belt neutron stars would provide a unique opportunity to constrain pulsar models to older ages and a variety of aspect angles, and to study the progenitor mass threshold for producing a neutron star. As supernova relics, they would bring valuable insight to the cosmic-ray production efficiency, the abundance of explosive nucleosynthesis products, and to the filling factor of hot interstellar gas and its connection to the halo. In other words, the Gould Belt is a lively and fascinating, but complex and out of the ordinary place to live in and explore.

References

1. Arzoumanian Z. *et al.* 2002, ApJ 568, 289
2. Berezhko, E. G. & Völk, H. J. 2004, A&A, 419, L27
3. Berkhuijsen E. M. 1973, A&A 24, 143
4. Blandford R. D. & Ostriker J. P. 1980, ApJ 237, 793
5. Büsching I. *et al.*, submitted to A&A, 2004
6. Cabrera-Caño J., Elias F., Alfaro E.J. 2000, Ap&SS, 272, 95
7. Cheng, K. S., Zhang, L., Leung, P., & Jiang, Z. J. 2004, ApJ, 608, 418
8. Comerón, F. 1999, A&A, 351, 506
9. Comerón, F. & Torra, J. 1992, A&A, 261, 94
10. Comerón, F. & Torra, J. 1994, A&A, 281, 35
11. Comerón, F., Torra, J., & Gómez, A. E. 1994, A&A, 286, 789
12. Dame, T. M., *et al.* 1987, ApJ, 322, 706
13. de Zeeuw, P. T., *et al.* 1999, AJ, 117, 354
14. Dickey, J. M. & Lockman, F. J. 1990, ARA&A, 28, 215
15. Drury, L. O. *et al.* 2001, Space Science Reviews, 99, 329
16. Figueras, F. & Blasi, F. 1998, A&A, 329, 957
17. Gehrels, N., *et al.* 2000, Nature, 404, 363

18. Harding, A. K., Gonthier, P. L., Grenier, I. A., & Perrot, C. A. 2004, AdSpR, 33, 571
19. Hartman R. C. *et al.* 1999, ApJS 123, 79
20. Gould, B. A. 1874, Proc. of the American Association for Advanced Science, 115
21. Gonthier, P. L., VanGuilder, R., Harding, A.K. 2004, ApJ, 604, 775
22. Gonthier, P. L., *et al.* 2004, Proc. of "The multiwavelength approach to unidentified γ-ray sources", Hong Kong, Eds. K. S. Cheng & G.E. Romero, Astrophysics and Space Sciences Journal, in press
23. Grenier, I. A. 2000, A&A, 364, L93
24. Grenier, I. A. 2004, Proc. of "The multiwavelength approach to unidentified γ-ray sources", Hong Kong, Eds. K. S. Cheng & G.E. Romero, Astrophysics and Space Sciences Journal, in press
25. Guillout, P., *et al.* 1998, A&A, 337, 113
26. Herschel, J. F. W. B. 1847, Results of astronomical observations made during the years 1834, 5, 6, 7, 8, at the Cape of Good Hope (London, Smith, Elder and co.)
27. Lallement, R., *et al.* 1999, A&A, 411, 447
28. Lindblad, P. O. 1967, Bull. Astron. Inst. Netherlands, 19, 34+
29. Lindblad, P. O., *et al.* 1997, in ESA SP-402: Hipparcos - Venice '97, Vol. 402, 507–512
30. Lindblad, P. O. 2000, A&A, 363, 154
31. Moreno, E., Alfaro, E. J., & Franco, J. . 1999, ApJ, 522, 276
32. Olano, C. A. 1982, A&A, 112, 195
33. Olano, C. A. 2001, AJ, 121, 295
34. Perrot, C. A. 2002, PhD thesis, Paris VII University
35. Perrot, C. A. & Grenier, I. A. 2003, A&A 404, 519
36. Pohl M., Perrot, C. A., Grenier, I. A., & Digel, S. 2003, A&A 409, 581
37. Pöppel, W. G. L. & Marronetti, P. 2000, A&A, 358, 299
38. Pöppel, W. G. L. 1997, Fundamentals of Cosmic Physics, 18, 1
39. Romero G.E., Grenier, I.A., Kaufman Bernado, M.M., Mirabel, I.F., Torres, D.F. 2004, astroph/0402285, Proc. 5th INTEGRAL Workshop, Munich
40. Slane, P., *et al.* 2001, ApJ, 548, 814
41. Tammann G. A. *et al.*, ApJS 92, 487, 1994.
42. Taylor, D. K., Dickman, R. L., & Scoville, N. Z. 1987, ApJ, 315, 104
43. Torra, J., Fernández, D., & Figueras, F. 2000, A&A, 359, 82
44. Tsunemi, H., *et al.* 2000, PASJ, 52, 887
45. White, R. E. & Bally, J. 1993, ApJ, 409, 234

PHOTOIONIZATION OF CIRCUMSTELLAR DISCS

Richard Alexander, Cathie Clarke & Jim Pringle
Institute of Astronomy, Madingley Road
Cambridge, CB3 0HA, UK

Models of discs around low-mass stars which couple photoevaporative mass-loss with viscous evolution have recently become important, as they are able to reproduce a number of observed disc properties successfully. However these models are subject to few observational constraints, and a number of issues remain unresolved and/or unexplored. In particular, the origin of the ionizing radiation required to drive the photoevaporation is not well-understood. In this contribution we review existing photoionization models, before going on to discuss recent and current work. Theoretical models of the accretion shock are considered, and we suggest a new observational diagnostic to quantify the chromospheric ionizing flux. We also consider the effects of X-ray photoionization in these models. We conclude that accretion powered UV and coronal X-rays are unlikely to influence disc evolution significantly. However the chromospheric Lyman continuum appears to be sufficient to drive disc photoevaporation, and so these models may indeed provide a realistic mechanism for dispersing circumstellar discs.

Keywords: accretion, accretion discs – stars: formation – circumstellar matter – planetary systems: protoplanetary discs – stars: pre-main sequence

1 Introduction

The existence of discs around young low-mass stars is now well established, and remains an important area of study as it has strong consequences for theories of both star and planet formation. Observations show us that at an age of $\sim 10^6$yr most low-mass stars are surrounded by discs that are optically thick to optical and near-infrared radiation (Kenyon & Hartmann 1995 [31]; Haisch et al. 2001 [24]; Lada & Lada 2003 [34]). These discs typically have masses of a few percent of a stellar mass (Beckwith et al. 1990 [6]) and are much more massive than the low-mass "debris discs" observed in older systems (Mannings & Sargent 1997 [37]). By an age of $\sim 10^7$yr, however, almost all of the discs have gone, and so this constrains the disc lifetimes to be of order a few million years. There is also evidence for an intrinsic spread in these disc lifetimes of up to an order of magnitude (Armitage et al. 2003 [5]).

However it is also well-established that the fraction of so-called transition objects, between disc-bearing Classical T Tauri stars and disc-less (or at least "optically thick disc-less") Weak-lined T Tauri stars (hereafter CTTS and WTTS), is small. This has been observed by a number of near-infrared studies (eg. Skrutskie et al. 1990 [46]; Kenyon & Hartmann 1995 [31]), and the effect has also been observed at mid-infrared (eg. Persi et al. 2000 [41]; Bontemps et al. 2001 [7]) and millimetre wavelengths (Simon & Prato 1995 [45]; Wolk & Walter 1996 [47]; Duvert et al. 2000 [14]). This constrains the transition time between the CTTS and WTTS to be $\sim 10^5$yr, with the disc vanishing simultaneously on spatial scales from 0.1-100AU on a timescale some 1-2 orders of magnitude shorter than the disc lifetime [a]. This effect is observed most clearly in low-mass star-forming regions such as Taurus-Auriga and ρ Ophiuchus, and so it seems likely that the mechanism responsible is something intrinsic to individual TTS systems rather than an environmental effect. However most mechanisms for disc clearing, such as viscous evolution (Hartmann et al. 1998 [26]) or magnetospheric clearing (Armitage et al. 1999 [4]), produce power-law declines in the disc surface density. Thus such models always produce a disc dispersal time that is comparable to the disc lifetime, and so fail to satisfy the two-timescale constraint required by the observations. Further, the simultaneous decline in the disc surface density observed across such a wide range of radii implies that the formation of a planet is unlikely to be responsible for this effect, as it is questionable whether a planet can account for such global changes in the disc properties.

One model which has been successful in reproducing the observed rapid disc dispersal times is the "UV switch" model of Clarke et al. (2001) [11]. This model couples a photoevaporative disc wind to viscous evolution of the disc, and results in a rapid decline in the inner disc at a late stage in the disc evolution. Models of photoevaporative disc winds were first produced by Hollenbach et al. (1994) [27], and were subsequently improved upon by a number of subsequent studies (eg. Richling & Yorke 1997 [43]; Font et al. 2004 [17]; see also the review by Hollenbach et al. 2000 [28]). In these models ultraviolet photons from the central star produce a thin, ionized layer on the disc surface, at a temperature of $\sim 10^4$K. Outside some gravitational radius ($\sim$ 10AU for a $1M_{\odot}$ star) the thermal energy of this ionized layer is such that it is greater than the gravitational binding energy, and so material can flow from the disc as a "disc wind". The mass-loss rate is low, typically of order $10^{-10}M_{\odot}yr^{-1}$, and depends only on the mass of the central object and the ionizing flux, with the mass-loss concentrated at or near to the gravitational radius. When these models are coupled to a model including viscous evolution of the disc the results at early times are the same as for a ordinary viscous evolution model. However at late times the mass accretion rate through the disc drops to a value comparable to the disc wind mass-loss rate. At this point the inner disc cannot be resupplied with material inside the gravitational radius, and so the inner disc drains on a viscous timescale. Thus after a disc lifetime of $\sim 10^7$yr the inner disc is dispersed on a timescale of $\sim 10^5$yr, satisfying the two-timescale constraint demanded by observations (Clarke et al. 2001 [11]).

However a number of problems and caveats still exist in this model, which we seek to address in this contribution. The primary uncertainty surrounds the ionizing flux produced by the central object. In order to succeed this model requires an ionizing flux on the order of 10^{40}–10^{43} photons s^{-1}, some ten orders of magnitude greater than that produced by a typical stellar photosphere. Further, this ionizing flux must be present at late times in the disc evolution, and

[a]This rapid dispersal is most clearly observed in the near-infrared. This near-infrared emission is due to warm dust in the disc, so it is only necessarily the *dust* which must disperse on this short timescale to satisfy the observations. However millimetre observations, which probe the gas in the disc, also show evidence for this rapid transition, and a strong correlation has been observed between the gas and dust emission (Najita et al. 2003 [39]), so we treat the gas and dust dispersal as simultaneous.

so ideally should not be powered by disc accretion. This problem is essentially unconstrained by observations, and so we investigate the production of Lyman continuum photons both by the accretion shock (Section 2) and the stellar chromosphere (Section 3). In contrast to the case of Lyman continuum photons, X-rays from TTS are well-studied, with typical luminosities of order 10^{30}erg s^{-1} (Feigelson & Montmerle 1999 [15]). Such energies are similar to that produced by the Lyman continuum, and so in Section 4 we consider whether this X-ray emission could also drive a disc wind. We do not yet address the other main problem with the model, that the outer disc, beyond the gravitational radius, is dispersed more slowly than demanded by observations (Clarke et al. 2001 [11]). In essence this contribution summarises the work of three papers in turn (Alexander et al. 2004a [1]; 2004b [2]; 2004c [3]), before bringing the separate conclusions together in a single summary.

2 Ionizing photons from the accretion shock

One possible source of Lyman continuum photons from TTS is from the "accretion shock" produced where disc materials falls onto the stellar surface. Discs around TTS are typically truncated by the magnetosphere at radii of 5-10R$_*$ (eg. Calvet & Gullbring 1998 [10]), and so material falling from the inner edge of the disc can attain extremely high velocities, of order $\sim$ 100km s^{-1}. This infalling material is channeled by the stellar magnetosphere and results in a so-called "accretion shock" where it impacts on the stellar surface. Existing models of the accretion shock (eg. Calvet & Gullbring 1998 [10]; Gullbring et al. 2000 [23]) have primarily focused on reproducing spectra observed at ultraviolet (1000–3000Å) and visible (3500–7000Å) wavelengths, and such emission spectra are now well understood. However absorption by interstellar HI makes observations at wavelengths shortward of the Lyman break (< 912Å) impossible, and so little is known about the Lyman continuum emission produced by the accretion shock. Observations indicate that the accretion shock has a typical temperature of 10,000–15,000K (eg. Johns-Krull et al. 2000 [30]), and so previous studies have estimated the ionizing flux produced by the accretion shock by assuming that the accretion shock emits like a black body "hotspot" on the stellar surface (Matsuyama et al. 2003 [38]). We contend that the ionizing flux produced by such a hotspot will be greatly suppressed, for two reasons. Firstly, the hotspot itself is likely to radiate like a heated stellar atmosphere rather than a simple black body, and in such a case photoionization of neutral hydrogen results in a strong "Lyman edge" in the spectrum at the Lyman break. Further, any ionizing photons produced by the hotspot must travel upwards through the accretion column in order to escape and ionize the disc surface. The accretion column is extremely optically thick to Lyman continuum photons due to its high density of HI, and so this provides an extremely strong suppression of the ionizing flux. We address each of these issues in turn.

2.1 Stellar Atmospheres

Previous studies (eg. Matsuyama et al. 2003 [38]) have assumed that the accretion shock can be modelled as a constant temperature hotspot, with the spectral energy distribution (SED) of the hotspot that of a $T = 15,000$K blackbody. Half of the accretion energy is assumed to be radiated by the hotspot, and so for a star of mass M_* and radius R_* the accretion luminosity is given by

$$L = \frac{GM_*\dot{M}_d}{2R_*} = A\sigma_{SB}T^4 \tag{1}$$

where $\dot{M}_d$ is the rate of mass accretion from the disc, A is the area of the hotspot, and σ_{SB} is the Stefan-Boltzmann constant. As the temperature is constant, the ionising photon rate Φ_a is proportional to the accretion rate $\dot{M}_d$. Matsuyama et al. (2003) [38] also include a photospheric

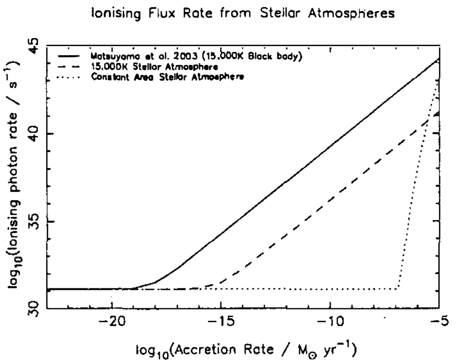

Figure 1: Ionising flux rates from different accretion shock models. The rate from a simple model atmosphere is some 3 orders of magnitude less than that from a blackbody, and the constant area case, with $T \propto \dot{M}_d^{1/4}$ decays more precipitously still. (Figure from Alexander at al. 2004a [1].)

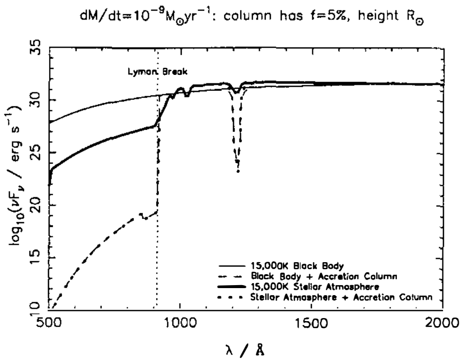

Figure 2: Spectra of light incident on and emitted by a constant density accretion column with a covering factor of 5% and a height of $1R_\odot$. Note the precipitous drop in the emitted spectra at the Lyman break, due to photoabsorption by HI. The deep absorption feature at 1215Å is Lyα. (Figure from Alexander at al. 2004a [1].)

contribution to the ionizing flux of $\Phi_p = 1.29 \times 10^{31}$photon s^{-1}, with the total ionizing flux given by $\Phi_a + \Phi_p$.

We propose two corrections to this model. Firstly, we assert that the high density of atomic hydrogen in the accretion shock will result in a SED that more closely matches that of a stellar atmosphere, showing a significant Lyman edge at 912Å. By repeating the calculation above, but this time adopting the SED of a 15,000K Kurucz stellar atmosphere (Kurucz 1992 [33]), we find that the ionizing flux from a 15,000K hotspot is reduced by 3 orders of magnitude. The second correction concerns the hotspot area. The formulation in Equation 1 uses a constant temperature, thus implying that the hotspot area decreases as the accretion rate drops. However if the accretion onto the stellar surface is channeled by the magnetosphere then the hotspot area should remain approximately constant with time. If the area of the blackbody hotspot A is indeed constant, then it is clear from Equation 1 that the hotspot temperature should vary as $T \propto \dot{M}_d^{1/4}$. As the *total* luminosity of the stellar atmosphere is very similar to that of a blackbody we adopted this criterion also. We then re-evaluate the ionizing flux from the hotspot as before, again keeping the scaling luminosity proportional to $\dot{M}_d$, but this time with the hotspot temperature given by

$$T = \left(\frac{GM_*}{2R_* A \sigma_{SB}} \dot{M}_d \right)^{1/4} \tag{2}$$

The results of both of these models are shown in Fig.1, with the blackbody result assumed by Matsuyama et al. (2003) [38] shown for comparison. In the case of constant area the fall in ionizing flux with accretion rate is much more dramatic than in the constant temperature case, with only high accretion rates ($> 10^{-7}\mathrm{M}_\odot\mathrm{yr}^{-1}$) producing ionizing photons at greater than the photospheric rate. The relationship between hotspot area and accretion rate is not well understood, with some evidence even suggesting an area that increases with $\dot{M}_d$ (Calvet & Gullbring 1998 [10]). However we go on to show that the presence of the accretion column above the hotspot is the dominant factor in determining Φ_a, and so the exact details of the hotspot area are not of great significance.

2.2 Accretion Columns

The other issue we consider is the presence of a column of accreting material directly above the hotspot. This accretion column absorbs Lyman continuum photons through photionization of neutral hydrogen, and so the ionizing flux is greatly supressed. The photoionization cross-section for absorption of Lyman continuum photons is $\sigma_{13.6\mathrm{eV}} = 6.3\times10^{-18}\mathrm{cm}^2$, and so a column density of $1.58\times10^{17}\mathrm{cm}^{-2}$ is equivalent to an optical depth of unity. The density of the infalling material is of order $10^{12}\mathrm{cm}^{-3}$ (Calvet & Gullbring 1998 [10]), and so the typical attenuation length is of order $10^{-5}\mathrm{R}_\odot$. Thus all Lyman continuum photons from the accretion shock are absorbed by the column, and the only significant source of ionizing photons that can escape the column is radiative recombination within the column, the so-called diffuse continuum.

In order to study the diffuse continuum we constructed models of the accretion column using the photoionization code CLOUDY (Ferland 1996 [16]). Our model uses the hotspots described above as a source, placed beneath a column which subtends a constant solid angle (ie. the column is a truncated radial cone). We assume a magnetospheric accretion model (eg. Ghosh & Lamb 1978 [18]), with the density of the column scaling as $R^{-5/2}$, and follow the parametrization of Calvet & Gullbring (1998) [10] in fixing the scaling density at the base of the column. As the diffuse continuum dominates, the ionizing flux emitted by the column is insensitive to the exact input SED and so the blackbody and stellar atmosphere hotspots both give the same diffuse Lyman continuum, as seen in Fig. 2. We compute these models for a broad range of accretion rates, column heights and covering fractions, and find that in all cases the flux emitted from the top of the column was much less than the photospheric level (a typical spectrum is shown in Fig. 2).

2.3 Discussion

The most obvious caveat in our model is that we only consider radial photons, and neglect emission from the "sides" of the columns. Given the enormous optical depth only a negligible fraction of the ionizing photons emitted near to the edge of the hotspot can escape. However the diffuse continuum emitted from the sides of the column is significant, and in fact is probably dominant. Given that this emission should be isotropic we can evaluate its value approximately by considering a column with a height equal to its diameter: in all cases the ionizing flux emitted is still less than the photospheric value. We also neglect both flaring and bending of the accretion column, but the uncertainties due to these effects are small. Even our "best-case" model, with parameters chosen so as to maximise the ionizing flux, fails to produce Lyman continuum photons at greater than the photospheric rate. The photospheric rate of 1.29×10^{31}photon s^{-1} is some 10 orders of magnitude less than the value required to drive disc photoevaporation in the models described in Section 1, and so we conclude that the accretion shock does not produce Lyman continuum photons at a rate likely to be significant in these models. Therefore, in order for photoevaporation to be a realistic means of disc dispersal the central source must sustain a source of ionizing photons that is not powered by disc accretion.

3 Ionizing photons from the chromosphere

A second possible source of Lyman continuum photons from TTS is the stellar chromosphere. Chromosperic emission from young stars is poorly understood, and no real constraints exist on the ionizing flux produced. However these stars are known to be magnetically active, and so some authors have argued that a chromosphere that resembles a "scaled-up" solar chromosphere seems likely (eg Costa et al. 2000 [12]). The rate of Lyman continuum photons from the solar chromosphere is $\sim 10^{38}$photon s^{-1}, and so a scaled up value would approach the rates required by photoevaporation models. However, as stressed by Clarke et al. (2001) [11], in addition to a strong ionizing flux merely being present around TTS, in order to drive the photoevaporation it must remain present at late times in the disc evolution. Thus we seek to place observational constraints on the chromospheric Lyman continuum emitted by TTS, both in terms of its magnitude and evolution.

There are, however, a number of observational issues that make this difficult. Most obviously, Lyman continuum photons are absorbed by interstellar HI and so direct measurements of the ionizing flux are not possible. Hydrogen recombination lines are of limited use as a diagnostic, as they are invariably optically thick. They also suffer from the fact that it is diffucult to separate the disc emission from that from the central source. Further, even when a diagnostic is found reddening is a significant problem, as small uncertainties in the extinction and reddening law at optical wavelengths result in much larger uncertainties when extrapolated to the ultraviolet.

In order to address this we make use of two techniques. Firstly, we use an emission measure (EM) analysis. In plasma physics, the EM is a measure of the mass of material emitting at a given temperature, and so combining the EM with a spectral synthesis package leads directly to a predicted spectrum. By assuming that the chromosphere around these objects radiates as an optically thin plasma, Brooks et al. (2001) [8] were able to derive volume emission measures for a sample of 5 CTTS. By utilising these EMs (kindly provided by David Brooks) we are able to derive reddening-dependent values of the ionizing flux emitted by these objects.

Secondly, we make use of the result noted by Brooks & Costa (2003) [9] that the total power radiated by the chromosphere is observed to correlate well with the flux in the CIV 1549Å doublet. We also note that the HeII 1640Å line is the equivalent of Hα for singly-ionized He, and is thought to be excited by radiative recombination. Thus the flux in the HeII line should provide an indicator of the ionizing flux present, and the HeII:CIV line ratio should provide a reddening-independent, normalised diagnostic. We then use archival (IUE) data to obtain HeII:CIV ratios for $\sim$ 40 TTS, both classical and weak-lined, in order to study the time evolution of the ionizing flux.

3.1 Emission Measures

In order to perform our EM analysis we make use of the EMs derived by Brooks et al. (2001) [8]. We use these EMs as input for the CHIANTI spectral synthesis code (Dere et al. 1997 [13]), and adopt the stellar parameters of Brooks & Costa (2003) [9]. We first attempt to reproduce the observed spectra, and find that the line ratios and intensities can generally be reproduced to within a factor of $\simeq 2$ of the observed values. (We note, however, that none of the synthetic spectra contain significant HeII 1640Å emission, in contrast to the observations. The plasma simulation only includes collisional excitation, and so we interpret this as evidence that the HeII 1640Å line is excited by radiative recombination.) We then use the synthetic SEDs to estimate the ionizing fluxes produced by these TTS. These values are obviously subject to large reddening uncertainties, and so are probably only accurate to order-of-magnitude level, but indicate that the ionizing fluxes fall in the range 10^{41}–10^{43}photon s^{-1}.

3.2 HeII:CIV Line Ratio

We also study the behaviour of the HeII:CIV line ratio, comparing the observed line ratios to the ratios of ionizing flux to total chromospheric power derived from the EM analysis above. The sample is small (5 objects), but it does indicate that a strong correlation between these two quantities, supporting the hypothesis that the line ratio is a useful diagnostic of the ionizing flux. In essence the ratio is a "hardness ratio", with a smaller value of the line ratio being indicative of a softer ionizing spectrum.

In order to study the evolution of the ionizing flux with time, we have made use of the data from the IUE final archive (Johns-Krull et al. 2000 [30]). From this we were able to obtain

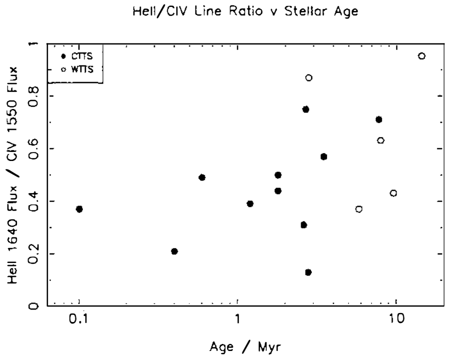

Figure 3: Plot of line ratio versus stellar age, with ages taken from Palla & Stahler (2002) [40]. The ratio stays approximately constant with age, as it does with all evolutionary indicators, and the highest values are from WTTS. (Figure from Alexander at al. 2004c [3].)

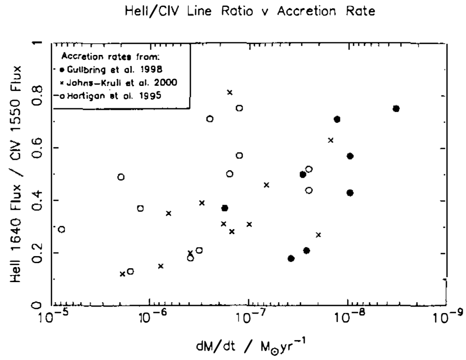

Figure 4: Plot of line ratio versus mass accretion rate, with objects "evolving" to the right. Three different sources are used for the accretion rates, each with their own different systematics, but the trend remains the same. (Figure adapted from Alexander at al. 2004c [3].)

HeII:CIV ratios for $\sim$ 40 sources. We then plot these line ratios against a number of evolutionary indicators, where such data exist (ie. mass accretion rate, stellar age, Hα equivalent width: see Figs.3 & 4). There is significant scatter in the data and the number statistics are unfavourable, but the general trends all show that the line ratio stays approximately constant against each age indicator, and if anything actually increases as the objects evolve. In addition, the highest values of the line ratio tend to come from WTTS, indicating that evolved systems do produce strong ionizing fluxes. The results show no dependence on other parameters (stellar M/R ratio, spectral type), and so we conclude that the ionizing flux produced by the chromosphere of TTS shows no evidence of any significant decline over the lifetime of the TTS phase of evolution.

3.3 Discussion

Our analysis is obviously crude, but given the lack of any existing observational constraints on this problem it does provide a valuable new insight. The dominant uncertainty in the ionizing flux values determined are due to reddening, and these are much greater than the uncertainties due to other potential sources of error. Thus we consider our order-of-magnitude estimates of 10^{41}–10^{43}photon s^{-1} to be plausible.

With regard to the line ratio, the dominant uncertainties lie in the use of the HeII 1640Å line. Firstly, the ionization energy for HeII is 54.4eV, and so the recombination lines only really give an indicator as to the presence of flux at wavelengths < 228Å, rather than 912Å. Thus we do not probe the region from 228Å–912Å directly. However it is difficult to envisage an emission mechanism which could produce photons in this spectra range without producing higher energy photons also, and so the HeII recombination lines should provide a reasonable indicator of the ionizing flux.

There is also the question of whether the HeII emission comes from radiative recombination or is due to collisional excitation. Studies of the solar corona show that both mechanisms play a role, and studies of the chromospheres of nearby bright stars have found similar results (eg. Linsky et al. 1995 [35], 1998 [36]). High resolution spectroscopy can be used to distinguish the two processes, as they result in very different line profiles, but unreasonably long exposure times are necessary when observing TTS (around 50 hours per source with HST!). However any plasma hot enough to produce significant collisional population of the $n = 3$ state of HeII (48.4eV above the ground state) would be expected to radiate significantly at wavelengths > 912Å through free-free radiation and bound-free transitions, and so the presence of strong HeII 1640Å emission should be a reliable indicator as to the presence of a strong ionizing flux in both cases. Also, the abscence of HeII 1640Å emission in the synthetic spectra derived from the EMs (which do not consider photo-excitation) supports the radiative recombination hypothesis. Other uncertainties, such as possible opacity in the CIV 1549Å line, are less significant that those discussed here.

The last potential problem regards getting the ionizing photons to the disc. We have already seen that the accretion shock is extremely optically thick to Lyman continuum photons, and the outflow/jet from the central source may be optically thick also (Shang et al. 2002 [44]). Thus it may be that chromospheric ionizing photons are absorbed before they can reach the disc. The location of the chromospheric emission is not well-established, however, and so this question remains open.

We have shown that TTS chromospheres do indeed seem to produce ionizing photons at a rate large enough to be significant in photoevaporation models, with ionizing fluxes in the range 10^{41}–10^{43}photon s^{-1}. Moreover we propose that the HeII:CIV line ratio may act as a diagnostic of the ionizing flux, and by studying archival data we find that the ionizing flux remains approximately constant as objects evolve. Thus chromospheric emission can be sufficient to drive disc photoevaporation, as required by the model of Clarke et al. (2001) [11].

4 X-ray driven disc winds?

A further possible source of disc heating is X-rays. Both CTTS and WTTS are known to be strong X-ray sources, with typical X-ray luminosities on the order of 10^{28}–10^{30}erg s^{-1} (eg. Feigelson & Montmerle 1999 [15]). Previous studies of the X-ray/disc interaction have focused primarily on using X-rays to sustain the low levels of ionization required to drive the magnetorotational instability (Glassgold et al. 1997 [20]; Igea & Glassgold 1999 [29]), or looked at the effect of X-ray heating on the observed spectrum (Glassgold & Najita 2001 [19]; Gorti & Hollenbach 2004 [22]). However they have not considered the potential this interaction has to drive a disc wind: here we make a preliminary study into the significance of this effect.

When soft X-rays, of the type emitted by TTS, are incident on a circumstellar disc a number of processes occur. These are discussed in great detail by Krolik & Kallman (1983) [32] (see also Glassgold et al. 2000 [21]); here we merely provide a short summary of the relevant points. The incident X-ray photons are absorbed by heavy elements (typically O or C, with some Fe absorption also). A single photoelectron is produced, with an energy essentially equal to that of the incident photon. This "primary" electron then collides with neutral hydrogen or helium in the gas, generating a large number ($\sim$ 30) of "secondary" electrons. This process accounts for the majority of the ionization, and thus heating, in our models. Collisional charge exchange between ionized heavy species and light neutrals accounts for a few percent of the total heating, and the Auger effect (2-electron decay) is negligible. In addition, we note that the probability of a diffuse X-ray field is very small, as recombinations producing X-rays are rare. Thus all the heating is along the line-of-sight - a significant difference from the UV case. Throughout the following modelling we assume solar gas composition, and adopt model parameters of $M_* = 1\mathrm{M}_\odot$ (stellar mass) and $M_d = 0.01\mathrm{M}_\odot$ (disc mass).

4.1 Basic Model

As a first iteration we construct a simple 1-dimensional model. Here we make the approximation that the disc can be divided into a series of concentric, non-interacting annuli. We adopt an initial steady disc model, with the disc surface density given by a R^{-1} power-law (eg. Beckwith et al. 1990 [6]) and the disc temperature given by

$$T(R) = \left(\frac{R}{1AU}\right)^{-1/2} 100\text{K} \tag{3}$$

Thus, by solving the equation of hydrostatic equilibrium, we can show that at each radius R the vertical structure of the disc is given by a Gaussian density profile (Pringle 1981 [42]) with a scale height

$$H(R) = \left(\frac{c_s^2 R^3}{GM_*}\right)^{1/2} \tag{4}$$

where c_s is the local isothermal sound speed.

We take our initial disc structure and, using the CLOUDY photoionization code, study what happens at each radius R when the disc is irradiated from above by X-rays. We adopt an X-ray source position of $R = 0$, $z_s = 10\text{R}_\odot$, a source luminosity of $L_X = 10^{30}\text{erg s}^{-1}$, and take the source spectrum to be that of 10^7K bremsstrahlung (typical of that observed in TTS). Thus we evaluate the flux, F_X, downwardly incident on each annulus as

$$F_\text{X} = \frac{L_\text{X}}{4\pi R^2} \frac{z_s}{\sqrt{R^2 + z_s^2}} \tag{5}$$

where the first term represents simple geometric dilution of the energy, and the second the sine of the incidence angle. For a given density structure CLOUDY returns a temperature profile $T(z)$. Thus by solving the equation of hydrostatic equilibrium in the non-isothermal case at each radius R we generate a new density profile and are able to iterate towards a self-consistent structure. The results of this procedure at $R = 10\text{R}_\odot$ are shown in Fig.5. Above some reference point, the temperature rises gradually to around 10,000K. In order to heat to higher temperatures than this the disc material must be mostly ionized, and so only the very low density upper regions of the disc are heated to >10,000K. The density structure is actually well-fit by a two-temperature structure, with a best-fit temperature of 6200K in the upper region. However this 1D model breaks down at radii $\gtrsim 30\text{R}_\odot$, as the disc expands to a height comparable to the source height, and so the approximation of downward incidence (Equation 5) is no longer valid. Thus we must construct a 2-dimensional model in order to study the behaviour at larger radii.

4.2 2D Model

We extend the model to consider a simple 2D case as follows. As the vertical structure of the disc is well-modelled by the two-temperature profile described above, the critical factor in determining the overal structure of the disc is the location of the transition point between the heated and cold regions. This in turn is determined by how far the X-rays penetrate into the disc. Thus we can solve for the location of the transition point we can determine the effects of the X-ray heating.

The X-rays penetrate the disc along the line-of-sight to a critical value of the parameter

$$\xi = \frac{L_X J_h}{nd^2} \tag{6}$$

where n is the local particle number density, d the distance along the line-of-sight to the source and where the factor J_h accounts for the attenuation of the flux due to absorption along the line-of-sight (Krolik & Kallman 1983 [32]). Essentially ξ represents the photon to particle density ratio at a given location. We evaluate the attenuation factor numerically by integrating the column along the line-of-sight, and then using the approximate parametrization for J_h derived by Glassgold et al. (1997) [20].

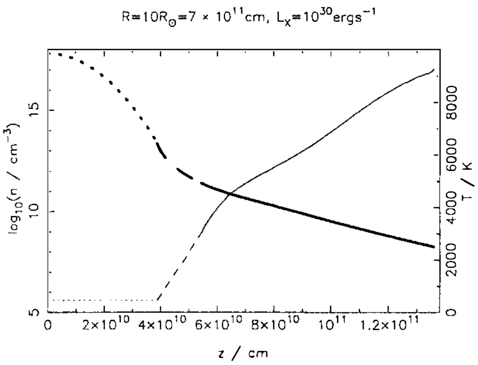

Figure 5: Density (heavy line) and temperature (lighter line) profiles evaluated by 1D model at a radius of $10R_\odot$. The solid region is calculated explicitly by the model, the dashed region is extrapolated, and the dotted region represents the isothermal midplane. The steepening of the $T(z)$ curve with decreasing z is due to the increased efficiency of 2-body cooling as the density incereases. (Figure from Alexander at al. 2004b [2].)

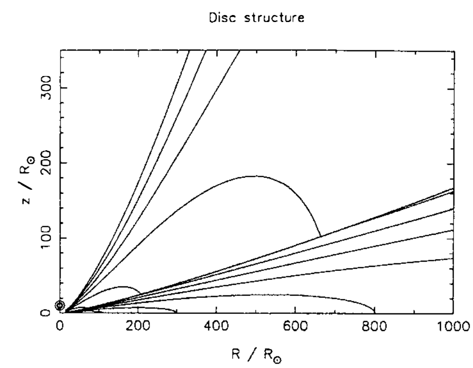

Figure 6: Structure of the X-ray heated disc evaluated by the 2D model. Density contours are drawn at $n = 10^{15}, 10^{14}, 10^{13}\ldots10^{3}$cm^{-3}. The location of the X-ray source at $R = 0$, $z_s = 10R_\odot$ is marked by circles. The transition point is clearly visible at the point where several contours are overlaid. Most of the X-ray attenuation occurs at $R \lesssim 100R_\odot$. (Figure from Alexander at al. 2004b [2].)

We use the inner disc structure obtained from our 1D model to produce a "starting" structure in the region $R = 10$–$20R_\odot$. From this we determine the critical value of the ionization parameter to be $\xi_c \simeq 10^{-8}$erg cm s^{-1}. As the attenuation through the disc to a given radius R depends only on the disc structure at radii less than R, we can evaluate ξ at all values of z at this radius. The value which gives $\xi = \xi_c$ is adopted as the transition point for radius R, and so we can generate a vertical structure at R and iterate outwards through the disc. Thus we solve for the disc structure on a regularly-spaced (R, z) grid, with grid spacings of $2R_\odot = 1.39 \times 10^{11}$cm in R and 10^9cm in z. Runs at higher resolution over a smaller spatial extent indicate that the numerical accuracy of this procedure is better than 10%. The disc structure obtained is shown in Fig.6.

We are able to make a crude estimate of the mass-loss that can be driven by X-rays by evaluating the mass-loss per unit area as ρc_s at the base of the heated column at the gravitational radius. The number density at the base of the column is $\simeq 10^5$cm^{-3}, which gives a value of for the mass-loss per unit area of $\simeq 10^{-13}$g cm^{-2} s^{-1}. This is comparable to the value for UV photoevaporation evaluated by Hollenbach et al. (1994) [27], who derive a value of 3.88×10^{-13}g cm^{-2} s^{-1} for an ionizing flux of 10^{41}photons s^{-1}. However our value is to be regarded as an upper limit, for the reasons outlined below, and so we find that X-ray photoevaporation is at most comparable to UV photoevaporation, and almost certainly much less significant.

4.3 Discussion

There are a number of simplifications in our model, but two are of particular significance. Firstly, there is the manner in which we evaluate the vertical structure. The 2-temperature structure is adopted as it is a good fit to the results of the 1D model. However in the 1D model the CLOUDY code only solves explicitly for the structure at temperatures greater than 3000K (the code is not stable below this point). We assume that the temperature gradient is smooth at temperatures below this, and extrapolate down to the midplane temperature linearly (see Fig.5). This essentially puts the hot/cold transition point at as low a vertical position, and therefore as high a density, as the model permits. In reality it seems likely that there will be an extended column of "warm" ($\sim$ 1000K) material (eg. Glassgold & Najita 2001 [19]; Gorti & Hollenbach 2004 [22]). In this case the hot temperatures required to drive mass-loss are only reached at higher z than in our model. As the density falls exponentially with z, even a relatively small warm column will significantly reduce the density at the base of the hot region, and so the "true" mass-loss rate will likely be significantly lower than that predicted by our model.

The other main simplification of our 2D model is the assumption of a constant temperature in the heated region. This is a best-fit, but tends to under-estimate the density at high z compared to the 1D models (as the temperature rises with increasing z). Most of the attenuation along the line-of-sight to the outer regions of the disc comes from material at radii $\lesssim 50R_{\odot}$, where the 1D approximation is still valid. By under-estimating the density at high z in this regions we in turn under-estimate the attenuation along the line-of-sight to the outer disc, and therefore in turn over-estimate the depth to which the X-rays penetrate the disc at larger radii. A more realistic temerature profile would therefore be expected to decrease the calculated mass-loss rate somewhat. A number of less significant approximations are also made, but are not discussed here for reasons of paper length.

Our 2D model is simplistic, and more realistic models are clearly needed to firm up our conclusion. However we are satisfied that our model represents a "best case" model, designed to maximise the mass-loss, and so we consider the derived mass-loss rate to be an upper limit. The true rate is most likely significantly lower. In the absence of any significant Lyman continuum flux an X-ray driven disc wind could be significant. However it seems that UV driven winds do exist, and so we do not consider it likely that X-ray driven disc winds are significant in dispersing circumstellar discs.

5 Summary

In this contribution we have reviewed models of disc photoevaporation, and considered several different means to resolve the major uncertainty with these models: the ionizing flux. We have shown that the accretion shock is unlikely to power disc photoevaporation, due to the extremely high optical depth of the accretion column. Similarly, it seems unlikely that X-rays can drive a significant disc wind, although more detailed calculations are needed to confirm this result. Studies of TTS chromospheres, however, seem to indicate that the chromosphere does produce a sufficient ionizing flux. Plasma modelling, using previously derived emission measures, indicate that the typical ionizing flux is in the range 10^{41}–10^{43}photon s^{-1}, and by using the ultraviolet HeII:CIV line ratio as a hardness ratio we have shown that this flux is not expected to change significantly as the TTS evolve. Thus there does appear to be an ionizing flux sufficient to drive these models, and so they remain an interesting area of study.

Acknowledgments

RDA acknowledges the support of a PPARC PhD studentship, and also thanks the EC-RTN for supporting his attendance at this conference. CJC gratefully acknowledges support from the Leverhulme Trust in the form of a Philip Leverhulme Prize.

References

1. Alexander, R.D., Clarke C.J., Pringle, J.E., 2004a, MNRAS, 348, 879
2. Alexander, R.D., Clarke C.J., Pringle, J.E., 2004b, MNRAS submitted
3. Alexander, R.D., Clarke C.J., Pringle, J.E., 2004c, in preparation
4. Armitage, P.J., Clarke, C.J., Tout, C.A., 1999, MNRAS, 304, 425
5. Armitage P.J., Clarke C.J., Palla F., 2003, MNRAS, 342, 1139

6. Beckwith S.V.W., Sargent A.I., Chini R.S., Güsten R., 1990, AJ, 99, 924
7. Bontemps, S., André, P., Kaas, A.A. et al., 2001, A&A, 372, 173
8. Brooks, D.H., Costa, V.M., Lago, M.T.V.T., Lanzafame, A.C., 2001, MNRAS, 327, 177
9. Brooks, D.H., Costa, V.M., 2003, MNRAS, 339,467
10. Calvet N., Gullbring E., 1998, ApJ, 509, 802
11. Clarke C.J., Gendrin A., Sotomayor M., 2001, MNRAS, 328, 485
12. Costa, V.M., Lago, M.T.V.T., Norci, L., Meurs, E.J.A., 2000, A&A, 354, 621
13. Dere, K.P., Landi, E., Mason, H.E., Monsignori Fossi, B.C., Young, P.R., 1997, A&AS, 125, 149
14. Duvert, G., Guilloteau, S., Ménard, F., Simon, M., Dutrey, A., 2000, A&A, 355, 165
15. Feigelson, E.D., Montmerle, T., 1999, ARA&A, 37, 363
16. Ferland G.J., 1996, *A Brief Introduction to* CLOUDY, University of Kentucky Department of Physics and Astronomy Internal Report
17. Font, A.S., McCarthy, I.G., Johnstone, D., Ballantyne, D.R., 2004, ApJ, 607, 890
18. Ghosh P., Lamb F.K., 1978, ApJ, 223, L83
19. Glassgold, A.E., Najita, J., 2001, in ASP Conference Series 244, 251
20. Glassgold, A.E., Najita, J., Igea, J., 1997, ApJ, 480, 344 (Erratum: ApJ, 485, 920)
21. Glassgold, A.E., Feigelson, E.D., Montmerle, T., 2000, in Mannings, V., Boss. A.P., Russell, S.S., eds, Protostars & Planets IV. Univ. Arizona Press, Tuscon, p. 429
22. Gorti, U., Hollenbach, D., 2004, ApJ in press (astro-ph/0405244)
23. Gullbring E., Calvet N., Muzerolle J., Hartmann L., 2000, ApJ, 544, 927
24. Haisch K.E., Lada E.A., Lada C.J., 2001, ApJ, 553, L153
25. Hartigan, P., Edwards, S., Ghandour, L., 1995,ApJ, 452, 736
26. Hartmann L., Calvet N., Gullbring E., D'Alessio P., 1998, ApJ, 495, 385
27. Hollenbach D., Johnstone D., Lizano S., Shu F., 1994, ApJ, 428, 654
28. Hollenbach, D.J., Yorke, H.W., Johnstone, D., 2000, in Mannings, V., Boss. A.P., Russell, S.S., eds, Protostars & Planets IV. Univ. Arizona Press, Tuscon, p. 401
29. Igea, J., Glassgold, A.E., 1999, ApJ, 518, 848
30. Johns-Krull C.M., Valenti J.A., Linsky J.L., 2000, ApJ, 539, 815
31. Kenyon, S.J., Hartmann, L., 1995, ApJS, 101, 117
32. Krolik, J.H., Kallman, T.H., 1983, ApJ, 267, 610
33. Kurucz R.L., 1992, in Barbuy, B., Renzini, A., eds, Proc. IAU Symp. 149, Stellar Populations of Galaxies. Kluwer, Dordrecht, p. 225
34. Lada, C.J., Lada, E.A., 2003, ARA&A, 41, 57
35. Linsky, J.L., Wood, B.E., Judge, P., Brown, A., Andrulis, C., Ayres, T.R., 1995, ApJ, 442, 381
36. Linsky, J.L., Wood, B.E., Brown, A., Osten, R.A., 1998, ApJ, 492, 767
37. Mannings V., Sargent A.I., 1997, ApJ, 490, 792
38. Matsuyama I., Johnstone D., Hartmann L., 2003, ApJ, 582, 893
39. Najita, J., Carr, J.S., Mathieu, R.D., 2003, ApJ, 589, 931
40. Palla, F., Stahler, S.W., 2002, ApJ, 581, 1194
41. Persi, P., Marenzi, A.R., Olofsson, G. et al., 2000, A&A, 357, 219
42. Pringle, J.E., 1981, ARA&A, 19, 137
43. Richling S., Yorke, H.W., 1997, A&A, 327, 317
44. Shang, H., Glassgold, A.E., Shu, F.H., Lizano, S., 2002, ApJ, 564, 853
45. Simon, M., Prato, L., 1995, ApJ, 450, 824
46. Skrutskie, M. F., Dutkevitch, D., Strom, S.E., Edwards, S., Strom, K.M., Shure, M.A., 1990, AJ, 99, 1187
47. Wolk, S.J., Walter, F.M., 1996, AJ, 111, 2066

SEARCHING FOR X-RAY IRRADIATION EFFECTS ON MOLECULAR CLOUDS

T. Montmerle (1), M.H. Vuong (2)

(1) Laboratoire d'Astrophysique de Grenoble
BP 53X, 38041 Grenoble Cedex, France
(2) ESO, DMD Division, 85748 Garching, Germany

All young stars emit X-rays at high levels: low-mass stars as a result of magnetic activity, high-mass stars as a result of shocks from instabilities in their radiative winds. In addition, diffuse X-ray emission is coming from large cavities created by the strong winds of very massive stars (spectral type O5 and earlier). Thus, in regions of massive star formation like M17, a new paradigm emerges to replace the traditional "Strömgren sphere": that of "hollow HII regions" filled with a multimillion-degree gas. The total X-ray emission is then shared roughly equally between pointlike (stars) and diffuse (hot gas) X-ray emission. This emission irradiates the surrounding molecular cloud, giving rise to a variety of effects, the main one being ionization and the associated gas chemistry involving radicals. However, UV photons are able to travel over large distances in the tenuous, external parts of molecular clouds, masking at least in part the effects of X-ray irradiation, as shown by a detailed multi-wavelength study of M17.

Keywords: HII regions, star formation, X-rays, stellar winds, ISM chemistry, M17

1 Introduction: Why should molecular clouds be irradiated by X-rays ?

1.1 "Internal" irradiation by Young Stellar Objects

After more than twenty years of observations of star-forming regions by X-ray satellites (i.e., since the pioneering days of X-ray imaging with the *Einstein Observatory* in the 80's), it is now well-known that young stars, both low-mass and high-mass, are conspicuous X-ray emitters. This is illustrated by two recent cases: the ρ Oph cloud core, with spectral types B2 and later, and the Orion Nebula Cluster (ONC), with spectral types O7 and later. Fig. 1 shows a 30 ksec XMM image of the ρ Oph cloud ($d \simeq 140$ pc) of $\sim 30'$ radius centered on the core F (Ozawa,

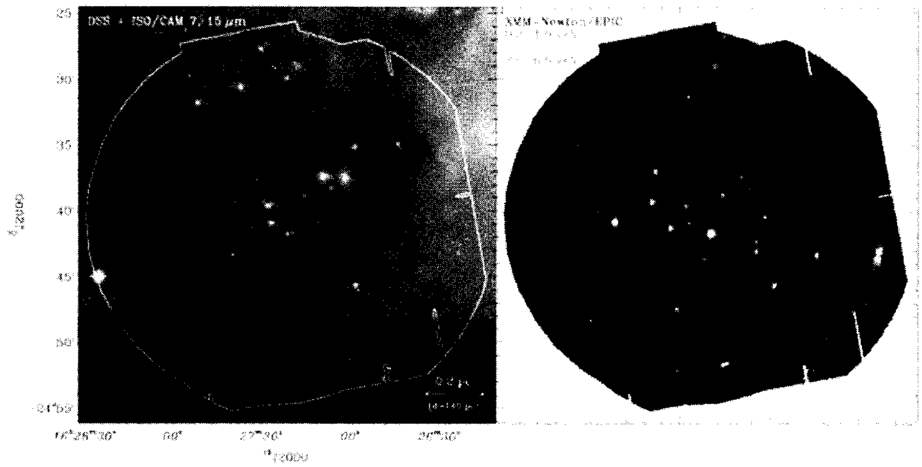

Figure 1: The ρOph cloud core F, where most of the star formation activity currently takes place. *Left:* ISOCAM mid-IR image, with the XMM field-of-view outlined. *Right:* XMM image of the same region. Note the tilted "Y"-shaped cluster of protostars at the center, conspicuous both in the IR and X-ray images (Ozawa et al. 2005)

Grosso, & Montmerle 2005) (right), together with the ISOCAM mid-IR image of the same area (Abergel et al. 1996) (left). The bright IR sources in the center are a cluster of so-called Class I protostars (evolved, accreting protostars with a thin circumstellar envelope, age $\approx 10^5$ yrs), embedded in the cloud core, surrounded by several dozens of fainter, more evolved T Tauri stars, with (Class II) and without (Class III) circumstellar disks, with ages $\sim 10^6 - 10^7$ yrs. With a nearly one-to-one correspondence, these IR sources have X-ray counterparts, numbering about 90 objects in ρ Oph (Ozawa et al. 2005). Similarly, as shown in Fig. 2 and perhaps even more spectacularly so, a deep (750 ksec) *Chandra* image of the ONC ($d \simeq 450$ pc), shows an excellent correspondence between stellar IR and X-ray sources for all spectral types (Getman et al. 2005), in a sample of over 1,600 sources concentrated in the $17' \times 17'$ field-of-view. In both cases, the mass range extends all the way down to the brown dwarf regime, with luminosities (in erg s^{-1}) from $\log L_X \sim 32$ down to $\log L_X \sim 27$, i.e. the X-ray luminosity of the active present-day Sun. On average, one finds $L_X/L_{bol} \sim 10^{-4} - 10^{-3}$ for low-mass stars, which generate X-rays via enhanced solar-like magnetic activity (e.g., Feigelson & Montmerle 1999, Favata & Micela 2003), and $L_X/L_{bol} \sim 10^{-6} - 10^{-7}$ for high-mass stars, which generate X-rays by radiative wind shocks (e.g., Owocki & Cohen 1999), either expanding freely or confined by a large-scale magnetosphere (e.g., Stelzer et al. 2005).

In other words, the surroundings of young stars, especially while these are embedded in molecular clouds (which is essentially the case for low-mass stars, which constitute the vast majority of the young stellar population), are exposed to the X-ray "internal" irradiation of hundreds to thousand stars.

1.2 "External" irradiation by OB associations

It is not always realized that molecular clouds are in general not truly isolated, but lie in the vicinity of other molecular clouds which, in turn, may harbor massive stars in various states of evolution, including *post-mortem* supernovae (SN). This is the case in particular for the Gould

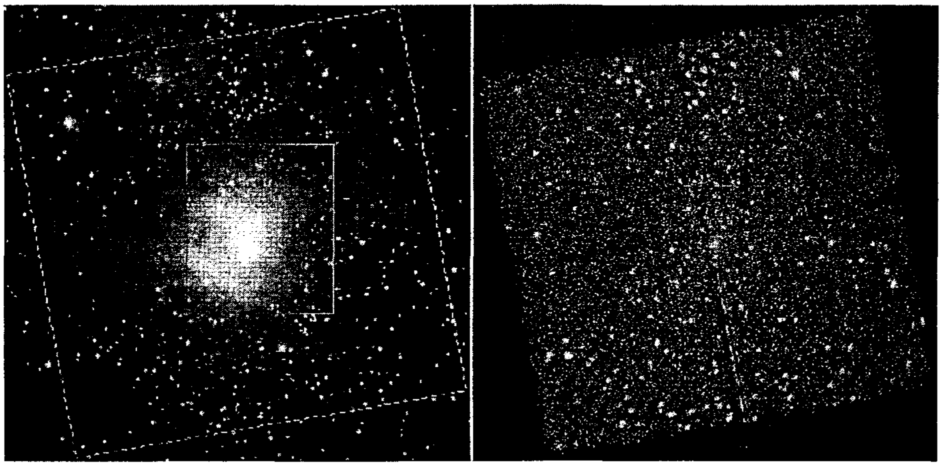

Figure 2: The Orion Nebula Cluster. Same as Fig. 1, but with different instruments. *Left:* 2MASS (near-IR) image. *Right: Chandra* image of the same region. Note the excellent visual correspondence between the IR and X-ray images, which is confirmed by a detailed study (Feigelson et al. 2002, Getman et al. 2005).

Belt, an expanding approximate ring of early-type stars and molecular clouds filled with the "Local Bubble", a hot, million-degree gas originating in SN explosions a few 10^7 yrs ago (e.g., Lallement 2004, and Breitschwerdt, this volume). For instance, the ρ Oph cloud mentioned above, a region of low-mass star formation, is located in front of the Sco-Cen-Lup-Crux chain of OB associations part of the Gould Belt. Under the influence of strong winds from massive stars, and/or SN explosions, an extended X-ray bubble is associated with this chain, irradiating the cloud from "outside". In this and other regions, the bubble is visible in the 0.1-2 keV ROSAT All-Sky Survey (Snowden et al. 1995), as shown in Fig. 3.

Another, novel situation may arise. In the early stages of an OB association, i.e., before any Wolf-Rayet star or SN explosion has appeared, the winds of the most massive stars will blow a cavity in the associated HII region. Due to the high velocity of these winds (typically a few 1,000 km s^{-1}), shocks will be generated at the cavity boundary, and diffuse X-rays will be emitted on a large scale, much like a "standing" supernova remnant. Theoretical predictions have been made for nearly 30 years (see next Section), but it is only recently that an unambiguous observational proof of the existence of diffuse X-rays has been obtained. In this paper, we will concentrate on this aspect of X-ray emission associated with molecular clouds and their resulting irradiation effects.

2 Diffuse X-ray emission from HII regions

2.1 M17: a case study

The M17 nebula, also known as the "Omega" nebula, is one of the brightest HII regions in the Milky Way. Located at $d \sim 2$ kpc from the Sun, it is excited by 13 O stars, with spectral types ranging from O3 (the most massive stars in the Galaxy) to O9.5, and 34 B stars (Townsley et al. 2003, and refs. therein). Whereas its appearance in Hα images is that of a filled nebula, in 2MASS images it appears as a "hollow" nebula, with a clear cavity around the O star cluster

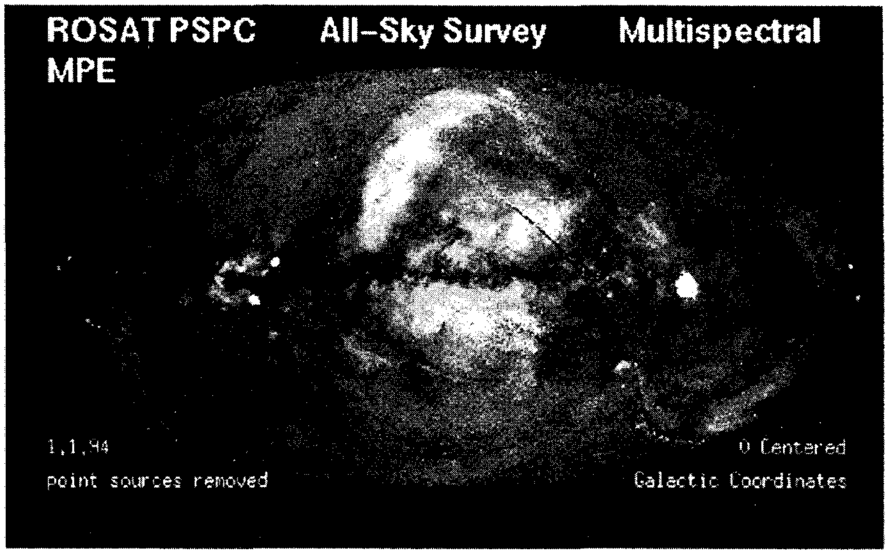

Figure 3: The "multispectral" X-ray sky, as seen by *ROSAT*. The X-ray energy is 0.1-2 keV, so is very sensitive to extinction along the line of sight at low energies. The very large extended structure, covering almost half of the sky in the direction of the Galactic Center, is the so-called "Local Bubble". This is a network of old supernova remnants (several million years at least), filling the interstellar medium up the the nearest star-forming regions of the "Gould Belt", like Ophiuchus or Orion (e.g., Lallement 2004).

(see Fig. 4), far from the classical picture of a Strömgren sphere. Thus a first question arises: what causes such a cavity to exist ?

X-ray observations recently completed with *Chandra*, as we will summarize in this contribution, hold the answer – for the first time. As explained above, one *a priori* expects X-ray emission to be stellar in origin. Low-mass stars (like T Tauri stars), with masses lower than a few solar masses, emit X-rays as a result of their magnetic activity. Making the reasonable assumption that the ONC X-ray luminosity function (XLF) holds in nebulae like M17, scaled in their overlapping intermediate- to low-mass ranges, *thousands* of X-ray sources associated with low-mass stars are expected to be present, each emitting $L_X \sim 10^{27}$ to 10^{32} erg s^{-1}, along with dozens of OB stars with L_X up to $10^{33} - 10^{34}$ erg s^{-1}. Altogether, thousands of intense *stellar* X-ray sources are necessarily present in regions of massive star formation.

However, the *Chandra* image revealed another component, in terms of *large-scale extended emission*, not only filling the 2MASS cavity, but stretching away form the O star cluster. In order to check whether this emission was diffuse or just the sum of unresolved faint sources (for example from a large number of X-ray faint very low-mass stars), it was necessary to proceed along several steps: (i) remove resolved point sources, via an appropriate "swiss-cheese" algorithm; (ii) based on the resulting X-ray luminosity function and making a reasonable assumption on its extrapolation to very low masses following the IMF, estimate the contribution of unresolved sources. In M17, Townsley et al. (2003) were able to remove $\sim$ 900 resolved sources, and estimate that $\sim$ 4500 unresolved faint sources contributed to the extended emission. In spite of this large number, the contribution of the unresolved sources turned out to be a small fraction ($\sim$ 8%) of the total extended emission. In other words, $\sim$ 92% of the extended emission had to be genuinely diffuse, as emitted by a large volume of hot ($T \sim 10^7$ K) gas. This result was confirmed by examining an archival pointed image from *ROSAT* (Dunne et al. 2003), which, by

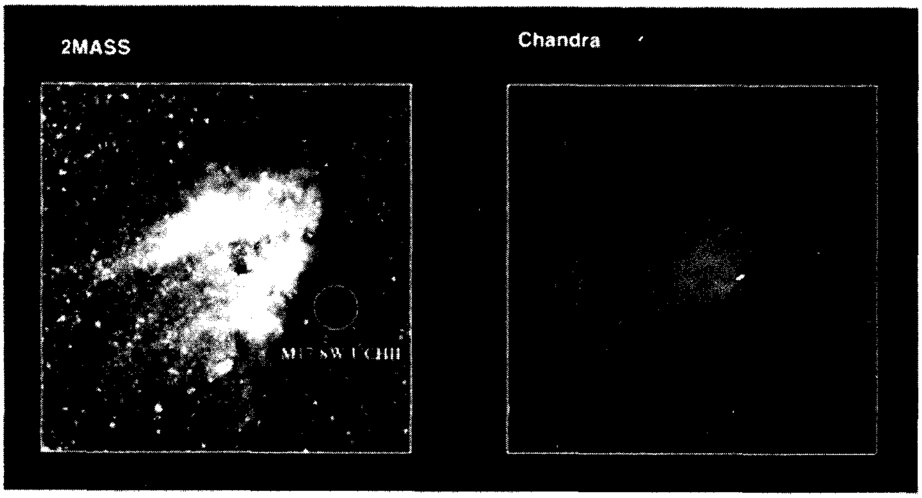

Figure 4: M17 seen by 2MASS (left), and by *Chandra* (right). The square is the *Chandra* field of view ($17' \times 17'$). The correspondance between the cavity around the cluster of exciting OB stars and the extended X-ray emission is striking, showing that a diffuse, hot X-ray emitting gas fills the cavity. See Fig. 2 for comparison.

itself, could not demonstrate the existence of truly diffuse emission because of its poor angular resolution (up to 10") compared with *Chandra*.

2.2 Hollow HII regions

Thus, at long last, a nearly 30-yr old prediction has become verified. This prediction was based on the fact that the winds from massive stars should create a hot, X-ray emitting bubble, heated by the wind terminal shock at the interface with the surrounding dense material (e.g., Castor, McCray & Weaver 1975, Weaver et al. 1977), shaping "hollow HII regions" (Dorland, Montmerle, & Doom 1986), and maintaining pressure equilibrium with an outer HII shell, ionized by the UV flux of the massive stars ("photodissociation regions", or PDR). Demonstrating the existence of diffuse hot gas in wind-powered nebulae had to wait for an unambiguous removal of the unresolved source component owing to both the superb angular resolution of *Chandra* ($\sim$ 0.7" FWHM on-axis), and to appropriate sofware for removing the resolved component. In addition to M17, other "hollow HII regions" associated with diffuse X-ray emission have been found with *Chandra*: RCW38 (Wolk et al. 2002), 9 Sgr (Rauw et al. 2002), etc. All these regions, however, are excited by stars of spectral type $\sim$ O5 and earlier (i.e., stars more massive than $M_\star \approx 30 - 40 M_\odot$), showing the importance of the "mechanical" wind component to generate diffuse X-rays, as opposed to the usual radiative UV component. By comparison, no diffuse X-rays are seen in the ONC (Fig. 2), in which the exciting stars do not have spectral types earlier than O7 ($M_\star \approx 20 M_\odot$).

For M17, the resulting census of the X-ray emission is as follows (Townsley et al. 2003):

- *Stellar component:* OB stars: $L_{X,OB} \simeq 6.1 \times 10^{33}$ erg s^{-1}; T Tauri stars (resolved): $L_{X,TTS} \simeq 4.1 \times 10^{33}$ erg s^{-1}.
- *Diffuse (gas) component:* $L_{X,gas} \simeq 3.4 \times 10^{33}$ erg s^{-1}
- Total X-ray luminosity: $L_{X,M17} \simeq 10^{34}$ erg s^{-1}, or $\approx$ 10,000 average T Tauri stars.

This X-ray luminosity, both its stellar and gaseous components, is spread over a large volume (> 10 pc^3), and thus is able to produce large-scale irradiation interactions with the surrounding molecular cloud, as described in the next section.

3 X-ray irradiation effects in a nutshell

When an X-ray photon interacts with the interstellar material, it interacts in practice with *heavy atoms*, in any form (ionized, neutral, or molecular, or in dust grains), by ioinizing them as a result of the photoelectric effect on their inner shells (K, L). The first ejected electrons carry away a substantial fraction of the X-ray incident energy (≈ 1 keV), and thus triggers a *secondary electron cascade*, which in turn ionizes other atoms. In the process, about 40 secondary electrons are produced per initial photoionization, so that each has an energy ≈ 25 eV, and thus is able to ionize in particular H and He (e.g., Wilms et al. 2000, Glassgold, Feigelson, & Montmerle 2000). Because molecules become ionized (radicals), they are able to react strongly with other molecules, producing a variety of chemical reactions.

X-rays are thus able, directly (via the photoelectric effect), or indirectly (via secondary electron cascades), to penetrate much deeper in molecular clouds than UV photons. The absorption cross-section varies with the X-ray energy E_X as $E_X^{\sim -2.5}$ (e.g. Galssgold et al. 2000); the opacity of interstellar material (gas + dust) for 1 keV photons is $\tau_{1keV} \sim 1$ for an equivalent column density $N_H \sim 5 \times 10^{21}$ cm^{-2}, or equivalently for a visual magnitude $A_V \sim 3 - 4$ (e.g., Vuong et al. 2003): hard X-rays ($\sim$ 2-3 keV) can penetrate up to $A_V \sim 100$, e.g., into dense cores where protostars form. Conversely, in tenuous media, such as the outer layers of molecular clouds ($n_H \sim 100$ cm^{-3}, say), X-rays can travel several pc, which is a significant fraction of the cloud size, before being significantly absorbed, hence leave a trace of their ionizing interactions all along the way, in the form of "anomalous" chermistry.

4 ISO spectral observations of M17: a mystery ?

ISO (1995-1998) was an ESA satellite equipped with a mid-IR camera (ISOCAM), a far-IR spectrograph (ISOPHOT), and two spectrometers, the SWS (Short-Wavelength spectrometer) and the LWS (Long-Wavelength spectrometer). As displayed in Fig. 5, a series of observations of M17 were made across the boundary between the cavity, the HII gas, and the molecular cloud (Cesarsky et al. 1996). These observations and the complementary analysis of the SWS and LWS archival results by Vuong (2004) revealed the existence of fine structure lines of highly ionized species along the line of sight. Also, the observations, summarized in Fig. 6, showed a large excess of C^+ in the direction of the supposedly neutral molecular cloud. Could this excess be evidence for X-ray irradiation ?

A powerful way to understand the origin of the extended ionized component is to consider the OIII line ratio diagnostic. According to the calculations of Rubin et al. (1994), the 52μm/88μm ratio is directly related to the density of the emitting gas. This is because OIII recombines mainly via charge exchange reactions. In order to keep a ratio ≈ 2, as observed in M17, with a recombination rate as fast as 10^{-9} s^{-1} (Honvault et al. 1995), a high photon flux has to be maintained. As shown by Vuong (2004), in spite of the fact that X-rays can ionize OI into OIII, the actual X-ray flux is insufficient to maintain the ionization level against the recombination rate. The OIII emission with the observed line ratio must therefore come from a *warm, low-density gas*, with a density $n < 100$ cm^{-3}. Such a gas is however invisible in "standard" Hα images; in the radio continuum range at 330 MHz , there is a sharp "wall" at the boundary of the molecular cloud (Subrahmanyan & Goss 1996). One can however calculate that the upper limit to the electron density along the line of sight to the cloud deduced from these radio observations is $n_e \simeq 100$ cm^{-3}, so that the OIII emitting material is in fact undetectable in the radio.

However, as displayed in Fig. 7 very faint Hα images (from *SuperCOSMOS*) do show emission past the radio "wall" towards the molecular cloud. Because the Hα image is uncalibrated, it

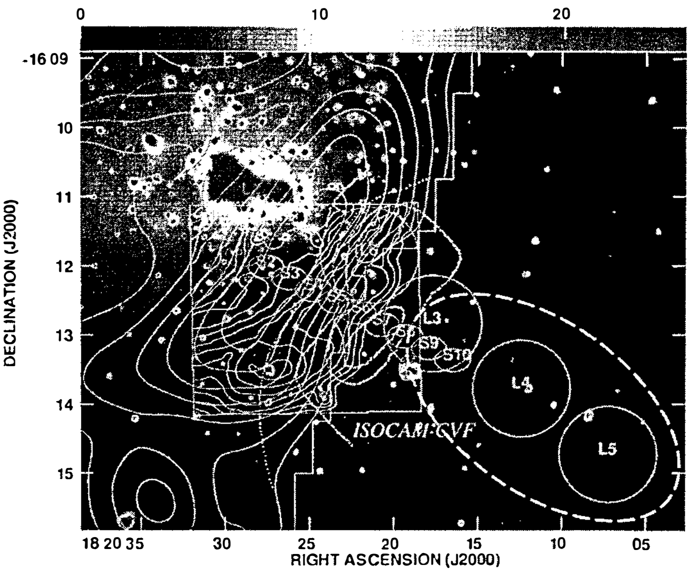

Figure 5: ISO pointings of M17, superimposed on the *Chandra* image, from the O star cluster (saturated region in the upper left corner) into the molecular cloud. Square: ISOCAM field of view; S*n*: SWS pointings; L*n*: LWS pointings (dashed ellipse: fields in the direction of the molecular cloud). Thin, closely spaced isophotes: 330 MHz emission; loose isophotes: IRAS 100 μm emission.

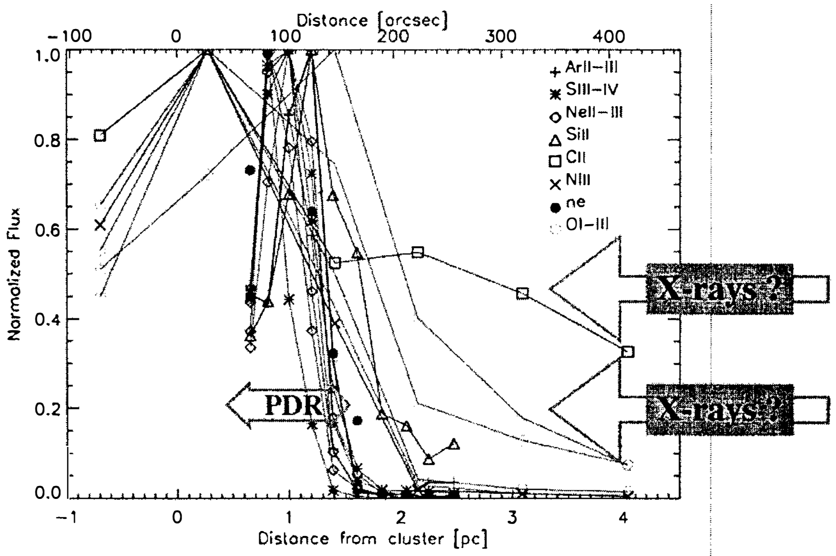

Figure 6: Line fluxes from SWS and LWS measurements, at the position indicated in Fig. 5, normalized to the peak of the emission. The peak corresponds to the PDR, as expected. However, substantial emission, mainly of OIII and CII, is detected past the PDR into the molecular cloud.

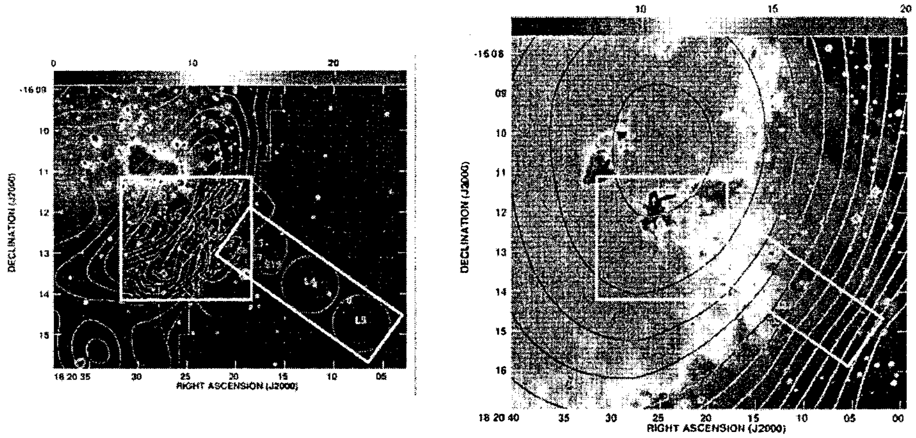

Figure 7: *Chandra* and *ISO* observations (identical to Fig.3, left), vs. the Hα emission (from *SuperCOSMOS*) overlapping the molecular cloud (right). Contours: 330 MHz emission. The LWS measurements turn out to be along the line of sight to a faint, extended Hα emission. The corresponding UV-ionized low-density gas is likely responsible for the OIII emission. *Squares:* ISOCAM field-of-view. *Rectangle:* LWS measurements, revealing the CII and OIII excess emission visible in Fig. 6.

is not possible to calculate the electron density in the gas responsible for the faint Hα emission, to verify that it is consistent with its non-detection at 330 MHz. But it does show that UV photons from the exciting O star cluster are able to "by-pass" the cloud and ionize its diffuse, low-density external regions, and that they must be responsible for the OIII emission. The case for the C^+ excess far from the exciting cluster is less clear, because it extends much farther than the faint Hα emission, over distances of a few pc comparable to the penetration depth of soft X-rays in a medium with estimated density $n_H \approx 100$ cm^{-3}: in that case, the X-rays may be responsible for the C^+ excess, but the actual volume density of the medium which the X-rays irradiate is unfortunately unknown. On the other hand, a contribution from the ambient interstellar UV field cannot be excluded.

5 Conclusions

M17 (and other massive star-forming regions with exciting stars of spectral types O5 and earlier), is the seat of an intense X-ray luminosity, shared roughly equally between the usual stellar emission from dozens of OB stars, from thousands of lower-mass, late-type stars, and from a hot gas filling a wind-supported cavity, predicted nearly 30 yrs ago. Therefore, strong X-ray irradiation effects are expected in the parent molecular cloud, in particular the existence of ionized species inside a normally neutral, molecular medium.

However, OB stars also generate a huge flux of UV photons, responsible for the very existence of the HII region in a shell around the central cavity (PDR). Apparently, a significant flux of UV photons manages to escape the densest parts of the parent molecular cloud and ionize the gas beyond the classical PDR. This diffuse, faint ionization, otherwise unseen, becomes visible in the form of the mid-IR OIII lines detected by the ISO spectrographs, and overrules the ionization expected from X-rays. Further away, a few pc from the exciting massive star cluster, X-ray ionization may be responsible for the extended C^+ emission, not excluding a contribution from the ambient interstellar UV field.

All in all, on the basis of the present tracers of low-density ionized gas alone like faint Hα, OIII, and even C^+, it seems difficult to disentangle the respective roles of UV and X-ray irradiation. Other tracers of *high-density* gas, such as HCO^+ or DCO^+, are needed to single out the effects of pure X-ray irradiation inside dense regions of molecular clouds, because the UV photons would then be entirely absorbed, but no such measurements exist for the time being in massive star-forming regions like M17.

References

1. Abergel, A., et al. 1996, A&A, 315, L329
2. Castor, J., McCray, R., & Weaver, R. 1975, ApJ, 200, L107
3. Cesarsky, D., et al. 1996, A&A, 315, L309
4. Dorland, H., Montmerle, T., & Doom, C. 1986, A&A, 160, 1
5. Dunne, D.C., et al. 2003, ApJ, 590, 306
6. Favata F. & Micela M., 2003, Sp. Sci. Rev., 108, 577
7. Feigelson E. D. & Montmerle T., 1999, ARA&A, 37, 363
8. Getman, K., et al. 2005, ApJ COUP Special Issue, in press
9. Glassgold, A. E., Feigelson, E. D., & Montmerle, T. 2000, in *Protostars and Planets IV* (Tucson: University of Arizona Press; eds Mannings, V., Boss, A.P., Russell, S. S.), p. 429
10. Honvault P., et al. 1995, A&A, 302, 931
11. Lallement R. 2004, A&A, 418, 143
12. Owocki S. P. & Cohen D. H., 1999, ApJ, 520, 833
13. Ozawa, H., Grosso, N., Montmerle, T. 2005, A&A, 429, 963
14. Rauw, G., et al. 2002, A&A, 394, 993
15. Rubin, R.H., et al. 1994, ApJ, 420, 772
16. Snowden, S.L., et al. 1995, ApJ, 454, 643
17. Stelzer, B., et al. 2005, ApJ COUP Special Issue, in press
18. Subrahmanyan, R., & Goss, W.M. 1996, MNRAS, 281, 239
19. Townsley, L.K., et al. 2003, ApJ, 593, 874
20. Vuong, M.H. 2004, PhD Thesis, Université Paris XI
21. Vuong, M.H., et al. 2003, A&A, 408, 581
22. Weaver, R., et al. 1977, ApJ, 218, 377
23. Wilms, J., Allen, A., & McCray, R. 2000, ApJ, 542, 914
24. Wolk, S.J., et al. 2002, ApJ, 580, 161

After the classes

SUPERSHELLS AND TRIGGERED STAR FORMATION

J. PALOUŠ(1) S. EHLEROVÁ(1) & R. WÜNSCH(1),(2)

(1) Astronomical Institute, Academy of Sciences of the Czech Republic, Prague, Czech Republic
(2) Nicolaus Copernicus Astronomical Center, Polish Academy of Science, Warszawa, Poland

We show supershells in the Milky Way as they have been identified in an automatic search of HI shells in 3D data cubes. They are compared to shells and supershells in LMC, SMC and other galaxies. We discuss their origins, particularly their connection to star formation, stellar winds and supernova explosions driving the turbulent ISM. We explore when they fragment and produce gravitationally bounded clumps, and derive their mass spectrum. An analytical approximation is compared to numerical simulations using ZEUS and ŠEMÍK codes. The mass spectrum fits a power law slope -2.3, which is close to the stellar IMF.

Keywords: Stars: formation; ISM: structure; ISM: supernova remnants; Galaxies: star clusters

1 Star formation triggering

The interstellar medium (ISM) in galaxies has the turbulent nature. It is composed of several coexisting intermixed phases influencing each other. The star formation plays a key role: the young stellar clusters produce stellar winds, ionizing radiation and supernovae initiating supersonic motions of shells and supershells. The dissipative shock waves heat the low density medium around the star forming regions to $10^6 - 10^7$ K creating the X-ray gas filling the HI cavities. The dense and expanding walls of hot bubbles, sheets and filaments collide and dissipate the kinetic energy. This energy is partly radiated away and partly heats the diluted medium. Cold high density shells, supershells and clouds composed of atomic and molecular gas are the sites of formation of new stars and stellar clusters.

Formation of stars in diffuse ISM clouds is a process which increases the original density of the parental cloud ($\sim 10^4$ cm^{-3}) to stellar density ($\sim 10^{24}$ cm^{-3}), e.g. by 20 orders of magnitude. It is a complex interaction between the gravitational instability, hydrodynamics of the collapse, cooling and radiative transfer inside of the collapsing cloud, magnetic fields supporting the local fragments, energy dissipation in the supersonic shock waves, and energy and mass feedback from young forming stars. The supersonic turbulence can suppress the global collapse of a cloud and transfer it to dense cores and sheets, where the individual members of the future star cluster form. Extended reviews on the interstellar turbulence and how it controls the star formation has been published by Mac Low & Klessen (2004), Elmegreen & Scalo (2004) and Scalo & Elmegreen (2004).

Internal or external agents may trigger the collapse and star formation. Internal agents are decay of the turbulence in the dense parts of a GMC or the ambipolar diffusion. External triggers may be a consequence of galaxy versus galaxy interactions and collisions, interaction of the galaxy with the intracluster gas in galaxy clusters, or gas compression and shocks connected to spiral arms, rings and bars. The large scale distribution of the ISM in the interacting galaxies maps the landscape of the gravitational potential. It is a result of the momentum conservation combined with the hydrodynamical effects, which pump the ISM along the tidal fields. On smaller scales, the stellar feedback is important: the stellar winds, fotoionizing radiation and supernova explosions not only stop the local collapse to stars, but they also push and compress the ambient ISM forming coherent dense and cold shells and supershells, which may become the sites of further star formation.

Here we focus on scales of $\sim$ 1 kpc and below, which are sizes of expanding supershells and shells. Shells originate from star formation, infall of HVCs to the galactic plane, or hypernovae. Some shells may be induced by galaxy rotation and other large scale motions and some structures may be formed in galaxy collisions. The dependence of shells on the galactic Star Formation Rate (SFR) should also be discussed in the future. In the next section we give examples of ISM structures in galaxies of the local universe. Later we discuss the question when the gravitational instability sets in and we give the mass spectrum of fragments.

2 Supershells in the ISM

Shells, supershells and holes in an HI distribution have been discovered in the Milky Way (Heiles 1979; 1984), M31 (Brinks & Bajaja 1986), M33 (Deul & den Hartog 1990), LMC (Kim et al. 1999), SMC (Stanimirovic et al. 1999), Ho II (Puche et al. 1992), Ho I (Ott et al. 2001), IC2574 (Walter & Brinks, 1999), and in other nearby galaxies within 10 Mpc. The most probable energy sources, which create HI shells, are massive stars. A part of shells might be produced by HVCs infall or by hypernovae (Efremov et al. 1999; Vorobyov & Basu, 2004). Some structures are probably results of the galactic rotation or the galaxy collisions. All these energy sources also drive the turbulence in the ISM.

The HI column density map of the LMC - SMC region is shown in Fig. 1 (Brüns et al., 2004). Large scale structures – Magellanic Bridge, Magellanic Stream and Leading Arm – are consequences of the interaction. Even on the scale of Fig. 1 and with its resolution we see the filaments and shell-like structures, bots in LMC and SMC galaxies and in tidal features. HI structures in Magellanic clouds are frequently connected to young stellar clusters. A comparison of HI structures in the Magellanic Bridge and the Magellanic Stream regions, where no stars are detected, to shells and supershells of the LMC and SMC, where stars actively form, would address the question of the origin of HI shells.

The HI structures in the Milky Way were identified with an automatic searching routine HOLMES (Ehlerová et al. 2004; Ehlerová & Palouš, 2004). This model independent searching algorithm was applied to the Leiden–Dwingeloo HI survey (Hartmann & Burton, 1997) and provided a sample of $\sim$ 600 structures, a more complete list compared to other catalogues (Heiles, 1974, 1984; Hu, 1981; McClure-Griffiths et al. 2002). In Fig. 2. we show structures discovered in the field $(l, b) = (99 - 117, -15 - +5)^o$ around the radial velocity -25 km s^{-1}. In the region also resides the Cep 3 OB association, which is marked with a diamond.

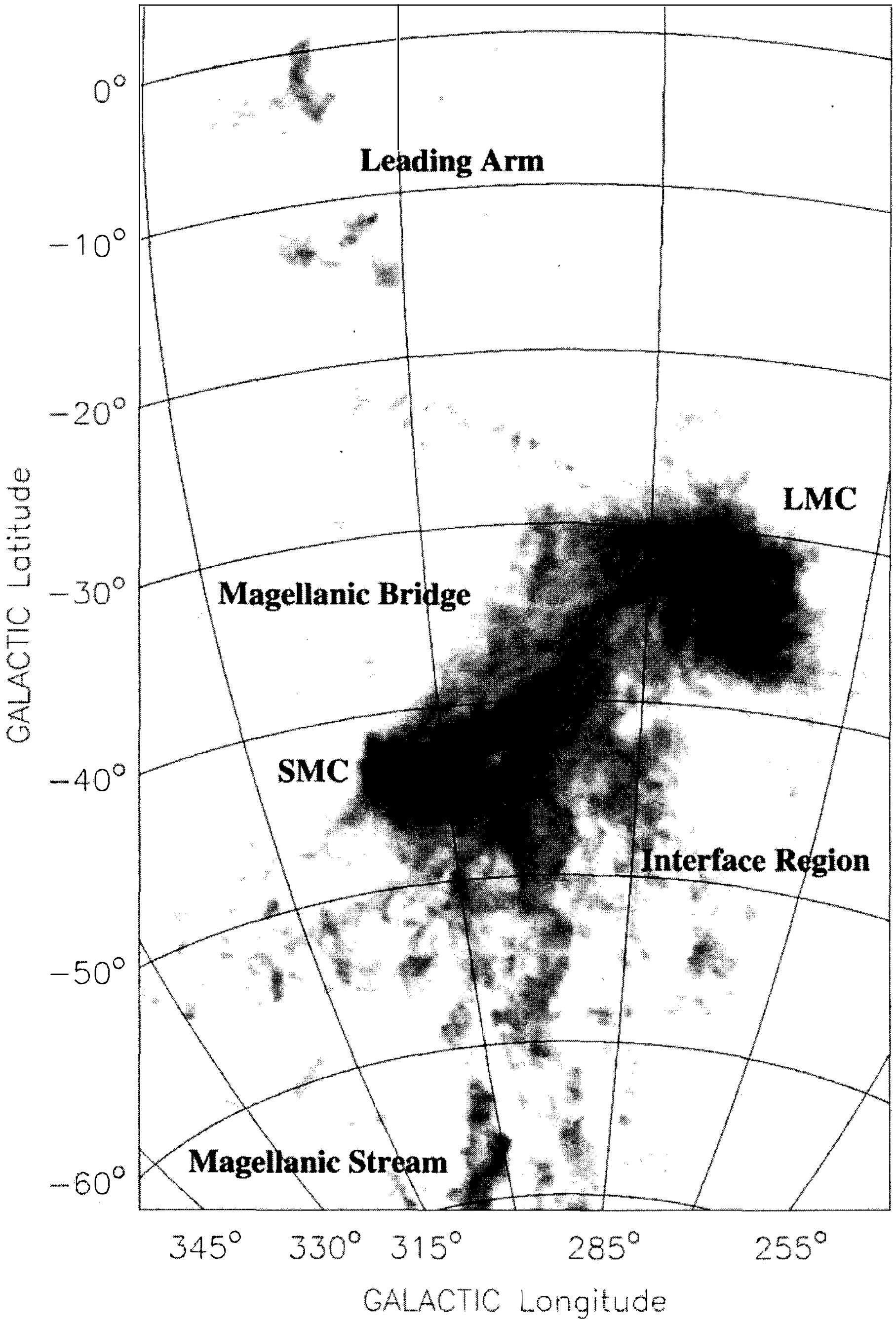

Figure 1: LMC & SMC: an interacting system of dwarf galaxies (Brüns et al. 2004).

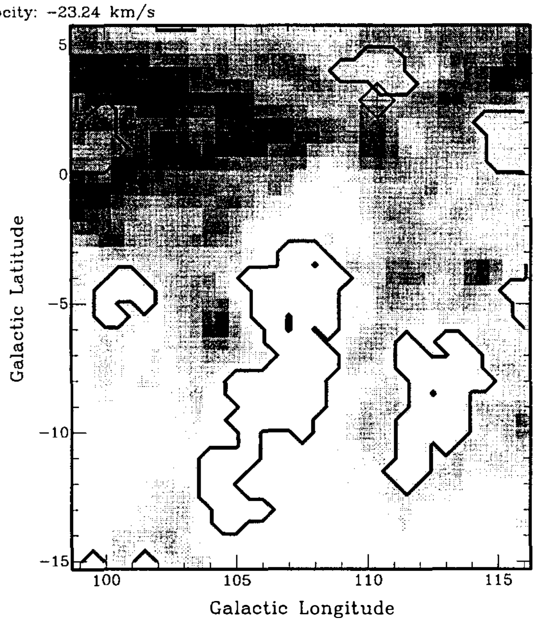

Figure 2: Supershells near the Cep 3 OB association (diamond) (Ehlerová & Palouš 2004). Structures discovered are shown with the contour line.

The distribution of shells and supershell discovered with the searching routine HOLMES in the Leiden–Dwingeloo survey is shown in Fig. 3. Structures concentrate to the galactic equator with the half-thickness 800 pc and show a trend for smaller shells to be closer to the central plane than the larger shells. This can be explained as a consequence of larger density of the shell ambient medium closer to the galactic plane able to slow down their expansion velocity more effectively than at high z, where the density of the ISM is low.

3 Triggering with Supershells

We discuss the supersonic expansion of shells and sheets from regions of localized deposition of energy and address the question when they are gravitationally unstable. The energy input from an OB association creates a blastwave which propagates into the ambient medium (Ostriker & McKee, 1988; Bisnovatyi-Kogan & Silich, 1995). The schematic representation of the situation is shown in Fig. 4. After the initial fast expansion the mass accumulated in the shell cools and collapses to a thin structure, which is approximated as infinitesimally thin layer surrounding the hot medium inside. Neglecting the external pressure and assuming the constant energy input L, the self-similar solution for radius R, expansion velocity V and column density Σ_{sh} is (Castor et al. 1975; Ehlerová & Palouš, 2002):

$$R(t) \qquad = 53.1 \times \left(\frac{L}{10^{51} \text{ erg Myr}^{-1}}\right)^{\frac{1}{5}} \times \left(\frac{\mu}{1.3}\frac{n}{\text{cm}^{-3}}\right)^{-\frac{1}{5}} \times \left(\frac{t}{\text{Myr}}\right)^{\frac{3}{5}} \text{pc} \qquad (1)$$

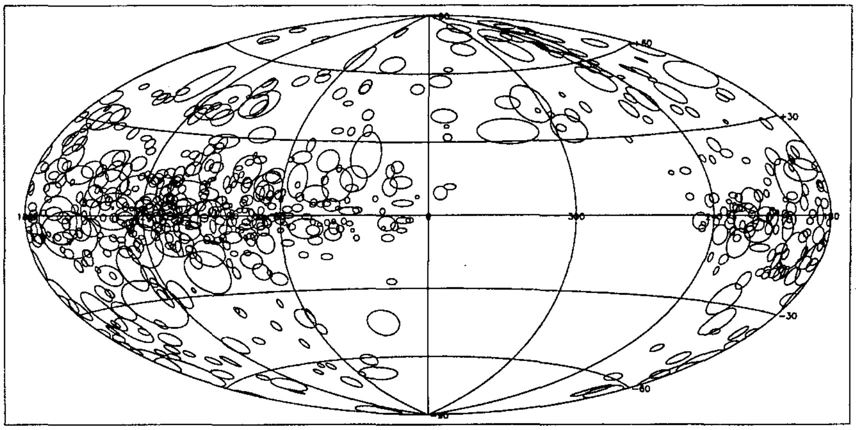

Figure 3: Shells and supershells in the Leiden-Dwingeloo survey (Ehlerová & Palouš, 2004).

c_{sh} $[kms^{-1}]$ n $[cm^{-3}]$	0.3	0.5	1.0
10^{-1}	43	59	91
1	14	19	29
10^2	1.4	1.9	2.9
10^6	0.01	0.02	0.03

Table 1: Values of t_b in Myr for $L = 10^{51} erg/Myr$ and $\mu = 1.3$.

$$V(t) = 31.2 \times \left(\frac{L}{10^{51}\ \mathrm{erg\ Myr^{-1}}}\right)^{\frac{1}{5}} \times \left(\frac{\mu}{1.3}\frac{n}{\mathrm{cm^{-3}}}\right)^{-\frac{1}{5}} \times \left(\frac{t}{\mathrm{Myr}}\right)^{-\frac{2}{5}} \mathrm{kms^{-1}} \qquad (2)$$

$$\Sigma(t)_{\mathrm{sh}} = 0.564 \times \left(\frac{L}{10^{51}\ \mathrm{erg\ Myr^{-1}}}\right)^{\frac{1}{5}} \times \left(\frac{\mu}{1.3}\frac{n}{\mathrm{cm^{-3}}}\right)^{\frac{4}{5}} \times \left(\frac{t}{\mathrm{Myr}}\right)^{\frac{3}{5}} \mathrm{M_{\odot}pc^{-2}}, \qquad (3)$$

where n is the density, μ is the mean atomic weight of the ambient medium and t is the time since the beginning of an expansion.

The linear analysis of hydrodynamical equations including perturbations on the surface of the shells has been performed by Elmegreen (1994) and Wünsch & Palouš (2001). The fastest growing mode is:

$$\omega = -\frac{3V}{R} + \sqrt{\frac{V^2}{R^2} + \left(\frac{\pi G \Sigma_{sh}}{c_{sh}}\right)^2}, \qquad (4)$$

where c_{sh} is the sound speed inside of the expanding shell.

In Fig. 5. we give the time evolution of the fastest mode. At early times, for $t < t_b$, the shell is stable, where t_b is the time, when the fastest mode starts to be unstable:

$$t_{\mathrm{b}} = 28.8 \times \left(\frac{c_{\mathrm{sh}}}{\mathrm{km\ s^{-1}}}\right)^{\frac{5}{8}} \times \left(\frac{L}{10^{51}\ \mathrm{erg\ Myr^{-1}}}\right)^{-\frac{1}{8}} \times \left(\frac{\mu}{1.3}\frac{n}{\mathrm{cm^{-3}}}\right)^{-\frac{1}{2}} \mathrm{Myr}. \qquad (5)$$

Later, for $t > t_b$, when the expansion slows down and reduces the stretching, which acts against gravity, and when the shell column density increases, the shell starts to be gravitationally unstable. Values of t_b are given in Tab. 1 as a function of n and c_{sh}. We see that for ambient densities similar to values in the solar vicinity, $n \sim 10^{-1} - 10^2$, t_b is a few $\times 10^7$ yr, which means that

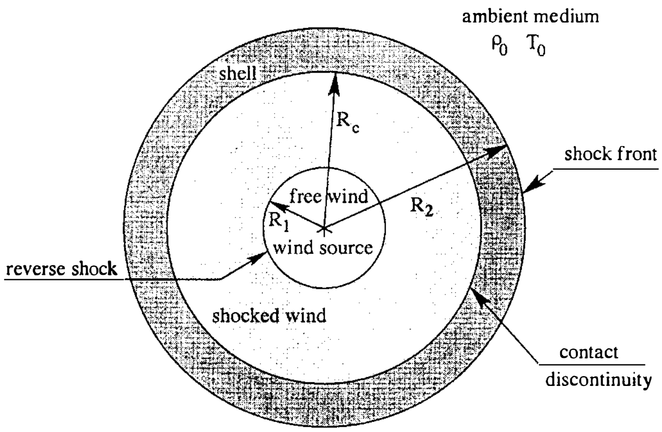

Figure 4: Schematic representation of a supershell expanding around an OB association.

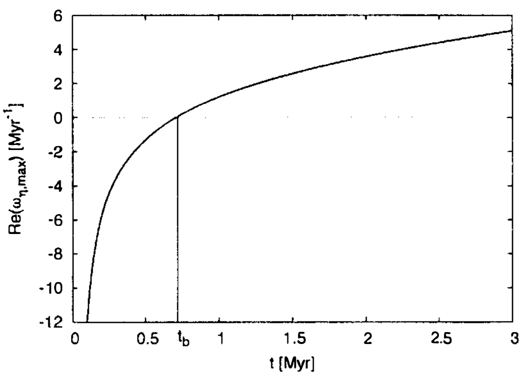

Figure 5: The fastest growing mode.

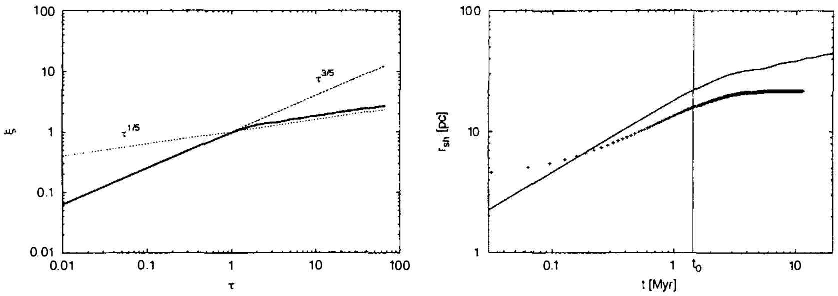

Figure 6: A comparison of the analytical solution by Whitworth & Francis (2002) - left panel - to the numerical solution with ZEUS + ŠEMÍK - right panel. The solid line is from the analytical solution and the crosses result from the numerical simulation.

the gravitational instability is rather slow compared to turbulent collision times and galactic differential rotation. t_b is much smaller in high density medium of GMC and dense cores, where it is $\sim 10^4$ yr only. Thus the shell gravitational instability is particularly important inside the GMCs.

4 Expansion with self-gravity

The evolution of the stellar-wind bubble expanding in a homogeneous and static medium with self-gravity was solved analytically by Whitworth & Francis (2002), and it is shown in Fig. 6 - left panel. The self-gravity becomes important at the time t_0 where the dependence $R(t)$ changes from $R \propto t^{3/5}$ to $R \propto t^{1/5}$:

$$t_0 = \left(\frac{3\pi}{32\ G\ n\ \mu}\right)^{1/2}. \tag{6}$$

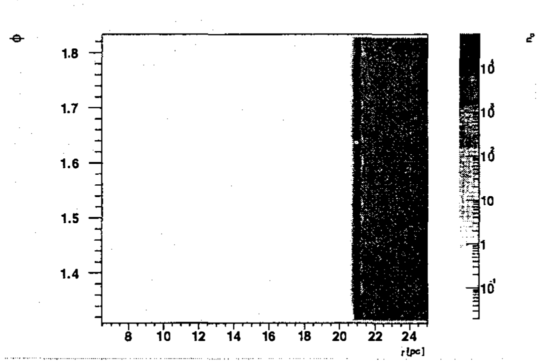

Figure 7: The density distribution in the simulation zone.

The analytical approximations using thin-shell approximation have been compared to numerical simulations with the ZEUS hydrocode combined with the new Poisson solver ŠEMÍK (Wünsch, 2003). The density distribution in the simulation zone is shown in Fig. 7. The analytical solution by Whitworth and Francis (2002) is compared to 3D simulations, where apart

n	t_0	$t_b(L=1, c_{sh}=1)$	$t_b(L=5, c_{sh}=1)$	$t_b(L=1, c_{sh}=2)$
10^{-1}	163	91.1	74.5	140
1	51.7	28.8	23.6	44.4
10^2	5.17	2.88	2.36	4.44
10^6	0.0517	2.88e-2	2.36e-2	4.44e-2

Table 2: Values of t_0 and t_b in Myr for $L = 10^{51} erg/Myr$ and $\mu = 1.3$.

from the self-gravity we include the pressure of the ambient medium (Fig. 6, right panel). The vertical line gives the time t_0 according to eq. 6. We see that the slope of $R(t)$ changes to lower values before t_0 and the average slope is less than 0.6, since the pressure of the ambient medium lowers the expansion speed.

We would like to know if the shell can form gravitationally bounded fragments. We think, that such fragments can only form during the time interval (t_b, t_0), when the shell is already unstable but still expands reasonably fast. When this interval is too short, fragments do not grow well or do not form at all. Values of t_b (eq. 5) and t_0 (eq. 6) are compared in Tab. 2.

5 Mass spectrum of fragments

The dispersion relation of the shell gravitational instability is:

$$\omega(\eta, t) = -\frac{3V}{R} + \sqrt{\frac{V^2}{R^2} - \frac{c_{sh}^2\eta^2}{R^2} + \frac{2\pi G\Sigma_{sh}\eta}{R}}, \tag{7}$$

where η is the dimensionless wavenumber and λ is the wavelength of the perturbation: $\eta = 2\pi R/\lambda$. It is shown in Fig. 8: it gives the wavelength interval of unstable perturbations.

The resulting number of fragments is inversely proportional to the fragment growth time $t_{growth} = \frac{2\pi}{\omega(\eta,t)}$. Rapidly growing fragments are more frequent in the final mass spectrum than the slowly growing fragments.

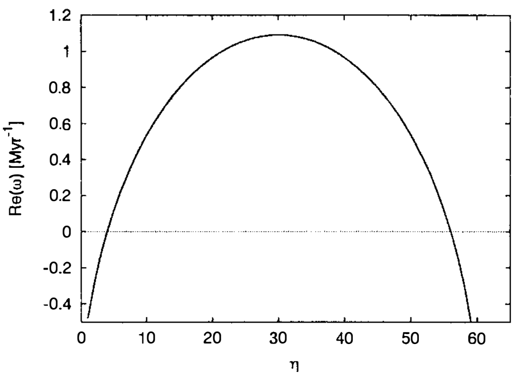

Figure 8: The dispersion relation

Thus the number of fragments in a given volume of radius R is

$$N = \omega\frac{R^3}{(\lambda/4)^3}. \tag{8}$$

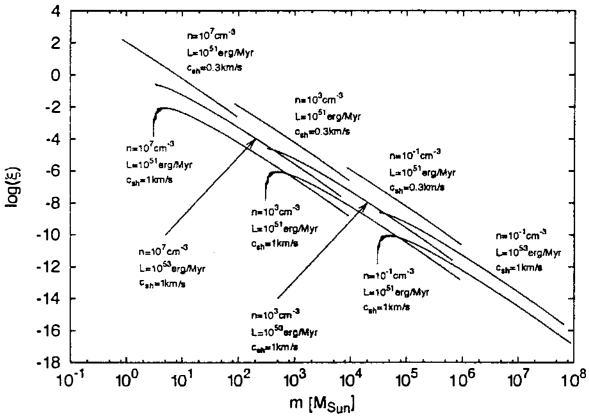

Figure 9: The mass spectrum of fragments of an expanding shell at time $5t_b$.

A fragment with the wavelength λ has the mass

$$m = \frac{4}{3}\pi(\lambda/4)^3\rho. \tag{9}$$

We derive the mass spectrum $\xi(m) = \frac{dN}{dm}$:

$$\xi(m) = -\frac{4}{3}\ \pi\ R^3\ \rho\,\omega\, m^{-2}. \tag{10}$$

If the dispersion relation $\omega(\eta)$ were a constant, the slope of the mass spectrum $\xi(m) \propto m^{-\alpha}$ would be exactly approximated with a power law slope α= 2. But in our case ω is not only the function of η but also of the time t.

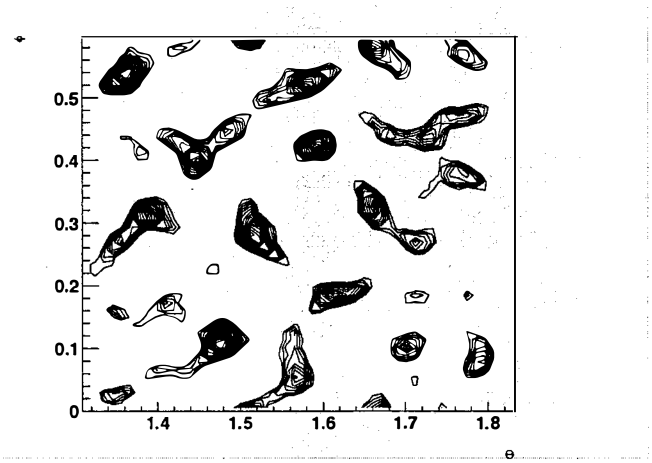

Figure 10: The 3D simulations with ZEUS + ŠEMÍK: the surface density in the shell.

We assume that t_{growth} for a given η is inversely proportional to the average value of ω for this η since the time $t_b(\eta)$ when a given mode starts to be unstable. The time average $\bar{\omega}$ for a given η is calculated using the equation:

$$\bar{\omega}(\eta) = \frac{\int_{t_b(\eta)}^{t} \omega(\eta, t')dt'}{t - t_b(\eta)}. \tag{11}$$

The resulting mass spectra for different values of n, c_{sh} and L, as they have been derived using the thin-shell approximation (1) - (3), are shown in Fig. 9. The high mass parts are well approximated by the power law with a slope $\alpha = 2.2 - 2.4$.

Results of 3D simulations using ZEUS hydrodynamical code in the combination with the Poisson solver ŠEMÍK are shown in Figs 10 and 11. Fig. 10 shows the surface density of the shell at time $t = 5 \times t_b$, Fig. 11 gives the mass spectrum of fragments. The results from simulations are in agreement with the analytically derived mass spectrum using the thin-shell approximation. The mass distribution of fragments fits the power law slope $\alpha = 2.2 - 2.4$.

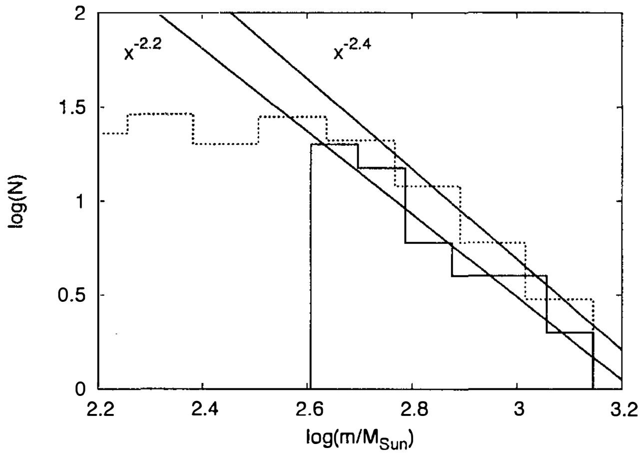

Figure 11: The 3D simulations with ZEUS + ŠEMÍK: the mass spectrum of fragments.

6 Conclusions

Supershells and shells are discovered in the Milky Way and other galaxies of the local universe. Their connection to the star formation have been explored. We show that under certain environmental conditions expanding supershells may be gravitationally unstable and produce fragments, thus triggering the star formation at other places in their home galaxy. Their mass spectrum is close to stellar IMF.

References

1. Bisnovatyi-Kogan, G. S. & Silich, S., S. A., 1995, RvMP 67, 661
2. Brinks, E. & Bajaja, E., 1986, A&A 169, 14
3. Brüns, C., Kerp, J., Staveley-Smith, L., Mebold, U., Putman, M. E., Hayenes, R. F., Kalberla, P. M. W., Muller, E. & Filipovic, M. D., 2004, A&A, in press
4. Castor, J., McCray, R. & Weaver, R., 1975, ApJ 200, L107

5. Deul, E. R. & den Hartog, R. H., 1990, A&A 229, 362
6. Efremov, Yu. N., Palouš, J., Ehlerová, S., 1999, A&A 350, 457
7. Ehlerová, S. & Palouš, J., 1996, A&A 313, 478
8. Ehlerová, S. Palouš, J., 2002, MNRAS 330, 1022
9. Ehlerová S. & Palouš J., 2004, A&A submitted
10. Ehlerová, S., Palouš, J. & Wünsch, R., 2004, Astrophys. and Space Sci. 289, 279
11. Elmegreen, B. G., 1994, ApJ 427, 384
12. Elmegreen, G. B. & Scalo, J., 2004, astro-ph/0404451
13. Hartmann, D. & Burton, W. B., 1997, Atlas of galactic neutral hydrogen, Cambridge University Press
14. Heiles, C., 1979, ApJ 229, 533
15. Heiles, C., 1984, ApJS 55, 585
16. Hu, E. M., 1981, ApJ 248, 119
17. Kim, S., Staveley-Smith, L., Dopita, M. A., Freeman, K. C., Sault, R. J., Kesteven, M. J. & McConnell, D., 1999, AJ 118, 2797
18. Mac Low, M.-M. & Klessen, R. S., 2004, RvMP 76, 125
19. McClure-Griffiths, N. M., Dickey, J. M., Gaensler, B. M. & Green, A. J., 2002, ApJ 578, 176
20. Ostriker, J. P. & McKee, C. F., 1988, RvMP 60, 1
21. Ott, J., Walter, F., Brinks, E., Van Dyk, S. D., Dirsch, B. & Klein, U., 2001, AJ 122, 3070
22. Palouš J., Wünsch R. & Ehlerová S., 2004, MNRAS, submitted
23. Puche, D., Westpfhal, D., Brinks, E.& Roy, J., 1992, AJ 103, 1841
24. Scalo, J. & Elmegreen, B. G., 2004, astro-ph/0404452
25. Stanimirovic, S., Staveley-Smith, L., Dickey, J. M., Sault, R. J., Snowden, S. L., 1999, MNRAS 302, 417
26. Vorobyov, E. I. & Basu, S., 2004, A&A, submitted
27. Walter, F. & Brinks, E., 1999, AJ 118, 273
28. Whitworth, A. P., Francis, N. 2002, MNRAS 329, 641
29. Wünsch, R., 2003, PhD thesis, Charles University, Prague
30. Wünsch, R. & Palouš, J., 2001, A&A 374, 746

Monsieur and Madame Tran, the spirit of Rencontres de Moriond

Part 4

Galactic and extragalactic modes of star formation

Star formation at the edge of Chaos: Self organized criticality and the IMF

Jorge MELNICK and Fernando SELMAN
European Southern Observatory, Alonso de Córdova 3107, Santiago, Chile

The IMF for stars more massive than a few solar masses appears to be a universal function that can be well approximated by a power-law of slope surprisingly close to the value found by Salpeter 50 years ago. We use the central cluster of 30 Doradus to determine an accurate value for the IMF slope, and we show that the few seriously discrepant IMF's reported in the literature are most likely due to systematics in the data processing. We propose that massive star formation shows this surprising regularity over a wide range of physical parameters because it is regulated by the laws of complexity. More precisely, we propose that the ISM is in a state of Self-Organized Criticality (SOC) which is a transition between order and chaos.

Keywords: IMF - ISM: Fractal structure - Stars: Massive

1 The Theme

Above a certain threshold mass, which appears to vary from cluster to cluster, but which is close to $1M_{\odot}$, there is strong observational evidence that the IMF is a universal function that can be approximated well approximated by power-law of slope very close, if not identical, to the value found by Salpeter 50 years ago: $\Gamma = -1.35$ (Salpeter, 1955; for a recent review see Kroupa, 2002). This is a very important result, but also a rather surprising one since *a priori* one would expect the physics of star formation to depend on ISM parameters such as temperature, density, pressure, or metallically. Yet, the IMF seems to be invariant over a reasonably wide range of these parameters.

There are, however, a few places where the (massive star) [a] IMF appears to depart significantly, and even dramatically, from the 'universal' power-law. The two most significant objects that apparently show discrepant IMF's are the extreme field in the LMC, and the Arches cluster near the Galactic center. Interestingly, these objects represent the extremes in the stellar (and therefore presumably also ISM) densities of objects for which reliable IMF's have been measured.

We will show in this paper that in both cases: the high density extreme (Arches), and the low density extreme (LMC field), that the discrepancy can be ascribed to systematics in the data. Thus, there is no convincing case yet of a well determined IMF that is different from the universal (Salpeter) function. We propose in this Paper that this is a natural consequence of the Fractal structure of the interstellar medium.

[a] Throughout this paper we use IMF to refer to the *massive star* IMF defined in the text.

2 The IMF

2.1 The IMF of 30 Doradus

Large telescopes, modern instrumentation, and powerful software tools allow the IMF of clusters and associations to be determined rather accurately. In fact, the accuracy is often limited by stochastic effects: a very massive cluster is required to properly sample the mass range (say 1-100$M_\odot$), but there are very few such clusters that can be resolved even using state-of-the art instrumentation on the ground or in space. We refer the reader to the paper by Kroupa (2002) for a comprehensive review of the IMF. Here we will restrict the discussion to the best studied of these clusters: 30 Doradus, for which the most accurate (both in terms of how the data was treated and in terms of stochastic fluctuations) IMF to date has been determined (Selman et al., 1999).

30 Dor is the largest HII region in the LMC, and one of the largest HII regions in the Local Group. It is ionised by a massive ($M \simeq 3 \times 10^5 M_\odot$), young (age$\lesssim$ 3Myrs) cluster containing about 8000 OB stars. Except for the very central regions, the 30 Dor cluster can be resolved by direct CCD imaging from the ground making it a unique laboratory to study the physics of massive star formation (see e.g. Selman, 2003, and references therein).

Technically, the most difficult problem in determining the IMF of any young cluster or association is the transformation of observables (e.g. UBV photometry) into physical parameters such as mass and age. The difficulty comes basically from two fronts: the rather low sensitivity of the UBV photometry to the effective temperatures of massive stars, and the fact that in young clusters the reddening varies significantly from star to star. Selman et al. (1999) introduced a new technique called the Colour-Magnitude Stereogram (CMS) to transform UBV photometry into mass and age. In the presence of variable reddening the theoretical evolutionary tracks become surfaces in the CMS, the *theoretical surfaces.* The job consists in transforming these surfaces from the theoretical (T_{eff}, M_{bol}, age) space into the observable [(B-V), (U-B), V] space, and to find, for each star, the most likely set of parameters. Figure 1 shows the CMS for 30 Dor together with 4.5Myr, 12Myr, and 50Myr isochrones. The theoretical surface is shown for the 12Myr isochrone and a range of $0 < A_V < 3$ mag in extinction.

Figure 2 shows the distribution of reddening obtained for the stars in the cluster divided in two mass bins. The extinction in V varies by more than 2 magnitudes from star to star. This means that, in order to be complete to any given mass, the photometry be complete at least two magnitudes fainter than the magnitude corresponding to a star of that mass. The figure also shows that there are no systematic differences in the reddening distributions as a function of mass. This makes it possible to statistically correct for the stars hidden by the variable reddening.

Figure 3 shows the IMF that obtains combining ground based IMF photometry for the whole cluster excluding the central core (Selman et al. 1999), with HST photometry of the central regions (Hunter et al. 1995, 1996). The three sets of points in the ground based data show the raw counts (triangles), the counts corrected for photometric incompleteness (squares), and the counts corrected for variable reddening using the distribution showed in Figure 2 (circles). Two sets of HST data are shown with open symbols for stars of mass lower than $10 M_\odot$. The error bars show the counting statistics which are acceptable even for the most massive bins. The power-law fit to the data gives a slope of $\Gamma = -1.37 \pm 0.05$.

The main conclusions from the study of 30 Doradus are: (a) the IMF is very well represented by a power-law of slope indistinguishable from the Salpeter value, and (b) the effect of variable reddening, if not corrected, is very severe near the magnitude limit of the photometry and can seriously *flatten* the slope.

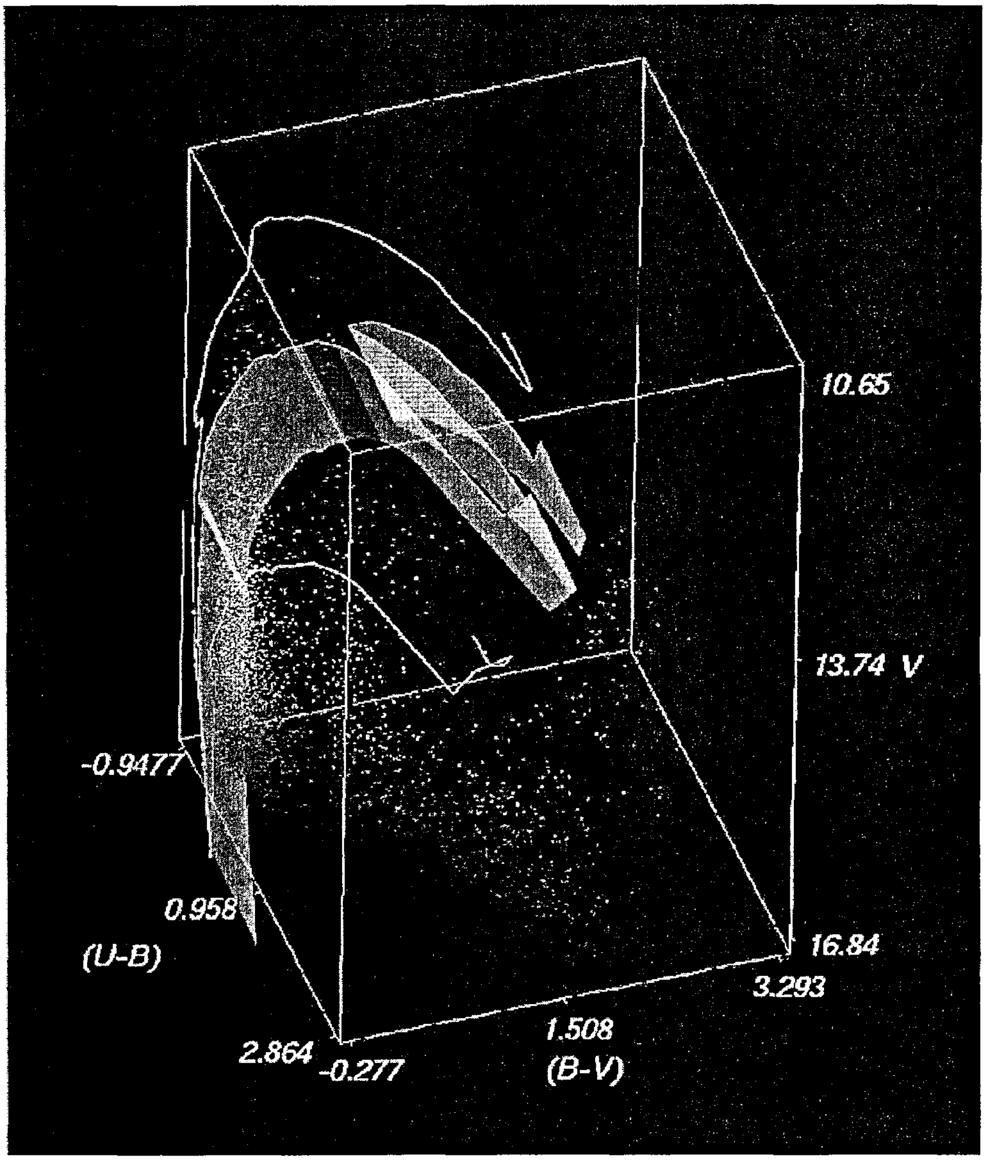

Figure 1: The colour-magnitude stereogram for 30 Dor. The theoretical surface is shown for a 12Myr isochrone and a range of 3 magnitudes in A_V

2.2 The discrepant cases: LMC and Arches

At the extreme ends of the range of stellar densities for which the IMF has been determined with reasonable accuracy lie two objects that show very discrepant IMF's. At the low density end, the LMC field far from even the smallest clusters and associations, is reported by Massey (2002) to have a slope $\Gamma = -3.8 \pm 0.6$, At the very high density end, the Arches cluster near

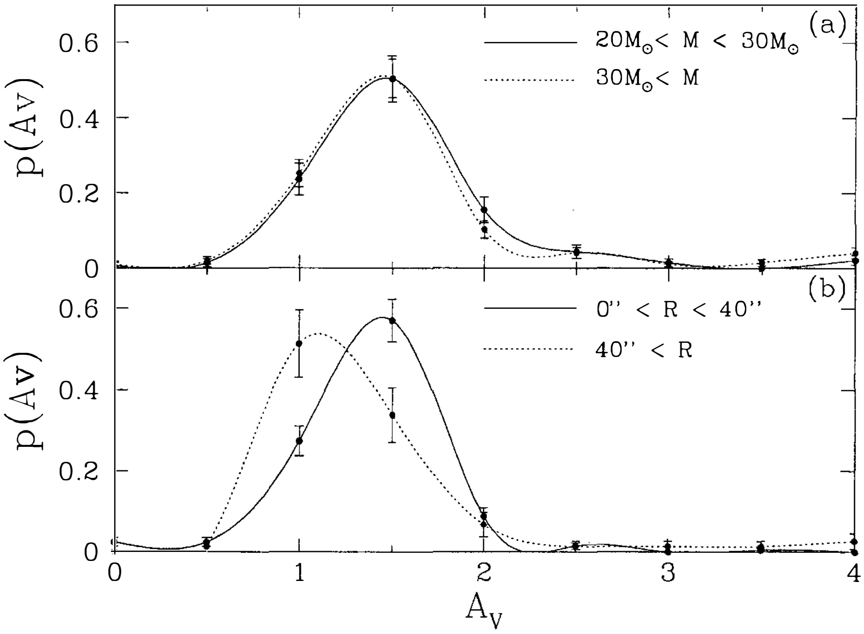

Figure 2: Top: V-band extinction distribution as a function of mass. Bottom: As a function of distance to the center of the cluster. The average extinction is larger in the central part of the cluster.

the center of the Milky Way , yields a slope ranging from $\Gamma = -0.6$ in the central region, to $\Gamma = -0.9$ elsewhere (Stolte et al., 2003). If these observations are correct, they point to a very strong dependency of the IMF on density which should provide crucial clues to understand the physics of star formation.

In the course of an investigation of the properties of the 30 Doradus super-association, we obtained a new determination of the IMF for the LMC field using the same techniques described above for the central cluster (Selman, 2003; Selman and Melnick 2004). This is shown in Figure 4 where we plot our results together with those of Massey (2002). The transformation from present day mass function (PDMF) to IMF is done assuming constant star formation in both cases. Our IMF is seen to be significantly flatter than that of Massey. The discrepancy is due saturation effects in the CCD which set-in at $V \simeq 12$i mag, or $\geq 40 M_\odot$ on the main sequence. Massey has only one mass-bin below this limit (Fig. 4). so he discarded stars brighter than V=12. Instead, since our data goes deeper (but also saturates at V=12), we were able to restrict the IMF to stars between 10 and $40 M_\odot$.

In order to check for systematic effects due to the different fields and difference mass ranges covered by the two data sets, we corrected Massey's data (in the for incompleteness using the theoretical evolutionary tracks and recovered our value for the IMF slope in the field in common.

Unfortunately, in the case of the Arches cluster we do not have independent data to check the published results. However, Stolte et al. (2002) reported significant variations in the extinction from star to star in the cluster. In fact, there seems to be a strong radial gradient in reddening, in the sense that the central parts of the cluster are less reddened. A close inspection of the

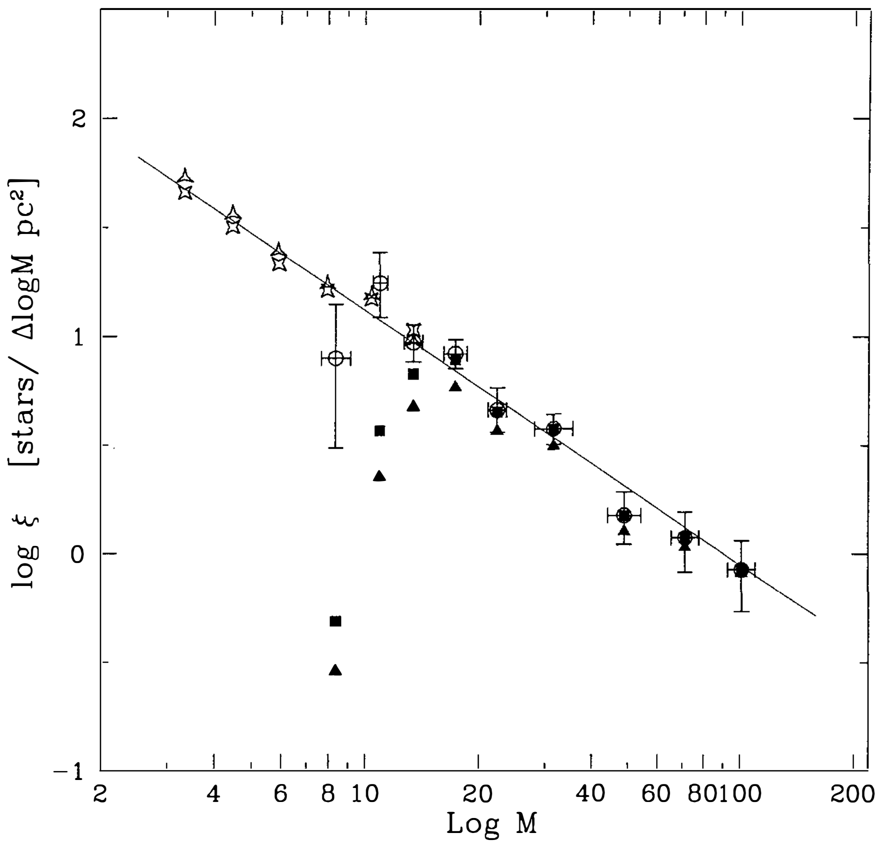

Figure 3: The IMF of the 30 Doradus cluster. Filled triangles show the raw counts; squares the counts corrected for photometric completeness; open circles correction for variable reddening. Two sets of HST data for the central region are shown (lower magnitudes)

2MASS images of the field reveal the presence of several dark patches in the vicinity of the cluster, suggesting that the observed gradient may be due to foreground extinction. Whatever its origin, the observed variance in extinction implies that, in order to be complete to any given mass, the photometry must go several magnitudes deeper than the K-magnitude corresponding to that mass. Contamination by Bulge stars adds a further complication that led Stolte et al. (2003) to limit their analysis to M$\geq$10$M_\odot$ ($K \sim$ 15.1). According to Stolte et al. (2002), the extinction in the cluster varies from A_K = 1.9 to A_K = 4.1. Therefore, in order to count all stars more massive than 10$M_\odot$ one has to reach K=15.1+4.1=19.2, well into the range of magnitudes where Bulge contamination is strong. If indeed the reddening variation is a function of radius, then by subtracting a radial component (as done by the authors) the variance is decreased but not avoided. Assuming the Bulge contamination to be small for stars brighter than, say, K=17.5, the corresponding completeness limit for mass would be K=17.5-4.1=13.4 or M$\sim$ 20$M_\odot$.

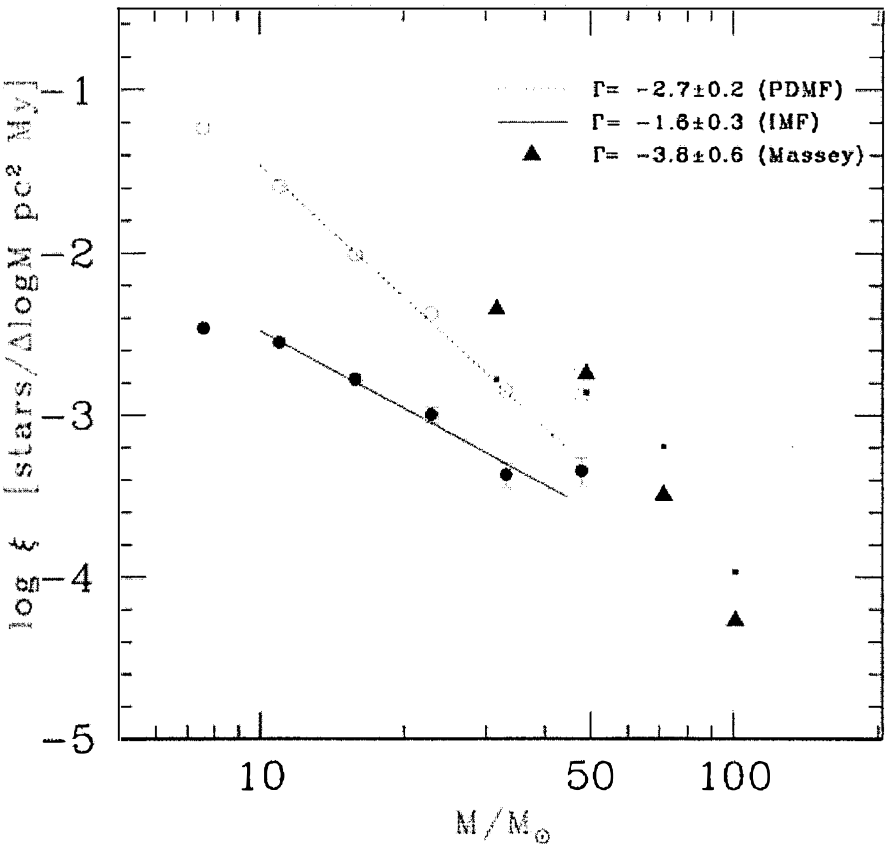

Figure 4: The IMF of the LMC field

Figure 5 shows the IMF of Stolte et al.(2003) for the cluster with their fit to the data. Clearly, if the fit is restricted to $M > 20M_{\odot}$, the IMF would be significantly steeper. The flattening observed in the central region, where the variance in extinction is much lower, may be real, but still needs to be confirmed with better and deeper data, particularly in the J-band. The origin of the radial gradient in reddening also needs to be confirmed since, contrary to the Arches, in 30 Dor, the average extinction is larger in the central regions (Figure 2), while the core of 30 Dor also contains large numbers of massive WR and Of stars.

Our strong conclusion for this section is all the available data are consistent with the hypothesis that the (massive star) IMF is a universal function that, within the uncertainties of state of the art observations, can be well approximated by a power-law of slope $\Gamma = -1.3$.

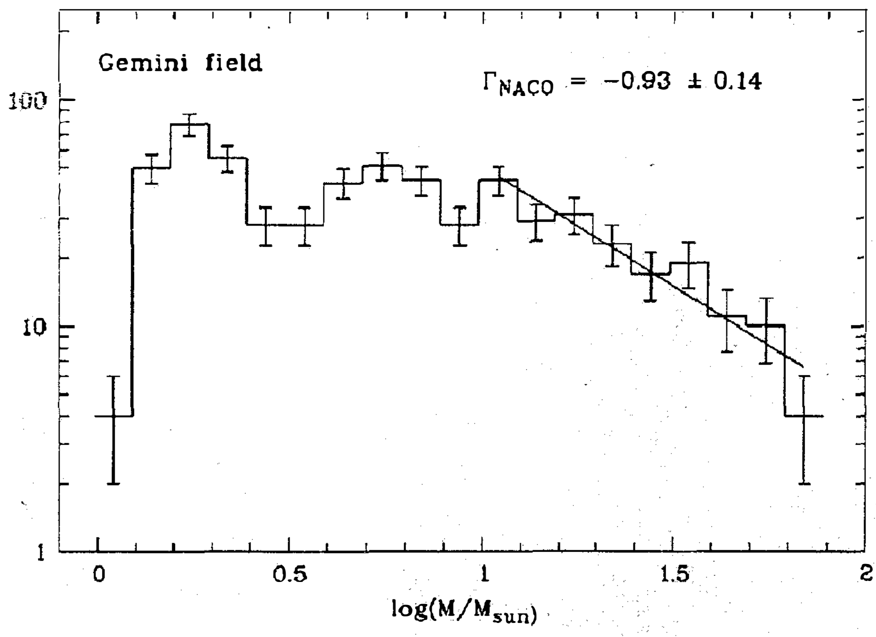

Figure 5: The IMF of the Arches cluster taken from Stolte et al. (2003). Due to differential reddening, only the $M > 20M_\odot$ bins are probably complete leading to a steeper IMF than is shown in the figure.

2.3 Caveats

Selman (2003) has discussed some of the systematic effects that may affect photometric determinations of the IMF (binaries, stellar rotation, fraction of Be stars, star formation history, etc.) Probably the most serious potential problem comes from binaries. We have explicitly assumed that all the stars in the cluster are single stars. Figure 6 shows the distribution of radial velocities for the central cluster of 30 Doradus. The velocity dispersion, $\sigma_o = 36.5 \mathrm{kms}^{-1}$, is much larger than the Virial dispersion of a cluster of the (photometric) mass and radius of 30 Doradus (Bosch et al., 2001). Thus, either the cluster is flying apart, contains large amounts of dark matter, or a large fraction of binaries. The latter case was modelled by Bosch et al., (2001) who showed that the observed velocity dispersion is consistent with the hypothesis that all the stars in the cluster are binaries.

There are no data (yet) to confirm or deny this hypothesis which we present here only to warn the reader that the last word on the IMF has not been said yet.

3 Fractals

There is good observational evidence (e.g. Elmegreen, 2002 and references therein) that the interstellar medium (ISM) has a fractal structure. It can be shown for arbitrary fractal geometry that the mass distribution of ISM clouds (or clumps) will be a power-law of slope very close to $\Gamma_{ISM} = -1$ (Elmegreen, 1997; Melnick and Selman, 2000). So, if we want to understand the IMF, we must first understand the origin of the fractal structure of the interstellar medium. Clearly, this is the result of the way galaxies are formed and evolve, and therefore, of a very complex process. However, we notice that power-law distributions of (log-log) slope ~ -1 occur

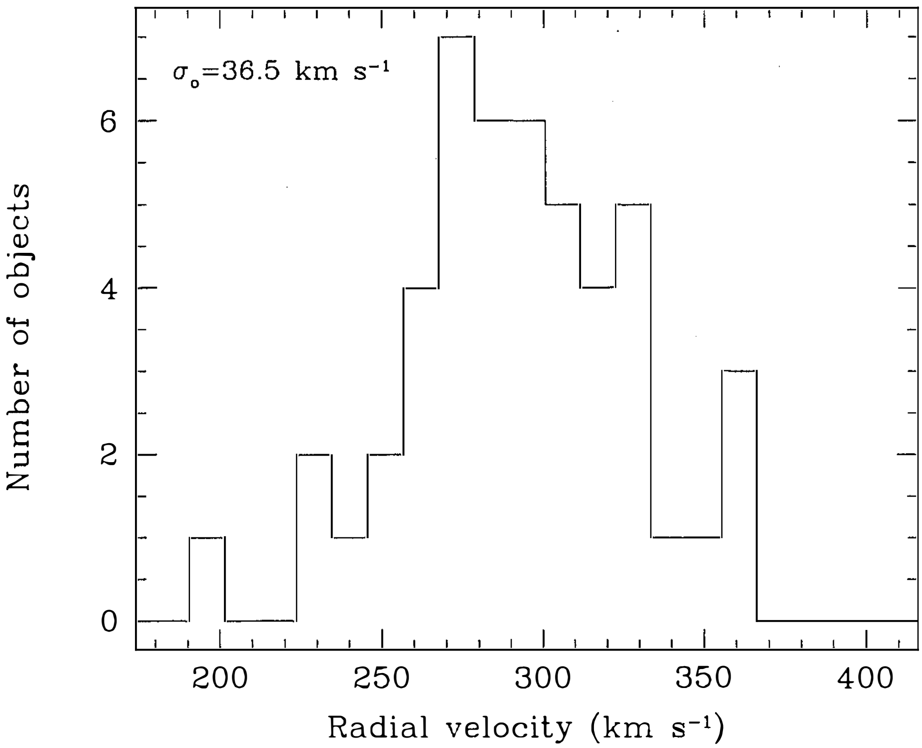

Figure 6: The radial velocity histogram for 30 Dor. The velocity dispersion corrected for instrumental effects is shown in the Figure

frequently in Nature. In fact, power-law distributions are the tell-tails of a highly self-regulated process known as Self Organized Criticality, or SOC (Bak, 1996). The prototypical example of SOC is the sand-pile. A pile of sand that is formed by slowly adding grains one-by-one reaches a stage where the addition of a single grain may cause avalanches of any size. (Figure 7). The system reaches a critical state where it self-organizes to maintain a stable configuration. In this state the distribution of avalanche sizes is a power-law of slope very close to -1. Other manifestations of this state are earthquakes (Richter law), Solar flares, traffic jams, internet traffic, etc. (see e.g. Valverde, and Sole, 2000). Since these processes are extremely complex, researchers in the field use toy models (i.e. blocks linked by springs for the earth-crust), or cellular automata to reproduce the observed behaviour, so the strongest indication of SOC in complex systems is a power-law distribution of events ('avalanches') with slope close to -1.

Therefore, we propose that due to extremely fine-tuned feed-back processes, the ISM has

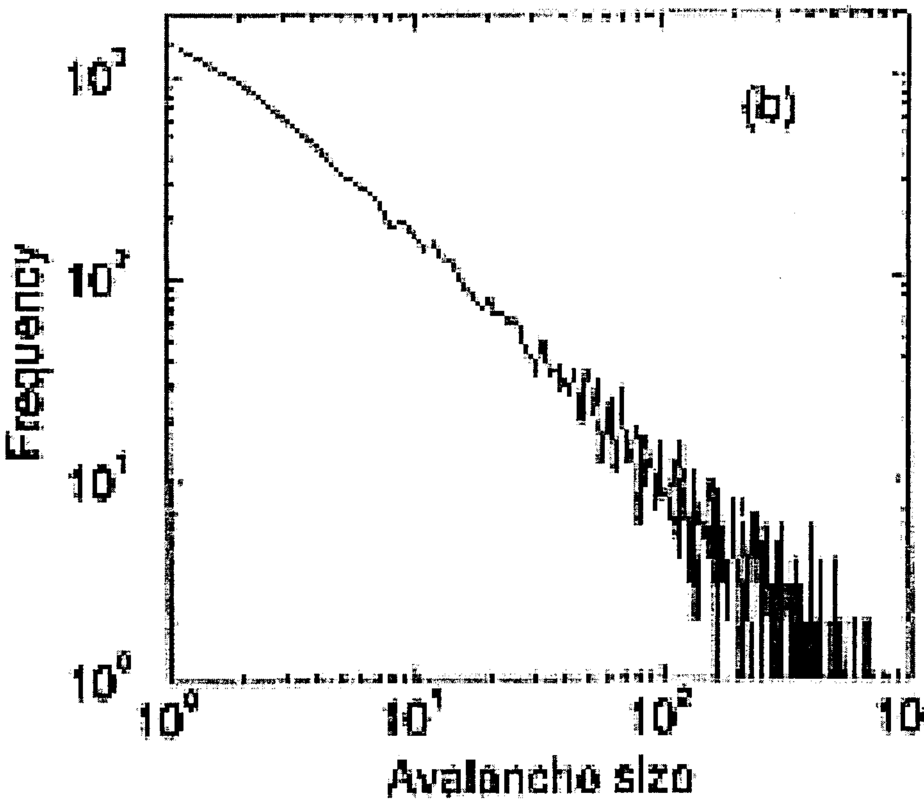

Figure 7: The size distribution of avalanches in a sand-pile (taken from Valverde and Solé, 2000)

reached a state of Self-organized criticality. Obviously stars form as the result of gravitational collapse of gas clumps, and it requires only a few straightforward assumptions to go from the mass distribution of clumps to the IMF of stars (Elmegreen, 1997). Self-organized criticality can be seen as an intermediate state between order and chaos. So the ISM is literally at the edge of chaos. Just as a sand-pile will collapse if one adds a lot of sand at once, the ISM may become chaotic if strongly disturbed. In that case the size distribution of 'avalanches' would become unpredictable and may well be dominated by very large avalanches. We do not have a toy model for the ISM, so it is hard to quantify what is meant by 'strong disturbance'. However, it is difficult to imagine a disturbance larger than a merger event. Therefore, the mass distribution of star clusters (super-clusters) formed in extreme mergers, ULIRGS, for example, could indeed provide a challenging test.

We conclude with another caveat. If the IMF is mostly determined by complexity, then the IMF slope will be a test of the complexity, but not necessarily of the physics, of numerical models.

References

1. Bak, P., 1996, *How Nature Works*, Springer-Verlag, New York
2. Bosch, G., Selman, F., Melnick, J., Terlevich, R., 2001, A&A, 380, 137
3. Elmegreen, B.G., 1997, ApJ, 486, 944.
4. Elmegreen, B.G., 2002, ApJ, 577, 206
5. Hunter D. A., Shaya E. J., Holtzman J. A., Light R. M., O'Neil E. J., Lynds R. 1995, ApJ, 448, 179
6. Hunter D. A., O'Neil E. J., Lynds R., Shaya E. J., Groth E. J., Holtzman J. A. 1996, ApJ, 459, L27
7. Kroupa, P., 2002, Science, 82, 295.
8. Massey, P., 2002, ApJS, 141, 81
9. Melnick, J., Selman, F. 2000, ASP Conference Series, 215, p.159
10. Selman, F., Melnick, J., Bosch, G., Terlevich, R., 1999, A&A, 347, 532
11. Selman, F., 2003, Ph.D. thesis, Caltech.
12. Selman, F, Melnick, J., 2004, preprint.
13. Salpeter, E., E., 1955, ApJ., 121, 161
14. Stolte, A., et al., 2003, *The Messenger*, 111, 9.
15. Stolte, A., Grebel, E.K., Brandner, W., Figer, D.F., 2002, A&A, 394, 459.
16. Valverde, S., and Sole, R.V., 2000, `http://complex.upc.es/˜sergi`

STAR FORMATION IN GALAXY MERGERS:
Scaling up a universal process or a violent mode of SF?

UTA FRITZE - V. ALVENSLEBEN

Universitätssternwarte Göttingen, Geismarlandstr. 11, 37083 Göttingen, Germany

I briefly review some measures of star formation rates in galaxies and discuss their respective uncertainties before outlining the range of star formation rates encountered in starbursts from isolated dwarf through massive gas-rich interacting systems. I present our current understanding of molecular cloud masses and structures and on star formation processes and efficiencies in starburst and interacting galaxies. Star cluster formation is an important mode of star formation, in particular in strong star formation regimes. I discuss the role of star clusters and their properties in helping us assess the question if star formation is a universal process allowing for considerable scaling or if there's two different regimes for normal and violent SF.

Keywords: Stars: formation, Galaxies: evolution, formation, interactions, ISM, starburst, star clusters, globular clusters: general, open clusters and associations: general

1 Motivation

Despite considerable efforts by many researchers over more than 30 yr, the question if **S**tar **F**ormation (**SF**) is basically described by one universal process that can be scaled up and down considerably from lowest levels in dwarf and low surface brightness galaxies to extremely high levels observed in massive gas-rich interacting galaxies, ULIRGs, and SCUBA galaxies or if, on the other hand, there are two fundamentally different modes or processes of SF – violent as opposed to normal SF – still is one of the major unresolved issues in astrophysics.

2 Star Formation Rates: Measures and Regimes

2.1 Star Formation Rates: Measures and Limitations

In nearby galaxies, spirals, irregulars and starburst galaxies, **SF Rates (SFRs)** are conventionally derived from H_α or FIR luminosities using handy formulae like

$$\mathrm{SFR}\ [\mathrm{M}_\odot/\mathrm{yr}] \ = \ \mathrm{L}(\mathrm{H}_\alpha\ /\ 1.26 \cdot 10^{41})\ [\mathrm{erg/s}] \quad \text{(Kennicutt 1998)}$$

$$\mathrm{SFR}\ [\mathrm{M}_\odot/\mathrm{yr}] \ = \ \mathrm{L(FIR)}\ /\ 5.8 \cdot 10^{9}\ [\mathrm{L}_\odot]$$

that are valid for a Salpeter IMF from 0.1 through 100 $M_\odot$, for constant or slowly varying SFRs and for metallicities close to solar.

Our evolutionary synthesis models GALEV for galaxies or star clusters of various metallicities do include gaseous emission in terms of lines and continuum on the basis of the time evolving and metallicity-dependent summed-up Lyman continuum photon rate (Smith et al. 2002, Schaerer & de Koter 1997) from all the hot stars present in a cluster or a galaxy. While hydrogen emission line strengths are taken from photoionisation models, the line ratios of heavy element lines relative to H_β for low metallicities are taken from empirical compilations by Izotov et al. (1994, 1997) and Izotov & Thuan (1998). Our models confirm the relations between $H_\alpha-$ and [OII]$-$ line luminosities in normal SF regimes and show their limitations: **1)** at significantly subsolar metallicities $Z \sim \frac{1}{20}\ Z_\odot$ SFRs estimated from $H_\alpha-$ luminosities by the above formula are overestimated by factors ≤ 3 for continuous SF regimes and by factors ≥ 3 for starbursts. This is due to the fact that low-metallicity stars are hotter and have stronger ionising fluxes. **2)** In case of SFRs fluctuating on short timescales ($\lesssim 10^7$ yr) errors up to factors of 100 can arise. For short-timescale fluctuations of the SFR, as e.g. in dwarf galaxies and their starbursts as well as in SF regions/complexes within larger galaxies, the delay of the $H_\alpha-$ luminosity maximum with respect to the maximum of the SFR due to the fact that massive supergiants have even stronger ionising fluxes than their main sequence progenitors increases the errors in the SFRs estimated from H_α beyond the metallicity effect discussed above. Fig. 1a shows the good agreement of our solar metallicity const. SF model with Kennicutt's relation and the differences arising for metallicities other than solar. Starbursts with durations from 10^5 to 10^8 yr are put on top of the constant SFR models around ages of 10 Gyr. The rapid rise of the SFR is not immediately reflected in a corresponding increase in $H_\alpha-$ luminosity: the ratio of $\log(L(H_\alpha)/\mathrm{SFR})$ decreases by a factor up to 10 for the shortest burst before it strongly increases by a factor $\lesssim 60$ in the course of the burst and comes down to the pre-burst value after the burst (see Fig. 1b and Weilbacher & FvA 2001 for details).

SFRs of distant galaxies are often estimated from their [OII]3727$-$ luminosities. The metallicity dependence of the [OII]3727$-$line is twofold. [OII] fluxes depend on the oxyen abundance and, hence, increase with increasing metallicity of the ionised gas, and on the strength of the ionising flux that decreases with increasing metallicity. The combination of both effects accounts for a factor ~ 2 change in the transformation factor between L([OII]) and SFR (see also Weilbacher & FvA 2001).

SFRs are particularly meaningful if expressed in relation to galaxy masses. In normal SF mode, spiral galaxies with typical masses of order 10^{10} $M_\odot$ have global SFRs around $1 - 3$ $M_\odot$/yr. Irregular and dwarf irregular galaxies with masses in the range 10^6 to 10^9 $M_\odot$ have SFRs of order $0.01 - 3$ $M_\odot$/yr. Starbursts in dwarf galaxies, e.g. **B**lue **C**ompact **D**warf **G**alaxies (**BCDGs**) feature SFRs of order $0.1 - 10$ $M_\odot$/yr.

2.2 Burst Strengths

Bursts strengths – defined as the relative increase in stellar mass during the burst $b := \Delta S_{\mathrm{burst}}/S$ – in BCDGs have been shown by Krüger, FvA & Loose (1995) with evolutionary synthesis

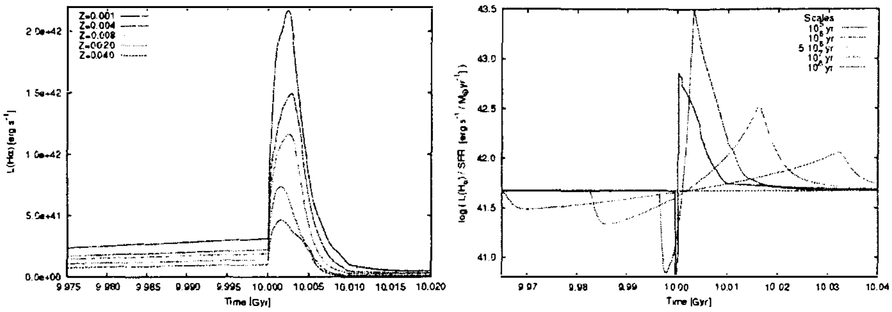

Figure 1: Time evolution of L(H$_\alpha$) for const. SF plus a burst of 10^6 yr duration starting after 10 Gyr in models with various metallicities (Fig. 1a) and of the ratio L(H$_\alpha$)/SFR for Gaussian shaped bursts of various durations for Z=0.001 (Fig. 1b).

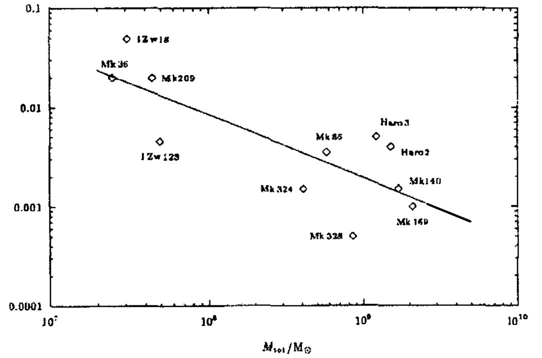

Figure 2: Burst strengths as a function of total dynamical galaxy mass, including HI, for the sample of BCDGs analysed by Krüger *et al.* (1995).

modelling compared to optical through NIR photometry to range from b = 0.001 to b = 0.05, and to decrease with increasing total mass of the galaxy, including M(HI), as shown in Fig. 2, in agreement with expectations from stochastic self-propagating SF scenarios.

All of the starbursting dwarf galaxies we have analysed so far, however, are fairly isolated. Note that accurate burst strengths can only be given for systems at the end of the burst, i.e. for young post-starburst galaxies. As post-starbursts galaxies age, the precision to which burst strengths can be measured starts to decrease significantly as soon as the peak of the strong Balmer absorption line phase is over about 1 Gyr after the burst. For galaxies with ongoing starbursts only lower limits to the burst strength can be estimated.

Massive gas-rich interacting galaxies feature high and sometimes very high SFRs of order 50, 100, and up to 1000 M$_\odot$/yr for Luminous and Ultraluminous IR Galaxies, LIRGs and ULIRGs, in their global or nuclear starbursts which typically last over a few 10^8 yr. Evolutionary synthesis modelling of post-starbursts in massive gas-rich spiral – spiral merger remnants like NGC 7252 have shown that these systems can also have tremendous bursts strengths that increase their stellar masses by 10 – 30 and possibly up to 50% (FvA & Gerhard 1994a, b). Starbursts in massive interacting galaxies hence are completely off the burst strength – galaxy mass relation for starbursts in non-interacting dwarf galaxies. Whether this is due to the presence/absence of an external trigger or due to the difference in gravitational potential and dynamical timescale between dwarf and giant galaxies is an open question still. Careful analyses of dwarf – dwarf or giant – dwarf galaxy mergers should tell the difference.

2.3 Star Formation Efficiencies

Even under the most conservative assumptions – that the pre-merger spirals were drawn from the high end of their type-specific luminosity function and were particularly gas-rich for their type – the **SF** Efficiencies (**SFEs**), defined in terms of SFE:=mass of stars/mass of gas available, in these cases must have been extremely high. For the global starburst happening slightly less than 1 Gyr ago during the merger of two bright gas-rich spirals now called NGC 7252, the analysis of the deep Balmer absorption line spectrum taken by F. Schweizer with our models indicated a SFE $\geq$ 40% – on a global scale (cf. FvA & Gerhard 1994a, b). This should be compared to the large-scale SFEs around $0.1-3\%$ as determined for normal spiral and irregular galaxies and for starbursts in (isolated) dwarf galaxies.

Small scale SFEs in Milky Way **M**olecular **C**louds (**MCs**) can be defined as the mass ratio of the core mass of a MC to its total mass, SFE:= M(MCcore)/M(MC), and also have values in the range $0.1 - 3\%$. I.e., a very small mass fraction of order 0.1 to few % of Galactic MCs has the high densities relevant for SF and makes up the cloud core.

On scales of $10-300$ pc, ULIRGs that all have been shown to be advanced stages of massive gas-rich galaxy mergers, feature SFEs in the range $30 - 100\%$. Their extremely strong nuclear starbursts are heavily dust-obscured, emitting the bulk of their bolometric luminosities at FIR wavelengths.

3 Molecular Clouds and Star Formation

3.1 Molecular Cloud Structure and Star Formation

In the Milky Way and nearby galaxies, molecular clouds are observed using sub-mm lines with different lines being tracers of molecular gas at different densities. The most often observed CO(1–0) line traces gas at densities $n \geq 100$ cm^{-3}, the HCN(1–0) line traces gas at $n \geq 30\,000$ cm^{-3}, and the CS(1–0) line traces gas at $n \geq 100\,000$ cm^{-3}. Within the Milky Way and the nearest Local Group galaxies detailed observations of MC complexes in these different lines allow to assess their internal structure. It is from this kind of observations that we know that MCs typically have much more than 90% of their mass in low density envelopes as traced by CO and only a few % in their high density cores as traced by HCN or CS. I.e., on small scales for Milky Way MCs

$$\mathrm{L(HCN,\ CS)/L(CO)} \sim 0.1\ -\ 3\%\ \sim\ \mathrm{M(MC\ core)/M(MC)}$$

For galaxies beyond the Local Group, only integrated measures of luminosities in these different lines are possible and allow to estimate integrated mass ratios of molecular gas at various densities. On scales of 10–300 pc it has been shown for ULIRGs that

$$\mathrm{L(HCN,\ CS)/L(CO)} \sim 30\ -\ 100\%\ \sim\ \mathrm{M(MC\ core)/M(MC)},$$

suggesting that the MC structure in these massive gas-rich interacting galaxies with their tremendous starbursts is drastically different from the MC structure in the Milky Way or the Magellanic Clouds. The dynamical mass in the central regions of ULIRGs is dominated by the mass of molecular gas at densities of MC cores. This is, in fact, predicted by hydrodynamical simulations of gas-rich spiral – spiral mergers and necessary if these mergers are to result in elliptical galaxies. The molecular gas densities in the centers of ULIRGs are similar to the central stellar densities in giant ellipticals, their SFRs high enough to transform the gas into stars within the typical duration of a ULIRG phase ($1 - 4 \cdot 10^8$ yr). These apparent drastic differences in MC structure immediately raise the question if the SF process in massive gas-rich galaxy mergers, in particular in those going through a LIRG or ULIRG phase, can be the same as for the normal SF mode of undisturbed galaxies or for the mini-starbursts in BCDGs – as they appear in comparison to those in LIRGs or ULIRGs? A scenario where increased rates of cloud – cloud collisions are at the origin of the enhanced SF is hard to imagine in view of the fact that the core of Arp 220 on a scale of several 10 to 100 pc resembles **one** ultra-giant MC core of order $10^{10}M_\odot$ (cf. FvA 1994).

Observationally, a very tight correlation between global SFRs measured from FIR luminosities and the total mass in MC cores measured in terms of HCN–luminosities is found to hold for normal spirals as well as for the most extreme LIRGs and ULIRGs, i.e. over 4 orders of magnitude in terms of both total MC core masses and SFRs (Solomon *et al.* 1992, Gao & Solomon 2004). At the same time, the ratio between SFR as measured from L_{FIR} and total MC core mass as measured by L_{HCN} is roughly constant for all SFing galaxies from spirals through ULIRGs (Gao & Solomon 2004), indicating that the SF efficiency when referred not to HI but to the amount of dense molecular gas as traced by HCN or CS is constant over all the dynamical range.

For all galaxies (BCDGs ... Irrs ... spirals ... ULIRGs), SF efficiencies quantitatively correspond to the ratio between the integrated mass of MC cores and the total mass of molecular gas. For BCDGs ... spirals the total mass of molecular gas exceeds that of the MC cores by a factor ≥ 100, for ULIRGs both quantities are comparable. Hence, SFE $\sim$ M(MC core)/M(MC) or L(FIR) $\sim$ L(HCN, CS)/L(CO).

The widely used Schmidt (1959) law relates the SFR density to the neutral or molecular gas density to a power n with n$\sim$ 1 for spirals, Irrs, and BCDGs, and n$\sim$ 2 for ULIRGs and holds over 5 orders in gas surface density and 6 orders in SFR density.

When expressed in terms of high density gas traced by HCN or CS, the Schmidt law takes the form

$$\text{SFR density} \sim (\text{gas(HCN, CS) density})^n$$

with n = 1 for **all** galaxies (spirals, . . ., ULIRGs) and all SF regimes, as also shown by Gao & Solomon (2004).

In the course of mergers among gas-rich galaxies, hydrodynamic models (SPH) as well as sticky particle codes predict strongly enhanced collision rates among MCs that push up their SFRs. Models also predict that shock compression of MCs should significantly raise SF efficiencies to values SFE $\leq 0.75 - 0.9$, already for small overpressures in the intercloud medium (Jog & Das 1992, 1996). Strong burst SFRs require not only pre-existing MCs to be efficiently transformed into stars but also the fast transformation of HI into molecular gas. McKee & Ostriker (1977) have shown that shocks are very efficient in promoting the transformation of HI, leaving the ISM behind strong shocks almost fully molecular.

It hence appears that once gas is compressed to MC core densities, it is with almost 100 % efficiency transformed into stars. The process that determines the SF timescale and the SF efficiency seems to be the compression of gas to these high densities. And this process, in turn, is apparently slow and has low efficiency in non-interacting spirals, irregulars and even starbursting dwarfs, while fast and very efficient in massive gas-rich interacting galaxies.

3.2 Molecular Cloud Mass Spectra

In spiral and irregular galaxies and normal SF mode MCs, their cores, and ultimately even the star clusters that form from them, all feature similar mass spectra that are power laws with index m $\sim -1.7 \ldots -2$.

Largely unexplored at present are the mass spectra of MCs and MC cores in strongly interacting galaxies due to the large distance of those systems. A first attempt in this direction is presented by Wilson *et al.* (2003) for the Antennae galaxy pair NGC 4038/39 at a distance of 15 Mpc, an ongoing merger of two Sc-type spirals as estimated from the HI-richness of their long tidal tails. NGC 4038/39 is a LIRG with the most vigorous SF going on in the overlap region between the two disks and huge amounts of star cluster formation. Ground- and space-based observations over a large wavelength range as well as extensive dynamical modelling is available for the Antennae galaxies, the youngest system in Toomre & Toomre's (1972) age sequence of interacting galaxies. Wilson *et al.* find the mass spectrum of MCs in the Antennae to obey a power-law with m in the range $-1.2 \ldots -1.6$ in the accessible mass range from 10^7 to 10^9 $M_\odot$. The mass range below 10^7 $M_\odot$ as well as the mass spectrum of MC cores remain inaccessible to present-day instrumentation. Although this slope is slightly flatter than for MC mass spectra in non-interacting galaxies, it is not clear yet, if the MC mass spectrum in the Antennae is really enhanced in massive MCs due to the high ambient pressure as could be expected from the above-quoted models.

4 Star Cluster Formation

Star cluster formation is an important mode of SF, in particular in starbursts. ~ 20 % of the UV luminosity of starburst galaxies is accounted for by Star Clusters, and the contribution of star clusters to the total UV luminosity seems to increase with increasing UV surface brightness (Meurer *et al.* 1995).

Star clusters observed with HST in a large number of interacting and merging galaxies and young merger remnants seem to span the full range from low mass clusters ($\sim 10^3$ $M_\odot$) through high and very high mass clusters ($\geq 10^7$ $M_\odot$), from weakly bound, short-lived clusters similar to the open clusters in nearby galaxies all through strongly bound and long-lived clusters analoguous to Globular Clusters.

It has been predicted by hydrodynamical cluster formation models that the formation of strongly bound and hence long-lived clusters requires very high SF efficiencies SFE ≥ 20 % (Brown *et al.* 1995), and is therefore generally not possible during normal SF in spiral or irregular galaxies, nor in the mini-starbursts in BCDGs.

The very existence of a large number of massive compact star clusters in the relatively old spiral – spiral merger remnant NGC 7252, in which a very strong burst ended more than Myr ago, proves that these clusters must be very strongly bound – like Globular Clusters – as they survived for that span of time in an environment where violent relaxation has been strong enough to transform the two spiral disks into an elliptical-like object with an $r^{1/4}$ light profile (Schweizer 2002).

In the Antennae NGC 4038/39 we have analysed the 550 star clusters that have been detected in V and I with HST WFPC1 by Whitmore & Schweizer (1995) with our GALEV models and derived ages from their V-I colors under the assumption that they have around half-solar metallicity – as expected if they form from the ISM of Sc spirals and confirmed by spectroscopy of the brightest of them by Whitmore *et al.* (1999). We found 480 of them to have ages $\leq 4 \cdot 10^8$ yr and 70 to be fiducially old Globular Clusters inherited from the progenitor galaxies (FvA 1998). We followed their evolution with our GALEV evolutionary synthesis models and showed that – provided they would all survive – they would develop a color distribution with the same width but somewhat redder, due to their enhanced metallicity, as those of metal-poor GCs and a Gaussian shape **L**uminosity **F**unction (**LF**) typical of old GC systems despite the fact that their observed LF is a power law. It is the age spread among the young star clusters, that is comparable to their age, in conjunction with the rapid luminosity evolution during these young ages and with the observational completeness limit that causes this apparent distortion in the LF.

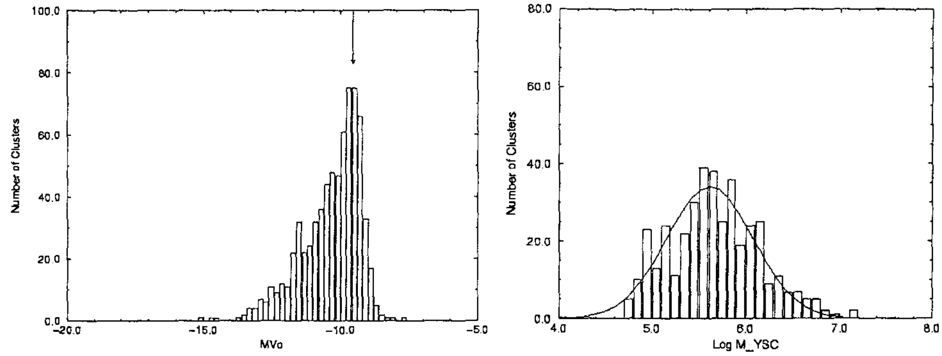

Figure 3: Observed LF of star clusters in NGC 4038/39 (Fig. 3a). The arrow indicates the observational completeness limit. Mass Function derived for the **young** clusters with a Gaussian fit as described in the text (Fig. 3b).

In FvA (1999) we derived masses from ages and model M/L-ratios for all the clusters and found the **M**ass **F**unction (**MF**) of the **young** star cluster system to be a Gaussian with $\langle \log \mathrm{M} \rangle = 5.6$ and $\sigma = 0.46$ very similar to that of GCs in the Milky Way and M31 with $\langle \log \mathrm{M} \rangle = 5.47$, $\sigma = 0.5$ and $\langle \log \mathrm{M} \rangle = 5.53$, $\sigma = 0.43$, respectively (cf. Ashman *et al.* 1995).

The major drawback in our analysis was our assumption of a uniform reddening for all young clusters lack of more detailed information about individual clusters. Zhang & Fall (1999) used reddening-free Q-parameters for their analysis of the same data and found a power-law mass function. The major drawback in their analysis was that they had to exclude an important fraction of clusters for which the Q-parameters did not yield an unambiguous age. Excluding this age group of clusters in our models also leads to a power-law MF. Hence, till today, the MF of young star clusters forming in merger-induced starburst is controversial. A multi-wavelength analysis should allow to independently determine metallicities, ages, extinction values, and masses of all the young star clusters provided accurate photometry in at least 4 reasonably spaced passbands is available, as shown by Anders *et al.* (2004a), and is currently underway using HST WFPC2, NICMOS and VLT data provided by our ASTROVIRTEL project (PI R. de Grijs).

The question is if and to what percentage the young star clusters copiously formed in galaxy mergers are open clusters or GCs and if they split into these two distinct classes of objects or if there is a continuum extending from losely bound and low-mass open clusters to strongly bound and high-mass GC. Key issues for this question are their mass range, their MF and their compactness. Size determinations for young star clusters require a careful analysis: small clusters are barely resolved even in the closest interacting systems, the galaxy background is bright and varies on small scales, and some clusters do not (yet?) seem to be tidally truncated, i.e. cannot be described by King models. The degree of internal binding, i.e. the ratio between mass and radius, however, is a key parameter for survival or destruction of a cluster in the violently changing environment of the merging and relaxing galaxy.

4.1 Globular Cluster Formation

GC formation requires extremely high SF efficiencies. It happened in the Early Universe and it apparently happens today in the strong starbursts accompanying the mergers of massive gas-rich galaxies. If it also happens in non-interacting massive starburst galaxies or in dwarf galaxy starbursts is an open question.

Our investigation of star clusters in the dwarf starburst galaxy NGC 1569, that was known

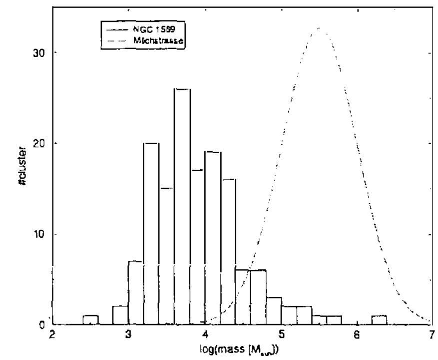

Figure 4: Mass Function of young star clusters in the dwarf starburst galaxy NGC 1569 as compared to the MF of Milky Way GCs.

before to host 3 super star clusters, revealed $\sim$ 160 young star clusters with good photometry in many bands in our ASTROVIRTEL data base. Analysis of their Spectral Energy Distributions (**SEDs**) in comparison with a large grid of GALEV models for star clusters with various metallicities and dust extinctions by means of a dedicated SED Analysis Tool yielded individual clusters ages – all $\leq$ 24 Myr –, metallicities, extinction values, and masses. As seen in Fig. 4, masses of all but 3 of these clusters turn out to be lower and most in fact much lower – of order $10^3 - 10^4$ $M_\odot$ – than those of GCs in the Milky Way despite their high luminosities that are due to their very young ages (Anders *et al.* 2004b).

Hence, with maybe 2 or 3 exceptions – depending on a careful determination of their sizes –, the rich bright young cluster population in the dwarf starburst galaxy NGC 1569 does not seem to comprise any young GCs, most of its low-mass clusters will probably not survive the next $1 - 2$ Gyr. This raises the question why GCs do not form in dwarf galaxy starbursts. Why are SF efficiencies low in dwarf starbursts as already found for BCDGs many years ago? Because of the short dynamical timescales or the shallower potential in dwarf galaxies or because of a lack of ambient pressure in these non-interacting galaxies as compared to massive interacting galaxies? An answer should be provided by careful analyses of the starburst and star cluster properties in dwarf – dwarf galaxy mergers.

4.2 Star Cluster vs. Field Star Formation

An intriguing example of episodes with and without cluster formation is provided by the LMC. It shows a clear gap in terms of star cluster ages (Rich *et al.* 2001) with no clusters in the age range from 4 – 10 Gyr. This gap, however, is not seen in field star ages and the metallicity apparently has also increased continuously over the cluster age gap. Star cluster formation epochs coincided with epochs of enhanced field star formation, probably associated with close encounters between the LMC and the Milky Way.

5 Conclusions and Open Questions

I have shown that global galaxy-wide SFRs span a huge range, even in relation to galaxy mass, from normal low-level SF in undisturbed disk galaxies to the extremely high SFRs in massive gas-rich interacting galaxies, ULIRGs, and SCUBA galaxies.

I cautioned that SFR estimates from H_α– or O[II]– luminosities are only valid for metallicities close to solar and for SFR fluctuations on timescales $\geq 10^8$ yr, hence not for dwarf galaxy starbursts, nor for SFing regions on subgalactic scales.

Concerning SF efficiencies, there is a clear dichotomy between normal galaxies and dwarf galaxy starbursts on the one hand and starbursts in massive interacting gas-rich galaxies on the other hand, with SFEs differing by factors 10−100 between them. It apparently originates in a similar dichotomy for the integrated mass ratio between molecular gas at low densities as traced by CO and the high density molecular gas of MC cores as traced by HCN or CS with the ratio M(MC core)/M(MC) differing by the same factor 10−100. The key process determining the SF efficiency seems to be compression of molecular gas to MC core densities. Once this is accomplished, the high density MC core material is transformed into stars with very high efficiency – in fact with the **same** efficiency in normal, starburst, and ULIRG galaxies.

The causes of these differences are not clearly identified yet. They could be differences in the dynamical timescales, in the depth of the potential or the dynamics of a merger. Detailed investigations into the starburst and its star and cluster formation in a dwarf – dwarf galaxy merger should tell.

While it will not be possible to resolve the masses of MCs and MC cores down to interesting values before ALMA – not even for the closest interacting galaxies, the comparison of integrated luminosities in lines tracing molecular gas at various densities should already yield interesting clues to the molecular cloud structure in various kinds of starbursts.

Star cluster formation is an important and sometimes dominant mode of SF. It is not clear yet if the mass ratio between SF going into field stars and SF going into star cluster formation – and, in particular, into the formation of compact massive long-lived GCs – scales with the strength of SF or burst, or with the SF efficiency. A comparative investigation of integrated starburst properties and those of the young star cluster populations should help.

A third dichotomy, probably related to the other two, was found concerning GC formation. While GC formation apparently is possible and wide-spread in high SF efficiency situations as in the Early Universe or in massive gas-rich spiral – spiral mergers, it does not seem to be possible, or at least not frequent, in isolated dwarf galaxy starbursts.

The age and metallicity distributions of GC (sub-)populations contain valuable information about the violent (star) formation histories of their parent galaxies and can reasonably be disentangled by means of multi-wavelength SED analyses.

Acknowledgments

I thank the organisers and the DFG (Fr 916/11-1) for partial travel support and gratefully acknowledge very efficient support from the ASTROVIRTEL team (project funded by the European Comm. under FP5 HPRI-CT-1999-00081).

References

1. Anders, P. & Fritze – v. Alvensleben, U., 2003, A&A 401, 1063
2. Anders, P., Bissantz, N., Fritze – v. Alvensleben, U., de Grijs, R., 2004a, MN 347, 196
3. Anders, P., de Grijs, R., Fritze – v. Alvensleben, U., Bissantz, N., 2004b, MN 347, 17
4. Ashman, K. M., Conti, A., Zepf, S. E., 1995, AJ 110, 1164
5. Brown, J. H., Burkert, A., Truran, J. W., 1995, ApJ 440, 666
6. Fritze – v. Alvensleben, U., 1994, in *Violent Star Formation*, ed. G. Tenorio – Tagle, Cambridge Univ. Press, p. 249
7. Fritze – v. Alvensleben, U., 1998, A&A 336, 83
8. Fritze – v. Alvensleben, U., 1999, A&A 342, L25
9. Fritze – v. Alvensleben, U., 2004, A&A 414, 515
10. Fritze – v. Alvensleben, U. & Gerhard, O. E., 1994a, A&A 285, 751

11. Fritze – v. Alvensleben, U. & Gerhard, O. E., 1994b, A&A 285, 775
12. Gao, Y. & Solomon, P. M., 2004, ApJS 152, 63
13. Izotov, Y. I., Thuan, T. X., Lipovetsky, V. A., 1994, ApJ 435, 647
14. Izotov, Y. I., Thuan, T. X., Lipovetsky, V. A., 1997, ApJS 108, 1
15. Izotov, Y. I., Thuan, T. X., 1998, ApJ 500, 188
16. Jog, C. J., Das, M., 1992, ApJ 400, 476
17. Jog, C. J., Das, M., 1996, ApJ 474, 797
18. Kennicutt, R. C., 1998, ARAA 36, 189
19. Krüger, H., Fritze – v. Alvensleben, U., Loose, H.-H., 1995, A&A 303, 41
20. McKee, C. F., Ostriker, J. P., 1977, ApJ 218, 148
21. Meurer, G. R., Heckman, T. M., Leitherer, C., Kinney, A., Robert, C., Garnett, D. R., 1995, AJ 110, 2665
22. Rich, R. M., Shara, M. M., Zurek, D., 2001, AJ 122, 842
23. Schaerer, D., de Koter, A., 1997, A&A 322, 598
24. Schmidt, M., 1959, ApJ 129, 243
25. Schweizer, F., 2002, IAU Symp. 207, 630
26. Smith, L. J., Norris, R. P. F., Crowther, P. A., 2002, MN 337, 1309
27. Solomon, P. M., Downes, D., Radford, S. J. E., 1992, ApJ 387, L55
28. Toomre, A. & Toomre, J., 1972, ApJ 178, 623
29. Weilbacher, P. & Fritze – v. Alvensleben, U., 2001, A&A 373, L9
30. Whitmore, B. C. & Schweizer, F., 1995, AJ 109, 960
31. Whitmore, B. C., Zhang, Q., Leitherer, C., Fall, S. M., Schweizer, F., Miller, B. W., 1999, AJ 118, 1551
32. Wilson, C. D., Scoville, N., Madden, S. C., Charmandaris, V., 2003, ApJ 599, 1049
33. Zhang, Q. & Fall, S. M., 1999, ApJ 527, L81

PERIODICALLY BURSTING STAR FORMATION IN DWARF IRREGULARS

F.I. Pelupessy, P.P. van der Werf, V. Icke

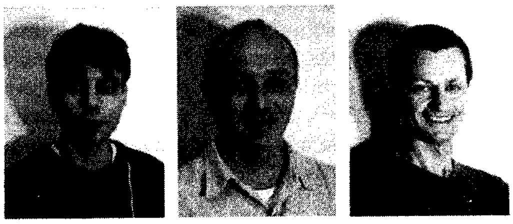

Leiden Observatory, PO Box 9513, 2300 RA Leiden, The Netherlands

We examine star formation in dwarf irregulars using N-body/SPH simulations. To represent the ISM of these systems in a realistic manner our code includes a detailed model for star formation and a new method of implementing feedback. We find a bursting star formation mode with the ISM of the galaxy regulated by stellar feedback processes. In the central parts of the galaxy triggered star formation is dominant. Outside the central 1.5 kpc it proceeds through a more quiescent mode. We also compare our simulation with an observed sample of isolated dwarfs. We find that our model is consistent with the observed distribution of instantaneous over mean star formation.

Keywords: methods: numerical, methods: N-body, galaxies: dwarf, galaxies: evolution, galaxies: ISM, galaxies: irregular

1 Introduction

On the small end of the galaxy size and mass spectrum, dwarf irregular galaxies form a group of gas-rich star forming galaxies characterized by disordered, patchy star formation and a complex HI morphology. These systems are in a sense the most clean examples of star forming galaxies, they lack spiral density waves and have rotation curves with low shear, and for this reason they have attracted much interest amongst observers.

Recently, they have been studied intensively with surveys of dwarf systems (Hunter 1997 [12], Stil 1999 [29], van Zee 2001 [31]) showing that they are not young systems, since they have old populations of stars. Their star formation has been roughly constant for Gyrs, and their current star formation is generally not extremely high, with gas consumption timescales of $t_c > 10^{10}$ yr. As a group they do exhibit widely varying star formation rate(SFR), the SFR per unit area spanning 4 orders of magnitude(Hunter 1997). However their star formation properties do not seem to be correlated to other physical parameters that are independent of star formation (van Zee 2000[30],2001 [31]). Also, Hunter et al.(1998 [13]) studied a number of possible mechanisms that could be responsible for regulating star formation(amongst which gravitational and thermal instabilities and shear regulation), but found none that could be responsible for observed star formation patterns.

Some tantalizing hints about star formation processes have come from the study of single systems. Detailed HI observations (e.g. Kim et al. 1998 [15], Wilcots & Miller 1998 [34], Puche et al. 1992 [20], Walter & Brinks 2001 [33]) reveal the complex 'frothy' structure of the ISM, dominated by holes, shells and filamentary structure. The energy associated with these structures is comparable to the available mechanical luminosity of the young stars, suggesting that star formation plays an important role in shaping the interstellar medium(ISM) of these systems. Star formation, on the other hand is found within the dense walls of the HI holes, and chains of star formation suggestive of propagating star formation have been found (Stewart et al. 2000 [28]).

This wealth of observational data does not mean however that we have a clear picture about star formation in dwarf galaxies. It is for example not clear whether the majority of isolated dwarf galaxies experiences constant, bursting, gasping or chaotic star formation or to what extent the superbubbles in the ISM are actually caused by feedback processes. Some doubt has been cast on the origin of the holes in what seemed to be the most clear example, Ho II (Rhode et al. 1999 [22]). And although the case for secondary star formation events is very strong in a number of systems(Stewart et al. 2000 [28]), it has not yet become clear to what extent there is real propagating star formation. Then there is also the more general question of the evolutionary relation between the different classes of dwarf galaxies, such as ellipticals, irregulars and blue compact dwarfs(BCD).

While it is clear that feedback processes play a major role one must be careful with arguments based on simple analytical estimates. The nature of the ISM, which is both kinematically and thermodynamically in a very dynamic state, means that numerical simulation is necessary to make realistic models that can follow the different processes important in these systems.

The possible consequences of propagating star formation were studied extensively in the context of *stochastic self-propagating star formation* (SSPSF) models. These showed that episodic star formation was a natural consequence of the small size of dwarf galaxies(Gerola & Seiden 1980 [11], Comins 1983 [6]). However, while they probably capture some general characteristics of the star formation pattern, these models are phenomenological and do not include the underlying physics of the ISM. Other theoretical studies of the influence of star formation on the ISM of dwarf galaxies have mainly concentrated on the effects of large (central) bursts and on questions concerning the ejection of gas and the distribution of metals(e.g. Mac-Low & Ferrara 1999 [17], Mori et al. 1997 [18]), without trying to set up self-consistent star formation and ISM models.

The importance of a good model for the ISM and feedback has been recognized by a number of authors working on codes for galactic evolution problems(a.o. Andersen & Burkert 2000 [1], Berczik & Hensler 2003 [2], Semelin and Combes 2002 [23], Springel & Hernquist 2003 [27]). However, relatively little effort has been directed towards resolving the normal evolution of irregular dwarfs and providing the connection with detailed studies of single systems and extensive unbiased samples. Dwarf galaxies are good test systems for exploring star formation in galaxies: they are dynamically simple systems in the sense that they do not exhibit spiral density waves or shear. Furthermore their small size means that simulations can follow the various physical processes at finer linear and density scales. Here we report on simulations we have performed of the evolution of a normal dwarf irregular galaxy, including a detailed model for the ISM, star formation and feedback. Our model does not explicitly postulate the presence of a two phase medium, rather it forms it as a result of the physics of the model. Furthermore we take special care in formulating a star formation model that is solely based on the Jeans instability, and we formulate a feedback scheme that gives us unambiguous control over the strength of the feedback. We will discuss the results of the simulation both in relation to detailed observations of comparable single systems, as well as in the context of recent surveys of dwarf galaxies.

Table 1: Overview of the processes included in the ISM model used. For H and He ionization equilibrium is explicitly calculated, for other elements collisional ionization equilibrium (CIE) is assumed. references: 1) Wolfire et al. 1995 [35], 2) Raga et al. 1997 [21] , 3) Verner & Ferland 1996 [32], 4) Silva & Viegas 2001 [25]

process	comment	ref.
heating		
Cosmic Ray	ionization rate $\zeta_{CR} = 1.8\ 10^{-17}\ s^{-1}$	1
Photo Electric	FUV field from stars	1
cooling		
e,H_0 impact	H,He,C,N,O,Si,Ne,Fe	2,4
ionization & recombination		
UV	ionization assumed for species with $E_i < 13.6$eV	
Cosmic Ray	H, He only; primary & secondary ionizations	1
Collisional	H, He only	3
Radiative recombination	H, He only	3
CIE	assumed for metals	

2 Method

To be able to characterize the star formation in dwarf galaxies we need to model the complex and dynamic system that is the ISM of a galaxy. This means that, in addition to self gravity and gasdynamics, we need to include realistic modelling of the ISM and star formation and feedback processes. We employ an N-body/SPH code, using the conservative SPH formulation of Springel & Hernquist(2002 [26]).

2.1 The ISM model

Our model for the ISM is qualitatively similar to the model for the Cold Neutral Medium (CNM) and Warm Neutral medium (WNM) of Wolfire et al. (1995 [35],2003 [36]). We solve for the ionization and thermal evolution of the gas including the various processes given in Table 1. A concise overview of the ISM model is given in Fig. 1. The plots in this figure show that as density varies, the equilibrium state of the gas changes from a high temperature/high ionization state ($T = 10^4$ K, $x_e \approx 0.1$) at low densities, to a low temperature/low ionization state ($T < 100$ K, $x_e < 10^{-3}$) at high densities. In between is a density domain where the negative slope of the P-n relation indicates that the gas is unstable to isobaric pressure variations, the classic thermal instability. The shape of these curves and hence the exact densities of the thermal instability vary locally throughout the simulation according to the conditions of UV and supernova heating. The gas in the simulation may be out of equilibrium, although the timescales for reaching equilibrium are generally short, $< 10^6$ yr. In principle the cooling properties of the gas depend on the local chemical composition. In practice, only small metallicity gradients are observed in dwarfs, so we take constant metallicity($Z = 0.2\ Z_\odot$). Potentially more serious is the fact that we assume a constant cosmic ray ionization rate ζ throughout the galaxy. We take a 'standard' value of $\zeta = 1.8\ 10^{-17}\ s^{-1}$. The low energy ($\approx$ 100 MeV) cosmic rays that are important for heating and ionization of the ISM, have short mean free paths($<$ 10 pc) so ζ is expected to vary substantially across a galaxy. However, the exact sources, let alone production rates, of these low energy cosmic rays are not well known.

The FUV luminosities of the stellar particles, which are needed to calculate the local FUV field used in the photoelectric heating, are derived from Bruzual & Charlot (1993 [3], and updated) population synthesis models for a Salpeter IMF with cutoffs at 0.1 $M_\odot$and 100 $M_\odot$. In the present work we do not account for dust extinction of UV light.

2.2 Star formation & Feedback

The coldest and densest phase in our model is best identified with the CNM. Giant molecular clouds(GMC) are embedded and form in the CNM, but we would have to take account of complex physics and extreme resolution demands to follow collapse further. Hence we use a simple prescription for star formation, based on the assumption that star formation is governed by the unstability of the parent GMCs. A region is considered unstable to star formation if the local Jeans mass M_J is smaller than the mass of a typical molecular cloud $M_{ref} \approx 10^5 M_\odot$. The rate of star formation is set to scale with the local free fall time: $\tau_{sf} = f_{sf} t_{ff} = \frac{f_{sf}}{\sqrt{4\pi G\rho}}$. The delay factor f_{sf} is uncertain, but from observations a value $f_{sf} \approx 10$ seems reasonable. The actual efficiency of star formation is then determined by balance between the cooling of the gas and the UV and SN heating.

Feedback from stellar winds and supernovae is essential for regulating the ISM. While the mechanical energy output of stars is reasonably well known, it has proven to be difficult to include it completely self-consistently in galaxy sized simulations of the ISM. The reason for this is that the effective energy of feedback depends sensitively on the energy radiated away in thin shells around the bubbles created. This will mean that the effect of feedback is not reliable unless prohibitively high resolution is used. In SPH codes there have been conventionally two ways to account for feedback: by changing the thermal energy input and by acting on particle velocities. Both are unsatisfactory, as the thermal method suffers from overcooling (Katz 1992 [14]) and the kinetic method seems to be too efficient in disturbing the ISM (Navarro & White 1993 [19]). Here we use a new method based on the creation at the site of young stellar clusters of *pressure particles* that act as normal SPH particles in the limit that mass of the particle $m \to 0$, for constant energy. For the energy injection rate we take $\dot{E} = \epsilon_{sn} n_{sn} E_{sn}/\Delta t$, with $E_{sn} = 10^{51}$ erg, $\epsilon_{sn} = .1$, $n_{sn} = 0.009$ per $M_\odot$ and $\Delta t = 3 \times 10^7$ yr. The efficiency ϵ_{sn} thus assumes that 90% of the energy is radiated away, a value which comes from more detailed simulations of the effect of supernova and stellar winds on the ISM (Silich et al. 1996 [24]), and is also used in other simulations of galaxy evolution(e.g. Semelin & Combes 2002 [23], Springel & Hernquist 2002 [26], Buonomo et al. 2000 [4]).

2.3 Initial conditions

We set up a model dwarf galaxy resembling current dIrrs. Although these exhibit a wide range of morphologies, they are very similar in their averaged radial profiles to scaled down versions of ordinary disk galaxies. Hence we take for the initial condition a three component model for a small disc galaxy, consisting of a gas disk, a stellar disk and a dark halo, modelled loosely on the properties of DDO 47 and similar dIrrs. The gas disk is constructed with a radial surface density profile,

$$\Sigma = \Sigma_g/(1 + R/R_g), \tag{1}$$

with central density $\Sigma_g = 0.01\ M_\odot/\mathrm{kpc}^2$ and radial scale $R_g = .75$ kpc, truncated at 6 kpc. An exponential stellar disk,

$$\rho_{disk}(R, z) = \frac{\Sigma_0}{2h_z} \exp(-R/R_d) \mathrm{sech}^2(z/h_z) \tag{2}$$

with central surface density $\sigma_0 = 0.3\ M_\odot/\mathrm{kpc}^2$, $R_d = 0.5$ kpc and vertical scale height $h_z =$ 0.2 kpc, is constructed as in Kuijken & Dubinski (1995 [16]). The total mass of the gas is $M_g =$

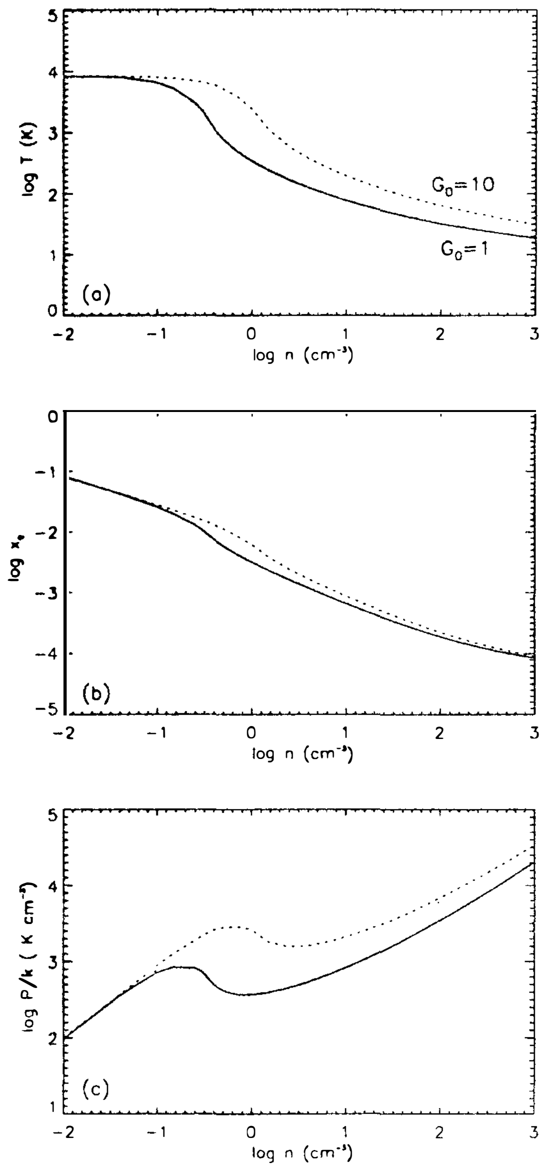

Figure 1: Overview of the ISM model: Equilibrium plots of (a) temperature T, (b) electron fraction x_e and (c) pressure P as a function of density n for two different values of the UV field G_0, drawn line: $G_0 = 1$, dotted: $G_0 = 10$ ($\times 1.6\ 10^{-3}$ ergs cm^{-2} s^{-1})

$2 \times 10^8 M_\odot$ and the total mass of the stellar disk is $M_d = 1.5 \times 10^8 M_\odot$. Both the gas disk and stellar disk are represented by $N = 10^5$ particles. The ages of the initial population of stars are distributed according to a constant SFR of 0.007 $M_\odot$/yr.

Dwarf galaxies are amongst the most dark matter dominated objects, exhibiting dark to luminous matter ratios of 10-100. Their rotation curves are best fit by flat central density cores (Flores & Primack 1994 [10], Burkert 1995 [5]). Therefore we take a halo profile

$$\rho_{\rm halo}(r) = \rho_0 \frac{\exp(-r^2/r_c^2)}{1 + r^2/\gamma^2} \tag{3}$$

with core radius $\gamma = 2$ kpc, cutoff radius $r_c = 20$ kpc and central density $\rho_0 = 2 \times 10^7\ M_\odot/\mathrm{kpc}^3$, for a total mass of $M_{\rm halo} = 15 \times 10^9 M_\odot$ and a peak rotation velocity of about 50 km/s. We represent the dark halo by a static potential.

3 Results

In Fig. 2, UBV snapshots of the simulated dwarf galaxy are shown, taken after about 1 Gyr of evolution and spaced about 50 million years apart. The appearance of the galaxy varies with time, episodes of strong star formation(e.g. at 1024 Myr) are followed by quiescent phases(1071 and 1118 Myr). During star formation bursts the galaxy is dominated by a few very active star formation sites, during quiet times the galaxy is relatively featureless. The brightness of the galaxy varies from approximately $M_B = -14.6$ in burst phase to $M_B = -14.2$ at quiescent phases, with colors varying from U-V=.13 and U-B=-.3 to U-V=.5 and U-B=-.03.

If we look at the HI (Fig. 3) we see that the HI distribution of the galaxy is dominated by holes of varying sizes. the ISM of the galaxy is in a very dynamical state. Dense shells of HI combine to form big HI clouds, which correspond to the sites of intense star formation. As the cold clouds move about in the galaxy they are in turn destroyed by mechanical feedback from the stars to perpetuate the cycle of star formation, cloud destruction and formation. Sometimes structures resembling spiral arms form, but generally there are no spiral density waves in gas or stars, and, due to the low shear, a flocculent spiral structure also does not develop.

The star formation history of the simulation is plotted in Fig. 4. It shows a gray scale plot of the temporal evolution of the (azimuthally averaged) star formation density and below it the resulting total SFR. We see that after an initial transient period the galaxy settles in a mode of periodically varying star formation, with a minimum SFR of about $0.003 M_\odot$/yr while the peak SFR is about a factor of 10 higher. Also plotted are the results for a run with reduced feedback strength. In this case variations are smaller in amplitude, and quasi-periodic.

The cyclical pattern of star formation raises a number of questions: What is the driver of these variations? What determines the period and amplitude of the oscillation? Why is star formation apparently synchronized over the whole galaxy? The period of the oscillation is about 165 Myr, which is slightly larger than double the dynamical time scale of the dark halo, ($t_{\rm dyn} = 80$ Myr). This suggests that cycle is governed by interplay of supernova feedback and gravity: feedback provides the kick for the oscillation, expelling gas and increasing the velocity dispersion and thus inflating the gas disk, after which the gas falls back for the next cycle on a dynamical time scale. Dwarf galaxies are in solid body rotation and their potential corresponds to a harmonic oscillator, which means that everywhere material flung out falls back to the same location in the same time, synchronizing the SFR over the whole galaxy. This effect can add to the phenomenon shown in Fig. 4, namely that the overall star formation cycle looks remarkably regular.

In the upper panel of Fig. 4 we see that star formation in the center is correlated. The azimuthally averaged density gives the impression that star formation is happening in inward and outward moving rings; however visual inspection shows that it moves around in patches

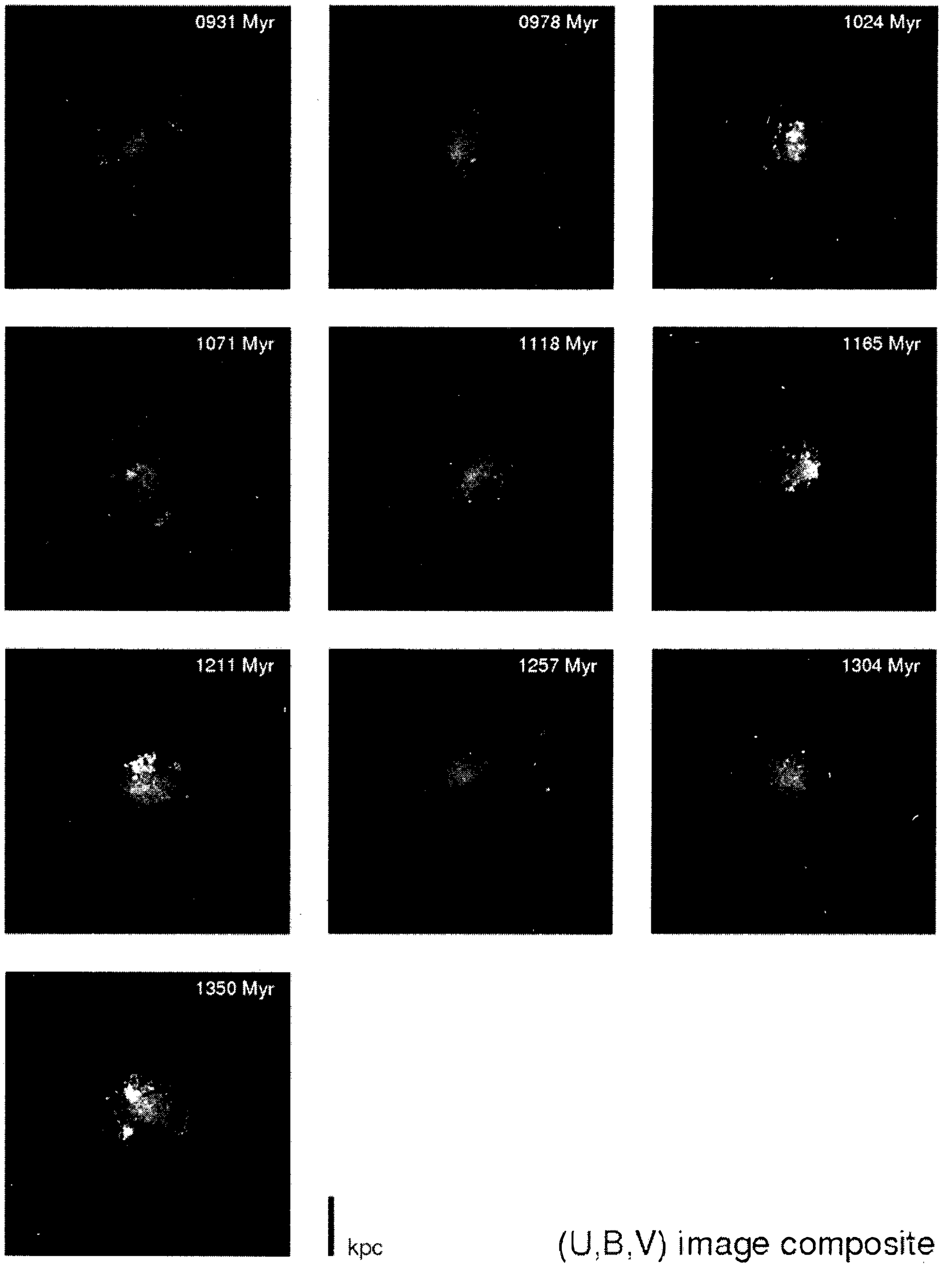

Figure 2: Simulated dwarf galaxy after ≈ 1 Gyr. Shown are UBV composite pictures at different times.

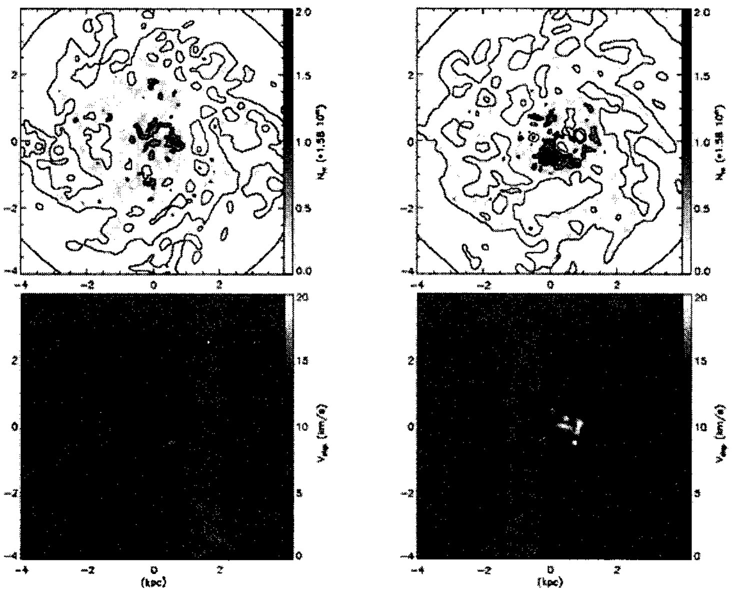

Figure 3: HI surface density & velocity dispersion map in quiescent phase(left, taken at 1165 Myr) and in burst phase(right, at 1211 Myr).

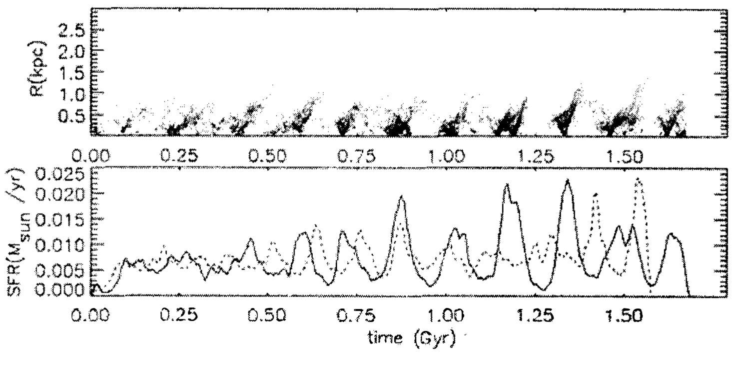

Figure 4: Star Formation History of a simulated dwarf galaxy. Upper panel: density plot of the azimutally averaged star formation rate. Lower Panel: total star formation rate. The dotted line indicates the SFR for a run with 50% reduced feedback strength.

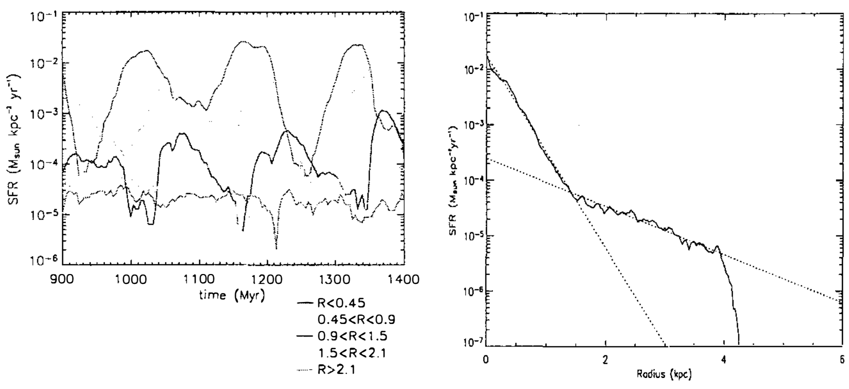

Figure 5: Left: SFR at different radii, right: radial profile of the mean star formation density(drawn line, dotted lines are exponentials with scalelengths of .25 and 1. kpc).

and partial rings: if some region starts to form stars, nearby dense regions will be triggered to form stars, often moving the star formation in a particular direction along a dense filament or bridge. Furthermore these periodic bursts happen only relatively close to the centre of the galaxy, whereas in the outer parts stars form at a more or less constant low rate. This difference in behaviour is illustrated by Figs 5. We see that in the inner part of the galaxy star formation is in a bursting mode, which due to the triggering gives rise to cyclical variations, whereas in the outer parts star formation happens in a more quiescent mode. This behaviour is expected (see Ehlerová & Palouš 2002 [9]) because star formation can only be triggered in the expanding shells around the holes induced by feedback if the column density is high enough, N $\approx 10^{20-21}$ cm^{-2}. Fig. 5 shows a plot of the resulting radial dependence of the star forming density, clearly visible are the three different regions with different star forming behaviour. The bursting region is confined within 1.5 kpc, while star formation extends further out, stopping abrubtly at $\approx$ 4kpc, well short of the edge of the gasdisk.

When we compare the star formation in our model and observed SFR (for example in Van Zee 2001 [31]) we see that the agreement is quite good: our values fall well within the range of observed rates of $0.001 M_\odot/yr$ to $0.1 M_\odot/yr$, although admittedly the star formation rate in our model does depend fairly strongly on poorly constrained quantities such as the shape of the IMF, the amount of energy released in SN and stellar winds, and the various parameters regulating star formation. It is however encouraging that we can use reasonable values for the parameters and get SFR that are close to observed rates.

It is difficult to verify whether variations of SFR in our model are realistic for real dwarf galaxies. Variations of within a factor $\approx$ 3 on timescales of 100s of Myr are difficult to track down. They do not leave clear signatures in CM diagrams and detection in detailed SFH derived from the ages of resolved populations of stars(possible for a select few galaxies using HST) is difficult due to the uncertainties inherent in this type of SFH derivation that go back more than few times 10^8 yr. On the other hand, there is evidence that bursts of roughly this amplitude do occur in dwarf galaxies(Dohm-Palmer et al. 1998 [7], 2002 [8]). Strong additional evidence for variations in the SFR is the observed scatter in the ratio of current star formation to past star formation: the Scalo b parameter. If the variations in our model are generic for isolated dwarf galaxies, this will explain the observed distribution of b. To verify this we have plotted in Fig. 6 the histograms of $\mathrm{SFR}/\langle\mathrm{SFR}\rangle_t$ for our simulation together with the distribution of b for a sample

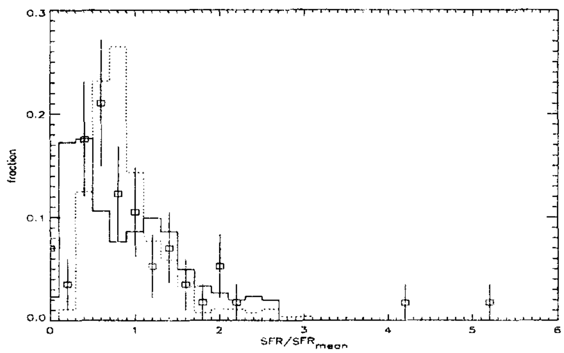

Figure 6: distribution of SFR/⟨SFR⟩$_t$ for a sample of isolated dwarfs (squares with error bars), a simulation with full feedback(drawn line) and a simulation with 50% feedback(dotted line). Data is taken from Van Zee 2001.

of isolated dwarf galaxies as derived by Van Zee 2001 ([31]). Clearly these two are qualitatively the same. We also have plotted the results for a run with 50% less feedback. In this case the amplitude of variations is somewhat too small(although both are in good agreement with the observed distribution given the uncertainties inherent in deriving it, see discussion in Van Zee 2001[31]). The distribution of b is a degenerate indicator of the SF history, and the above comparison assumes a.o. that dwarf galaxies form a homogeneous population; that variations in SFR are assumed to be of similar strength and shape, independent of galaxy properties(although the b distribution is independent of the period); and that the variations in SFR are periodic. Nevertheless we think that variations in SFR as a generic property for dwarf galaxies is the simplest explanation for the observed scatter and that our model captures a number of essential features of the these variations, namely: moderate bursting, long periods of low SF, and the 'peakiness' of the SF enhancements, all encoded in the specific shape of the distribution of Fig. 6.

4 Conclusions

Our model suggests that a large part of the current dIrr population is in a (quasi-)periodic burst mode of star formation. The scatter in observed properties in this picture is mainly due to the fact that galaxies are observed at different phases of their evolution. In our models variations are due to the interplay of stellar feedback and gas dynamics, the galaxy being periodically stirred by bursts of star formation after which a quiescent period occurs during which gas falls back to the disk. Our model predicts that the amplitude of the variations depends on the strength of the feedback and that the period depends on the dynamical time scale. Also, the surface density of gas determines whether star formation happens in a propagating mode. Therefore we expect to see differences in star forming behaviour and ultimately in observational properties depending on the parameters of the dark matter and gas distribution, that may explain differences between the types of star forming dwarf galaxies. We intend to study this question in future work by running different models of dwarf galaxies.

Acknowledgments

This work was sponsored by the stichting Nationale Computerfaciliteiten (National Computing Facilities Foundation) for the use of supercomputer facilities, with financial support from the Nederlandse Organisatie voor Wetenschappelijk Onderzoek (Netherlands Organisation for Scientific Research, NWO). FIP was supported by a grant from NWO.

References

1. Andersen, R.-P. & Burkert, A. 2000, ApJ, 531, 296
2. Berczik, P., Hensler, G., Theis, C., & Spurzem, R. 2003, Ap&SS, 284, 865
3. Bruzual A., G. & Charlot, S. 1993, ApJ, 405, 538
4. Buonomo, F., Carraro, G., Chiosi, C., & Lia, C. 2000, MNRAS, 312, 371
5. Burkert, A. 1995, ApJ, 447, L25+
6. Comins, N. F. 1983, ApJ, 266, 543
7. Dohm-Palmer, R. C., Skillman, E. D., Gallagher, J., et al. 1998, AJ, 116, 1227
8. Dohm-Palmer, R. C., Skillman, E. D., Mateo, M., et al. 2002, AJ, 123, 813
9. Ehlerová, S. & Palouš, J. 2002, MNRAS, 330, 1022
10. Flores, R. A. & Primack, J. R. 1994, ApJ, 427, L1
11. Gerola, H., Seiden, P. E., & Schulman, L. S. 1980, ApJ, 242, 517
12. Hunter, D. 1997, PASP, 109, 937
13. Hunter, D. A., Elmegreen, B. G., & Baker, A. L. 1998, ApJ, 493, 595
14. Katz, N. 1992, ApJ, 391, 502
15. Kim, S., Staveley-Smith, L., Dopita, M. A., et al. 1998, ApJ, 503, 674
16. Kuijken, K. & Dubinski, J. 1995, MNRAS, 277, 1341
17. Mac Low, M. & Ferrara, A. 1999, ApJ, 513, 142
18. Mori, M., Yoshii, Y., Tsujimoto, T., & Nomoto, K. 1997, ApJ, 478, L21+
19. Navarro, J. F. & White, S. D. M. 1993, MNRAS, 265, 271
20. Puche, D., Westpfahl, D., Brinks, E., & Roy, J. 1992, AJ, 103, 1841
21. Raga, A. C., Mellema, G., & Lundqvist, P. 1997, ApJS, 109, 517
22. Rhode, K. L., Salzer, J. J., Westpfahl, D. J., & Radice, L. A. 1999, AJ, 118, 323
23. Semelin, B. & Combes, F. 2002, A&A, 388, 826
24. Silich, S. A., Franco, J., Palous, J., & Tenorio-Tagle, G. 1996, ApJ, 468, 722
25. Silva, A. I. & Viegas, S. M. 2001, Computer Physics Communications, 136, 319
26. Springel, V. & Hernquist, L. 2002, MNRAS, 333, 649
27. Springel, V. & Hernquist, L. 2003, MNRAS, 339, 289
28. Stewart, S. G., Fanelli, M. N., Byrd, G. G., et al. 2000, ApJ, 529, 201
29. Stil, J. M. 1999, Ph.D. Thesis, Leiden
30. van Zee, L. 2000, AJ, 119, 2757
31. van Zee, L. 2001, AJ, 121, 2003
32. Verner, D. A. & Ferland, G. J. 1996, ApJS, 103, 467
33. Walter, F. & Brinks, E. 2001, AJ, 121, 3026
34. Wilcots, E. M. & Miller, B. W. 1998, AJ, 116, 2363
35. Wolfire, M. G., Hollenbach, D., McKee, C. F., Tielens, A. G. G. M., & Bakes, E. L. O. 1995, ApJ, 443, 152
36. Wolfire, M. G., McKee, C. F., Hollenbach, D., & Tielens, A. G. G. M. 2003, ApJ, 587, 278

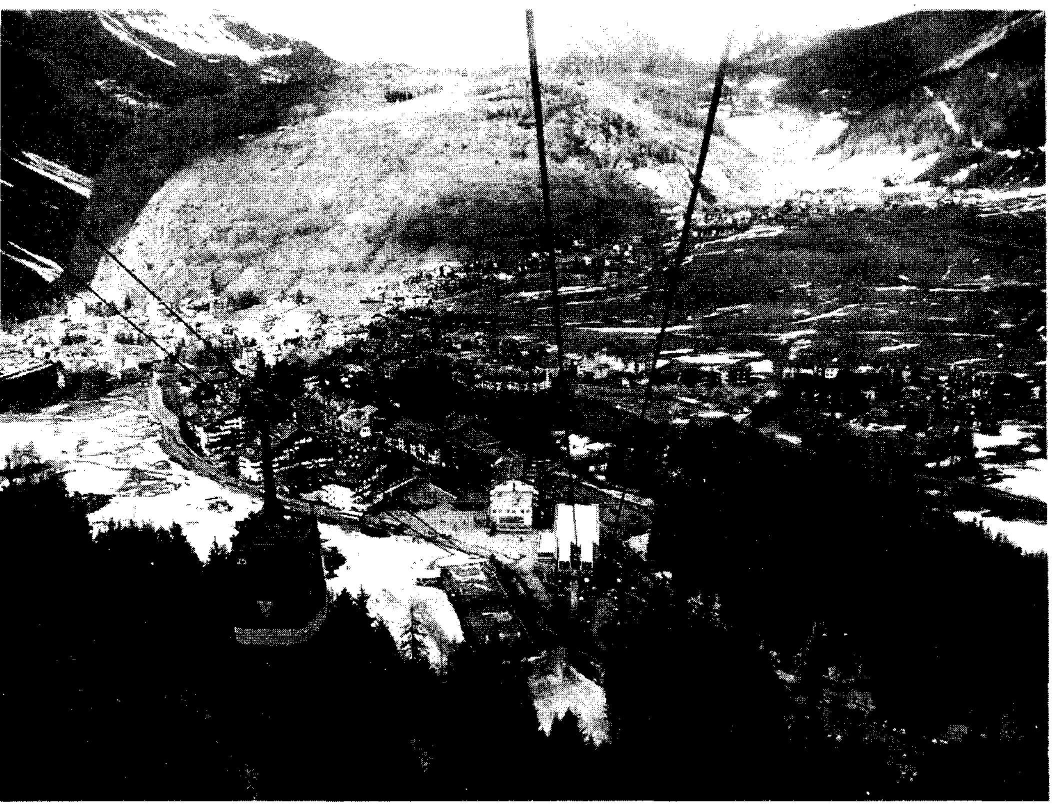

La Thuile village

TIDAL DWARF GALAXIES: DARK MATTER AND STAR FORMATION IN UNUSUAL ENVIRONMENTS

JONATHAN BRAINE
Observatoire de Bordeaux, B.P. 89, 33270 Floirac, France

The study of how star formation, and particularly the star formation efficiency (SFE), is affected by the large-scale environment is difficult. It is generally accepted that stars form from molecular gas, making the measure of molecular gas a critical ingredient. The molecular gas is typically and probably best traced by the CO lines, such that it is difficult to estimate the molecular gas mass in small galaxies as they are generally metal-deficient.
Due to their high metallicity, Tidal Dwarf Galaxies provide a possibly unique means of studying star formation in a dwarf galaxy environment (dominated by the gas mass, little or no rotation) and comparing with spiral galaxies (rotating disks dominated by the stellar mass). They also provide a means of probing the dark matter content of the disk material from which they form. Another unusual environment in which CO can be used to trace H_2 but where the SFE is extremely low is discussed as well.

Keywords: Stars: formation – ISM: molecules – Galaxies: formation – Galaxies: interactions – Cosmology: dark matter – Galaxies: evolution

1 Introduction

One of the main problems in studying star formation outside of our own galaxy is that the fuel for star formation, molecular gas, is typically traced by the CO lines at 2.6 and/or 1.3 mm and these lines are very difficult to detect outside of the disks of spiral galaxies. Tidal Dwarf Galaxies (TDGs), are ideal because they are morphologically small dwarf galaxies but have a higher metallicity as they are formed from the tidal debris torn off from the outer parts of spiral galaxies by tidal forces during a galaxy-galaxy interaction. Some of the ejected gas, which is mostly atomic, then starts to collapse near the end(s) of the tidal tail(s), forming molecular hydrogen and allowing star formation to start anew in an object which is now a dwarf galaxy. The time required from ejection into the intergalactic medium to formation of a TDG is generally a few 10^8 years. A more complete description of TDGs can be found in Duc et al.

(2000)[7]. The observations of molecular gas in TDGs are described in Braine et al. (2000, 2001)[1,2]. Simulations of TDG formation are described in Duc et al. (2004)[8]. Does star formation proceed in the same way in a rotating disk galaxy and in a small irregular? We can now study the two environments in the same way.

In this presentation I will also discuss star formation in the gaseous bridges left over after head-on collisions of spiral disks. Again, this is an environment where we can use the same tools (*i.e.* CO lines and Hα emission).

Given their formation mechanism, the total mass of the TDG is ideally traced by the CO line because the molecular gas forms only in the condensing gas whereas some of the HI traces gas in the tidal tail which will not become part of the bound object. Thus, in addition to investigating star formation outside of spiral galaxy environments, I will present some new work on the dark matter content of the tidal dwarf galaxy VCC 2062.

2 Star Formation in TDGs and other Dwarf Galaxies

The most striking difference between TDGs and Dwarf Galaxies not identified as tidal is their high CO luminosities (see Fig. 1), roughly a factor 100 higher than for other dwarf galaxies of similar luminosity and star formation rate. The most important factor responsible for this difference is certainly the metallicity. As the metallicity increases, the CO lines become optically thick over a larger area and larger velocity range. Furthermore, the shielding against UV radiation due to both CO molecules and dust increases as well. For this reason, a change in metallicity is expected to have a stronger effect in a UV-bright environment.

Fig. 1 shows that while the luminosity range of TDGs is indeed typical of dwarf galaxies, their star formation efficiency (SFE) as traced by the M_{mol}/SFR ratio (equivalent to CO/Hα becuase the CO is used to estimate the H_2 mass and the Hα the Star Formation Rate) is rather typical of spirals and much higher (about a factor of 100) than in dwarf galaxies. The current observations show that in TDGs, as in spiral galaxies, CO is likely a good tracer of H2 and the $N(H_2)/I_{CO}$ conversion factor does not seem to be radically different in TDGs and in spirals. The similar gas consumption times also indicate that star formation proceeds in a similar way in both spiral disks and small irregular systems as TDGs.

What can we learn about star formation from the apparent similarity of TDGs and spirals? Star formation in spiral disks can be well described by a Schmidt law (SFR $\propto$ (M_{gas}/surface area)^n), with a constant exponent n, when including a threshold for the onset of star formation (Kennicutt 1989)[9]. The similarity of the SFE in TDGs and spirals provides evidence that a similar discription might be valid in TDGs. From our data we cannot say anything about the threshold for the onset of star formation because we lack spatial resolution. (Kennicutt 1989)[9] derived coherent results when applying the Toomre 'Q' criterion $Q = \frac{v_{gas}\kappa}{\pi G \Sigma_{gas}}$ – where κ is the epicyclic frequency, v_{gas} the velocity dispersion of the gas, and Σ_{gas} the gas surface density – to a sample of spirals. This is, however, no definite proof that the large-scale elements in 'Q' are indeed those that determine whether the star formation, which is small-scale physics, occurs. The Toomre criterion as it stands is by definition not appropriate in systems which are not clearly rotating. If the threshold for the onset of star formation would be found to be similar in spirals and in TDGs, then the 'Q' criterion is likely not the appropriate controlling factor in spirals. It is, however, remarkable that the gas consumption time, the inverse of the SFE, appears not very different in spiral disks, dominated by the stellar mass, and dwarf galaxies which are dominated by the gaseous mass.

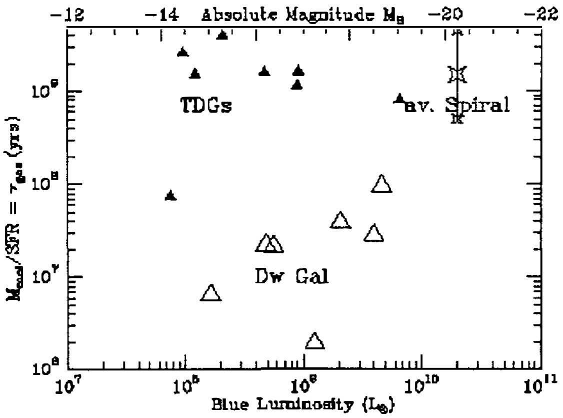

Figure 1: The star formation efficiency is plotted as a function of the Blue luminosity for Tidal Dwarf Galaxies, "classical" Dwarf Galaxies, and the average of a sample of spiral galaxies, the dispersion of which is shown by the error bars. In all cases the Star Formation Rate (SFR) is determined through Hα observations and the molecular gas mass through CO observations using the same conversion factor to translate CO intensity to H_2 column density.

3 Bridges between colliding galaxies

Another unusual environment is provided by the molecular gas bridges in the UGC 12914/5 and UGC 813/6 galaxy pairs. These spiral-spiral pairs have undergone head-on collisions in which the interstellar media of the galaxy disks have collided and been left in the space between the receding galaxies. It was initially expected that molecular gas would be absent from these systems but in fact it is the dominant gas phase. The distribution and line widths indicate that unlike the TDGs the molecular gas was pulled out of the disks rather than forming *in situ*. The reader is referred to Condon et al. (1993)[5] and Braine et al. (2003)[3] for further information on the UGC 12914/5 (Taffy) system and to Condon et al. (2002)[4] and Braine et al. (2004)[6] for the U813/6 pair.

From the CO emission from the bridges, the SFRs expected in the UGC 12914/5 and UGC 813/6 bridges are about 9 and 2 $M_{\odot}\mathrm{yr}^{-1}$ respectively. In both cases, only a single HII region is observed in the bridge and the SFR is only some 10% of what would be expected in "normal" molecular gas. To be ejected into the bridge region, however, the cores have experienced a sudden deceleration of several 100 km/s. Just as for the rest of the cloud, the collision necessarily ionizes the dense cores as well. However, because the probability of a dense core encountering another dense core is low, the dense core will continue deeper into the incoming cloud, ending up in a lower density medium than the barycenter of the two clouds. It may then be able to expand and lose its "pre-stellar" nature. The ionization and subsequent cooling of the clouds may result in some degree of homogenizing of the clouds, such that time is required before overdensities can become pre-stellar cores. *Our tentative conclusion is that star formation in the bridge material has been retarded or even suppressed by the recent collision.*

4 Dark Matter

In addition to investigating star formation outside of spiral galaxy environments, I will present some new work on the dark matter content of the tidal dwarf galaxy VCC 2062.

In Braine et al. (2001) we showed that it was not necessary to invoke the presence of dark matter to explain the dynamics of the molecular gas in the TDGs in which CO was detected. The distances of the objects and the uncertainties in their geometries made the individual mass determinations quite approximate. Now we present a closer TDG, VCC 2062, for which we believe we have a much more accurate mass determination. The NGC 4694 – VCC 2062 system is shown in Fig. 2 with contours showing the atomic gas column density distribution.

Dark matter being the difference between the "dynamical mass" and the "visible mass", we will successively estimate these and then compare. A velocity gradient can be seen in Figure 3 going from southwest to northeast, with the SW side approaching. Attributing the gradient to rotation implies a rotation velocity of about (6 km/s)/sin$i$ where i is the inclination of the rotation plane. The elliptical isophotes in all bands elongated along the dynamical major axis suggests that $i \gtrsim 45°$ such that most of the rotation is observed. Assuming all the support is due to rotation, an inclination angle of $i = 45°$, and a distance of 17 Mpc, we derive a dynamical mass of 2×10^7 $M_\odot$.

It is also possible to estimate the mass the same way as in Braine et al. (2001) $M \approx R\,\Delta V^2/G$ where R is the size of the system and ΔV the CO line width. However, unlike the objects presented in Braine et al. (2001), VCC 2062 is resolved in CO and the geometry is not a major uncertainty. The central line width is 24 km/s but all of the other positions yield lower values. A more average line width is is 15 km/s. Using a 15 km/s line width in the formula above gives a total mass of 8×10^7 $M_\odot$.

The visible mass can be decomposed into the stars, the atomic gas, and the molecular gas. The blue luminosity of VCC 2062 is slightly over 10^7 $L_\odot$ so the stellar mass can be roughly estimated to be 10^7 $M_\odot$, although as we shall see this is of little importance. Summing the atomic gas mass over the area observed in CO and including the associated Helium yields M(HI) $\approx 4.5 \times 10^7$ $M_\odot$. Again including the Helium associated with the H_2, the molecular gas mass is 2×10^7 $M_\odot$ for a rather conservative $N(\mathrm{H_2})/I_{\mathrm{CO}}$ of 2×10^{20} cm^{-2} per K km/s. The visible mass is therefore in the range $7 - 8 \times 10^7$ $M_\odot$, in almost exact agreement with the dynamical mass estimate of the preceding paragraph. Apparently, little or no additional mass (*i.e.* dark matter) is necessary to explain the internal motions in TDGs.

Following the results presented here for VCC 2062 and the earlier work by Braine et al. (2001) [2], it seems increasingly clear that TDGs are galaxies dominated by their visible mass component. So far, they are the only galaxies with little dark matter. Two conclusions come naturally from this: (*a*) most dwarf galaxies are probably *not* TDGs because most dwarf galaxies for which total masses are available are dark matter dominated; (*b*) The fraction of the mass in the outer parts of spiral disks in the form of dark baryons is not sufficient to be detectable through the dynamics of TDGs. VCC 2062 is the subject of an article in preparation.

Acknowledgments

The work presented here is a collaborative effort including particularly Pierre-Alain Duc, Ute Lisenfeld, Elias Brinks, Vassilis Charmandaris, Stéphane Leon, and Emmanuel Davoust.

I would also like to thank the Université Bordeaux 1 for the "Bonus Qualité Recherche" funding that made my participation possible.

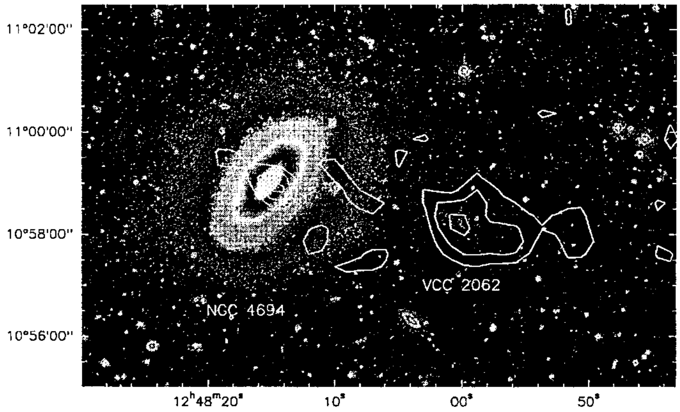

Figure 2: Optical image of the NGC 4694 – VCC 2062 system with HI column density contours (yellow) superposed. The TDG VCC 2062 is nearly independent of the parent system and the HI is clearly concentrated.

References

1. Braine, J. *et al.* 2000, *Nature* **403**, 867
2. Braine, J. *et al.* 2001, A&A, **378**, 51
3. Braine, J.*et al.*, 2003, *A&A*, **408**, L13
4. Condon, J. J., Helou, G., & Jarrett, T. H. 2002, AJ, **123**, 1881
5. Condon, J. J., Helou, G., Sanders, D. B., & Soifer, B. T. 1993, AJ, **105**, 1730
6. Braine, J. *et al.*, 2004, *A&A*, **418**,419
7. Duc, P. A. *et al.* 2000, *AJ* **120**, 1238
8. Duc, P. A. *et al.* 2004, *A&A* submitted
9. Kennicutt, R. C., J. 1989, ApJ, **344**, 685

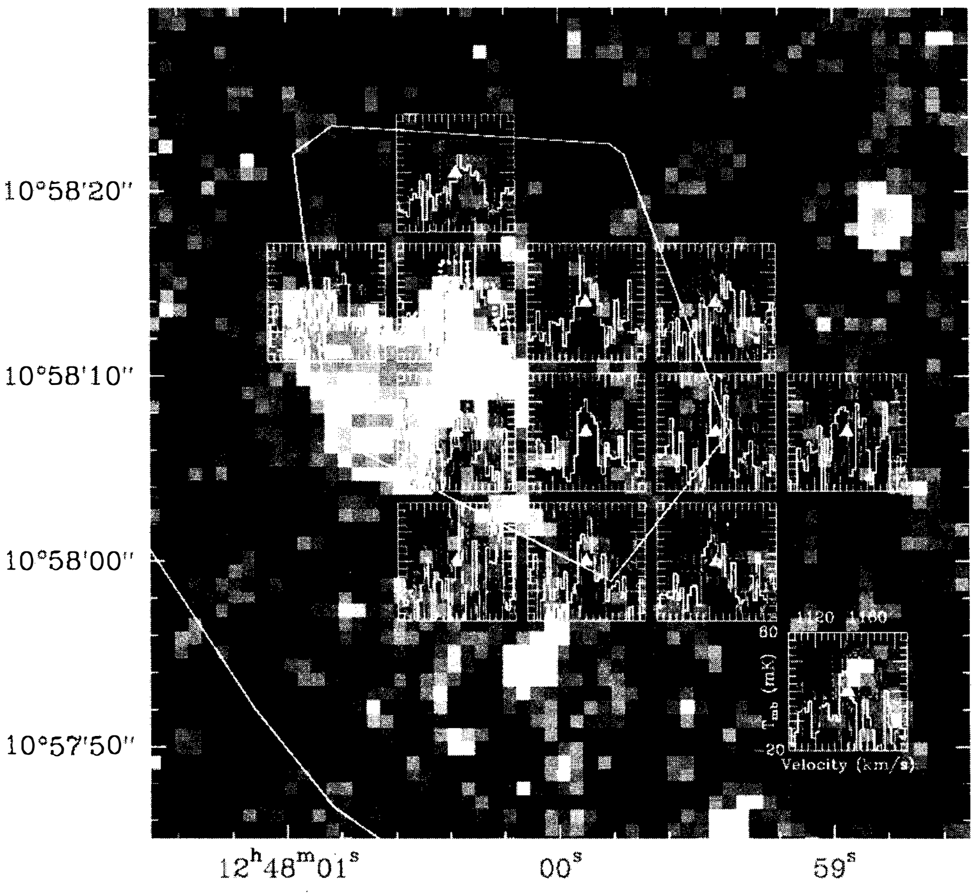

Figure 3: Close up of the VCC 2062 system with the same HI contours as in Fig. 2. The spectra shown are the CO(1–0) line (white, solid), the CO(2–1) line (red, dashed), and the HI line (green, dotted).

THE GALAXY EVOLUTION EXPLORER : GALEX

Denis BURGARELLA[1], C. Kevin XU[2], Véronique BUAT[1] & THE GALEX TEAM
[1] *Observatoire Astronomique Marseille Provence / LAM*
traverse du siphon, B.P. 8, 13376 Marseille Cedex 12, France
E-mail : denis.burgarella@oamp.fr
[2] *California Institute of Technology, MC 405-47, 1200 East California Bd, PAsadena, CA 91125, USA*

This paper presents GALEX, the Galaxy Evolution Explorer (P.I. C. Martin) and the planned imaging and spectroscopic surveys that will be carried out by GALEX in the Far Ultraviolet (153 nm) and Near Ultraviolet (251 nm) bands. A first sample of GALEX data was made public through the Early Release of October 2003 and the Data Release 1 including a much larger amount of data will be released in Fall 2004. Some results related to the Young Local Universe are presented featuring studies of ultraviolet images of local galaxies and a spectroscopic analysis of the ELAIS South 1 field as observed by GALEX.

Keywords: galaxies : ultraviolet – galaxies : infrared – galaxies extinction – galaxies evolution;

1 What is GALEX ?

GALEX, the Galaxy Evolution Explorer was launched by a PEGASUS rocket on 28 April 2003. GALEX is a $50 - cm$ telescope devoted to observing the Ultraviolet (UV) in two bands centered at about 153m and 231nm (Martin et al. 2004, Barlow et al. 2004). In Section 2, a sample of Early release Observations data will be shown. In Section 3 a few results from local galaxy imaging will be presented and in Section 4 the analysis of the ELAIS South 1 spectroscopic observations that are part of the ERO.

Figure 1 lists the main GALEX surveys with the planned observed areas, sensitivities, spectral and angular resolutions. The estimated number of galaxies and the average distances for each survey are strongly related and selected to address the GALEX science objectives that will be presented in the next Section.

One of the main features of this list is the All-sky Imaging Survey (AIS) that will be carried by GALEX over its lifetime. The previous largest UV dataset was observed from the French balloon-borne telescope FOCA that covered about 70 square degrees in the Northern Hemisphere. All the other UV telescopes : the International Ultraviolet Explorer - IUE, ASTRO-1 and ASTRO-2 to quote only a few

Surveys	AIS	DIS	WSS	MSS	DSS
Area (deg^2)	40000	160	160	16	2
Sensitivity (mAB)	21	26	20-22	22-24	23-25
Estimated Mean Redshift	0.2	1.2	0.2	0.5	1
Estimated Number of Galaxies	10^7	10^7	6.10^4	5.10^4	3.10^4
Spectral Resolution R	2 bands	2 bands	100-200	100-200	100-200
Angular Resolution (FWHM arcsec)	4 - 5	4 - 5	4 - 5	4 - 5	4 - 5

Figure 1: List of GALEX main surveys in UV.

of them were essentially target-oriented as is, of course, the Hubble Space Telescope (HST). Such surveys were already performed at other wavelength ranges (e.g. IRAS) but UV was left over with only small portions of the sky until Martin's GALEX was accepted by NASA as a SMall Explorer Mission. France and Korea joined the US team to build GALEX. In addition to these surveys a Guest Investigator Program offers GALEX observation time to the astronomical community. The deadline was on 16 April 2003 and the selected programs should be announced around July 2004. To get used to the data and better know what GALEX characteristics and performances are, an Early Release Observation (ERO) is available since October 2003.

The GALEX Science Project is strongly related to galaxies and to their evolution. The main objectives is to map the history and evolution of the universe over 80% of its history. The main questions that we can find on GALEX web site are :

What is the history of star formation in the Universe ?

What do nearby galaxies look like in UV light ?

When and where did the stars and elements that we see today have their origin ?

Schematically, GALEX Science Goals could be divided into i) local ones where we will try to better understand and calibrate the UV observations of local galaxies and ii) evolutive ones where we will investigate the evolution of galaxies and their star formation and of some of the main related parameters : dust, morphology, metallicity, etc.

2 The Early Release Observations

This description of the Early Data Release is a summary of the more detailed document avalaible on GALEX public web site :

http://www.galex.caltech.edu/EROWebSite/Early_release_data_description_part1.htm

GALEX Early Release data contains images and catalogs generated by the GALEX data pipeline as of November - December 2003. These data are representative of GALEX data and are intended to provide data in a format similar to those that will be delivered to the Guest Investigators and to the astronomical community, through the first major Data Release (DR1) planned for the end of 2004.

At the beginning of December 2003, GALEX had observed more than 3000 square degrees of sky during more than 2000 orbits. For the all-sky and medium imaging surveys, the early release observations contain less than 1 % of what had been collected, with the single DIS/WSS field one of 10-15 deep fields that had been observed.

The ERO fields and exposure times were selected to provide a representative data set for use by prospective investigators.Targets observed at different Galactic latitudes with varying infrared cirrus levels (100 mm) have a wide range of extinction values and UV background levels.The median cirrus level over the whole sky is about 3.0 MJy/sr. GALEX deep imaging and spectroscopy fields are generally selected to have $I_{100} < 1.0$ MJy/sr. Currently the All-sky survey is limited to fields with cirrus levels below 3.0 MJy/sr.

Two sorts of files are included in the ERO release. A first set provides a minimal source extraction catalog and images that would be useful to have a quick look at the data. Moreover, an advanced set contains the full data coming out from the pipeline. This is the information needed to 'test' GALEX performances, get used to the format and make potential Guest Investigators ready to submit good proposals.

In Figures 2 & 3, we present some instances of the data that can be found on GALEX Web Site.

We assume a cosmology with $H_0 = 70 km.s^{-1}.Mpc^{-1}$, $\Omega_M = 0.3$ and $\Omega_{VAC} = 0.7$ in this paper.

Figure 2: GALEX Early Release Observations : Color Image of the field containing M81 and M82

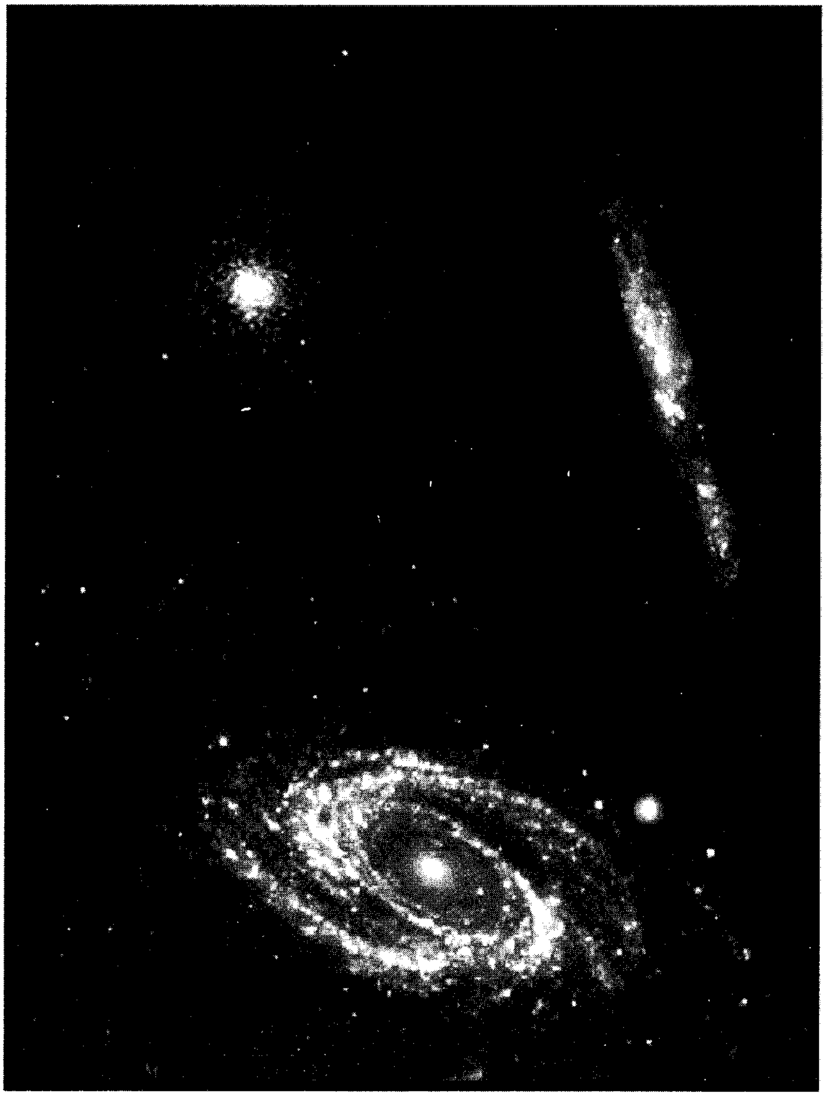

Figure 3: GALEX Early Release Observations : Mosaic image containing GALEX color images of M81, the globular cluster M2 and the galaxy NGC 55

3 Local Galaxies : the Stefan's Quintet

A number of UV images of local galaxies have been already analysed and the first analysis will be published in a special issue of ApJ Letters. To cite a few of them : Bianchi et al. (2004) on M51 and M101, Popescu et al. (2004) carried out a comparison of UV and FIR fluxes of M101, Boissier et al. (2004) performed a radial analysis of the dust attenuation and star formation rate of M83, Hoopes et al. (2004) studied the UV haloes of NGC 253 and M82, Hibbard et al. (2004) studied the tidal tails of the Antennae (NGC 4038/NGC 4039). In this paper, we will have a more detailed look at the paper from Xu et al. (2004) on Stefan's Quintet.

The first UV images of this famous interacting group contain NGC 7317 (E), the binary galaxies NGC 7318a (E) and NGC 7318b (Sbc pec), the Sy2 galaxy 7319 (Sbc pec) and the foreground galaxy NGC 7320 (Sd). Most of the UV emission is located in regions associated to NGC 7319, NGC 7318b and the starburst region in the intragroup medium SQ-A.The total star formation rate (SFR) of Stefan's Quintet is about 6.7 $M_{sol}.yr^{-1}$ and the main contributors are SQ-A : 1.3 $M_{sol}.yr^{-1}$ in excellent agreement with the Hα luminosity corrected for dust extinction, 2 $M_{sol}.yr^{-1}$ for NGC 7319, most (68 %) of which coming from the disk of the galaxy and 15 % from the loop-shaped young tail. The UV emission associated with NGC 7318b is emitted from a 80-kpc disk and amounts to 3.4 $M_{sol}.yr^{-1}$.

4 The ELAIS South 1 Field : Galaxy UV Extinction

The ELAIS S1 field was observed by GALEX in both its Wide Spectroscopic and Deep Imaging Survey modes (Figure 4). This field was previously observed by the Infrared Space Observatory and Burgarella et al. (2004) made use of the catalogue of multi-wavelength data published by the ELAIS consortium (Rowan-Robinson et al. 2004) to select galaxies common to the two samples. Among the 959 objects with GALEX spectroscopy, 88 are present in the ELAIS catalog and 19 are galaxies with an optical spectroscopic redshift. The distribution of redshifts covers the range $0 < z < 1.6$. The selected galaxies have bolometric IR luminosities $10 < Log(L_{IR}) < 13$ (deduced from the 15μm flux) which means that we cover a wide range of galaxies from normal to Ultra Luminous IR Galaxies. The mean (σ) UV luminosity (not corrected for extinction) amounts to $Log(\lambda.L_{1530}) = 9.8(0.6)$ L_{sol} for the low-z ($z \leq 0.35$) sample. The UV slope β (assuming $f_\lambda \propto \lambda^\beta$) correlates with the GALEX FUV-NUV color if the sample is restricted to galaxies below $z < 0.1$. Taking advantage of the UV and IR data, we estimate the dust attenuation from the IR/UV ratio and compare it to the UV slope β. We find that it is not possible to uniquely estimate the dust attenuation from β for our sample of galaxies (Burgarella et al. 2004). These galaxies are highly extinguished with a median FUV dust attenuation $A_{FUV} = 2.7 \pm 0.8$ in agreement with the median value deduced from a photometric survey from GALEX carried out by Buat et al. (2004). Once the dust correction applied, the UV- and IR-based SFRs correlate. For the closest galaxy with the best quality spectrum, we see a feature consistent with being produced by a bump near 220nm in the attenuation curve (Figure 5).

4.1 GALaxy UV Attenuation Models

Light do not undergo the same extinction when it is emitted by young stars (i.e. age < 10 Myrs) as compared to older stars (age > 10 Myrs). Young stars probably undergo more dust extinction because they are still concentrated and embedded in the remaining of the molecular cloud. Old stars probably destroyed their cocoon and move away. In our models, we assume an attenuation law for young stars which is identical to Calzetti et al. (2000) attenuation law while the Milky Way ou LMC attenuation law is assumed for old stars. Dust associated to old stars is either mixed with the stars i.e. optical depth proportional to the starburst optical depth (multiplied by 5 & 1, divided by 2, 5 & 10) or concentrated in clumps (5, 10, 15, 20 clumps) with optical depths proportional to young star optical depth (/5 up /80). We show in Figure 6 how the GALEX colors (FUV-NUV) evolves. When a MW extinction law is assumed for old stars, the Log (FIR/UV) ratio (which is directly related to the dust attenuation) could be totally decoupled from the FUV-NUV color. A same trend is observed for the UV slope β (assuming $f_\lambda \propto \lambda^\beta$). It seems that the degeneracy could prevent us from determining the dust attenuation from the UV slope for Luminous IR galaxies (LIRGs) and Ultra-LIRGs (see also Fig. 5).

Figure 4: GALEX Early Release Observations : Color Image of the ELAIS South 1 Field (top) and the 2-D spectroscopic image of the same field. The fireworks-like aspect of the latter is due to the fact that the grism is rotated for each sub-exposure, changing the direction of the dispersion.

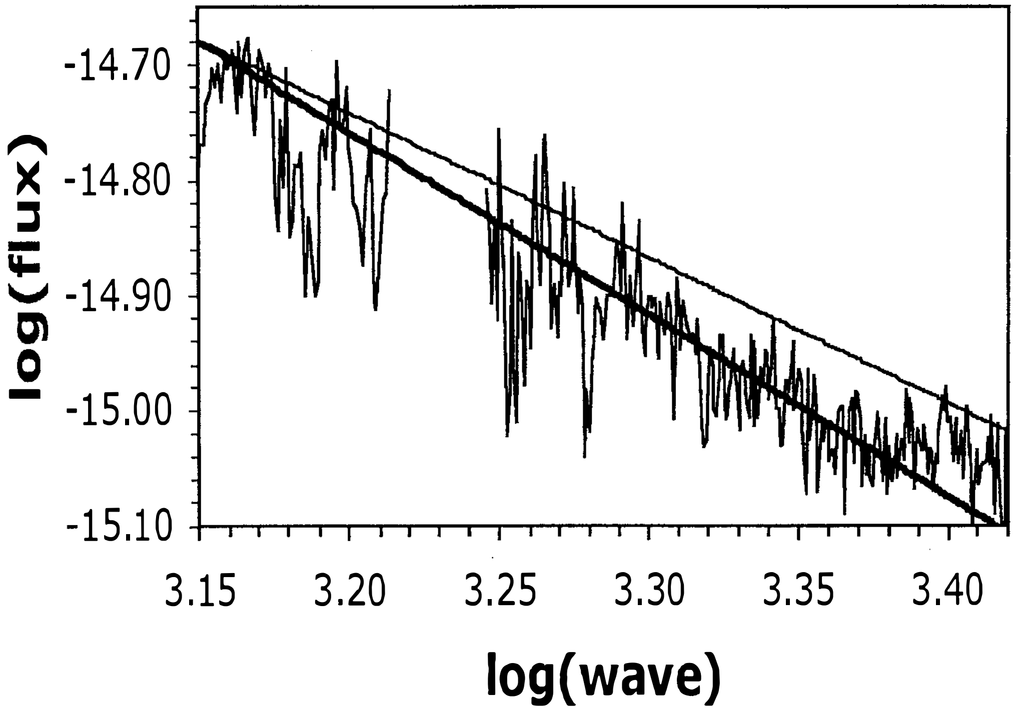

Figure 5: The highest-quality spectra is shown with its fits ($f_\lambda \propto \lambda^\beta$). This object seems to exhibit a trough consistent with being due to a bump around 220 nm ($log_{10}(\lambda) = 3.34$) similar to the Milky Way Extinction law. The regular fit (heavy line) gives β = -1.58 $\pm$0.04. If we estimate β without the trough by exluding pixels in the range $1900\AA - 2500\AA$, i.e. $3.28 \leq log_{10}(\lambda) \leq 3.39$ (thin line), we obtain $\beta = -1.26$ at 8 σ from the previous value.

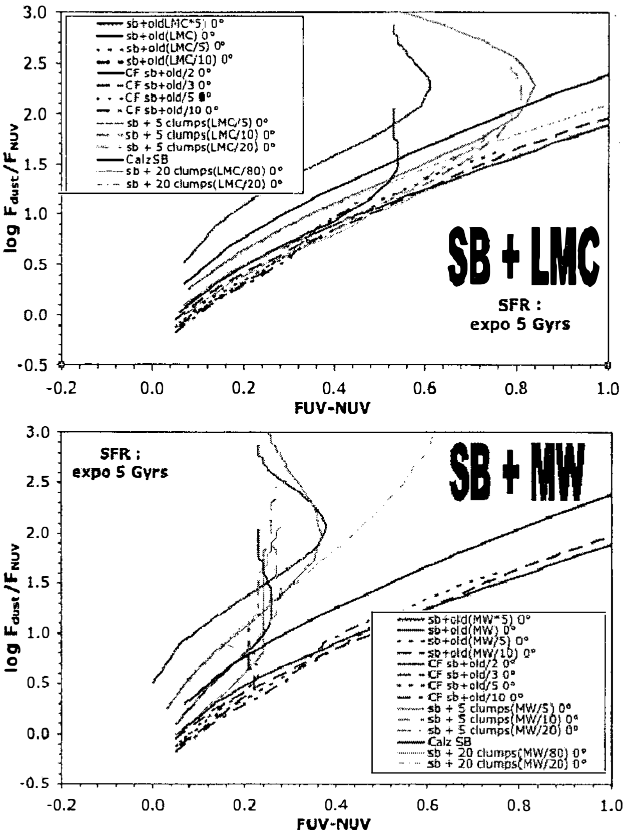

Figure 6: We show the resulting models in a Log(F_{dust}/F_{NUV}) vs. FUV-NUV for several configurations : Calzetti law for young stars (age < 10 Myrs) plus LMC (top) and MW (bottom) for older stars. We assume, here, a exponential SFR with a decaying rate of 5 Gyrs. Other laws e.g. Charlot & Fall (2000), Meurer et al. (1999) are also shown for comparison.

References

1. Barlow T. et al. 2004, ApJ Letters, in press
2. Bianchi L. et al. 2004, ApJ Letters, in press
3. Boissier S. et al. 2004, ApJ Letters, in press
4. Buat V. et al. 2004, ApJ Letters, in press
5. Burgarella D. et al. 2004, ApJ Letters, in press
6. Calzetti D., Harmus L., Bohlin R.C., Kinney A.L., Koornneef J., Storchi-Bergmann T., 2000 ApJ 533, 682
7. Charlot S. & Fall S.M. 2000, ApJ 539, 718
8. Goldader. J.D., Meurer G., Heckman T.M., Seibert M., Sanders D.B., Calzetti D., Steidel C.C. 2002, ApJ 568, 651
9. Hibbard J.E. et al. 2004, ApJ Letters, in press
10. Hoopes C.G. et al. 2004, ApJ Letters, in press
11. Martin C. et al. 2004, ApJ Letters, in press
12. Meurer G.R., Heckman T.M. & Calzetti D. 1999, ApJ 521, 64
13. Popescu C.C. et al. 2004, ApJ Letters, in press
14. Rowan-Robinson et al. 2004, MNRAS 351, 1290
15. Xu C.K. et al. 2004, ApJ Letters, in press

Hans and his fans

Star clusters near intermediate and high mass young stars

W.J. de Wit (1), F. Palla (1), L. Testi (1), H. Zinnecker (2)

(1) INAF-Osservatorio Astrofisico di Arcetri, Largo E. Fermi 5, 50125 Florence, Italy
(2) Astrophysikalisches Institut Potsdam, An der Sternwarte 16, 14482 Potsdam, Germany

Abstract

A number of 43 high mass O-type stars within 2 kpc of the Sun are not known to be current, nor former member of clusters/OB-associations. We try to elucidate their formation history by looking deeper into their local stellar environment, by evaluating their spatial velocities, and their location in the Galaxy with respect to young stellar clusters. We find that 5 stars are in fact member of a small cluster and that nearly half (22 objects) could have undergone a dynamical ejection from a young cluster. Based on the current available data, 6% of the Galactic O-type stars cannot be associated with a stellar cluster. Finally by assuming that all stars are formed in clusters, that follow a powerlaw in size distribution we calculate the expected statistics regarding isolated O stars and O stars in OB-associations.

Keywords: Stars: formation - - Stars: early-type - Stars: statistics

1 Introduction: forming a high-mass star

The observational fact that the majority of the high-mass stars are found in physical stellar groups (star clusters or OB-associations) has prompted the assumption that the formation of a high-mass star is inescapably linked to the formation of a stellar cluster. From the initial formation of lower mass objects out of a turbulent molecular cloud, a high-mass star can subsequently be assembled by coalescence of molecular cores in very early embedded stages (Stahler, Palla & Ho 2000)[36] or by the direct collision of low-mass stars in competitive accretion in somewhat later stages (Bonnell, Bate & Zinnecker 1998; Bonnell & Bate 2002)[3 5]. The formation of a high-mass star may require the optically thick, merging bodies, as they can overcome the copious stellar radiation. The exerted pressure may halt and reverse spherically infalling gas when the accreting object attains a mass of $\sim 10\,M_\odot$ (Wolfire & Cassinelli 1987; Edgar & Clarke 2004)[43 11].

Disk accretion on the other hand can increase the final stellar mass up to $\sim 40\,M_\odot$ (Yorke & Sonnhalter 2001)[44], and is therefore the competing alternative to merging scenarios. The recent detections of accretion disks near high-mass stars in the submm (see Beltran et al., this volume) and even near-infrared silhouetted disks (Chini et al., this volume) does not favour the merging scenario, provided that the detected disk structures are dynamically stable, delivering the bulk of the final stellar mass. On face value it is safe to state that if nature forms high-mass stars according to the coalescence scenario, a single high-mass star does not form in isolation (see also the poster contribution by Dobbs et al., this volume). The coalescence picture predicts thus that all high-mass stars form in clusters. This prediction is however seems to be contested by extragalactic observations and possibly by Galactic observations of isolated high-mass stars, as we report in this contribution.

2 Absence of clusters near young high mass stars in external Galaxies

That visually single high-mass stars form outside stellar clusters in the Large Magellanic Cloud (LMC) is inferred in a number of papers by Massey and collaborators (1995, 1998) [27,28]. Intriguingly their observations seem to indicate that the LMC field is capable of producing isolated stars up to spectral type O3e, i.e. stars with masses $\gtrsim 80\,M_\odot$ and ages $\lesssim 2$ Myr. "Isolated" in this case means that there is *no collection of young stars* visible within 100 pc radius (Massey 1998) [28]. The latter distance limit an O3e star is able to cover in its lifetime at a velocity of $50\,\mathrm{km\,s^{-1}}$. Such velocities are easily attainable if the high-mass star would be formed in a populous young cluster and liable to undergo energetic dynamical interactions leaving the cluster at high spatial velocities (see Sect. 5). Without any hint of a nearby young population, the suggestion is therefore that the field of the LMC is able to form single, isolated O3e stars.

A similar claim is proposed for the bulge of the interacting spiral Galaxy M 51 (Lamers et al. 2002) [23]. These authors show on the basis of HST WFPC2 observations that a number of bright blue point sources, generally regarded as super star clusters (e.g. Larsen 2000; Bik et al. 2002) [24,1] are better fitted to stellar atmospheres rather than cluster evolutionary models. In addition these sources have two characteristics that are not expected for clusters; they follow the Humphreys-Davidson upper luminosity limit in an HR-diagram and their distribution in effective temperature shows evidence for a gap. This is expected for a collection of luminous red and blue supergiants, but not for star cluster. It is proposed that due to a high radiation field emanating from the bright nuclear starburst cluster in the centre of M 51, molecular clouds in the bulge are depleted in CO and are best described by a stiff equation of state. This prevents a collapsing cloud from fragmenting and therefore produces single high-mass objects (see Spaans & Silk 2000; Li, Klessen & Maclow 2003) [35,25].

At odds with the merging scenarios proposed for the formation of high-mass stars, the LMC and M 51 seem to be capable of producing high-mass stars without producing a cluster at the same time. Of course, the angular resolution achieved for the studies towards M 51 and even the LMC may have hampered the detection of such clusters, where in the latter case 1" equals 0.25 pc. This size scale is found typical for embedded clusters in the Galaxy (e.g. Lada & Lada 2003) [22]. The same cluster size scale is also found for clusters near the less massive intermediate mass pre-main sequence stars, as we discuss in the following section.

3 Sub-parsec scale clusters near HAeBe stars

Herbig Ae/Be stars (HAeBe) are intermediate mass ($2 \lesssim M/M_\odot \lesssim 15$) pre-main sequence (PMS) stars generally found away from active star formation sites. This mass range covers the important gap between low mass, "isolated" star formation in which the forming star has only a minor effect on the circumstellar medium, and high mass, "clustered" star formation where the forming stars may have a decisive influence on the environment. HAeBe stars are the most massive stars for which the PMS contraction time scale is longer than their main gas accretion (protostellar) time scale, that is in a non-merging scenario. It becomes therefore attractive to probe HAeBe stars for instance on the presence of accretion disks (e.g. Millan-Gabet et al. 2001; Vink et al. 2003; Eisner et al. 2004) [30,41,12], and it is expected that HAeBe stars can provide evidence for the role of stellar clusters on the formation of intermediate and high-mass stars.

Results of searches for clusters near HAeBe stars have been presented by Hillenbrand (1995) [18] and Testi, Palla & Natta (1998; 1999) [37,38]. These authors convincingly show the increase of the number of companion stars (i.e. the cluster richness) with increasing mass of the HAeBe star.

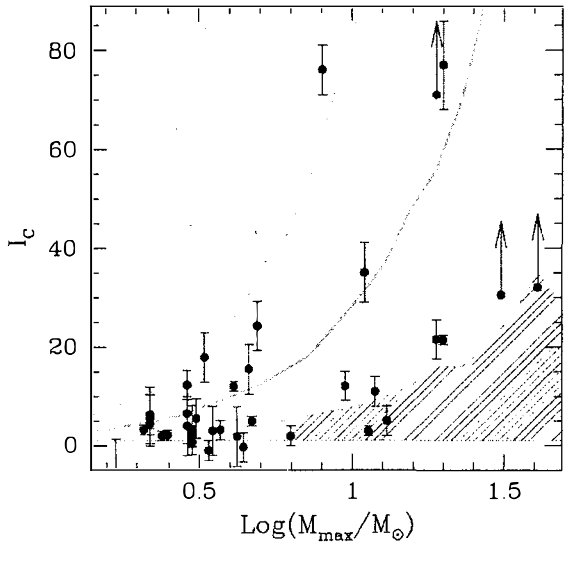

Figure 1: The distribution of the cluster richness (I_C) near HAeBe stars (dots) as function of the mass of the HAeBe stars (from Testi et al. 1999). The full lines are the results of model calculation by Bonnell & Clarke (1999), involving stellar mass functions and a cluster size distributed according to a powerlaw with slope -1.7. The median value for the richness of the model clusters per stellar mass is given by the full line, the dashed lines indicate the 75% and 25% percentile. The hatched area is the region where 25% of the new-born stars more massive than 6 $M_\odot$ should be located.

This is illustrated in Fig. 1, where the cluster richness (indicated by the I_C parameter [a] Testi et al. 1998) is plotted against the mass of the HAeBe star. The figure shows clearly that the more massive HAeBe stars are more likely to be accompanied by much richer clusters than the lower-mass HAeBe stars. Effectively the increase in stellar densities of the clusters with HAeBe stellar masses bridges the gap between single isolated star formation of the low mass stars as for example in Taurus (Gomez et al. 1993) [16] and the densities found in a high-mass star formation site like that of Orion, with stellar densities reaching 10^4 stars per cubic parsec (Hillenbrand & Hartmann 1998) [19]. Whether this result reflects the need for a cluster in the formation of a high-mass star (e.g. Bonnell et al. 2004) [6] or a universal stellar IMF has been calculated by Bonnell & Clarke (1999) [4]. Their models populate clusters drawn from a cluster size distribution with standard stellar mass functions. The cluster size distribution is assumed to be a powerlaw (see also Sect. 6). The results of these calculations are represented by the various curves in Fig. 1. The data on the HAeBe star clusters are compatible with the model calculations. The clusters near HAeBe stars may therefore simply reflect the statistics arising from an IMF combined with a certain size distribution for stellar clusters.

The study of clusters near HAeBe stars reveal two other remarkable results. First is that there seems to be a rather constant cluster radius of ~ 0.25 pc regardless of cluster richness. The cluster radius is here defined as the distance for which the stellar density reaches the background level. Secondly, Fig. 1 makes clear that single HAeBe stars can be found up to stellar masses of $\sim 10\,M_\odot$. This limit is similar to the upper mass limit for which the spherical accretion models of Wolfire & Cassinelli (1987) [43] (see also Edgar & Clarke 2004) [11] are able to produce a star.

Given the size scale of the clusters found near HAeBe stars and its independence of cluster richness, clusters near high-mass stars in external galaxies like the LMC would be difficult to

[a] which is the integral over distance of the source density subtracted by the average source density measured at the edge of each field.

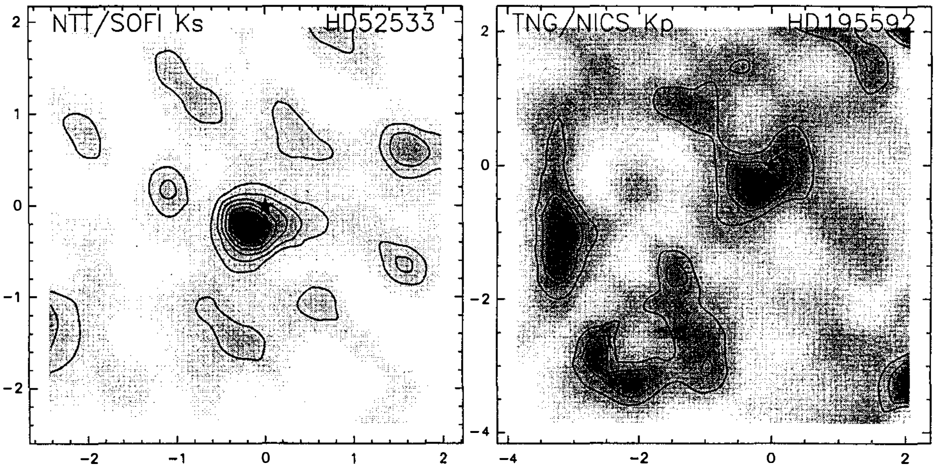

Figure 2: Clusters detected near the O-type field stars HD 52533 and HD 195592. The stellar density maps have been constructed from K-band imaging and probe masses down to a tenth solar mass. The contours are 1σ spaced deviations from the average stellar density value in the field of view. Location of the target star is indicated by an asterisk. The ordinates are in arcminutes and correspond roughly to a few parsecs. The clusters have radial sizes of $\sim$ 0.25 pc.

detect using ground-based telescopes; 1" in the LMC corresponds to the median cluster radius of the Galactic HAeBe stars, i.e. 0.25 pc. Admittedly, the O3 type stars located in the general stellar field of the LMC (Massey et al. 1998) are about the most massive stars known and are therefore from IMF considerations required to be accompanied by even richer stellar clusters than the Galactic HAeBe stars. On the other hand the trend seen among the Galactic HAeBe stars could also well be tested by probing for clusters near more massive, isolated stars in the Galaxy, i.e. the O-type stars that are located in the Galactic field.

4 A search for clusters near Galactic high-mass field stars

The general definition of a field star is a negative one. Field stars are those objects that are *not* members of any known spatial concentration of stars, either a cluster or an association of stars. In general, field stars form the old population of a galaxy and should therefore be of low mass. However, there exists a number of stars among the field population that are known to be massive and therefore are much younger than the average age of the field. They come in two varieties. Historically, most attention was devoted to those massive field stars that are known to have (or have had) high spatial velocities, i.e. the runaway stars (see Blaauw 1961) [2]. From a stellar population point of view these stars are a subset of the field, however when deriving physical quantities of stellar clusters, runaways should be considered as cluster members.

The second group of high-mass stars that are located in the field are simply those O-type stars without large spatial velocities. They have received less attention in the literature as a group, since it may be expected that they are either unrecognized runaway stars (without yet determined accurate proper motions) or that they are part of an unrecognized cluster or star forming region. The primary cause for the unknown origin of this subgroup of the O stars is that they are generally distant. For clarity, we will make the explicit distinction between field O stars and runaway O stars, in the sense that runaway stars are not considered to be part of the group of field O stars, following the above reasoning.

Some 70% of the O-type stars in the Galaxy are found in clusters or in OB-associations, $\sim$ 10% are the runaway stars, and $\sim$ 20% are the field O stars (see Gies 1987; Mason et al. 1998; Maíz-Apellániz et al. 2004) [43 15 26]. The O-type field stars (43 objects) were discussed as a group by Gies et al. (1987) in terms of their radial velocities, binarity, and multiplicity properties. These properties of the field O-stars are found to be intermediate between the corresponding properties of O-stars in OB-associations and the runaway stars. Gies suggested that the O-type field stars could well have a similar history as the runaway O (and B) stars, that is through dynamical interaction and ejection. However some of the O-type field stars are found to consist of multiple visual objects, a configuration that is not likely to have undergone dynamical interaction.

The existence of isolated O-type stars in the Galactic field, combined with the knowledge of the clustering of low-mass stars near HAeBe stars, prompted us to investigate in more detail the level of isolation of the Galactic field population. In de Wit et al. (2004a) [8] we search for hitherto unknown stellar clusters centred on all 43 known field stars within 2 kpc of the Sun as catalogued in Mason et al. (1998). High resolution stellar density maps were constructed from deep K-band images taken with NTT/SOFI and TNG/NICS, probing scales of ~ 0.25 pc. Lower resolution maps were constructed from 2MASS K-band covering tens of parsecs with a resolution of ~ 1.0 pc. A 3σ deviation from the average stellar density was considered to be a cluster provided that it was centred on the target star. The maps are presented in de Wit et al. (2004a) along with the K-band images. In 5 cases we detect a clear stellar density enhancement near the field O star, four of which were previously thought to be visually single objects. The two best examples of newly detected clusters are given in Fig. 2 for stars HD 52533 and HD 195592. Converting the detected density enhancements into stellar spatial densities, we obtain $\sim$ 1000 stars per cubic parsec. The radii of these clusters are measured to be 0.30 pc and 0.25 pc respectively, comparable to the HAeBe clusters. The main result of de Wit et al. (2004a) is however that $\sim$ 85% of the field O-type stars are not associated with sub parsec scale clusters, similar to the ones detected near HAeBe stars.

5 Field O stars: a runaway history?

Within a 2 kpc radius from the Sun, the percentage of confirmed O-type runaway stars is $\sim$ 10%. Runaway OB stars acquire high spatial velocities after dynamical interactions in the centres of young dense stellar clusters or due to a binary supernova explosion (Blaauw 1961; Poveda et al. 1967; Gies & Bolton 1986; Clarke & Pringle 1992; Hoogerwerf et al. 2001) [32 14 7 20]. The higher average peculiar radial velocity (Gies 1987) for the field O stars compared to O stars in OB-associations, suggests that some fraction of the field O stars may have a history of dynamical interactions. In this view, high-mass stars can be dynamically ejected with "intermediate" velocities, that are less than the velocities of the runaway OB stars.

In an attempt to exclude runaway O stars (i.e. dynamically ejected stars) from the field O stars (i.e. formation in the Galactic field?), we have re-examined for the sample of field O stars the spatial velocity distribution using Hipparcos, their distribution above the Galactic plane, and the proximity to known young clusters. Basically this exercise is similar to detecting runaway OB stars but with much more relaxed constraints than usually adopted in the literature.

5.1 Space velocities

Traditionally the minimum peculiar velocity for classifying a runaway star is $40\,\mathrm{km\,s^{-1}}$ (Blaauw 1961). Peculiar space velocities for 35 field O stars are derived in de Wit et al. (2004b) [9] using Hipparcos (ESA 1997) proper motions. These measurements were converted into space velocities using the published radial velocities and distances by Gies (1987) and Mason et al. (1998). The uncertainty on the distance of the target O stars was assumed to be 30%, and is propagated into the error estimate.

Fig. 3 demonstrates that the Hipparcos proper motions allow the identification of seven candidate runaway O stars by applying the velocity limit of $40\,\mathrm{km\,s^{-1}}$. Some of them have already been suggested as runaways in the literature (for references see de Wit et al. 2004b). Apart from the double line spectroscopic binary HD 15137, each of the other six stars is both optically and spectroscopically a single object. A single nature would corroborate the hypothesis of a dynamical origin, since the ejection of a multiple system has a small probability.

We note that the objects with clusters reported in the Sect. 4 in general do not have large spatial velocities. They occupy the same region of Fig. 3 as the rest of field population. However, an exception is the star HD 57682, that has the highest space velocity of all. The stellar surface density enhancement marginally detected in de Wit et al. (2004a) could be a statistical fluctuation rather than a stellar cluster.

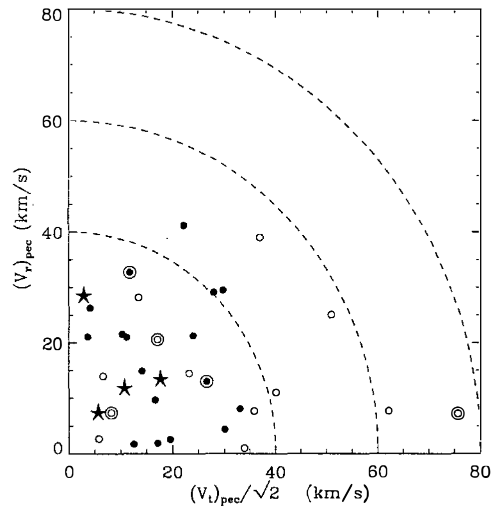

Figure 3: The peculiar space velocity for 35 O-type field stars that were found to have Hipparcos proper motion measurements. Symbols are as follows: asterisks indicate a peculiar space velocity with an absolute uncertainty less than $10\mathrm{kms}^{-1}$, filled circles an uncertainty between $10\text{-}20\mathrm{km\,s}^{-1}$, and empty circles $>20\mathrm{km\,s}^{-1}$. Some field O stars have space velocities negligible different from the bulk of the Galactic field. Encircled symbols indicate stars that are found to reside in small scale clusters, as depicted in Fig. 2. Note that not all field O stars have Hipparcos proper motions.

5.2 Distance from the Galactic plane

Massive star formation is confined to a distance of ~200 pc from the Galactic plane, as illustrated in Fig. 4. It shows the spatial distribution of the OB associations within 3 kpc of the Sun (Mel'Nik & Efremov 1995) [29]. Star formation is probably not occurring in the halo of Galaxy (e.g. Ramspeck et al. 2001) [33].

The threshold distance for identifying runaway OB star is generally taken to be 500pc. This translates into a perpendicular Z-component velocity of ~ 30 km s^{-1}, adopting the maximum distance of ~200pc from the Galactic plane for star formation to occur. Field O stars have an average peculiar radial velocity of 6.4 km s^{-1} (Gies 1987) and, moving ballistically, may wander ~ 65 pc in an average lifetime of 10^7 yr. We use a value of Z = 250 pc as the maximum allowed distance for the field O stars. Any O field star with Z-value larger than this is regarded as a possible runaway star. This leads to the identification of eleven field O stars as runaway candidate stars, three of which (HD 15137, HD 91452, HD 201345) were also found to have large spatial velocities in Sect. 5.1.

5.3 Ejection from young stellar clusters

The location of a young stellar cluster in the proximity of an isolated field O star suggests a possible physical connection between the two. De Wit et al. (2004a) reports for each field O star all clusters known in the literature (if any) that have an age estimate less than 10 Myr and are found within a projected distance of 65 pc (the "wander distance"). These candidate host clusters are obviously required to have similar distances to the Sun as the field O star, adopting again a distance uncertainty for the O field stars of 30%. In seven cases a candidate young host cluster is found to exist within the set distance boundary of the field O star. As far as these clusters have been studied, their nature supports an history of gravitational interaction and the ejection of high-mass stars. We briefly describe two examples.

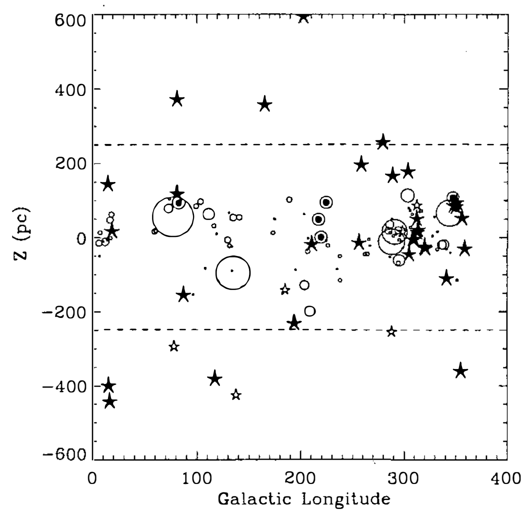

Figure 4: Projection of O stars perpendicular to the Galactic plane. The open circles show OB-associations within 3 kpc of the Sun from Mel'Nik & Efremov (1995). The size of the circle is proportional to the estimated stellar richness of each association. Filled encircled dots correspond to field O stars found to reside in small scale clusters, as depicted in Fig. 2. The remaining field O stars are all indicated by asterisks: open asterisks for those that have peculiar spatial velocities larger than 40 km s^{-1}.

The O field star HD 117856 (O9.5 III) is found at a projected distance of 60 pc from the 4 Myr cluster Stock 16 (Turner 1985) [39]. Stock 16 is known to be a massive young cluster lying in the H II region RCW 75. Its most luminous member has been identified as O7.5 III((f)) star by Walborn (1973) [42]. This particular cluster stands out due to a large proportion of close binary systems among its present population (Dokuchaev & Ozernoi 1981) [10] possibly indicative of a dynamical past with frequent gravitational encounter between its members. The second example is the O-type field star HD 125206 (O9.5 IV), located at a projected distance of 45 pc from the 7 Myr cluster NGC 5606 (Vazquez et al. 1994) [40]. The core of NGC 5606 is reported by Vazquez et al. 1994 to be underpopulated in low-mass stars and showing "five bright stars forming a compact group". Such a hierarchical situation is expected to exist in a cluster able to expel high-mass stars (e.g. Clarke & Pringle 1992) [7].

In conclusion, the search of de Wit et al. (2004b) for runaway O-type candidate stars among the O-type field stars (using more relaxing constraints than generally adopted in identifying runaways) has yielded 22 new candidate runaway O stars. Conversely, that is to say that the number of O-stars in the Galactic field for which it is safe to state, given the current available data, that they do not find an origin in a cluster/OB association is 12, or $\sim$ 6% of all O-stars, adopting a number of 193 for Galactic O-stars with V $< 8^{m}$ (Mason et al. 1998). We see thus that in the solar neighborhood, such a low percentage of field O-stars (following the definition of Sect. 4) renders the formation of a high-mass star in a isolated mode unlikely, although admittedly it cannot be excluded completely.

6 The stellar and cluster mass function: the expected number of isolated O stars

Statistical IMF arguments allow for a finite probability of forming a high-mass star without the required cluster and indirectly provide support for the formation of a high-mass star set by conditions other than a stellar cluster, e.g. a sufficiently massive, non-fragmenting dense molecular core in combination with an accretion disk (e.g. Yorke & Sonnhalter 2002; Li et al. 2003) [44 25]

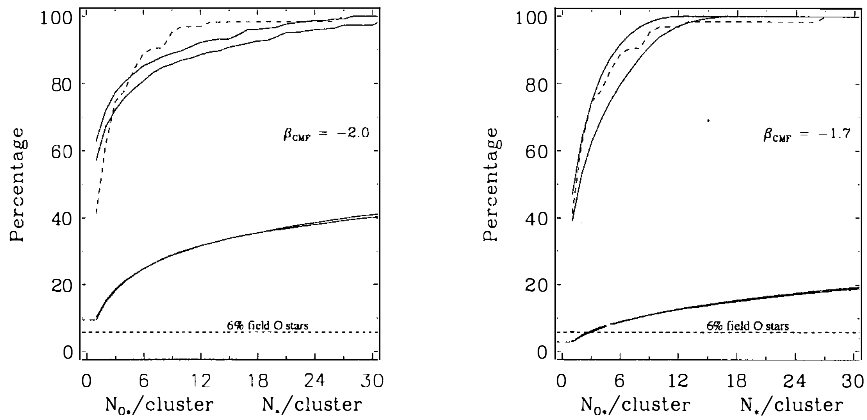

Figure 5: Both panels show the cumulative distribution of (1) the number of O stars per cluster (two upper full lines) and (2) the number of stars per cluster that have at least 1 O star (two lower full lines). The left and right display the same quantities for two different slopes of the cluster distribution by N_*. The dashed curve is the observed distribution of O-type stars per OB-association (Mason et al. 1998). Indicated by the dashed horizontal line is the percentage of Galactic field O-type stars, as proposed in this contribution.

Probability calculations for the clusters found near HAeBe stars were done by Bonnell & Clarke (1999). Similar calculations applied to the statistics of the O-type stars are presented in de Wit et al. (2004b).

That stellar clusters are distributed in mass according to a power law is now an established idea. The cluster mass function (CMF) is consistent with a value of -2 for the power index in different astrophysical environments like super star clusters (Zhang & Fall 1999) [45] or globular clusters (Harris & Pudritz 1994; see also Elmegreen & Efremov 1997) [17] [13]. Using a cluster distribution by number of OB stars (N_*) instead of by mass, Oey, King & Parker (2004) [31] showed recently that the clusters/associations in the Small Magellanic Cloud (SMC) also appear to be distributed by a power law with index of -2. Their main finding is that this cluster distribution by N_* can account for all observed OB clusters/association down to clusters containing only one OB star. Extrapolating this result, de Wit et al. (2004b) calculate the expected number of field O stars by assuming that all high mass and low mass stars are formed in clusters distributed according to the same power law, down to "clusters" containing only one member.

The results of the Monte Carlo simulations are presented in the form of cumulative distributions in Fig. 5. The distributions in each panel correspond to runs of 0.5×10^6 clusters. Each panel shows the cumulative distribution of two different parameters as indicated on the x axis, namely (1) the number of stars per cluster when the most massive cluster member is at least of O-type, [b] represented by the two *lower* full curves in each panel. And (2) the two *upper* full curves in each panel represent the cumulative distribution of the number of O-type stars per cluster. The upper and lower full curves are represented twice, corresponding to calculations with different shape of the stellar IMF, viz. a Salpeter (1955) [34] and a Kroupa (2002) [21].

The upper two full curves in the left panel thus show that for a CMF with slope -2 that $\sim$60% of the O-type stars are expected to be in clusters containing only 1 O-type star. Comparing this to the observed number (the dashed line) of O stars per OB association from M98, we see that the predicted number is a somewhat high. The model with power slope -2 also predicts that about 10% of the O-type stars are single stars (lower curves). This prediction is nearly independent of the adopted stellar IMF and somewhat higher than the revised percentage of field O stars of 6%

[b]an O-type star in this case would be a star more massive than 17.5 $M_\odot$.

(indicated by the dashed horizontal line) as reported in the previous section. A CMF with power -2 therefore predicts too many single O-type stars and too many clusters with only one O-type star, than observed. In the right panel we actually try to fit the observations, and find that the Galactic data for O-type stars would be best fitted with a value of -1.7 for the CMF power index. Interestingly, such a power law was also preferred by Bonnel & Clarke (1999)[4] in their calculations to fit the size distribution of the small clusters near HAeBe stars (Testi et al. 1999), presented in Fig. 1.

These calculations are found to depend critically upon the mass of the most massive cluster; more massive clusters have more O-type stars and the cumulative distribution tend to rise more slowly. In the calculations presented in the left panel of Fig. 5 we applied the value of the most massive OB-association in the sample of M98. The largest association in M98 is Sco OB 1 that contains 27 O-type stars, equivalent to $\sim 1.2 \times 10^4\,M_\odot$. The fit to the data in the right panel required the maximum number of stars per cluster to be 3×10^3.

We conclude that although the number of O field stars in the Galaxy is small, such a small fraction is actually expected when clusters follow a cluster mass distribution function with a power index of -1.7. This result is reasonably independent of the shape of the stellar IMF.

7 Summary and conclusions

In this contribution we have discussed some of the statistical properties of Galactic field O stars. It is for a large part the combination of two papers written on the subject by the same authors. We have tried to see whether there exists Galactic evidence for such a thing as the isolated formation of a high-mass star (produced in the Galactic field). The motivation for this study comes from the ongoing discussion whether high-mass stars should necessarily form in a cluster of stars. High-mass stars are claimed to have formed as single entities in external galaxies, such as the LMC and M 51.

In an attempt to clarify the origin of Galactic O star field population, we presented deep near infrared imaging of these 43 stars in a search for their membership of yet unknown host clusters. In 5 cases we have found the evidence of the existence of such clusters. The large majority of the field O stars is therefore not in a cluster. The next step consisted in evaluating a possible runaway nature for the field O stars. We plausibly relaxed the criteria for the identification of such stars and attempted to identify the parent cluster. This exercise lead us to propose the total of 22 field O stars to be runaway candidate stars.

Effectively our study of the Galactic O field stars shows that only 12 O stars (or 6%) cannot be associated with a cluster. This of course does not proof that they formed in the Galactic field, in an isolated mode. However if one would adopt the assumption that all stars are formed in clusters, and clusters are distributed in size according to a powerlaw with a slope of -1.7, all the way down to clusters with a single member, one finds a number of field O-type stars that is consistent with the revised statistics presented here. This may therefore indicate that the Galaxy is able to form a single high-mass star without the requirement of a stellar cluster.

Acknowledgments

WJDW acknowledges financial assistance from the European Union Research Training Network 'The Formation and Evolution of Young Stellar Clusters' (RTN1-1999-00436). This research has made use of the Simbad database, operated at the Centre de Donnees Astronomiques de Strasbourg (CDS), andof NASA's Astrophysics Data System Bibliographic Services (ADS). This publication makes use of data products from the Two Micron All Sky Survey, whichis a joint project of the University of Massachusetts and the Infrared Processing and Analysis Center/California Institute of Technology, funded by the National Aeronautics and Space Administration and the National Science Foundation.

References

1. Bik, A., *et al.* 2003 A&A 397, 473.
2. Blaauw, A. 1961 Bull. Astr. Inst. Neth. 15, 265.
3. Bonnell, I. A., *et al.* 1998 MNRAS 298, 93.

4. Bonnell, I. A., & Clarke, C. J. 1999 MNRAS 309, 461.
5. Bonnell, I. A., & Bate, M. R. 2002 MNRAS 336, 659
6. Bonnell, I. A., *et al.* 2004 MNRAS 349, 735.
7. Clarke, C. J., & Pringle, J. E. 1992 MNRAS 255, 423.
8. de Wit, W. J., *et al.* 2004 A&A 425, 937
9. de Wit, W. J., *et al.* 2005 A&A , subm.
10. Dokuchaev, V. I., & Ozernoi, L. M. 1981 Soviet Astronomy Letters 7, 52.
11. Edgar, R., & Clarke, C. 2004 MNRAS 349, 678.
12. Eisner, J., *et al.* 2004 astro-ph/0406356.
13. Elmegreen, B. G., & Efremov, Y. N. 1997 ApJ 480, 235.
14. Gies, D. R., & Bolton, C. T. 1986 ApJS 61, 419.
15. Gies, D. R. 1987 ApJS 64, 545.
16. Gomez, M., *et al.* 1993 AJ 105, 1927.
17. Harris, W. E., & Pudritz, R. E. 1994 ApJ 429, 177.
18. Hillenbrand, L. A. 1995 Ph.D. Thesis.
19. Hillenbrand, L. A., & Hartmann, L. W. 1998 ApJ 492, 540.
20. Hoogerwerf, R., *et al.* 2001 A&A 365, 49.
21. Kroupa, P. 2002 Science 295, 82.
22. Lada, C. J., & Lada, E. A. 2003 ARA&A 41, 57.
23. Lamers, H. J. G. L. M., *et al.* 2002 ApJ 566, 818.
24. Larsen, S. S. 2000 MNRAS 319, 893.
25. Li, Y., *et al.* 2003 ApJ 592, 975.
26. Mason, B. D., *et al.* 1998 AJ 115, 821.
27. Massey, P., *et al.* 1995 ApJ 438, 188.
28. Massey, P. 1998 In ASP Conf. Ser. 142: The Stellar Initial Mass Function (38th Herstmonceux Conference) pp. 17.
29. Mel'Nik, A. M., & Efremov, Y. N. 1995 Astronomy Letters 21, 10.
30. Millan-Gabet, R., *et al.* 2001 ApJ 546, 358.
31. Oey, M. S., *et al.* 2004 AJ 127, 1632.
32. Poveda, A. 1967 AJ 72, 824.
33. Ramspeck, M., *et al.* 2001 A&A 378, 907.
34. Salpeter, E. E. 1955 ApJ 121, 161.
35. Spaans, M., & Silk, J. 2000 ApJ 538, 115.
36. Stahler, S. W., *et al.* 2000 Protostars and Planets IV pp. 327.
37. Testi, L., *et al.* 1998 A&A Suppl. 133, 81.
38. Testi, L., *et al.* 1999 A&A 342, 515.
39. Turner, D. G. 1985 ApJ 292, 148.
40. Vazquez, R. A., *et al.* 1994 A&A Suppl. 106, 339.
41. Vink, J. S., *et al.* 2003 In ASP Conf. Ser. 287: Galactic Star Formation Across the Stellar Mass Spectrum pp. 319.
42. Walborn, N. R. 1973 AJ 78, 1067.
43. Wolfire, M. G., & Cassinelli, J. P. 1986 ApJ 310, 207.
44. Yorke, H. W., & Sonnhalter, C. 2002 ApJ 569, 846.
45. Zhang, Q., & Fall, S. M. 1999 ApJ 527, L81.

Induced Star Formation around Young HII regions : a detailed study of the Trifid nebula

B. Lefloch (1)
J. Cernicharo (2)
(1) Laboratoire d'Astrophysique de Grenoble
BP 53X, 38041 Grenoble Cedex, France
(2) DAMIR, IEM
C. Serrano, 121, 28006, Madrid, Spain

There is large observational evidence that triggered modes of star formation may be important at the Galactic scale. Large-scale surveys suggest that HII regions are efficient in spreading star formation and producing high-/intermediate-mass objects but the details of the mechanisms are not well constrained, so that the role of HII regions in triggering SF is still questioned. We present here an observational study of the Trifid nebula, a young HII region, and its protostellar population. in relation with the parental cloud. Several massive protostellar cores (60 to 200 $M_{\odot}$) are detected, which harbour intermediate-mass objects. We find direct evidence that several of the cores are experiencing shock conditions which probably caused their gravitational collapse.

Keywords: ISM : HII regions, clouds; stars; Stars : formation

1 HII regions in the Galaxy

There is large observational evidence that HII regions play an important role in spreading Star Formation throughout the Galaxy. In the solar neighborhood, most of the embedded young stellar clusters are adjacent to HII regions excited by older stars and/or clusters. This is the case of Orion and other well-known regions such as the Rosette nebula, the W3/W4/W5 complex or M17.

Several systematic studies based on IRAS data [14,3] have shown that the dense condensations at the border of HII regions are common sites of Star Formation. The ysos identified in these clouds are, on average, one order of magnitude more massive than their counterparts in dark clouds. These studies were biased towards luminous sources; moreover, the poor angular resolution a priori excluded the youngest HII regions, whose nebular emission may dominate the ysos emission. Because of these instrumental limitations, the low-mass objects remained out of reach until the advent of SPITZER. Another consequence is that most of the studies were restricted to evolved regions, which have already reached sizes of tens of parcsecs. Under such conditions, the cometary globules are exposed to reduced ionizing and UV radiation fields, so that the radiation impact on the dynamics is then limited. In parallel to these large surveys, only very few detail studies of Cometary Globules have been carried out until now [2,11], so that the cloud physical properties are not well characterized. On the theoretical side, numerical modelling has allowed to get a clear view of the evolution of these structures exposed to the strong ionizing radiation of the nebula, in good agreement with the observations[9,10].

The possibility of triggering star formation in the environment of HII regions has long attracted the attention of theoreticians[4,16]. Several models have been proposed and revisited since (see Whitworth and Deharveng for a review). However, it is still not clear today if triggering is important in all star forming regions (SFRs) and which triggering mode is efficient. It is therefore not surprising that the properties of the protostellar population that forms in the vicinity of an HII region, its relation to the parental cloud, are not well understood.

It is in this context that we decided to start a systematic study of a young HII region, close enough to allow a complete census of the young stellar and protostellar population: the Trifid nebula (M20). The emission of the nebula and its environment were systematically observed from centimeter to optical wavelengths. The free-free radiation of the nebular gas and in the ionization fronts was observed with the VLA. The cold dust and gas emission was observed at IRAM, SEST and CSO. The emission of the Photon-Dominated Regions was observed with the instruments onboard ISO. Such a large database is necessary to disentangle the various processes at work in and around the HII region.

2 The Trifid at large-scale

The Trifid nebula (Fig. 1) is located in the Sagittarius arm of the Galaxy at a distance of 1.7 kpc, close to the young supernova remnant W28SNR and other massive SFRs. The nebula is rather compact, with a diameter of 3.5 pc, which allows a comprehensive study of the HII region and the parental molecular cloud. Subsequently, the measured electron density in the nebular gas is high ($100-200\,\mathrm{cm}^{-3}$). The spectral type is still somewhat debated, O7.5 III or O7 V, but the Lyman-c photon rate is well characterized : $\dot{N}_L = 10^{49}\,\mathrm{s}^{-1}$. The exciting star of the nebula (HD 164492A) is accompanied by a cluster of five objects (components B to F), some of which are still surrounded by their protostellar disks, undergoing heavy photoevaporation[7], which suggests a young evolutionary age for the nebula. Indeed, numerical modelling of cometary globules at the border of the Trifid indicate a dynamical age of 0.3 Myr[8].

The low-density gas emission was mapped in the millimeter lines of CO and its isotopes (^{13}CO, C^{18}O) at the IRAM 30m telescope and at the CSO over an area of 20' by 30'. At the distance of the Trifid, the beam size of $10''$ corresponds to a linear size of 0.1 pc. We detected hardly any neutral gas inside the HII region, apart from tiny photoionized globules. The line profiles are characterized by a broad plateau covering a velocity range of $80\,\mathrm{km\,s}^{-1}$. On top of this plateau are detected narrower components (typically $1-3\,\mathrm{km\,s}^{-1}$ wide). The high-velocity components (up to $40\,\mathrm{km\,s}^{-1}$ with respect to the cloud velocity) are distributed in thin sheets of gas blown away from the nebula. The narrow components arise from denser regions, in particular the dust lanes. These are detected in absorption against the optical nebula, which means they are located on the front side of the ionized gas; it allows to derive the kinematical structure of the Trifid (see Fig. 2). Based on CS and C^{18}O line analysis, the typical H_2 density of these components is $\sim 5\times10^3\,\mathrm{cm}^{-3}$ and the gas column density is $N(H_2) \sim 5\times10^{21}\,\mathrm{cm}^{-2}$. It implies a thickness of 0.3 pc, comparable to the transverse size (in the plane of the sky). In other words, the gas around the nebula is distributed in filaments. The size of these filaments ranges from $1-2$ pc, for the lanes, up to 10 pc for gas in the filament on the Western side of the nebula. On the front side, the gas exhibit a much more fragmented appearance than what is derived from the optical. The lanes appear to have been accelerated to $\approx 10\,\mathrm{km\,s}^{-1}$ with respect to the ambient cloud, and they undergo strong velocity gradients, of several $\mathrm{km\,s}^{-1}\,\mathrm{pc}^{-1}$.

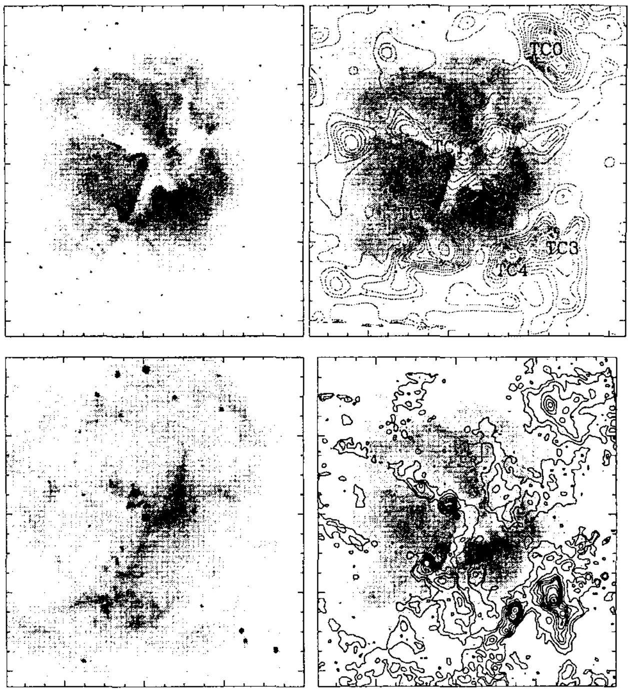

Figure 1: The Trifid nebula : (up. left) in the optical ($H\alpha$); (low left) at 11.5μm seen with ISOCAM; (up. right) in the $HCO^+ J = 1 \rightarrow 0$ line seen with the SEST; (low. right) at 1.3mm with the IRAM 30m telescope. Location of the protostellar sources TC1-TC4 is indicated in the HCO+ emission map.

3 Massive Protostellar Cores

The cold dust emission was mapped at 1.3mm with the MPIfR-37 channel bolometer array over an area of 15' by 30' (Fig. 3). Our sensitivity was good enough to detect the extended emission from the gas filaments and fragments inside these filaments. Seven condensations were identified in total : TC0N, TC0,1,2,..,5. Whereas five condensations are directly exposed to the influence of the nebula (TC0,..,4), two others are more distant but still associated with the parental molecular cloud.

Four of them (TC0N, TC0, TC3, TC5) are identified in the Western filament with masses ranging from about $200\,M_\odot$ up to $800\,M_\odot$. The fragments have a typical size of 1.5 pc and are equally separated by 10^{19} cm(3.3 pc). This value is in very good agreement with the most unstable mode that propagates in a purely hydrodynamically supported filament[12]. The mass of the fragments is being accreted from the filament itself, as suggested by the velocity field obtained in the CS $J = 2 \rightarrow 1$ line, that shows the molecular gas of the filament flowing onto the massive fragments. The total mass of the filament and the fragments are very similar ($\sim 2000\,M_\odot$). The condensations TC1-2 are located in the dust lanes at the border of the HII region, i.e. they are directly exposed to the high-energy radiation of the nebula. They have smaller sizes ($\sim$ 0.3 pc) and masses ($\sim 60\,M_\odot$). Molecular line observations have allowed to derive the condensation structure to 6" resolution and showed that a radiatively-driven shock propagates inside the condensations, whereas a Photon-Dominated Region has formed below the surface[8]. The filament associated with TC4 appears to be fragmented in at least three condensations.

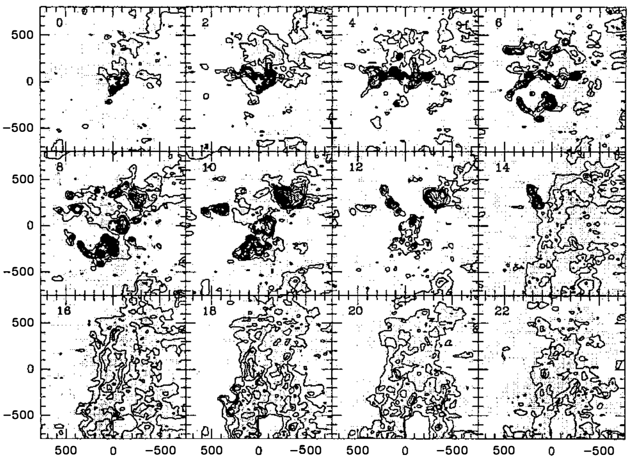

Figure 2: Map of the CO $J = 3 \rightarrow 2$ emission integrated per velocity channels observed at the CSO. Channel velocity is indicated in the upper right corner. A white star marks the position of the exciting star of the nebula.

The two other condensations have smaller masses ($\sim 10\,M_{\odot}$). The distribution of the dense gas and its kinematics are consistent with condensations forming **from** the fragmentation of the filament, compressed by the shock preceding the ionization front[6].

Several cores could be identified in the most massive condensations (TC1-5), which appear strongly peaked (Fig. 3). The cores are compact, with sizes of $0.1 - 0.2$ pc. We focus here on the brightest cores identified in each condensation. TC0N and TC0 differ somewhat from the rest of the sample in that their flux distribution is much shallower and does not present any strong peak. Comparison with the $12\mu m$ maps obtained ISOCAM shows that only two sources (TC4-5) exhibit a counterpart in the mid-IR, indicating all the millimeter sources to be deeply embedded. Indeed, the Spectral Energy Distribution obtained with ISO for some of them (TC2,4,5) indicates dust temperatures of $15-20$ K and dust column densities of a few 10^{23} cm^{-2}. The core properties are summarized in Table 1. They are massive ($M = 20 - 200\,M_{\odot}$) and their luminosity is typical of intermediate-mass objects.

Detailed studies of the molecular content of TC1-5 have confirmed the protostellar nature of these cores[6,8] : evidences of outflowing gas were discovered in all the cores. TC2 is somewhat an exception as the outflow is oriented almost in the plane of the sky, so that the wings were too weak to be detected at the IRAM 30m telescope. However, the source powers the splendid HH399 photoionized jet[13]. The various molecular tracers observed (HCO^+,CS,SiO) show bright lines, comparable to those detected in the Orion protostellar cores, once scaled at the same distance[6]. The ratio of their millimeter to bolometric luminosity is found large, with values typical of "Class 0" protostars, i.e. all the protostars are very young, still in the phase of accreting the bulk of mass from their parental envelope. The cores TC3-4-5 appear to be very dense, with densities $n(H_2) = (1-5)\times 10^6$ cm^{-3} at the emission peak, and in the envelope ($n(H_2) = (2-4)\times 10^5$ cm^{-3}). The line profiles of the high-density gas tracers (CS, SiO) are characterized by bipolar wings

Table 1: Physical properties of the protostellar cores detected around the Trifid nebula. In the last column is given the flux scaled at the distance of the nearest SF complexes (ρ Oph and Taurus; 160 pc). We adopt a dust temperature of 20 K and a dust spectral index of 2 (derived from the SED obtained with ISO/LWS). A dust absorption coefficient $\kappa = 0.1\,\mathrm{cm^2\,g^{-1}}$ at $250\mu m$ was assumed. We follow the convention $a(b) = a \times 10^b$

Source	$S_{1.3}^{peak}$ (Jy)	$S_{1.3}^{int}$ (Jy)	M_t ($M_\odot$)	N_H ($\mathrm{cm^{-2}}$)	L_{bol} (L_{bol})	S^* (Jy)
TC0	0.10	0.70	46	1.0(23)	-	
TC1	0.16	0.20	23	1.7(23)	-	16
TC2	0.15	0.18	27	1.6(23)	500-1200	15
TC3	0.39	0.92	90	3.7(23)	-	39
TC4	0.29	0.60	58	2.8(23)	520-2400	29
TC5	1.03	2.0	200	1.0(24)	3900	-

that reach velocities up to $30\,\mathrm{km\,s^{-1}}$ with respect to the ambient gas for some of these sources. The outflow properties could be derived in the case of TC3-4-5 and are found consistent with those powered by intermediate-mass protostars[15]. TC1 and TC2 exhibit similar properties : their peak density, as derived from CS, is less (typically $2-4\times10^5\,\mathrm{cm^{-3}}$), as well as their mean envelope density ($\sim 2\times10^4\,\mathrm{cm^{-3}}$). The TC1 and TC2 protostars are detected in condensations less massive and less dense than the TC3-4-5 sources. As such, they are a good illustrative case of star formation going on at the same time as the protostellar envelope is photoevaporated. We did not find any strong evidence the star formation process was triggered by the radiatively-driven implosion of the condensations[8]; observations at a better angular resolution would help ascertain this conclusion. The gas properties of TC0 are rather similar to those of TC1-2. The core does not exhibit any sign of gravitational collapse : it appears to be still in a quiescent stage while it is hit by the ionization front of the HII region.

4 Triggered Star Formation around the Trifid

Analysis of the gas kinematics in the Western filament yields interesting constraints on the star formation that took place. A map of the $C^{18}O$ emission per velocity channels (Fig. 3) in the region near TC3 and TC4 shows that the emission from the cores is anticorrelated with the rest of the filament : there is a perfect match between the cores and the apparent "hole" in the filament. The emissions are separated by about $3\,\mathrm{km\,s^{-1}}$ (compare the panels at $v = 18\,\mathrm{km\,s^{-1}}$ and $v = 21\,\mathrm{km\,s^{-1}}$). This is a direct evidence that TC3 and TC4 are forming in **shocked** material of the filament. Dense molecular gas tracers such as CS, SiO, $H^{13}CO^+$ peak exactly at the same velocity despite their different optical depth, hence probing different gas layers. It is consistent with star formation occuring **after** the shock impact. In the opposite case, one would expect optically thin tracers to keep track of the initial velocity distribution in the inner core regions. A detailed analysis of TC5 has been carried out and leads to the conclusion that TC5, too, is forming inside a shocked core. The most plausible trigger would be W28SNR, at the border of which lies TC5. Interestingly, in the Western filament, the evidences of ongoing star formation are found only in the cores which show evidences of shock.

Numerical simulations of a filament impacted by an HII region[5] show that the timescales involved to form the first and the subsequent generation(s) of cores are always several times the crossing time of the filament : ≈ 1.5 Myr for the Western filament, much more than the age of the Trifid and W28SNR. The fragmentation of the filament is therefore related to some older event, and the protostellar cores were pre-existing the ignition of the nebula. The very short dynamical timescale of the cores ($\sim 10^4$ yr) is consistent with a very recent gravitational

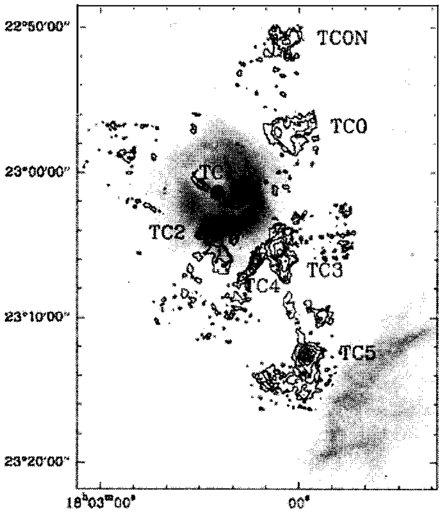

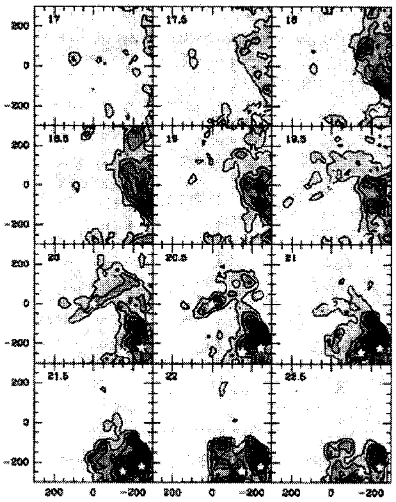

Figure 3: *(left)* 1.3mm dust emission map (contours) superposed on a 20cm VLA image of the region. *(right)* Map of the $C^{18}O$ $J = 1 \rightarrow 0$ emission per velocity channels on the Western side of the Trifid. White stars mark the position of HD 164492A, TC3 and TC4.

collapse, following immediately the shock compression of the cores.

The Trifid nebula is a good illustrative case of a young HII region formed in a dense cloud. The exciting star was born inside a web of filaments. The destabilization of these filaments has led to their fragmentation. The formation of new generation of stars in these fragments has been triggered by shock interaction with the ambient medium, probably the Trifid and/or W28SNR. High-angular resolution observations as well as numerical modelling should be undertaken to understand the peculiar kinematical structure of these cores, and how strongly it can affect the gravitational collapse and the source multiplicity.

References

1. Cernicharo, J., Lefloch, B., Cox, P., et al., 1998, Science, 282, 462
2. Cernicharo, J., Bachiller, R., Duvert, G., et al., 1992, A&A, 261, 589
3. Dobashi, K., Yokenura, Y., Matsumoto, T., et al., 2001, PASJ, 53, 85 233, 190
4. Elmegreen, C.J., Lada, 1977, ApJ, 214, 725
5. Fukuda, N., Hanawa, T., 2000, ApJ, 533, 911
6. Lefloch, B., Cernicharo, J., 2000, ApJ, 545, 340
7. Lefloch, B., Cernicharo, J., Cesarsky, D., et al., 2001, A&A, 368, L13
8. Lefloch, B., Cernicharo, J., Rodriguez, L.F., et al., 2002, A&A, 581, 335
9. Lefloch, B., Lazareff, B., 1994, A&A, 289, 559
10. Lefloch, B., Lazareff, B., 1995, A&A, 301, 522
11. Lefloch, B., Lazareff, B., Castets, A., 1997, A&A, 324, 249
12. Nakamura, F., Hanawa, T., Nakano, T., 1993, PASJ, 45, 551
13. Rosado,M., Esteban, C., Lefloch, B., et al., 1999, AJ, 118, 2962
14. Sugitani, K., Fukui, Y., & Ogura, K., 1991, ApJS, 77, 59
15. Shepherd, D., Churchwell, E., 1996, ApJ, 472, 225
16. Whitworth, A. P.; Bhattal, A. S.; Chapman, S. J., et al., 1994, MNRAS, 268, 291

SEQUENTIAL FORMATION OF MASSIVE STARS OR CLUSTERS AT THE PERIPHERY OF H II REGIONS

L. DEHARVENG, A. ZAVAGNO, J. CAPLAN
Laboratoire d'Astrophysique de Marseille
2 Place le Verrier, 13248, Marseille Cedex 4

Several physical processes can trigger star formation at the periphery of classical H II regions. We present and discuss some of them.

Keywords: stars: formation - stars: early-type - ISM: H II regions.

1 Introduction

In this presentation we will concentrate on star formation observed at the periphery of *classical H II regions.* We will review different processes, linked to H II regions, which can trigger star formation at their border. We will present the models, and then some observations to illustrate these models. In the discussion we would like to draw up the balance sheet between what we know or understand and what we still do not understand and cannot explain.

First we can turn to statistics. The presence of an H II region adjacent to a molecular cloud has two effects: i) it favours star formation; ii) it favours the formation of massive objects. Dobashi et al. (2001)[3] have investigated the luminosity of protostars forming in molecular clouds as a function of the parental cloud mass, in a sample of about five hundred molecular clouds taken from the literature; half of these clouds are associated with protostellar candidates selected from the IRAS point source catalogue. They have shown that *the protostars in clouds associated with H II regions are more luminous that those in clouds away from H II regions.* In addition, Dobashi et al. have shown the existence of well-defined upper and lower limits in the luminosity distribution; they propose a very simple model which assumes that the luminosity function of protostars is controlled by the mass of the parental cloud and by some external pressure imposed on the cloud surface. The lower and upper limits in the luminosity distribution correspond respectively to $P_{\rm external} = 0$ and $P_{\rm external}/k \sim 10^{5.5}$ K cm^{-3}; this last figure is a reasonable value for the pressure of the ionized gas in a classical H II region.

A complete review of the processes triggering star formation has been given by Elmegreen (1998) [7].

2 Model 1 - Radiation-driven implosions - Bright rims and cometary globules

Due to the high pressure of the ionized gas relatively to that of the surrounding neutral material, H II regions expand. Their expansion velocity, $\sim$11 km s^{-1} just after the ionization of the gas and the formation of the initial Strömgren sphere, decreases with time (Dyson & Williams, 1997 [5]).

In this scenario the H II region expands in a medium containing *pre-existing dense molecular clumps.* The pressure exerted by the ionized gas on the surface of a clump can lead to its implosion, and to the formation of a 'cometary globule ' surrounded by dense ionized gas forming a 'bright rim'.

This configuration has been simulated by Lefloch & Lazareff (1994) [11]. These authors follow the evolution of a 20 $M_\odot$ clump submitted to the ionizing flux of a O7V star situated at 5 pc from the clump. A shock front progresses in the clump, leading to the formation of a dense core, near the centre of the initial clump. The maximum compression is obtained after 0.2 Myr. This collapse phase is followed by a transient phase of re-expansion, and by a quasi-stationary cometary phase. During this last phase the cometary globule presents a dense head and a tail extending away from the ionization source; it evaporates slowly, as the dense ionized gas flows away from the globule; it moves away from the ionizing star with a velocity of a few km s^{-1}. It is entirely ionized and disappears after 2.7 Myr. The collapse phase is rapid, lasting about 10% of the lifetime of the globule. It is possibly during this phase that star formation occurs.

Numerous observations of bright rims have been performed recently, at various wavelengths, mainly to study the structure of the molecular globules and their stellar content. Most of these observations show very good agreement between the models and the observations with regard to the morphology of the globules and to their velocity field; cf. Sugitani et al. (1997) [17], De Vries et al. (2002) [2], Thompson et al. (2004) [19].

Signposts of star formation are often observed in the direction of cometary globules: IRAS sources with colours of protostellar objects, MSX point sources, near-IR reddened objects, CO outflows, Herbig-Haro objects, Hα emission stars, etc. We will illustrate this by two examples.

- Fig. 1 shows the Bright Rim Cloud (BRC) no. 5 in the catalogue of Sugitani et al. (1991) [16]. The MSX emission at 8.3 μm is shown as contours, superimposed on an image of the bright rim (DSS-2 red survey); a bright MSX point source is observed *in the direction of the head of the globule*, which is also an IRAS source with a luminosity of $\sim$ 1100 $L_\odot$. A near-IR cluster (2MASS survey) is detected in the same direction; it contains two bright K stars presenting a near-IR colour excess, probably indicative of an accretion disk (Lada & Adams, 1992) [10]. A CO outflow, with a dynamical age of 1.5 10^4 yr, has been detected in the direction of the head of the globule (Duvert et al. 1990 [4], Lefloch et al. 1997 [12]).

- BRC 44, also from the catalogue of Sugitani et al., presents a somewhat different configuration. Fig. 2 shows how it appears in the optical (DSS-2 red survey); the ionizing radiation comes from the south. CO observations (Ridge et al. 2003) [14] and 2-mm observations (Sugitani et al. 2000) [18] show the presence of a dense globule in the direction of the region of high absorption (Fig. 2). An IRAS point source of $\sim$ 700 $L_\odot$ lies in the direction of the globule. A CO outflow has possibly been detected in this direction (Sugitani et al. 1989) [15]. A cluster containing Hα emission stars lies at the periphery of the globule (Ogura et al. 2002) [13], in the direction of the ionized gas. The near-IR image of this region shows a small very red cluster (Fig. 2); it contains a very bright star (with a strong near-IR colour excess according to the 2MASS catalogue) which is probably a young object with an associated accretion disk. This

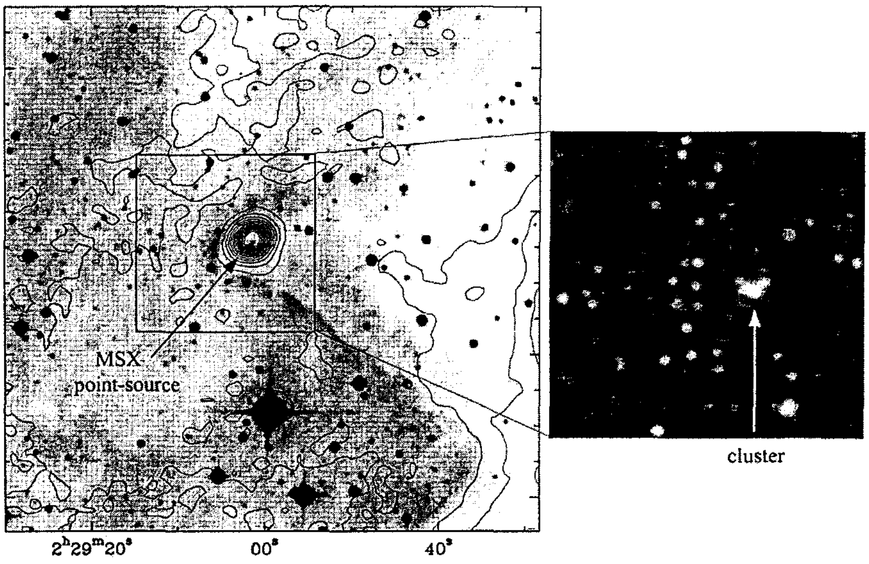

Figure 1: BRC 5. *Left:* The MSX emission at 8.3μm (contours) is superimposed on a DSS red frame (grey scale). *Right:* Colour composite JHK image (from 2MASS) of the head of the globule.

star lies at the border of the dense globule and definitively not inside. Only a faint but very red object lies in the direction of the globule.

Ogura et al. (2002) [13] present this region as a case of *small-scale sequential star formation.* If star formation occurs during the very short implosion phase, near the maximum contraction phase of the globule, small-scale sequential star formation is difficult to understand. The case of BRC 44 suggests that star formation occurs at the periphery of the globule more than in its centre, and with time moves away from the first-generation star(s) exciting the H II region. Ogura et al. present several other such cases.

3 Model 2 - The collect and collapse model

During the expansion of an H II region the ionization front (IF) is supersonic, and it is preceded by a shock front (SF) on the neutral side. Neutral material accumulates between the two fronts, forming a layer of dense shocked material. Instabilities can develop, on various time scales, within this compressed layer.

1. Dynamical instabilities can develop on a short time scale; a two-dimensional simulation of this process is presented by García-Segura & Franco (1996) [8]. According to these authors, the resulting structures are very similar to the bright rims and 'elephant trunks' observed at the periphery of H II regions. If confirmed, this process is interesting as it allows the formation of dense clumps in a formerly rather homogeneous medium.

2. Gravitational instabilities can develop on a long time scale, along the length of the layer. This process is interesting because it leads to the formation of *massive* fragments: because of the long time scale, the compressed layer becomes very massive, and it fragments into massive pieces. For example, according to Whitworth et al. (1994) [20], for an H II region evolving in a medium of density 1000 cm^{-3}, where the rms velocity dispersion is 0.5 km s^{-1},

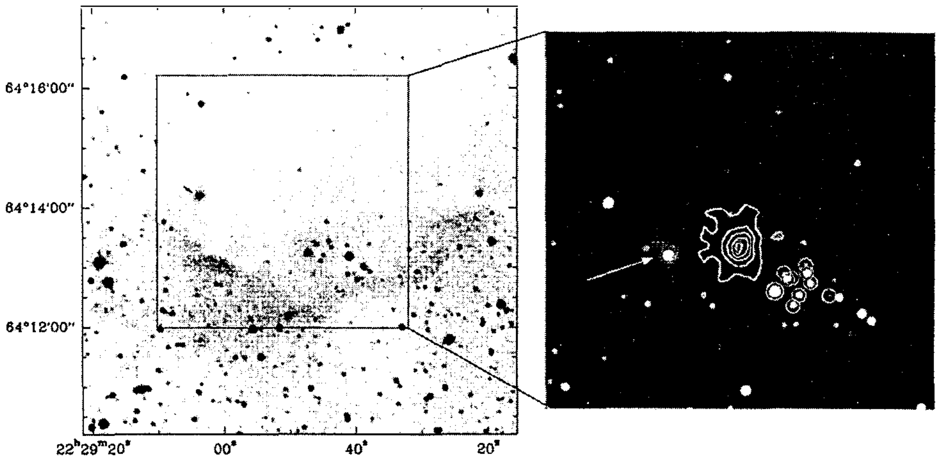

Figure 2: BRC 44. *Left:* DSS red frame (grey scale). *Right:* The 2-mm emission (contours) is superimposed on a colour composite JHK image (2MASS); the Hα emission stars are identified by circles; the arrow points to the K star with a strong near-IR colour excess.

fragmentation into seven parts occurs after about 3 Myr, with masses of about 600 $M_{\odot}$. These fragments are very dense, and they fragment in turn, very quickly, leading to the formation of clusters. Because these second-generation stars conserve the velocity of the medium in which they form, they ought to be observable later on, in the direction of the layer.

This model has never been convincingly confirmed, mostly because the morphology of H II regions is generally complicated. To study the collect and collapse process, we have selected about twenty H II regions with a very simple morphology, allowing us to locate the ionization front, and separate the ionized and the surrounding neutral media. Each of these regions has a red cluster at its periphery (Deharveng et al., in preparation). Sh 104 is the prototype of such regions; it is spherically symmetric around a central exciting O6V star. A ring of molecular and dust emission (MSX emission at 8.3 μm, mainly due to PAHs) surrounds the ionized gas, showing the existence of a layer of dense molecular material surrounding the H II region. An MSX point source which is observed at the periphery of the H II region, in the direction of the ring, is also an IRAS source with a luminosity of $\sim$3 10^4 $L_{\odot}$; an ultra-compact (UC) H II region and a near-IR cluster are detected in the same direction. The mass of the molecular ring is $\sim$6000 $M_{\odot}$. This molecular ring contains four fragments regularly spaced along the ring. The brightest fragment, with a mass $\sim$670 $M_{\odot}$, contains several dense cores; the near-IR cluster, exciting the UC H II region, is observed in the direction of the brightest fragment. Details and illustrations can be found in Deharveng et al. (2003) [1]. The presence of *four fragments regularly spaced along the molecular ring* is a strong argument in favour of the collect and collapse model; it allows us to reject the spontaneous collapse or the implosion of a pre-existing molecular clump, the collision of the compressed layer with a pre-existing molecular clump, and the collapse of post-shock cores formed in a supersonic turbulent medium (Elmegreen et al. 1995) [6]. Also, the estimated star formation efficiency is high. The second-generation cluster contains at least a B1V star, exciting the ultra-compact H II region; assuming a standard IMF, the mass of the cluster is $\sim$330 $M_{\odot}$. The remaining parental fragment has a mass of 670 $M_{\odot}$, and thus a star formation efficiency of around 33%.

4 Discussion and conclusions

In this section I will try to summarize what we know about triggered star formation, and what is still uncertain.

Star formation is triggered by H II regions. I will illustrate this assertion by the case of the well-known H II region IC1848. Karr & Martin (2003) [9] have presented a multi-wavelength study of this region and have compared the distributions of the ionized gas (via radio continuum emission), the associated molecular material (via ^{13}CO emission), the associated dust (via the MSX emission at 8.3μm), and IRAS sources with colours corresponding to young stellar objects. Most of the IRAS sources lie at the periphery of the H II region. The number of IRAS sources per unit CO area is 4.8 times higher inside the zone of influence of the H II region than outside.

Young stars or clusters formed in clouds adjacent to H II regions are more luminous, and thus more massive, then those away from H II regions. For example in the Vela molecular ridge, Yamaguchi et al. (1999) [21] have shown that the mean IR luminosity of IRAS sources in clouds adjacent to H II regions is 780 $L_{\odot}$, whereas it is 63 $L_{\odot}$ for sources in clouds away from H II regions. The luminosity of the second-generation clusters formed by the collect and collapse process in the Sh 104, Sh 217, and RCW 79 regions is respectively 30000 $L_{\odot}$, 22700 $L_{\odot}$, and 55000 $L_{\odot}$ (Deharveng et al., in preparation). These clusters contain B stars exciting UC H II regions.

The radiation-driven implosion model is well-verified by numerous observations. But we do not know if the molecular clumps pre-exist, or if they are formed either by dynamical instabilities in the compressed layer surrounding the ionized gas or by supersonic turbulence. Also, we do not know where (in the core, or at its periphery) and when (during the maximum compression phase, or earlier) star formation occurs. Thus, at present, we do not understand the small-scale sequential star formation observed in the vicinity of bright rims.

The collect and collapse process (on the long time scale) works, at least in its basic trends, if not in all its details. It leads to the formation of relatively massive clusters with a high efficiency, of the order of 30%. But we do not yet know its relative importance compared with other star-formation processes.

An important future goal is to determine what fraction of star formation is triggered by massive stars and H II regions, and which process is dominant in the formation of massive objects.

Acknowledgments

We thank B. Lefloch, F. Massi and J. Brand for many interesting discussions on this subject. This work has made use of the Simbad astronomical database operated at CDS, Strasbourg, France. It has used the NASA/IPAC Infrared Science Archives (MSX, IRAS, and 2MASS surveys), operated by the Jet Propulsion Laboratory, California Institute of Technology, under contract with the National Aeronautics and Space Administration.

References

1. Deharveng, L., Lefloch, B., Zavagno, A., Caplan, J., Whitworth, A.P., Nadeau, D., Martin, S., 2003, A&A 408, L25
2. De Vries, C.H., Narayanan, G., Snell, R.L., 2002, ApJ 577, 798
3. Dobashi, K., Yonekura, Y., Matsumoto, T., Momose, M., Sato, F., Bernard, J-P., Ogawa, H., 2001, PASJ 53, 85
4. Duvert, G., Cernicharo, J., Bachiller, R., Gómez-González, J., 1990, A&A 233, 190

5. Dyson, J.E., Williams, D.A., 1997, The physics of the interstellar medium, 2nd ed., eds R J Tayler & M Elvis, Published by Institute of Physics Publishing, Bristol and Philadelphia
6. Elmegreen, B. G., Kimura, T., Tosa, M., 1995, ApJ 451, 675
7. Elmegreen, B. G. 1998, in ASP Conf. Ser., 148, 150, eds. C. E. Woodward, J. M. Shull & H. A. Tronson
8. Garcia-Segura, G., Franco, J., 1996, ApJ 469, 171
9. Karr, J.L., Martin, P.G., 2003, ApJ 595, 900
10. Lada, C.J., Adams, F.C., 1992, ApJ 393, 278
11. Lefloch, B., Lazareff, B., 1994, A&A 289, 559
12. Lefloch, B., Lazareff, B., Castets, A., 1997, A&A 324, 249
13. Ogura, K., Sugitani, K., Pickles, A., 2002, AJ 123, 2597
14. Ridge, N., Wilson, T.L., Megeath, S.T., Allen, L.E., Myers, P.C., 2003, AJ 126, 286
15. Sugitani, K., Fukui, Y., Mizuno, A., Ohashi, N., 1989, ApJ 342, L87
16. Sugitani, K., Fukui, Y., Ogura, K., 1991, ApJSS 77, 59
17. Sugitani, K., Morita, K.I., Nakano, M., Tamura, M., Ogura, K., 1997, ApJ 486, L141
18. Sugitani, K., Matsuo, H., Nakano, M., Tamura, M., Ogura, K., 2000, AJ 119, 323
19. Thompson, M.A., White, G.J., Morgan, L.K., Miao, J., Fridlund, C.V.M., Huldtgren-White, M., 2004, A&A 414, 1017
20. Whitworth, A.P., Bhattal, A.S., Chapman, S.J., Disney, M. J., Turner, J.A., 1994, MNRAS 268, 291
21. Yamaguchi, N., Mizuno, N., Matsunaga, K., Mizuno, A., Ogawa, H., Fukui, Y., 1999, PASP 51, 775

Part 5

Extreme conditions for star formation

Did most local stars form in a starburst mode?

D. ELBAZ

CEA Saclay/DAPNIA/SAp
F-91191 Gif-sur-Yvette Cedex, France

We discuss the implications of the ISO, SCUBA and Spitzer extragalactic surveys, combined with the COBE cosmic infrared background, on the star formation history of galaxies. A class of galaxies is emerging, similar to local luminous infrared galaxies, that appears to play a dominant role in the shaping of present-day galaxies. Instead of a class, these observations suggest that these "dusty starbursts" should be considered as a common phase experienced by most if not all galaxies, once or even several times in their lifetime.

Keywords: Galaxies: starbursts - star formation rates - dust: extinction

1 Introduction

It is widely accepted that in the local universe stars form in giant molecular clouds (GMCs) where their optical and mostly UV light is strongly absorbed by the dust which surrounds them. Whether extinction was already taking place in the more distant universe where galaxies are less metal rich was less obvious ten years ago. Galaxies forming stars at a rate larger than about 20 $M_\odot\,an^{-1}$ were known to radiate the bulk of their luminosity above 5 μm thanks to IRAS, the so-called luminous (LIRGs, $12 > log(L_{IR}/L_\odot) \geq 11$) and ultra-luminous (ULIRGs, $log(L_{IR}/L_\odot) \geq 12$) infrared (IR) galaxies. In the following, we will call these galaxies "dusty starbursts". The bolometric luminosity of galaxies experiencing such large star formation rates is dominated by the radiation of their young and massive stars. In the local universe, such objects are very rare and indeed "dusty starbursts" radiate only 2 % of the bolometric luminosity of galaxies at z$\sim$0. In the past, galaxies were more gaseous and formed the bulk of their present-day stars, hence we may expect to find more of these violent star formation events. Already IRAS observations indicated a rapid decline of the comoving number density of ULIRGs since $z\sim0.3$ (Kim & Sanders 1998, see also Oliver et al 1996), but this was over a small redshift range and with small number statistics. However, the idea that "dusty starbursts" should have been common in the past was not accepted until a combination of observations arised during the last ten years. Distant galaxies were expected to be only marginally affected by dust extinction by reference to local galaxies and because they were less metal rich. Star formation rates were commonly measured from optical emission lines uncorrected for extinction, such as [OII] or [Hα] or the UV continuum. The first version of the cosmic star formation history of the universe (Madau et al 1995) was published without accounting for any extinction effect. However several independant sources converged towards another scenario, where most star formation that took place in the universe was obscured by dust, such as:

1. extragalactic source counts at 15 μm (Elbaz et al 1999, Metcalfe et al 2003, Gruppioni et al 2003, Rodighiero et al 2004, Fadda et al 2004, see Fig. 1) exhibit a slope which cannot be reconciled with model expectations unless strong evolution is advocated, either in luminosity and/or density of the mid infrared luminosity function, hence of the amount of star formation hidden by dust (e.g. Chary & Elbaz 2001).

2. the nearly simultaneous discovery of the cosmic infrared background (CIRB, Puget et al 1996, Fixsen et al 1998, Hauser & Dwek 2001 and references therein), at least as strong as the UV-optical-near IR one, whereas local galaxies only radiate about 30 % of their bolometric luminosity in the IR above $\lambda \sim 5\,\mu$m.

3. the 850 μm number counts from the SCUBA sub-millimeter bolometer array at the JCMT (Hughes et al 1998, Barger et al 1998, Smail et al 2002, Chapman et al 2003, and references therein) which also indicate a strong excess of faint objects in this wavelength range, implying that even at large redshifts dust emission must have been very large in at least the most active galaxies.

4. the most distant galaxies, individually detected thanks to the photometric redshift technique using their Balmer or Lyman break signature showed the signature of a strong dust extinction. The so-called "β-slope" technique (Meurer et al 1999) used to derive the intrinsic luminosity of these galaxies and correct their UV luminosity by factors of a few (typically between 3 and 7, Steidel et al 1999, Adelberger & Steidel 2000) was later on shown to even underestimate the SFR of LIRGs/ULIRGs (Goldader et al 2002).

5. the slope of the sub-mJy deep radio surveys (Haarsma et al 2000).

6. More recently, extragalactic source counts at 24 μm with MIPS onboard Spitzer confirmed the strong evolution found at 15 μm (Chary et al 2004, Papovich et al 2004).

It has now become clear that the cosmic history of star formation based on rest-frame UV or emission line indicators of star formation such as [OII] or [Hα] strongly underestimates the true activity of galaxies in the past if not corrected by strong factors due to dust extinction (Flores et al 2004, Liang et al 2004, Cardiel et al 2003). Although distant galaxies were less metal rich and much younger, they must have found the time to produce dust rapidly in order to efficiently absorb the UV light of their young stars.

2 Towards a coherent picture of the cosmic star formation history

We have produced a compilation of the versions of the comoving density of star formation for different star formation indicators references existing at the time of the conference in the Fig. 2 (see figure caption for the references). Fig. 2a shows the very large dispersion of all these measurements, leading the reader to the impression that they provide no valuable constraint on what really happened. However, once we take out data points providing only lower limits because they are not corrected for dust extinction, we get a much sharper scenario (Fig. 2b).

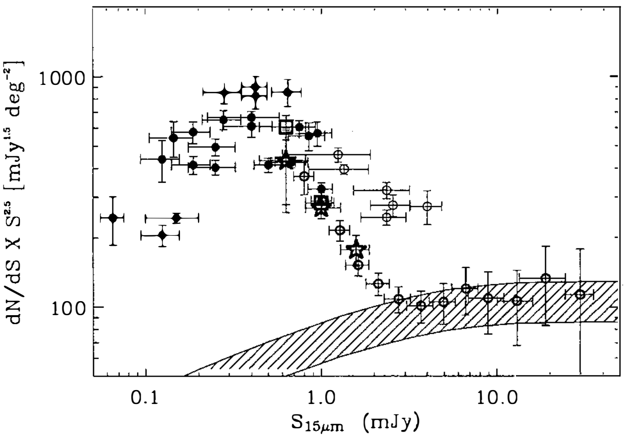

Figure 1: $15\,\mu$m differential counts (with 68 % error bars). The counts were normalized to the euclidean distribution without evolution, i.e. dN/dS $\propto$ $S^{-2.5}$. This figure is an extension of Fig.2 from Elbaz et al (1999) including the new analysis of the Lockman Hole Deep (Fadda et al 2004, bold squares) and Shallow (Rodighiero et al 2004, bold stars) surveys using the "Lari technique". The hatched area indicates the location of models if the mid infrared luminosity function was not evolving with redshift. The local luminosity function at $15\,\mu$m is from Fang et al (1998) and we used the template SED of M51 for the computation the k-correction. The width of the hatched area indicates an uncertainty of 20 %.

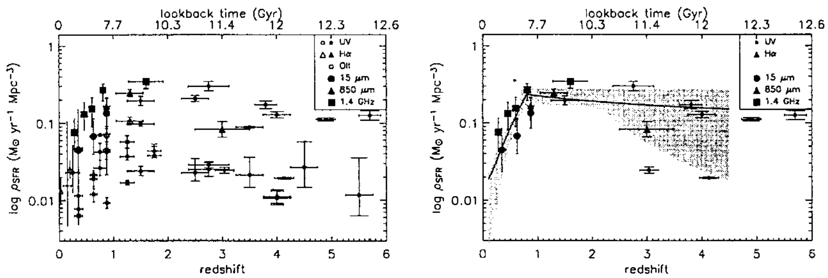

Figure 2: Density of star formation per unit comoving volume as a function of redshift (or lookback time, upper axis), i.e. cosmic star formation history. Cosmology: H_0=70 km s^{-1} Mpc^{-1}, Ω_m=0.3, Ω_Λ=0.7. The origin of the data points is given in the upper-right box. Data are from 1500Å(Massarotti et al 2001, Madau et al 1998, Pascarelle et al 1998), 1700Å(Steidel et al 1999), 2000Å(Treyer et al 1998), 2800Å(Connolly et al 1997, Lilly et al 1996, Cowie et al 1999), 3000Å(Sawicki et al 1997), *OII* (Hammer et al 1997), H_α (Gallego et al 1995, Tresse & Maddox 1998, Glazebrook et al 1999, Yan et al 1999), $15\,\mu$m (Flores et al 1999), $850\,\mu$m (Hughes et al 1998), 21 cm (Haarsma et al 2000). **left (a):** empty symbols are only modestly corrected for dust extinction (except for H_α uncorrected) following the recipee of Ascasibar et al. (2002): A(1500-2000 Å)=1.2 mag and A(2880 Å, 3000 Å, OII)= 0.625 mag, i.e. factors of 3 and 1.8 respectively. The filled symbols are corrected by extinction or do not require any correction (as for the 15, 850 μm and 1.4 GHz) data). We used the corrections quoted by the authors except for H_α for which no correction was available. We applyied a correction of a factor 2.3 to this indicator, i.e. half the one observed for ISOCAM galaxies (see Hammer et al 2004, Liang et al 2004). **right (b):** only the filled points are represented and compared to the range of possible star formation histories derived from source counts in the mid IR, far IR, sub-mm and the CIRB by Chary & Elbaz (2001).

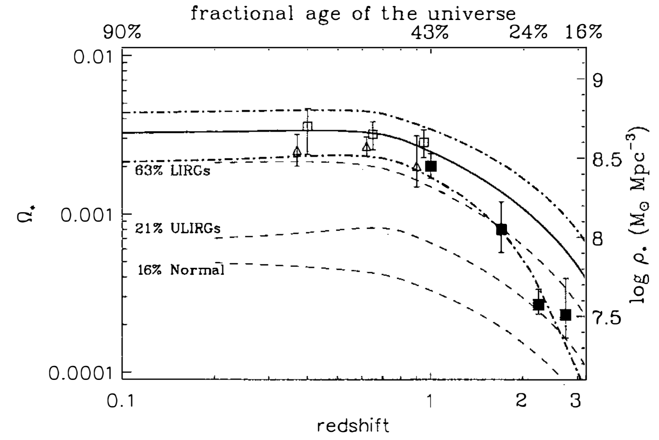

Figure 3: Redshift evolution of the comoving density of stars or Ω_* (divided by the critical density of the universe). Data from Dickinson et al (2003). The plain line is the best fit model of Chary & Elbaz (2001), including both luminosity and density evolution. The dashed lines represent the range of possible models within 1-σ of the observational constraints.

The grey area represents the range of possible scenarios from Chary & Elbaz (2001) fitting the combination of mid IR, far IR, sub-mm counts, the cosmic infrared background (CIRB) and the redshift distribution of the 15 μmISOCAM sources. A revised version including Spitzer MIPS 24 μm counts will soon be submitted. It does not require a major revision of this scenario. These data suggest that a strong evolution took place below $z \sim 2$ that gave rise to a large fraction of present-day stars. The main actors of this scenario are the "dusty starbursts", which are required to explain the source counts as well as the CIRB. An interesting test for this scenario consists in integrating the cosmic star formation history and to compare it to the observed evolution of the cosmic density of stars in the universe. This integral (for a Gould IMF, Gould et al 1996) is compared to the compilation of measurements from Dickinson et al (2003) in the Fig. 3. We have assumed a fraction of 20 % of the counts and infrared background to be due to active galactic nuclei (AGNs, see Fadda et al 2002). Although the best fitting model from Chary & Elbaz (2001) slightly overpredicts the comoving stellar mass density above $z \sim 1$, data are consistent with the broad region permitted by the range of valid models (region within the two dot-dashed lines). Note that the LIRGs by themselves provide about 63 % of present-day stars in this framework and fit the observed stellar mass density by themselves.

The excess of stellar mass derived from the integration of the cosmic star formation history (Fig. 2b) could be produced by several causes:

- a larger fraction of AGNs above $z \sim 1.5$

- a top-heavy initial mass function in dusty starbursts

- a change of the IR spectral energy distribution of galaxies that would imply that the SFR that we derived is overestimated for distant galaxies.

However, the global agreement of the two cosmic histories - of star formation and of stellar mass density- suggest that we are getting close to a coherent picture in which dusty starbursts play a major in shaping present-day galaxies. In this scenario, SCUBA galaxies of a few mJy with redshifts measured around $z \sim 2.5$ (Chapman et al 2003) are the tip of the iceberg, i.e. ULIRGs, while most of the evolution is due to LIRGs.

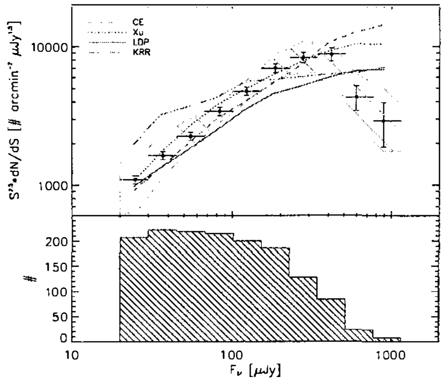

Figure 4: Completeness corrected galaxy counts in the MIPS 24 μm channel from Spitzer observations of the ELAIS-N1 field (from Chary et al 2004). The error bars reflect the Poissonian uncertainty. The horizontal bars represent the minimum and maximum flux density in that bin. The lines show four models for 24 μm counts: King & Rowan-Robinson (2003, KRR), Xu et al (2001, Xu), Chary & Elbaz (2001, CE), Lagache, Dole & Puget (2003, LDP). The symbols are plotted at the average of the flux densities of the detected sources in that bin for the data while the lines are plotted at the counts-weighted flux average for the models. The lower plot in the figure shows the histogram of the actual number of sources detected in each flux bin without any completeness correction.

3 From ISO to Spitzer

On August 23rd, 2003, NASA's Spitzer space telescope (formerly SIRTF) was launched. Among its first results came the source counts at 24 μm down to $\sim$ 20 μJy which confirmed what ISO deep surveys already saw: a strong excess of faint sources indicating a rapid redshift evolution of IR luminous galaxies. When compared to models developped to fit the ISO counts, the faint end of the Spitzer counts are fitted as shown in the Fig. 4 reproduced from Chary et al (2004). On the high flux density range, around 1 mJy and above, less galaxies are found than predicted by those models (see also Papovich et al 2004). This is partly, if not integrally, due to the fact that even ISOCAM-15 μm number counts were initially overestimated above $S_{15} \sim 1$ mJy.

In Fig. 1, we have separated the data points from the IGTES (Elbaz et al 1999) between those below and above $S_{15} = 1$ mJy, with filled and open dots respectively. Data above this flux density from Elbaz et al (1999) appear to be inconsistent with those derived from ELAIS-S1. Most of those points were derived from the Shallow Survey of the Lockman Hole within the IGTES, which suffered from having less redundant observations of a given sky pixel. At that time, ISOCAM data reduction methods were not optimized for such surveys, but since then, they have been improved to better deal with such shallow surveys. A recent analysis of the Lockman Hole Deep (Fadda et al 2004, large open squares) and Shallow (Rodighiero et al 2004, large open stars) surveys from the IGTES provided new number counts at these flux densities perfectly consistent with those derived from ELAIS-S1 by Gruppioni et al (2003) using the same data reduction technique. Note that the models designed to fit the ISOCAM number counts were constrained by the Elbaz et al (1999) counts, hence overproduce the number of sources above $S_{15} \sim 2$ mJy. As a natural result, they also overpredict the number of sources detected in the high flux density regime at 24 μm with Spitzer (see Papovich et al 2004, Chary et al 2004).

Although some refinement of the template SEDs used in the models might be considered (as suggested by Lagache et al 2004), the 24 μm number counts appear to be perfectly consistent with the up-to-date 15 μm counts. Moreover, the high flux density range does not strongly

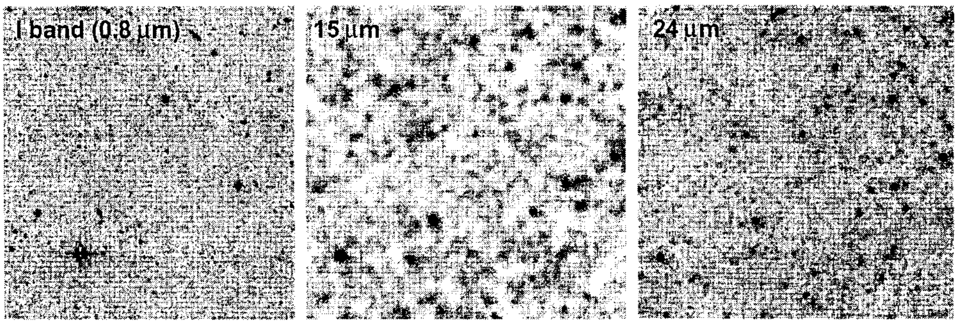

Figure 5: Images of the Ultra-Deep Survey in the Marano FIRBACK field in the I-band (left), ISOCAM $15\,\mu$m band (middle; depth $140\,\mu$Jy, 80 % completeness) and Spitzer MIPS-24 μm band (right; depth $110\,\mu$Jy, 80 % completeness).

affect the conclusions of the models based on previous $15\,\mu$m counts since bright objects do not contribute significantly to the CIRB and to the cosmic density of star formation. Hence these refinements are not strongly affecting the conclusions derived on galaxy formation and evolution based on the ISO deep surveys and summarized in the previous sections (see also Dole et al 2004 for the Spitzer counts in the far IR).

Another hint on the consistency of Spitzer MIPS-24 μm surveys with ISOCAM-15 μm is given by the comparison of the images themselves. Galaxies detected at 15 and 24 μm are clearly visible in both images in Fig. 5, although several 24 μm sources do not have a 15 μm counterpart. This results from the combination of the better sensitivity of MIPS, by a factor 2 or slightly more for the deepest surveys and of the k-correction. For galaxies above $z \sim 1$, the PAH bump centered on the PAH feature at 7.7 μm starts to exit to 15 μm broadband while it remains within the MIPS-24 μm band up to $z \sim 2$. The combination of ISOCAM and MIPS can be used to test whether the library of template SEDs that were used to derive total (from 8 to 1000 μm) IR luminosities for the 15 μm galaxies, based on local correlations, remains valid with increasing redshift. One of the most important tests is to check whether the 7.7 μm PAH bump is still present at $z \sim 1$ and whether the 24 over 15 μm flux density ratio is consistent with the template SEDs used by the models from which star formation histories were derived. The template SEDs designed by Chary & Elbaz (2001) provide a very good fit to the combination of both mid IR values for a sample of 16 galaxies detected by ISOCAM and MIPS (see Fig. 6). The $L_{\rm IR}$(8-1000 μm) derived from either the 15 or 24 μm luminosities or the combination of both to constrain the SED fit present a 1-σ dispersion of only 20 % (Elbaz et al 2004). For galaxies located around $z \sim 1$, the relative 15 and 24 μm luminosities clearly suggest the presence of a bump at 7.7 μm as observed in nearby galaxies and due to PAHs.

4 Conclusions

Many questions remain unsolved that will be addressed by future missions, staring with Spitzer. Only when a fair sample of redshifts will have been determined for the distant LIRGs will we be able to definitely ascertain the redshift evolution of the IR luminosity function. Already for the brightest part of it, campaigns of redshift measurements have started, on ELAIS fields for the nearby objects, and on the Marano field with VIMOS and the Lockman Hole with DEIMOS for more distant objects. The fields selected for Spitzer legacy and garanteed time surveys were also carefully selected to be covered at all wavelengths and followed spectroscopically, so that this issue should be addressed in the very near future. Due to confusion and sensitivity limits, direct

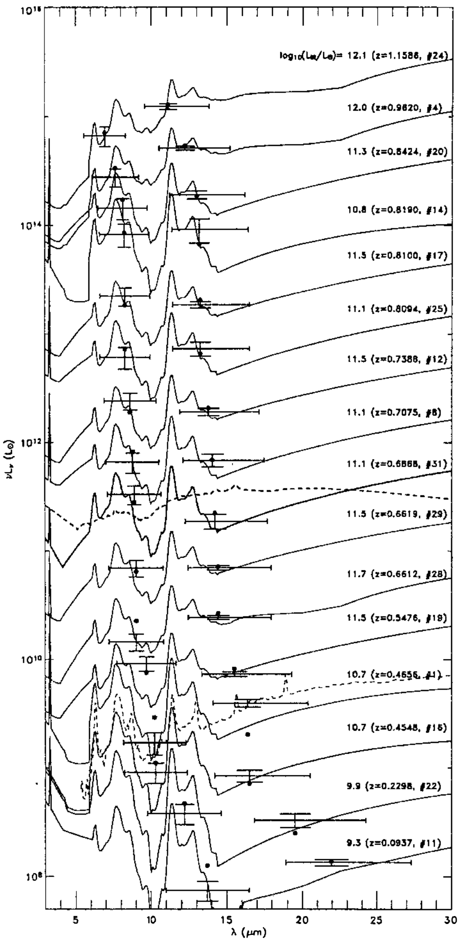

Figure 6: All SEDs sorted (from top to bottom) by decreasing redshift. The SEDs are shifted by an arbitrary offset in νL_ν for visibility; wavelengths are rest-frame. ISOCAM 15 μm and MIPS 24 μm luminosities are reported with the filter bandwidth and the 1-σ uncertainty. The label indicates the logarithm of the IR luminosity as well as the redshift and ID of each source, e.g. ID #4 is the galaxy UDSF04 in Liang et al (2004). The filled dots are the luminosities that would be measured in both filters for the plotted SED from the library of template SEDs of Chary & Elbaz (2001). Bold dashed line on gal.#31: SED of the AGN NGC 1068 normalized to best fit the measured 15 and 24μm luminosities of the galaxy. Dashed line on gal.#1: SED of NGC 7714 (Brandl et al 2004).

observations in the far IR will not reach the same depth than mid IR ones until the launch of Herschel scheduled for 2007. The direct access to the far IR distant universe with Herschel will certainly bring major information on galaxy formation, together with the James Webb Space Telescope (JWST) up to 30 μm and the Atacama Large Millimeter Array (ALMA), which will bring an improved spatial resolution for the $z \sim 2$ and above universe.

Many questions remain unsolved:

- What is the triggering mechanism for the distant dusty starbursts ? Major mergers are not numerous enough top explain such numbers of dusty starbursts in the past. Other dynamical processes such as "passing by" objects, may represent an important alternative to major mergers that should be carefully considered in hierarchical simulations. A recent study by Moy et al (2005, in prep.) indeed suggests that clustering plays a major role in triggering these phases.

- What is the present-day counterpart of distant LIRGs ? A discussion of the relative contribution of dusty starbursts as a function of morphological type is provided by Hammer et al (2004), who suggest that the disks of spiral galaxies may have been destroyed and recen tly rebuilt.

- Have we underestimated the contribution of Compton thick AGNs to infrared counts ? A population of such objects might not have been detected by XMM-Newton and Chandra but could still provide an important contribution to the peak of the cosmic X-ray background at 30 keV (see Worsley et al 2004).

Acknowledgments

We wish to thank the Centre National d'Etudes Spatiales (CNES) for their financial support.

References

1. Adelberger, K.L., Steidel, C.C., 2000, ApJ 544, 218
2. Ascasibar, Y., Yepes, G., Gottlöber, S., Müller, V., 2002, A&A 387, 396
3. Barger, A.J., Cowie, L.L., Sanders, D.B. et al , 1998, Nature 394, 248
4. Brandl, B.R., Devost, D., Higdon, S.J.U. et al , 2004, ApJS, 154, 188
5. Cardiel, N., Elbaz, D., Schiavon, R. P. et al , 2003, ApJ 584, 76
6. Chapman, S.C., Blain, A.W., Ivison, R.J., Smail, I. 2003, Nature 422, 695
7. Chary, R.R., Elbaz, D. 2001, ApJ 556, 562
8. Chary, R.R., Casertano, S., Dickinson, M.E. et al , 2004, ApJS 154, 80
9. Connolly, A. J., Szalay, A. S., Dickinson, M., et al 1997, ApJ, 486, L11
10. Cowie, L. L., Songaila, A., & Barger, A. J. 1999, AJ118, 603
11. Dickinson, M., Papovich, C., Ferguson, H.C., Budaári, T., 2003, ApJ 587, 25
12. Elbaz, D., Cesarsky, C.J., Fadda, D. et al , 1999, A&A 351, L37
13. Fadda, D., Flores, H., Hasinger, G. et al , 2002, A&A 383, 838
14. Fadda, D., Lari, G., Rodighiero, G. et al , 2004, A&A 427, 23
15. Fixsen, D. J., Dwek, E., Mather, J.C., Bennett, C.L., Shafer, R.A. 1998, ApJ 508, 123
16. Flores, H., Hammer, F., Thuan, T. X. et al 1999, ApJ517, 148
17. Flores, H., Hammer, F., Elbaz, D., et al., 2004, A&A 415, 885
18. Gallego, J., Zamorano, J., Aragon-Salamanca, A., & Rego, M. 1995, ApJ455, L1
19. Giavalisco, M., et al , 2004, ApJ, 600, L103
20. Glazebrook, K., Blake, C., Economou, F., Lilly, S., & Colless, M. 1999, MNRAS306, 843
21. Goldader, J.D., Meurer, G., Heckman, T.M., et al , 2002, ApJ 568, 651
22. Gould, A., Bahcall, J. N., Flynn, C., 1996, ApJ, 465, 759
23. Gruppioni, C., Pozzi, F., Zamorani, G. et al , 2003, MNRAS 341, L1

24. Haarsma, D. B., Partridge, R. B., Windhorst, R. A., & Richards, E. A. 2000, ApJ544, 641
25. Hammer, F., Flores, H., Lilly, S. J. et al 1997, ApJ481, 49
26. Hammer, F., Flores, H., Elbaz, D., et al , 2004, A&A 430, 115
27. Hauser, M.,& Dwek, E., 2001, ARAA, 37, 249
28. Hughes, D. H., Serjeant, S., Dunlop, J. et al 1998, Nature, 394, 241
29. Kim, D.-C., Sanders, D. B., 1998, ApJS 119, 41
30. King, A. J., & Rowan-Robinson, M., 2003, MNRAS 339, 260
31. Lagache G., Dole H., Puget J-L., 2003, A&A MNRAS 338, 555
32. Lagache G., Dole H., Puget J-L. et al , 2004, ApJS 154, 112
33. Liang, Y., Hammer, F., Flores, H., Elbaz, D., Marcillac, D., Cesarsky, C.J., 2004, A&A 423, 867
34. Lilly, S. J., Le Fevre, O., Hammer, F., & Crampton, D. 1996, ApJ 460, L1
35. Madau, P., Ferguson, H. C., Dickinson, M. E., et al 1996, MNRAS283, 1388
36. Madau, P., Pozzetti, L., & Dickinson, M. 1998, ApJ498, 106
37. Massarotti, M., Iovino, A., Buzzoni, A., 2001, ApJL 559, 105
38. Metcalfe, L., Kneib, J.-P., McBreen, B. et al , 2003, A&A 407, 791
39. Meurer, G.R., Heckman, T.M., Calzetti, D., 1999, ApJ 521, 64
40. Oliver S. et al , 1996, MNRAS, 280, 673
41. Papovich, C., Dole, H., Egami, E. et al , 2004, ApJS 154, 70
42. Pascarelle, S. M., Lanzetta, K. M., & Fernández-Soto, A. 1998, ApJ508, L1
43. Puget, J-L., Abergel, A., Bernard, J-P. et al , 1996, A&A 308, L5
44. Rodighiero, G., Lari, C., Fadda, D. et al , 2004, A&A 427, 773
45. Sawicki, M. J., Lin, H., & Yee, H. K. C. 1997, AJ113, 1
46. Smail, I., Ivison, R.J., Blain, A.W., Kneib, J.-P. 2002, MNRAS 331, 495
47. Steidel, C. C., Adelberger, K. L., Giavalisco, M., Dickinson, M., & Pettini, M. 1999, ApJ519, 1
48. Tresse, L. & Maddox, S. J. 1998, ApJ495, 691
49. Treyer, M. A., Ellis, R. S., Milliard, B., Donas, J., & Bridges, T. J. 1998, MNRAS300, 303
50. Yan, L., McCarthy, P. J., Freudling, W., et al 1999, ApJ519, L47
51. Worsley, M.A., Fabian, A.C., Barcons, X., et al 2004, MNRAS 352, L28
52. Xu, C., Lonsdale, C., Shupe, D. et al , 2001, ApJ 562, 179

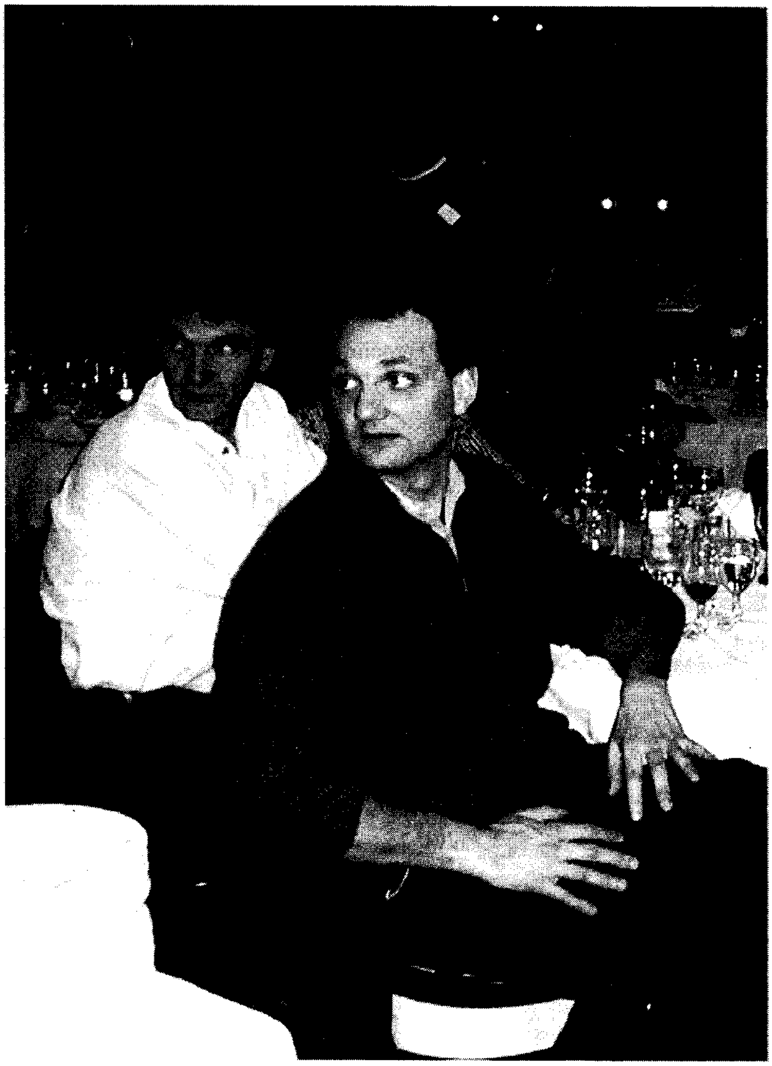

Alignments

CENSUS OF THE GALACTIC CENTRE EARLY-TYPE STARS USING SPECTRO-IMAGERY

T. PAUMARD (1), R. GENZEL (1), J.P. MAILLARD (2), T. OTT (1), M. MORRIS (3), F. EISENHAUER (1), R. ABUTER (1)
(1) Max-Planck-Institut für extraterrestrische Physik
Giessenbachstrasse, Postfach 1312, D-85741 Garching, Germany
(2) Institut d'astrophysique de Paris
98bis bvd. Arago, F-75014 Paris, France
(3) University of California, Los Angeles
Div. of Astronomy, Dept of Physics and Astronomy
Los Angeles, CA 90095-1562, USA

The few central parsecs of the Galaxy are known to contain a surprising population of early-type stars, including at least 30 Wolf-Rayet stars and luminous blue variables (LBV), identified thanks to their strong emission lines. Despite the presence of emission from ionised interstellar material in the same lines, the latest advances in spectro-imaging have made it possible to use the absorption lines of the OB stars to characterise them as well. This stellar population is particularly intriguing in the deep potential well of the 4 million solar mass black hole Sgr A*. We will review the properties of these early-type stars known from spectro-imagery, and discuss possible formation scenarios.

Keywords: Galaxy: centre, stars: early-type, infrared: stars, instrumentation: spectrographs, instrumentation: adaptive optics.

1 Introduction

The Galactic Centre (GC) is the closest of all galactic nuclei in the universe. It is also a galactic nucleus which shows some traces of activity: it features one of the best supermassive black hole (SMBH) candidates (Sgr A*), the densest star cluster in the Galaxy, an H II region (Sgr A West or the Minispiral), and a torus of molecular gas (the Circumnuclear Disk, CND). The region also contains three high-mass star clusters: the Quintuplet, the Arches, and the parsec-scale cluster around Sgr A*. This region therefore presents very interesting evidence of star formation in this peculiar part of a galaxy and should help in understanding starburst galaxies as well as high-mass star formation.

In the early images of the central region of the GC recorded in the near infrared, at the best seeing-limited resolution, several bright point sources dominate the $\sim 20'' \times 20''$ field centred on Sgr A*. Among these, source GCIRS 16[a] was extremely bright and an intense point source of He I λ 2.058 μm. This source has been since then resolved into a cluster of six stars, but the same remarks still apply to each of the components: these six stars are very bright, and exhibit

[a]The sources named "GCIRS" for Galactic Centre Infrared Source are often referred to simply as "IRS" sources in the GC-centric literature.

intense He I lines. Stellar classification of these stars can now be attempted: they are very likely evolved OB stars in a transitional phase (Morris et al. 1996), very close to the Luminous Blue Variable (LBV) stage. Several dozens of even more evolved stars (Wolf-Rayet stars) have been observed in the same region (Krabbe et al. 1995; Paumard et al. 2001), and massive stars are known to orbit the central black mass at distances as short as a few light-days (Schödel et al. 2003; Ghez et al. 2003, 2004).

These observations show that massive star formation has occurred at or near the GC within the last few million years. Neither the mechanisms that lead to massive star formation nor those that may lead to any star formation at all in the vicinity of a SMBH are currently known. Two basic types of scenarios have been developed to explain the presence of these stars where they are: either they have been formed *in situ*, or they have been formed at some distance, and then drifted to where we see them. Both hypotheses are problematic; they will be discussed in Sect. 6. In any case, the exact properties of these stars must be studied in order to provide ground on which to build formation scenarios. These properties include exact stellar type, stellar rotation, spatial distribution, radial velocity and proper motion, and require both high-resolution imaging on a large enough time baseline and spectroscopy of each source to provide all this information.

Spectroscopic analysis with adaptive optics of GC sources has been performed a number of times using long slits. However, this approach can lead only to limited results, because the data contain information only for a very limited number of sources, and because it is not possible to unambiguously associate a given spectrum with a particular star. The second classical approach is to use either multi-band imaging to determine colour indices and thereby colour temperatures, or narrow band imaging around spectral lines typical of certain stellar classes. Proper reduction of these imaging data is however extremely difficult because of the highly variable extinction (Blum et al. 1996), that makes it quite hard to resolve the degeneracy between temperature and A_V (we will however show a successful, though limited, use of this technique in Sect. 4). Concerning narrow band techniques, even using a very nearby continuum filter, it is necessary to apply a different reddening to each star in order to avoid false detections. As the non-homogeneous extincting material is mingled with the stellar content, even very nearby stars (in projection) can be affected by a different reddening. It is therefore ultimately not possible to create a perfect extinction map. Furthermore, a number of spectral features are complex, showing both emission and absorption (for instance P Cygni profiles), which can cancel each other.

For all these reasons, it appears that significant progresses can be made in the field of stellar populations studies in the GC by means of spectro-imaging techniques, which allow one to simultaneously obtain spectra for *all* the stars contained within a field of view. We have used successively two instruments in order to perform such a study, BEAR and SPIFFI. The characteristics of both instruments will be discussed in Sect. 2, the reduction techniques in Sect. 3 and the results obtained in the Galactic Centre in Sect. 5.

2 Instruments and observations

BEAR is a prototype, made of the CFHT Fourier Transform Spectrometer (FTS), coupled with a NICMOS 3 camera. As such, it is an Imaging Fourier Transform Spectrometer. The FTS provides a very high spectral resolution, which can indeed be chosen at observation time depending on the target. In practice, resolutions up to 30,000 have been obtained in this mode. The field of view is set by the original design of the FTS, which was not built with spectro-imaging in mind, and is thus limited to 24″. This prototype does not make use of an adaptive optics system and its spatial resolution is therefore seeing-limited. Finally, the bandwidth of data is limited, for two reasons: first, to limit both observing time and data size, and second because the multiplex property of the FTS makes the S/N ratio lower when the bandwidth increases.

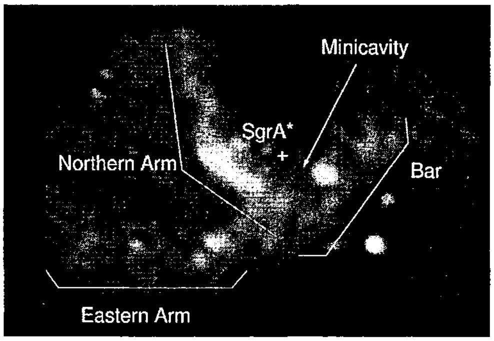

Figure 1: The Minispiral as seen by BEAR in Brγ [b]. This picture is a composite of three images obtained from the BEAR cube through three virtual filters. The colours give therefore the velocity field of the Minispiral, from -350 km s^{-1} (red) to $+350$ km s^{-1} (purple). The standard names of some ISM features are given. A few emission line stars show up as point sources: GCIRS 16NE and 16C just east of Sgr A*, The AF and AF NW stars below the Bar, and the GCIRS 13E cluster on the western edge of the Minicavity.

We have obtained several datasets concerning the Galactic Centre: in He I λ 2.058 μm at a spectral resolution of 52.9 km s^{-1}, as a mosaic of three subfields; and in Brγ (2.166 μm), at a spectral resolution of 21.3 km s^{-1}, as a mosaic of two subfields. These data are presented in depth in Paumard et al. (2004). They cover most of a $40'' \times 40''$ field at a resolution of $\simeq 0.5''$. This instrument has now been decommissioned with the closure of the CFHT infrared focus; however, a specifically designed instrument following the basic concept of BEAR with adaptive optics would provide a very useful observing mode for the new telescopes, allowing for large field, high spectral and spatial resolution spectro-imaging.

SPIFFI (Thatte et al. 1998; Eisenhauer et al. 2000, 2003) is a near-infrared integral field spectrograph to be commissioned as part of SINFONI at the VLT in June 2004. It allows observers to obtain simultaneously spectra of 1024 pixels in a 32×32 pixel field-of-view. In conjunction with the adaptive optics system MACAO it will be possible to perform spectroscopy with slit widths sampling the diffraction limit of an 8m-class telescope. SPIFFI covers the near-infrared wavelength range from 1.1 μm to 2.45 μm with a moderate spectral resolving power ranging from $R = 1000$ to $R = 4000$, and is based on a reflective image slicer and a grating spectrometer. K-band data have been obtained during a test run on 2003 April 8/9 as a mosaic of about two dozen subfields covering a total field of about $10'' \times 10''$ centred on Sgr A* at an excellent seeing-limited resolution of $\simeq 0.25''$. The spectral resolution is 85 km s^{-1}.

3 Data reduction

3.1 The ISM and its subtraction

The first treatment to find the spectral features is to remove the continuum emission from the stars to obtain the *line cubes.* This can be done by linear interpolation between two neighbouring continuum regions if the cube contains only a narrow band (case of BEAR) or by fitting a simple function, like a polynomial, if the continuum is not nearly linear (case of SPIFFI). Once the stellar continuum is subtracted, the BEAR Brγ data are dominated by the extended emission from the ionised ISM (Fig. 1[b]). In Paumard et al. (2004), we have decomposed each spectrum in the field into several velocity components of the same line. Assuming that the ISM is made of clouds of finite velocity gradient material, we have decomposed the Minispiral into 9 components that are often superimposed on each other. In this paper, we have shown that these features are sufficiently thick to be responsible for a significant extinction, on the order of half of the K flux. This is consistent with the high spatial variability of A_V in this region. This decomposition required the very high spectral resolution provided by BEAR, because the lines from two structures along the same line of sight are often very close to one another in

[b]The figures are available in colour at http://www.mpe.mpg.de/~paumard/YLU/ and various archives.

the spectral domain. In some cases indeed, this spectral separation goes down to 0 km s^{-1}. In these cases, interpolation must be used to perform the decomposition using information from neighbouring points where the two structures are sufficiently separated.

These ISM features are really intermingled with the stellar content. It is therefore necessary to subtract the interstellar contribution in order to analyse this stellar population. In Paumard et al. (2001), updated in Paumard et al. (2003), we have again used both the high spectral resolution of BEAR and its spatial properties in the He I λ 2.058 μm to discriminate between the stellar and interstellar lines, showing that some previous reports of Helium stars were indeed false, and due to insufficient correction of the extended emission. To clean the BEAR stellar spectra, we simply cut out the ISM lines manually. These lines were identified by visually exploring the cube and using the 2D information it contained. This simple correction was of good enough quality because at this very high resolution, the observed ISM line width ($\lesssim$ 20 km s^{-1}) was much smaller than the spectral scale of the stellar features ($\gtrsim$ 150 km s^{-1}). For these data, we had extracted the spectra of previously reported He-stars, and visually inspected the cube for more stars. We hence reported three new detections in the field, out of which one (N6) turned out to be essentially an unresolved thread of ionised ISM, the two others being now confirmed by SPIFFI.

The SPIFFI data lack the spectral resolution required to clean each individual spectrum of the narrow ISM lines it contains, but the spatial resolution is so high (and it will still improve with the upcoming adaptive optics system) that it is now possible to reliably estimate the extended line emission component by interpolating each frame of the cube over the locations of the point line emission or absorption sources. More specifically, the steps that have been applied for this correction are the following: (1) determination of the CO index (a measure of the depth of the 2.3 μm CO absorption band) of each star using narrow-band NACO images; (2) the stars with a low CO index are suspected early-type stars; (3) for each spectral channel of the line cube (i.e. continuum subtracted), an aperture corresponding to each possible early-type star is marked as unavailable data; (4) each frame of the line cube is interpolated over these unavailable regions; (5) a low spatial-frequency pass filter is applied to each frame, the cube resulting from these steps is the ISM cube, it normally contains only the ISM emission plus most of the noise; (6) this ISM cube is then subtracted from both the original cube and the line cube to obtain the *stellar cube* and *stellar line cube*, out of which a spectrum for each suspected early-type star is extracted.

3.2 Identification of the featured stars

This leads to over 100 spectra, most of which actually show spectral signatures typical of early-type stars. However, at this point, it is not clear which feature really belongs to which star, as the spectrum of every star is contaminated by the wings of the neighbouring stars. The most straightforward way of resolving this degeneracy is visual inspection: for each feature of each spectrum, it is possible to extract from the stellar line cube an image integrated exactly over the spectral domain corresponding to the maximum emission (resp. absorption) of the given feature. In most cases, a local maximum (resp. minimum) appears on this image in the vicinity of the studied star. The exact location of this extremum reveals to which star the feature belongs, i.e., to the studied star or to one of its neighbours. This visual method is inappropriate for heavy duty work such as that implied by the analysis of the GC content, which, as already mentioned, contains hundreds of candidates and dozens of stars actually showing features accessible to SPIFFI. In particular, this method requires considerable interaction by the observer, and does not make use of the fact that a given early-type star should typically show more than one feature. Furthermore, the features do not have to be simple, the lines often show P Cygni profiles, or consist of several lines from different species, both in emission and absorption (for instance, a

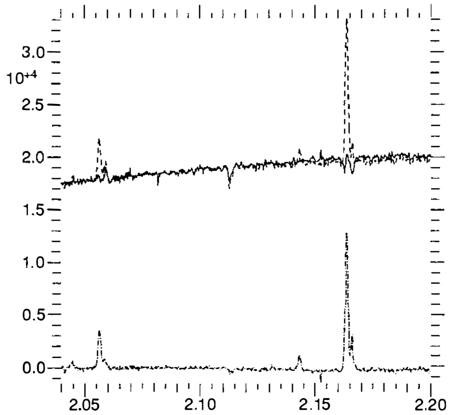

Figure 2: Dashed spectrum: one of the original spectra (GCIRS 33N); dash-dotted: the corresponding ISM spectrum; solid: the corrected stellar spectrum.

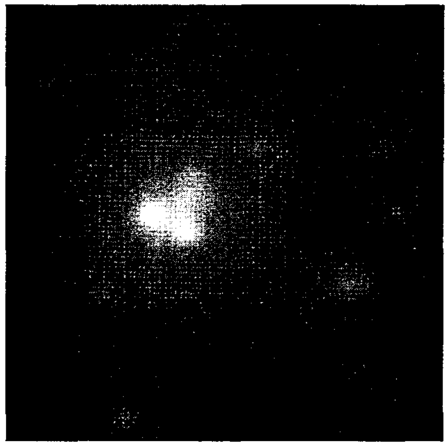

Figure 3: HK'L composite image of GCIRS 13E [b].

typical feature at 2.11 μm is made of two He I lines, often in absorption, one of which is itself a doublet, and one N line, often in emission for O stars). It would therefore be more appropriate to use the entire spectra to determine the spatial location of the stars to which they belong.

We have developed a method specifically to achieve this purpose. Each extracted stellar spectrum can be considered as a template that we want to compare with the individual spectra at each pixel of the field, in order to determine the point in the field from which this spectrum arises and spreads because of the spatial PSF. This comparison is done by means of correlation: for each template spectrum (each spectrum previously extracted from the stellar line cube), a correlation map is built. This map contains, for each pixel in the field, the correlation factor between the template and the spectrum contained in the stellar line cube at this location. This map normally contains a local maximum at the true location of the star to which the features of the template spectrum belong. This technique can easily be automated, and takes the entire continuum-subtracted spectrum of the stars into account. Furthermore, this technique can be generalised to provide both a complementary detection technique of the candidate early-type stars, and a first automated spectral classification of the stars. In the method described above, one can allow for a Doppler shift between the template spectrum and the spectra in the cube. This corresponds to tracing the maximum of the cross-correlation function for each spatial location rather simply using correlation. In that case, every other star in the field showing a spectrum similar to the template will show up as a local maximum on the map. It will therefore be possible to automatically determine which stars have a spectrum similar to the template.

When this cross-correlation work has been done, many candidates can be rejected, as they do not show detectable features. Other stars can be added to the list of candidates because they have been found on the cross-correlation map of one of the templates. The extraction procedure described above can then be iterated to take this information into account. This is necessary because information concerning the ISM emission should not be wasted by blanking out the region containing a candidate early-type star that has been shown indeed not to show detectable features; and on the contrary the features from the newly detected candidates must be cleared out as well as possible. This second extraction led to 29 spectra, all of them showing recognisable features typical of early-type stars, and associated unambiguously with a single star (within the precision allowed by the spatial resolution of the instrument).

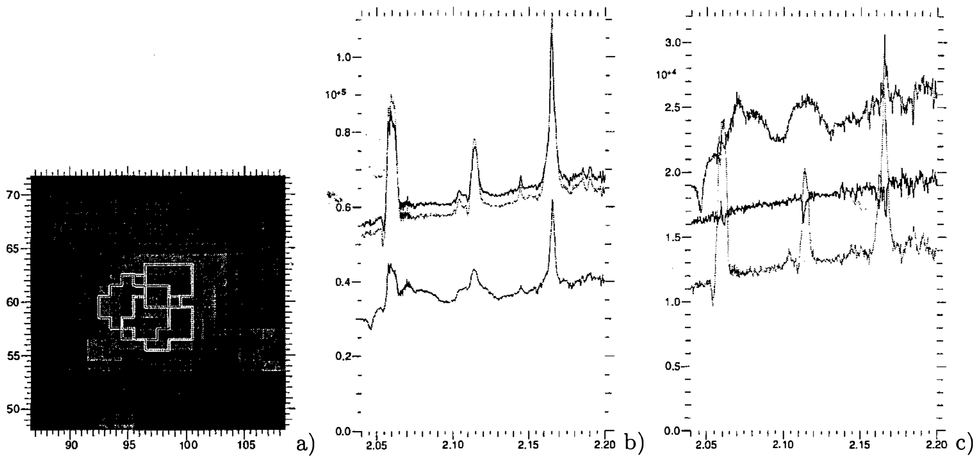

Figure 4: SPIFFI spectra of GCIRS 13E: **a)** apertures used, **b)** raw (blended) spectra, **c)** final object spectra.

All the stars previously studied with BEAR within the field of SPIFFI are detected here as well. As already stated, object N6 from Paumard et al. (2001) does not correspond to an He star but to a tiny ISM feature; however, this ISM feature coincides in projection, and may be physically associated, with four stars that indeed show some He feature (ID 24, 26, 31 and 33). Furthermore, for the first time, thanks to their high spatial resolution as well as high signal-to-noise ratio, these SPIFFI data allow detection of faint emission lines as well as absorption lines, which are totally filled by ISM emission on the raw data. Fig. 2 shows one of the original spectra, the ISM profile determined as in Sect. 3.1, and the inferred stellar spectrum. After correction for the very intense interstellar Brγ line, a complex stellar feature made of Brγ and He I in absorption appears.

4 GCIRS 13E: a case for spectro-imaging

Among these objects, GCIRS 13E deserves special attention. This source is bright at all wavelength from sub-mm to X rays. A three colour high-resolution image (Fig. 3) made from Gemini H and K' and ESO 3.6m L band data illustrates that it contains three blue stars and a very red core. Deconvolution of these three images plus narrow band NICMOS images (Maillard et al. 2004) has shown that GCIRS 13E is indeed a cluster of at least seven evolved massive stars: even the three red objects at the cluster core can be interpreted as dusty Wolf-Rayets. A_V can be derived from the two assumptions that it does not vary significantly within the cluster and that the bluest star is in the Rayleigh-Jeans regime ($T_{\rm eff} \gtrsim 25\,000$ K at this wavelength), which is proven by the fact that two of the stars show emission in a NICMOS Paα image. This multi-wavelength, high spatial resolution study can be considered as a kind of low spectral resolution attempt. However, the exact spectral type of these hot stars cannot be unambiguously established by this technique, because more spectroscopic information is needed. Therefore, spectra of the individual components are required to achieve this purpose.

The sources are too close to one another to allow for individual aperture spectroscopy. Any attempt to do this is doomed to give spectra significantly affected by one another. In Fig. 4, we show three spectra obtained from the SPIFFI data through three overlapping virtual apertures; two of them seem identical, whereas the third is clearly affected by a blend with these. Reducing these apertures would reduce the signal-to-noise ratio while not providing much better results.

Table 1: Translation of ID numbers in the figures to common names. Offsets from Sgr A* (RA, dec. in arcsec) are given for so far anonymous stars.

Fig. 5	Fig. 6	Name	Fig. 5	Fig. 6	Name	Fig. 6	Name
N1	41	IRS 16NE	B8		AF NW	33	MPE 1.6-6.8
N2	14	IRS 16C	B9		HeIN3	34	IRS 29NE1
N3	17	IRS 16SW	B10		BSD WC9	53	IRS 13E1
N4	13	IRS 16NW	B11	27	IRS 29N	57	IRS 13E north[b]
N5	48	IRS 33SE	B12		IRS 15NE	72	0.774, −4.047
N7	75	IRS 34W	B13	46	IRS 16SE2	81	IRS 34NW
B1		ID 180[a]		1	S2 (S0-2)	87	IRS 1W
B2		IRS 7E2		7	S1-3	97	3.195, −4.842
B3	178	IRS 9W		23	IRS 16CC	110	6.372, 0.227
B4		IRS 15SW		24	1.447, −1.49	179	1.8, −6.3
B5	61	IRS 13E2		26	1.593, −1.355	180	IRS 3[c]
B6		IRS 7W		31	IRS 16SE1	181	0.665, −1.608
B7		AF star		32	IRS 33N		

a: in Ott et al. (1999); *b*: north of the cluster, exact identification uncertain; *c*: the emission line star is offset by about 0.1″ from the bright K-band source.

However, the spectrum obtained through each of the apertures is a linear combination of the spectra of all the stars (at least seven indeed). It is therefore possible to obtain three independent spectra by linear combination of these three observed spectra, leading to spectra typical of three of the types discussed below (Fig. 4c), although it is not yet clear whether the upper spectrum in this figure belongs to the blue star north of the cluster or to the red stars in the middle.

5 The (known) stellar population of early-type stars

The main results obtained with BEAR (Paumard et al. 2001, 2003) are that the He stars can indeed be classified in two groups, from their line width (mean FWHM $\simeq 225 \pm 75$ km s^{-1} for the narrow line stars and 1025 ± 400 km s^{-1} for the broad line stars) and K magnitude: all the narrow line stars are more luminous than the broad line stars, by more than 2 magnitudes in average (in Paumard et al. 2001, we reported that one narrow line star, GCIRS 34W, was less luminous than the others, but that was due to a temporary obscuration event, as discussed in Paumard et al. 2003 and below). A third, striking property of these two stellar classes is their spatial distribution (Fig. 5): the narrow line stars are concentrated in the GCIRS 16 complex, whereas the broad line stars are distributed in the entire field. Table 1 gives the translation between the identification numbers used in Fig. 5, in Figs. 6 to 12, and common names.

The SPIFFI data set that we have analysed so far has a smaller field, and therefore does not add much information on these two different spatial distributions. However, thanks to their other characteristics already discussed (wide band, high spatial resolution, and high signal-to-noise ratio), they give a lot of interesting results. We will hereafter present the spectra of all the early-type stars that we have found, together with a discussion of their data type. The spectra presented here are limited to the range 2.04 − 2.20 μm, for comparison with Hanson et al. (1996). The reduction software being still under heavy development, some artifacts remain, which take the form of strong noise spikes. The spectra are given in Figs. 7 to 12, and their spatial distribution is given in Fig. 6. The various vertical lines on Figs. 7 to 12 mark several atomic lines: green: He I, pink: carbon, red: H (Brγ), blue: He II.

Early Wolf-Rayet stars: Six stars show very broad features mainly from C IV and/or N; they are early Wolf-Rayet stars (WC and WNE). Some of them also show some Brγ emission.

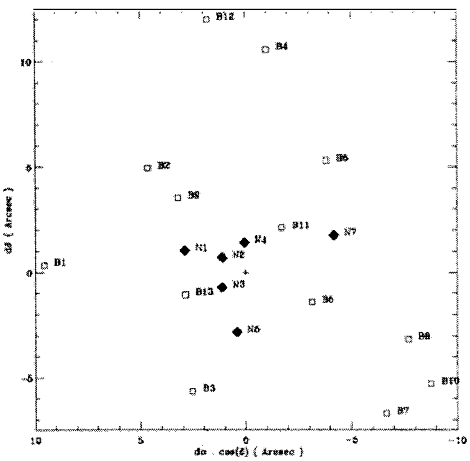

Figure 5: Spatial distribution of the narrow (N) and broad (B) line stars.

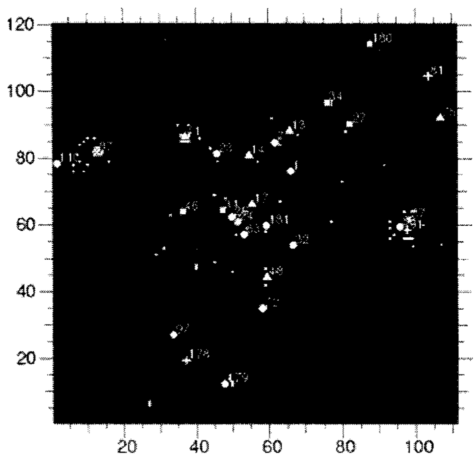

Figure 6: Spatial distribution of the 6 stellar types: early (squares) and late (vertical crosses) Wolf-Rayet stars, LBVs (triangles), OBN stars (circles), a candidate Be star (diagonal cross), and a few more OB stars.

GCIRS 16SE2 had been mistaken for a broad He I emission line star in Paumard et al. (2003). This was due to the fact that an unidentified absorption feature at roughly 2.045 μm lays in our short wavelength continuum region, which mimicked a low signal-to-noise, broad emission line on a very red continuum. GCIRS 29N shows broad and tenuous features of C IV and N, but also He I; it was the broad He I-line stars B11 in Paumard et al. (2003) and may be of a slightly later type than the other stars of this group. Its weak He I λ 2.058 μm resembles that of the star Blum WC9 (B10), which could therefore be of the same type. These seven stars are randomly spread over the entire field.

Late Wolf-Rayets: The second subset of stars is typical of late Wolf-Rayet stars (WNLs), with rather broad and bright He I, He II, Brγ and N lines. Two of them show a broad He I λ 2.058 μm line, typical of the broad-line He-stars discussed in Sect. 5. All these broad-line stars (except B10, B11 and B13 already discussed) therefore seem to be WNLs as well.

Luminous Blue Variables: The third subset corresponds exactly to the narrow-line stars discussed in Sect. 5. In this wavelength domain, they are characterised by their rather strong, narrow He I λ 2.058 μm line with a clear P Cyg profile; an equally strong feature at 2.166 μm made mainly of Brγ as well as a clear contribution of He I λ 2.163 μm; this complex does not show a P Cyg profile, but that may be mainly because of the blending; a complex of He I (in absorption for all but one star) and N (in emission) around 2.11 μm. These spectra are typical of so called "transitory" stars, Ofpe/WN9 and Luminous Blue Variables (LBVs). Morris et al. (1996) seems to show that all these types may relate to objects of the same nature, maybe in different states. As already stated these stars are all within the GCIRS 16 cluster. GCIRS 34W deserves special attention: this is the only one to have already shown an obscuration event, which fully qualifies it as an LBV; this is the only one that shows the He I λ 2.11 μm complex in emission; and this is the star for which the spatial association with the GCIRS 16 cluster is the most controversial. The first point above does not mean that the other stars are not LBVs as well, as obscuration events of LBV stars are indeed rare (Humphreys et al. 1999). Neither does the second, as the spectra of LBVs are variable as well as their luminosity: the fact that the He I λ 2.11 μm complex of GCIRS 34W is currently in emission could be related to its obscuration event.

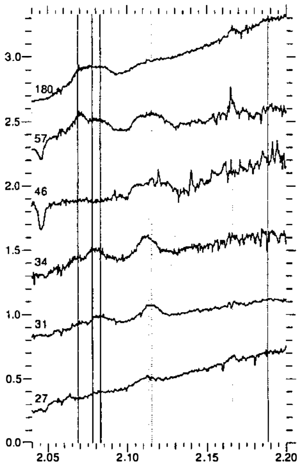

Figure 7: Early Wolf-Rayets.

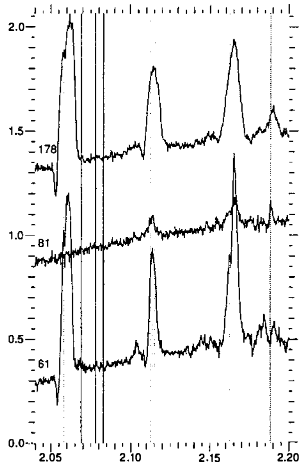

Figure 8: Late Wolf-Rayets.

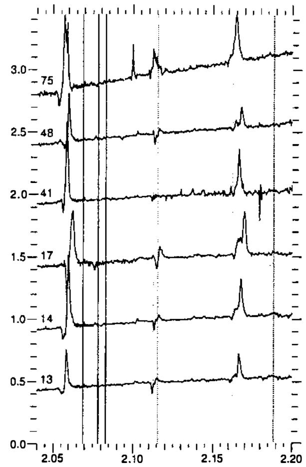

Figure 9: Luminous Blue Variables.

OBN stars: The third type is defined by stars which show: He I λ 2.058 μm (often with a complex structure); the He I λ 2.11 μm complex in absorption; often N λ 2.11 μm in emission; comparable Brγ and He I λ 2.163 μm, mostly in absorption, but sometimes with some emission in-between. Note that the three stars that show emission at 2.166 μm are in a crowded area, and two of them are superimposed upon a very compact thread of ISM material. The ISM correction at this very location is therefore somewhat suspicious. We had reported a He star at this location with BEAR, but the same comment applies to this detection as well.

Following the independent stellar classification scheme in the K-band (hence the "k" prefix) by Hanson et al. (1996), these stars can be classified in various kOB subtypes (kOBh+, kOBh-, kO7-O8, kO9-B1b+, kOBb and kOBbh+). It is hard to give an unambiguous classification in the MK system for these stars, for two reasons: a unambiguous relationship between the MK system and the K band classification scheme by Hanson et al. (1996) does fundamentally not seem to exist; and very few standard stars have been studied so far both in the optical and infrared to provide ground for comparison. This is particularly true for OB stars.

However, when one compares directly these stars to the templates shown in Hanson et al. (1996), it appears clearly that only two stars exhibit a similar feature at 2.166 μm, with comparable Brγ and He I: HD 191781 (kOBbh+) and HD 123008 (kO7-O8bh-). Both are ON9.7 supergiants. ON and BN stars (generically called OBN stars) are particular kinds of O and B stars which show unusual N lines in the optical. They are also known to show unusually strong He lines, and to be particularly bright because of a lower atmospheric opacity (Langer 1992). Indeed, our 9 stars are particularly bright, as a typical O9 supergiant should be at most 1.4 magnitudes brighter than S2 (a O8-B0V star according to Ghez et al. 2003, of $m_K = 13.95$), whereas their K magnitudes span the 10.43–12.63 range. It therefore seems likely that these nine stars are indeed N- and He-rich stars that would appear in the optical as OBN stars.

GCIRS 1W: a Be star? GCIRS 1W is known to exhibit a very flat and very red spectrum, to be embedded within the Northern Arm and to interact with it to form a bow shock (Tanner et al. 2004). Study of this star is made difficult by the fact that it is a local source of excitation for the ISM, and is therefore coincident with a local maximum of the ionised gas emission. However, the correction described in Sect. 3.1 allows us to unambiguously identify the He I λ 2.06 μm line in absorption as well as the Brγ line in emission. This spectrum is similar to that of the Be star DM +49 3718 in Hanson et al. (1996). Indeed, all the stars in this atlas which show Brγ in

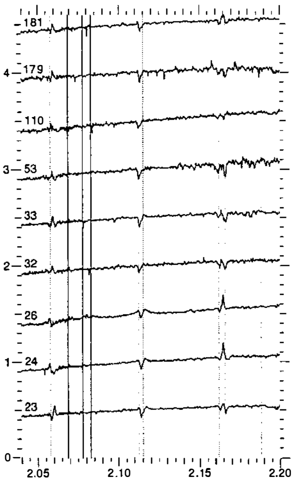

Figure 10: N- and He-rich stars (OBN).

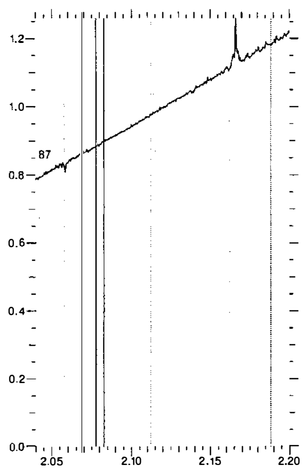

Figure 11: GCIRS 1W, a candidate Be star.

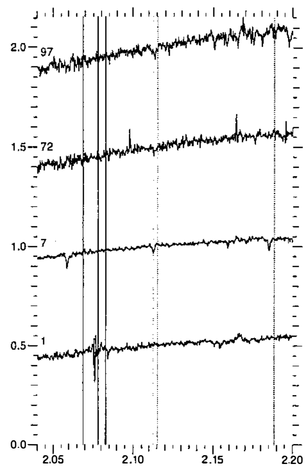

Figure 12: More OB stars.

emission and no He I λ 2.11 μm are Oe or Be stars.

More OB stars: Finally, a few more stars exhibit at least one He I line or the Brγ line. Star number 1 (S2) shows only to a detectable level the Brγ line, and we are mostly able to detect it because a very high Doppler shift (about 1400 km s^{-1}) puts it away from the ISM residuals, at about 2.155 μm. This star and others of its kind will be more easily studied when SPIFFI is equipped with adaptive optics. The three other stars show mostly the He I λ 2.163 μm line. The absence of detection of Brγ is certainly due to the noise in that region of the spectrum, which comes from the residuals of the ISM feature.

6 Formation scenarios

The existence of the early-type stars at their current position can basically be explained in two ways: either they have been formed *in situ*, or they have been formed somewhere else in the Galaxy before they have been drawn here. Various items in the literature argue that gravitational collapse of a gas cloud is prevented in the tidal field of Sgr A*, and that therefore star formation cannot have occurred *in situ*. However, Levin & Beloborodov (2003) show that stellar formation in the vicinity of a SMBH is likely to occur if the black hole possesses a massive enough accretion disk. This consideration transforms the problem into: did Sgr A* possess a massive, parsec scale accretion disk 10^6 years ago? The fact is that Sgr A* does not appear to possess a disk, of any observable scale, right now. The ISM that can be seen at the parsec scale is concentrated in the CND (which may contain about 10^4 M$_\odot$ of material, Christopher & Scoville 2003) and in the Minispiral, for which 10^3 M$_\odot$ seems to be a reasonable upper limit, as the estimates for two of the nine components of the Minispiral are $\simeq$ 10 M$_\odot$ (Liszt 2003; Paumard et al. 2004). However, Morris et al. (1999) show that current absence of a disk remains compatible with *in situ* formation within an accretion disk in the context of a limit cycle.

The other possibility is that these stars have been formed at some distance, and then moved into the central parsec. The presence of the Arches and Quintuplet clusters at a distance of about 35 pc shows that massive star cluster formation is indeed possible at these distances. According to McMillan & Portegies Zwart (2003), a cluster with a dense enough core ($\gtrsim 10^5$ M$_\odot$), formed within 20 pc, could spiral down to the central parsec within the lifetime of the most massive stars. It would however be stripped during its cruise, so that it would eventually deposit only a small fraction of its mass into the central region. However, it is not yet clear whether this scenario could explain the stars closest to Sgr A*, at only a few light days, and Kim & Morris (2003) and Kim et al. (2004) conclude that they are unable to find realistic initial conditions to their simulations that would lead to the observed situation through infall of a cluster.

These two possibilities should lead to somewhat different clusters in the end: for instance, the spiralling-in cluster scenario probably predicts that a significant number of young stars of all masses, co-eval with the inner parsec early-type stars, should be found in the few central tens of parsecs, as a byproduct of the stripping of the infalling cluster. Such a population is not yet known. Actually observing it would require at least deep imaging in the J, H and K bands, at the best available resolution and over a field of about 3×3 arcmin^2.

The observed properties of the early-type stars that need to be addressed are the following: a group of 15 N- and He-rich stars (the LBVs and the ON stars) are seen within a small region (about $5''$ or one light-year), offset from Sgr A* by about $1''$; there are about two dozen Wolf-Rayet stars dispersed apparently randomly (in projection) in the central few parsecs; and there is a compact cluster of evolved stars (GCIRS 13E), that contains members of both the above-mentioned groups of stars. These properties can be classified in two types: first, the spatial distribution of the stars, and second their spectral types. The actual spatial distribution is clearly subject to caution as we only have access to a projected distribution. However, at least two velocity components are available for all the stars within the central two parsecs, and a radial velocity is also being obtained for a growing number of them: these four to five dimensions should be enough to constrain the dynamical models. An important point in the spatial distribution is that several groups of stars are observed. One of the groups, GCIRS 13E, is a compact cluster. It is proposed in Maillard et al. (2004) that this could be the remaining core of an infalling cluster. However, it must be asked whether such a compact cluster could itself form *in situ*.

Concerning the spectral types, the fact reported here that more stars within the GCIRS 16 cluster are N- and He-rich should also be addressed by the models. These kinds of stars have experienced an unusual mixing. It can be the trace of a fast initial rotation of the proto-stars, that would be due to the initial conditions. It may be explained by the shear if the stars have been formed within an accretion disk. The efficient mixing within the GCIRS 16 stars could also come from close-by interactions with Sgr A*, but it would be hard to explain how these stars can be seen know as an offset group, rather than a spheroidal cluster centred on Sgr A*.

7 Conclusion

Spectro-imaging techniques have been applied to the GC, providing very valuable information on the nature of the early-type stars lying there, and on their spatial distribution. Upcoming commissioning of the adaptive optics system that will be used in conjunction with SPIFFI must be anticipated to give even more spectacular results. These stars appear to belong to several segregated groups, distinct in their spatial distribution and stellar types, but not apparently in their age. One of these groups is made of moderately evolved stars that show core-processed material at their photosphere, which is not exceptional, but unusual. The more evolved stars, already at the WR stage, have probably lost any spectral signature that would have shown whether they were already N- and He-rich before they reached this stage. All these observations are far from trivial and should give strong constraints on the formation scenarios.

Acknowledgements

T. Paumard wants to thank Sergei Nayakshin for fruitful discussions about the possibility of stellar formation in a parsec-scale accretion disk.

References

Blum, R. D., Sellgren, K., & Depoy, D. L. 1996, ApJ, 470, 864

Christopher, M. H. & Scoville, N. Z. 2003, in ASP Conf. Ser. 290: Active Galactic Nuclei: From Central Engine to Host Galaxy, 389

Eisenhauer, F., Abuter, R., Bickert, K., et al. 2003, in Instrument Design and Performance for Optical/Infrared Ground-based Telescopes, ed. Masanori Iye & Alan F. Moorwood, Proc. SPIE, 4841, 1548

Eisenhauer, F., Tecza, M., Mengel, S., et al. 2000, in Optical and IR Telescope Instrumentation and Detectors, ed. Masanori Iye & Alan F. Moorwood, Proc. SPIE, 4008, 289

Ghez, A. M., Duchêne, G., Matthews, K., et al. 2003, ApJ, 586, L127

Ghez, A. M., Salim, S., Hornstein, S. D., et al. 2004, ApJ, submitted, astro-ph/0306130

Hanson, M. M., Conti, P. S., & Rieke, M. J. 1996, ApJS, 107, 281

Humphreys, R. M., Davidson, K., & Smith, N. 1999, PASP, 111, 1124

Kim, S. S., Figer, D. F., & Morris, M. 2004, ApJ, 607, L123

Kim, S. S. & Morris, M. 2003, ApJ, 597, 312

Krabbe, A., Genzel, R., Eckart, A., et al. 1995, ApJ, 447, L95

Langer, N. 1992, A&A, 265, L17

Levin, Y. & Beloborodov, A. 2003, ApJ, 590, L33

Liszt, H. S. 2003, A&A, 408, 1009

Maillard, J. P., Paumard, T., Stolovy, S. R., & Rigaut, F. 2004, A&A, accepted, astro-ph/0404450

McMillan, S. L. W. & Portegies Zwart, S. F. 2003, ApJ, 596, 314

Morris, M., Ghez, A. M., & Becklin, E. E. 1999, Advances in Space Research, 23, 959

Morris, P. W., Eenens, P. R. J., Hanson, M. M., Conti, P. S., & Blum, R. D. 1996, ApJ, 470, 597

Ott, T., Eckart, A., & Genzel, R. 1999, ApJ, 523, 248

Paumard, T., Maillard, J. P., & Morris, M. 2004, A&A, accepted, astro-ph/0405197

Paumard, T., Maillard, J. P., Morris, M., & Rigaut, F. 2001, A&A, 366, 466

Paumard, T., Maillard, J. P., & Stolovy, S. R. 2003, in Galactic Center Workshop 2002: The Central 300 parsecs, ed. A. Cotera, S. Markoff, T. R. Geballe & H. Falcke, Astron. Nachr., 324 S1/2003, 303

Schödel, R., Ott, T., Genzel, R., et al. 2003, ApJ, 596, 1015

Tanner, A., Ghez, A., & Morris, M. 2004, ApJ, submitted

Thatte, N. A., Tecza, M., Eisenhauer, F., et al. 1998, in Adaptive Optical System Technologies, ed. Domenico Bonaccini & Robert K. Tyson, Proc. SPIE, 3353, 704

THE RECENT STAR FORMATION ACTIVITY IN THE GALACTIC CENTRE

F. SCHULLER[1,2], A. OMONT[2], M. FELLI[3], L. TESTI[3]

(1) Max Planck Institut für Radioastronomie
Auf dem Hügel 69, D-53121 Bonn, Germany
(2) Institut d'Astrophysique de Paris, CNRS
98 bis, bd Arago, F-75014 Paris, France
(3) Osservatorio Astrofisico di Arcetri
Largo E. Fermi, 5, I-50125 Firenze, Italy

The Galactic star formation activity is mainly concentrated in the inner Disk, and in particular in the Central Molecular Zone (CMZ, $|l| \leq 1.5°$, $|b| \leq 0.5°$), where giant very active star forming complexes (Sgr B2, Sgr C) and exceptional massive young clusters that formed a few Myr ago (the Arches, the Quintuplet and the central helium star clusters) are present. In addition, massive stars are currently being formed outside of these peculiar regions, as clearly indicated by the emission of warm dust in the mid-infrared. Here we show how it is possible to extract the young stellar population from large scale mid-infrared surveys, such as ISOGAL and MSX. A sample of 360 massive YSO candidates was selected from these surveys over the entire CMZ. This provides a rough estimate of the average star formation rate in this extreme environment over the last million years. We also mention planned and ongoing follow-up observations, aimed at confirming the young stellar nature of these candidates, and at deriving their physical properties.

Keywords: Stars: formation – Stars: pre-main sequence – Galaxy: centre – Infrared: stars – Surveys

1 Introduction

The central region of our galaxy shows a quite unusual environment, with a very high stellar density and large amounts of interstellar matter in various phases, from cold molecular gas to hot gas ionised by recently formed massive stars. This high concentration of matter is clearly seen at various wavelengths, for example in the four IRAS bands in the infrared (see Launhardt et al. 2002 [1] for a recent review).

The star formation in this region is also atypical, with on one hand three very massive starburst clusters (the Arches, Quintuplet and Central clusters) that formed a few million years ago, and on the other hand active star formation all over the central few hundred parsecs, as clearly indicated by the emission of warm dust. In the present study, we will focus on the inner Galactic Bulge, or Central Molecular Zone, delimited by $|l| \leq 1.65°$ and $|b| \leq 0.5°$. We will show that stars are actually being formed there, as derived from large scale mid-infrared surveys (ISOGAL and MSX); finally, we will give a rough estimate of the average star formation rate in this region over the last million years.

2 The ISOGAL survey

The ISOGAL survey (Omont et al. 2003) [2] was one of the largest programs observed by the ISO satellite. Almost 500 raster images were taken at 7 or 15 μm with the ISOCAM instrument, covering a total area of $\sim$16 deg^2 in the Galactic disk and bulge. The coverage of the inner bulge was almost complete, as illustrated in Fig. 1. The extraction of point sources led to the publication of a catalogue containing 10^5 infrared objects (Schuller et al. 2003) [3] in the most obscured regions of the Milky Way, down to a sensitivity usually of order 10 mJy, nearly two orders of magnitude deeper than IRAS. The ISO data were combined with near-infrared data from the DENIS survey (Epchtein et al. 1994, 1997) [4,5], providing additional photometry in the I, J and K_s bands and an astrometric accuracy better than 1" for most sources.

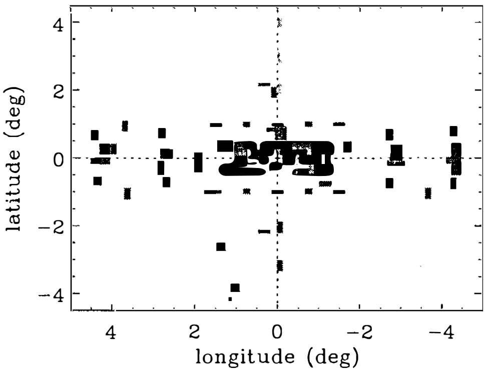

Figure 1: Galactic map of ISOGAL fields in the inner Galactic bulge. The light gray symbols represent fields observed only at 7 μm, medium gray symbols are for fields observed only at 15 μm, and the black ones correspond to fields with both 7 and 15 μm observations.

The bulk of the extracted point sources are evolved stars on the asymptotic giant branch (AGB), and the combined use of the mid infrared and near infrared data enables to derive some of their properties, including foreground interstellar extinction, mass loss rates, luminosities and indication of age (Jiang et al. 2003 [6], Ortiz et al. 2002 [7], Ojha et al. 2003 [8], van Loon et al. 2003 [9]; see also Omont et al. 2003 [2]). However, a few percent of the ISOGAL sources are interpreted as young stellar objects (YSO), as we will show in this contribution.

3 Identification of evolved stars

We used various published studies of stellar populations close to the Galactic Centre over a 0.1 deg^2 area to infer the nature of a large fraction of the brightest ISOGAL sources. In particular, monitoring observations over a 24×24 arcmin^2 area centred on the Galactic Centre were performed by Glass et al. (2001) [10] to detect and characterise long period variable (LPV) stars.

From this catalogue of LPVs, we can extract 216 sources located inside the ISOGAL observations. Then, 178 of them can be associated with ISOGAL point sources within a 3" search radius. Confusion issues, as well as variability may explain why no association could be found for most of the remaining 38 sources.

A compilation of catalogues of OH/IR stars was also associated with the ISOGAL data by Ortiz et al. (2002) [7], who found 30 OH/IR stars in this 0.1 deg^2 test area, for which an ISOGAL counterpart can be found within a 4" search radius. Nineteen of these OH/IR stars are also included in the catalogue of LPV stars, so that together we find 189 ISOGAL sources associated with late evolved stars.

4 Identification of massive YSOs and candidates

In the same 0.1 deg^2 test area, we can consider as previously known young stellar objects the sources that we associate with IRAS sources that satisfy the selection criteria defined by Wood and Churchwell (1989) [11] for ultra-compact HII regions, and those associated with radio continuum sources with thermal spectral index. Thirteen ISOGAL sources can thus be interpreted as YSOs in this region.

In addition, we used the MSX point source catalogue (Egan et al. 1999) [12] which covers all the Galactic Plane in the 8–21 μm range, with sensitivities of order 100 mJy at 8 μm and ~1 Jy at longer wavelengths. MSX counterparts can be found for most of the brightest ISOGAL sources. Then, we used the colour criterion $F_{21\,\mu m}/F_{15\,\mu m} \geq 2$ (or D–E ≥ 1.57 mag) to select YSO candidates from the MSX data. In our test area, 11 ISOGAL sources with MSX associations satisfy this criterion. We will consider them as good YSO candidates in the following.

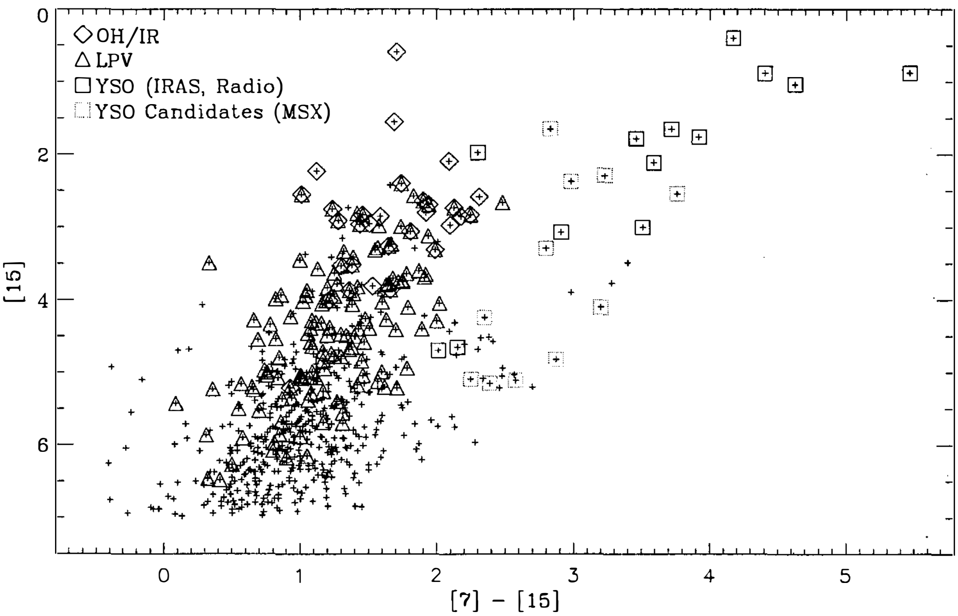

Figure 2: [15] vs. [7]–[15] colour magnitude diagram for all sources detected at both wavelengths in the area covered by the Glass et al. (2001) observations. Sources identified with objects of various natures are represented with different symbols, as shown in the upper left.

5 Selection criteria of ISOGAL YSO candidates

5.1 Colour criterion

As can be seen in the colour-magnitude diagram shown in Fig. 2, most sources associated with AGB stars (LPV and OH/IR stars) are found in the most populated sequence seen in this diagram, with colours [7]–[15] usually below 2 mag. On the other hand, sources interpreted as YSOs from their IRAS or radio counterparts, and those called YSO candidates because they show MSX flux ratios $F_{21\,\mu m}/F_{15\,\mu m} \geq 2$, are mainly located in the reddest part of this diagram. Also note that most sources brighter than [15] = 4.5 mag (108 out of 149, or 72%) are identified either with late evolved stars or with YSOs, so that the distinction between these two classes of objects seems relatively clear for the brightest population.

Similar conclusions were derived from the analysis of 5 ISOGAL fields at $l = +45°$ (Felli et al. 2000) [13], and from the associations between ISOGAL sources and radio sources detected at 5 GHz by Becker et al. (1994) [14], in the $-10° \leq l \leq +40°$ range (Felli et al. 2002) [15]. The latter study enabled us to extract more than 700 YSO candidates from the complete ISOGAL dataset, using the simple criteria [15] $\leq$ 4.5 and [7]–[15] $\geq$ 1.8. An analysis similar to that presented here was also carried out for one ISOGAL test field, centred at $(l, b) = (-0.27°, -0.06°)$ (Schuller et al. 2004) [16].

5.2 Extension criterion

The analysis of the ISO data revealed another difference between evolved stars and YSOs. The former appear point-like in the images, while the latter are often slightly extended. This may be explained by very different morphologies, since LPV and OH/IR stars do not show any resolvable spatial extension, while the sources that we interpret as YSOs may correspond to star forming regions, in which small groups or clusters of young stars are embedded in dusty cocoons.

In the ISOGAL catalogue, the quantity σ_{15} directly indicates if a source is point-like or slightly extended. This number is derived from the correlation between the profile of a source and the point spread function that was used to extract the sources (see Schuller et al. 2003) [3], and increases for slightly extended sources. The morphological difference between AGB stars and YSOs is illustrated in the left panel of Fig. 3.

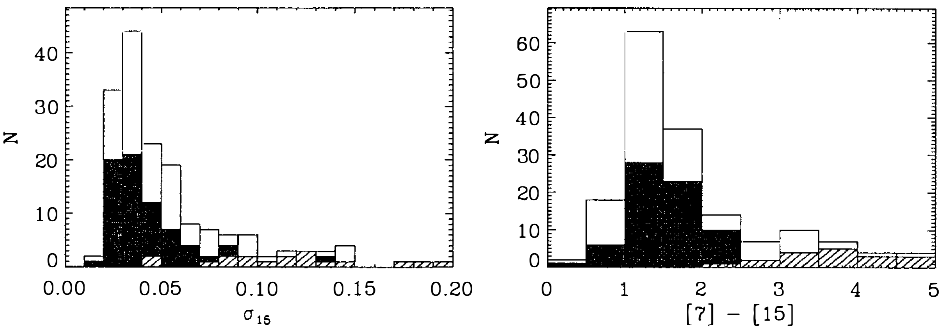

Figure 3: Distributions of extensions σ_{15} (left panel) and colours [7]–[15] (right panel) for all sources detected at both wavelengths and brighter than [15]=4.5 in one ISOGAL test field. The fractions of each bin filled with dark gray show the numbers of sources associated with AGB stars, and those filled with line patterns indicate the numbers of sources associated with YSO candidates.

5.3 Extraction of YSO candidates from the ISOGAL data

We have defined selection criteria that combine red [7]–[15] colour and signs of spatial extension, in order to limit the contamination of this sample by late evolved stars. Also, we have limited the present analysis to sources brighter than 5 mag at 15 μm, because the distinction between young and evolved objects obviously becomes less clear for fainter sources.

In detail, the selection criteria that we used are:

$$[15] \leq 5 \,\text{and:} \begin{cases} 2 < [7]-[15] \leq 2.5 \,\text{and}\, \sigma_{15} \geq 0.1 \\ 2.5 < [7]-[15] \leq 3 \,\text{and}\, \sigma_{15} \geq 0.05 \\ [7]-[15] \geq 3 \end{cases} \tag{1}$$

We find 232 sources satisfying these criteria in the ISOGAL fields covering the inner Galactic bulge. In addition, 99 sources are detected only at 15 μm in the fields also observed at 7 μm, with magnitudes $[15] \leq 5$ and $\sigma_{15} \geq 0.05$. Since the 50%-completeness limit is around 10 mag at 7 μm, these sources are also very red and can thus be considered as good YSO candidates. However, 29 sources cannot really be considered as YSOs, because they are identified with OH/IR stars (seven of them), or because the 7–15 μm association doesn't seem correct. Thus, we were able to select a sample of 302 YSO candidates from the ISOGAL data over the inner Galactic bulge.

These sources are located in the well known large star forming complexes (Sgr B, Sgr C...), but also scattered in a ~0.2° wide strip around the Galactic plane over the ±1° range in longitude (see Fig. 4).

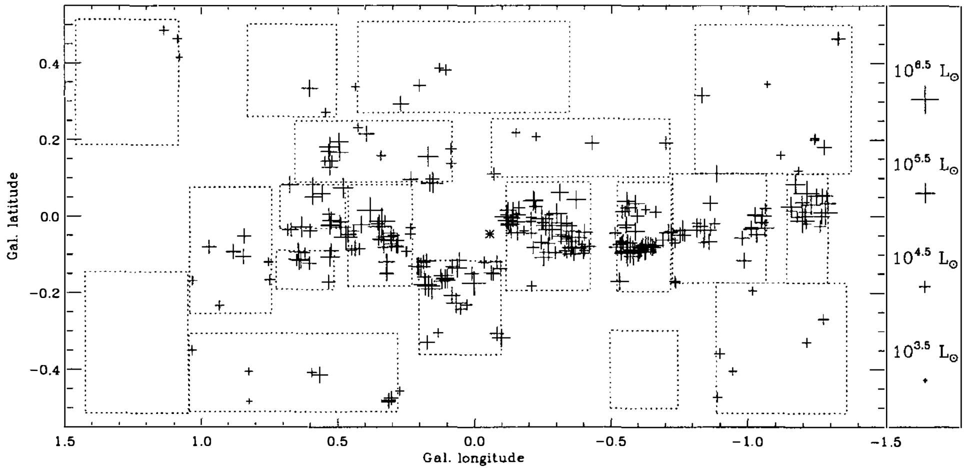

Figure 4: Distribution in galactic coordinates of the 300 ISOGAL-selected YSO candidates. The symbol sizes reflect the bolometric luminosity, as computed with Eq. 2. The frames drawn with dotted lines show the limits of the ISOGAL fields. The star symbol in the centre shows the position of Sgr A*.

6 Census of recent star formation in the inner Galactic bulge

6.1 Determination of bolometric luminosities

Starting from the IRAS sources interpreted as ultra-compact HII regions, we have been able to derive a simple relation between the flux density at 15 μm and the bolometric luminosity for these objects (see Felli et al. 2002) [15]. This relation is:

$$\frac{L}{D^2} \approx 300 \, \frac{F_{15}}{\mathrm{Jy}} \, \mathrm{L}_\odot \, \mathrm{kpc}^{-2} \tag{2}$$

The coefficient 300 may be uncertain by a factor ~2, and certainly varies with the nature and evolutionary state of the sources. Moreover, aperture photometry must be performed on these sources, for which the PSF-fitting photometry is often underestimated by up to ~1 mag. We also corrected for foreground extinction towards each source, as derived from the extinction map published by Schultheis et al. (1999) [17]. As a result, the total luminosity arising from this sample is almost 5×10^7 L$_\odot$. The distribution of the luminosities that we have estimated is shown in the left panel of Fig. 5. It appears clearly that our sample becomes incomplete below 10^5 L$_\odot$.

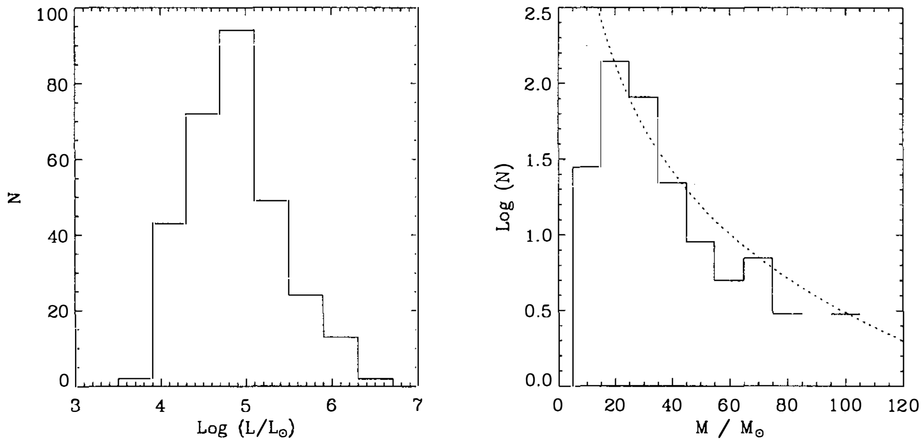

Figure 5: Distributions of luminosity (left panel) and mass (right panel) estimates for the 300 ISOGAL-selected YSO candidates. The dotted line on the right panel corresponds to a Salpeter initial mass function.

We have then converted the bolometric luminosities to masses of the embedded stars, using the simple assumption that each source corresponds to one single zero age main sequence star. It is highly probable that small groups or clusters of young stars are actually embedded in each source, which would increase the total mass of recently formed stars by a large factor that depends on the initial mass function and the lower and upper mass cutoffs that we assume. However, we used this trivial assumption to derive a first order estimate of the recent star formation rate in this region. The distribution of masses that we derived is shown in the right panel of Fig. 5, and seems reasonably consistent with a Salpeter IMF, as indicated by the dotted line.

6.2 Selection of MSX YSO candidates

To get a complete census of the recently formed stars in the CMZ, we used the MSX catalogue to select YSO candidates in the regions not observed with ISOGAL. Using the simple criterion $F_{21\,\mu\mathrm{m}}/F_{15\,\mu\mathrm{m}} \geq 2$ (or D-E $\geq$ 1.57 mag), we found 57 additional sources. We then derived their bolometric luminosities from their flux densities at 21 μm with a relation similar to Eq. 2. We found that the total luminosity of these 57 sources, mainly concentrated in the brightest regions of Sgr A and Sgr B (not observed by ISO to avoid saturation problems), is comparable to that of the 300 ISOGAL candidates.

6.3 Estimate of the average star formation rate

To appear as bright mid-infrared sources, these young massive stars must still be deeply embedded in their parent dusty cocoons. As shown by Wood and Churchwell (1989) [11], O-type stars might spend about 15% of their lifetime in this dusty phase, or about 0.5 Myr for a typical O-type star. We can then convert our estimated total mass of young stars to an average star formation rate, saying that our sample contains all (bright) stars that formed over the last 0.5 Myr.

Since we considered only the sources brighter than 5 mag at 15 μm, corresponding to the most luminous end of the distribution, the total mass that we derive gives only a lower limit to the star formation rate. Using an age of 0.5 Myr, we find that:

$$\mathrm{SFR} > 0.08\,\mathrm{M}_{\odot}/\mathrm{yr} \tag{3}$$

Finally, we can extrapolate the integrated mass that we observe to lower masses assuming a typical initial mass function. Using a Salpeter IMF from 0.1 $\mathrm{M}_{\odot}$to 120 $\mathrm{M}_{\odot}$, we find:

$$\mathrm{SFR}\,(0.1 - 120\,\mathrm{M}_{\odot}) \approx 0.2 - 0.4\,\mathrm{M}_{\odot}/\mathrm{yr} \tag{4}$$

where the factor 2 uncertainty mainly reflects the inaccuracy in our luminosity estimates.

However, some other studies of recent star formation in the Galactic Centre seem to indicate that the low mass cutoff of the IMF is somewhat higher in that peculiar region. Extrapolating our mass estimate only down to 1 $\mathrm{M}_{\odot}$, one finds:

$$\mathrm{SFR}\,(1 - 120\,\mathrm{M}_{\odot}) \approx 0.1 - 0.2\,\mathrm{M}_{\odot}/\mathrm{yr} \tag{5}$$

This results should be regarded as preliminary, since several steps in our computations remain quite uncertain. In particular, we have to make sure that the candidates we have selected are really of young stellar nature, and to improve the bolometric luminosity estimates. Several follow-up programs have been initiated for this purpose, as described in the next section.

7 Follow-up observations

7.1 Search for H_2O masers

Water maser emission is believed to be a typical signature of the early phases of massive star formation. A program aiming at detecting water masers towards some 300 YSO candidates in the Galactic bulge and disk is ongoing with the Effelsberg 100 m radio telescope. Up to now, 24 sources have been observed, including seven in the inner bulge region, but no water maser was detected. The one-σ rms noise was typically between 100 and 300 mJy.

These non-detections may be explained by a too low sensitivity, in particular in the direction of the Galactic Centre, hardly observable from the Effelsberg site. Another possibility could be that our YSO candidates correspond to star forming regions with no very massive star, or with no molecular gas dense enough for water masers to be excited. However, note that if each source correspond to a cluster of low to intermediate mass stars, the derived mass of formed stars would have to be much higher to account for the observed luminosity.

It may also be that these sources are actually massive stars recently formed, but already in a quite evolved state of the star formation process, while water maser emission is thought to arise during the very early stages of this process. Finally, this could mean that some sources in our sample are not of young stellar nature; additional observations at other wavelengths, with better spatial resolution than ISO or possibly spectroscopic observations are clearly required to answer this question.

However, we cannot conclude from these non-detections that the observed sources are not massive YSOs. Indeed, earlier studies also showed that the detection rate of H_2O masers is unusually low in the Galactic Centre region (Taylor et al. 1993) [18], which may be explained as an effect of higher metalicity. Even in the general environment of the Galactic disk, the detection rate of water masers towards HII regions detected in hydrogen recombination lines is only of order 20% (Codella et al. 1994) [19].

7.2 Mid-infrared spectro-imaging with Spitzer

Another follow-up program that was just accepted as a Spitzer general observer program will certainly provide more constraints on the nature of a subsample of our YSO candidates. In the region also covered by the Glass et al. (2001) [10] observations, we have selected 68 good candidates, not associated with LPV nor with OH/IR stars. We will use the IRS spectrometer in scan mapping mode to observe small maps (up to 90" extension) around the ISO detected sources, and get their spectra in the 5–38 μm range, with a moderate spectral resolution of order 100.

The main goals of this program are: i) to derive the exact nature of these sources from the spectral features observed, including emission lines from ionised species in high mass star forming regions, or bending modes of H_2O and CO_2 ices in low mass star forming regions; ii) to improve our luminosity estimates using the spectral energy distribution at longer wavelengths. We expect to find a rising continuum emission longwards of the 15–20 μm limit provided by ISO and MSX, from which dust temperature and therefore bolometric luminosities can be more accurately estimated; iii) we also expect to resolve substructures in some sources, if they correspond to small groups or clusters of embedded stars. The spatial resolution of these observations will roughly be limited by the 3.6" width of the IRS slit, which translates to 0.15 pc at the distance of the Galactic Centre, well suited to resolve dense cores or massive proto-clusters. Actually, some of the sources that appear extended at 15 μm seem to be resolved into at least two sources at 7 μm with ISO, as illustrated in Fig. 6.

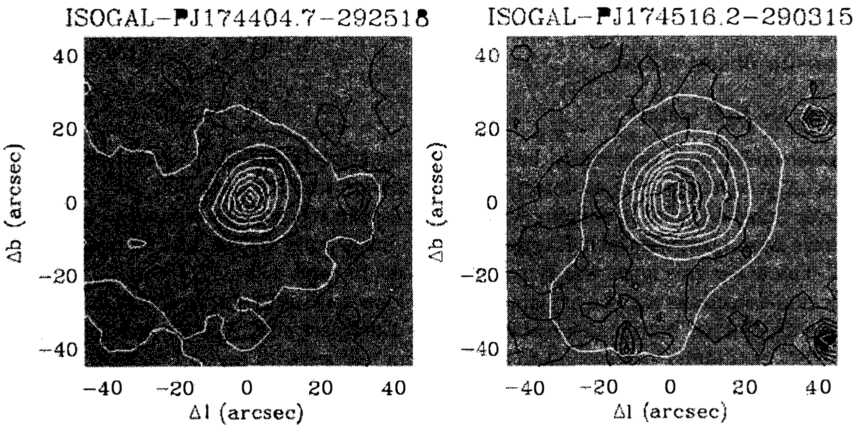

Figure 6: Two examples of YSO candidates, where an extended source is seen at 15 μm (white contours), overlapping at least two point sources at 7 μm (black contours).

This program should also serve as a template to better characterise the larger sample of ISOGAL selected YSO candidates. The 68 targets that will be observed with Spitzer cover most of the mid-infrared parameter space (colour, magnitude, spatial extension). Therefore, if any general trend can be evidenced between these parameters and physical properties of the sources (e.g. bolometric luminosities), it could be applied to all other objects in our sample, providing a much more accurate census of the recent star formation in the inner Galactic bulge.

7.3 Galactic Plane surveys at other wavelengths

Several large scale surveys of the Galactic plane that are currently in preparation will certainly improve our understanding of the Galactic star formation in the coming years. This include surveys in the submillimetre that will make use of new large bolometer arrays, such as SCUBA-2 at the James Clerk Maxwell telescope, and LABOCA at the APEX telescope. Observations carried out at 850 μm will mainly reveal the coldest components of the interstellar medium, and in particular the dense cores which correspond to the earliest stages of star formation.

Most of the infrared range will also become observable with the Herschel satellite in 2007. A project of a complete or very large survey of the Galactic plane in the far-infrared with Herschel is now being discussed. Observations between 60 and 600 μm will provide very strong constraints on the physical properties of dusty material (temperature, emissivity index...) in star forming regions, and in the various phases of the interstellar medium.

Additional follow-up programs are foreseen for a longer term. For example, newly discovered sources may be observed in various molecular lines, using heterodyne instruments at the APEX telescope, or the HIFI spectrometer on board Herschel. Also, the ALMA interferometer will be a very powerful tool for targeted follow-up observations, aimed at studying the velocity fields in these sources, searching for infall or outflow signatures, and analysing the chemical processes occurring at various evolutionary stages.

8 Conclusion

We have shown in this paper how it is possible to extract the most luminous young stellar objects from the two mid infrared band ISOGAL survey. We have used a simple colour criterion, combined with an indication of spatial extension, to extract 300 good YSO candidates from a 3 deg^2 area covering the inner Galactic bulge. Then, using a linear relation to roughly derive bolometric luminosities from the 15 μm flux densities, we have been able to estimate an average star formation rate of order 0.2 $M_\odot$/yr in that region over the last $\sim$0.5 Myr.

However, the accuracy of our results may be greatly improved with complementary observations, and much care has to be taken to interpret the nature of the sources observed in the very peculiar environment of the Galactic Centre. The star formation processes may be slightly different there than in nearby giant molecular clouds. This is shown by the low detection rate of water masers towards massive star forming sites, and indications that the initial mass function may be truncated to somewhat higher masses than in other places of the Galaxy.

Follow-up observing programmes are already ongoing or in preparation. These observations should provide improved spatial resolution with respect to ISO, in order to resolve structures or groups of objects in these slightly extended sources. Also, data at complementary wavelengths, from the mid infrared to the (sub)millimetre, will be of great use to derive the physical properties of these objects.

Acknowledgements

This research is based on observations with ISO, an ESA project with instruments funded by ESA Member States (especially the PI countries: France, Germany, the Netherlands and the United Kingdom) and with the participation of ISAS and NASA.

This research also made use of data products from the Midcourse Space Experiment. Processing of the data was funded by the Ballistic Missile Defense Organization with additional support from NASA Office of Space Science.

References

1. R. Launhardt, R. Zylka, and P. G. Mezger. *A&A*, 384:112, 2002.
2. A. Omont, G. F. Gilmore, C. Alard, et al. *A&A*, 403:975, 2003.
3. F. Schuller, S. Ganesh, M. Messineo, et al. *A&A*, 403:955, 2003.
4. N. Epchtein, B. de Batz, E. Copet, P. Fouqué, et al. *Ap&SS*, 217:3, 1994.
5. N. Epchtein, B. de Batz, L. Capoani, et al. *The Messenger*, 87:27, 1997.
6. B. W. Jiang, A. Omont, S. Ganesh, G. Simon, and F. Schuller. *A&A*, 400:903, 2003.
7. R. Ortiz, J. A. D. L. Blommaert, E. Copet, et al. *A&A*, 388:279, 2002.
8. D. K. Ojha, A. Omont, F. Schuller, et al. *A&A*, 403:141, 2003.
9. J. T. van Loon, G. F. Gilmore, A. Omont, et al. *MNRAS*, 338:857, 2003.
10. I. S. Glass, S. Matsumoto, B. S. Carter, and K. Sekiguchi. *MNRAS*, 321:77, 2001.
11. D. O. S. Wood and E. Churchwell. *ApJ*, 340:265, 1989.
12. M. P. Egan, S. D. Price, M. M. Moshir, et al. The Midcourse Space Experiment Point Source Catalogue Version 1.2 Explanatory Guide. Technical Report AFRL-VS-TR-1999-1522, Air Force Research Laboratory, June 1999.
13. M. Felli, G. Comoretto, L. Testi, A. Omont, and F. Schuller. *A&A*, 362:199, 2000.
14. R. H. Becker, R. L. White, D. J. Helfand, and S. Zoonematkermani. *ApJ Sup. Series*, 91:347, 1994.
15. M. Felli, L. Testi, F. Schuller, and A. Omont. *A&A*, 392:971, 2002.
16. F. Schuller, A. Omont, I. S. Glass, and M. Schultheis. *A&A, in prep.*, 2004.
17. M. Schultheis, S. Ganesh, G. Simon, A. Omont, et al. *A&A*, 349:L69, 1999.
18. G. B. Taylor, M. Morris, and E. Schulman. *AJ*, 106:1978, 1993.
19. C. Codella, M. Felli, V. Natale, F. Palagi, and F. Palla. *A&A*, 291:261, 1994.

The detection of molecular gas with peculiar velocity toward the Galactic center

Hiroaki Yamamoto, Toshikazu Onishi, and Yasuo Fukui

Department of Astrophysics, Nagoya University, Chikusa-ku, Nagoya 464-8602

We have carried out ^{12}CO (J=1–0) observations toward the Galactic center by using the NANTEN 4-m mm-submm telescope of Nagoya University. The observations cover $-12° \leq l \leq 12°$ and $-5° \leq b \leq 5°$ with a grid spacing of 4 arc-minutes. The wide coverage along the Galactic latitude succeeded to obtain a distinctive result from the previous studies; a detection of many features of gas perpendicular to the Galactic plane. These features well demonstrate the existence of energetic events at the Galactic center in the past. One of the peculiar features is the existence of molecular clouds with forbidden velocities out of a Galactic rotation model that is located far from the Galactic center of $\sim$ 1 kpc. In order to derive the accurate physical properties, we made deep ^{12}CO and ^{13}CO (J=1–0) observations toward the corresponding HI features distributed above the Galactic plane at negative longitude and below it at positive longitude revealed by van der Kruit (1970). We detected ^{12}CO emission whose total luminosity is about 3.6×10^5 (K km s^{-1} pc^{-2}). The ^{13}CO (J=1–0) observation was made toward the 5 points of and around each peak position of 24 of 42 molecular clouds identified by the ^{12}CO emission. We detected the significant emissions toward 8 of them. When we assume that molecular clouds are in virial equilibrium with the external pressure, the total molecular mass was estimated to be 2.9×10^5 $M_\odot$. We estimated that the external pressure is 1.0×10^5 [cm^{-3} K] which is $\sim$5 times higher than that in the 2nd quadrant (Heyer et al. 2001) and $\sim$3 times lower than that of the Galactic center (Oka et al. 1998). The X_{factor} derived is 0.6×10^{20} (cm^{-2} [K km s^{-1}]$^{-1}$). Most of these molecular clouds distributed over the forbidden velocity region of the Galactic rotation model. It may suggest that these molecular clouds are the remnant of the past phenomena in the Galactic center.

Keywords: Radio lines: ISM – ISM: clouds

1 Introduction

The central region of the Galaxy is one of the most active sites in the Milky Way. It has been known for years that there is a quite massive molecular gas complex. The radio observations are the powerful tool to investigate the faraway inner region such as the Galactic center because the radio lines are not affected by the obscuration of dust along the line of sight. So, many astronomers have observed molecular clouds in the Galactic center with various molecular spectra (e.g., Bally et al. 1987; Bania 1977; Oka et al. 1998). The latitude coverage of previous observations on this region was typically only $\pm$ 0.5 degrees corresponding to some 150 pc and these have revealed the distribution and kinematics at the only center of our Galaxy. Figure 1 shows an HI map of the Galactic center derived by van der Kruit 1970. This figure indicates that the neutral hydrogen is extended far beyond the previous CO coverage. And this HI feature is not associated with the structure in the plane. We have carried out the ^{12}CO(J=1–0) observation in the Galactic center with wider range as never before and high sensitive, and high resolution ^{12}CO(J=1–0) and ^{13}CO(J=1–0) observations toward those features in dotted lines in figure 1 for the first time. The distance to the Galactic center is assumed to be about 8.5 kpc throughout this paper.

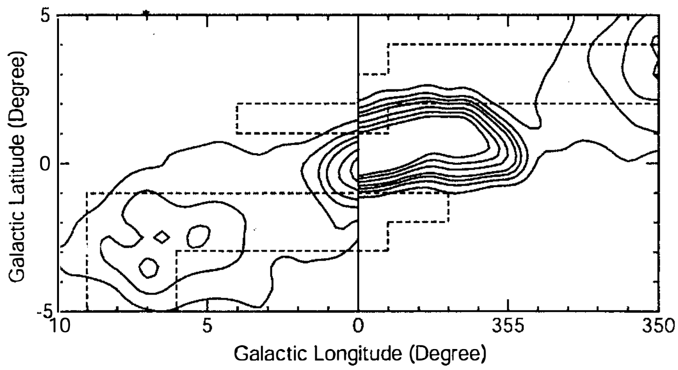

Figure 1: The surface density map of neutral hydrogen derived by van der Kruit 1970. The velocity range at positive and negative longitude is -300 to -30 km s^{-1} and 30 to 300 km s^{-1}, respectively. The lowest contour is 4.5×10^{19} cm^{-2} and the separation between contours is 5.0×10^{19} cm^{-2}. The dotted lines indicate the observed region with high sensitivity.

2 Observations

Observations of the J=1–0 transition of ^{12}CO and ^{13}CO were made with NANTEN, a 4m mm - sub mm telescope at Las Campanas Observatory, Chile. The system noise temperature was 220 K (SSB) at 115 GHz and 120 K (SSB) at 110 GHz. The beam size was $\sim2'.6$ at $\sim$115 GHz and $\sim2'.7$ at $\sim$110 GHz.

First of all, we carried out the ^{12}CO observation toward $-12° \leq l \leq 12°$ and $-5° \leq b \leq 5°$ at a grid spacing of $4'$, corresponding to 10 pc at 8.5 kpc, and next we carried out the ^{12}CO observation with high sensitivity in the dotted lines in figure 1. The ^{13}CO observation was made toward the 5 points of and around each peak position identified by the ^{12}CO emission. All observations were performed by the position-switching technique. The velocity resolution was 0.6 km s^{-1} for all ^{12}CO observations and 0.1 km s^{-1} for ^{13}CO observations. The typical noise fluctuations of ^{12}CO observation, that with high sensitivity and ^{13}CO observation were $\sim$ 0.36, $\sim$ 0.18 and $\sim$ 0.10 K per channel, respectively.

We employed a room-temperature chopper wheel for the intensity calibration (Kutner & Ulich 1981). An absolute intensity calibration was made by observing ρ Oph East [$\alpha(1950)$ = $16^{\rm h}29^{\rm m}20^{\rm s}.9$, $\delta(1950)$ = $-24°22'13''$] for ^{12}CO and ^{13}CO and we observed them every 2 hours. We assumed the $T_{\rm R}^*$ of ρ Oph East to be 15.0 K for ^{12}CO and 10.0 K for ^{13}CO.

3 Results

The total integrated intensity map of $^{12}CO(J=1\text{–}0)$ in the Galactic center is shown in Figure 2. There are a number of filamentary features perpendicular to the Galactic plane. In particular, these features located at high latitude are local. Some of them are located near the Galactic center and these features well demonstrate the existence of energetic events at the Galactic center in the past.

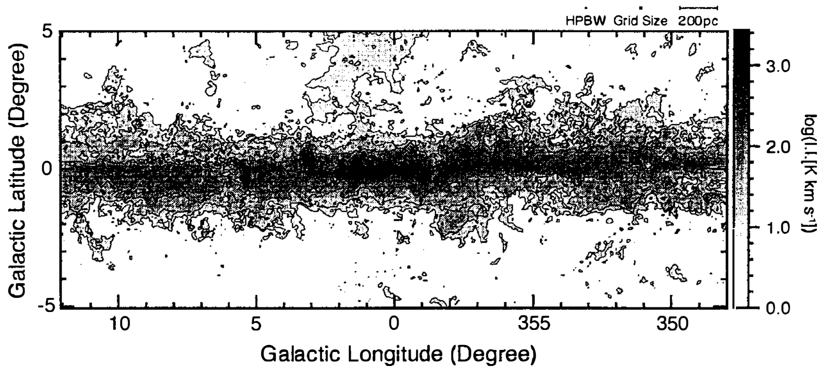

Figure 2: Total integrated intensity map of $^{12}CO(J=1\text{–}0)$ emission in the Galactic center. The gray scale is indicated by the logarithm. The lowest contour and the separation between contours are log(1.0) K km s^{-1} and log(0.5) K km s^{-1}, respectively.

Figure 3 shows the velocity integrated intensity map of ^{12}CO superposed on the surface density map of HI derived by van der Kruit 1970. We could not detect ^{12}CO emission above the Galactic plane at negative longitude at all. CO emissions were located beyond $-4°$ in Galactic latitude and most of CO emissions were localized toward $l \sim 4°.5$ and $b \sim -2°$. ^{12}CO clouds are defined as a collection of more than 2 contiguous observed positions at each position exceeds 7 K km s^{-1} (3σ). Based on this definition, we identified 42 molecular clouds. For 42 clouds, the maximum brightness temperature, FWHM line width derived by a single gaussian fitting, and the V_{LSR} range from 0.64 to 3.03 K, 5 to 54 km s^{-1}, -164 to -21 km s^{-1}, respectively. The radius of a cloud defined by as the radius of an equivalent circle having the same area, i.e., $(Radius) = \sqrt{(Area/\pi)}$, ranges 2.1 to 14.5 pc. The total luminosity in the observed region was $\sim 3.6\times10^5$ K km s^{-1} pc^{-2}.

The crosses in figure 3 indicate the positions where we observed ^{13}CO emission. The ^{13}CO ($J=1\text{–}0$) observation was made toward the 5 points of and around each peak position of 24 of 42 molecular clouds identified by the ^{12}CO emission. We detected the significant emissions toward 8 of them, indicating by bold crosses in figure 3. Figure 4 shows the typical profiles of ^{12}CO and ^{13}CO emission. Each profile toward this have the velocity around -50 km s^{-1}. The r.m.s. noise fluctuation of 0.18 K was enable us to detect very weak ^{12}CO emission ever not detected until now. The line width of spectra, $\sim$ 10 km s^{-1}, is broader than the typical ^{12}CO spectra in Galactic disk (e.g., Solomon et al. 1987).

4 Didcussion

4.1 The mass of Molecular clouds

Generally, to derive the mass of molecular clouds from integrated intensity of ^{12}CO, we use a useful factor, $N(H_2)/W(CO)$ (hereafter, X_{factor}). Figure 5 (a) shows the correlation diagram

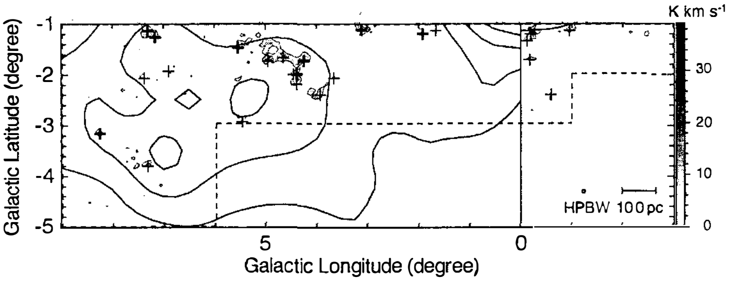

Figure 3: HI surface density map superposed on the Integrated intensity map of ^{12}CO(J=1–0) emission with high sensitivity. Thick and thin lines indicate the contour of HI and the boundary of ^{12}CO clouds, respectively. The lowest contour and the separation between contours of HI are the same as figure 1. The dotted lines are the same as figure 1. The crosses indicate the positions where we observed ^{13}CO emission. The bold crosses indicate the positions detected ^{13}CO emission.

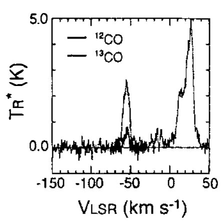

Figure 4: Typical spectra of ^{12}CO and ^{13}CO. Thick and dotted lines indicate the spectra of ^{12}CO and ^{13}CO emission, respectively.

between the mass of molecular cloud estimated from the integrated intensity of CO, $M_{\rm CO}$, and Virial mass, $M_{\rm vir}$. To drive the mass of molecular clouds we assume that the X_{factor} is 3.0×10^{20} cm^{-2} (K km s^{-1})$^{-1}$ which is typical value of the Milky Way (Young & Scoville 1991). The $M_{\rm vir}$ was derived by using the following equation, assuming isothermal, spherical, and uniform density distribution with no magnetic and external pressure: $M_{\rm vir}=209\times R\times V_{\rm comp}^2$, where R and $V_{\rm comp}$ are the radius of molecular cloud (pc) and line width (km s^{-1}) of the composite profile obtained by averaging all of the spectra within a cloud. As the diagram indicates, $M_{\rm vir}$ is one order of magnitude larger than $M_{\rm CO}$. But here, $M_{\rm vir}$ is not taken into account the external pressure. It is likely that the external pressure in and around Galactic center is higher than that in Galactic plane. Our taking into account the external pressure, we re-estimated the X_{factor} and estimated the external pressure as the same as Oka et al. 1998 (See sec. 5.1 in his paper) and estimated the mass of molecular clouds. Figure 5 (b) shows the correlation diagram between $M_{\rm CO}$ and $M_{\rm vir}$ taken into account the external pressure. We got the best agreement between $M_{\rm vir}$ and $M_{\rm CO}$ with p/k = 1.0×10^5 cm^{-3} K. Oka et al. 1998 estimated the external pressure(p/k) to be 3×10^5 cm^{-3} K. Present value is $\sim$3 times lower than the estimation of Oka et al. 1998 and $\sim$5 times higher than that of 2nd quadrant (Heyer et al. 2001) whose mean external pressure was 1.8×10^4 cm^{-3} K. But since the external pressure of each objects ranges from over 10^5 cm^{-3} K to 10^2 cm^{-3} K in 2nd quadrant, it may be that there are a wide variety of the external pressure toward the present observed region. These indicate that the external pressure deceases from the Galactic center to outer galaxy with one order of magnitude in a large sense, even though the external pressure is quite high in some regions, for instance near the O.B. stars. Using the X_{factor} redefined for pressure bound clouds, new X_{factor} = 0.6×10^{20} cm^{-2} (K km s^{-1})$^{-1}$, the total molecular mass in the observed region becomes 2.9×10^5 $M_\odot$. The mass range of molecular clouds is from 2.3×10^2 $M_\odot$ to 7.5×10^4 $M_\odot$. Oka et al. 1998 estimated the molecular mass to be about 2×10^7 $M_\odot$ within the inner 400 pc of the Galaxy. Our present value, the mass of the isolated structure far from Galactic plane, is about 1% within that of the inner 400 pc of the Galaxy.

4.2 Velocity structure of the structure isolated far from Galactic plane

As the comprehensive structure, toward Galactic center the velocity of molecular clouds is distributed to the positive $V_{\rm LSR}$ in positive longitude because of the Galactic rotation. Figure 6 shows the $V_{\rm LSR}$ distribution of the CO emission, integrated over -5 to 5 degrees in Galactic

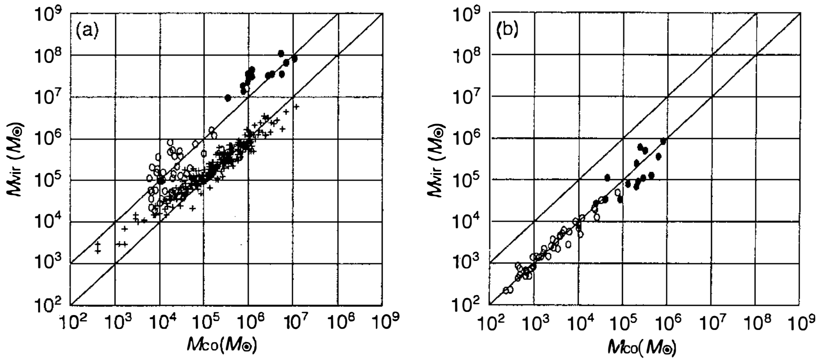

Figure 5: Virial mass, M_{vir}, plotted against the mass derived by ^{12}CO integrated intensity, M_{CO}, before (a) and after (b) taking into account the external pressure. Open circles , filled circles and crosses indicate ^{12}CO data in present observation, Oka et al. 1998 and Galactic plane, respectively. The two solid lines represent M_{vir}=10M_{CO} and M_{vir}=M_{CO} from the top.

latitude, in Galactic longitude whose range is from −12 degrees to 12 degrees. The velocity structure is very complication but in a large sense the CO emission is localized to the positive V_{LSR} in positive longitude, and the negative V_{LSR} in negative longitude. The component from −60 km s^{-1} to −20 km s^{-1} in positive longitude is the 3kpc arm (Bania 1977). Present clouds were localized under the 3 kpc arm. The velocity range of present clouds was from −21 km s^{-1} to −190 km s^{-1} This is the forbidden region out of a Galactic rotation model and it is likely that these molecular clouds would not be in any gravitationally bound orbit because they are far from the Galactic plane. These molecular clouds which have the opposite velocity out of a Galactic rotation should be affected by the past and/or present exclusive event. As there is a very good correlation between molecular clouds and HI cloud in terms of the velocity (van der Kruit 1970), it was likely that there was the effect of the past and/or present exclusive events in more larger scale. We suggest that they may represent a remant of a past active explosive event near the Galactic nucleus, perhaps a black hole. In this senario, the timescale of this event is roughly estimated to be 10^7 years ago.

5 Summary

We have carried out the ^{12}CO(J=1–0) observations in the Galactic Cetner. We revealed the comprehensive structure in the Galactic center and discovered a number of filamentary features perdendicular the Galactic plane. These features well demonstrate the existence of energetic events at the Galactic center in the past. And We have carried out high sensitiveity ^{12}CO(J=1–0) observations toward HI features derived by van der Kruit 1970. We have discovered 42 molecular clouds far above the Galactic plane and ^{13}CO(J=1–0) observations toward the peak position of 24 of 42 molecular clouds identified by the ^{12}CO emission. We detected the significant emissions toward 8 of them. The total mass of molecular clouds is estimated to be $\sim 2.9 \times 10^5$ $M_\odot$ and the external pressure is estimated to be $\sim 1.0 \times 10^5$ cm^{-3} K. This value is three times lower than the Galactic center and five times higher 2nd quadrant. These molecular clouds have the forbidden velocity out of a Galactic rotation model. They are most likely expanding from the Galactic center. If they are expanding, they may represent a past active event near the Galactic nucleus. The timescale of this event is roughly estimated to be 10^7 years ago.

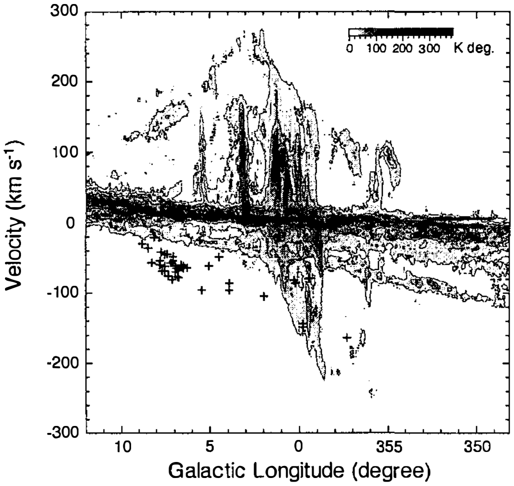

Figure 6: The longitude – latitude diagram in the Galactic center. The crosses indicate the locations of ^{12}CO clouds identified by this observation.

References

1. Bally, J., Stark, A. A., Wilson, R. W., & Henkel, C. 1987, ApJS, 65, 13
2. Bania, T. M. 1977, ApJ, 216, 381
3. Heyer, H. M., Carpenter, J. M., & Snell, R. L. 2001, ApJ, 551, 852
4. Kutner, M. L., & Ulich, B. L. 1981, ApJ, 250, 341
5. Oka, T., Hasegawa, T., Hayashi, M., Handa, T., & Sakamoto, S. 1998, ApJ, 493, 730
6. Oka, T., Hasegawa, T., Sato, F., Tsuboi, M., & Miyazaki, A. 1998, ApJS, 118, 455
7. Solomon, P. M., Rivolo. A, R., Barrett, A., & Yahil. A. 1987, ApJ, 319, 730
8. van der Kruit, C. P. 1970, A&A, 4, 462
9. Young, J. S., & Scoville, N. Z. 1991, ARA&A, 29, 581

The Fate of Lyman photons in local Starburst: new ACS/HST images

Daniel Kunth (1), M. Hayes (2), G. Östlin (2), M.J. Mas–Hesse (3), C. Leitherer (4), A. Petrosian (5)

(1) Institut d'Astrophysique de Paris 98 bis Bld Arago, 75014 Paris, France
(2) Stockholm Observatory, SE-106 91 Stockholm, Sweden
(3) Centro de Astrobiologia (CSIC–INTA), Madrid, Spain
(4) Space Telescope Science Institute, 3700 San Martin Dr., Baltimore, MD 21218, USA
(5) Byurakan Astrophysical Observatory, Byurakan 378433, Armenia

Abstract

We review the imaging and spectroscopic properties of the $Ly\alpha$ emission in starburst galaxies. The $Ly\alpha$ photons escape is largely driven by kinematical and orientation effects related to the presence of large scale expanding shells of neutral hydrogen. The various $Ly\alpha$ profiles can be linked to the evolutionary state of the starburst. Our recent $Ly\alpha$ imaging study using the HST-ACS is presented here: it highlights the presence of diffuse extended emission of low intensity leaking out the diffuse HI components. The similarities with the line profiles observed on high redshift galaxies is an important fact that cautions the use of $Ly\alpha$ to derive the cosmic star formation rate and constrains the search for high redshift galaxies.

1 Introduction

Star-formation rates in primeval galaxies are expected to reach hundreds of $M_{\odot}\mathrm{yr}^{-1}$ (Partridge & Peebles,1967). For a normal Salpeter IMF this corresponds to total bolometric luminosities in excess of $10^{11}L_{\odot}$, which is similar to the values in luminous IRAS galaxies (Heckman 1993). The ionizing radiation from the newly formed young stars should lead to prominent $Ly\alpha$ emission due to recombination of hydrogen in the ambient interstellar medium. Therefore, the $Ly\alpha$ line could be an important spectral signature in young galaxies at high redshift since the expected $Ly\alpha$ luminosity amounts to a few percent of the total galaxy luminosity (Schaerer 2003; Stiavelli et al. 2003).

From the above estimates, typical $Ly\alpha$ fluxes of 10^{-15} erg s^{-1} cm^{-2} are expected. Such values are within easy reach of present instruments. Over the past 20 years major observational efforts were undertaken to search for $Ly\alpha$ emission from faint galaxies at high redshift (Djorgovski & Thompson 1992). Although many $Ly\alpha$ emitters have been found (e.g., Frye et al. 2002; Malhotra & Rhoads 2002; Fujita et al. 2003; Ouchi et al. 2003, Schaerer, this conference), their numbers are smaller than predicted. Where is the population of $Ly\alpha$ emitting field galaxies, which should exist at high redshift?

The assumption of the $Ly\alpha$ intensity as produced by pure recombination in a gaseous medium may be too simple. Meier & Terlevich 1981, Hartmann et al. 1988, Neufeld 1990, and Charlot & Fall 1993 considered the effects of dust on $Ly\alpha$. $Ly\alpha$ photons experience a large number of resonant scatterings in neutral atomic hydrogen, thereby increasing the path length and the likelihood of dust scattering and absorption. This process can be very efficient in removing $Ly\alpha$ photons from the line of sight to the observer, leading to much lower line strengths in comparison with the idealized Case B. Depending on the aspect angle of the galaxy as seen from the observer, this may lead to a decrease of the $Ly\alpha$ equivalent width. On the other hand, $Ly\alpha$ may actually be enhanced due to the presence of many supernova remnants which form during the starburst (Shull & Silk 1979). The net result is controversial. Bithell (1991) finds supernova remnants to be an important contributor to the $Ly\alpha$ strength whereas Charlot & Fall (1993) reach the opposite conclusion.

The theoretical situation is sufficiently complex that observational tests are required. The most obvious test are measurements of $Ly\alpha$ in local starburst galaxies whose redshifts are sufficiently large to permit observations of their intrinsic $Ly\alpha$ outside the geocoronal and Galactic interstellar $Ly\alpha$. Observations of local starbursts have indeed been performed with the *IUE* satellite, (Meier & Terlevich 1981; Hartmann et al. 1988; Calzetti 2001; Terlevich et al. 1993; Valls-Gabaud 1993). Again, the results are controversial. For instance, Calzetti & Kinney (1992) and Valls-Gabaud find $Ly\alpha$ strengths in agreement with pure recombination theory whereas Hartmann et al. and Terlevich et al. conclude that significant dust trapping of $Ly\alpha$ photons must occur.

2 The role of kinematics in HI gas

Finally, and most importantly, the kinematic properties of the interstellar medium may very well be the dominant escape or trapping mechanism for $Ly\alpha$ (Kunth et al. 2003). The complex nature of the $Ly\alpha$ escape probability has been revealed by the HST/GHRS spectroscopy (Kunth et al. 1998) and raised additional questions. They detected $Ly\alpha$ emission in half of them, with clear asymmetric P–Cyg profiles, as shown in Fig. 1a, while the other half showed prominent damped $Ly\alpha$ absorptions. The sample was extended at lower resolution by Thuan & Izotov (1997). In Fig. 1b we show the 3 characteristic $Ly\alpha$ profiles that can be found in star-forming galaxies: pure emission with symmetric profile, P–Cyg emission and broad, damped absorption profile.

The analysis of these data yielded the following results:

- As $Ly\alpha$ is detected in emission, a clear P–Cyg profile is seen in most cases. Also the interstellar neutral metallic lines appear blueshifted by 200–400 km/s.
- When the neutral gas is static with respect to the HII region, a damped broad absorption profile is detected.

Hence HST-GHRS data clearly showed that the kinematics of the gas was one major parameter determining the visibility of the $Ly\alpha$ line. However, if the dust content is small, the $Ly\alpha$ photons may, after multiple resonant scatterings could diffuse out over a larger area. This would create a bias in the spectroscopic studies which usually target the regions of peak UV intensity - under this scenario the places where we do *not* expect to see $Ly\alpha$ in emission. Another possibility is that the UV-continuum sources are partly shielded by a clumpy medium, in which case we would see mixed absorption and emission. In cases where the ISM has a non-zero radial velocity with respect to the UV continuum source, $Ly\alpha$ may appear in emission with a characteristic P-Cygni profile. Depending on the morphology and kinematics of the galaxy this can occur in different regions, and e.g. in a galaxy merger the escape probability may be enhanced.

Further on, Mas-Hesse et al. (2003) have performed 2–D observations using HST-STIS in order to analyze the spatial structure of the emission profile, and look for areas where the $Ly\alpha$ photons could be leaking. Three objects were included in the sample: 2 showing

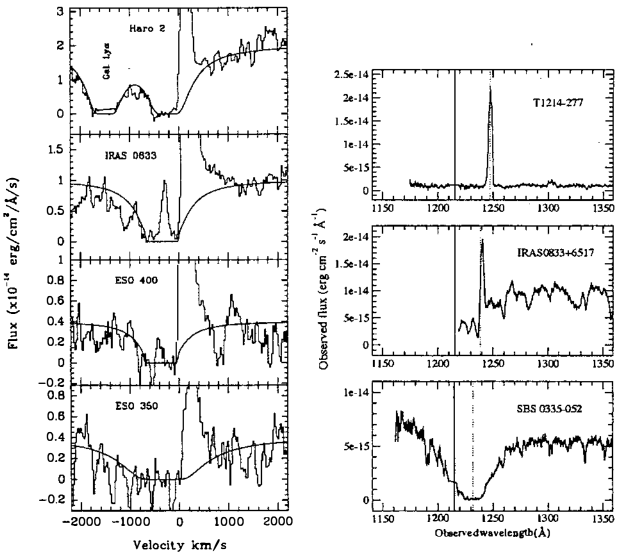

Figure 1: a) Starburst galaxies showing $Ly\alpha$ emission lines with P–Cyg profiles, as shown by Kunth et al. (1998); b) prototypical examples of the three cases discussed in the text: pure emission, P–Cyg profile and damped absorption.

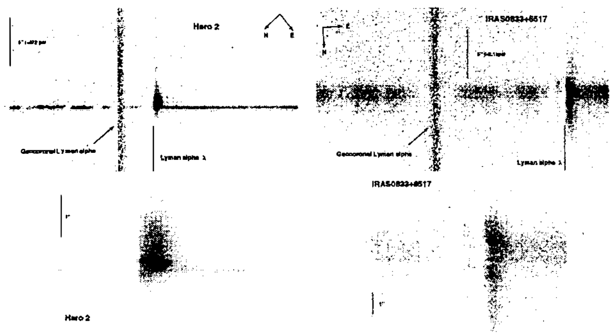

Figure 2: a) Spectral HST–STIS image of Haro 2 around the $Ly\alpha$ region. Wavelength increases upwards. The $Ly\alpha$ emission is extended over around 8 arcsec (1 kpc). Note the extended low density component and the sharpness of the blue absorption edge. b) Spectral image of IRAS 0833+6517. The $Ly\alpha$ emission is extended over around 10 arcsec (5 kpc). Note the presence of a secondary emission peak located at the center of the absorption profile.

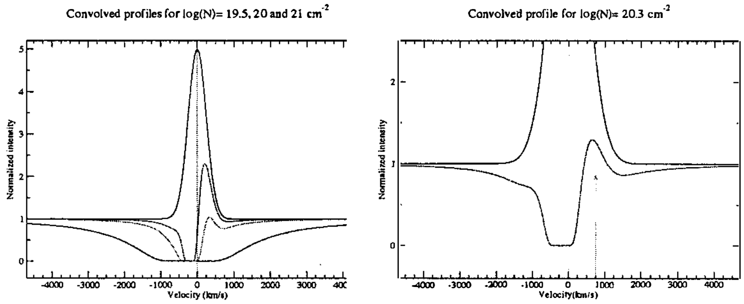

Figure 3: Effects of an expanding shell on the $Ly\alpha$ emission profile. The left panel shows the intrinsic emission line, and the resulting profiles for different column densities of neutral Hydrogen. On the right panel we show that the resulting emission might appear artificially redshifted by several hundreds of km/s.

a strong P–Cyg profile (Haro 2 and IRAS 0833+6517) and 1 showing a damped absorption (IZw18).

No emission whatsoever was detected from IZw18 along the STIS slit. The spectral images for Haro 2 and IRAS 0833+6517 are shown in Fig. 2. The main results drawn from these data are:

- No velocity structure has been detected on the sharp edge of the P–Cyg profiles on scales of 1–5 kpc.
- These profiles imply the presence of large column densities of neutral gas outflowing from the HII region at velocities of 200 – 400 km/s, acting practically as a moving plane-parallel slab on kpc scales.
- Detection of broad and extended emission components of low intensity.

3 Interpretation: an evolutionary view

These observational results suggest that the central starbursts in these galaxies are driving a huge expanding shell of neutral gas. One can postulate that the interaction of the ionizing flux and the shell itself with the surrounding medium can lead to different configurations which could explain the variety of $Ly\alpha$ profiles. Moreover, these scenarios could be correlated with the evolutionary state of the starburst process.

Mas-Hesse et al. (2003) show first in Fig. 3 the predicted effect of an expanding shell of neutral Hydrogen for different column densities. P–Cyg profiles similar to the observed ones are produced for column densities $\log(n_H) \approx 19 - 20$ cm^{-2}, moving at velocities around 300 km/s with respect to the HII region where the $Ly\alpha$ emission line is produced. For higher column densities the absorption is completely damped, and no $Ly\alpha$ photons can escape. On the other hand, for much higher outflowing velocities, the absorption takes place so much to the blue of the emission profile, that this wouldn't be affected at all. Note that as a result of this saturated absorption by neutral gas, the centroid of the emerging $Ly\alpha$ emission line might appear artificially redshifted by a significant amount (see Fig. 3b) with respect to the HII region. This effect can be mistaken as an evidence for the presence of receding flows of ionized gas, which is not the case since the line is indeed emitted by the HII region.

As discussed in detail in Tenorio-Tagle et al. (1999) and Mas-Hesse et al. (2003), the interaction of bubbles and superbubbles as the starburst episode evolves may lead to different scenarios affecting the properties of the $Ly\alpha$ emission line profiles. We have identified 4 basic steps:

i) Initially, when a star-forming episode starts, a central HII region begins to develop. At this phase, if the neutral gas surrounding the starburst region has HI column densities above 10^{14-15} cm^{-2}, an absorption line centered at the systemic velocity of the galaxy will be visible, independently on the viewing angle. If the total HI column density along the line of sight is higher than around 10^{18} cm^{-2}, a damped $Ly\alpha$ absorption profile will be detectable. It is important to stress that during this early phase of a starburst the Balmer emission lines will be strongest, due to the high ionizing flux produced by the most massive stars.

ii) The situation changes drastically and becomes a strong function of viewing angle, once the mechanical energy released by the starburst is able to drive a shell of swept up matter exceeding the dimensions of the central disk. Then, upon the acceleration that this shell experiences as it enters the low density halo, it becomes Rayleigh–Taylor unstable and fragments. This event allows the hot gas (composed basically by matter recently processed by the starburst), to stream with its sound speed between fragments and follow the shock which now begins to form a new shell of swept-up halo matter, expanding at a velocity v_{exp}. Another consequence of the blowout is the fact that the ionizing photons from the recent starburst are now able to penetrate into the low density halo, and manage to produce an extended conical HII region that reaches the outskirts of the galaxy. An observer looking then at the starburst through the conical HII region will be able to detect the strong $Ly\alpha$ emission line produced by the central HII region, centered at the systemic velocity of the galaxy, and without any trace of absorption by neutral gas. On the other hand, an observer looking far away from the conical HII region will detect a broad absorption profile at any evolutionary state.

iii) Sooner or later, recombination will begin in the expanding shell. This will cause a strong depletion of the ionizing radiation which formerly was able to escape the galaxy after crossing the extended conical HII region. Recombination in the expanding shell will produce an additional broad $Ly\alpha$ component of low intensity.

iv) The ionization front becomes eventually trapped within the expanding shell by basically 3 effects. First, by the increasingly larger amount of matter swept into the expanding shell, as this ploughs into the halo. Second, the growth of the shell dimensions also implies less UV photons impinging, per unit area, at the inner edge of the shell. And third, in the case of a nearly instantaneous starburst, the production of UV photons starts to decrease drastically (as t^{-5}) after the first 3.5 Myr of evolution.

The trapping of the ionization front will lead to the formation of a neutral layer at the external side of the expanding shell. All these effects result in an increasingly larger saturated absorption, as the external neutral layer will resonantly scatter the $Ly\alpha$ photons. This absorption will appear blueshifted with respect to the $Ly\alpha$ emitted by the central HII region by $-v_{exp}$ leading so to the formation of a P–Cyg profile where a variable fraction of the intrinsic $Ly\alpha$ emission would be absorbed.

In addition, the profile will be contributed by the $Ly\alpha$ radiation arising from the receeding section of the shell, both by recombination on the ionized layer, and by backscattering of the central $Ly\alpha$ photons by the neutral layer.

Under some circumstances, the leading shock front on the external surface of the shell can be heated and become ionized, producing so an additional $Ly\alpha$ emission which would be detected blueshifted by $-v_{exp}$ and not affected by absorption. This could be the case of the secondary emission peak detected in IRAS 0833+6517.

4 The ACS imaging studies

In the distant universe, $Ly\alpha$ imaging and low resolution spectroscopic techniques are now successfully used to find large numbers of galaxies. However, without a proper understanding of the $Ly\alpha$ emission processes this line cannot be used to estimate astrophysical quantities such as star formation rates and fluxes for reionisation and it becomes dubious to use it to study clustering if the biases are not properly known. If the star forming activity of a high redshift galaxy is connected with its environment, the $Ly\alpha$ escape probability will not be independent of this parameter.

These considerations led us to start a pilot programme to image *local* starburst galaxies in the $Ly\alpha$ line using the solar blind channel (SBC) of the Advanced Camera for Surveys (ACS) onboard HST, allowing us to study the $Ly\alpha$ emission and absorption morphology in detail. A sample of six galaxies with a range of luminosities ($M_V = -15$ to -21) and metallicities ($0.04Z_\odot$ to $\sim Z_\odot$), including previously known $Ly\alpha$ emitters as well as absorbers, were selected and observed during 30 orbits in Cycle 11. The observations were obtained through the F122M ($Ly\alpha$) and F140LP (continuum) filters.

Table 1: Targets for ACS $Ly\alpha$ imaging project

Galaxy	M_B	12+log(O/H)	emitter/absorber
SBS 0335-052	−17	7.3	absorber
NGC 6090	−21	8.8	emitter
ESO 350-38	−20	7.9	emitter
Tol 1924-416	−19	7.9	emitter
Tol 65	−15	7.6	absorber
IRAS 08+65	−21	8.7	emitter

4.1 First continuum subtractions

The first results for two of the galaxies, ESO 350-38 and SBS 0335-052, were presented in Kunth et al. (2003). The images were drizzled to correct for geometric distortion, aligned and background subtracted. In order to subtract the continuum (F140LP) from the on-line (F122M) images to construct line-only $Ly\alpha$ images it is necessary to assume a shape of the continuum. As the UV spectra of starbursts are fairly well described by power-law spectral energy distributions (SEDs), a natural first step would be to adopt a power-law, $f_\lambda = \lambda^\beta$, with the slope β derived from, e.g. IUE spectra in the range $\lambda \sim 1300$Å. The relative scaling factors between the filters differs by a factor 1.7 for assumptions of $\beta = -2$ and 1. The $Ly\alpha$ images in Kunth et al. (2003) were obtained in this way, by assuming $\beta = 0$, however it was noted that β was variable over the face of each galaxy.

The results presented in Kunth et al. (2003) give a view of $Ly\alpha$ that is complementary to the results of previous HST/GHRS spectroscopy by Kunth et al. (1998). Moreover, they reveal the complex nature of $Ly\alpha$ emission and absorption in starburst galaxies. ESO350-IG038 shows $Ly\alpha$ in emission from several knots (A and C following Vader el. al 1993). By using the F140LP image, and an archival F606W WFPC2 image these knots were found to have very blue UV/optical colours ($f_{\lambda,F140LP}/f_{\lambda,F606W} = 15$). In knot B and the surrounding region, $Ly\alpha$ is seen in absorption. Here, colours are much redder ($f_{\lambda,F140LP}/f_{\lambda,F606W} = 1$). Knot A also shows a P Cygni profile and and diffuse $Ly\alpha$ emission is seen in numerous regions, particularly to the south-west of the image.

The image of SBS0335-052 shows broad damped $Ly\alpha$ absorption almost throughout, confirming the reports of Thuan et al. (1997). Diffuse $Ly\alpha$ emission is seen towards the north of the image (around SSC 5 following Thuan et al.) although it is very sensitive to the assumptions in the continuum subtraction.

Clearly, in order to separate emission from absorption in the less obvious cases, and in order to obtain photometrically valid images, a continuum subtraction procedure that takes the spatial variation of the continuum slope into account, is necessary.

4.2 Continuum subtractions using a β-map

A more realistic way of estimating the scaling factor would be to use photometric maps of the ultraviolet continuum slope, so called "β-maps". A β-map can be constructed from the F140LP images and an HST image in another, preferably blue, passband. Many of the target galaxies have been previously imaged e.g. with WFPC2 and β-maps were constructed based on these. A general feature of such continuum subtractions is that the continuum is oversubtracted. This calls for several explanationss: i) The continuum often starts to deviate

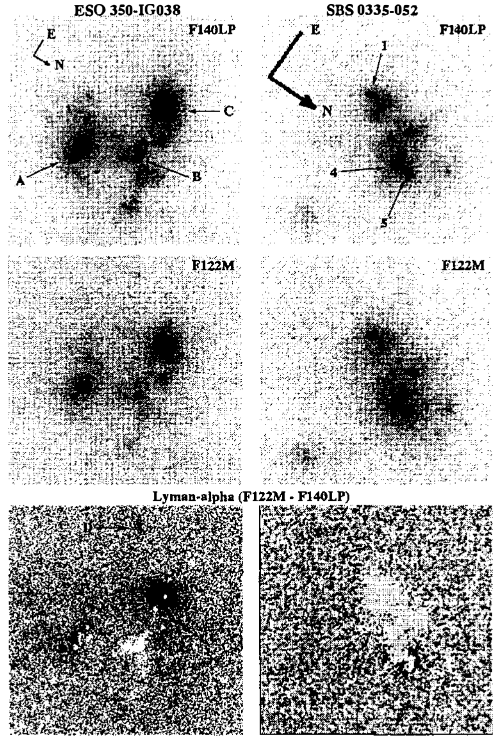

Figure 4: **Top:** UV continuum (F140LP) images of ESO 350-38 (field shown is 13 arcsec x 13 arcsec) and SBS 0335-052 (4.4 arcsec x 4.4 arcsec). The different knots discussed in the text are labeled. **Middle:** F122M images. **Lower panels:** continuum subtracted $Ly\alpha$ image assuming $\beta = 0$. Emission is shown in black and absorption in white. Note the faint $Ly\alpha$ emitting blob (labeled D) in ESO 350-38 and the possible faint emission to the north of '4' and '5' in SBS 0335-052.

from a power-law at wavelengths $\lambda < 1300$ Å, and in addition, absorption features may be present. Moreover, this λ-region is sensitive to extinction and the the extinction near $Ly\alpha$ is greater than for the continuum. ii) The F122M filter also covers, in addition to $Ly\alpha$ in the target galaxies, $Ly\alpha$ absorption from gas in the Milky Way. This means that a fixed fraction of the photons with wavelength $\lambda_{\rm obs} = 1216\mathring{A} \pm \delta\lambda$ will be lost. Since the solid angle covered is very small, this fraction will be fixed for each galaxy and will depend only on the column density of neutral hydrogen along the sightline.

It should be pointed out that the first point concerns also high-z $Ly\alpha$ galaxies where continuum subtraction is a potential, yet little discussed, problem. In addition there might be an effect of intergalactic dust along the sightline. What is needed is a way to relate the correct continuum level at $Ly\alpha$ to the colours at longer wavelength.

We proceeded by switching our attention to another galaxy in our sample, ESO338-IG04 (Tololo 1924-416) where we have deep HST/WFCP2 images in the F218W, F336W, F439W, F555W and F814W filters (Östlin et al. 1998, 2003), as well as STIS long slit spectra with G140L available (Leitherer et al. in preparation). The combination of spectroscopic and imaging data over a wide wavelength interval meant that this target was ideal for a thorough investigation of the continuum subtraction procedures. From IUE spectra (e.g. Giavalisco et al. 1996) this target was known to be one of the brighter $Ly\alpha$ emitters in the local universe.

Preliminary continuum subtractionsusing a flat ($\beta = 0$) continuum, similar to those produced for ESO350-IG038 and SBS0335-052 had already shown ESO338-IG04 to be a bright $Ly\alpha$ emitter over nearly all of the starburst region. This can be seen in Figure 5. Small offset absorption holes appeared in the brightest regions, similar to those announced for ESO350-IG038 in Kunth et al. (2003) and a feature consistent with a P-Cygni profile was visible in the brightest central star cluster. Also, a lot of diffuse $Ly\alpha$ was seen leaking out from regions approximately east and west of the central starburst. Adopting the normal β-map procedure again lead to the usual oversubtraction of the continuum, even after experimenting with β-maps constructed from a variety of filter combinations.

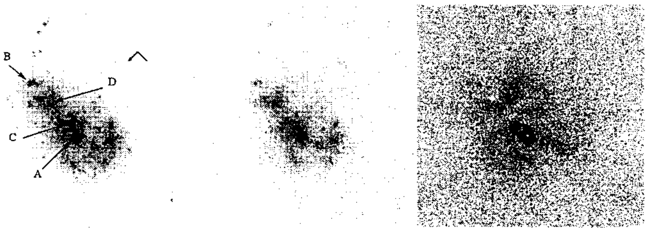

Figure 5: **Left:** UV continuum (F140LP) image of ESO 338-IG04. The different knots discussed in the text are labeled. **Middle:** F122M image. **Right:** continuum subtracted $Ly\alpha$ image assuming $\beta = 0$. Emission is shown in black and absorption in white. The field shown is 14 arcsec x 14 arcsec.

Comparison with the low resolution STIS spectrum of the central regions proved this continuum subtraction to be inaccurate. The spectrum shows $Ly\alpha$ emission from regions were the β-map subtracted image shows absorption. Comparison of the β values from the images and spectra in several star forming regions revealed that photometrically determined β values were usually more negative than those determined by fitting a power law to the slope of the spectrum. It is clear that in at least some cases, the method of continuum subtraction using β-maps substantially underestimates the scaling factor between the F122M and F140LP filters, leading to the subtraction of too much continuum.

The method of using a β-map to estimate the scaling factor indeed relies upon the power-law being continuous at wavelengths $\lambda < 1400$Å. The IUE spectrum of this galaxy seems to indicate that this is not the case. The spectrum seems to flatten off slightly at around 1500Å, increasing (making less negative) the value of β between out online and offline filters. Moreover there is no one-to-one relationship between the βs obtained through β-maps and power-law fitting to the STIS spectrum at shorter wavelengths, i.e. there is no simple relationship that describes the flattening of the spectrum shortwards of the F140LP filter.

4.3 Synthetic spectra techniques

The way forward is to use synthetic UV-spectra of starbursts (these are either based on model atmospheres or use empirical data, the latter being more realistic but there is a general lack of data for hot stars with low metallicities and there may be contaminations from interstellar absorption lines).

High resolution synthetic stellar evolutionary spectra (M. Cerviño, private communication) were used to approximate the SED of the central cluster of the galaxy. Our aim was to try and recreate the observed spectra of ESO338-IG04. The chosen synthetic spectra were generated using a Salpeter IMF, solar metalicity and burst ages ranging from 3 to 6 Myr. We took the low-resolution STIS spectrum of the central star cluster and fitted a Voigt profile to the wings of the damped Galactic $Ly\alpha$ absorption profile (giving a Galactic HI column density of 20.7 cm^{-1}, independently confirming the value of 20.8 cm^{-1} from Galactic HI maps). This Voigt profile was then convolved with the spectrum to simulate Galactic $Ly\alpha$ absorption. We then applied Galactic reddening using the Cardelli law with values A_V=0.288 and E(B-V) = 0.087 taken from NED. We fitted the synthetic spectrum to the real spectrum, fitting parameters were burst age and internal reddening using the SMC law. The best fit synthetic spectrum was then convolved with the HST/ACS/SBC

F122M and F140LP instrument throughput profiles obtained using the SYNPHOT package in IRAF/STSDAS and synthetic fluxes in these filters were computed. The F122M-F140LP scale factor required to produce a net flux of zero in a continuum subtraction was calculated as $scalefactor = f_{F140LP}/f_{F122M}$. This method therefore gives us the scale factor depending only on the flux through the online and offline filters; totally independent of the shape of the slope at longer wavelengths. It is not dependent on the parameterisation of the continuum slope. For the central region, this gave a scale factor of 8.89 which corresponds to a β of -0.86. While significantly less negative than the value of β = -2.08 (Calzetti et al 1994), it does represent the continuum slope in exactly the region of interest.

This method works well for the bright clusters along the STIS slit where the starburst is young but is less applicable as the burst has aged. The general problem is that the aging of a burst and interstellar extinction have very similar but non-identical effects (reddening of the SED). Moreover, we need to find a method that does not rely on spectra, but allow us to use images. To do so we calculated a model for the appropriate metallicity (Z = 0.001), and Salpeter 0.1–120 $M_\odot$ IMF using the Starburst99 code (Leitherer et al. 1999). We also included nebular emission lines through the interface with Starburst99 to the "Mappings" code. The model spectra were convolved with the WFPC2 and ACS/SBC filter profiles for all burst ages from 1 to 900 Myr and for a range of reddenings from E(B−V)=0 to 0.25 using the SMC law. We then calculated the scale factor in the above manner (taking the Galactic $Ly\alpha$ absorption into account) for all grid points.

We then investigated the relation between the scale factor and observed colours using various filter combinations, i.e. we are not primarily interested in resolving the age–reddening degeneracy, but to get a correct scale factor as a function of colour, whatever its reason. We quickly concluded that a single colour index can not uniquely determine the scale factor. Based on our experience with β-maps and fitting of the spectra, this was not, of course, a surprise.

However, when using some filter combinations involving at least two different colour index, the scale factor can be tightly constrained. The best combinations in this case were F140LP-F218W vs. F336W-F439W and F140LP-F336W vs. F336W-F439W, the latter is presented here.

The model data points were used to populate a lookup table where the scale factor could be looked up from any pair of F140LP-F336W and F336W-F439W colours. In between evolutionary steps in the models (jumps in burst age), more colours and scale factors were interpolated linearly. Using this lookup table, the ACS F140LP image and WFPC2 F336W and F439W images were used to create a map of the scale factor over the whole starburst region. This scale factor map was then used to make a continuum subtraction.

A scale factor map and associated continuum subtraction are shown in Fig 6. The first continuum subtracted $Ly\alpha$ image shows excellent agreement with features in the spectrum. $Ly\alpha$ is seen in both emission and absorption across the starbusrt region. Emission is seen from knot A and the region surrounding knot C with a P-Cygni profile at knot A. Diffuse emission is seen around knot D but not emission from this knot itself. Diffuse emission is also visible in large regions outside starburst regions. These are $Ly\alpha$ photons produced elsewhere that, after multiple scatterings, manage to leave the cloud thanks to a low dust content. Little is seen around knot B which is really strong in continuum but shows almost nothing in the low-res STIS spectrum.

We are now in the process of refining this procedure and will apply it to our whole sample using available HST images. In principle the method is applicable also to ground based data of high-z $Ly\alpha$ galaxies.

5 Implications for high-redshift galaxies

In many respects, $Ly\alpha$ could be a fundamental probe of the young universe. It suffers from fewer luminosity biases than Lyman-break techniques so that $Ly\alpha$ surveys become a more efficient way to trace the fainter end of the luminosity function, i.e., it traces the building blocks of present-day galaxies in the hierarchical galaxy formation paradigm (Hu, Cowie, & McMahon 1998; Fynbo et al. 2001). Early results paint a complex picture. The equivalent widths of the sources are much larger than expected for ordinary stellar populations (Malhotra & Rhoads 2002). They could be explained by postulating an initial mass function (IMF) biased towards more massive stars, as predicted theoretically for a very metal-poor stellar population (Bromm, Coppi, & Larson 2001). The combined effect of low metallicity and flat IMF, however, can only partly explain the anomalous equivalent widths. Additional mechanisms must be at work (AGN activity?). Could spatial offsets between the escaping $Ly\alpha$ and the stellar light, together with higher extinction of the dust shrouded stars be important? Our HST spectroscopy and recent ACS imagery cautions against using the $Ly\alpha$ equivalent width as a star-formation indicator in the absence of spatial information.

The source numbers themselves are only about 10% of the numbers expected from an extrapolation of the Lyman-break luminosity function. Malhotra & Rhoads speculate if the youngest galaxies are preferentially selected, whereas older populations are excluded, the results are skewed towards large $Ly\alpha$ equivalent widths. Could dust formation after 10^7 yr destroy the $Ly\alpha$ photons? The results in the low-redshift universe suggests otherwise. We find little support for dust playing a *major* role in destroying $Ly\alpha$ photons. Rather, the ACS images favor the complex morphology as key to understanding the $Ly\alpha$ escape mechanism.

Haiman & Spaans (1999) proposed $Ly\alpha$ galaxies as a direct and robust test of the reionization epoch (see Schaerer, this conference). Prior to reionization, these galaxies are hidden by scattering of the neutral intergalactic medium (IGM). Therefore, a pronounced decrease in the number counts of *galaxies* should occur at the reionization redshift, independent of Gunn-Peterson trough observations using *quasars*. $Ly\alpha$ in galaxies would have the additional appeal of being sensitive at much higher IGM optical depths since its red *wing* coincides with the red damping wing of intergalactic $Ly\alpha$ only. While this idea is attractive in principle, our ACS imagery calls for caution. In practice, $Ly\alpha$ is a complex superposition of emission and absorption in the star-forming galaxy itself. The resulting $Ly\alpha$ profile will be strongly affected by absorption from the continuum. This becomes even more of a concern when imaging data are interpreted. When integrating over the filter bandpass, the emission part of the profile is partly compensated by the absorption. As a result, we measure significantly lower $Ly\alpha$ fluxes than with spectroscopic methods, and the escape fraction of $Ly\alpha$ photons is significantly underestimated.

The $Ly\alpha$ line is a premier star-formation tracer, in particular at high z where traditional methods, such as $H\alpha$ or the far-IR emission, become impractical. Radiative transfer effects in the surrounding interstellar gas make its interpretation in terms of star-formation rates less straightforward than often assumed. Clearly, a better understanding of the complex $Ly\alpha$ escape mechanisms, both empirically and theoretically, is required before we can attempt to interpret large-scale $Ly\alpha$ surveys. Future high-resolution imagery of local starburst galaxies may provide the necessary calibrations.

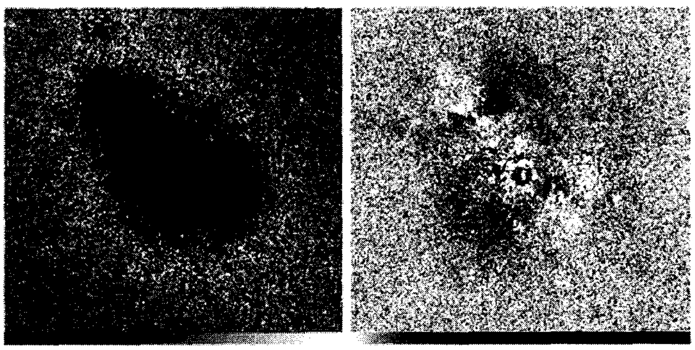

Figure 6: **Left**: Scale factor map, ramp scale. Cuts levels are set to show the interesting intensity levels: lcuts=7 (black) to hcuts=14 (white). **Right**: Continuum subtracted $Ly\alpha$ image, created using the scale factor map.

6 References

1. Bithell, M. 1991, MNRAS, 253, 320
2. Bromm, V., Coppi, P. S., & Larson, R. 2001, ApJ, 564, 23
3. Calzetti, D. 2001, PASP, 113, 1449
4. Calzetti, D., Kinney, A. L. & Storchi-Bergmann, Th. 1994, ApJ, 429, 582
5. Charlot, S., & Fall, S. M. 1993, ApJ, 415, 580
6. Deharveng, J. M., Joubert, M., & Kunth, D. 1986, in Star-Forming Dwarf Galaxies and Related Objects, ed. D. Kunth et al. (Paris: Editions Frontieres), p. 431
7. Djorgovski, S., & Thompson, D. J. 1992, in IAU Symp. 149, Stellar Populations, ed. B. Barbuy & A. Renzini (Kluwer: Dordrecht), p. 337
8. Frye, B., Broadhurst, T., & Benitez, N. 2002, ApJ, 568, 558
9. Fujita, S. S., et al. 2003, AJ, 125, 13
10. Fynbo, J. U., Möller, P., & Thomsen, B. 2001, A&A, 374, 443
11. Giavalisco, M., Koratkar, A., & Calzetti, D. 1996, ApJ, 466, 831
12. Haiman, Z. & Spaans, M. 1999, ApJ, 518, 138
13. Hartmann, L., Huchra, J. P., Geller, M. J., O'Brien, P., & Wilson R. 1988, ApJ, 326, 101
14. Heckman, T. M. 1993, in The Environment and Evolution of Galaxies, ed. S. M. Shull & H. Thronson (Kluwer: Dordrecht), p. 155
15. Hu, E. M., Cowie, L. L., & McMahon, R. G. 1998, ApJ, 502, L99
16. Kunth, D., Leitherer, C., Mas-Hesse, J. M., stlin, G., & Petrosian, A. 2003, ApJ, 597, 263
17. Kunth, D., Mas-Hesse, J. M., Terlevich, E., Terlevich, R., Lequeux, J., & Fall, S. M. 1998, A&A, 334, 11
18. Leitherer, C., Schaerer, D., Goldader, J. D., Gonzlez Delgado, R. M., Robert, C., Kune, D. F., de Mello, D. F, Devost, D., & Heckman, T. M. 1999, ApJS, 123, 3
19. Malhotra, S., & Rhoads, J. E. 2002, ApJ, 565, L71
20. Mas-Hesse, J. M., Kunth, D., Tenorio-Tagle, G., Leitherer, C., Terlevich, R. J., & Terlevich, E. 2003, ApJ, 598, 858
21. Meier, D.L. & Terlevich, R. 1981, ApJ, 246, L109
22. Neufeld, D. A. 1990, ApJ, 350, 216
23. Ouchi, M., et al. 2003, ApJ, 582, 60
24. Östlin, G., Bergvall, N. & Rönnback, J. 1998, A&A, 335, 85
25. Östlin, G., Zackrisson, E., Bergvall, N. & Rönnback, J. 2003, A&A, 408, 887
26. Partridge, R.B. & Peebles, P.J.E. 1967, ApJ, 147, 868
27. Schaerer, D. 2003, A&A, 397, 527
28. Shull, J. M., & Silk, J. 1979, ApJ, 234, 427
29. Stiavelli, M., Fall, S. M., & Panagia, N. 2004, ApJ, 600, 508
30. Tenorio-Tagle, G., Silich, S.A., Kunth, D., Terlevich, E., & Terlevich, R. 1999, MNRAS, 309, 332
31. Terlevich, E., Diaz, A. I., Terlevich, R., & Vargas, M.L. 1993, MNRAS, 260, 3
32. Thuan, T.X. & Izotov, Y.I. 1997, ApJ, 489, 623
33. Thuan, Izotov & Lipovetsky ApJ, 477, 661
34. Vader, P., Frogel, J., Terndrup, D. & Heisler, C. 1993, AJ, 106, 1743
35. Valls-Gabaud, D. 1993, ApJ, 419, 7

Evening at La Thuile

EXTREME CONDITIONS FOR STAR FORMATION IN STARBURST GALAXIES

Andrew J. Baker
Max-Planck-Institut für extraterrestrische Physik
Postfach 1312, D-85741 Garching, Germany

Almudena Alonso-Herrero
Steward Observatory, The University of Arizona
933 N. Cherry Ave., Tucson, AZ 85721, United States;
&
Departamento de Astrofísica Molecular e Infrarroja, IEM
Consejo de Investigaciones Científicas, Serrano 113b, 28006 Madrid, Spain

Linda J. Tacconi
Max-Planck-Institut für extraterrestrische Physik
Postfach 1312, D-85741 Garching, Germany

Local starburst galaxies serve as important stepping stones in propagating our understanding of star formation from the Milky Way to the high-redshift universe. Here we focus on two types of local starbursts in which certain of the preconditions and/or products of star formation are extreme– dwarf galaxies with low mass and metallicity, which exhibit massive young star clusters and intense UV radiation fields, and merging galaxies with high mass and infrared luminosity, in which the entire ISM appears to be molecular in phase. As instructive examples, we discuss the dwarf starburst NGC 5253 and the ultraluminous merger IRAS 17208–0014.

Keywords: Galaxies: ISM — Galaxies: starburst — Galaxies: star clusters

1 Introduction

As reviewed in detail by Kennicutt (1998), star formation in galaxies proceeds in two modes. The first is "quiescent": stars form at a relatively modest rate for a relatively long timescale, across the entirety of a galaxy's disk. In the second, "starburst" mode, gas is turned into stars relatively rapidly, over a spatially compact region that may represent part or all of the galaxy in which it is found. Starbursts are often triggered by external dynamical disturbances– tidal encounters, gas accretion events, or large-scale mergers– which can extract angular momentum from a galaxy's gas and drive it to small radii. Current star formation in the Milky Way is plainly proceeding in the former, quiescent mode. Critically, this statement applies to all of the local star-forming regions whose observed properties provide the bedrock for our models of how star formation proceeds on the scale of a single Giant Molecular Cloud (GMC). Whether star formation in the latter, starburst mode proceeds identically on GMC scales is an open question. To address it, we must study the initial conditions for and final products of star formation in reasonable samples of galaxies beyond the Milky Way, where both may be different from what we are able to measure in the solar neighborhood.

The basic definition of a starburst in fact encompasses a wide variety of galaxy populations. In this contribution, we focus on two [extremely different] types of systems exhibiting extreme properties of one sort or another, in which virtually the entire galaxy is participating in the burst. The first category comprises dwarf irregulars, in which low mass, often low metallicity, and a lack of spiral density waves can in the right circumstances allow the triggering of extremely intense global starbursts. The second category comprises the Ultra-Luminous Infrared Galaxies (ULIRGs: Sanders & Mirabel 1996), whose exceptional bolometric luminosities are triggered by the merger of two or more gas-rich disk progenitors. These two populations represent the low and high-mass extremes of the starburst phenomenon in the local ($D < 100\,$Mpc) universe. We focus our discussion on one illustrative example from each category– the dwarf galaxy NGC 5253, and the ULIRG IRAS 17208-0014.

2 The double star cluster in the center of NGC 5253

NGC 5253 is one of the nearest ($D = 4.1\,$Mpc) and youngest dwarf starbursts in the local universe. Its metallicity is approximately one-half solar (Storchi-Bergmann et al. 1995), and its bolometric luminosity of $\sim 2.5 \times 10^9\, L_\odot$ (Gorjian et al. 2001) is being powered by a remarkably small reservoir of molecular gas. Meier et al. (2002) estimate from CO interferometry that the gas mass available for forming stars is only a few times $10^6\, M_\odot$, of which only a small fraction directly coincides with the nuclear source responsible for most of the galaxy's $L_{\rm bol}$. Turner et al. (1997) were the first to suggest that the current burst in NGC 5253 might have been triggered by the infall of a metal-poor gas cloud along the galaxy's minor axis.

The extreme properties of NGC 5253's deeply embedded nuclear star-forming region have been the focus of a series of increasingly detailed studies over the past decade. Beck et al. (1996) and Turner et al. (1998) concluded that free-free emission from the galaxy's central regions was optically thick at 2 cm, suggesting the presence of an ensemble of ultracompact H II regions. Turner et al. (2000) and Mohan et al. (2001) concluded from independent observations of radio continuum and recombination line emission that if the power source is a UCH II region, the ionizing flux requires more than 2000 O stars to occupy a volume only 1-2 pc in diameter. Gorjian et al. (2001) used 8.7 and 11.7 μm photometry to exclude the possibilities that either a dust-enshrouded supernova or an AGN could be responsible for the system's observed luminosity. Most recently, Turner et al. (2003) measured narrow Brγ linewidths and concluded that the gas responsible for obscuring the central cluster is gravitationally bound to it.

The newest observations of NGC 5253, described in detail by Alonso-Herrero et al. (2004; hereafter AH04), have been obtained with the NICMOS camera on the *Hubble Space Telescope*. Broad-band imaging in filters approximating J, H, and K has revealed that the bright central "cluster" in NGC 5253 is in fact *double*. This conclusion is reinforced by the double morphology in NICMOS Pa$\,\alpha$ imaging, which together with H-band continuum is shown in Figure 1. The two clusters are separated by $0.3 - 0.4''$ on the sky, corresponding to 6-8 pc in projection. Broad-band colors are consistent with the evidence of 1.3 cm continuum mapping (Turner et al. 2000) in revealing the western cluster– C2 in the nomenclature of AH04– to be considerably more embedded than the eastern cluster C1. As a result, it is possible to identify C2 as the unambiguous origin of most of the "supernebula" emission seen in the mid-infrared and at all longer wavelengths.

Because the two members of the double cluster can be spatially resolved, it is possible to translate their distinct observed properties into distinct star formation histories and stellar masses. From their (identical) Pa$\,\alpha$ quivalent widths and a *Starburst99* model for an instantaneous burst with a $1 - 100\, M_\odot$ Salpeter IMF (Leitherer et al. 1999), we can conclude that both clusters have identical ages of $3.3 \pm 1.0\,$Myr. From the same model and the observed $J - H$ colors, we can estimate (assuming a foreground screen geometry) that C1 has $A_V = 2 \pm 2$ and

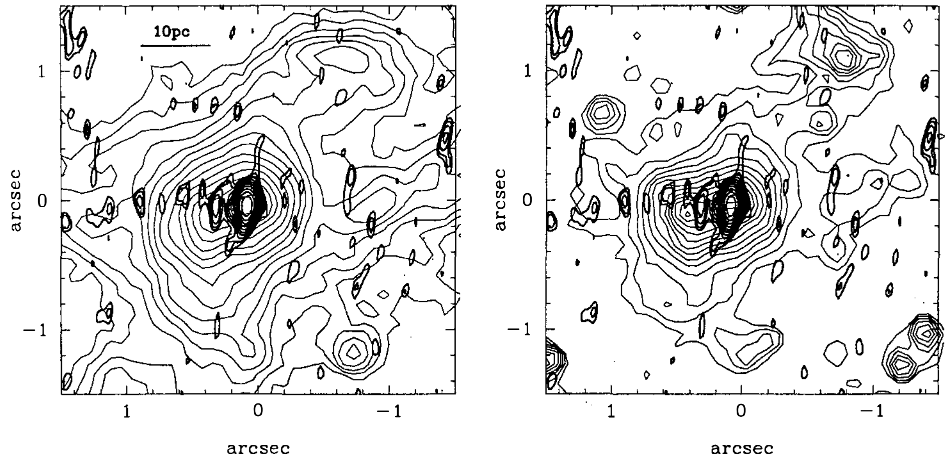

Figure 1: The central $3'' \times 3''$ of NGC 5253 (reproduced from AH04). Thin contours trace continuum–subtracted Pa α emission (left panel) and 1.6 μm continuum emission (right panel); in both panels, thick contours trace 1.3 cm continuum emission from Turner et al. (2000). North is up and east is to the left.

C2 has $A_V = 14 \pm 2$. Finally, from the population synthesis model, the inferred extinctions, and the observed H–band magnitudes, we can estimate stellar masses: $\sim 5 \times 10^4 \, M_\odot$ for C1, and from 3×10^5 to $1 \times 10^6 \, M_\odot$ for C2 (the spread for the latter results from the uncertain degree of contamination by hot dust in K). We conclude that the two nuclear clusters are twins, in the sense of being born at the same time, but are definitely *not* identical; in a situation not commonly seen in hospitals, one is a factor of ten more massive than the other.

NGC 5253 is not the only dwarf starburst galaxy to contain an extremely compact and intense star–forming region at its center; radio continuum mapping reveals $\geq 10^5 \, M_\odot$ star clusters embedded within "ultra-dense H II regions" in SBS 0335–052 (Plante & Sauvage 2002) and Henize 2–10 (Johnson & Kobulnicky 2003). In addition, NGC 5253 is not the only dwarf starburst galaxy to have formed a massive double cluster with a small separation. In NGC 1569, the bright "A" cluster has been resolved (De Marchi et al. 1997) into two components separated by $\sim$ 1.5pc in projection (for $D = 1.7$ Mpc). Although these have a common $\sim$ 5 Myr age, they can be unambiguously identified as separate structures on the basis of their clearly different stellar populations (Maoz et al. 2001). The kinematic masses of these two components are both $\sim 3 \times 10^5 \, M_\odot$ (Gilbert 2002), in the same regime that we infer for C2 in NGC 5253.

The detailed properties of all such young, close cluster pairs may represent an interesting challenge for theories of cluster formation and evolution. Fujimoto & Kumai (1997) propose that double clusters can be formed from the oblique collisions of massive molecular clouds, a scenario that can account for pair ages that are predominantly coeval in the LMC (Dieball et al. 2002) as well as in NGC 1569 and NGC 5253. However, it is not clear whether this formation mechanism can naturally account for a cluster mass ratio as high as that (10:1) seen in NGC 5253. In both NGC 1569 and NGC 5253, we would also expect the disruption of the clusters to proceed relatively quickly. de Oliveira et al. (1998) show N–body simulations of cluster interactions for a 10:1 mass ratio (albeit with a smaller total mass than we observe for C1 and C2), and find that disruption of the smaller cluster occurs on $\sim$ 10 Myr timescales for any pericenter separations less than 4.3 times the half-light radius. This threshold would almost certainly be crossed in the case of NGC 5253, meaning that whatever formation mechanism *does* account for its coeval but unequal–mass double cluster must also avoid too rapid disruption on timescales less than

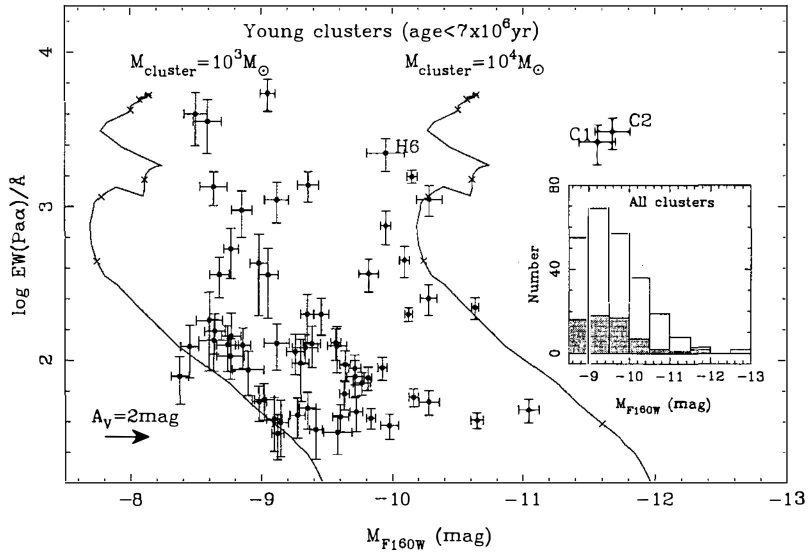

Figure 2: Paα equivalent width vs. absolute F160W magnitude for the 65 H–band selected clusters in NGC 5253 (reproduced from AH04). Theoretical curves show the predicted tracks of $10^3\,M_\odot$ and $10^4\,M_\odot$ clusters, with age from an instantaneous burst increasing from top left to bottom right (crosses mark 1 Myr intervals). The two members of the central double cluster fall well to the right– at higher masses– than the bulk of the star cluster population in this galaxy, even before correction for extinction. The inset shows the absolute magnitude distribution for all clusters (white) and young clusters (solid) in NGC 5253; the 20–30% fraction of young clusters is roughly constant in all magnitude bins.

its inferred ~ 3 Myr age.

3 Star formation across the center of NGC 5253

In addition to the nuclear double cluster, our *HST* imaging allows us to identify a number of other star clusters in the central regions of NGC 5253. Some 20–30% of all clusters selected from the H–band image have Pa α equivalent widths corresponding to ages of ≤ 7 Myr; these are plotted in Figure 2. We can combine the absolute H–band magnitudes of these sources with *Starburst99* modelling as described above to compute cluster masses. These generally lie– modulo correction for extinction– in the regime of $10^3 - 10^4\,M_\odot$. It is obvious from Figure 2 that the two members of the nuclear double cluster (plotted as C1 and C2) have masses significantly above the median for NGC 5253, even before (substantial) correction for extinction is applied. This deviation reinforces our conclusion that C1 and C2 are physically associated, rather than projected by chance along the line of sight, and were formed in a single event.

The vigorous, ongoing formation of star clusters across the central regions of NGC 5253 implies that the galaxy's interstellar radiation field should be quite intense. AH04 confirm this expectation by examining the strength of the galaxy's polycyclic aromatic hydrocarbon (PAH) feature at 3.3 μm. In general, PAH emission tends to avoid the regions of most intense star formation in starburst galaxies, due to either the photoionization or the destruction of the molecules carrying the PAH structures (e.g., Normand et al. 1995; Tacconi–Garman et al. 2004). The L–band spectra reproduced in Figure 3 show that the central regions of NGC 5253 are indeed entirely devoid of 3.3 μm PAH emission. In this respect, NGC 5253 differs from the starbursts NGC 4945 and He 2–10, and from a bright H II region in NGC 2903.

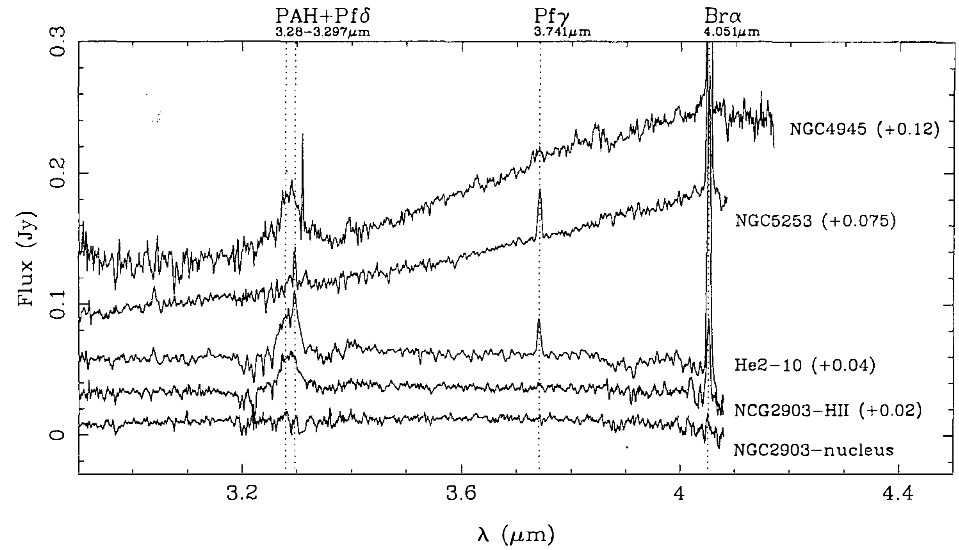

Figure 3: Integrated $3-4\,\mu$m spectra of NGC5253 and other local starburst galaxies (reproduced from AH04). The broad $3.3\,\mu$m feature present in most of these objects is absent from NGC5253 (as from the nucleus of NGC 2903), pointing to a combination of low metallicity and intense UV flux capable of destroying the PAH carriers.

NGC 5253's highly subsolar metallicity offers two likely explanations for this difference. First, massive stars forming from lower–metallicity gas naturally produce harder ionizing spectra. Second, massive stars forming from low–metallicity reservoirs may also be less effectively shielded from the rest of the ISM by dust than would be the case in $\sim Z_{\odot}$ systems. Rigby & Rieke (2004) have effectively demonstrated the latter effect by population synthesis fits to the mid–infrared spectroscopy of a broad set of starburst galaxies from Thornley et al. (2000). Of the full sample of 27, the three systems with the highest [Ne III]/[Ne II] ($15.6\,\mu$m/$12.8\,\mu$m) intensity ratios have uniformly low mass and metallicity (NGC 5253, II Zw 40, and NGC 55). Rigby & Rieke show that– even using the appropriate low–metallcity stellar atmosphere models– the intensity ratios in these systems can only be explained by a Salpeter mass function extending above $40\,M_{\odot}$. Intensity ratios in the remaining 24 starbursts can be accounted for if the ISM is ionized by a mass function cutting off *below* $40\,M_{\odot}$– as would (effectively) be the case if their highest–mass stars remain deeply embedded for most of their lives. The extreme harshness of the radiation field in NGC 5253 is thus intimately connected with other aspects of its mode of star formation.

4 The molecular gas conditions in the centers of ULIRGs

In comparison to the UV–bright starburst population that is represented by NGC 5253, ULIRGs are entirely different. Defined as having $L_{\rm IR}(8-1000\,\mu{\rm m}) \geq 10^{12}\,L_{\odot}$, they are invariably found to have the telltale signs (tidal tails, distorted isophotes, etc.) of the mergers of two gas–rich risk galaxies. They have substantial molecular gas reservoirs (e.g., Downes & Solomon 1998; Bryant & Scoville 1999), which power their enormous luminosities by a combination of intense star formation and accretion onto a central black hole in varying mixtures (e.g., Genzel et al. 1998). Because these systems are more heavily dust–enshrouded, as well as rarer and therefore more distant than UV–selected starbursts like NGC 5253, it is not possible to study them at an equivalent spatial resolution. Nevertheless, observations of their molecular ISM with millimeter

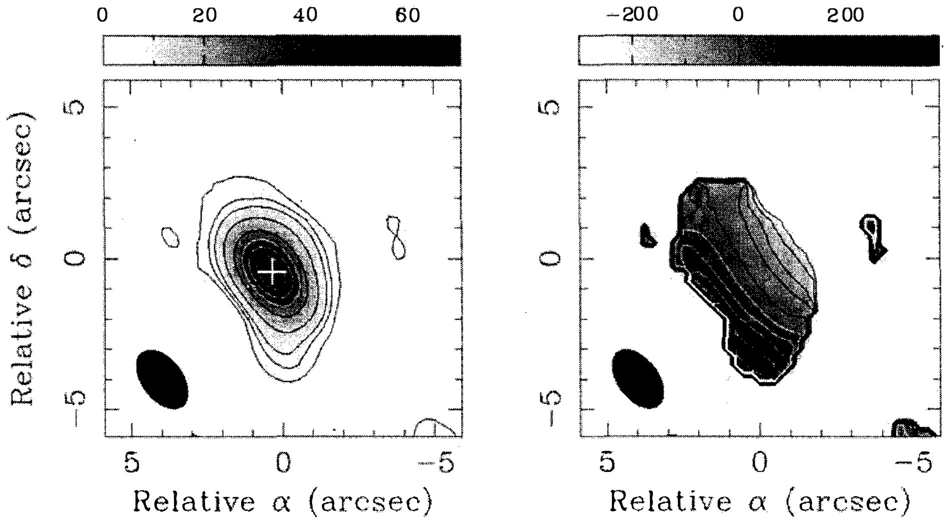

Figure 4: PdBI maps of CO(1–0) emission from IRAS 17208–0014, with ellipses showing the 2.2″ × 1.3″ synthesized beam. Left panel: zeroth moment, with contours {1,3,5,10,20,30,40,50} ×1.2 Jy beam^{-1} km s^{-1}; the cross marks the dynamical center. Right panel: first moment, with contours separated by 50 km s^{-1} steps relative to z_{sys}.

interferometers can already reveal important differences with more run–of–the–mill star–forming systems.

To illustrate what can be learned from such observations, we focus on one example from our ongoing molecular line survey of ULIRGs. IRAS 17208–0014, at $z = 0.0428$, has mid–infrared spectral properties that suggest it is primarily powered by star formation (Genzel et al. 1998). Figure 4 shows new high–resolution mapping of its CO(1–0) emission obtained with the IRAM Plateau de Bure Interferometer (PdBI); these data recover some 60% of the galaxy's total CO(1–0) line flux as measured by single–dish observations. The high (13.6 km s^{-1}) velocity resolution afforded by heterodyne spectroscopy, together with a steeply rising rotation curve, means that by fitting a parametric model to the data cube we can constrain the parameters of the molecular gas on scales that are smaller than the 2.2″ × 1.3″ synthesized beam. We have modelled this galaxy's CO(1–0) emission as an axisymmetric disk rotating in a potential assumed to be be logarithmic. We find that χ^2 is minimized for an inclination $i = 44°$, a terminal velocity $v_{\rm rot} = 262\,{\rm km\,s^{-1}}$, and an outer disk radius of $450\,h_{0.7}^{-1}$ pc (for a flat cosmology with $\Omega_\Lambda = 0.7$ and $H_0 = 70\,h_{0.7}\,{\rm km\,s^{-1}\,Mpc^{-1}}$). The dynamical mass within this radius– thanks to our modelling, no longer subject to the usual degeneracy between rotational velocity and inclination– is $7.1 \times 10^9\,h_{0.7}^{-1}\,M_\odot$.

From our measured CO(1–0) line flux (97 Jy km s^{-1}) we can infer a CO(1–0) line luminosity $L'_{\rm CO} = 8.2 \times 10^9\,h_{0.7}^{-2}\,{\rm K\,km\,s^{-1}\,pc^2}$. In the Milky Way and nearby disk galaxies of reasonably high metallicity, the conversion factor $\alpha_{\rm CO} \equiv M_{\rm gas}/L'_{\rm CO}$ is nearly constant (e.g., Young & Scoville 1991). Naively using $\alpha_{\rm CO} \simeq 4.8\,M_\odot\,({\rm K\,km\,s^{-1}\,pc^2})^{-1}$ as calibrated from the Milky Way and its nearest neighbors (and including a factor of 1.36 for helium), we would infer that IRAS 17208–0014 has a molecular gas mass of $3.9 \times 10^{10}\,h_{0.7}^{-2}\,M_\odot$. This is an unphysical factor of 5 larger than the dynamical mass enclosed within the same radius. Similarly problematic comparisons arise for other ULIRGs (e.g., Shier et al. 1994) and even Luminous Infrared Galaxies (LIRGs) satisfying only $L_{\rm IR} \geq 10^{11}\,L_\odot$ (e.g., Alonso–Herrero et al. 2001). Conflicts can be explained away for a limited number of systems– in which only $v_{\rm rot} \sin i$ has been measured– under the assumption that such cases are being viewed almost face-on and should be subject to large $\sin i$ corrections. However, it is implausible for *every* LIRG and ULIRG molecular disk to be viewed face-on, and for cases (like IRAS 17208–0014 above) in which kinematic modelling breaks the degeneracy between $v_{\rm rot}$ and $\sin i$, simple geometrical explanations are completely excluded.

The resolution of this paradox was first established by Downes et al. (1993). Use of a constant $\alpha_{\rm CO}$ in normal galaxies is predicated on the assumption that molecular line emission arises from an ensemble of small, virialized clouds whose areal filling factor within the telescope beam is small at any given velocity. In this case (e.g., Dickman et al. 1986), we have

$$\alpha_{\rm CO} = M_{\rm gas}/L'_{\rm CO} \propto \frac{\sum R_i^3\, n_i}{\sum R_i^2\, \Delta v_i\, T_i} \rightarrow \frac{\sqrt{n}}{T} \tag{1}$$

In contrast, if molecular gas is not found in discrete GMCs but instead smoothly fills the beam, the observed CO velocity width will reflect the *total* dynamical rather than merely the molecular mass, and $\alpha_{\rm CO}$ goes down in consequence, to $\simeq 0.8\,M_\odot\,({\rm K\,km\,s^{-1}\,pc^2})^{-1}$ (Downes & Solomon 1998). A similar effect may also hold, albeit at a less extreme level, in the centers of nearby disk galaxies where the ambient pressure may be high enough to maintain an ISM that is predominantly molecular in phase (e.g., Regan et al. 2001).

For ULIRGs, the parameters of the ISM in compact molecular disks correspond to mean densities $\sim 10^3\,{\rm cm^{-3}}$, which facilitate the formation of H_2 and CO molecules and more easily thermalize the CO transitions (Downes & Solomon 1998). Substantial gas masses can also reach densities of $\geq 10^4\,{\rm cm^{-3}}$ as well, which elevate the global ratio $L'_{\rm HCN}/L'_{\rm CO}$ above the levels seen in nearby disk galaxies (Gao & Solomon 2004). Large quantities of dense gas translate to high rates of star formation, and in turn to high rates of feedback: Rupke et al. (2002), for example, estimate mass loss rates in ULIRGs of $13 - 133\,M_\odot\,{\rm yr^{-1}}$ from Na D absorption-line spectroscopy. The extreme results of star formation in ULIRGs are a direct consequence of the extreme (pre)conditions for star formation prevailing in their molecular gas reservoirs. However, an important caveat is in order: with the nearest ULIRG (Arp 220) lying at a distance of 78 Mpc, it remains difficult to assess whether the formation of individual stars and star clusters in ULIRGs is *qualitatatively* as well as (in normalization) quantitatively different from the process we observe in the Milky Way.

5 Linking Galactic and extragalactic star formation

An ongoing challenge for theories of galaxy formation is understanding exactly how star formation proceeds in the youngest galaxies at the highest redshifts. The availability of starbursts with extreme physical conditions in the local universe means that we may already have a reasonably complete set of easily studied templates to use in improving our intuition. Recent case studies of high-redshift galaxies in which gravitational lensing permits the robust measurement of key physical parameters suggest such analogies may not be unreasonable. Among high-redshift populations, Lyman break galaxies (LBGs) are typically assumed to be the scaled-up analogues of local UV-bright starbursts. In the $z \sim 2.7$ LBG MS 1512–cB58, star formation appears to be proceeding in a disk with a Schmidt-law dependence on the surface density of molecular gas (Baker et al. 2004). High-redshift submillimeter galaxies (SMGs), selected on the basis of their dust luminosities, are widely considered to be the scaled-up analogues of local ULIRGs. In SMM J14011+0252, a $z \sim 2.5$ SMG, nebular emission line strengths indeed indicate (via the standard R_{23} indicator) an oxygen abundance that is supersolar on large spatial scales (Tecza et al. 2004). If these results are representative, it may not be necessary to invoke exotic modes of star formation at the redshifts ($z \sim 1 - 3$) when most of the universe's stars were formed (e.g., Dickinson et al. 2003).

A major theme of the formal talks and informal discussions at this meeting was the importance of building a bridge between studies of star formation within and beyond the Milky Way. In this regard, J. Alves proposed early in the week that astronomers' understanding of star formation physics improves with redshift– represented mathematically, that $U(\mathrm{SFP}(z)) \propto z^n$ for some $n \geq 1$. From our point of view, this seems unduly disrespectful of the enormous strides that have been made in understanding how star formation proceeds on GMC scales. Instead, we view the steepest challenge as being to propagate our understanding of star formation out of the Milky Way and into the nearest galaxies; beyond this point, provided one's definition of "local" encompasses the nearest LIRGs at $\sim 15\,\mathrm{pc}$ and the nearest ULIRGs at $\sim 100\,\mathrm{Mpc}$, local templates can be used as analogues for star formation in systems out to the very high redshifts beyond which subsolar metallicities begin to affect the formation of the bulk of the stars (e.g., Schaerer in this volume). In this view, a better description of our current plight is $U(d\mathrm{SFP}(z)/dz) \propto z^n$ for $z \leq 5$. Once the gap to the nearest galaxies is bridged, it should be possible to think of most of the universe's star formation as effectively "local."

Acknowledgments

AJB and LJT thank the scientific and technical staff at the Institut für Radioastronomie im Millimeterbereich (IRAM), which is itself supported by the INSU/CNRS (France), the MPG (Germany), and the IGN (Spain). AAH acknowledges support from NASA contract 960785 through the Jet Propulsion Laboratory, and the Spanish Programa Nacional de Astronomía y Astrofísica under grant AYA2002–01055.

References

1. Alonso–Herrero, A., Engelbracht, C. W., Rieke, M. J., Rieke, G. H., & Quillen, A. C. 2001, ApJ, 546, 952
2. Alonso–Herrero, A., Takagi, T., Baker, A. J., et al. 2004, ApJ, in press (astro-ph/0405093)
3. Baker, A. J., Tacconi, L. J., Genzel, R., Lehnert, M. D., & Lutz, D. 2004, ApJ, 604, 125
4. Beck, S. C., Turner, J. L., Ho, P. T. P., Lacy, J. H., & Kelly, D. M. 1996, ApJ, 457, 610
5. Bryant, P. M. & Scoville, N. Z. 1999, AJ, 117, 2632
6. De Marchi, G., Clampin, M., Greggio, L., et al. 1997, ApJ, 479, L27
7. de Oliveira, M. R., Dottori, H., & Bica, E. 1998, MNRAS, 295, 921
8. Dieball, A., Müller, H., & Grebel, E. K. 2002, A&A, 391, 547
9. Dickinson, M., Papovich, C., Ferguson, H. C., & Budavári, T. 2003, ApJ, 587, 25
10. Dickman, R. L., Snell, R. L., & Schloerb, F. P. 1986, ApJ, 309, 326
11. Downes, D. & Solomon, P. M. 1998, ApJ, 507, 615
12. Downes, D., Solomon, P. M., & Radford, S. J. E. 1993, ApJ, 414, L13
13. Fujimoto, M. & Kumai, Y. 1997, AJ, 113, 249
14. Gao, Y. & Solomon, P. M. 2004, ApJS, 152, 63
15. Genzel, R., Lutz, D., Sturm, E. et al. 1998, ApJ, 498, 579
16. Gilbert, A. M. 2002, Ph.D. thesis, University of California at Berkeley
17. Gorjian, V., Turner, J. L., Beck, S. C. 2001, ApJ, 554, L29
18. Johnson, K. E. & Kobulnicky, H. A. 2003, ApJ, 597, 923
19. Kennicutt, R. C., Jr. 1998, ARAA, 30, 189
20. Leitherer, C., Schaerer, D., Goldader, J. D., et al. 1999, ApJS, 123, 3
21. Maoz, D., Ho, L. C., & Sternberg, A. 2001, ApJ, 554, L139
22. Meier, D. S., Turner, J. L., & Beck, S. C. 2002, AJ, 124, 877
23. Mohan, N. R., Anantharamaiah, K. R., & Goss, W. M. 2001, ApJ, 557, 659
24. Normand, P., Rouan, D., Lacombe, F., & Tiphene, D. 1995, A&A, 297, 311

25. Plante, S. & Sauvage, M. 2002, AJ, 124, 1995
26. Regan, M. W., Thornley, M. D., Helfer, T. T., et al. 2001, ApJ, 561, 218
27. Rigby, J. R. & Rieke, G. H. 2004, ApJ, 606, 237
28. Rupke, D. S., Veilleux, S., & Sanders, D. B. 2002, ApJ, 570, 588
29. Sanders, D. B. & Mirabel, I. F. 1996, ARAA, 34, 749
30. Shier, L. M., Rieke, M. J., & Rieke, G. H. 1994, ApJ, 433, L9
31. Storchi–Bergmann, T., Kinney, A. L., & Challis, P. 1995, ApJS, 98, 103
32. Tacconi–Garman, L. E., Sturm, E., Lehnert, M., et al. 2004, A&A, submitted
33. Tecza, M., Baker, A. J., Davies, R. I., et al. 2004, ApJ, 605, L109
34. Thornley, M. D., Förster Schreiber, N. M., Lutz, D., et al. 2000, ApJ, 539, 641
35. Turner, J. L., Beck, S. C., Crosthwaite, L. P., et al. 2003, Nature, 423, 621
36. Turner, J. L., Beck, S. C., & Ho, P. T. P. 2000, ApJ, 532, L109
37. Turner, J. L., Beck, S. C., & Hurt, R. L. 1997, ApJ, 474, L11
38. Turner, J. L., Ho, P. T. P., & Beck, S. C. 1998, AJ, 116, 1212
39. Young, J. S. & Scoville, N. Z. 1991, ARAA, 29, 581

Lounge. — At last!

MODES OF STAR FORMATION IN AND AROUND INTERACTING SYSTEMS

P.-A. DUC

CNRS FRE 2591 and CEA-Saclay, Service d'astrophysique
91191 Gif sur Yvette cedex, France

Interacting systems and mergers are particularly well known for the exceptionally strong starburst that some of them – the so-called ultraluminous infrared galaxies – host in their nuclear region. The massive gas clouds that have accumulated there condense and form stars with a rate of several hundreds of solar masses per year. At such a rate the gas reservoir is exhausted within typically 100 Myr. For long, the dazzling nuclear starbursts have diverted our attention from the fact that star formation in interacting systems may be spatially extended. Other modes of star formation that are much quieter but last longer actually occur in interacting systems: in the interface region between the colliding galaxies, along tidal bridges and tails, at the tip of long tidal tails, in the so-called Tidal Dwarf Galaxies, or even in the intergalactic medium surrounding the parent galaxies, at more than 100 kpc from their nucleii. I present in this review the variety of SF modes encountered in and around interacting systems and a few numerical models that might account for them.

Keywords: Galaxies: interactions; Galaxies: starburst; Galaxies: ISM

1 Introduction

Galactic collisions are rather rare in the Local Universe, at least those involving two massive galaxies. Less than a few percent of spirals are currently involved in a tidal interaction. Why then bother studying the different modes of star formation in colliding galaxies ? First of all, major collisions where much more frequent in the past. The HST optical surveys have shown that the number of disturbed galaxies raises to several 10% at a redshift of 0.7–1 (e.g. Griffiths et al., 1994; Le Fèvre et al., 2000)[12,15]. Beside, infrared surveys indicate that a large proportion of the stars in the Universe have probably formed during a luminous infrared phase (see contribution by D. Elbaz in this volume). The fraction of interacting galaxies among the Luminous Infrared Galaxies (LIRGs) is high (Flores et al., 1999)[9]. Therefore, a significant, if not the majority, of

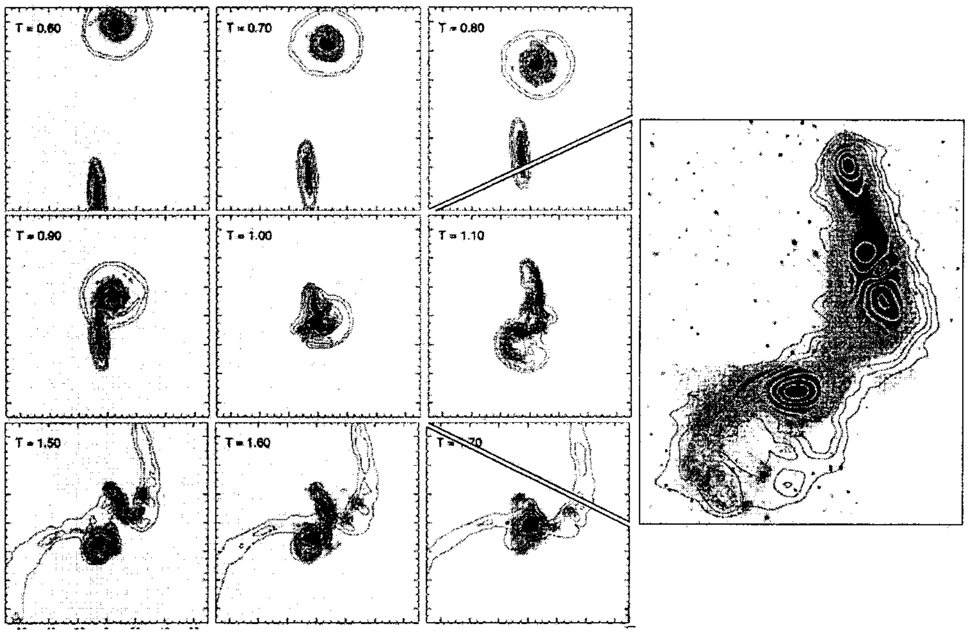

Figure 1: Simulated sequence of a galaxy collision, corresponding to the interacting system Arp 245 (NGC 2992/3). The stellar component is represented by the grayscale, and the gaseous component by the contours. The real system (inset to the right) is well matched at T=1.1 or about 100 Myr after the periapse (Adapted from Duc et al., 2000).

stars in the Universe could have been formed, triggered by a large-scale event, such as a major galaxy collision.

Second, interacting systems are rather easy to model with numerical simulations. The shape of their long tidal tails, and their kinematics, provide strong constraints on the orbital parameters of the collision (i.e., the impact parameter, relative velocities, position of the orbital planes), and on the initial conditions in the colliding galaxies (i.e., relative distributions of the stellar and gaseous components, rotational velocity, etc ...). For instance, a fast encounter at more than 500 km s^{-1} will have less impact on the morphology of the target galaxy than a slow encounter for which tidal perturbances have more time to develop. A prograde encounter (the rotation of the target galaxy and its orbital trajectory have the same direction) will produce longer and sharper tails than a retrograde encounter. Once best guesses for the initial conditions are determined, one may run a numerical model and, comparing it with the real system at different stages of the collision, estimate its dynamical age (see Fig. 1). Thus the simulations set the clock. The ability of dating some particular events associated with the collision is particularly useful and lacks in isolated galaxies. The typical time scale unit for galaxy interactions is 100 Myr. Mergers typically occur 500 Myr after the initial encounter. Long tidal tails survive for about 1 Gyr, while morphological disturbances can be seen for a few Gyr (See the comprehensive review on mergers by Struck, 1999)[30].

Finally, interacting systems appear as multiple–usage laboratories. Indeed, within one single system, one may encounter a unique variety of physical conditions that would not be accessible in an isolated spiral galaxy, starting with the most extreme conditions in the nucleii of merging galaxies. Indeed, the galaxies known to form, in the nearby Universe, stars at the highest rates (several hundreds of solar masses per year) are all advanced mergers showing a compact infrared

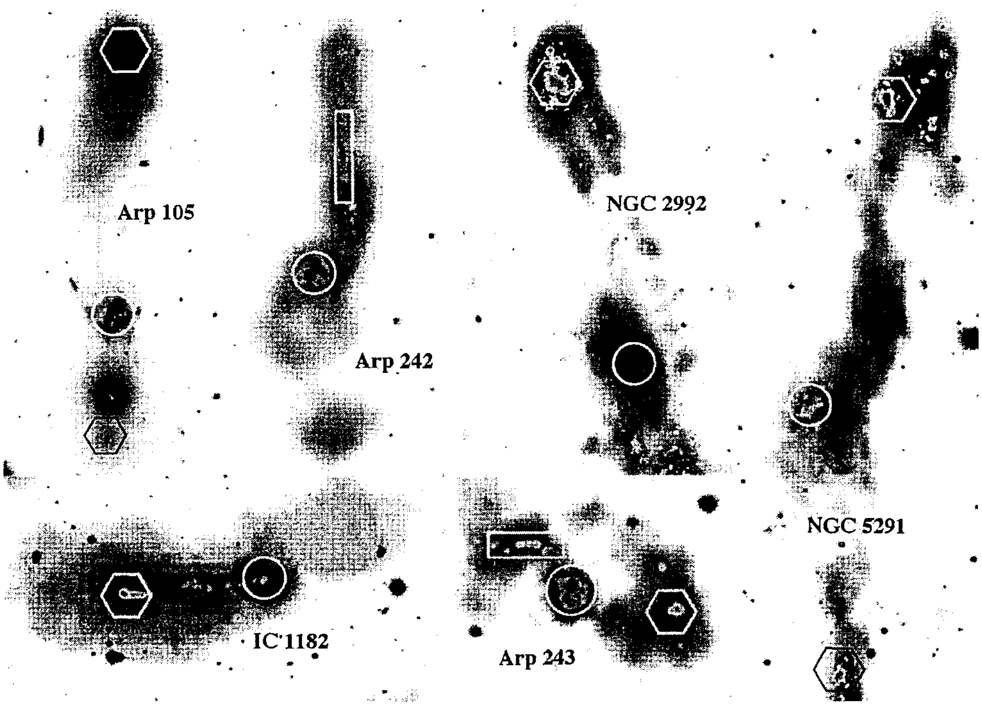

Figure 2: Composite image of six interacting systems showing the old stellar component (optical image), the atomic hydrogen (VLA HI map) and in light grey the regions of current star formation (Fabry-Perot Hα image). The nuclear starbursts are indicated by the circle, the star-forming regions along the tails by a rectangle and in Tidal Dwarf Galaxies by a polygon (HI courtesy of J. Dickey, P.–A. Duc, J. Hibbard, B. Malphrus and B. Smith)

emission excess. On the other hand, conditions in the external regions of mergers are milder, while the tip of the tidal tails may show an unexpectedly high level of activity.

In the following, we systematically explore the various conditions exhibited by mergers from the most central regions (less than 100 pc) to the most external ones (at radial distances greater than 100 kpc). Note that I do not address here the triggering of star formation by minor mergers, i.e. when the respective masses of the target and bullet galaxies differ than more than a factor of 3–5.

Fig. 2 shows a composite image of several interacting systems observed at different wavelengths. The star-forming regions in various environments are highlighted.

2 The central regions

2.1 Observations: the nuclear starburst

Soon after the discovery of the Ultraluminous Infrared Galaxies (ULIRGs) by IRAS, optical and near-infrared ground-based observations revealed that almost all of them were advanced mergers (Sanders et al., 1988)[28]. IRAS did not have the spatial resolution to pinpoint the precise location of the emitting region. It was even difficult to tell which of the two merging galaxies showed the infrared excess at 60 and 100 μm. However, studies at other wavelengths revealed that the IR emission was very compact and centered on the merging nucleii. The very good correlation between the radio and far infrared on one hand, and between the far infrared and the mid-infrared on the other ensured that the emission came from the nuclear region at all these wavelengths. For instance ground-based mid-infrared imaging in the N-band indicates that the 10 μm emission is less extended than 500 pc (Soifer et al., 2000)[29]. The 20 cm emission of ULIRGs is also very compact. It has been debated for almost 20 years whether an AGN or a nuclear starburst is responsible for the heating of the dust and subsequent IR emission (Sanders & Mirabel, 1996)[26]. Most likely, both contribute. Converted into a star formation rate, the IR emission corresponds, if powered by star-formation, to values as high as several hundreds of solar masses per year. Whether stars in these extreme conditions form with a different efficiency than in more quiescent star-forming regions is debated (see the contribution by U. Fritze in this volume). Large quantities of highly concentrated gas are available in the central dust enshrouded regions for fueling the nuclear starburst or the AGN (Sanders et al., 1991)[27]. It is most often observed in molecular phase, as if the atomic hydrogen had been compressed locally and transformed into H_2 (Mirabel & Sanders, 1989)[23]. Given the high SFRs, this gas will be rapidly consumed, typically with a time scale of only 100 Myr, i.e. much less than the time scale of the merging process. At which stage of the collision did the IR phase occur ? How the gas originally distributed all over the disks could end up in the inner 1 kpc ? Numerical simulations may once again help in answering these questions.

2.2 Simulations: transporting gas via bars

Feeling a dynamical friction, the gas which was initially in rotation in the disk of the merging galaxies looses its angular momentum, before being funneled into the central regions via stellar bars. Such a simple scenario is qualitatively very well reproduced by numerical simulations (Barnes & Hernquist, 1996)[2]. However, one single bar may only drive material in the inner kpc. A supplementary mechanism is required to push the gas further inside. The formation of a "bar within a bar", i.e. a nuclear bar (Friedli & Martinet, 1993; Maciejewski et al., 2002)[10,18] may help.

When does the nuclear starburst start ? How long does it last ? This can be studied in numerical simulations that implement simple rules for the star formation, such as a Schmidt law – the SFR is proportional to the gas density. Whereas no significant increase of the star-forming activity is observed before the first encounter between the colliding galaxies at the periapse, the SFR will either peak before or after the final merging depending on the orbital parameters and initial conditions in the merging galaxies. For instance, in a prograde/prograde encounter involving galaxies with massive stellar bulges, the starburst occurs later, after the merging occurred (Mihos et al., 1992; Mihos & Hernquist, 1994)[22,21], and the overall production of stars is less. Indeed, the strength of the bars may depend on these initial conditions. Also, as we will see later, the ability for a merging system to form or not long tidal tails is primordial. With long tails (favored by a prograde merger and a small bulge) a significant fraction of the gas can escape, leaving less gas for the central regions.

3 The interface regions

3.1 Observations: star formation in bridges and tails

Not all the star-forming regions in mergers are concentrated in the central regions. Extended star forming regions are also observed, in particular in the so-called "interface" regions of overlapping disks, in the bridges linking still well-separated galaxies, or along the tidal tails emanating from each of them. These star-forming regions are generally revealed by their blue optical color, their associated HII regions and the presence of Giant Molecular Clouds. Like in the nuclear regions, they can also be dust enshrouded – see for instance the prominent dusty condensations in the

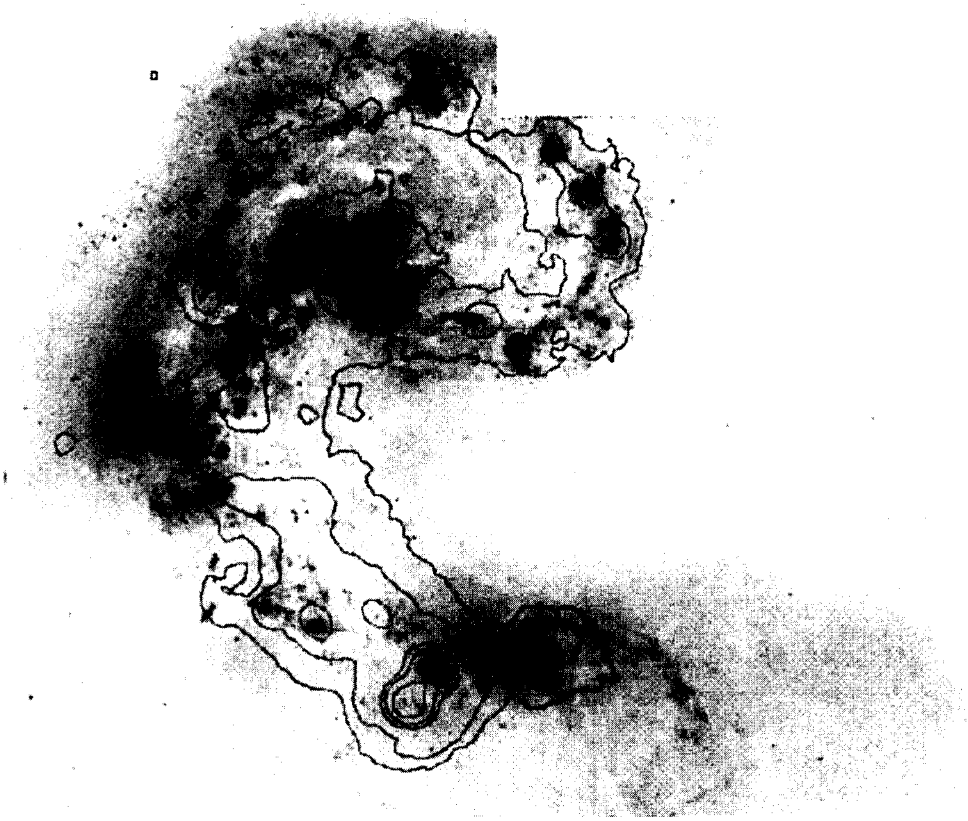

Figure 3: ISOCAM mid-infrared contours superimposed on an HST image of the Antennae (Adapted from Mirabel et al., 1998)

interface region of the Antennae shown in Fig. 3 (Mirabel et al., 1998)[24]. In some tidal tails, the Hα luminosity of individual giant HII complexes (GHCs) may even exceed that of the Giant HII Regions of normal disks (Weilbacher et al., 2003)[31]. Star formation may locally be efficient enough to produce Super Star Clusters and even Globular Clusters.

3.2 Simulations: rules for the extended star formation

Simple, density dependent models for star formation are actually not able to properly reproduce the extended SF observed in interacting systems. Pinpointing the problem, Barnes(2004)[1] recently proposed to implement a new rule for star formation that takes into account the mechanical heating due to shocks and hence direct cloud–cloud collisions. Such a model appears to be more realistic.

The formation of star–forming gravitationally bound objects along tidal tails – the possible progenitors of Super Star Clusters –, is also observed in numeral simulations (Barnes & Hernquist, 1996)[2]. They have initially typical masses of a few 10^7, up to 10^8 $M_\odot$(see also Fig. 4).

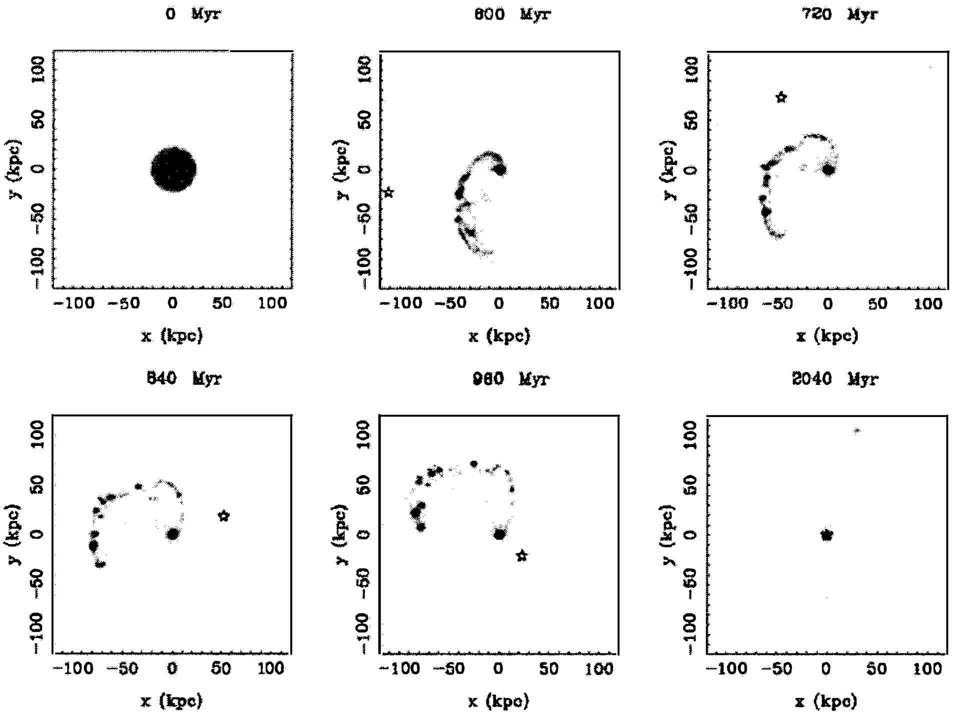

Figure 4: Formation of the Super Star Clusters progenitors along tidal tails in N-body simulations of a collision between two spirals surrounded by a truncated dark matter halo. The gas of only one galaxy is shown (from Bournaud et al., 2003)

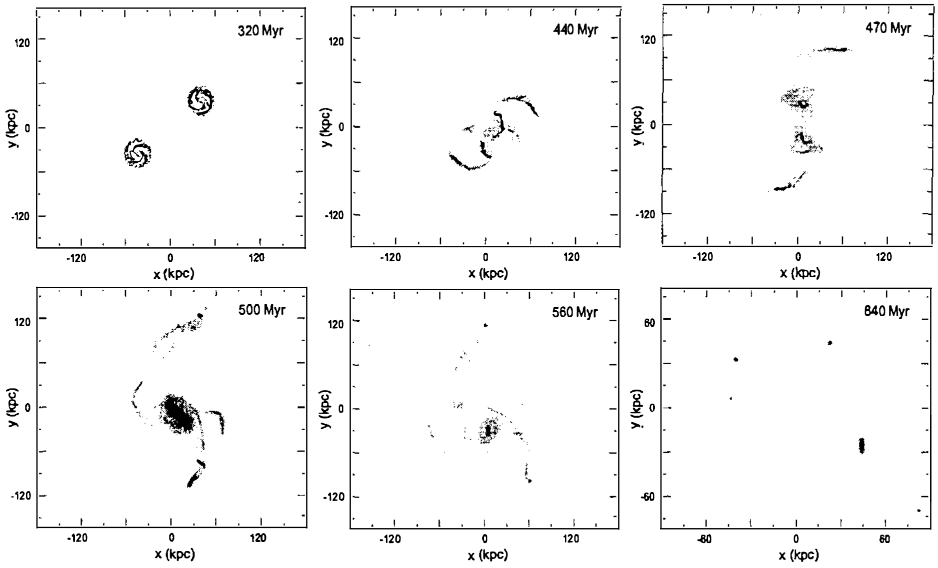

Figure 5: Formation of Tidal Dwarf Galaxies in full N-body simulations of a collision between massive spirals surrounded by an extended dark matter halo. The system is seen face-on. The gas is displayed with a logarithm intensity scale (from Duc et al., 2004)

4 The tip of tidal tails

4.1 Observations: Tidal Dwarf Galaxies

Star formation may extend even further, up to the very tip of long tidal tails, more than 100 kpc from the nucleus of the parent galaxy. There, large accumulations of tidal material were reported in several interacting systems (see a few of them in Fig. 2). As these objects have apparent masses and sizes comparable to dwarf galaxies, they are referred to Tidal Dwarf Galaxies (TDGs) (e.g. Duc et al., 2000)[8]. They contain large quantities of gas in atomic, molecular and ionized form and have luminous masses of typically 10^9 $M_\odot$ (See the contribution by J. Braine in this volume and Braine et al., 2001[5]). Because they are most often observed at or near the tip of long optical tidal tails, the very existence of such massive objects has been challenged. Indeed an apparent accumulation of tidal material could be artificial. In 3–D space, tidal tails are curved. Seen edge-on, they appear as linear structures and may show at their tip fake mass concentrations caused by material projected along the line of sight (Hibbard, 2004; Mihos, 2004)[13,20]. Kinematical studies of tidal tails help in identifying such projection effects (Bournaud et al., 2004)[3]. The spatial and velocity coincidence of the different phases of the tidal gas towards a TDG candidate adds circumstantial evidence as to its reality (Braine et al., 2001) [5].

The Star Formation Rate so far measured in TDGs vary from 0.01 $M_\odot$/yr to 0.5 $M_\odot$/yr. TDGs seem to form stars with an efficiency (defined as the ratio between the SFR and the molecular gas content) comparable to that measured in spiral disks (Braine et al., 2001)[5], i.e. less than in typical dwarf irregular galaxies. Note however that the H_2 mass in classical dwarfs, and hence the star formation efficiency, is difficult to estimate because of their low metallicity and thus weak CO emission. Having a prominent gas reservoir, TDGs can sustain star formation for more than 1 Gyr, i.e. ten times longer than the infrared luminous nuclear starburst. Therefore, in advanced mergers, the only on-going activity may actually take place at the tip of tidal tails.

4.2 *Simulations: forming proto-TDGs in extended dark matter haloes*

If the formation of bound intermediate-mass clumps along tidal tails has been reproduced in numerical simulations for more than a decade, the genesis of massive proto-TDGs at the tip of the tails has just recently been achieved by Bournaud et al. (2003)[4]. Their simulations (see Fig. 5) include extended dark matter haloes (at least ten time the stellar radii), which turned out to be a key ingredient. Indeed, within extended haloes, the tidal field can efficiently carry away from the parent disk a large fraction of the gas, while maintaining its surface density to a high value. This creates a density contrast near the tip of the tail. Otherwise, outside a truncated dark matter halo, the tidal material is diluted along the tail. Later-on, self-gravity takes over; the gas clouds collapse and start forming stars. Thus, such TDGs were fundamentally formed following a kinematical process, according to a top-down scenario (Duc et al., 2004)[7]. Their origin hence differs from the less massive Super Star Clusters that are also present around mergers, but were formed from growing local instabilities.

5 Up to the intergalactic medium

5.1 *Intergalactic HII regions*

In some specific environments, such as compact groups of galaxies or clusters, emission line regions, characterized by a very low underlying old stellar content, and sometimes by their compact aspect (the so-called *EL-Dots*) were detected even further away from their parent galaxy, in what could already be considered as the intergalactic medium (see for instance the spectacular Stephan's Quintet shown in Fig. 6) Their optical spectra are typical of star-forming HII regions (e.g. Gerhard et al., 2002; Cortese et al., 2004; Ryan-Weber et al., 2004; Mendes de Oliveira et al., 2004) [11,6,25,19]. Each individual region has a modest star-formation rate, usually of the order of 0.001–0.005 $M_\odot$/yr. Their rather high oxygen abundances indicate that they are formed of pre-enriched gas most probably stripped from spiral disks. However, contrary to the objects in stellar tidal tails, the umbilical cord linking them to their parent galaxies is much more difficult to observe, at least through the optical window. Given the distance to their progenitors and the time scale for the gas removal (at least 100 Myr), star–formation has started in situ in the IGM.

5.2 *Enriching the intergalactic medium*

The stripping of the gaseous material fueling the intergalactic star–forming regions could either be due to tidal interactions, as discussed above and/or to ram-pressure if the parent galaxy is moving through a dense medium. Because this mode of star–formation occurs outside any pre-formed local galactic potential (although in the outskirts of the dark matter halo around the parent galaxy), it should contribute to the IGM enrichment in a particularly efficient way. Indeed the supernovae ejecta are directly transfered into the IGM.

6 Back to the galaxies

6.1 *Observations: shells and rings around mergers*

Advanced mergers, such as NGC 7252, and old mergers (among them, some "disturbed" elliptical galaxies) are surrounded by stellar rings, loops and shells. These remnants of a past collision are probably tidal material falling back onto the galaxies. Their presence on optical images illustrates the fact that the most likely fate of the tidal material sent into the IGM is to simply return to their progenitors. Gravity and dynamical friction cause their orbital decay. Thus, the merger that temporarily lost part of its gas will be supplied again and able to form stars long

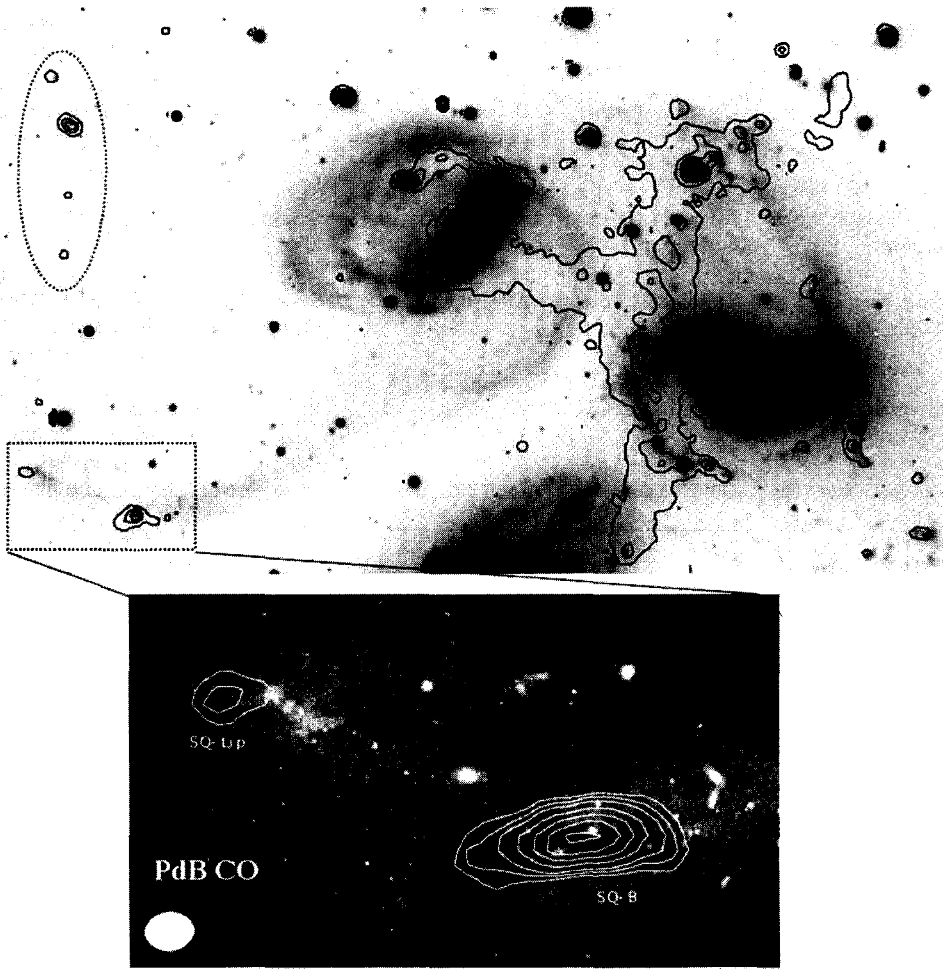

Figure 6: Star forming regions in the intragroup medium of the Stephan's Quintet. Top: Hα contours (courtesy of Jorge Iglesias-Paramo) superimposed on an optical CFHT image of the group. The location of several apparently isolated intergalactic HII regions is delineated by the ellipse. They actually lie within an extended HI structure not shown on the figure. Bottom: close-up around the SQ-B area showing the Plateau de Bure CO(1–0) contours superimposed on an HST image (adapted from Lisenfeld et al., 2004). In this region located near the tip of an optical tidal tail, large quantities of molecular gas, equivalent to the total H_2 content of the Milky Way, were found (Lisenfeld et al., 2002). The PdB CO emission closely matches the morphology of an optical dust lane and of an associated, partly obscured, HII–region. SQ–B was also detected at mid–infrared wavelengths (Xu et al., 2003). Its inferred integrated SFR is as high as 0.5 $M_\odot$/yr. Its properties resemble more those of Tidal Dwarf Galaxies than the intergalactic star–forming regions located further to the North, where no CO signal was detected.

Table 1: Modes of star-formation in and around mergers

Mode	Location	Onset Time	Duration	Triggering Mechanism
Nuclear starburst	Central regions	Between the periapse and final merger	Less than 100 Myr	Condensation of gas transported via bars
Extended Star Formation	Bridges, tails, interface region	Around the periapse	Several 100 Myr	ISM-ISM shocks
Star Formation in TDGs	Tip of tidal tails	After the periapse	Several 100 Myr	Kinematical origin + in situ collapse of massive gas clouds
Intergalactic Star Formation	In the IGM/ICM	??	10 Myr ?	Tidal or ram-pressure stripping
Delayed Star Formation	Outer regions	Soon after peripase	up to several Gyr	Return of tidal material

after the central starburst has ceased. The tidal interaction is hence responsible for a delayed SF episode.

6.2 Simulations: the return of tidal material

Using a numerical model of NGC 7252, Hibbard & Mihos (1995)[14] computed how long it takes for tidal material to fall back. They showed that this rate decreases with time but, depending on its initial location along the tidal tail, the return may take several Gyrs for material at the tip of the tail or only a few Myr for material at the base of the tail.

7 Conclusions

Table 1 summarizes the different modes of star formation taking place in and around mergers and discussed in this review. Some of them may actually be weak or absent in a given interacting system. Depending on the initial physical conditions in the parent galaxies (in particular the amount, location and kinematics of the gas reservoirs), the geometrical parameters of the collision (in particular, whether the collision is prograde or retrograde) and the large-scale environment (whether the collision occurs in a void, in a group or a cluster), one mode of star-formation or another may be favored.

One should, in any case, keep in mind that although the particularly active but short-lived nuclear starbursts have received a lot of attention, star formation in major mergers may be, spatially, extended, and, as a result, last much longer than usually believed.

Acknowledgments

I wish to thank all my colleagues working on extended star–formation in interacting systems and on Tidal Dwarf Galaxies, in particular Philippe Amram, Frédéric Bournaud, Jonathan Braine,

Elias Brinks, Vassilis Charmandaris, Stéphane Leon, Ute Lisenfeld, Frédéric Masset and Peter Weilbacher.

References

1. Barnes, J. E., 2004, MNRAS 350, 798
2. Barnes, J. E., Hernquist, L., 1996, ApJ 471, 115
3. Bournaud, F., Duc, P. ., Amram, P., et al., 2004, A&A in press (astro-ph/0406169)
4. Bournaud, F., Duc, P.-A., Masset, F., 2003, A&A 411, L469
5. Braine, J., Duc, P.-A., Lisenfeld, U., et al., 2001, A&A 378, 51
6. Cortese, L., Gavazzi, G., Boselli, A., Iglesias-Paramo, J., 2004, A&A 416, 119
7. Duc, P.-A., Bournaud, F., Masset, F., 2004, submitted to A&A
8. Duc, P.-A., Brinks, E., Springel, V., et al., 2000, AJ 120, 1238
9. Flores, H., Hammer, F., Thuan, T. X., et al., 1999, ApJ 517, 148
10. Friedli, D., Martinet, L., 1993, A&A 277, 27
11. Gerhard, O., Arnaboldi, M., Freeman, K. C., Okamura, S., 2002, ApJ 580, L121
12. Griffiths, R. E., Casertano, S., Ratnatunga, K. U., et al., 1994, ApJ 435, L19
13. Hibbard, J., Barnes, J. E., 2004, in: IAU Symposium 217, Recycling intergalactic and interstellar matter, eds. Duc, P. A., Braine, J., Brinks, E., ASP, in press
14. Hibbard, J. E., Mihos, J. C., 1995, AJ 110, 140
15. Le Fèvre, O., Abraham, R., Lilly, S. J., et al., 2000, MNRAS 311, 565
16. Lisenfeld, U., Braine, J., Duc, P.-A., et al., 2002, A&A 394, 823
17. Lisenfeld, U., Braine, J., Duc, P.-A., et al., 2004, A&A , submitted
18. Maciejewski, W., Teuben, P. J., Sparke, L. S., Stone, J. M., 2002, MNRAS 329, 502
19. Mendes de Oliveira, C., Cypriano, E. S., Sodré, L., Balkowski, C., 2004, ApJ 605, L17
20. Mihos, C., 2004, in: IAU Symposium 217, Recycling intergalactic and interstellar matter, eds. Duc, P. A., Braine, J., Brinks, E., ASP, in press (astro–ph/0401557)
21. Mihos, J. C., Hernquist, L., 1994, ApJ 431, L9
22. Mihos, J. C., Richstone, D. O., Bothun, G. D., 1992, ApJ 400, 153
23. Mirabel, I. F., Sanders, D. B., 1989, ApJ 340, L53
24. Mirabel, I. F., Vigroux, L., Charmandaris, V., et al., 1998, A&A 333, L1
25. Ryan-Weber, E. V., Meurer, G. R., Freeman, K. C., et al., 2004, AJ 127, 1431
26. Sanders, D. B., Mirabel, I. F., 1996, ARA&A 34, 749
27. Sanders, D. B., Scoville, N. Z., Soifer, B. T., 1991, ApJ 370, 158
28. Sanders, D. B., Soifer, B. T., Elias, J. H., et al., 1988, ApJ 325, 74
29. Soifer, B. T., Neugebauer, G., Matthews, K., et al., 2000, AJ 119, 509
30. Struck, C., 1999, Physics Reports 321, 1
31. Weilbacher, P. M., Duc, P.-A., Fritze-v. Alvensleben, U., 2003, A&A 397, 545
32. Xu, C. K., Lu, N., Condon, J. J., et al., 2003, ApJ 595, 665

Evening looks...

Star formation history of distant luminous infrared galaxies

D. Marcillac D. Elbaz, S. Charlot, Y. Liang, F. Hammer, H.Flores C.Cesarsky
SAp/DAPNIA/DSM/CEA Saclay
Bat. 709, Porte 230B, Orme des Merisiers
91191 Gif sur Yvette Cedex
the other adresses are given in marcillac et al (2004)

We present a determination of the recent past star formation histories of a sample of Luminous Infrared Galaxies (LIRGs) selected on their mid infrared emission thanks to Spitzer and ISO. We used a Monte Carlo simulation of 2 10^5 synthetic spectra to derive what happened in the latest Gyear. We derived a burst duration of about 0.1 Gyr which produce about 10 % of the stellar mass. Details results are given in marcillac et al (in prep).

Keywords: Stars: formation, Galaxies: evolution, interaction, starburst

1 introduction

While local galaxies radiate on average ~ 30 % of their bolometric luminosity in the $[8 - 1000\,\mu\text{m}]$ range (Soifer & Neugebauer 1991), luminous IR galaxies (LIRGs and ULIRGs) radiate more than 90 % of their light at these wavelengths. Although LIRGs ("luminous infrared galaxies", $10^{11}\text{L}_{\odot} \leq \text{L}_{\text{IR}} = L[8 - 1000\,\mu\text{m}] < 10^{12}\text{L}_{\odot}$) and ULIRGs ("ultra luminous infrared galaxies", $L_{\text{IR}} \geq 10^{12}\,\text{L}_{\odot}$) are only responsible for about 6 % of the integrated IR emission of local galaxies, their number density was already found to rapidly evolve with redshift ($\sim (1+z)^{7.6\pm3.2}$; Kim & Sanders, 1998) up to $z \sim 0.2$ from IRAS observations. The rapid redshift evolution of the number density of LIRGs and ULIRGs was later on confirmed with the ISOCAM (Cesarsky et al. 1996) and ISOPHOT (Lemke et al. 1996) instruments onboard ISO (Kessler et al. 1996) up to about $z \sim 1$ and with SCUBA for ULIRGs only but up to larger redshifts (Chapman et al., 2004).

In the local universe LIRGs and ULIRGs are associated to unusual, rare and violent events such as galaxy-galaxy strong interactions or major mergers. They show disturbed systems of several objects with recent traces of tidal interactions or of a recent merger (Sanders & Mirabel 1996) as it can be seen in the Antennae, the prototype merger of two late type spiral galaxies (Mirabel et al 1998, Vigroux et al 1996). It is therefore logical to expect that the distant population of LIRGs is due to interactions such as observed locally and indeed a large fraction of ISOCAM galaxies do show a disturbed morphology (Zheng et al. 2004).

The so-called Madau plot which presents the cosmic star formation history (CSFH) in the universe was strongly revised since its first appearance in Madau et al. (1995), where it was computed on the sole basis of UV light uncorrected for extinction. We know that most star formation in the history of the universe was hidden by dust and a strong correction for dust extinction needs to be applied to the CSFH, where LIRGs and ULIRGs appear to play a major role. IR observations (number counts, Cosmic InfraRed Background) suggest that more than half of the present-day stars formed during intense star formation events, during which galaxies appeared as LIRGs/ULIRGs to us (Chary & Elbaz 2001 and references therein). More specifically, although ULIRGs also rapidly evolve as a function of redshift, they are more extreme and rare than LIRGs which are the dominant contributors to the CIRB . It has now become clear that even though distant galaxies were less metal rich, they were forming stars in dust embedded regions such as the giant molecular clouds that we see in local galaxies.

The contribution of active galactic nuclei (AGNs) to the IR luminosity of these distant LIRGs was found to be less than 20 % by combining mid-IR with hard X-ray observations from the Newton and Chandra X-ray observatories (Fadda et al. 2002).

The present study shows that absorption lines such as the combination of Balmer absorption lines with the 4000Å break provide strong constraints on both the intensity and the duration of the burst, in addtition to what roughly happened in the last Gyears. Our strategy is similar to the one employed by Kauffmann et al. (2003) to derive the recent star formation history of SDSS (Sloan Digital Sky Survey).

2 sample selection

The sample of distant LIRGs we have studied was selected from three deep ISOCAM 15 μm surveys (Liang et al, 2004). One hundred and five galaxies were selected on the basis of their 15 μm flux density in three different regions of the southern hemisphere, hence avoiding a strong contamination by cosmic variance: the ISOCAM Ultra-Deep Surveys in the FIRBACK (UDSF) and ROSAT (UDSR) fields and the CFRS 3^h field. All three fields were selected for their low cirrus contamination and high galactic latitude. The UDSF (9 arcmin $\times$9 arcmin) is located at the center of the "far infrared background" survey at 175 μm with ISOPHOT onboard ISO ('FIRBACK'; Puget et al. 1999, Lagache & Dole 2001). The UDSR is centered at the position of a deep ROSAT survey (Zamorani et al. 1999). The UDSR and UDSF are both close to the position of the so-called 'Marano Field' originally selected for an optical survey of quasars (Marano et al. 1988), but are separated by 21 arcmin with respect to each other. The third field is one of the Canada France Redshift Survey fields (CFRS 3^h) combining deep infrared, optical and radio data as well as spectra from the MOS multiobject spectrograph on the 3.6m CFHT.

The observations were performed during three nights with FORS2 on the ESO-VLT with the combination of the grisms R600 and I600 to cover the wavelength range 5000 to 9200 Å at a resolution of 5 Å (R=1200). At the median redshift of the objects of $z \sim 0.6$, the resolution is equivalent to 3 Å (R=2000).

The data reduction was performed using IRAF packages (Liang et al, 2004).

We applied a wavelet transform analysis to increase the signal to noise ratio of the absorption lines.

In the following, we will only use spectra with a signal to noise $\geq$ 3.0 in the absorption lines which reduced our sample to 22 galaxies.

3 How to study the past star formation of distant LIRGs

3.1 Presentation of the Balmer absorption lines and D4000

The 4000 Å break (D4000) is created by absorption lines located in the narrow 4000 Å region; it is the biggest discontinuity observed in a galaxy optical spectrum. It is mainly sensitive to temperature and metallicity : metals in the atmosphere of O and B stars are strongly ionised hence producing a weaker opacity and 4000 Å break. Reversely with decreasing atmospheric temperatures metallic ions become less ionised and stars exhibit a D4000 rise, which is therefore a good tracer of age. However, D4000 rises strongly only around one Gyr and after; therefore it is mostly an indicator of the oldest stellar population. In order to trace back the recent star formation history of galaxies, it is necessary to use another tracer of stellar age such as the Balmer absorption lines.

The Balmer absorption lines are dominantly produced by the atmosphere of A to G stars. However O and B stars, which do not exhibit strong absorption lines, indirectly affect them by diluting them in the continuum. We used the $H8$ (3889 Å), $H9$ (3835 Å) and $H\delta$ (4101 Å) Balmer absorption lines and checked that they provide consistent results. The two former lines present the advantage to be located at lower wavelengths, hence accessible to higher redshifts and are less affected by the underlying nebular emission lines. While the $H\delta$ pseudo–equivalent width indice is already defined in the Lick system (Worthey & Ottavianni 1997), we had to define new indices for the high order Balmer absorption lines. We have primarily used $H8$, which is better determined for most of our spectra . Before measuring these absorption features, we have corrected them from the underlying nebular emission line (unless impossible, which we indicate in the paper).

To illustrate the time evolution of these features, we have synthesized a single stellar population without extinction using the latest version of the 'GALAXEV' code from Bruzual & Charlot (2003).

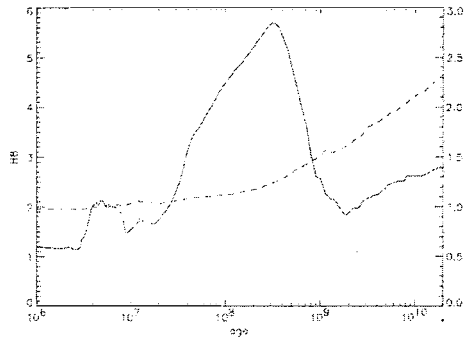

Figure 1: Time evolution of H8 and D4000 for a single stellar population synthesized with the GALAXEV Code (Bruzual & Charlot 2003) for a solar metallicity. **Solid line : H8. Dashed line : Hδ**

This version presents the important improvement of including the spectral library STELIB whose spectral resolution is $3\AA$ across the whole range from 3200 to 9500 $\AA$, i.e. a resolution equivalent to our data in the rest-frame of the galaxies. Fig. 3.1 presents the evolution with time of the H8 absorption lines and and the 4000 $\AA$ break for a solar metallicity.

3.2 Presentation of the simulations

We performed a Monte Carlo simulation to try to recover the past star formation of our LIRG galaxies. Wesynthesized model spectra for 2 10^5 objects with different star formation histories in order to compare their D4000 and H8 features.
The model spectra were synthesized assuming a combination of continuous star formation ($SFR^{cont}(t) \propto exp^{-\gamma t_{Gyr}}$ where γ is a parameter to define) and several bursts at random times. The burst of star formation rate is supposed to be constant during a burst duration of τ_B. The fraction of stars created during the burst, f_B, is defined as the ratio of the mass of stars formed during the burst over the mass of stars formed by continuous star formation since its formation, $M_\star^{cont}$. Note that $M_\star^{cont}$ is equal to the integrated mass of stars born through the continuous star formation without accounting for the gas returned to the ISM by evolved stars , hence it is larger than the real stellar mass of the galaxy at the time, t_{form}, of the observation. We also defined a range of metallicity, attenuation and velocity dispersion for each synthesized galaxy: in fact adaptated priors must be chosen for each free parameter, because if only few model spectra are generated assuming that the galaxies are presently experimenting a strong burst of star formation, this possibility will be under-represented, which may lead to a bad estimation of the parameters we want to constraint.
Since LIRGs are thought to be strong IR emitters and then, hightly extincted, we needed to include the effect of dust in the simulations. Dust attenuation was introduced following the attenuation law described in Charlot & Fall (2000) which assumes a differential attenuation depending on the age of the stars. Stars younger than 10^7 years, the typical lifetime of a giant molecular cloud (GMC), are assumed to be embedded by dust in their parent GMC with an optical depth τ_λ which is defined as a power-law function of λ. On the contrary, stars older than this timescale are supposed to have escaped their parent GMC and their ambient medium's optical depth is assumed to be μ times smaller. This extinction law presents the advantage to reproduce well the correlation observed for UV selected starbursts of the FIR over UV ratio with the UV slope, β, as well as the $L_{H\alpha}$ over $L_{H\beta}$ ratio.
We have then calculated a χ^2 using D4000 and H8 to put constraints on the burst duration and strength. The other parameters do not play a role as strong as the burst parameters . This technique will provide probability distribution functions (PDF) for these two parameters. Figure 1 shows a simulation whose priors cover a range of typical field galaxies, while in figure 2 the parameters were optimized to sample the locus of the distant LIRGs.

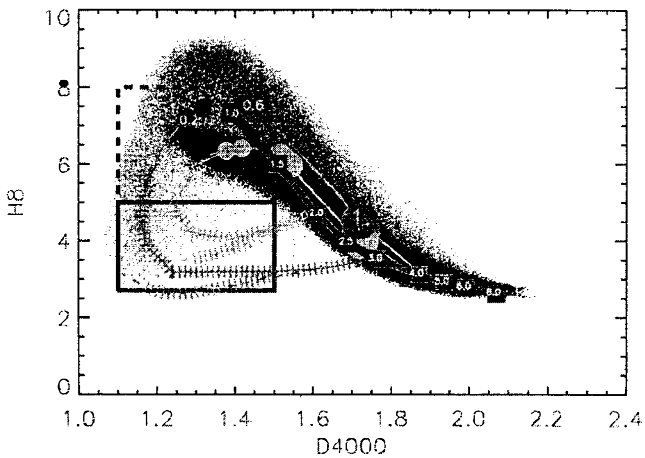

Figure 2: Monte-Carlo simulation of 200 000 virtual galaxies (individual points) plotted in the H8 versus 4000 Å(D4000) break for a range of parameter typical of field galaxies. **Light grey points (lower-left):** starbursting galaxies. **Dark grey points (upper part):** post-starburst galaxies (starbursts which have finished to burst in the past two Gyears). **Dark points:** galaxies whith a continuous star formation in the two past Gyears. **Bold line:** track followed by an individual galaxy with continuous star formation (numbers in squares= age in Gyr) generated with GALAXEV (γ=4, μ=0.3, τ_V=3.0,V_{disp}=200 km.s^{-1}). **loops:** effect of starburst of 5×10^7 (dashed line) and 10^8 (plain line) years starting after 2 Gyr (light orange) and 3 Gyr (dark orange) of continuous star formation. The line is hatched during the starburst phase. The size of the orange dots is proportional to the time counted in 10^8 years unit after the beginning of the burst. **The dark rectangle with a dashed line:** area where are located the distant LIRGS. **The dark rectangle with a solid line:** area where are lying 75 % of the sample (see Fig. 3 for the position of the individual galaxies with error bars).

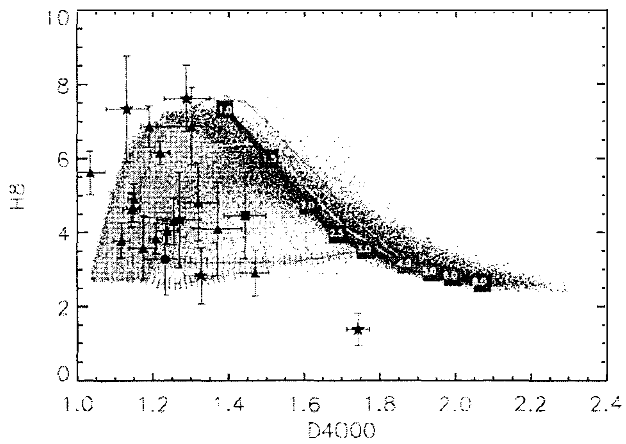

Figure 3: onte-Carlo simulation of 200 000 virtual galaxies whose priors better sample the locus of distant LIRGs. The distant LIRGs are represented with green points with error bars. **Triangles:** galaxies corrected for the underlying nebular emission line in H8 derived from the observed lower order Balmer emission lines corrected for extinction from the Balmer lines ratio. **Stars:** galaxies with negligible emission Balmer line in emission, hence uncorrected because no effect on the H8 absorption line EW. **Square:** corrected for the underlying H8 emission line using only one Balmer emission line available, hence the dust attenuation was computed from the IR (from the ratio of SFR(IR) over SFR(Hβ)). **Circle:** no correction for the underlying potential emission line because no information available on the Balmer emission lines.

4 Results

We performed the previously described analysis for galaxies which presented a signal to noise ratio greater than 3 for H8 which lead to 22 galaxies. Here are presented the mean values of several parameters.

4.1 The Scalo parameter

The Scalo parameter, i.e. the present SFR divided by the mean SFR averaged over the whole lifetime of a galaxy, measures the relative intensity of the present star formation activity in the galaxies. The Monte Carlo realizations which are favoured by the bayesian analysis converge to a clear determination for 14 of the 22 distant LIRGs. The best-fit models to the data exhibit a SFR/<SFR>$\sim$ 5$\pm$3 (1-σ). This indicates that these galaxies are experiencing a major phase of star formation in their lifetime, during which they form stars on average five times faster than averaged over their lifetime. This result is consistent with the large $L_{\rm IR}$ and SFR(IR) of these galaxies of several ten solar masses per year.

4.2 Duration of the burst of star formation

Only 20 % of the sample have a burst duration greater than 3 10^8 years, while 80 % of them peak around 10^8 years. In fact, the galaxies with a long burst of star formation can be also explained by 2 burst of about 10^8 years separated by a few 10^8 years.

4.3 Fraction of stars created during the burst of star formation

We were able to calculate a lower limit to $f_{\rm B}$ for only 7 galaxies because its determination requires a good detection of both the young and the old population of stars. Consequently it is only possible to determine the amount of stars created for galaxies which have just started a burst, i.e the young population does not dominate too strongly the optical emission. As a result, the burst fraction for these galaxies is very low, i.e 2-5 %.

One can predict the average stellar mass fraction born during the starburst taking place in distant LIRGs by assuming their SFR_{IR} to be constant during their burst duration ; we derive a real burst fraction f_B of 10 %. Note that this fraction is the ratio of the mass of stars born during the stars over the actual mass of the galaxy, which is not the one defined in the Monte Carlo code but the one which is observed.

4.4 The multiple burst scenario

A sub-sample of galaxies lying on the upper-left side of the Fig. 2 are better reproduced when including a series of two successive bursts in the model, so that they are detected during the second burst. In the local universe, LIRGs and ULIRGs show the morphological signature of galaxies in the process of merging (Borne et al, 1999, Sanders et al, 1988) and simulations of such processes predict that the two galaxies cross each other several times inducing a series of several bursts (Mihos & Hernquist, 1994). In order to quantify the probability that the distant LIRGs studied here experienced another starburst prior to the present one, we have specifically designed another Monte Carlo simulation with the same parameters as in figure 2, but forcing the presence of previous burst during the last 2 Gyrs of the galaxy lifetime for a fraction of the Monte Carlo realizations.

Galaxies in the central part of the diagram, i.e 80 % of the sample, present a probability that a previous burst ended up less than 1 Gyear ago which is lower than 20 %. On the contrary, this probability rises to more than 50 % for the galaxies located in the upper left part of figure 2. Consequently the majority of our LIRGs do not exhibit a stong episode of star formation just before the one which is observed. This result is consistent with the fact that LIRGs do not exhibit the strongly perturbed morphology often seen for ULIRGs (Zheng et al. 2004). Their strong starbursts may instead be triggered by tidal effects and minor mergers in regions of the universe where the local density of galaxies is larger as suggested by Elbaz & Cesarsky (2004) and Elbaz & Moy (2004).

References

1. Adelberger, K. L. & Steidel, C. C., 2000, ApJ, 544, 218
2. Bruzual, G. & Charlot,S.2003, MNRAS, 344, 1000
3. Cesarsky, C.J., *et al.* 1996, A&A, 315, L32
4. Chary, R., Elbaz, D., ApJ, 2001, 556, 562
5. Charlot & Fall 2000, ApJ, 539, 518
6. Chapman et al, 2004, ApJ, 606, 85
7. Elbaz, D., Cesarsky, C.J., 2003, Science, 300, 270
8. Fadda, *et, al.*, 2002, A&A, 383, 838
9. Kauffmann, G. *et, al.* 2003, MNRAS, 341, 54
10. Kessler, M., *et, al.* 1996, A&A, 315, L27
11. Kim, D.-C., Sanders, D.B. 1998, ApJS, 119, 41
12. Lagache, G., Dole, H. 2001, A&A, 372, 702
13. Lemke, D., et al 1996, A&A, 315, L64
14. Liang, Y.C., *et, al.*, 2004, A&A, 423,867
15. Madau, P., *et, al.*, 2000, MNRAS, 312, L9.
16. Marcillac, D., *et, al.*, in prep
17. Mirabel, I. F.,*et, al.* 1998, A&A, 333, L1
18. Moy, E., *et, al.*, in prep
19. Puget, J. L., *et, al.* 1999, A&A, 345, 29P
20. Sanders, D.B., & Mirabel,I.F. 1996, ARA&A, 34, 749
21. Soifer, B. T., & Neugebauer, G. 1991, AJ, 101, 354
22. Vigroux, L., *et, al.*, 1996, A&A, 315, L93
23. Worthey, G., Ottavianni, D.L. 1997, ApJS, 111, 377
24. Zamorani, G., *et, al.*, 1999, A&A 346, 731
25. Zheng, .,Z., *et, al.*, 2004, A&A, 421, 847

**The Initial Conditions to Star Formation:
Low-Mass Star Formation at Low Metallicity**

Martino Romaniello

European Southern Observatory
Karl-Schwarzschild-Strasse 2
D-85748 Garching b. Muenchen, Germany

We summarize the current status and future developments of an on-going effort to identify and characterize the properties of low-mass ($\sim 1\ M_\odot$) pre-Main Sequence stars with sub-solar metallicity ($\sim Z_\odot/3$). The selection criteria of the sample are presented, together with selected properties of the candidate pre-Main Sequence stars: • the spatial distribution, which is conclusively less clustered than that of the high mass stars of the same young generation; • the accretion rate onto the central star, which is found to be significantly higher than in the Galaxy; • and the Initial Mass Function, with a logarithmic slope $\Gamma \gtrsim -1.7$. The systematic uncertainties on this latter quantity are thoroughly discussed.

Keywords: Stars: formation, Stars: mass function, Stars: pre-main sequence, Galaxies: Large Magellanic Cloud, Galaxies: stellar content

1 Introduction

The processes at play during star formation determine much of the appearance of the visible Universe. The shape of the stellar Initial Mass Function (IMF) and its normalization (the star-formation rate) are, together with stellar evolution theory, key ingredients in determining the chemical evolution of a galaxy and its stellar content. Yet, our theoretical understanding of the processes that lead from diffuse molecular clouds to stars is still very tentative, as many complex physical phenomena concur in producing the final results. While clear variations in the star-formation rate are observed in different regions of the Milky Way and in external galaxies, with their histories showing bursts and lulls (e.g., Tolstoy 2003), the observational evidence for (or against) variations in the IMF is often contradictory

From an observational standpoint, most of the effort to characterize and understand the process of star formation has traditionally been devoted to nearby Galactic star-forming regions, such as the Taurus-Auriga complex, Orion, etc. If this, on the one hand, permits one to observe very faint objects at the best possible angular resolution, on the other it is achieved at the expense of probing only a very limited set of initial conditions for star formation (all these clouds have essentially solar metallicity, e.g., Padget 1996).

With a typical metallicity of about a third of the solar value (e.g., Hill et al 1995, Geha et al 1998, Cole et al 2000) the Large Magellanic Cloud (LMC) provides an ideal environment to study low-mass young stars:

- with a distance modulus of 18.57 ± 0.05 (see the discussion in Romaniello et al 2000), the LMC is our closest galactic companion after the Sagittarius dwarf galaxy. At this distance one arcminute corresponds to about 15 pc and, thus, one pointing with a typical imaging instrument comfortably covers almost any star forming region in the LMC (10 pc see, e.g., Hodge 1988);

- the depth of the LMC along the line of sight is negligible, at least in the central parts we consider (van der Marel & Cioni 2001). All of the stars can, then, effectively be considered at the same distance, thus eliminating a possible spurious scatter in the Color-Magnitude Diagrams;

- the extinction in its direction due to dust in our Galaxy is low, about $\mathrm{E(B-V)} \simeq 0.05$ (Bessell 1991) and, hence, our view is not severely obstructed.

Studying the effects of a lower metallicity on star formation is also essential to understand the evolution of both our own Galaxy, in which a large fraction of stars were formed at metallicities below solar, and what is observed at high redshifts. As a matter of fact, the global star formation rate appears to have been much more vigorous at $z \simeq 1.5$ than it is today (Madau 1996 and subsequent incarnations of the so-called "Madau plot"). At that epoch the mean metallicity of the interstellar gas was similar to that of the LMC at present (e.g., Pei, Fall & Hauser 1999). This fact makes the study of star forming regions in the LMC especially important for the understanding of galaxy evolution.

Here we will concentrate on the detection and characterization of solar-type pre-Main Sequence (PMS) stars around SN 1987A in the LMC. We have chosen this particular field for several reasons: the occurrence of a type II supernova ensured the presence of a young generation of stars, the mild crowding, which allows for accurate photometry and, finally, the availability of superb data originally designed to study the Supernova itself.

2 Observations and data reduction

The field of SN 1987A in the LMC was repeatedly imaged over the years with the WFPC2 onboard the HST to monitor the evolution of its Supernova remnant. We have taken advantage of this wealth of data and selected from the HST archive a uniform dataset providing broad-band coverage from the ultraviolet to the near infrared, as well as imaging in the Hα line. A description of the camera and its filter set can be found in Heyer et al (2004). All images are centered with the Planetary Camera chip on SN 1987A ($\alpha_{2000} = 05:35:28.26, \delta_{2000} = -69:16:13.0$), but have different position angles on the sky, resulting in complete coverage of an almost circular region of 130″ (about 30 pc) in radius.

The data were processed through the standard Post Observation Data Processing System pipeline for bias removal and flat fielding. In all cases cosmic ray events were removed combining the available images after accurate registration and alignment.

The plate scale is 0.045 and 0.099 arcsec/pixel in the Planetary Camera and in the three Wide Field chips, respectively. We performed aperture photometry following the prescriptions by Gilmozzi (1990) as refined by Romaniello (1998), *i.e.* measuring the flux in a circular aperture of 2 pixels radius and the sky background value in an annulus of internal radius 3 pixels and width 2 pixels. Due to the undersampling of the WFPC2 Point Spread Function, this prescription leads to a smaller dispersion in the Color-Magnitude Diagrams, *i.e.* better photometry, than PSF fitting for non-jittered observations of marginally crowded fields (Cool & King 1995, Romaniello 1998). Photometry for the saturated stars was recovered by either fitting the unsaturated wings of the PSF for stars with no saturation outside the central 2 pixel radius, or by following the method developed by Gilliland (1994) for the heavily saturated ones. The flux calibration was done using the internal calibration of the WFPC2 Whitmore (1995), which is typically accurate to within 5% at optical wavelengths. The spectrum of Vega is used to set the photometric zeropoints (VEGAMAG system).

2.1 From magnitudes and colors to luminosity and temperature

Once the observed fluxes of the stars are carefully measured, we derive their intrinsic properties, *i.e.* luminosity and temperature, as well as the extinction caused by the intervening interstellar dust along the line of sight, using the prescriptions developed by Romaniello et al (2002). The intrinsic stellar parameters and their associated errors are derived with a minimum χ^2 technique by comparing the observed magnitudes to the ones expected based on the theoretical stellar atmosphere models of Bessel et al (1998) computed in the HST-WFPC2 bands using the IRAF *synphot* task. In order to cope with the effects of interstellar dust we have used the the extinction law appropriate for this region of the LMC (Scuderi at al 1996). Let us stress here that, by convolving the theoretical spectra with the filter sensitivity curves provided in IRAF, we ensure that the observations are faithfully modeled. In particular, the red leak that affects the WFPC2 F336W (U-band-like) filter is properly taken into account.

The dereddening method is extensively described in Romaniello et al (2002), but let us briefly summarize it here:

1. stars for which both $E(B-V)$ and T_{eff} can be simultaneously derived are selected according to their small photometric error and their location in the Q_{UBI} vs $(U-I)$ plane. Q_{UBI} is a reddening-free color defined as:

   $$Q_{UBI} \equiv (U-B) - \frac{E(U-B)}{E(B-I)}\,(B-I)$$

   This color-based selection is aimed at solving the possible non-monotonicity of broad-band colors with temperature (see, for example, Allen 1973). The stars for which $E(B-V)$ and T_{eff} can be derived simultaneously turn out to be hotter than 10,000 K or between 6,750 and 8,500 K.

   Also, a star's location in the Q_{UBI} vs $(U-I)$ plane provides a first guess of its temperature and reddening;

2. for the stars selected in step 1, $E(B-V)$, T_{eff}, L and their associated uncertainties are derived starting from the first guesses by performing a minimum χ^2 multi-band fit of synthetic colors from Bessel (1998) to the observed magnitudes;

3. for each star for which $E(B-V)$ and T_{eff} cannot be derived simultaneously because of its intrinsic temperature and/or too large errors, the reddening is set as the mean of the ones of its 4 closest neighbors with direct reddening determination. The corresponding rms is used as an estimate of the uncertainty on the adopted value of $E(B-V)$. The effective temperature, luminosity and associated errors are, then, derived from a minimum χ^2 multi-band fit.

In the case of the field discussed here, there is, on average, one star with direct $E(B-V)$ determination every 13 arcsec^2. Of course, it is possible that a few stars have, in reality, extinction values significantly different from the local mean, but the global effect is negligible.

The errors on $E(B-V)$ and T_{eff} are computed from the χ^2 maps and propagated to the luminosity. A full discussion on the errors is reported in Romaniello et al (2002), but it is important to keep in mind here that the procedure outlined above does not introduce any systematic errors on the derived stellar parameters.

The resulting HR diagram for the field of SN 1987A is displayed in Figure 2, together with selected stellar isochrones. As it can be seen, the most luminous stars in the field have an age of about 12 Myrs.

3 Selection of candidate PMS stars

The task of identifying the candidate PMS stars is a particularly challenging one because they have the same optical broad-band properties as the much older population (1 Gyr of age and older) of stars of comparable mass ($1-2\ M_{\odot}$) that constitute the diffuse population in the LMC (cfr. the HR diagram in Figure 2). As a diagnostics of their PMS nature, then, we use two well-known features of Galactic Classical T Tauri stars, namely the Hα and Balmer continuum excesses[a].

Both the Balmer continuum and Hα emissions are thought to be linked to the accretion process from the circumstellar disk (e.g., Calvet et al 2002). As such, a correlation is to be expected between these two quantities. In Figure 1 we plot the excess Balmer emission versus the one in Hα: $m_{\mathrm{F336W,obs}}$ is the observed magnitude in the HST-WFPC2 F336W, *i.e.* U-band-like, filter $m_{\mathrm{F336W,mod}}$ is the corresponding photospheric one from the models of Bessel et al (1998), while the ($m_{\mathrm{F675W}} - m_{\mathrm{F656N}}$) color measures the H$\alpha$ equivalent width. Indeed, the correlation between U and Hα activity is apparent, providing a very important sanity check as to the pre-Main Sequence nature of these stars.

The location in the HR diagram of the stars with Balmer continuum excess is displayed in Figure 2 as black dots, overlaid on the general stellar population (grey squares).

Of course, this selection criterion based on Hα and/or Balmer continuum excess does not provide a complete census of all of the PMS stars in the field. Rather, it privileges stars with high enough excesses to be detectable in our data. It would be highly desirable to use X-ray observations to select the PMS stars, a technique that has proven to be extremely successful in identifying low-mass PMS stars in Galactic star-forming regions. Regrettably, though, the current generation of X-ray instruments do not have enough sensitivity to reach as far out as the LMC.

4 The properties of candidate PMS stars in the LMC

4.1 The spatial ditribution

In Figure 3 we display the spatial distribution of massive stars, *i.e.* stars with M>6 M$_{\odot}$, and candidate PMS stars as defined above through their Hα excess ($M \lesssim 2\ M_{\odot}$). We see that massive stars are strongly concentrated near SN 1987A (14 out of a total of 55 are within 20$''$ of the supernova), and that 31 out of the remaining 41 are mostly located East of SN 1987A. The PMS stars, on the other hand, do not show any strong spatial concentration, although one

[a]Only stars with a measured Hα equivalent width larger than 3 Å, or ($m_{\mathrm{F675W}} - m_{\mathrm{F656N}}$) > 0.15, are considered. Emission below this threshold could be contaminated by normal chromospheric activity (Frasca & Catalano 1994).

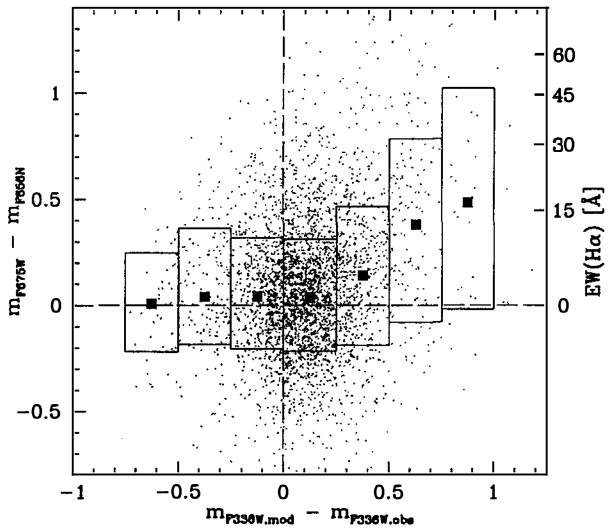

Figure 1: F336W vs Hα excess for our sample of candidate pre-Main Sequence stars in the field of SN 1987A (gray dots). $m_{F336W,obs}$ is the observed magnitude, $m_{F336W,mod}$ is the photospheric one from the models of Bessell et al (1998) and the ($m_{F675W} - m_{F656N}$) color measures the Hα equivalent width, as shown on the right vertical axis. The filled squares represent the median ($m_{F675W} - m_{F656N}$) value in the ($m_{F336W,mod} - m_{F336W,obs}$) bins marked by the rectangles, whose vertical extent includes 66% of the stars in each bin. The high statistical correlation between the two quantities is apparent and is confirmed by the high value of Spearman's coefficient $\rho = 7.9$, which implies a probability of less than 10^{-4} that the two variables are uncorrelated.

can notice that the number density of PMS stars on the NE side of SN 1987A is appreciably lower than on the SW side. It is apparent, then, that high and low-mass stars belonging to the same young generation are spatially distributed in substantially different manners, indicating that star formation processes for different ranges of stellar masses are rather different and/or require different initial conditions.

We do not find any significant difference in ages among PMS stars at different spatial locations, suggesting that, rather than dealing with some sort of propagating star formation, the key factor here is the overall efficiency of the star formation process that varies from place to place. Also, we note that there is no enhancement in the density of candidate PMS stars around the SN 1987A cluster, nor near the brightest star in the observed field lending support to the idea that the process of formation of low mass stars may be distinct from the one leading to the formation of massive stars.

4.2 The accretion rate

There is currently a widespread agreement that low mass stars form by accretion of material until their final masses are reached (e.g., Bonnell et al 2001 and references therein). As a consequence, the accretion rate is arguably *the* single most important parameter governing the process of low-mass star formation and its final results, including the stellar Initial Mass Function. Ground and HST-based studies show that there may be significant differences between star formation processes in the LMC and in the Galaxy. For example, Lamers et al (1999) and de Wit et

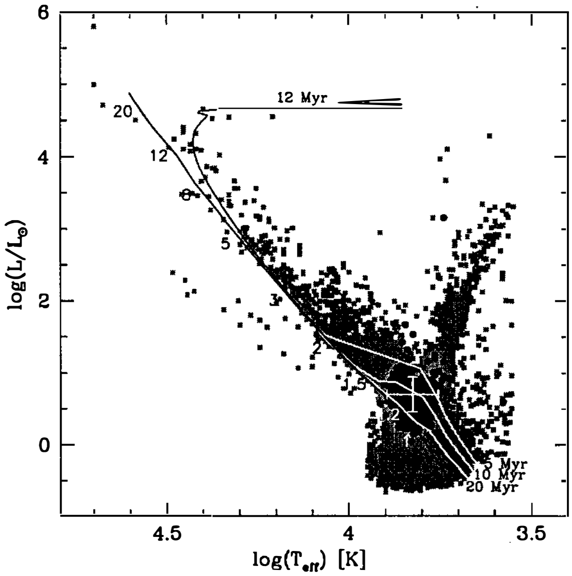

Figure 2: HR diagram displaying the position of the stars with U excess (black dots) overlaid on the general stellar population (gray squares) found in the WFPC2 field. Luminosities and temperatures for the stars with excess were computed excluding the F336W magnitude from the fit to the model atmospheres and adopting for each star the mean $E(B-V)$ value of its 4 closet neighbors. The typical uncertainties on the luminosity and temperature for the stars with U excess, computed as the mean of the uncertainties on the individual stars, is shown as a cross. For reference, we also plot the theoretical Zero Age Main Sequence, with the position of stars of various masses marked on it, and a 12 Myr post-Main Sequence isochrone ($Z = 0.3\ Z_\odot$, Brocato & Castellani 1993). Also shown are 5-20 Myrs pre-Main Sequence isochrones (Siess et al 1997), again computed for $Z = 0.3\ Z_\odot$.

al (2002) have identified by means of ground-based observations high-mass pre-Main Sequence stars (Herbig AeBe stars) with luminosities systematically higher than observed in our Galaxy, and located well above the "birthline" of Palla & Staler (1990). They attribute this finding either to a shorter accretion timescale in the LMC or to its smaller dust-to-gas ratio. Whether such differences in the physical conditions under which stars form will generally lead to differences at the low mass end is an open question, but Panagia et al (2000) offer tantalizing evidence of a higher accretion also for LMC low mass stars.

We have measured the accretion rate onto our solar-type candidate PMS star by means of their Balmer excess (Romaniello et al 2004). The idea that the strong excess emission observed in some Galactic low-mass, pre-Main Sequence stars (Classical T Tauri stars) is produced by accretion of material from a circumstellar disk dates back to the pioneering work of Lynden-Bell & Pringle (1974). The excess luminosity is, then, related to the mass accretion rate. In particular, the Balmer continuum radiation produced by the material from the disk as it hits the stellar surface has been used as an estimator of the mass infall activity (see, for example, Gullbring et al 1998 and references therein).

We have, then, derived the accretion rate onto the central star ($\dot{M}$) with the following equations:

$$\left\{ \begin{array}{l} L_{acc} \simeq \frac{GM_*\dot{M}}{R_*}\left(1 - \frac{R_*}{R_{in}}\right) \\ \log\left(\frac{L_{acc}}{L_\odot}\right) = 1.16\ \log\left(\frac{L_{\mathrm{F336W},exc}}{L_\odot}\right) + 1.24 \end{array} \right. \quad (1)$$

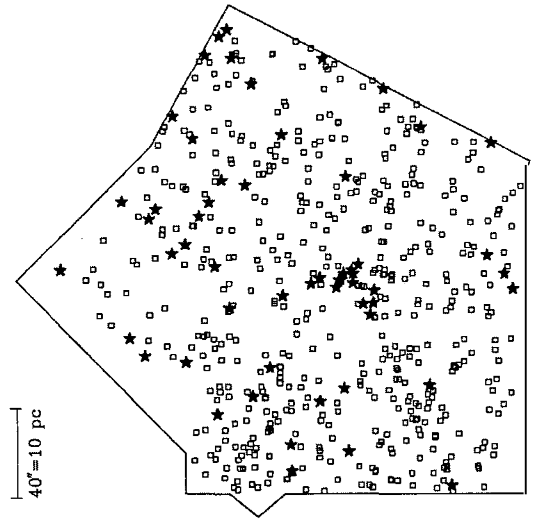

Figure 3: Comparison of the spatial distributions of massive stars ($M \gtrsim 6M_{\odot}$, filled star symbols) and PMS stars ($M \lesssim 2M_{\odot}$, open squares) belonging to the same younger population. North is up and East is to the left. As it can be seen, the stars of different mass have conclusively different spatial distributions.

The second equation is the Gullbring et al (1998) empirical relation between the accretion luminosity L_{acc} and the Balmer excess luminosity, as transformed by Robberto et al (2004) to the WFPC2 F336W filter. The reader is referred to Romaniello et al (2004) for a thorough description of the derivation of $\dot{M}$.

When interpreted as pre-Main Sequence stars, the comparison of the objects' location in the HR diagram with theoretical evolutionary tracks (see Figure 2) allows one to derive their masses ($\sim 1 - 1.4\ M_{\odot}$) and ages ($\sim 12 - 16$ Myrs). At such an age and with an accretion rate as measured using equations (1) in excess of $\sim 1.5 \times 10^{-8} M_{\odot}\ yr^{-1}$, these candidate pre-Main Sequence stars in the field of SN 1987A are both older and more active than their Galactic counterparts known to date. In fact, the overwhelming majority of T Tauri stars in Galactic associations seem to dissipate their accretion disks before reaching an age of about 6 Myrs (Haisch et al 2001; Armitage et al 2003). Moreover, the oldest Classical T Tauri star know in the Galaxy, TW Hydræ, at an age of 10 Myrs, *i.e.* comparable to that of our sample stars, has a measured accretion rate some 30 times lower than the stars in the neighborhood of SN 1987A (Muzerolle et al 2000).

The situation is summarized in Figure 4, where we compare the position in the age-$\dot{M}$ plane of the stars described here with that of members of Galactic star-forming regions. An obvious selection bias that affects our census is that we only detect those stars with the largest Balmer continuum excesses, *i.e.* highest accretion rates. There might be stars in the field with smaller accretion rates, either intrinsically or because they were observed when the accretion activity was at a minimum, which fall below our detection threshold. This selection effect is rather hard to quantify, but it is clear that the locus of the accreting stars that we do detect in the neighborhood of SN 1987A is significantly displaced from the one defined by local pre-Main Sequence stars.

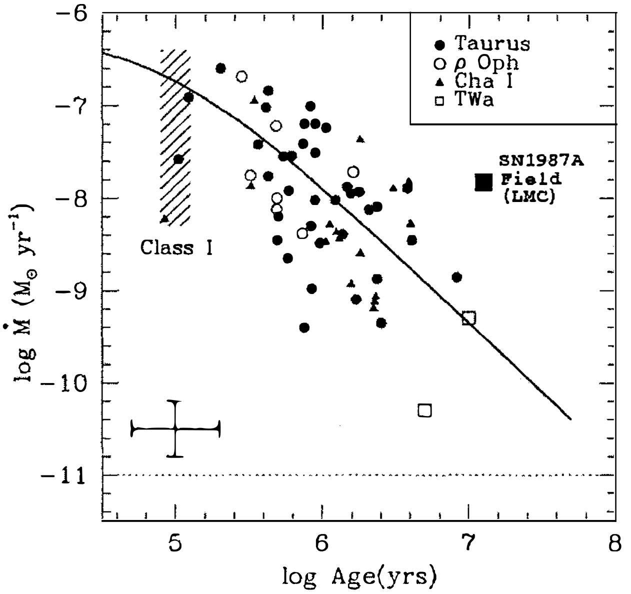

Figure 4: Mass accretion rate as a function of age for Classical T Tauri stars in different star-forming regions (adapted from Muzerolle et al 2000). Our result for the field of SN 1987A is marked with a black square.

4.3 The Initial Mass Function

The almost anti-correlation of the spatial distributions of high mass and low mass stars of a coeval generation (cfr. Section 4.1 and Figure 3) indicates that star formation processes for different ranges of stellar masses are rather different and/or require different initial conditions. An important corollary of this result is that the very concept of an "initial mass function" may not have validity in detail, but rather be the result of a chaotic process. It would, then, only make sense to talk about an *average IMF* over a suitably large area in which all different star formation processes are concurrently operating. Actually, if we just take the ratio of the total numbers of massive to low-mass stars belonging to the young population as identified through their Balmer continuum excess, and interpret them in terms of a power-law IMF adopting mass intervals of 6-15 $M_\odot$ and 1-2 $M\odot$ for massive stars and for PMS stars, respectively, we would derive a slope of the initial mass function of $\Gamma = dlogN/dlogM \simeq -1.7$ with a purely statistical uncertainty of ± 0.1. This value is somewhat steeper than the classical Salpeter's (1955) slope $\Gamma = -1.35$ for the Solar neighborhood and is valid over essentially the same mass interval as the original Salpeter's analysis, *i.e.* ~2-10 $M_\odot$. However, this is a conclusion drawn without taking into account of possible incompleteness effects.

On the one hand, for both massive and low mass stars above $\sim 1 M_\odot$, incompleteness due to missed detection and/or to crowding/blending is a negligible effect because all of these stars are well above our detection limit and their surface density in not so high (1 star per $\sim$ 170 WF pixel area, or, equivalently, an average separation of stars of $\sim$ 13 WF pixels). On the other hand, for PMS stars one has bear in mind that we can reliably identify only stars with strong excess and that the *total* number of PMS stars of comparable masses may be considerably larger. For example, Alcalá et al (1996) have shown that in the Orion region the number of weak-line T Tauri stars, *i.e.* low-mass PMS stars that do not exhibit strong emission features, is at least comparable to, and possibly larger than that of strong-line T Tauri stars.

Moreover, T Tauri stars are known to exhibit photometric variability on short timescales (e.g., Smith et al 1999, and references therein). As a consequence, at any one time one may be able to detect only a fraction of the entire population of strong-line T Tauri stars. Indeed, preliminary comparisons of overlapping regions in fields imaged at two different epochs (about 15% of the entire field around SN 1987A) have shown that, while the number of stars with a significant excess at any one time is essentially constant, no more than half of the candidate PMS stars display a significantly strong Hα excess at both epochs (Romaniello et al, in preparation). This suggests that the "true" Initial Mass Function could significantly steeper than $\Gamma \simeq -1.7$ quoted above.

It is important to realize how crucial it is to *individually* identify and characterize each and everyone of the PMS stars if one wants to evaluate an IMF reliably, because using just the location of stars in the HR diagram as the criterion to recognize PMS stars will unavoidably introduce some heavy contamination from old stars in the process of leaving the Main Sequence. One can argue that, for a fixed surface density of old population stars, such an effect is much reduced when studying regions containing large concentrations of young stars. For instance, the possible contamination by older populations could be, say, 10% or less, if the surface density of young stars in a given region were higher than 200-400 times the density of young stars around SN 1987A or, equivalently, 10 times the density of old population stars in the SN 1987A vicinities. However, since the density of old population stars with luminosities in the range $1 < L/L_{\odot} < 10$ is about 0.2 stars per square arcsecond, exceeding that density by a factor of 10, at least, would imply an average density of young population, low mass stars ($1 < L/L_{\odot} < 10$) higher than 2 stars per square arcsecond, and at least ten times higher for stars in the next 1-*dex* bin in luminosity. It is easy to realize that with such high stellar densities another problem is bound to arise, at least for low mass stars, namely confusion/blending due to crowding. These effects will both "drown" faint stars into a "sea" of even fainter stars and/or would artificially create brighter stars by confusing nearby stars into one more luminous, apparently point-like source.

5 Future directions

From the discussions presented above, it is clear that it is essential to have *spectroscopic* criteria that allow one to discern PMS stars from field stars unambiguously and completely. Hα and/or UV excess are possible ways of accomplishing this goal, but even these methods need confirmation, calibration and sharpening, in that we still have to compare our multi-band photometry with *real* spectra before a 100% reliable of identification of PMS stars can be claimed. In order to fill this gap we have just secured medium-resolution spectra of a number of our best PMS candidates at the ESO-VLT with the VIMOS instrument in IFU mode. The data reduction and analysis are currently in progress and should result in the first ever statistically significant sample of extragalactic low-mass pre-Main Sequence stars with a spectroscopic confirmation.

References

1. Allen, C.W., 1973, Astrophysical Quantities (3rd ed.: London: Athlone)
2. Armitage, P.J., Clarke, C.J., and Palla, F. 2003, MNRAS, 342, 1139
3. Bessell, M.S. 1991, A&A, 242, L17
4. Bessell, M.S., Castelli, F., and Plez, B. 1998, A&A, 333, 231 (erratum 337, 321)
5. Bonnell, I.A., Clarke, C.J., Bate, M.R., and Pringle, J. E. 2001, MNRAS, 324, 573
6. Brocato, E., and Castellani, V. 1993, ApJ, 410, 99

7. Calvet, N., Hartmann, L., and Strom, S.E. 2002, in "Protostars and Planets IV", eds. V. Mannings, A.P. Boss, and S.S. Russell (Tucson: University of Arizona Press), 377
8. Cole, A.A., Smecker-Hane, T.A. and Gallagher, J.S., III 2000, AJ,120, 1808
9. Cool, A.M, and King, I.R. 1995, in "Calibrating HST: Post Servicing Mission", eds. A. Koratkar and C. Leitherer (Baltimore: STScI), 290
10. de Wit, W. J., Beaulieu, J. P., and Lamers, H.J.G.L.M. 2002, A&A, 395, 829
11. Frasca, A., and Catalano, S. 1994, A&A, 284,883
12. Geha, M.C., Holtzman, J.A., Mould, J.R., et al 1998, AJ, 115, 1045
13. Gilliland, R.L. 1994, ApJ, 435, L63
14. Gilmozzi, R. 1990, Core Aperture Photometry with the WFPC, STScI Instrum. Rep. WFPC-90-96 (Baltimore: STScI)
15. Gullbring, E., Hartmann, L., Briceño, C., and Calvet, N. 1998, ApJ, 492, 323
16. Haisch, K.E., Jr., Lada, E.A, and Lada, C.J. 2001, ApJ, 553, L153
17. Heyer, I., Biretta, J. et al. 2004, WFPC2 Instrument Handbook, Version 9.0 (Baltimore: STScI)
18. Hill, V., Andrievsky, S., and Spite, M. 1995, A&A, 293, 347
19. Hodge, P.W. 1988, PASP, 100, 1051
20. Lamers, H.J.G.L.M., Beaulieu, J. P., and de Wit, W. J. 1999, A&A, 341, 827
21. Lynden-Bell, D., and Pringle, J.E. 1974, MNRAS, 168, 603
22. Madau, P., Ferguson, H.C., Dickinson, M.E., et al 1996, MNRAS, 283, 1388
23. Muzerolle, J., Calvet, N., Briceño, C., Hartmann, L., and Hillenbrand, L. 2000, ApJ, 535, L47
24. Padgett, D.L. 1996, AJ, 471, 874
25. Palla, F., and Stahler, S. 1991, ApJ, 360, 47
26. Panagia, N., Romaniello, M., Scuderi, S., and Kirschner, R.P. 2000, ApJ, 539, 197
27. Pei, Y.C., Fall, S.M., and Hauser, M.G. 1999, ApJ, 522, 604
28. Romaniello, M. 1998, Ph.D. Thesis, Scuola Normale Superiore, Pisa
29. Romaniello, M., Salaris, M., Cassisi, S., and Panagia, N. 2000, APJ, 530, 738
30. Romaniello, M., Panagia, N., Scuderi, S., and Kirshner, R.P. 2002, AJ, 123, 91
31. Romaniello, M., Robberto, M., and Panagia, N. 2004, ApJ, 608, 220
32. Scuderi, S., Panagia, N., Gilmozzi, R., Challis, P.M., and Kirshner, R.P., 1996, ApJ, 465, 956
33. Siess, L., Forestini, M., and Dougados, C. 1997, A&A, 324, 556
34. Tolstoy, E. 2003, in "A decade of Hubble Space Telescope science", eds. M. Livio, K. Noll and M. Stiavelli, Space Telescope Science Institute symposium series, Vol. 14, Cambridge University Press, 128
35. van der Marel, R.P., and Cioni, M.-R.L. 2001, AJ, 122, 1807
36. Whitmore, B. 1995, in "Calibrating HST: Post Servicing Mission", eds. A. Koratkar and C. Leitherer (Baltimore: STScI), 269

Suzanne Aigrain
Institute of Astrophysics
Madingley road
CB3 0HA Cambridge
UK
suz@ast cam.ac.uk

Richard Alexander
Institute of Astrophysics
Madingley road
CB3 0HA Cambridge
UK
rda@ast.cam.ac.uk

Joao Alves
ESO
Karl Schwarzschild Str. 2
Garching
Germany
jalves@eso.org

Philippe André
CEA
Sce Astrophysique
91191 Gif sur Yvetee
France
pandre@discovery.saclay.cea.fr

Andrew Baker
MPI Extr. Physik
Postfach 1312
85741 Garching
Germany
ajb@mpe.mpg.de

Shantanu Basu
University of Western Ontario
1151 Richmond St London
N6A 3K7 London Ontario
Canada
basu@astro.uwo.ca

Maité Beltran
INAF
Astroph. Dept
Largo E. Fermi 5
50125 Firenze
Italy
mbeltran@arcetri.astro.it

Leo Blitz
Berkeley University
Astro. Dept
94720 Berkeley CA
USA
blitz@astro.berkeley.edu

Ian Bonnell
St Andrews University
North Haugh
KY16 9SS St Andrews
UK
iab1@st-and.ac.uk

Jérôme Bouvier
Observatoire
Labo astro.
bp 53
38041 Grenoble
France
jbouvier@obs.ujf-grenoble.fr

Jonathan Braine
Observatoire
11 rue Edmond Blanc
33290 Blanquefort
France
braine@obs.u-bordeaux1.fr

Dieter Breitschwerdt
University of Vienna
Inst. Astronomie
Vienna
Austria
breitschwerdt@astro.univie.ac.at

Denis Burgarella
LAM

Traverse du Siphon
13376 Marseille cedex 12
France
denis.burgarella@oamp.fr

Almas Chalabaev
LAOG
BP 53 X
38041 Grenoble cedex 9
France
chalabae@obs.ujf-grenoble.fr

Rolf Chini
Institute of Astrophysics
Universitat St. 150
44780 Bochum
Germany
chini@astro.rub.de

Paul Clark
St Andrews University
Dept Astro.
The North Haugh
KY16 8SS St Andrews
UK
pcc@st-andrews.ac.uk

Miguel De Avillez
University of Evora
R. Romao Ramalho 59
7000 Evora
Portugal
mavillez@galaxy.lca.uevora.pt

Willem-Jan De Wit
INAF
Astroph. Dept
Largo E. Fermi 5
50125 Firenze
Italy
dewit@arcetri.astro.it

Lise Deharveng
Laboratoire d'Astrophysique

2 place le Verrier
13248 Marseille cedex 4
France
lise.deharveng@oamp.fr

Clare Dobbs
St Andrews University
North Haugh
KY16 8SS St Andrews
UK
cld2@st-and.ac.uk

Pierre-Alain Duc
CEA
Astroph.
91191 Gif sur Yvetee
France
paduc@cea.fr

David Elbaz
CEA
Astrophysique
Orme des Merisiers Bat 709
91191 Gif sur Yvetee
France
delbaz@cea.fr

Wilfred Frieswijk
Kapteyn Institute
Landleven 12
9700 AV Groningen
The Netherlands
frieswyk@astro.rug.nl

Uta Fritze
Sternwarte University

Gottingen
Germany
ufritze@uni-sw.gwdg.de

Yasuo Fukui
Nagoya University
Dept Astro.
Furo-Cho Chikusa-ku
464-8602 Nagoya
Japan
fukui@a.phys.nagoya-u.ac.jp

Danièle Galli
INAF
Oss. Astrofisico
Largo E. Fermi 5
50125 Firenze
Italy
galli@arcetri.astro.it

Jose Goncalves
University of Lisboa, CAAUL
Astro. Astrofisica Dept
Tapada da Ajuda
1349-018 Lisbon
Portugal
goncalve@arcetri.astro.it

Simon Goodwin
Cardiff University
The Parade 5
CF24 3YB Cardiff
UK

Simon.Goodwin@astro.cf.ac.uk

Isabelle Grenier
CEA
Univ. Paris 7
91191 Gif sur Yvetee
France

isabelle.grenier@cea.fr

Sylvain Guieu
Laboratoire d'Astrophysique
414 rue de la Piscine
38041 Grenoble
France

Sylvain.Guieu@obs.ujf-grenoble.fr

Patrick Hennebelle
Observatoire de Paris
Ecole Normale Sup.
24 rue Lhomond
75005 Paris
France
patrick.hennebelle@ens.fr

Simon Hodgkin
Institute of Astrophysics
Madingley road
CB3 0HA Cambridge
UK

sth@ast.cam.ac.uk

David Hubber
Cardiff University
The Parade 5
CF24 3YB Cardiff
UK

David.Hubber@astro.cf.ac.uk

Kim Kendall
LAOG
414 rue de la Piscine
38041 Grenoble cedex 9
France

tkendall@obs.ujf-grenoble.fr

Jürgen Knödlseder
CESR
9 avenue du Colonel Roche
31028 Toulouse
France

knodlseder@cesr.fr

Daniel Kunth
IAP
98 bd Arago
75014 Paris
France

kunth@iap.fr

Ralf Launhardt
Max Planck Institut
Koenigstuhl 17
69117 Heidelberg
Germany

rl@mpia.de

Bertrand Le Floch
LAOG
414 rue de la Piscine
38041 Grenoble cedex 9
France

lefloch@obs.ujf-grenoble.fr

Nicolas Lodieu
Institute of Astrophysics
An der Sternwarte 16
14482 Postdam
Germany

nlodieu@aip.de

Delphine Marcillac
CEA
Sce Astrophysique
Bat 709
91190 Gif sur Yvetee
France
marcilla@cea.fr

Eduardo Martin
Institute of Astrophysics Canarias
Via Lactea
38200 Languna
Canaries Islands

ege@ll.iac.es

Fabrizio Massi
INAF
Astroph. Dept
Largo E. Fermi 5
50125 Firenze
Italy
fmassi@arcetri.astro.it

Mark McCaughrean
Institute of Astrophysics
An der Sternwarte 16
14482 Postdam
Germany

mjm@aip.de

Gwendolyn Meeus
Institute of Astrophysics
An der Sternwarte 16
14483 Postdam
Germany

gwen@aip.de

Jorge Melnick
ESO
Alonso de Cordova
3107 Vitacura
Chile

jmelnick@eso.org

Giuseppina Micela
Osservatorio Astronomico
Piazza del Parlamento 1
90134 Palermo
Italy

giusi@astropa.unipa.it

Vincent Minier
CEA
Astroph.
SAP/DAPNIA.DSM.
91191 Gif sur Yvetee
France
Vincent.Minier@cea.fr

Thierry Montmerle
LAOG

38043 Grenoble
France

montmerle@obs.ujf-grenoble.fr

Estelle Moraux
Institute of Astrophysics
Madingley road
CB3 0HA Cambridge
UK

moraux@ast.cam.ac.uk

Sebastien Muller
Institute of Astrophysics ASIAA
BP BOX 23
1 Roosevelt Rd Sec 4
141 31 Taipei
Taiwan
muller@asiaa.sinica.edu.tw

Toshikazu Onishi
Nagoya University
Dept Astro.
Furo-Cho Chikusa-ku
464-8602 Nagoya
Japan
ohnishi@a.phys.nagoya-u.ac.jp

Paolo Padoan
University of California
Gilman Drive
95100 La Jolla
USA

ppadoan@ucsd.edu

Francesco Palla
INAF
Astroph. Dept
Largo E. Fermi 5
50125 Firenze
Italy
palla@arcetri.astro.it

Jan Palous
Academy of Sciences
Astro. Inst.
141 31 Prague
Rep. Czech

palous@ig.cas.cz

Thibaut Paumard
Max Planck Institut
Extraterrest. Physik
Giessenbachstr.
85748 Garching
Germany
paumard@iap.fr

Inti Pelupessy
Sterrewacht Leiden
Niels Bohrweg 2
2333 Leiden CA
Netherlands

pelupes@strw.leidenuniv.nl

Nicolas Peretto
CEA
Sce Astrophysique
BAT 709
91190 Gif sur Yvetee
France
peretto@cea.fr

Neal Potter
Cardiff University
The Parade 5
School of Physics
CF24 3YB Cardiff
UK
neal.potter@astro.cf.ac.uk

Martino Romaniello
ESO

Karl Schwarzschild Str. 2
85748 Garching
Germany
mromanie@eso.org

Daniel Schaerer
Geneva Observatory
51 chemin des Maillettes
1290 Sauverny
Switzerland

daniel.schaerer@obs.unige.ch

Frédéric Schuller
Max Planck Institut
Auf dem Hugel 69
53121 Bonn
Germany

schuller@mpifr-bonn.mpg.de

Salvatore Sciortino
INAF
Piazza del Parlamento 1
90134 Palermo
Italy

sciorti@oapa.astropa.unipa.it

Joe Silk
Oxford University
Keble Road
OX1 3RH Oxford
UK

silk@astro.ox.ac.uk

Dimitris Stamatellos
Cardiff University
The Parade 5
CF24 3YB Cardiff
UK

D.Stamatellos@astro.cf.ac.uk

Jonathan Tan
Princeton University
Peyton Hall
08544 Princeton NJ
USA

jt@astro.princeton.edu

Anthony Whitworth
Cardiff University
The Parade 5
CF24 3YB Cardiff
UK

ant@astro.cf.ac.uk

Hiroaki Yamamoto
Nagoya University
Dept Astro.
Furo-Cho Chikusa-ku
464-8602 Nagoya
Japan
hiro@a.phys.nagoya-u.ac.jp

Hans Zinnecker
Institute of Astrophysics
An der Sternwarte 16
14483 Postdam
Germany

hzinnecker@aip.de